Transactions of the ASME®

Transactions of the ASME, Journal of Heat Transfer (ISSN 0022-1481) is published quarterly (Feb., May, Aug., Nov.) for $165.00 per year by The American Society of Mechanical Engineers, 345 East 47th Street, New York, NY 10017. Second class postage paid at New York, NY and additional mailing offices. POSTMASTER: Send address changes to Transactions of the ASME, Journal of Heat Transfer, c/o THE AMERICAN SOCIETY OF MECHANICAL ENGINEERS, 22 Law Drive, Box 2300, Fairfield, NJ 07007-2300.
CHANGES OF ADDRESS must be received at Society headquarters seven weeks before they are to be effective. Please send old label and new address.
PRICES: To members, $40.00, annually: to nonmembers, $165.00.
Add $24.00 for postage to countries outside the United States and Canada.
STATEMENT from By-Laws. The Society shall not be responsible for statements or opinions advanced in papers or . . . printed in its publications (B7.1, para. 3).

INDEXED by Applied Mechanics Reviews and Engineering Information, Inc.
Canadian Goods & Services Tax Registration #126148048.

Journal of Heat Transfer

Published Quarterly by The American Society of Mechanical Engineers

VOLUME 115 • NUMBER 2 • MAY 1993

ANNOUNCEMENTS

TECHNICAL PAPERS

Heat Conduction With Solidification

Forced Convection

Natural and Mixed Convection

Radiative Transfer

(Contents continued)

Boiling and Condensation

Materials Processing

TECHNICAL NOTES

A New Method for Thermal Analysis of Die Casting

M. R. Barone

D. A. Caulk

Engineering Mechanics Department,
General Motors Research,
Warren, MI 48090-9055

A new approach is developed for solving the initial value, steady periodic heat conduction problem in steady-state die casting. Three characteristics found in nearly all die casting processes are exploited directly: The casting is thin compared with its overall size, its thermal conductivity is high compared with that of the mold, and the cycle time is short compared with the start-up transient of the process. Under these conditions, it is reasonable to neglect the transverse temperature gradients in the casting and assume that all die temperatures below a certain depth from the cavity surface are independent of time. The transient die temperatures near the cavity surface are represented by a polynomial expansion in the depth coordinate, with time-varying coefficients determined by a Galerkin method. This leads to a set of ordinary differential equations on the cavity surface, which govern the transient interaction between the casting and the die. From the time-averaged solution of these equations, special conditions are derived that relate the transient solution near the cavity surface to the three-dimensional steady solution in the die interior. With these conditions, the steady temperatures in the bulk of the die can be determined independently of the explicit surface transients. This reduces the effort of solving a complex transient heat conduction problem to little more than finding a steady solution alone. The overall approach provides a general analytical tool, which is capable of predicting complex thermal interactions in large multicomponent dies.

1 Introduction

Die casting is a foundry process in which liquid metal is injected under high pressure into a permanent, water-cooled die, where it solidifies to a precise shape. The die performs two basic functions in making the casting: It imparts shape and it removes heat. In most situations, the second function is more difficult to control, probably because the thermal characteristics of the die affect so many aspects of the process. For example, the die surface must cool the metal rapidly, but not so rapidly that solidification occurs during cavity fill. Die temperatures should be fairly uniform or they will distort cavity dimensions and impair the precise fit between mated die components. The casting should eject with a relatively uniform temperature as well, or it may distort as it cools outside the die. Finally, if transient extremes in die temperature are too large, the die surface may prematurely crack, or heat check, due to thermal fatigue.

Although die cooling affects all these conditions, the relationships involved are often too subtle and too complex to predict how a given die will perform before it is built. Even when testing reveals certain design deficiencies, it is no easier to suggest what changes would make the die perform better. In spite of such a clear opportunity, however, thermal analysis is used far less in die casting than in other foundry processes. The primary reason appears to be the unusual mathematical structure of the die casting problem.

Die casting is distinguished from most other foundry processes by the fact that the same mold is used to make more than one casting. This means that the thermal disturbance caused by the first casting remains in the die to affect solidification of the next casting, and so on. The die temperatures gradually increase as more castings are made, until the process reaches steady state and the die temperatures become periodic. The solution at steady state is usually the most important. But at steady state, the heat conduction problems in the casting and the die are fundamentally different: The casting temperature is known explicitly at the moment of injection, whereas the initial die temperatures are determined implicitly by the fact that they are periodic. The combination of these two problems is very difficult to solve directly.

Previous attempts to analyze heat conduction in steady-state die casting have approached the solution in one of two ways: (1) Some distribution of die temperatures is arbitrarily assigned at the beginning of a steady-state cycle, e.g., Riegger (1981), Ohtsuka et al. (1982), and Granchi et al. (1983), or (2) the steady periodic solution in the die is approached asymptotically by starting the die at room temperature and solving for the entire start-up transient, e.g., Grant (1981) and Kearns (1986). The first approach relies on an ad hoc assumption, and the second, though rigorous, can lead to unacceptably long computations, especially in large dies.

The arbitrariness of prescribing the initial die temperatures for a steady-state casting cycle is now generally recognized and most commercial software vendors, e.g., Kallien and Sturm (1991), recommend the second approach described above. But since the transient time step must be small to follow accurately the rapidly fluctuating temperatures during the cycle, and many cycles are typically needed to reach steady state, computation times can be enormous, especially in large dies (Kearns, 1986).

In this paper, we develop a new approach to thermal analysis of die casting, which is capable of predicting the periodic die temperatures at steady state without solving for the start-up transient. The validity of this approach depends on three special conditions, which are found in nearly all die casting processes: The casting is thin compared with its overall size, its thermal conductivity is high compared with that of the mold, and the cycle time is short compared with the start-up transient of the process. Under these conditions, nearly all transient heat conduction is directed perpendicular to the casting and the periodic temperatures in the die penetrate only a short distance below the cavity surface. We idealize the temperature solution in the die by assuming that the die temperatures below a certain distance from the cavity surface are independent of time (Caulk, 1990). In the transient surface layer, the solution is represented as a finite polynomial in the transverse coordinate, with coefficients that depend on time. These coefficients satisfy a set

Contributed by the Heat Transfer Division for publication in the JOURNAL OF HEAT TRANSFER. Manuscript received by the Heat Transfer Division May 1992; revision received September 1992. Keywords: Conduction, Materials Processing and Manufacturing Processes. Technical Editor: R. Viskanta.

of ordinary differential equations determined by a Galerkin method. From the solution of these equations, it is possible to construct a set of linear equations relating the time-averaged die surface temperatures on both sides of the casting. In this way, the time-averaged die temperatures can be determined independently of the explicit surface transients, and the effort of solving the entire transient problem is reduced to little more than finding the steady solution alone.

To calculate the steady die temperatures, we use a boundary element method with special one-dimensional elements to represent cooling lines (Barone and Caulk, 1985). Unlike the finite element method, a boundary element model requires no interior mesh, making the die models easier to build and cooling lines easier to change. The combination of the local transient analysis near the casting with the boundary element analysis of the steady die temperatures provides a powerful analytical tool, which is applicable to a large class of die casting and permanent mold processes.

To evaluate the accuracy of the various assumptions, we compare the results of this new approach with finite difference calculations in a number of one-dimensional examples based on a typical aluminum process. Remarkably accurate results are achieved, even for moderately thick castings. Finally, we illustrate the practical utility of the method by considering several two-dimensional examples with nontrivial die geometry.

2 The Heat Conduction Problem

Before we develop the details of our modeling approach, it is useful first to formulate the general heat conduction problem for steady-state die casting. This will include certain basic assumptions that are common in nearly all analyses of this sort.

Depending on the size of the part, the liquid metal can take from 10 to 500 ms to fill the die cavity. As a first approximation, we adopt the usual approach of neglecting the heat transferred during flow—the so-called "instant fill" assumption. With this assumption, the casting cycle is divided into two parts: the *residence time*, when metal is in the die cavity, and the *open time*, when it is not. For convenience we let the cycle begin at the moment of injection. Let t_r represent the residence time and t_c the total cycle time.

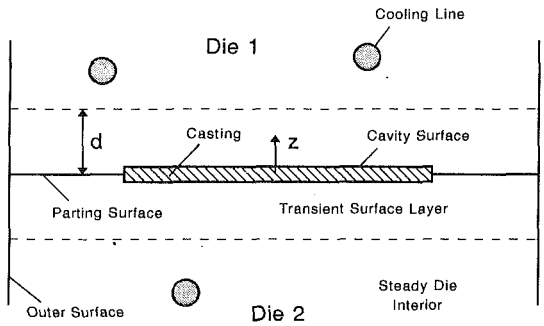

Fig. 1 Schematic illustration of a die-casting die

Let the three-dimensional region in the die cavity be denoted by $\mathcal{C}$ and the collection of die components by $\mathcal{D}$. The boundaries of the die components are divided into four surfaces: the *cavity surface*, where the die is in contact with the casting; the *parting surfaces*, where the die components are in contact with each other when the die is closed; the *cooling surfaces*, which are just the internal surfaces of the cooling lines; and the *outer surfaces*, which are in contact either with the die casting machine or the outside air. The cavity surface is denoted by $\partial\mathcal{C}$, the parting surfaces by $\partial\mathcal{P}$, the cooling surfaces by $\partial\mathcal{W}$, and the outer surfaces by $\partial\mathcal{D}$. A schematic illustration of the die and cavity is given in Fig. 1.

The temperature at any point x_i ($i = 1, 2, 3$) and time t is denoted by $\theta(x_i, t)$. Thermal conductivity is designated by k, mass density by ρ, heat capacity by c, and thermal diffusivity by $\alpha = k/\rho c$. The temperature and properties associated with the die have no subscripts and those associated with the casting are distinguished by adding a subscript c. The thermal resistance of the die lubricant is represented by an effective heat transfer coefficient h specified on the cavity surface. The contact resistance between the die components at the parting sur-

Nomenclature

$A_{\beta\gamma}$, $a_{\beta\gamma}$ = coefficients in the contact surface conditions on the cavity surface
b_β = coefficients in the contact surface conditions on the parting surface
c = heat capacity
C_0 = sensible heat capacity
C_β = relative cooling load
$\mathcal{C}$ = cavity region
$\partial\mathcal{C}$ = cavity surface
d = depth of the transient surface layer
D = water depth in die
$\mathcal{D}$ = die region
$\partial\mathcal{D}$ = die surface
h = heat transfer coefficient on the cavity surface
h_o = heat transfer coefficient on the outer surface
h_p = heat transfer coefficient on the parting surface
k = thermal conductivity
N = number of polynomial terms in the temperature representation
$\partial\mathcal{P}$ = parting surface
q = heat flux normal to the cavity surface
$\bar{q}$ = time-averaged heat flux
Q_L = latent heat per unit mass
t = time
t_c = cycle time
t_r = residence time
$\partial\mathcal{W}$ = cooling line surface
x_i = Cartesian coordinates
x_α = curvilinear coordinates on the contact surface
z = thickness coordinate in the surface layer
α = thermal diffusivity
θ = temperature
$\bar{\theta}$ = time-averaged temperature
θ_m = temperature coefficients in the surface layer
$\bar{\theta}_m$ = time-averaged temperature coefficients
θ_{liq} = liquidus temperature
θ_{sol} = solidus temperature
θ_c^* = initial casting temperature including equivalent sensible heat
μ = casting mass density per unit area
ρ = mass density

Subscripts

a = ambient
c = casting property or variable
i = interface between the surface layer and the die interior
p = parting surface
s = cavity surface
w = water
β = index denoting casting side associated with a property (= 1, 2)

Superscripts

A = antisymmetric part
S = symmetric part
β = index denoting casting side associated with a variable (= 1, 2)

faces is represented by an equivalent heat transfer coefficient h_p. The water temperature in the cooling lines is denoted by θ_w and the associated heat transfer coefficient by h_w. Similarly, the ambient temperature on the outer die surfaces is denoted by θ_a and the heat transfer coefficient by h_o. The temperature in the casting alloy at the beginning of the cycle is θ_c^0, which is assumed to be uniform throughout the die cavity.

The heat conduction equation in the casting is

$$\frac{\partial \theta_c}{\partial t} = \alpha_c \nabla^2 \theta_c, \quad \text{in } \mathcal{C} \text{ for } 0 \le t \le t_r, \tag{2.1}$$

where the heat capacity c_c of the casting material is taken as a function of temperature to account for the latent heat of solidification. The boundary condition on the cavity surface is given by

$$-k_c \frac{\partial \theta_c}{\partial n} = h(\theta - \theta_c) \quad \text{on } \partial\mathcal{C} \text{ for } 0 \le t \le t_r, \tag{2.2}$$

where n is directed along the outward normal to the die surface. The casting temperature satisfies the initial condition

$$\theta_c(x_i, 0) = \theta_c^0. \tag{2.3}$$

Like the casting, the heat conduction equation in the die components is given by

$$\frac{\partial \theta}{\partial t} = \alpha \nabla^2 \theta, \quad \text{in } \mathcal{D} \text{ for } 0 \le t \le t_c. \tag{2.4}$$

The thermophysical properties of the die material are assumed to be constant. The boundary conditions during the residence time are given by

$$-k \frac{\partial \theta}{\partial n} = \begin{cases} h(\theta - \theta_c) & \text{on } \partial\mathcal{C} \\ h_p[\![\theta]\!] & \text{on } \partial\mathcal{P} \\ h_o(\theta - \theta_a) & \text{on } \partial\mathcal{D} \\ h_w(\theta - \theta_w) & \text{on } \partial^T\mathcal{W} \end{cases} \quad \text{for } 0 < t < t_r, \tag{2.5}$$

where the notation $[\![\theta]\!]$ denotes the jump in temperature at a parting surface due to the finite contact resistance represented by the coefficient h_p. During the open time, the corresponding boundary conditions are

$$-k \frac{\partial \theta}{\partial n} = \begin{cases} h_o(\theta - \theta_a) & \text{on } \partial\mathcal{C} + \partial\mathcal{P} + \partial\mathcal{D} \\ h_w(\theta - \theta_w) & \text{on } \partial^T\mathcal{W} \end{cases} \quad \text{for } t_r < t < t_c. \tag{2.6}$$

Unlike the casting temperatures, the steady-state die temperatures are not known at $t = 0$. Instead, they are determined indirectly through the periodicity condition

$$\theta(x_i, 0) = \theta(x_i, t_c). \tag{2.7}$$

Even though the heat conduction problems in the casting and the die are governed by the same differential equation, the solutions are fundamentally different in character: The initial casting temperature is specified explicitly by Eq. (2.3), whereas the initial die temperatures are determined implicitly by satisfying the periodicity condition (2.7). More formally, the casting temperatures satisfy an *initial value problem*, while the die temperatures satisfy a *steady periodic problem*. Either one of these problems would not be difficult to solve by itself. But since both solutions are coupled through the boundary conditions (2.2) and $(2.5)_1$ on the cavity surface, they must be solved together. This gives the problem a mixed character that rules out traditional methods for solving it directly.

The classical method for solving steady periodic problems is to express the boundary condition in a series of harmonics and use Fourier transforms. But since the boundary condition on the cavity surface is linked to an initial value problem in the casting, this representation cannot be applied in this context. The only other alternative is to treat both the casting and the die as initial value problems and integrate both solutions through enough consecutive casting cycles for the die temperatures to become periodic. The obvious drawback of this approach is the need for extremely long computation times (Kearns, 1986). But other, more subtle, numerical problems can occur in some cases. If the time step is not small enough, the limiting solution can have spurious oscillations (Myers, 1978). Moreover, when a large contrast exists between the cycle time and the length of the start-up transient, the differential equations can be numerically stiff, requiring elaborate methods of integration (Gear, 1971).

3 Modeling Idealizations

To simplify the general heat conduction problem outlined in the previous section, we make three physical assumptions, which are valid in nearly all die casting processes:

1 The nominal thickness of the casting is small compared with its overall size.
2 The thermal conductivity of the casting alloy is much greater than that of the die steel.
3 The casting cycle is short compared with the start-up transient in the die.

These assumptions permit several idealizations in both the casting and the die. First we consider the casting.

Since the casting is thin and the casting alloy has a high thermal conductivity, we neglect the transverse temperature gradient in the casting compared with that in the die. We also neglect the casting thickness compared with the major die dimensions, so that the die cavity $\mathcal{C}$ collapses to zero volume. The casting is represented as a surface coincident with $\partial\mathcal{C}$, with a single temperature and a two-dimensional mass density defined at every point. Although the casting temperature may vary with position on $\partial\mathcal{C}$, the heat flux associated with these gradients is neglected, compared with the transverse component into the die.

In the die, we use the approach developed by Caulk (1990) and restrict the region affected by the periodic transient temperatures. When the casting cycle is short compared with the characteristic time scale for heat conduction in a die component, the periodic temperature transients associated with the repeated injection of liquid metal into the die cavity penetrate only a short distance into the die. Although the temperature near the cavity surface can vary as much as several hundred degrees during the cycle, the die temperatures are virtually steady only a few centimeters below the cavity surface. The actual attenuation is exponential, but we idealize it here by assuming that all transient die temperatures occur in a finite boundary layer of uniform depth, called the *transient surface layer* (Fig. 1). The depth of the transient surface layer depends on the thermal diffusivity of the die material and the cycle time of the process. Below the transient surface layer, in what is called the *steady die interior*, the temperatures are assumed to be independent of time. A transient surface layer also exists along the parting surfaces. Here the transient die temperatures result from periodic contact between die components with unequal temperatures rather than direct exposure to molten casting material.

We assume that temperature is continuous at the interface between the steady die interior and the transient surface layer, but only require continuity of the normal heat flux in a time-averaged sense. As in the casting, the temperature in the surface layer may vary with position along the cavity surface, but the associated heat flux is neglected compared with the transverse component. This makes the problem in the casting and the adjacent surface layers locally one dimensional, with all spatial coupling between different points along the casting occurring because of compatibility with the three-dimensional solution in the steady die interior. For convenience in what follows, we

refer to the idealizations introduced in this section as the *surface layer model.*

4 Governing Equations

Transient surface layers exist along both the cavity and parting surfaces. In what follows, we refer to the combination of these surfaces as the *contact surface.* Let x_α ($\alpha = 1, 2$) be curvilinear coordinates on the contact surface $\partial\mathcal{C} + \partial\mathcal{P}$, which we assume has a unique normal, except along isolated *branch lines* where two different parts of the casting surface intersect, or along isolated *parting lines* where a parting surface intersects the casting surface. At all other points, the casting is bounded by die material on two distinct sides, which we distinguish by the labels 1 and 2.

The heat conduction problem in the casting and transient surface layers is formulated by generalizing the approach by Caulk (1990), which did not include interaction between die components. In each die component, we define z as a third coordinate along the inward normal to the cavity surface. The transient surface layer is defined by $0 \le z \le d$, where the layer depth d must be specified in advance (Fig. 1). The specific value of d turns out to be relatively unimportant as long as it is large enough to include most of the region actually affected by transient temperatures. Based on the results of Caulk (1990), we assume that

$$d = 1.5\ (\alpha t_c)^{1/2}. \tag{4.1}$$

The temperature in each surface layer is represented by the finite polynomial

$$\theta(x_\alpha, z, t) = \theta_0(x_\alpha) + \sum_{m=1}^{N} \theta_m(x_\alpha, t)\,(1 - z/d)^m, \qquad 0 \le z \le d, \tag{4.2}$$

where θ_0 is the constant temperature at the interface with the steady die interior. The coefficient functions $\theta_m(x_\alpha, t)$ in Eq. (4.2) are determined by neglecting the heat flux parallel to x_α and requiring that the heat conduction equation (2.4) be satisfied in the following integrated sense:

$$\int_0^d \left(\rho c \frac{\partial\theta}{\partial t} + \frac{\partial q}{\partial z}\right)(1 - z/d)^n dz = 0, \quad (n = 0, 1, \ldots, N) \tag{4.3}$$

where q is the heat flux parallel to z. Let q_s and q_i represent values of the heat flux at the cavity surface $z = 0$ and the interface $z = d$, respectively. Then, following Caulk (1990), Eq. (4.3) can be integrated with the help of Eq. (4.2) to yield

$$\rho_\beta c_\beta d_\beta \sum_{m=1}^{N} \frac{1}{m+1}\,\dot\theta_m^\beta + q_i^\beta = q_s^\beta, \tag{4.4}$$

$$\rho_\beta c_\beta d_\beta \sum_{m=1}^{N} \frac{1}{m+n+1}\,\dot\theta_m^\beta + (k_\beta/d_\beta) \sum_{m=1}^{N} \frac{mn}{m+n-1}\,\theta_m^\beta = q_s^\beta, \qquad (\beta = 1, 2;\ n = 1, 2, \ldots, N) \tag{4.5}$$

where a superposed dot denotes a partial derivative with respect to time. Greek superscripts are used to distinguish values of dependent variables on the two sides of the casting and subscripts are used to distinguish values of material properties. The $2N$ equations in Eq. (4.5), together with the boundary condition on the cavity surface, are sufficient to determine the surface flux $q_s^\beta(x_\alpha, t)$ and the temperature coefficients $\theta_m^\beta(x_\alpha, t)$ in both surface layers. Equation (4.4) merely determines q_i^β, which does not appear in any of the other equations. The solution of Eq. (4.5) converges very rapidly with increasing order of the polynomial representation (4.2) (Caulk, 1990). We used $N = 4$ for the examples in this paper.

Let $\mu(x_\alpha)$ represent the mass density of the casting, per unit area on $\partial\mathcal{C}$. Then during the residence time the casting temperature $\theta_c(x_\alpha, t)$ is governed by the equation

$$-\mu c_c \dot\theta_c = q_s^1 + q_s^2 \quad \text{on } \partial\mathcal{C} \text{ for } 0 \le t \le t_r, \tag{4.6}$$

which equates the energy removed from the casting to the heat flux into the surface layers on each side. To represent the latent heat of solidification, we assume the heat capacity c_c of the casting alloy is a function of temperature. Let Q_L denote the latent heat per unit mass and let θ_{liq} and θ_{sol} denote the liquidus and solidus temperatures, respectively. Then, we assume that c_c depends on temperature in the form

$$c_c = \begin{cases} c_o & \theta_c > \theta_{\text{liq}}, \\ c_o + Q_L/(\theta_{\text{liq}} - \theta_{\text{sol}}) & \theta_{\text{liq}} > \theta_c > \theta_{\text{sol}}, \\ c_o & \theta_{\text{sol}} > \theta_c, \end{cases} \tag{4.7}$$

where c_o is the sensible heat capacity of the casting material. From Eq. (2.5), the heat flux on the cavity surface during the residence time is

$$q_s^\beta = h_\beta(\theta_c - \theta_s^\beta) \quad \text{on } \partial\mathcal{C} \text{ for } 0 < t < t_r, \tag{4.8}$$

where $\theta_s^\beta(x_\alpha, t)$ is the cavity surface temperature, and from Eq. (4.2)

$$\theta_s^\beta = \theta_0^\beta + \sum_{m=1}^{N} \theta_m^\beta. \tag{4.9}$$

On the parting surface, the surface layer solutions are coupled through continuity of the heat flux when the die is closed,

$$q_s^2 = -q_s^1 = h_p(\theta_s^1 - \theta_s^2) \quad \text{on } \partial\mathcal{P} \text{ for } 0 < t < t_r. \tag{4.10}$$

When the die is open, the heat flux on either surface is simply

$$-q_s^\beta = h_o(\theta_s^\beta - \theta_a) \quad \text{on } \partial\mathcal{P} + \partial\mathcal{C} \text{ for } t_r < t < t_c. \tag{4.11}$$

The temperature coefficients θ_m^β must be continuous at $t = t_r$ and satisfy the periodicity conditions

$$\theta_m^\beta(x_\alpha, 0) = \theta_m^\beta(x_\alpha, t_c). \tag{4.12}$$

The casting temperature satisfies only the initial condition

$$\theta_c(x_\alpha, 0) = \theta_c^0. \tag{4.13}$$

For convenience, we call Eqs. (4.4)–(4.13) the *surface layer equations.*

The steady temperatures in the interior of each die component are governed by the three-dimensional Laplace equation, subject to the boundary conditions in Eqs. (2.5) and (2.6) on the cooling lines and outer surfaces. In addition, the steady interior solution must satisfy continuity of temperature and time-averaged heat flux at the interface with the transient surface layer at $z = d_\beta$. Instead of imposing the latter conditions directly, we follow Caulk (1990) and extend the interior solution to the contact surface by identifying it with the time-averaged solution in the surface layer. This satisfies the interface conditions identically and eliminates the need to solve the steady problem over a subregion of the die. For clarity in what follows, we refer to the extended interior solution as the *time-averaged interior solution* and denote it by $\bar\theta(x_i)$. Throughout the die, the time-averaged interior solution is governed by

$$\nabla^2\bar\theta = 0 \quad \text{in } \mathcal{D}. \tag{4.14}$$

Although Eq. (4.14) is a linear equation, the time-averaged solutions in the separate die components are coupled at points along the contact surface through conditions that follow from the time-averaged solution of the nonlinear surface layer equations (4.5) and (4.6). These conditions, which relate the time-averaged temperature and heat flux on the two sides of the contact surface, are called the *contact surface conditions.* Since the surface layer equations are nonlinear, the contact surface conditions are nonlinear as well. This presents a formidable numerical problem that, while soluble, would require considerable computational effort. To avoid this, we introduce an additional assumption on the latent heat.

For purposes of calculating the time-averaged solution, we

set $c_c = c_o$ and account for the latent heat by raising the initial casting temperature to

$$\theta_c^* = \theta_c^0 + Q_L/c_o \tag{4.15}$$

at every point x_α. This assumption removes the nonlinearity from Eq. (4.6) by replacing the latent heat with an equivalent amount of sensible heat. The higher initial casting temperature (4.15) increases the rate of heat transfer to the die near the beginning of the cycle, but this difference should rapidly disappear after the casting cools below its solidus temperature. Since the total casting energy has not been altered, the time-averaged die temperatures should not be affected significantly. The accuracy of this assumption will be examined in more detail later.

5 Solution

The entire solution consists of three parts: determination of the contact surface conditions from the transient surface layer equations (4.4)–(4.13), the solution of Eq. (4.14) subject to these conditions, and the recovery of the surface transients based on the interior solution.

5.1 Contact Surface Conditions. First we derive some general results for the time-averaged solution in the transient surface layer, which hold regardless of the specific boundary conditions on the cavity surface. Let an overbar designate the average value of a function over the casting cycle. Then from the time integral of Eqs. (4.4) and (4.5), together with the periodicity conditions (4.12), we obtain

$$\bar{q}_i^\beta = \bar{q}_s^\beta = (k_\beta/d_\beta) \sum_{m=1}^{N} \frac{mn}{m+n-1} \bar{\theta}_m^\beta, \qquad (n = 1, 2, \ldots, N). \tag{5.1}$$

These are the time-averaged surface layer equations. The unique solution of this system is

$$\bar{\theta}_1^\beta = (d_\beta/k_\beta)\bar{q}_s^\beta, \tag{5.2}$$

$$\bar{\theta}_m^\beta = 0, \quad (m = 2, \ldots, N). \tag{5.3}$$

Hence the average temperature distribution in the transient surface layer is always linear. From Eqs. (4.9) and (5.3)

$$\bar{\theta}_s^\beta = \theta_0^\beta + \sum_{m=1}^{N} \bar{\theta}_m^\beta = \theta_0^\beta + \bar{\theta}_1^\beta. \tag{5.4}$$

This expression is valid for any periodic solution. Since the casting equation (4.6) and the boundary conditions (4.8) and (4.10) cannot be time-averaged in the same way, we must solve the full transient system, Eqs. (4.5)–(4.13), to proceed beyond this point.

First, consider the solution on the cavity surface. For convenience, we replace the casting temperature by the two auxiliary variables

$$\theta_c^\beta = \theta_c - \theta_0^\beta. \tag{5.5}$$

Then, from Eqs. (4.5), (4.6), (4.8), and (4.9), the governing equations during the residence time $0 \le t \le t_r$ are

$$-\mu c_o \dot{\theta}_c^\beta = \sum_{\gamma=1}^{2} h_\gamma \left(\theta_c^\gamma - \sum_{m=1}^{N} \theta_m^\gamma \right), \tag{5.6}$$

$$\rho_\beta c_\beta d_\beta \sum_{m=1}^{N} \frac{1}{m+n+1} \dot{\theta}_m^\beta + (k_\beta/d_\beta) \sum_{m=1}^{N} \frac{mn}{m+n-1} \theta_m^\beta = h_\beta \left(\theta_c^\beta - \sum_{m=1}^{N} \theta_m^\beta \right), \tag{5.7}$$

and during the open time $t_r \le t \le t_c$ they are

$$\rho_\beta c_\beta d_\beta \sum_{m=1}^{N} \frac{1}{m+n+1} \dot{\theta}_m^\beta + (k_\beta/d_\beta) \sum_{m=1}^{N} \frac{mn}{m+n-1} \theta_m^\beta = 0. \tag{5.8}$$

For simplicity, we have set $h_o = 0$ on the cavity surface when the die is open. Although the new variables in Eq. (5.5) create an additional casting equation in Eq. (5.6), they make the resulting system homogeneous. The solution must satisfy the periodicity conditions (4.12) and the initial conditions (4.13). In terms of the new variables (5.5) and the assumption (4.15), the initial conditions can be written in the form

$$\theta_c^\beta(x_\alpha, 0) = \theta_c^* - \theta_0^\beta. \tag{5.9}$$

But since the entire system is now linear and homogeneous, the solution for θ_m^β must be linear and homogeneous in the initial temperatures $\theta_c^* - \theta_0^\beta$. In particular, the time-averaged solution for θ_1^β can be expressed in the form

$$\bar{\theta}_1^\beta = \sum_{\gamma=1}^{2} A_{\beta\gamma}(\theta_c^* - \theta_0^\gamma), \tag{5.10}$$

where the coefficients $A_{\beta\gamma}$ are constants. In this form the result is not very useful, because it is expressed in terms of the interface temperatures θ_0^β. But we can use the general result in Eq. (5.4) to eliminate θ_0^β in favor of the time-averaged surface temperature $\bar{\theta}_s^\beta$. Combining Eqs. (5.4) and (5.10) we have

$$\bar{\theta}_1^\beta = \sum_{\gamma=1}^{2} a_{\beta\gamma}(\theta_c^* - \bar{\theta}_s^\gamma), \tag{5.11}$$

where, in standard indicial notation,

$$a_{\beta\gamma} = (\delta_{\beta\lambda} - A_{\beta\lambda})^{-1} A_{\lambda\gamma}. \tag{5.12}$$

It follows from Eqs. (5.2) and (5.11) that

$$\bar{q}_s^\beta = (k_\beta/d_\beta) \sum_{\gamma=1}^{2} a_{\beta\gamma}(\theta_c^* - \bar{\theta}_s^\gamma). \tag{5.13}$$

These two linear equations, which relate the time-averaged temperature and heat flux on both sides of the casting, are the desired contact surface conditions on the cavity surface. By rearranging terms, these conditions can be expressed in the more revealing form

$$\bar{q}_s^1 = (k_1/d_1)[(a_{11} + a_{12})(\theta_c^* - \bar{\theta}_s^1) + a_{12}(\bar{\theta}_s^1 - \bar{\theta}_s^2)],$$
$$\bar{q}_s^2 = (k_2/d_2)[(a_{22} + a_{21})(\theta_c^* - \bar{\theta}_s^2) + a_{21}(\bar{\theta}_s^2 - \bar{\theta}_s^1)]. \tag{5.14}$$

Each of the two terms in Eq. (5.14) represents a different contribution to the time-averaged heat flux on the cavity surface. The first term represents heat transferred from the casting to the die, and the second represents thermal interaction between die components. The remarkable conditions in Eq. (5.14) incorporate the entire effect of the transient temperatures near the casting on the time-averaged temperatures throughout the die.

A similar analysis leads to the following conditions on the parting surface:

$$\bar{q}_s^\beta = (k_\beta/d_\beta) b_\beta (\bar{\theta}_s^1 - \bar{\theta}_s^2), \tag{5.15}$$

where the two constants b_1 and b_2 are not independent since $\bar{q}_s^1 = -\bar{q}_s^2$. Unlike Eq. (5.14), these conditions have the form of a standard contact resistance. The coefficients b_β, however, include both the physical contact resistance represented by h_p, and the time-averaged effect of the transient solution in the two surface layers adjacent to the parting surface.

The five independent coefficients in Eqs. (5.13) and (5.15) must be computed from explicit solutions of the surface layer equations. Since these are linear ordinary differential equations with constant coefficients, the solution can be obtained by an eigenvalue analysis. The procedure is straightforward but involved, and so we omit the details here.

5.2 Steady Interior Solution. Although several numerical methods may be used to solve the Laplace equation (4.14), the boundary element method is a natural choice in this application because the surface mesh does not depend on the cooling line

locations inside the die. This means that individual cooling lines can be changed without affecting the rest of the die model.

Since the diameter of the cooling lines is usually small compared with other dimensions in the die (Fig. 1), we use a special form of the boundary element method developed by Barone and Caulk (1985) for geometric regions with slender circular holes. In this approach, the solution on the surface of the cooling line is assumed to be locally axisymmetric, and circumferential boundary integration is performed explicitly. Cooling lines are represented by one-dimensional line elements, with an associated radius at every node. Not only does this further simplify the modeling effort, but it reduces the number of unknowns, thereby improving the efficiency of the analysis when the number of cooling lines is large.

5.3 Transient Solution in the Surface Layer. The transient surface layer equations (4.5)–(4.13) depend on the steady interior solution through the constant interface temperature $\theta_0^\beta(x_\alpha)$ in Eq. (4.9). From Eqs. (5.2) and (5.4),

$$\theta_0^\beta = \bar{\theta}_s^\beta - (d_\beta/k_\beta)\bar{q}_s^\beta, \tag{5.16}$$

so that θ_0^β can be calculated directly from the time-averaged solution on the contact surface. The transient surface layer equations depend parametrically on x_α through nonuniformities in θ_0^β, but they are not spatially coupled. We recover the explicit transient solution in the surface layer by using the full nonlinear equations (4.5)–(4.13), without invoking the equivalent sensible heat assumption in Eq. (4.15). This assumption is still reflected in the transient results, but only through their dependence on θ_0^β in Eq. (4.9). In practice, the magnitude of this residual effect turns out to be quite small.

We seek a steady periodic solution in the transient surface layer, consistent with the initial casting temperature (4.13) prescribed at the beginning of every cycle. Since the casting equation is nonlinear, the solution must be obtained by choosing initial values for the temperature coefficients θ_m^β based on the linear solution and integrating the nonlinear equations (4.5) and (4.6) through successive casting cycles until a periodic solution is reached. Convergence can only be measured in a relative sense, but in most cases Eq. (4.12) was satisfied to within 0.1 percent in just a few casting cycles.

Since the boundary element solution yields a time-averaged temperature and heat flux at every boundary node on the cavity surface, θ_0^β can be computed at the same nodes and the associated transient temperatures calculated from the explicit solution of Eqs. (4.5)–(4.13). The transient solution between surface nodes can be obtained by interpolation.

The nonlinear system of ordinary differential equations (4.5)–(4.13) can be solved by a variety of numerical schemes. We used the routines developed by Shampine and Gordon (1975), which are based on the Adams methods.

6 A Special Case

In this section we discuss simplifications that occur in the surface layer equations when the die materials and the heat transfer coefficients are the same on both sides of the casting. These conditions are frequently encountered in actual die casting practice and the reduced equations yield important physical insight. In this case, the only source of asymmetry in the surface layer equations would be an imbalance in the steady interior solutions, reflected in unequal values for θ_0^1 and θ_0^2.

For convenience, we combine the temperature coefficients θ_m^β to form the symmetric and antisymmetric parts

$$\theta_m^S = \frac{1}{2}(\theta_m^1 + \theta_m^2), \quad \theta_m^A = \frac{1}{2}(\theta_m^1 - \theta_m^2). \tag{6.1}$$

With the help of Eqs. (4.5)–(4.11), the governing equations in the casting and the surface layers can be expressed in terms of the new variables (6.1). During the residence time $0 \le t \le t_r$ they are

$$-\frac{1}{2}\mu c_c \dot{\theta}_c + h\sum_{m=1}^{N}\theta_m^S = h(\theta_c - \theta_0^S), \tag{6.2}$$

$$\rho cd\sum_{m=1}^{N}\frac{1}{m+n+1}\dot{\theta}_m^S + \frac{k}{d}\sum_{m=1}^{N}\frac{mn}{m+n-1}\theta_m^S + h\sum_{m=1}^{N}\theta_m^S = h(\theta_c - \theta_0^S), \tag{6.3}$$

$$\rho cd\sum_{m=1}^{N}\frac{1}{m+n+1}\dot{\theta}_m^A + \frac{k}{d}\sum_{m=1}^{N}\frac{mn}{m+n-1}\theta_m^A + h\sum_{m=1}^{N}\theta_m^A = -h\theta_0^A, \tag{6.4}$$

During the open time $t_r \le t \le t_c$, the corresponding equations are

$$\rho cd\sum_{m=1}^{N}\frac{1}{m+n+1}\dot{\theta}_m^S + \frac{k}{d}\sum_{m=1}^{N}\frac{mn}{m+n-1}\theta_m^S = 0, \tag{6.5}$$

$$\rho cd\sum_{m=1}^{N}\frac{1}{m+n+1}\dot{\theta}_m^A + \frac{k}{d}\sum_{m=1}^{N}\frac{mn}{m+n-1}\theta_m^A = 0. \tag{6.6}$$

Since it is no longer necessary to distinguish between properties on different sides of the casting, we have dropped the subscripts from the material coefficients.

Two important observations can be made from the structure of Eqs. (6.2)–(6.6). First, the symmetric and antisymmetric temperature coefficients appear in separate equations. This means that for a given pair of interface temperatures θ_0^β, each part of the solution can be determined independently. Second, the casting temperature θ_c appears only in the symmetric equations (6.2) and (6.3). Therefore, only the symmetric solution is nonlinear.

The symmetric and antisymmetric solutions represent complementary modes of heat transfer. The symmetric solution represents a net flux away from the casting with no net flux between the die components. On the other hand, the antisymmetric solution represents a net flux between the die components with no net flux from the casting. Hence, the symmetric mode controls the solidification of the casting, while the antisymmetric mode controls thermal interaction between die components.

7 A One-Dimensional Example

In this section, we consider a simple example that illustrates how the surface layer model predicts specific features in the temperature response of the casting and die. So that physical effects are not obscured by geometric details, we first consider a one-dimensional problem in which the die temperatures are assumed to be independent of x_1 and x_2. For simplicity, we also assume that $h_o = 0$ in Eq. (4.11). The only source of asymmetry between the two die halves is an imbalance in cooling, represented by placing water at two different depths ($D_1 = 12$ cm and $D_2 = 36$ cm) below the cavity surface. The die materials, heat transfer coefficients, and water temperatures are the same on both sides of the casting. The specific values for these and other parameters (given in Table 1) reflect a typical die casting process for an aluminum transmission case.

In this example, the time-averaged die temperatures are linear in z, and so

$$\bar{q}_s^\beta = \left[\frac{h_w k_\beta/D_\beta}{h_w + k_\beta/D_\beta}\right](\bar{\theta}_s^\beta - \theta_w), \quad (\beta = 1, 2). \tag{7.1}$$

These equations, combined with the two contact surface con-

Table 1

Casting Properties

Heat capacity, c_c	1000 J/kg K
Density, ρ_c	2570 kg/m^3
Conductivity, k_c	108 W/m K
Latent heat, Q_L	390000 J/kg
Liquidus, θ_{liq}	593 °C
Solidus, θ_{sol}	538 °C

Die Properties

Heat capacity, c	584 J/kg K
Density, ρ	7760 kg/m^3
Conductivity, k	29 W/m K
Coating conductance, h	10000 W/m^2 K

Process Parameters

Injection temperature, θ_c^0	620 °C
Cycle time, t_c	80 s
Residence time, t_r	30 s
Water temperature, θ_w	25 °C
Water heat transfer coefficient, h_w	10000 W/m^2 K

ditions in Eq. (5.13), yield coupled solutions for $\overline{q}_s^\beta$ and $\overline{\theta}_s^\beta$. From these, the transient temperatures in the casting and the die can be recovered by the procedure in Section 5.3. Specific results for this example are shown as solid lines in Fig. 2. The casting temperature is shown only for the residence time, and the two cavity surface temperatures are displayed for the whole cycle.

Early in the cycle, the casting temperature drops abruptly as it loses sensible heat to the die. This is accompanied by a corresponding rise in the cavity surface temperatures. When the casting reaches liquidus temperature, it begins to cool more slowly since the die must now absorb the latent heat of solidification. After reaching solidus, the casting temperature drops rapidly again as it approaches equilibrium with the cavity surface.

The large difference between the water depths in the two dies produces a finite antisymmetric solution, which is reflected in the unequal die temperatures throughout the cycle. But before the casting reaches its solidus temperature, the difference between the two die temperatures is much smaller than the temperature difference between either die and the casting. This means that during solidification, the symmetric mode dominates the solution and both dies absorb roughly the same amount of energy.

After the casting solidifies, it cools very quickly until it falls below the temperature of the hotter die surface. Once this occurs, it cools at the same rate as both die surfaces, following a temperature curve about midway between the two. During this part of the residence time, the antisymmetric mode begins to dominate the solution. Heat transfer between the casting and the die becomes small compared to that between the two die surfaces.

During the latter part of the residence time, the transient surface layers are emptied of the energy they accumulated during solidification. On the cooler side, all of this accumulated heat is conducted back into the die, but on the hotter side, some of it also escapes across the casting into the other die.

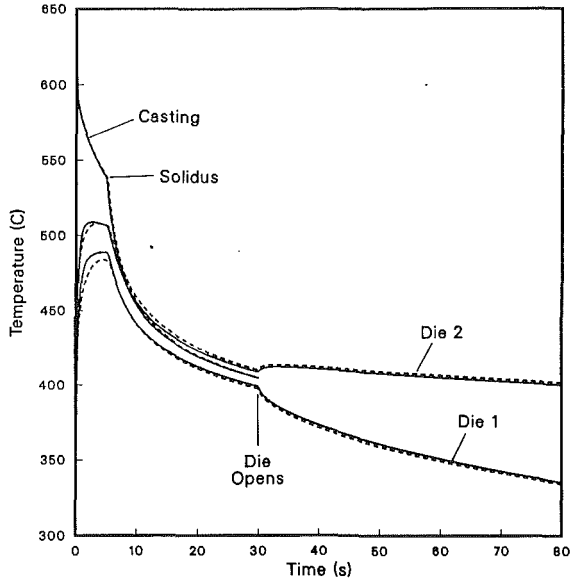

Fig. 2 Comparison of transient surface layer solution (solid lines) with the finite difference results (dashed lines) for a 6-mm-thick casting

Dramatic evidence of heat conduction from one die surface to the other can be seen in the sharp upward rebound in the surface temperature on the hotter die immediately after the die opens.

Before going on, we want to use the results of this example to clarify a misunderstanding in the die casting literature. First, we define the *relative cooling load* between opposite die surfaces by the ratio

$$C_\beta = \frac{\overline{q}_s^\beta}{\overline{q}_s^1 + \overline{q}_s^2}, \quad (\beta = 1, 2), \tag{7.2}$$

where $C_1 = C_2 = 0.5$ corresponds to perfectly balanced cooling. This quantity measures the relative participation of the two die surfaces in removing heat from the casting. Herman (1968) suggested that Eq. (7.2) be used to locate what he called the *neutral thermal axis*, or the line of porosity inside the casting marking the place where the metal solidifies last. Although C_β does measure the relative heat transfer to both die surfaces over the entire residence time, is is clear from the earlier discussion that it may not give an accurate accounting of the relative heat transfer up to the point of solidification. In the present example, the hotter die surface absorbs about 45 percent of the heat before the casting solidifies. But since much of this heat is lost to the other die surface later in the residence time, only 27 percent of the total is left by the time the casting is ejected. In this case, the relative cooling load ($C_2 = 0.27$) exaggerates what is actually a rather mild offset in the neutral thermal axis. A ratio like Eq. (7.2) would be useful for locating the neutral thermal axis, but only if the accumulated heat flux is calculated at the moment of solidification.

8 Comparison With Finite Difference Results

In this section, we evaluate the accuracy of our assumptions by comparing the results of the previous section with the long-time limit of a straightforward finite difference solution. The finite difference analysis was started with an initially uniform die temperature and continued until the die temperatures became periodic. To avoid a relative measure of periodicity, we took advantage of the fact that in one dimension the time-averaged die temperatures approach a linear distribution as the process reaches steady state. Depending on the water depth, from 50 to 300 cycles were necessary before the time-averaged die temperatures became linear in both sides of the die.

Table 2

	Surface Layer Model			Finite Difference Method			
Casting Thickness (mm)	6	12	18	6	12	18	
Depth Ratio	Average Cavity Surface Temperatures						Die Surface
1	310.9	312.4	311.4	310.6	310.6	306.4	1
	310.9	312.4	311.4	310.6	310.6	306.4	2
3	386.2	377.1	367.1	384.3	369.6	350.1	1
	421.8	441.1	453.6	423.1	443.9	453.9	2
5	409.3	398.5	386.8	406.3	387.8	362.8	1
	455.9	483.8	503.8	456.9	486.0	503.6	2
	Casting Ejection Temperatures						
1	310.8	325.7	347.4	310.6	326.8	352.1	
3	404.6	424.0	449.2	404.6	425.5	454.9	
5	433.7	457.9	489.7	433.0	458.4	496.8	
	Solidification Times						
1	2.74	6.22	9.67	2.83	6.74	10.84	
3	5.02	11.46	17.35	5.19	12.34	19.06	
5	6.53	15.18	22.77	6.72	16.07	24.61	

A direct comparison between the two solutions is possible everywhere except in the casting, where the finite difference results yield a distributed rather than a lumped solution. To compare the two solutions there, we reduced the finite difference results to a uniform temperature based on an equivalent casting energy. Finite difference results are shown as dashed lines in Fig. 2.

The first thing we observe is that the surface layer model predicts slightly lower casting temperatures and shorter solidification times than the finite difference results. This happens because the conductive resistance of the casting is not present in the surface layer model, and so the casting energy is able to reach the die more easily.

The second thing that is apparent in these results is that the error in die temperature is much greater on the cooler side than on the warmer side, especially during the early part of the cycle. Again, this can be explained by the fact that the transverse temperature gradient was neglected in the casting. The actual temperature distribution is nonuniform and can be expressed as the sum of symmetric and antisymmetric parts in the same way as in Section 6. Neglecting the symmetric part increases the flow of energy from the casting, and so it increases the temperature of both die surfaces equally. On the other hand, by neglecting the antisymmetric distribution, we increase the flow of energy between the dies, which increases the temperature of the cooler die and decreases the temperature of the warmer die. The two sources of error are summed on the cooler surface and subtracted on the warmer surface, producing the difference seen in Fig. 2.

The equivalent sensible heat approximation (4.15) also contributes to some of the error in Fig. 2. To isolate this assumption, we redid the finite difference analysis with no conductive resistance in the casting. This reduced the difference between the finite difference and layer results by about two thirds. Hence, the lumped representation for the casting is the major source of error in the surface layer model.

In spite of the noted discrepancies, it turns out that the surface layer model does predict very accurate results when the casting is thin. Table 2 shows the comparison between selected results for casting thicknesses of 6, 12, and 18 mm, and water depth ratios varying from 1 to 5. Corresponding to the three different casting thicknesses, the shorter water depth was chosen at 12, 6, and 4 cm to keep the temperatures within normal operating ranges for aluminum die casting. Consistent

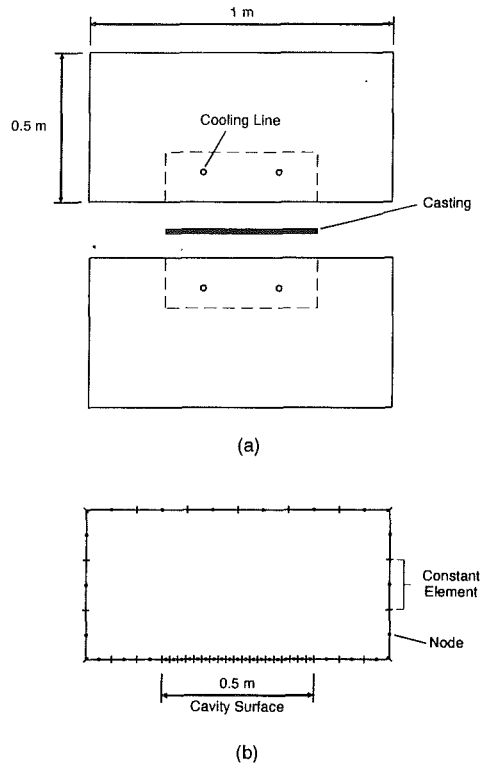

Fig. 3 Boundary element model for the symmetric two-dimensional example die. All the cooling lines in the examples that follow are contained in the region enclosed by the dashed line.

with the results in Fig. 2, the average cavity surface temperature shows a larger error on the cooler die surface. This error increases as the cooling gets more asymmetric. Nevertheless, the worst errors for the 6-mm casting are less than 3°C, and for the 18-mm casting, they are no greater than 20°C.

The error in solidification time varies from 3 percent for a 6-mm casting to about 9 percent for an 18-mm casting, with almost no effect of cooling asymmetry. Since the ejection temperatures reflect the accuracy of the symmetric mode alone, they turn out to be much better than the die surface results. Even for the 18-mm casting with the greatest amount of cooling asymmetry, the error in ejection temperature is less than 7°C.

At worst, the relative cooling load is accurate to within 1 percent. This good accuracy can be explained if we decompose the average heat flux into its symmetric and antisymmetric parts and express the relative cooling loads (7.2) in the alternative form

$$C_1 = \frac{1}{2}\left(1 + \bar{q}_s^A/\bar{q}_s^S\right); \quad C_2 = \frac{1}{2}\left(1 - \bar{q}_s^A/\bar{q}_s^S\right). \tag{8.1}$$

Both $\bar{q}_s^S$ and $\bar{q}_s^A$ will err on the large side because the conductive resistance of the casting has been neglected. Since the relative cooling load depends on the ratio of these quantities, its error is reduced accordingly.

9 Two-Dimensional Examples

Although the one-dimensional examples of the last section were useful for gaging the accuracy of the assumptions in the surface layer model, they are not general enough to illustrate the spatial coupling that can occur within a die component because of nonuniform interior temperatures. These nonuniformities stem from three basic sources: die geometry, cooling line positions, and casting thickness. In this section we examine several two-dimensional examples that illustrate the effect of each of these variables.

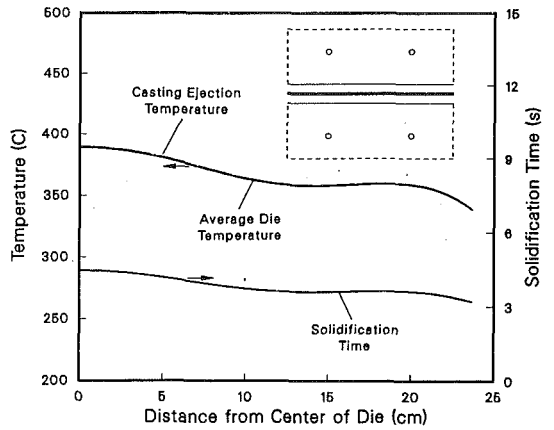

Fig. 4 Two-dimensional solution for symmetric cooling and a uniform casting thickness. In this case the casting ejection temperature (chain dot) and the average die temperature (solid) curves happen to be virtually indistinguishable.

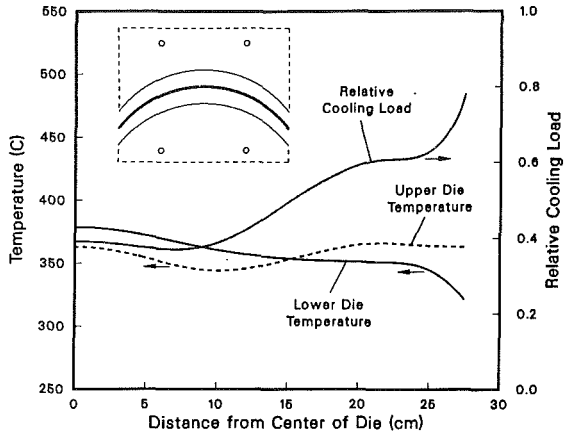

Fig. 6 Two-dimensional solution for a curved casting with uniform thickness

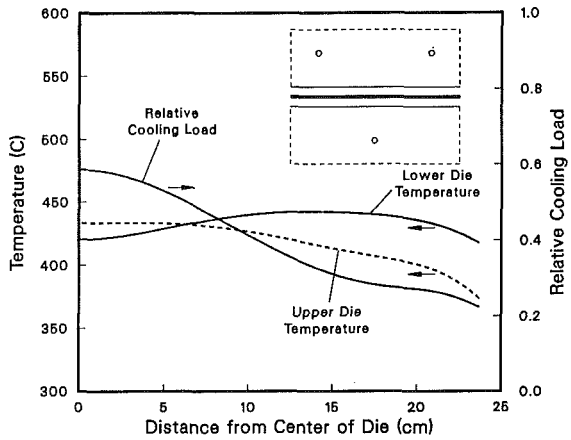

Fig. 5 Two-dimensional solution for unsymmetric cooling and a uniform casting thickness

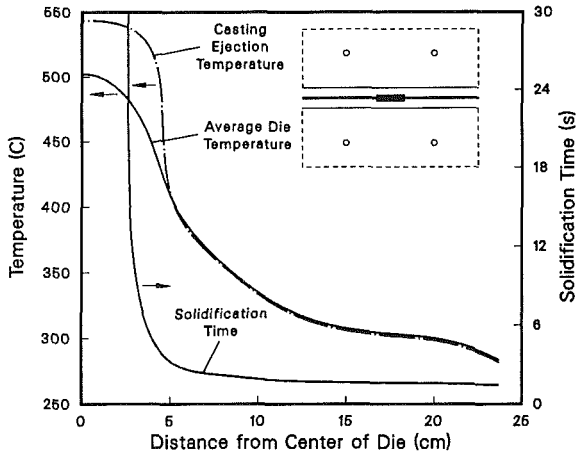

Fig. 7 Two-dimensional solution for symmetric cooling and a stepped casting

Consider the two-dimensional die geometry illustrated in Fig. 3(*a*). The 0.5-m long die cavity is centered between identical die components 1-m long by 0.5-m deep. For simplicity, we assume a zero heat flux on the parting and outer surfaces of the die, as well as on the cavity surface during the open time. Although the cooling lines take different positions in the various examples, they are always 15 mm in diameter and located inside the dashed line in Fig. 3(*a*). We consider castings with uniform and nonuniform thickness, but the total casting volume is held constant for consistent comparison. Since each example has complete symmetry about the center of the die, the results of the analysis are reported only from the center to the edge of the die cavity. In every case, the process variables and material properties are the same as in the last section (Table 1). The time-averaged die temperatures are computed on the basis of the boundary element model in Fig. 3(*b*), assuming a uniform distribution of temperature and heat flux on each element.

First, we consider a uniform casting thickness and a symmetric arrangement for the cooling lines (Fig. 4). Two cooling lines are spaced 25 cm apart and 10 cm away from the cavity surface in each die half. The average die temperatures decrease about 50°C from the center to the edge of the die cavity, with a slight local depression near the cooling lines. The decrease in surface temperature near the edge of the cavity is caused by the cooling influence of the mass of die steel under the insulated parting surface. Corresponding to the die temperature, the solidification time and ejection temperature also decrease from the center to the edge of the cavity. (In this case, the ejection temperature happens to be so close to the average die temperature, that the two curves are almost indistinguishable.) Because of the symmetry between the two die halves, the cooling load is perfectly balanced.

To see how an asymmetric cooling design affects these results, we put two cooling lines in the upper die half and only one in the lower (Fig. 5). The cooling line in the lower die half is located at the center of the casting, and the cooling lines in the upper die half are placed 16.7 cm on either side of the center. Each cooling line is still 10 cm from the cavity surface. This cooling design produces a strong variation in relative cooling load, especially near the edges of the cavity. But even where 80 percent of the casting energy goes into the upper die, the two surface temperatures differ by only 50°C. Evidently, a moderate imbalance in cavity surface temperature is sufficient to support a rather large difference in relative cooling load.

Variations in die geometry can also produce an asymmetric cooling load between die components. Consider the curved geometry in Fig. 6. Here the cavity forms a circular arc, which begins and ends at the same points as in the previous two examples, but projects 125 mm into the upper die component. The casting thickness is still uniform, but it is reduced from 6 to 5.17 mm to maintain the same overall casting mass. Again, the relative cooling load varies significantly from the center to the edge of the die cavity, but this time it occurs because of the curvature in the cavity surface.

In the next example (Fig. 7), we return to the original die

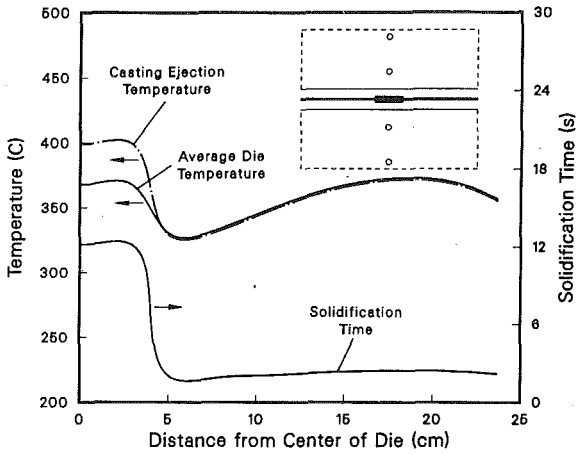

Fig. 8 Modified cooling design for the stepped casting

geometry and cooling line positions of Fig. 4, but introduce a sudden change in casting thickness from 4 to 16 mm about 40 mm from the center of the casting. The center of the die is now so hot that the casting is unable to solidify in the prescribed residence time. One way to correct this problem is to concentrate the cooling near the center of the die. It turns out that the relatively simple two-line arrangement in Fig. 8 is sufficient to both solidify the casting and smooth out the ejection temperatures. The closer cooling line acts as a strongly focused heat sink and the line above it helps to smooth the transition between the sharply different cooling requirements in the two areas of the casting.

Acknowledgments

We would like to express our appreciation to Ed Herman of GM Advanced Engineering for generously sharing helpful insights from his considerable experience in the die casting process. In addition, Dr. Andrew Schoene was helpful in implementing the nonlinear algorithms for solving the ordinary differential equations in the surface layer.

References

Barone, M. R., and Caulk, D. A., 1985, "Special Boundary Integral Equations for Approximate Solution of Potential Problems in Three-Dimensional Regions With Slender Cavities of Circular Cross-Section," *IMA Journal of Applied Mathematics*, Vol. 35, pp. 311–325.

Caulk, D. A., 1990, "A Method for Analyzing Heat Conduction With High-Frequency Periodic Boundary Conditions," ASME JOURNAL OF HEAT TRANSFER, Vol. 112, pp. 280–287.

Gear, C. W., 1971, *Numerical Initial Value Problems in Ordinary Differential Equations*, Prentice Hall, Englewood Cliffs, NJ.

Granchi, M., Vettori, E., and Cerini, E., 1983, "Computer Thermal Analysis of Die Casting Dies," *Proceedings, 12th International Die Casting Congress and Exposition*, Minneapolis, MN.

Grant, J. W., 1981, "Thermal Modeling of a Permanent Mold Casting Cycle," in *Modeling of Casting and Welding Processes*, Metallurgical Society of AIME, Warrendale, PA, pp. 19–37.

Herman, E. A., 1968, "The Influence and Control of the Neutral Thermal Axis in Die Casting," *Proceedings, 5th National Die Casting Congress*, Paper No. 54, Detroit, MI.

Kallien, L., and Sturm, J. C., 1991, "Simulation Aided Design for Die Casting Tools," *Proceedings, 16th International Die Casting Congress and Exposition*, Paper No. T91-102, Detroit, MI.

Kearns, K. J., 1986, "Computer Simulation of the Permanent Mold Process," *Modern Casting*, pp. 29–32.

Myers, G. E., 1978, "The Critical Time Step for Finite-Element Solutions to Two-Dimensional Heat-Conduction Transients," ASME JOURNAL OF HEAT TRANSFER, Vol. 100, pp. 120–127.

Ohtsuka, Y., Mizuno, K., and Yamada, J., 1982, "Application of a Computer Simulation System to Aluminum Permanent Mold Castings," *Transactions, American Foundrymen's Society*, Vol. 90, pp. 635–645.

Riegger, O. K., 1981, "Application of a Solidification Model to the Die Casting Process," in: *Modeling of Casting and Welding Processes*, Metallurgical Society of AIME, Warrendale, PA, pp. 39–72.

Shampine, L. F., and Gordon, M. K., 1975, *Computer Solution of Ordinary Differential Equations: The Initial Value Problem*, W. H. Freeman, San Francisco, CA.

A Perturbation Analysis of Transient Freezing of a Laminar Liquid Flow in a Cooled Two-Dimensional Channel

B. Weigand

W. Höhn

H. Beer

Technische Hochschule Darmstadt,
Institut für Technische Thermodynamik,
6100 Darmstadt, Federal Republic of Germany

The paper shows the applicability of a regular perturbation method for predicting the transient development of the ice layer thickness inside a cooled planar channel subjected to laminar flow. Applying the perturbation expansion to the conservation equations, closed-form solutions for the velocity and temperature distributions in the fluid for an arbitrarily shaped channel could be derived under the assumption that the axial variation in solid layer thickness is small. The distributions obtained for the steady-state ice layer thickness and the velocity were checked by numerical calculations and compared with the measurements of Kikuchi et al. (1986) and a generally good agreement was found.

Introduction

Problems of solidification or freezing of liquids inside cold channels have been encountered in numerous engineering applications. Because the freezing shut of systems may lead to a destruction of the equipment (for example, freezing shut of a water pipe in winter or freezing of molten sodium in a nuclear reactor), it is advisable to prevent blockage. If solidification on the cooled walls cannot be suppressed, steady-state conditions must be sought.

Many theoretical and experimental studies have been performed for fluid flow with solidification in circular tubes. An early investigation was reported by Zerkle and Sunderland (1968) for the steady-state freezing of laminar flow inside a horizontal tube. Under the assumption of a parabolic axial velocity distribution throughout the full axial length of the tube and with an appropriate coordinate transform, they were able to reduce the problem to the classical Graetz problem without solidification. Özişik and Mulligan (1969) used a slug flow approximation for the liquid core to analyze transient freezing in an isothermal circular tube. They applied integral transforms to obtain the transient development of the ice layer inside the tube. Bilenas and Jiji (1970) solved the boundary layer equations applying a finite-difference scheme, but they used a wide-meshed grid for their calculations. Chida (1983) calculated numerically the steady-state ice layer thickness, under consideration of axial conduction. Bilenas and Jiji (1970) and Chida (1983) assumed a fully developed parabolic axial velocity distribution at the entrance of the cooled section.

Despite its relevance to any important technological and physical problems, the freezing of liquid flows through a cooled two-dimensional channel has not been studied as intensively as the freezing in a cooled circular pipe. An early investigation of this problem was reported by Lee and Zerkle (1969). They assumed the axial velocity to be parabolic throughout the whole chill region, which was in analogy to Zerkle and Sunderland (1968). With the approximated velocity profile and with an appropriate coordinate transform, the energy equation could be reduced to a Graetz problem, and the steady-state ice layer was calculated. An experimental investigation of the effect of freezing a liquid in case of laminar flow between two cooled plates has been performed only by Kikuchi et al. (1986). They used water as the working fluid. Both plates were maintained at the same temperature, which was below the freezing temperature of the water and varied from $-2°C$ to $-7°C$. A numerical calculation of the steady-state ice layers for an arbitrary velocity profile at the entrance of the chill region was given by Weigand and Beer (1991), who solved the boundary layer equations with the help of a finite-difference method. For the case of a fully developed parabolic velocity distribution at the entrance of the cooled channel, the results of Weigand and Beer (1991) were compared with the experimental findings of Kikuchi et al. (1986) and a generally good agreement was found. Bennon and Incropera (1988) studied numerically the influence of free convection effects on the axial distribution of the steady-state solid–liquid interface by solving the conservation equations for laminar flow without simplified assumptions. The transient development of the solidified crust in a planar channel has been studied only by Weigand and Beer (1992). They obtained an approximate analytical solution for the distribution of the ice layer thickness under the assumption that the axial variation in solid layer thickness could be neglected. Their analysis is based on the boundary layer equations.

The subject of this paper is the presentation of an approximate solution of the boundary layer equations with the help of a regular perturbation method. Under the assumption that the axial variation in solid layer thickness is small, closed-form solutions for the velocity and temperature distributions in the fluid for an arbitrarily shaped channel could be developed. The given method is quite flexible and can be used to calculate the velocity and temperature distributions in a channel with an arbitrary cross section, if the axial variation in the free channel height is comparatively small. Finally, it can be shown that the solutions of Zerkle and Sunderland (1969) and Weigand and Beer (1992) can be obtained as the zero-order solution of the regular perturbation expansion, presented here.

Moreover, it should be pointed out that the present paper deals solely with smooth ice layers in laminar liquid flow. This means that the ice layers are assumed to increase monotonously in thickness with increasing values of the axial coordinate.

Analysis

Basic Equations and Assumptions. Figure 1 shows the geometric configuration and the coordinate system for a planar symmetric channel. The fluid enters the chilled region at $x=0$ with a fully developed laminar velocity profile and with a

Contributed by the Heat Transfer Division for publication in the JOURNAL OF HEAT TRANSFER. Manuscript received by the Heat Transfer Division February 1992; revision received September 1992. Keywords: Forced Convection, Phase-Change Phenomena, Transient and Unsteady Heat Transfer. Associate Technical Editor: Y. Bayazitoglu.

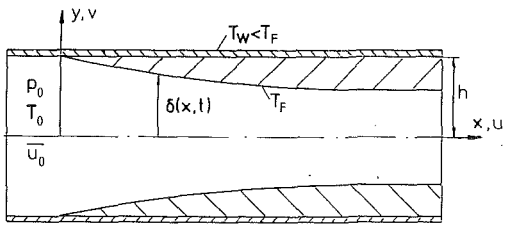

Fig. 1 Physical model and coordinate system

constant temperature T_0. In the cooled section, the wall temperature is maintained at a constant value T_W, which is lower than the freezing temperature T_F of the fluid. The frozen layers are generated on both walls as the fluid proceeds along the channel. Assuming an incompressible, Newtonian fluid with constant fluid properties, the quasi-steady conservation equations for the fluid may be written in the following form:

$$\frac{\partial \tilde{u}}{\partial \tilde{x}} + \frac{\partial \tilde{v}}{\partial \tilde{y}} = 0 \tag{1}$$

$$\tilde{u}\frac{\partial \tilde{u}}{\partial \tilde{x}} + \tilde{v}\frac{\partial \tilde{u}}{\partial \tilde{y}} = -\frac{\partial \tilde{p}}{\partial \tilde{x}} + \frac{1}{\mathrm{Re}_h}\frac{\partial^2 \tilde{u}}{\partial \tilde{y}^2} \tag{2}$$

$$0 = \frac{\partial \tilde{p}}{\partial \tilde{y}} \tag{3}$$

$$\tilde{u}\frac{\partial \theta}{\partial \tilde{x}} + \tilde{v}\frac{\partial \theta}{\partial \tilde{y}} = \frac{1}{\mathrm{Re}_h\,\mathrm{Pr}}\frac{\partial^2 \theta}{\partial \tilde{y}^2} \tag{4}$$

with the dimensionless quantities

$$\tilde{x} = \frac{x}{h},\quad \tilde{y} = \frac{y}{h},\quad \tilde{u} = \frac{u}{\overline{u}_0},\quad \tilde{v} = \frac{v}{\overline{u}_0},\quad \tilde{p} = \frac{p}{\rho \overline{u}_0^2},\quad \tilde{\delta} = \frac{\delta}{h}$$

$$\theta = \frac{T - T_F}{T_0 - T_F},\quad \mathrm{Re}_h = \frac{\overline{u}_0 h}{\nu},\quad \mathrm{Pr} = \frac{\nu}{a} \tag{5}$$

where $\overline{u}_0$ denotes the axial mean velocity for $\tilde{x} = 0$. The boundary conditions belonging to Eqs. (1)–(4) are

$$\tilde{x} = 0:\ \tilde{u} = \frac{3}{2}(1 - \tilde{y}^2),\quad \tilde{p} = \tilde{p}_0,\quad \theta = 1$$

$$\tilde{y} = 0:\ \frac{\partial \tilde{u}}{\partial \tilde{y}} = 0,\quad \tilde{v} = 0,\quad \frac{\partial \theta}{\partial \tilde{y}} = 0$$

$$\tilde{y} = \tilde{\delta}:\ \tilde{u} = 0,\quad \tilde{v} = 0,\quad \theta = 0 \tag{6}$$

By deriving Eqs. (1)–(4), the usual boundary-layer assumptions were made, which are a common treatment of the conservation equations for channel flows (Cebeci and Chang, 1978). The assumption of quasi-steady conditions, which was incorporated into Eqs. (1)–(5), is justified for water flow because of the small value of the Stefan number, which is about $\mathrm{Ste} \approx 0.1$ (Cervantes et al., 1990). The conservation of mass in integral form is given by

$$1 = \int_0^{\tilde{\delta}} \tilde{u}\, d\tilde{y} \tag{7}$$

where the mass that gets lost by freezing at the channel walls was neglected as the change in the density between fluid and solid is very small for water and quasi-steady conditions are assumed. As a consequence of these assumptions, the resulting velocity at the freezing front in Eq. (6) is taken to be zero.

In addition to Eqs. (1)–(7), the energy equation for the solid region is required. Assuming constant properties in the solid region and negligible axial conduction, the heat conduction equation for the solid phase reduces for quasi-steady conditions to

$$\frac{\partial^2 \theta_S}{\partial \tilde{y}^2} = 0 \tag{8}$$

with the boundary conditions

$$\tilde{y} = \tilde{\delta}:\ \theta_S = 1$$

$$\tilde{y} = 1:\ \theta_S = 0 \tag{9}$$

The dimensionless temperature θ_S is defined as $\theta_S = (T - T_W)/(T_F - T_W)$. Equations (1)–(6) and Eqs. (8)–(9) are coupled by the interface energy equation

$$\frac{\partial \theta_S}{\partial \tilde{y}} - \frac{1}{B}\frac{\partial \theta}{\partial \tilde{y}} = \frac{\partial \tilde{\delta}}{\partial \tau}\left[1 + \left(\frac{\partial \tilde{\delta}}{\partial \tilde{x}}\right)^2\right]^{-1},\quad \tilde{y} = \tilde{\delta} \tag{10}$$

with the following dimensionless quantities:

$$B = \frac{k_s}{k}\frac{T_F - T_W}{T_0 - T_F},\quad \tau = \mathrm{FoSte},\quad \mathrm{Fo} = \frac{t a_S}{h^2},$$

$$\mathrm{Ste} = \frac{c_S(T_F - T_W)}{r_S} \tag{11}$$

where B denotes a dimensionless freezing parameter.

Velocity and Temperature Distribution in the Liquid Phase. The velocity and the temperature distribution in the liquid can be calculated from Eqs. (1)–(7). Introducing a streamfunction, defined by

$$\tilde{u} = \frac{\partial \psi}{\partial \tilde{y}},\quad \tilde{v} = -\frac{\partial \psi}{\partial \tilde{x}} \tag{12}$$

into Eqs. (1)–(7) and applying the coordinate transformation

$$\eta = \frac{\tilde{y}}{\tilde{\delta}},\quad \xi = \frac{1}{\mathrm{Re}_h}\int_0^{\tilde{x}} \frac{d\tilde{x}}{\tilde{\delta}} \tag{13}$$

Nomenclature

a = thermal diffusivity
B = dimensionless freezing parameter, Eq. (11)
$B_m(\xi)$ = functions, Eq. (43)
Fo = Fourier number
F_n = eigenfunctions
h = distance from centerline to wall
k = thermal conductivity
L = channel length
p = pressure
Pr = Prandtl number
r_s = heat of fusion
Re_h = Reynolds number $= \overline{u}_0 h/\nu$
Re_{4h} = Reynolds number $= \overline{u}_0 4h/\nu$
Ste = Stefan number, Eq. (11)
T = temperature
T_F = freezing temperature of the liquid
T_0 = fluid temperature at the entrance
T_W = wall temperature
t = time
u, v = fluid velocity components
$\overline{u}_0$ = mean velocity at the entrance
x, y = coordinates
δ = distance from centerline to the solid–liquid interface
η = modified vertical coordinate, Eq. (13)
θ = dimensionless temperature of the fluid $= (T - T_F)/(T_0 - T_F)$
θ_S = dimensionless temperature of the solid $= (T - T_W)/(T_F - T_W)$
λ_n = eigenvalues
ν = kinematic viscosity
ξ = integral coordinate, Eq. (13)
ρ = density
τ = dimensionless time
ψ = streamfunction

to the resulting equations, the following set of partial differential equations can be derived:

$$\frac{\partial\psi}{\partial\eta}\frac{\partial^2\psi}{\partial\xi\partial\eta}-\frac{\partial\psi}{\partial\xi}\frac{\partial^2\psi}{\partial\eta^2}-\frac{1}{\bar{\delta}}\frac{\partial\bar{\delta}}{\partial\xi}\left(\frac{\partial\psi}{\partial\eta}\right)^2=-\bar{\delta}^2\frac{\partial\tilde{p}}{\partial\xi}+\frac{\partial^3\psi}{\partial\eta^3} \tag{14}$$

$$0=\frac{\partial\tilde{p}}{\partial\eta} \tag{15}$$

$$\frac{\partial\psi}{\partial\eta}\frac{\partial\theta}{\partial\xi}-\frac{\partial\psi}{\partial\xi}\frac{\partial\theta}{\partial\eta}=\frac{1}{\mathrm{Pr}}\frac{\partial^2\theta}{\partial\eta^2} \tag{16}$$

The boundary conditions, according to Eq. (6), are given by

$$\xi=0:\ \psi=\frac{3}{2}\left(\eta-\frac{1}{3}\eta^3\right)-1,\quad \tilde{p}=\tilde{p}_0,\quad \theta=1$$

$$\eta=0:\quad \frac{\partial^2\psi}{\partial\eta^2}=0,\quad \psi=-1,\quad \frac{\partial\theta}{\partial\eta}=0$$

$$\eta=1:\ \frac{\partial\psi}{\partial\eta}=0,\quad \psi=0,\quad \theta=0 \tag{17}$$

Without loss of generality, the streamfunction was assumed to be zero for $\eta=1$. The evaluation of the conservation of mass in integral form leads to $\psi=-1$ for $\eta=0$. In Eq. (17) the inlet boundary condition for $\bar{u}$ was replaced by a condition for the stream function at $\xi=0$.

The coordinate transform, according to Eq. (13), is very useful in order to solve the conservation equations, because the duct with variable distance between the wall and the centerline is transformed into a duct with constant height.

Equation (15) states that the pressure is not a function of the coordinate η. Therefore, one obtains the following partial differential equation for ψ by differentiating Eq. (14) with respect to η

$$\frac{\partial\psi}{\partial\eta}\frac{\partial^3\psi}{\partial\xi\partial\eta^2}-\frac{\partial\psi}{\partial\xi}\frac{\partial^3\psi}{\partial\eta^3}=\frac{\partial^4\psi}{\partial\eta^4}+\frac{2}{\bar{\delta}}\frac{\partial\bar{\delta}}{\partial\xi}\frac{\partial\psi}{\partial\eta}\frac{\partial^2\psi}{\partial\eta^2} \tag{18}$$

The last term on the right-hand side of Eq. (18) is of the order $(1/\delta)\ (\partial\bar{\delta}/\partial\xi)$. This term represents the effect of acceleration due to the converging ice layers. For moderate values of the cooling parameter B this term is relatively small. Therefore, this quantity will be treated as a perturbation parameter. Let us assume an expansion for the streamfunction ψ and also for the temperature distribution θ of the form

$$\psi=\psi_0+\frac{1}{\bar{\delta}}\frac{\partial\bar{\delta}}{\partial\xi}\psi_1+\left(\frac{1}{\bar{\delta}}\frac{\partial\bar{\delta}}{\partial\xi}\right)^2\psi_2+\frac{1}{\bar{\delta}}\frac{\partial^2\bar{\delta}}{\partial\xi^2}\psi_3+\ldots \tag{19}$$

$$\theta=\theta_0+\frac{1}{\bar{\delta}}\frac{\partial\bar{\delta}}{\partial\xi}\theta_1+\left(\frac{1}{\bar{\delta}}\frac{\partial\bar{\delta}}{\partial\xi}\right)^2\theta_2+\frac{1}{\bar{\delta}}\frac{\partial^2\bar{\delta}}{\partial\xi^2}\theta_3+\ldots \tag{20}$$

whereby the perturbation quantity is a function of ξ for a fixed value of time. Inserting the expansions, according to Eqs. (19) and (20), into the conservation Eqs. (16), (18) and into the boundary conditions (17), results in the following set of partial differential equations:

Zero-Order Equations (~ 1).

$$\frac{\partial\psi_0}{\partial\eta}\frac{\partial^3\psi_0}{\partial\xi\partial\eta^2}-\frac{\partial\psi_0}{\partial\xi}\frac{\partial^3\psi_0}{\partial\eta^3}=\frac{\partial^4\psi_0}{\partial\eta^4} \tag{21}$$

$$\frac{\partial\psi_0}{\partial\eta}\frac{\partial\theta_0}{\partial\xi}-\frac{\partial\psi_0}{\partial\xi}\frac{\partial\theta_0}{\partial\eta}=\frac{1}{\mathrm{Pr}}\frac{\partial^2\theta_0}{\partial\eta^2} \tag{22}$$

with the boundary conditions

$$\xi=0:\ \psi_0=\frac{3}{2}\left(\eta-\frac{1}{3}\eta^3\right)-1,\quad \theta_0=1$$

$$\eta=0:\ \psi_0=-1,\quad \frac{\partial^2\psi_0}{\partial\eta^2}=0,\quad \frac{\partial\theta_0}{\partial\eta}=0$$

$$\eta=1:\ \psi_0=0,\quad \frac{\partial\psi_0}{\partial\eta}=0,\quad \theta_0=0 \tag{23}$$

First-Order Equations ($\sim(1/\bar{\delta})(\partial\bar{\delta}/\partial\xi)$).

$$\frac{\partial\psi_0}{\partial\eta}\frac{\partial^3\psi_1}{\partial\xi\partial\eta^2}+\frac{\partial\psi_1}{\partial\eta}\frac{\partial^3\psi_0}{\partial\xi\partial\eta^2}-\frac{\partial\psi_1}{\partial\xi}\frac{\partial^3\psi_0}{\partial\eta^3}-\frac{\partial\psi_0}{\partial\xi}\frac{\partial^3\psi_1}{\partial\eta^3}=\frac{\partial^4\psi_1}{\partial\eta^4}+2\frac{\partial\psi_0}{\partial\eta}\frac{\partial^2\psi_0}{\partial\eta^2} \tag{24}$$

$$\frac{\partial\psi_0}{\partial\eta}\frac{\partial\theta_1}{\partial\xi}-\frac{\partial\psi_0}{\partial\xi}\frac{\partial\theta_1}{\partial\eta}=\frac{1}{\mathrm{Pr}}\frac{\partial^2\theta_1}{\partial\eta^2}-\frac{\partial\psi_1}{\partial\eta}\frac{\partial\theta_0}{\partial\xi}+\frac{\partial\theta_0}{\partial\eta}\frac{\partial\psi_1}{\partial\xi} \tag{25}$$

with the homogeneous boundary conditions

$$\xi=0:\ \psi_1=0,\quad \theta_1=0$$

$$\eta=0:\ \psi_1=0,\quad \frac{\partial^2\psi_1}{\partial\eta^2}=0,\quad \frac{\partial\theta_1}{\partial\eta}=0$$

$$\eta=1:\ \psi_1=0,\quad \frac{\partial\psi_1}{\partial\eta}=0,\quad \theta_1=0 \tag{26}$$

It should be noted that only the zero-order and first-order problem are given here. This is done in view of the fact that only these two problems will be solved subsequently. The extrapolation to higher-order problems is straightforward, because the perturbation equations can be solved in succession.

The zero-order equation, Eq. (21), for the streamfunction, with the boundary conditions given by Eq. (23), can easily be solved. The resulting expression for ψ_0 is

$$\psi_0=\frac{3}{2}\left(\eta-\frac{1}{3}\eta^3\right)-1 \tag{27}$$

Equation (27) states the fact that the axial velocity profile is parabolic through the whole chill region. After inserting the expression for the streamfunction ψ_0 into the energy Eq. (22), the following Graetz problem will be obtained:

$$\frac{3}{2}(1-\eta^2)\frac{\partial\theta_0}{\partial\xi}=\frac{1}{\mathrm{Pr}}\frac{\partial^2\theta_0}{\partial\eta^2} \tag{28}$$

Equation (28) can be solved easily by applying the method of separation of variables to θ_0 in the form

$$\theta_0=F(\eta)H(\xi) \tag{29}$$

The temperature distribution θ_0, which satisfies Eq. (28) and the given boundary conditions according to Eq. (23), is found to be

$$\theta_0=\sum_{n=1}^{\infty}A_nF_n(\eta)\exp\left(-\frac{2}{3}\frac{\xi}{\mathrm{Pr}}\lambda_n^2\right) \tag{30}$$

The eigenvalues λ_n^2 and the constants A_n are given for example by Shah and London (1978). It is interesting to note that the zero-order solution for the velocity and temperature distributions in the fluid represents those given by Lee and Zerkle (1969) for steady-state conditions. Hence, it can be concluded that Lee and Zerkle (1969) ignored in their analysis the effect of acceleration due to converging ice layers on the velocity and temperature distributions in the fluid and calculated the thermal development of a hydrodynamically fully developed flow in the transformed (ξ, η) plane.

Inserting the expression for the streamfunction ψ_0, Eq. (27), into Eq. (24), results in the following linear partial differential equation for ψ_1:

$$\frac{3}{2}(1-\eta^2)\frac{\partial^3\psi_1}{\partial\xi\partial\eta^2}+3\frac{\partial\psi_1}{\partial\xi}=\frac{\partial^4\psi_1}{\partial\eta^4}-9\eta(1-\eta^2) \tag{31}$$

with the boundary conditions given by Eq. (26). Equation (31) can be solved with the aid of the Laplace transform

$$L\{\psi_1(\xi,\eta)\}\equiv\int_0^{\infty}\psi_1(\xi,\eta)\exp(-s\xi)d\xi\equiv\bar{\psi}_1(s,\eta) \tag{32}$$

with respect to the axial coordinate ξ. This results in an ordinary differential equation for the transformed function $\bar{\psi}_1$

$$\frac{3}{2}(1-\eta^2)\, s\frac{d^2\bar{\psi}_1}{d\eta^2}+3s\bar{\psi}_1=\frac{d^4\bar{\psi}_1}{d\eta^4}+\frac{9}{s}(\eta^3-\eta) \tag{33}$$

with the transformed boundary conditions

$$\eta=0:\ \bar{\psi}_1=0,\quad \frac{d^2\bar{\psi}_1}{d\eta^2}=0$$

$$\eta=1:\ \bar{\psi}_1=0,\quad \frac{d\bar{\psi}_1}{d\eta}=0 \tag{34}$$

Equation (33) can be solved by assuming a series solution for $\bar{\psi}_1$ of the form

$$\bar{\psi}_1=\sum_{\nu=1}^{\infty} a_{2\nu-1}\eta^{2\nu-1}+\sum_{\nu=1}^{\infty} a_{2\nu}\eta^{2\nu} \tag{35}$$

Inserting the above given power series for $\bar{\psi}_1$ into the differential Eq. (33) and into the boundary conditions (34), it can easily be shown that the coefficients $a_{2\nu}$ for the even-powered terms are identically zero. Therefore, the first sum appearing in Eq. (35) represents the complete solution for $\bar{\psi}_1$:

$$\bar{\psi}_1=\sum_{\nu=1}^{\infty} a_{2\nu-1}\eta^{2\nu-1} \tag{36}$$

It is obvious that Eq. (36) automatically satisfies the boundary conditions on $\bar{\psi}_1$ for $\eta=0$. Using expression (36) for $\bar{\psi}_1$ in Eqs. (33) and (34) results in a system of infinite coupled linear algebraic equations for the unknown $a_{2\nu-1}$.

The power series solutions for $\bar{\psi}_1$ converges very rapidly with an increasing number of terms for arbitrary values of s. Therefore, only a five-term expansion was used to approximate the distribution of $\bar{\psi}_1$. After calculating the coefficients $a_1, \ldots, a_9$, a rational function for $\bar{\psi}_1$ of s and η is obtained. Using partial fraction expansions, $\bar{\psi}_1$ can be written as

$$\bar{\psi}_1=\frac{A(\eta)}{s+b}+\frac{B(\eta)s+C(\eta)}{(s+a)^2+\omega^2}+\frac{1}{s}f_2(\eta) \tag{37}$$

with the following abbreviations:

$$f_0(\eta)=\frac{1}{149}(-840\eta^9+3312\eta^7-7056\eta^5+7536\eta^3-2952\eta)$$

$$f_1(\eta)=\frac{1}{5215}(1575\eta^9+1302\eta^7-8379\eta^5+6552\eta^3-1050\eta)$$

$$f_2(\eta)=\frac{1}{840}(-9\eta^7+63\eta^5-99\eta^3+45\eta)$$

$$A(\eta)=\frac{f_0(\eta)-bf_1(\eta)-b^2f_2(\eta)}{\omega^2+(a-b)^2}$$

$$B(\eta)=-(f_2(\eta)+A(\eta))$$

$$C(\eta)=-\frac{\omega^2+a^2}{b}A(\eta)-f_0(\eta) \tag{38}$$

and the constants

$$a=5.04390800,\ b=11.80480144,\ \omega=22.57064595 \tag{39}$$

The inverse Laplace transformation $\bar{\psi}_1$, according to Eq. (37), can be obtained directly from existing tables of transforms (see, e.g., Andrews and Shivamoggi, 1988). This results in

$$\psi_1(\xi,\eta)=A(\eta)\exp(-b\xi)+\exp(-a\xi)\times\left[B(\eta)\left(\cos(\omega\xi)-\frac{a}{\omega}\sin(\omega\xi)\right)+\frac{C(\eta)}{\omega}\sin(\omega\xi)\right]+f_2(\eta) \tag{40}$$

The functions $f_0(\eta)$, $f_1(\eta)$, and $f_2(\eta)$ satisfy independently the boundary conditions for $\eta=0$ and $\eta=1$, according to Eq. (26).

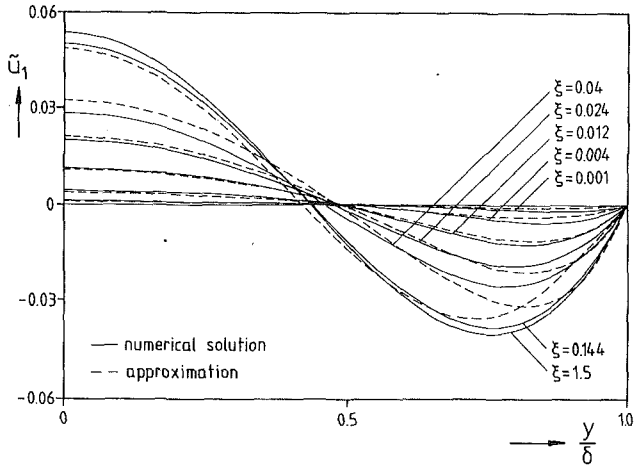

Fig. 2 Perturbation velocity $\tilde{u}_1$ as a function of η for various values of the axial coordinate ξ

The function $f_2(\eta)$, which appears as the last term on the right-hand side of Eq. (40), represents the solution of Eq. (31) for large values of ξ. Further, it is interesting to note that the monotonously decreasing part of the solution $A(\eta)\exp(-b\xi)$ tends more rapidly to zero for increasing values of ξ than the second term on the right-hand side Eq. (40), which contains oscillating terms in ξ. In order to check the accuracy of the given solution for ψ_1, the linear partial differential Eq. (31), with the boundary conditions (26), was solved numerically with a finite-difference method. The applied implicit finite-difference scheme was the Keller-box method (Cebeci and Bradshaw, 1984). This method has several very desirable features that make it appropriate for the solution of parabolic partial differential equations. One of them is that it allows nonuniform ξ and η spacings by second-order accuracy. Because the box scheme is a common method for solving parabolic differential equations, only a brief outline is provided here. First of all, the parabolic differential equation of order n is reduced to a system of n first-order equations. These equations were approximated by difference equations, using central differences at each nodal point. The ensuing algebraic equations, which show a block tridiagonal structure, can be solved easily.

The numerical calculations concerning Eq. (31) were performed with the help of a uniform grid in the ξ and η directions. Numerical runs showed that approximately 50 points in the η direction and approximately 400 points in the axial direction ($0 \le \xi \le 1.6$) guaranteed sufficient accuracy.

Figure 2 shows the perturbation velocity $\tilde{u}_1=\partial\psi_1/\partial\eta$ calculated from Eq. (40), compared with the numerical solution of Eq. (31). It can be seen that the simple five-term expansion, according to Eq. (40), approximates the numerical solution quite well. Only for greater values of the axial coordinate, the deviation from the numerical calculation is more pronounced. However, for $\xi\to\infty$, the perturbation velocity $\tilde{u}_1$, calculated from Eq. (40), and the numerically calculated distributions are identical.

Inserting the expressions for the streamfunctions ψ_0 and ψ_1, given by Eqs. (27) and (40), respectively, into the energy Eq. (25) for the quantity θ_1, the following partial differential equation for θ_1 can be obtained by using Eq. (30) for θ_0:

$$\frac{3}{2}(1-\eta^2)\frac{\partial\theta_1}{\partial\xi}-\frac{1}{\mathrm{Pr}}\frac{\partial^2\theta_1}{\partial\eta^2}=\frac{\partial\psi_1}{\partial\xi}\sum_{n=1}^{\infty}A_nF_n'(\eta)\exp\left(-\frac{2}{3}\frac{\xi}{\mathrm{Pr}}\lambda_n^2\right)+\frac{\partial\psi_1}{\partial\eta}\sum_{n=1}^{\infty}\frac{2}{3\mathrm{Pr}}\lambda_n^2A_nF_n(\eta)\exp\left(-\frac{2}{3}\frac{\xi}{\mathrm{Pr}}\lambda_n^2\right) \tag{41}$$

The boundary conditions belonging to Eq. (41) are

$$\xi = 0:\ \theta_1 = 0$$

$$\eta = 0:\ \frac{\partial \theta_1}{\partial \eta} = 0$$

$$\eta = 1:\ \theta_1 = 0 \tag{42}$$

By ignoring all terms on the right-hand side of Eq. (41) it can be seen that the resulting homogeneous equation reduces to Eq. (28). Therefore, the solution of Eq. (41) can be assumed in the form (see, e.g., Myers, 1987)

$$\theta_1 = \sum_{m=1}^{\infty} B_m(\xi) F_m(\eta) \tag{43}$$

Equation (43) satisfies identically the boundary conditions on θ_1 for $\eta = 0$ and $\eta = 1$ because of the used eigenfunctions $F_m(\eta)$ according to Eq. (30). Inserting the expression for θ_1, given by Eq. (43), into Eq. (41) and using the orthogonality relation for the eigenfunctions $F_m(\eta)$, results in a linear differential equation for the functions $B_m(\xi)$

$$\frac{dB_m(\xi)}{d\xi} = -\frac{2}{3}\frac{\lambda_m^2}{\mathrm{Pr}} B_m(\xi) + \frac{2}{3}\frac{1}{K_m}\int_0^1 F_m(\eta) Q(\xi, \eta) d\eta \tag{44}$$

with the abbreviations

$$K_m = \int_0^1 (1-\eta^2)\, F_m^2(\eta) d\eta$$

$$Q(\xi, \eta) = \frac{\partial \psi_1}{\partial \xi}\sum_{n=1}^{\infty} A_n F_n'(\eta) \exp\left(-\frac{2}{3}\frac{\xi}{\mathrm{Pr}}\lambda_n^2\right) + \frac{\partial \psi_1}{\partial \eta}\sum_{n=1}^{\infty}\frac{2}{3\mathrm{Pr}}\lambda_n^2 A_n F_n(\eta) \exp\left(-\frac{2}{3}\frac{\xi}{\mathrm{Pr}}\lambda_n^2\right) \tag{45}$$

The resulting boundary condition for $B_m(\xi)$ was obtained from Eq. (42)

$$\xi = 0:\ B_m = 0 \tag{46}$$

Equation (44) can be solved analytically. After some routine but rather longish algebra the following expression for $B_m(\xi)$ was obtained:

$$\begin{aligned} B_m(\xi) = {} & \frac{2}{3}\frac{1}{K_m}\sum_{n=1}^{\infty}\int_0^1 A_n F_n'(\eta) F_m(\eta) \left(\exp\left(-\frac{2}{3}\frac{\xi}{\mathrm{Pr}}\lambda_n^2\right) \times D_1(\xi, \eta) - \exp\left(-\frac{2}{3}\frac{\xi}{\mathrm{Pr}}\lambda_m^2\right) D_1(0, \eta)\right) d\eta \\ & + \frac{4}{9}\frac{1}{K_m \mathrm{Pr}}\sum_{n=1}^{\infty}\int_0^1 \lambda_n^2 A_n F_n(\eta) F_m(\eta) \left(\exp\left(-\frac{2}{3}\frac{\xi}{\mathrm{Pr}}\lambda_n^2\right) \times D_2(\xi, \eta) - \exp\left(-\frac{2}{3}\frac{\xi}{\mathrm{Pr}}\lambda_m^2\right) D_2(0, \eta)\right) d\eta \\ & + \frac{4}{9}\frac{1}{K_m \mathrm{Pr}}\sum_{n=1,\, m\neq n}^{\infty}\int_0^1 \frac{\lambda_n^2 A_n F_n(\eta) F_m(\eta)}{\frac{2}{3\mathrm{Pr}}(\tilde{\lambda}_m^2 - \tilde{\lambda}_n^2)} \left(\exp\left(-\frac{2}{3}\frac{\xi}{\mathrm{Pr}}\lambda_n^2\right) \times D_3(\xi, \eta) - \exp\left(-\frac{2}{3}\frac{\xi}{\mathrm{Pr}}\lambda_m^2\right) D_3(0, \eta)\right) d\eta \\ & + \frac{4}{9}\frac{\xi}{K_m \mathrm{Pr}}\exp\left(-\frac{2}{3}\frac{\xi}{\mathrm{Pr}}\lambda_m^2\right)\int_0^1 \lambda_m^2 A_m F_m^2(\eta) D_3(\xi, \eta)\, d\eta \end{aligned} \tag{47}$$

In Eq. (47) the functions $D_1(\xi, \eta)$, $D_2(\xi, \eta)$ and $D_3(\xi, \eta)$ were used. These functions are given by

$$D_1(\xi, \eta) = \frac{bA(\eta)}{\frac{2}{3\mathrm{Pr}}(\tilde{\lambda}_m^2 - \tilde{\lambda}_n^2) + b} \exp(b\xi) + \frac{1}{\left(\frac{2}{3\mathrm{Pr}}(\tilde{\lambda}_m^2 - \tilde{\lambda}_n^2) + a\right)^2 + \omega^2} \exp(a\xi) + \left[\left(B(\eta)\frac{a^2}{\omega} + C(\eta)\frac{a}{\omega} - B(\eta)\omega\right)\left(\left(\frac{2}{3\mathrm{Pr}}(\tilde{\lambda}_m^2 - \tilde{\lambda}_n^2) + a\right) \times \sin(\omega\xi) - \omega\cos(\omega\xi)\right)\left(2B(\eta)a + C(\eta)\right) \times \left(\left(\frac{2}{3\mathrm{Pr}}\left(\tilde{\lambda}_m^2 - \tilde{\lambda}_n^2\right) + a\right)\cos(\omega\xi) + \omega\sin(\omega\xi)\right)\right]$$

$$D_2(\xi, \eta) = \frac{A'(\eta)}{\frac{2}{3\mathrm{Pr}}(\tilde{\lambda}_m^2 - \tilde{\lambda}_n^2) + b} \exp(b\xi) + \frac{1}{\left(\frac{2}{3\mathrm{Pr}}(\tilde{\lambda}_m^2 - \tilde{\lambda}_n^2) + a\right)^2 + \omega^2} \exp(a\xi) \left[B'(\eta)\left(\left(\frac{2}{3\mathrm{Pr}}(\tilde{\lambda}_m^2 - \tilde{\lambda}_n^2) + a\right)\cos(\omega\xi) + \omega\sin(\omega\xi)\right) + \left(\frac{C'(\eta)}{\omega} + B'(\eta)\frac{a}{\omega}\right)\left(\left(\frac{2}{3\mathrm{Pr}}\left(\tilde{\lambda}_m^2 - \tilde{\lambda}_n^2\right) + a\right)\sin(\omega\xi) - \cos(\omega\xi)\right)\right]$$

$$D_3(\xi, \eta) = \frac{9}{168} - \frac{99}{280}\eta^2 + \frac{9}{24}\eta^4 - \frac{9}{120}\eta^6 \tag{48}$$

Inserting Eq. (47) into Eq. (43) results in the solution θ_1, which satisfies the given boundary conditions according to Eq. (42).

The Temperature Distribution in the Solid Region. With the boundary conditions (9), the temperature distribution in the solid phase is easily calculated from Eq. (8). The temperature distribution adopts the following form:

$$\theta_S = \frac{1-\tilde{y}}{1-\tilde{\delta}} \tag{49}$$

The temperature gradient at the solid-liquid interface is given in dimensionless form by

$$\frac{\partial \theta_S}{\partial \tilde{y}} = -\frac{1}{1-\tilde{\delta}} \tag{50}$$

The Solid-Liquid Interface. After solving Eqs. (21)–(26), the temperature gradient in the fluid at the solid-liquid interface is known. Therefore, the development of the ice layer thickness can be calculated from Eq. (10) at every axial position. Introducing Eq. (50) into Eq. (10) results in

$$\left(\frac{\partial \tilde{\delta}}{\partial \tau}\right)_{\tilde{x}} = \frac{1}{\tilde{\delta} - 1} - \frac{1}{B\tilde{\delta}}\frac{\partial \theta}{\partial \eta}\bigg|_{\eta=1} \tag{51}$$

in which terms of the order $(\partial^2\tilde{\delta}/\partial\xi^2)$ were neglected.

The temperature gradient in the fluid at the solid-liquid interface, which appears in Eq. (51), is given by

$$\frac{\partial \theta}{\partial \eta}\bigg|_{\eta=1} = \frac{\partial \theta_0}{\partial \eta}\bigg|_{\eta=1} + \frac{1}{\tilde{\delta}}\frac{\partial \tilde{\delta}}{\partial \xi}\frac{\partial \theta_1}{\partial \eta}\bigg|_{\eta=1} + \ldots \tag{52}$$

with the known functions $\partial\theta_0/\partial\eta|_{\eta=1}$ and $\partial\theta_1/\partial\eta|_{\eta=1}$, which can be calculated from Eqs. (30) and (43) by differentiating the expressions with respect to η and evaluating the resulting functions at $\eta = 1$. It should be noted here that $\partial\theta_0/\partial\theta\eta|_{\eta=1}$

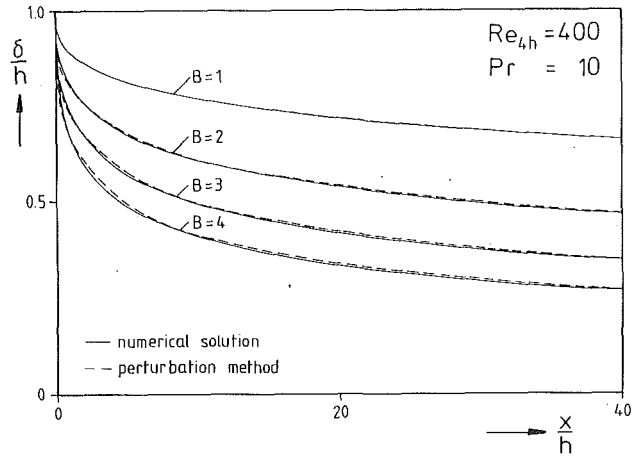

Fig. 3 Steady-state ice layer thickness as a function of x/h for $Re_{4h} = 400$, $Pr = 10$, and various B

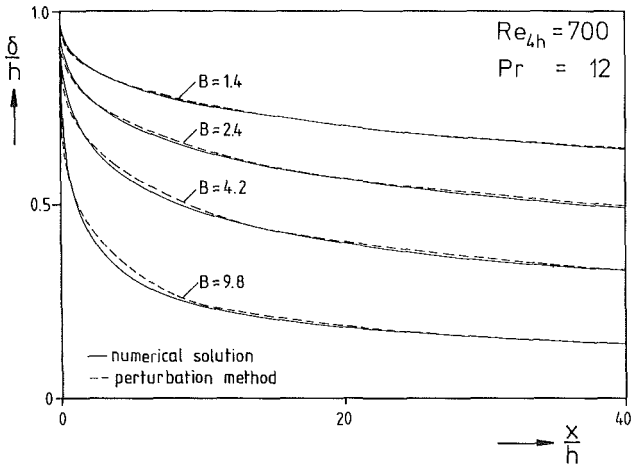

Fig. 4 Steady-state ice layer thickness as a function of x/h for $Re_{4h} = 700$, $Pr = 12$, and various B

and $\partial\theta_1/\partial\eta|_{\eta=1}$ are only functions of ξ and Pr. They do not depend explicitly on $\tilde{\delta}$ or Re_h.

Equation (51) is a nonlinear integrodifferential equation, because the derivation of $\tilde{\delta}$ with time has to be taken at constant $\tilde{x}$ and the temperature gradient in the fluid at the solid–liquid interface is a function of the integral coordinate ξ, defined in Eq. (13).

By ignoring terms of the order $(\partial\tilde{\delta}/\partial\tilde{x})$ in Eqs. (51) and (52), Weigand and Beer (1992) were able to derive a simple approximative solution for the transient development of the frozen layer. They obtained the free channel height $\tilde{\delta}$ as an implicit function of $\xi/Re_h/Pr$ for a given value of the freezing parameter B. The distribution of $\tilde{\delta}$ for the steady-state solution and for a parabolic entrance velocity profile was identical to the solution given by Lee and Zerkle (1969).

Taking terms into account of the order $(\partial\tilde{\delta}/\partial\tilde{x})$ in Eqs. (51) and (52), Eq. (51) must be integrated numerically. This was done by using the Runge–Kutta method. Approximately 200 grid points in the axial direction were used for the calculation of the development of the frozen crust at the cooled channel walls ($0 \le \tilde{x} \le 20$). The calculations were performed with a time step $\Delta\tau$ of approximately 10^{-4}. It must be pointed out that the calculation of $\tilde{\delta}$ at each time step involves an iteration, because the perturbation quantity $(1/\tilde{\delta})(\partial\tilde{\delta}/\partial\xi)$ for the temperature gradient at the solid–liquid interface appears in Eq. (52) and, therefore, Eqs. (51) to (52) are coupled. However, by performing some numerical calculations, it could be shown that the perturbation quantity $(1/\tilde{\delta})(\partial\tilde{\delta}/\partial\xi)$, appearing in Eq. (52), could be approximated with good accuracy by taking the zero-order solution of Weigand and Beer (1992). This makes superfluous the iteration for $\tilde{\delta}$ at a fixed value of time. The resulting error is negligible (the ice layers obtained with the two methods coincide). The steady-state solution was reached, if

$$\left|\frac{\partial\tilde{\delta}}{\partial\tau}\right|_{\tilde{x}} < 10^{-4}; \quad \tilde{x} = \frac{L}{h} \tag{53}$$

was satisified at the end of the cooled test section.

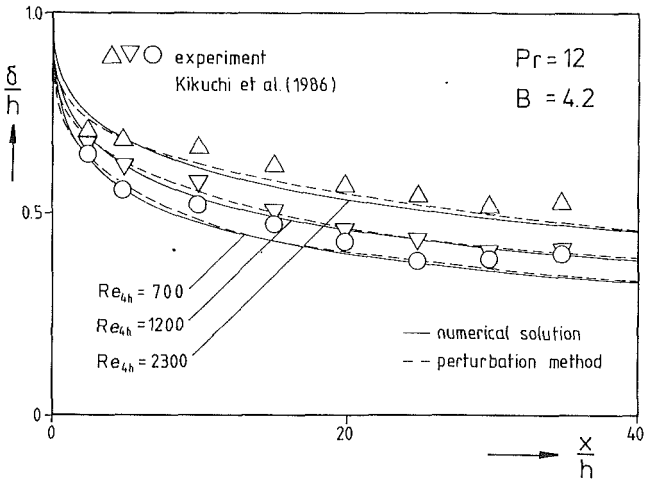

Fig. 5 Effect of Reynolds number on the axial distribution of $\tilde{\delta}$ for $Pr = 12$ and $B = 4.2$

Results and Discussion

Steady-State Freezing Fronts. The validity of the given perturbation analysis will be checked for the steady-state solution. This yields an upper limit of error, as $(1/\tilde{\delta})(\partial\tilde{\delta}/\partial\xi)$ will reach its maximum for steady-state conditions. In Figs. 3 and 4 the steady-state ice layer thickness is plotted as a function of the dimensionless downstream coordinate x/h. It can be observed that the ice layer thickness increases with growing values of B for a given Reynolds number. The two figures elucidate the deviation of the presented perturbation solution from the numerical calculation. The numerical solution was obtained by solving Eqs. (1)–(6) with a finite-difference scheme (Weigand and Beer, 1991). It can be seen that the perturbation solution is in good agreement with the numerical calculations, also for high values of the cooling parameter B, as it is shown in Fig. 4 for $B = 9.8$.

Figure 5 elucidates the effect of increasing Reynolds number on the axial distribution of $\tilde{\delta}$ for $B = 4.2$ and $Pr = 12$, compared with experimental data of Kikuchi et al. (1986). It is obvious that the ice layer thickness decreases with an increasing Reynolds number. This is due to the increasing heat flux from the liquid to the solid–liquid interface for growing values of Re_{4h}. The calculated results agree well with measurements of Kikuchi et al. (1986). It can also be observed that the deviation between the numerically calculated ice layers and the perturbation solution increases with growing Reynolds number, because the perturbation quantity is proportional to Re_{4h}. Therefore, the perturbation solution will approximate the numerical solution closer for smaller values of $(1/\tilde{\delta})(\partial\tilde{\delta}/\partial\xi)$.

In case of the experimental results for $Re_{4h} = 2300$, plotted in Fig. 5, the flow was still laminar. This is because of the acceleration of the flow due to converging ice layers, which tends to stabilize the laminar boundary layer and shifts the transitional Reynolds number to higher values.

The accuracy of the given perturbation analysis can be checked more precisely by comparing the axial velocity distribution given by Eqs. (27) and (40) with numerically calcu-

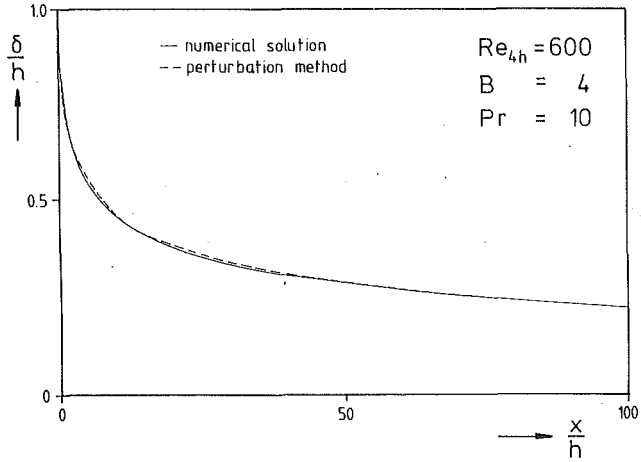

Fig. 6 Steady-state ice layer thickness as a function of x/h for $Re_{4h} = 400$, $Pr = 10$, and $B = 4$

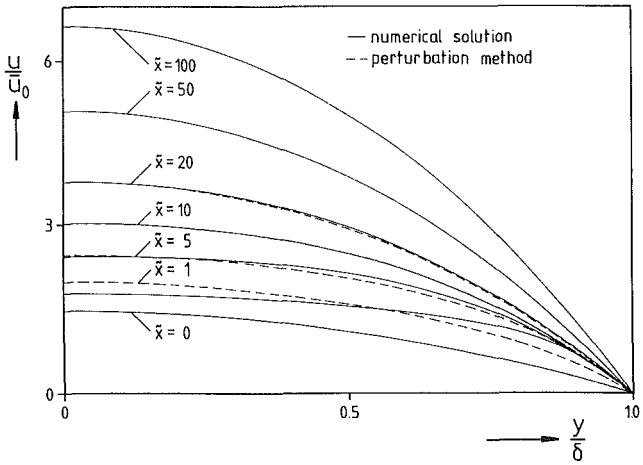

Fig. 7 Axial velocity distributions $u/\bar{u}_0$ for various x/h

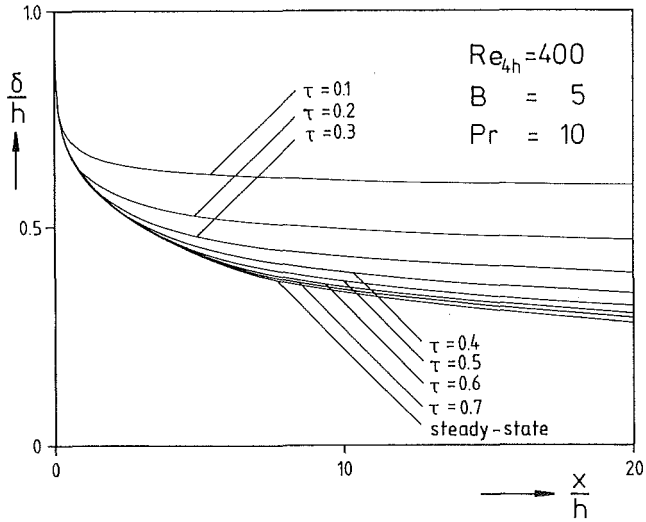

Fig. 8 Transient development of the freezing front as a function of x/h

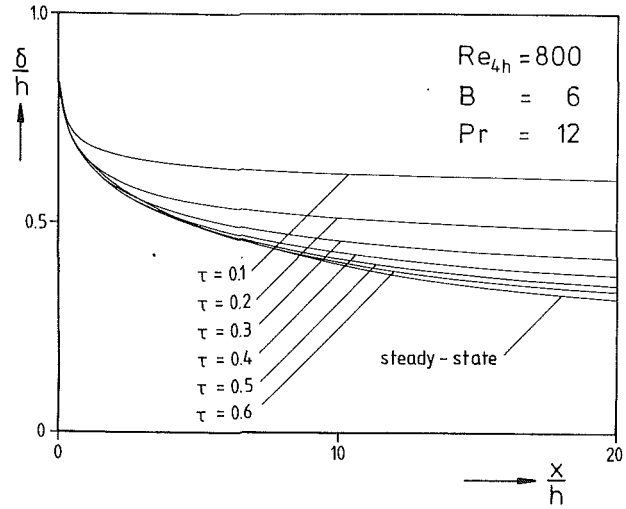

Fig. 9 Transient development of the freezing front as a function of x/h

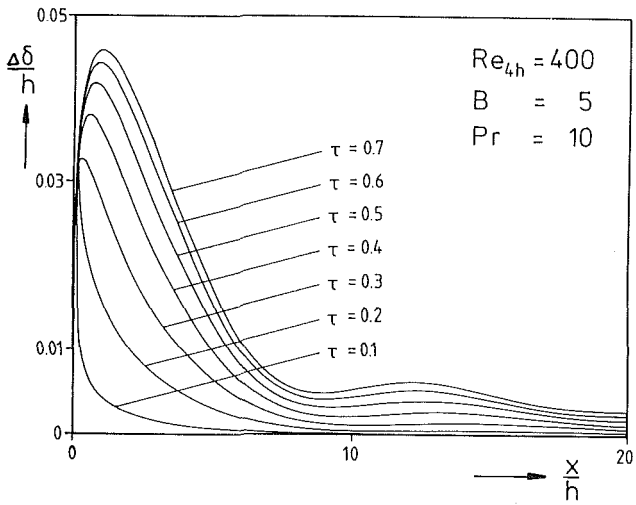

Fig. 10 Development of the absolute deviation between the perturbation solution and the approximation according to Weigand and Beer (1992) as a function of x/h

lated values. Figure 6 shows a steady-state ice layer for $Re_{4h} = 600$, $Pr = 12$. It can be observed that the numerical solution for $\tilde{\delta}$ and the results obtained by the perturbation analysis nearly coincide.

Figure 7 illustrates the development of the axial velocity profile for the ice layer shown in Fig. 6. The axial velocity is scaled with the axial mean velocity $\bar{u}_0$ at the entrance of the chill region. The profiles elucidate the effect of acceleration due to converging ice layers for various axial positions. It can be seen that the profiles are flattened for small values of the axial coordinate, while they approach a nearly parabolic shape for large values of the axial coordinate. The profiles obtained by the perturbation analysis are in good agreement with the numerical calculations, except for $\tilde{x} = 1$, where the deviation between the two solutions is more pronounced. This can be attributed to the sharply increasing ice layer thickness near the entrance of the test section. Consequently, the term $\partial\tilde{\delta}/\partial\tilde{x}$ adopts higher values in this region and the linearization of the conservation equations given by Eq. (19) may lead to some error. Nevertheless, the agreement between the numerical calculation and the perturbation solution is very good for $\tilde{x} > 5$.

Transient Development of the Freezing Fronts. Figures 8 and 9 illustrate the time-dependent development of the freezing fronts at the channel walls for different values of the cooling parameter B. In the early stage of the freezing process the ice layer thickness remains approximately constant over the channel length, except for the near entrance region, as can be seen from Fig. 8 for $\tau = 0.1$. This is evidenced by Eq. (51). If one excludes small values of the axial coordinate $\tilde{x}$, the first term on the right-hand side of Eq. (51) dominates the second term.

This means that for small values of τ the growth of the frozen layer at the channel walls is dominated by heat conduction in the thin ice layer.

Because there exists no numerical solution concerning the quasi-steady development of the ice layer in a planar channel, the given results can only be compared with the approximate solution of Weigand and Beer (1992). Figure 10 shows the distribution of the absolute deviation between the perturbation solution and the approximation during the transient development of the ice layer shown in Fig. 8. It is evident that the maximum deviation is obtained for steady-state conditions, because the solution of Weigand and Beer (1992) coincides with the approximation of Lee and Zerkle (1969) for the stationary case. Moreover it can be seen that the deviation between the two solutions is maximum for small values of x/h. This can be easily understood if one recognizes that the quantity $\partial\tilde{\delta}/\partial\tilde{x}$ reaches its maximum for low values of the axial coordinate. Because the effect of this term on the distribution of the ice layer thickness was ignored in the analysis of Lee and Zerkle (1969) and Weigand and Beer (1992), the maximum deviation must be in this region. However, the deviation $\Delta\tilde{\delta}$ between the two solutions is smaller than 0.05. Therefore, it can be stated that the solution given by Weigand and Beer (1992) approximates the time-dependent development of the freezing fronts in a cooled parallel plate channel relatively well.

Conclusions

A quite flexible method has been developed for calculating the velocity and temperature distributions in a planar channel with arbitrarily shaped walls under the assumptions that the perturbation quantity $(1/\tilde{\delta})(\partial\tilde{\delta}/\partial\xi)$ is sufficiently small. The applicability of the method was provided by calculating the transient development of the ice layers in a parallel plate channel for quasi-steady conditions. By comparing the obtained steady-state solutions with the numerical calculations of Weigand and Beer (1991) and the experiments of Kikuchi et al. (1986), it was demonstrated that the perturbation solution yields sufficient accuracy for a wide range of Reynolds numbers and cooling parameters B.

It could be shown that the transformed Navier–Stokes equations and the energy equation, for the quasi-steady conditions and written in ξ, η coordinates, contain only powers and derivatives of $(1/\tilde{\delta})(\partial\tilde{\delta}/\partial\xi)$, but not explicitly $\tilde{\delta}^n$. Therefore, application of this method to the complete conservation equations for quasi-steady conditions is straightforward.

References

Andrews, L. C., and Shivamoggi, B. K., 1988, *Integral Transforms for Engineers and Applied Mathematicians*, Macmillan, New York.

Bennon, W. D., and Incropera, F. P., 1988, "Developing Laminar Mixed Convection With Solidification in a Vertical Channel," ASME JOURNAL OF HEAT TRANSFER, Vol. 110, pp. 410–415.

Bilenas, J. A., and Jiji, L. M., 1970, "Numerical Solution of a Nonlinear Free Boundary Problem of Axisymmetric Fluid Flow in Tubes With Solidification," *Proceedings, 4th International Heat Transfer Conference*, Vol. 1, pp. 1–11.

Cebeci, T., and Chang, K. C., 1978, "A General Method for Calculating Momentum and Heat Transfer in Laminar and Turbulent Duct Flows," *Numerical Heat Transfer*, Vol. 1, pp. 39–68.

Cebeci, T., and Bradshaw, P., 1984, *Physical and Computational Aspects of Convective Heat Transfer*, Springer, New York.

Cervantes, J., Trevino, C., and Méndez, F., 1990, "An Asymptotic Analysis for the Transient Freezing and Laminar Flow in a Circular Pipe," *Proceedings, 9th International Heat Transfer Conference*, Vol. 4, pp. 321–326.

Chida, K., 1983, "Heat Transfer in Steady Laminar Pipe Flow With Liquid Solidification," *Heat Transfer: Japanese Research*, Vol. 81, pp. 81–94.

Kikuchi, Y., Shigemasa, Y., Oe, A., and Ogata, T., 1986, "Steady-State Freezing of Liquids in Laminar Flow Between Two Parallel Plates," *Journal of Nuclear Science and Technology*, Vol. 23, pp. 979–991.

Lee, D. G., and Zerkle, R. D., 1969, "The Effect of Liquid Solidification in a Parallel-Plate Channel Upon Laminar-Flow Heat Transfer and Pressure Drop," ASME JOURNAL OF HEAT TRANSFER, Vol. 91, pp. 583–585.

Myers, G. E., 1987, *Analytical Methods in Conduction Heat Transfer*, Genium Publishing Corporation, Schenectady, NY.

Özişik, M. N., and Mulligan, J. C., 1969, "Transient Freezing of Liquids in Forced Flow Inside Circular Tubes," ASME JOURNAL OF HEAT TRANSFER, Vol. 26, pp. 233–240.

Shah, R. K., and London, A. L., 1978, "Laminar Flow Forced Convection in Ducts," *Advances in Heat Transfer*, Academic Press, New York.

Weigand, B., and Beer, H., 1991, "Heat Transfer and Solidification of a Laminar Liquid Flow in a Cooled Parallel Plate Channel: The Stationary Case," *Wärme- und Stoffübertragung*, Vol. 26, pp. 233–240.

Weigand, B., and Beer, H., 1992, "Transient Freezing of Liquids in Forced Laminar Flow Inside a Parallel Plate Channel," *Wärme- und Stoffübertragung*, Vol. 27, pp. 77–84.

Zerkle, R. D., and Sunderland, J. E., 1968, "The Effect of Liquid Solidification in a Tube Upon Laminar-Flow Heat Transfer and Pressure Drop," ASME JOURNAL OF HEAT TRANSFER, Vol. 90, pp. 183–190.

Magnetically Damped Convection During Solidification of a Binary Metal Alloy

P. J. Prescott

F. P. Incropera

Heat Transfer Laboratory,
School of Mechanical Engineering,
Purdue University,
West Lafayette, IN 47907

The transient transport of momentum, energy, and species during solidification of a Pb–19 percent Sn alloy is numerically simulated with and without magnetic damping. The system is contained in an axisymmetric, annular mold, which is cooled along its outer vertical wall. Since thermosolutal convection accompanies solidification and is responsible for final macrosegregation patterns, application of a steady magnetic field, which is parallel to the axis of the mold, has the potential to reduce macrosegregation by damping buoyancy-driven flow during solidification. Results show that, during early stages of solidification, the magnetic field significantly affects thermally driven flow in the melt, as well as interactions between thermally and solutally driven flows. However, interdendritic flows and macrosegregation patterns are not significantly altered by moderate magnetic fields. Scaling analysis reveals that extremely strong fields would be required to effectively dampen convection patterns that contribute to macrosegregation.

1 Introduction

It is well known that buoyancy-induced flow during the solidification of alloys is the major cause of macrosegregation in ingots (Flemings, 1974; Fisher, 1981). Buoyancy forces arise from temperature and solute concentration gradients in interdendritic liquid, and macrosegregation refers to large-scale redistribution of solute in the fully solidified ingot. Recent modeling efforts have successfully predicted various forms of macrosegregation in binary alloys (Bennon and Incropera, 1987c; Neilson and Incropera, 1991; Prescott and Incropera, 1991) and have related segregation patterns to fluid flow phenomena that accompany the freezing process. Similar solidification models amenable to numerical solution also appear in the literature (Voller and Prakash, 1987; Beckermann and Viskanta, 1988; Voller et al., 1989; Ganesan and Poirier, 1990; Poirier et al., 1991; Felicelli et al., 1991; Amberg, 1991; Heinrich et al., 1991; Oldenburg and Spera, 1991), and reviews of existing models are available (Viskanta and Beckermann, 1987; Viskanta, 1988, 1990; Rappaz, 1989). In addition, complete two-phase models for solidification of binary mixtures are emerging (Prakash, 1990a, b; Ni and Beckermann, 1991; Beckermann and Ni, 1992).

Naturally occurring fluid flow in binary solidification systems may be altered in different ways. For example, solutally driven flow in the two-phase (mushy) zone may be controlled indirectly by increasing the freezing rate (Prescott and Incropera, 1991), which increases the rate at which the dendritic array becomes less permeable to fluid flow. Other means of altering convection patterns include changing the initial superheat of the melt, imparting centrifugal forces by rotating the mold, and imposing a magnetic field on the system.

The purpose of this study is to investigate the effects of magnetic damping on thermosolutal convection during solidification of a binary metal alloy and on the resulting macrosegregation. Magnetic damping forces are included in a continuum model for momentum, energy, and species transport in binary, solid–liquid phase change systems (Bennon and Incropera, 1987a), and numerical simulations are performed to assess the effects of a uniform magnetic field, aligned with the vertical axis of an axisymmetric, annular mold, on fluid flow and macrosegregation during the solidification of a Pb–19 percent Sn alloy. This composition is attractive by virtue of its wide freezing range ($T_{LIQ} - T_{SOL} = 96°C$) and hence its susceptibility to macrosegregation.

Magnetic damping occurs when an electrically conducting fluid flows transversely to a steady magnetic induction field. An electric current is induced

$$\mathbf{J} = \sigma_e \mathbf{V} \times \mathbf{B} \tag{1}$$

which, in turn, interacts with the magnetic field to yield a Lorentz damping force on the fluid

$$\mathbf{F}_L = \mathbf{J} \times \mathbf{B} = \sigma_e (\mathbf{V} \times \mathbf{B}) \times \mathbf{B} \tag{2}$$

Hence, the magnetic damping force is proportional to the square of the induction field and opposes the fluid velocity component from which it originates. A magnetic induction field therefore provides a preferred flow direction, since flow that is parallel (or antiparallel) to the induction field is not damped.

Magnetic damping has been studied both experimentally (e.g., Hoshikawa et al., 1984; Hirata and Inoue, 1985; Kim and Smetana, 1985) and numerically (e.g., Oreper and Szekely, 1984; Langlois, 1984; Lee et al., 1984; Mihelcic and Wingerath, 1985; Organ, 1985; Kim and Langlois, 1986) for the growth of single crystals, as in the Czochralski or Bridgman–Stockbarger processes. The effect of magnetic damping on the metallurgical grain structure in a solidified metal alloy has been investigated experimentally (Uhlmann et al., 1966), and experiments have been performed under more controlled conditions to study the effects of a magnetic field on convection during solidification (Vives and Perry, 1987). However, there are no published investigations regarding the effects of magnetic damping on fluid flow in both the melt and mushy zones during the casting of metal alloys; nor has the relationship between magnetic damping and macrosegregation in alloy castings been studied.

2 The Model

Simulations of this study are based on a continuum model for transport phenomena in dendritic solidification systems (Bennon and Incropera, 1987a). The salient features of this

Contributed by the Heat Transfer Division and presented at the National Heat Transfer Conference, San Diego, California, August 9–12, 1992. Manuscript received by the Heat Transfer Division July 1992; revision received November 1992. Keywords: Double Diffusion Systems, Liquid Metals, Materials Processing and Manufacturing Process. Associate Technical Editor: L. C. Witte.

model, as it applies to a Pb–Sn system, are described in a previous study (Prescott and Incropera, 1991). In this study, the model has been extended to include magnetic damping effects, and the mold containing the Pb–Sn charge is included in the simulations.

It is assumed that the magnetic field is axisymmetric and purely axial, a condition that is closely approximated in the interior of a solenoid. The flow field is assumed to be axisymmetric and without swirl. Thus, it follows from Eqs. (1) and (2) that the current density field is purely tangential and the Lorentz force is purely radial. In accordance with the revised continuum momentum equation (Prescott et al., 1991), the Lorentz force acting on the liquid phase must be included in the radial momentum equation. With electric current determined by a *volume*-averaged velocity, $g_l\mathbf{V}_l + g_s\mathbf{V}_s = \mathbf{V} + (\rho/\rho_l - 1)(\mathbf{V} - \mathbf{V}_s)$, it follows that

$$\mathbf{F}_{L,l} = \sigma_{e,l}[\mathbf{V}\times\mathbf{B} + (\rho/\rho_l - 1)(\mathbf{V}-\mathbf{V}_s)\times\mathbf{B}]\times\mathbf{B} \approx \sigma_{e,l}(\mathbf{V}\times\mathbf{B})\times\mathbf{B} \tag{3}$$

The approximation in Eq. (3) is based on recognition of the fact that $|(\rho/\rho_l - 1)(\mathbf{V}-\mathbf{V}_s)| \ll |\mathbf{V}|$. Therefore, the radial damping force is

$$F_{L,l,r} = -\sigma_{e,l}B_z^2 v \tag{4}$$

and the radial momentum equation is

$$\frac{\partial}{\partial t}(\rho v) + \nabla\cdot(\rho\mathbf{V}v) = \nabla\cdot\left(\mu_l\frac{\rho}{\rho_l}\nabla v\right) - \mu_l\frac{\rho}{\rho_l}\frac{(v - f_s v_s)}{r^2} - \frac{\mu_l}{K}\frac{\rho}{\rho_l}(v - v_s) - \sigma_{e,l}B_z^2 v - \frac{\partial P}{\partial r} \tag{5}$$

The axial momentum, energy, and species equations are, respectively,

$$\frac{\partial}{\partial t}(\rho u) + \nabla\cdot(\rho\mathbf{V}u) = \nabla\cdot\left(\mu_l\frac{\rho}{\rho_l}\nabla u\right) - \frac{\mu_l}{K}\frac{\rho}{\rho_l}(u - u_s) + \rho_l g[(\rho_{l,\mathrm{ref}}/\rho_l - 1) + \beta_T(T - T_{\mathrm{ref}})] - \frac{\partial P}{\partial z} \tag{6}$$

$$\frac{\partial}{\partial t}(\rho h) + \nabla\cdot(\rho\mathbf{V}h) = \nabla\cdot\left(\frac{k}{c_s^*}\nabla h\right) + \nabla\cdot\left[\frac{k}{c_s^*}\nabla(h_s^* - h)\right] - \nabla\cdot[f_s\rho(\mathbf{V}-\mathbf{V}_s)(h_l - h_s)] + |\mathbf{J}|^2/\sigma_e \tag{7}$$

and

$$\frac{\partial}{\partial t}(\rho f^\alpha) + \nabla\cdot(\rho\mathbf{V}f^\alpha) = \nabla\cdot(\rho D\nabla f^\alpha) + \nabla\cdot[\rho D\nabla(f_l^\alpha - f^\alpha)] - \nabla\cdot[f_s\rho(\mathbf{V}-\mathbf{V}_s)(f_l^\alpha - f_s^\alpha)] \tag{8}$$

The magnetic damping term in Eq. (5) is implemented numerically as a linearized source term (Bennon and Incropera, 1988). That is, $\bar{S}^M = S_p^M v(r\Delta r\Delta z)$ where $S_p^M = -\sigma_{e,l}B_z^2$. Although the last term on the right-hand side of Eq. (7) accounts for Joulean dissipation, it represents less than 0.1 percent of the external heat loss for the strongest magnetic field considered in this study. The third and second terms, respectively, on the right-hand sides of Eqs. (5) and (6) are D'Arcy damping terms, which account for relative phase motion within the mushy zone. The permeability K is assumed to be isotropic and is evaluated from the Blake–Kozeny model (Bennon and Incropera, 1987b):

$$K = K_0\left[\frac{g_l^3}{(1-g_l)^2}\right] \tag{9}$$

where the constant $K_0 = 2.8\times10^{-11}$ m^2 was determined from representative dendrite arm spacings for the Pb–Sn system (Nasser-Rafi et al., 1985). The buoyancy term in Eq. (6) is discussed elsewhere (Prescott and Incropera, 1991). The continuum model requires specification of the solid velocity $\mathbf{V}_s$, and in this study a stationary mushy zone is assumed ($\mathbf{V}_s = 0$).

Figure 1 shows the problem domain and the numerical mesh used for its discretization. The system is axisymmetric and is patterned after an experimental apparatus for which $H = 150$ mm, $H/(r_o - r_i) = 3.2$, and $r_o/r_i = 4$. The outer and inner mold wall thicknesses are $t_o/r_o = 0.037$ and $t_i/r_i = 0.20$, respectively, and the bottom mold wall thickness is $t_b/H =$

Nomenclature

- $\mathbf{B}$ = magnetic induction field, T
- B_z = axial component of magnetic induction, T
- c = specific heat, J/kg•K
- c_s^* = specific heat of solid at an arbitrary reference state, J/kg•K
- D = binary mass diffusion coefficient, m^2/s
- Da = D'Arcy number (see Eq. (13))
- f = mass fraction
- $\mathbf{F}_L$ = Lorentz force, N/m^3
- g = volume fraction; acceleration of gravity, m/s^2
- h = enthalpy, J/kg
- h_s^* = $c_s^* T$, J/kg
- H = height of mold cavity, m
- k = thermal conductivity, W/m•K
- K = permeability, m^2
- $\mathbf{J}$ = electric current density field, A/m^2
- Ly = Lykoudis number (see Eq. (12))
- m = slope of liquidus line on the equilibrium phase diagram, K
- M = Hartmann number (see Eq. (11))
- N = buoyancy parameter (see Eq. (14))
- P = pressure, N/m^2
- q'' = heat flux, W/m^2
- r, z = radial and axial coordinates, m
- r^*, z^* = dimensionless coordinates $(r - r_i)/(r_o - r_i)$ and z/H, respectively
- $\bar{S}$ = discretized source term
- S_p = linearized source coefficient
- t = time, s; wall thickness, m
- T = temperature, °C or K
- u, v = axial and radial velocity components, m/s
- U = overall heat transfer coefficient, W/m^2•K
- $\mathbf{V}$ = velocity, m/s
- β_S = solutal expansion coefficient
- β_T = thermal expansion coefficient, K^{-1}
- μ = dynamic viscosity, N•s/m^2
- ρ = density, kg/m^3
- σ_e = electrical conductivity, A/V•m
- ψ = streamfunction, defined by $\rho ur = \partial\psi/\partial r$ and $\rho vr = -\partial\psi/\partial z$, kg/s•rad

Subscripts

- b = bottom
- c = coolant
- i = inner; initial
- l = liquid
- LIQ = liquidus
- max = maximum
- min = minimum
- o = outer
- r = radial component
- ref = reference value
- s = solid
- SOL = solidus
- z = axial component

Superscripts

- M = magnetic damping
- α = constituent α

0.053. It was determined in a previous study (Prescott and Incropera, 1991) that a 50 × 50 mesh is suitable for the mold cavity. Additional nodes were added to accommodate the inner and outer vertical mold walls and the mold bottom, bringing the mesh size to 54 radial nodes by 53 vertical nodes. The portion of the grid that represents the mold cavity was biased in the radial direction, such that the total cavity volume was equally distributed among all respective control volumes. Time steps of 0.25 s were used to resolve the system transients in a control-volume based finite-difference method (Patankar, 1980), with a fully implicit time marching scheme.

Initially, both the melt and the mold are isothermal at 305°C, which is 20°C above the liquidus temperature. Also, at $t = 0$ the melt is chemically homogeneous and quiescent. Cooling occurs through the outer vertical surface of the mold, where the heat flux is expressed as

$$q'' = U[T(r_o + t_o, z, t) - T_c] \tag{10}$$

The overall heat transfer coefficient, U, is set at 35 W/m²•K, which effects a cooling rate associated with large macrosegregation (Prescott and Incropera, 1991), and $T_c = 13$°C. The top, bottom, and inner boundaries are adiabatic. The interface between the mold and the melt is modeled to be slip-free and impermeable, while the meniscus is shear-free.

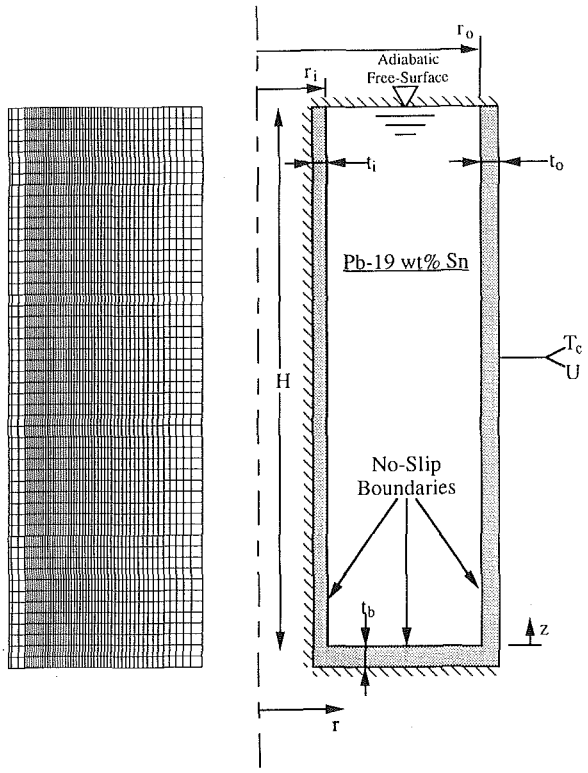

Fig. 1 The simulation system

The constituent properties are listed in Table 1, along with those of the stainless steel mold. Solid and liquid phase properties are found using a linear combination of the constituent properties (Prescott and Incropera, 1991), although the electrical conductivity of the liquid is assumed to be constant.

3 Results of Simulations

Three simulations were performed to examine the effects of magnetic damping. The first simulation includes no magnetic field and serves as a base case. To verify the model, results from the base case are compared with those from experiments, the details of which are documented elsewhere (Prescott, 1992). The second and third simulations have induction fields of 0.1 T and 0.5 T, respectively.[1]

Cooling curves predicted by the base case simulation are compared with those determined experimentally (Prescott, 1992) at $z^* = 0.083$ and 0.83 in Figs. 2(*a*) and 2(*b*), respectively. Overall, the predicted cooling rate exceeds measured values, with differences attributable to model assumptions and/or uncertainties in prescribed model parameters. Also, because the model assumed local equilibrium, it was unable to predict undercoolings and recalescences, which are evident in the experimental data.

Measured and predicted macrosegregation patterns at $z^* = 0.083$ and 0.83 are shown in Figs. 3(*a*) and 3(*b*), respectively, where data from six different azimuthal planes are plotted. Macrosegregation was measured using atomic absorption spectrophotometry to analyze small samples (weighing approximately 100 mg) from large ingot sections (Prescott, 1992). Zero Δ%Sn (Fig. 3) corresponds to the nominal composition; positive values represent Sn enrichment; and negative values represent Sn depletion. Although there is considerable scatter in the data, general trends are predicted by the model. That is, the concentration of Sn increases with increasing height and, at $z^* = 0.83$, with decreasing radius. The average estimated uncertainty in the measurements is 0.4 percent Sn and does not account for the scatter in the data, which is as large as 4 percent. The scatter is attributed to three-dimensional distributions of Sn in the experimental ingots (Prescott, 1992) and is a manifestation of discrete channels, which were dispersed about the circumference of the mushy zone during solidification. The assumption of axial symmetry precludes prediction of such channels.

With impediments related to uncertainties in prescribed model parameters and the influence of three-dimensional effects on solute distribution, it is unreasonable to expect complete agreement between measured and predicted results. Nevertheless, important trends are predicted, and the model may be used as a reliable tool to assess the influence of magnetic damping on solidification.

[1] A 0.1 T (Tesla) induction field requires approximately 8×10^4 A•turns/m in an ideal solenoid.

Table 1 Physical properties of Pb, Sn, and the mold

	Properties	Pb	Sn	Mold
h_f	Fusion enthalpy (J/kg)	23,020	59,020	
T_f	Fusion temperature (°C)	327	232	
c_s	Solid specific heat (J/kg•K)	132	243	535
c_l	Liquid specific heat (J/kg•K)	159	249	
k_s	Solid thermal conductivity (W/m•K)	34	62	18
k_l	Liquid thermal conductivity (W/m•K)	16	51	
μ	Viscosity (N•s/m²)	2.4×10^{-3}	1.78×10^{-3}	
ρ	Density (kg/m³)	10,600	7000	7900
D_l	Binary diffusion coefficient, Sn in Pb (m²/s)	1.5×10^{-9}		
β_T	Coefficient of thermal expansion (K^{-1})	1.09×10^{-4}		
β_S	Solutal expansion coefficient	0.354		
K_o	Permeability coefficient (m²)	2.8×10^{-11}		
σ_e	Electrical conductivity (A/V•m)	1.5×10^{6}		

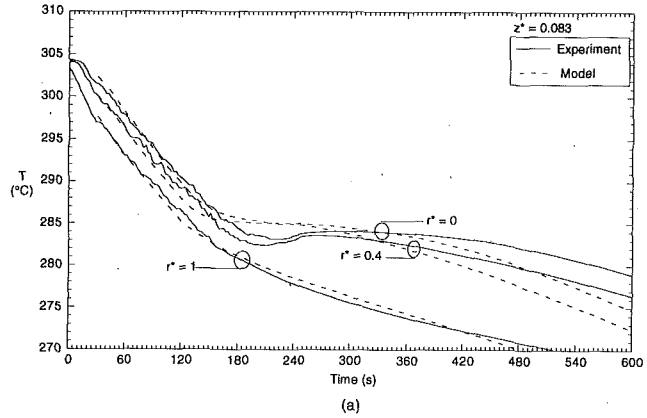

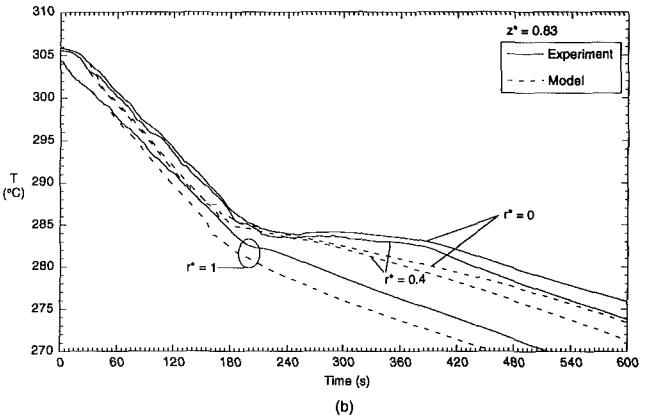

Fig. 2 Measured and predicted cooling curves at (*a*) $z^* = 0.083$ and (*b*) $z^* = 0.83$

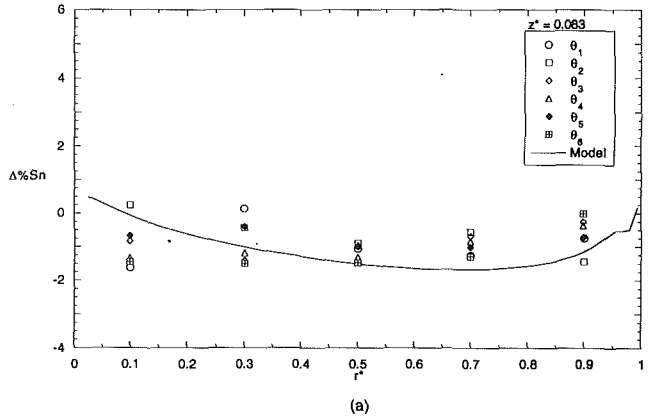

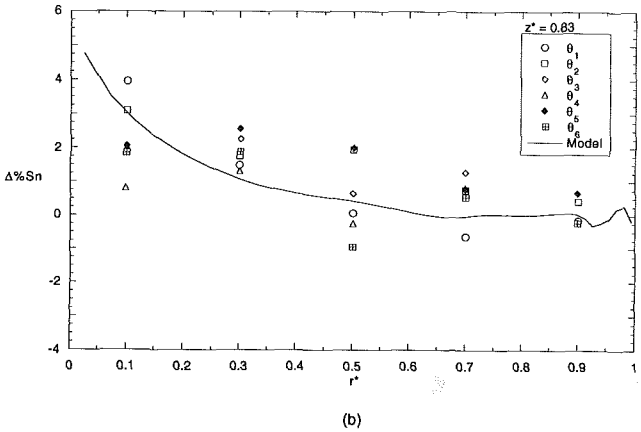

Fig. 3 Measured and predicted macrosegregation patterns at (*a*) $z^* = 0.083$ and (*b*) $z^* = 0.83$

Convection conditions are represented by field plots of velocity vectors, streamlines, isotherms, and liquid isocomposition lines (liquid isocomps). The liquidus interface, which represents the boundary between the melt and mushy zones, is indicated as a heavy line on each plot. Fully solidified regions and the solidus interface do not appear in any of the plots in this paper. Velocity vectors are scaled according to the current maximum velocity, which is indicated at the top of each velocity vector plot. Streamlines associated with clockwise recirculation have negative values and are plotted in ten equal increments between Ψ_{min} and 0, while counterclockwise recirculation cells have positive values, which are plotted in ten equal increments between 0 and Ψ_{max}. Isotherms and liquid isocomps (expressed as mass fraction Sn) are plotted in 20 equal increments between minimum and maximum values. In general, the minimum temperature and maximum liquid composition are found near the outer (left) boundary of the mold cavity. In addition, macrosegregation plots, which indicate mixture (solid + liquid) composition, are presented with legends to facilitate interpretation.

Figure 4 shows velocity, streamfunction, temperature, and liquid composition fields for the base case at $t = 140$ s, which is soon after solidification commenced. Temperature gradients, Fig. 4(*c*), are responsible for a relatively strong counterclockwise convection cell, Figs. 4(*a*, *b*), which thermally stratifies the interior of the melt during the early cooling period, Fig. 4(*c*). Thermal convection is enhanced during the early cooling stages by heat transfer from the bottom and inner tube walls of the mold, Fig. 4(*c*). Solutal buoyancy forces act upward, opposing thermal buoyancy, within the mushy zone, where interdendritic liquid is enriched with Sn, Fig. 4(*d*). Interdendritic liquid leaving the mushy zone, at $z^* \approx 0.27$, Fig. 4(*b*), is turned downward along the liquidus interface by the momentum of the thermal convection cell, thereby confining the liquid composition gradient primarily within the mushy zone, Fig. 4(*d*). The interdendritic liquid that leaves the mushy zone is replaced with liquid from the bulk melt near the bottom of the cavity, Figs. 4(*a*, *b*).

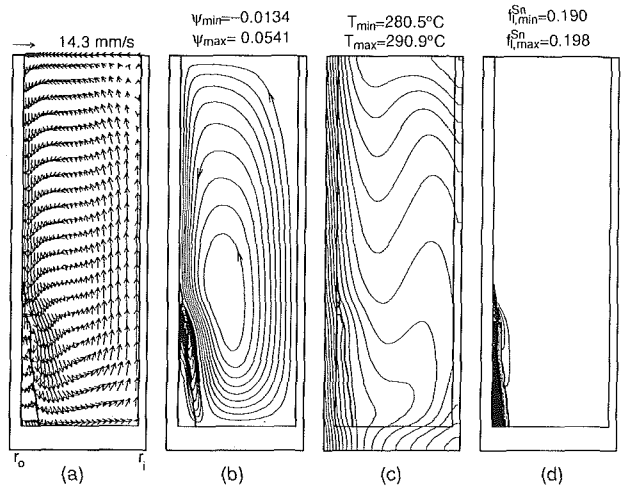

Fig. 4 Convection conditions after 140 s of cooling without magnetic damping: (*a*) velocity vectors, (*b*) streamlines, (*c*) isotherms, and (*d*) liquid isocomps

With time, the liquidus interface moves both radially inward and vertically upward along the cooled mold wall. At $t = 155$ s (Fig. 5), the mushy zone covers approximately 75 percent of the inside surface of the outer mold wall. Fluid is exchanged between the mushy and melt zones in a relatively confined region near the top of the mushy zone, Fig. 5(*b*), where a

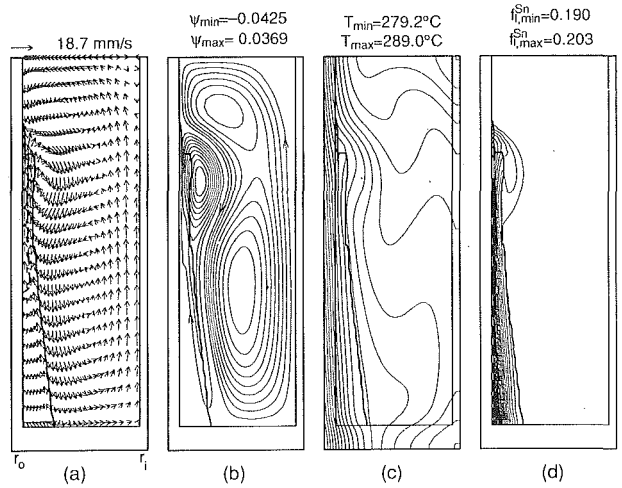

Fig. 5 Convection conditions after 155 s of cooling without magnetic damping: (*a*) velocity vectors, (*b*) streamlines, (*c*) isotherms, and (*d*) liquid isocomps

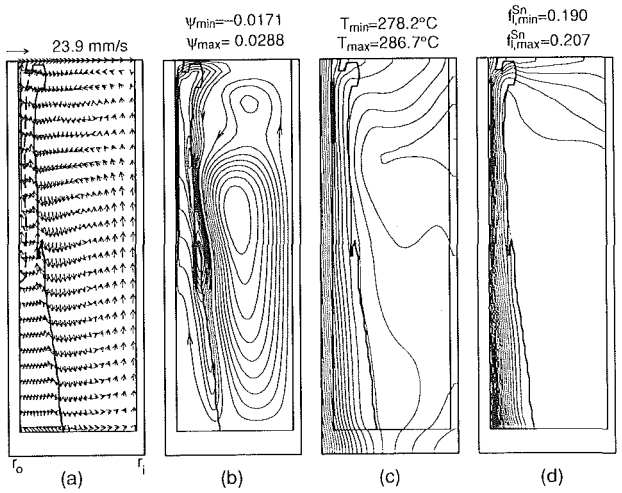

Fig. 6 Convection conditions after 170 s of cooling without magnetic damping: (*a*) velocity vectors, (*b*) streamlines, (*c*) isotherms, and (*d*) liquid isocomps

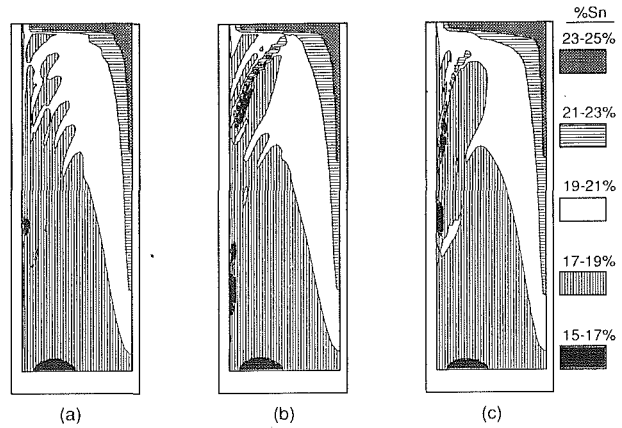

Fig. 7 Macrosegregation patterns after 600 s of cooling: (*a*) without magnetic damping, (*b*) with B_z = 0.1 T, and (*c*) with B_z = 0.5 T

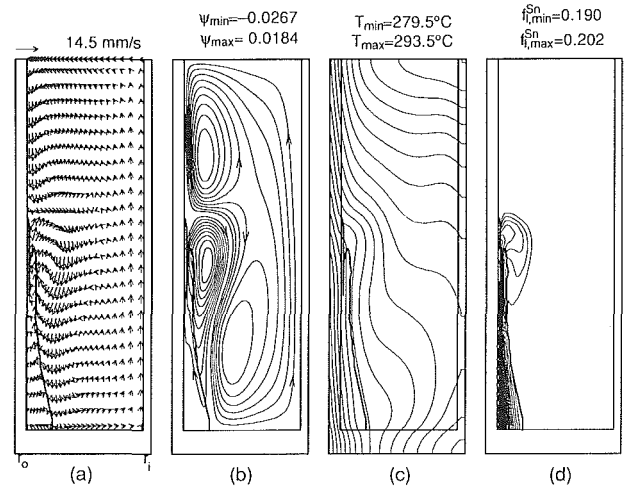

Fig. 8 Convection conditions after 140 s of cooling with B_z = 0.1 T: (*a*) velocity vectors, (*b*) streamlines, (*c*) isotherms, and (*d*) liquid isocomps

strong, solutally driven flow, emerging from the mushy zone, interacts with thermally driven flow in the bulk melt. The interaction turns both flows radially inward, thereby constricting the thermal cell. This double-diffusive convection pattern ultimately advects warmer fluid from the bulk melt into the mushy zone, and the attendant heating, combined with local Sn enrichment by ascending interdendritic fluid, favors remelting and/or dissolution of dendrites and the development of a channel. The channel, although not fully melted, is aligned vertically and is located along the mold wall for $z^* \gtrsim 0.5$. It is delineated by a heavy dashed line in Fig. 5(*a*).

Convection conditions at t = 170 s are shown in Fig. 6. The channel along the top half of the cooled mold wall draws Sn-enriched interdendritic fluid into it, Figs. 6(*b*, *d*), and fluid in the channel is accelerated toward the top of the cavity, where Sn rich layers are formed, Figs. 6(*a*, *d*). In addition to the exchange of fluid between the mush and melt promoted by the channel, two small recirculation cells are active along the liquidus interface at $z^* \approx 0.5$ and $z^* \approx 0.75$, Fig. 6(*b*). Such recirculations are responsible for establishing preferred flow paths of interdendritic liquid at later times. That is, channels, although not fully melted, are established by small recirculations along the liquidus interface during early solidification stages. Fluid of nominal composition enters the mushy zone at the bottom of these recirculation zones and displaces fluid of higher Sn concentration. Thus, a small Sn-depleted region, with an increased solid fraction and decreased permeability, is created. At the top of a recirculation cell, there exists a Sn enriched zone with decreased solid fraction and increased permeability. The position of these interfacial recirculation cells moves as the liquidus interface advances inward and upward, thereby creating a series of channels. These channels manifest themselves as A-segregates in the final casting (Flemmings, 1974; Fisher, 1981).

Figure 7(*a*) shows the macrosegregation pattern that exists at t = 600 s. Although the ingot is not fully solidified at this time, fluid flow is virtually nonexistent due to the small permeability of the dendritic structure, and macrosegregation is essentially complete (Prescott and Incropera, 1991). The A-segregates in Fig. 7(*a*) are the series of Sn-rich pockets extending upward and radially inward from the Sn depleted region in the upper portion of the ingot. In addition to the A-segregate pattern, a large cone of Sn-rich material, which results from the solutally induced recirculation of interdendritic fluid during the intermediate stages of solidification (300 < t < 600 s) (Prescott and Incropera, 1991), extends down from the top of the ingot.

Convection conditions associated with application of a 0.1 T induction field are shown in Figs. 8–10, and the resultant macrosegregation pattern is shown in Fig. 7(*b*). At t = 140 s (Fig. 8), a nonuniform mushy zone is attached to the lower half of the cooled mold wall. With the magnetic field,

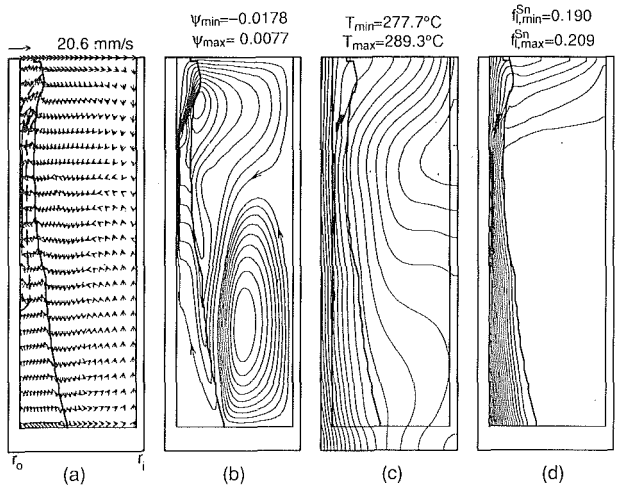

Fig. 9 Convection conditions after 170 s of cooling with B_z = 0.1 T: (*a*) velocity vectors, (*b*) streamlines, (*c*) isotherms, and (*d*) liquid isocomps

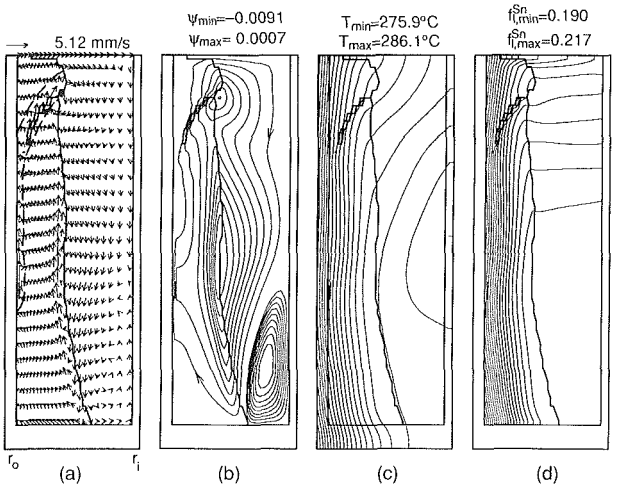

Fig. 10 Convection conditions after 210 s of cooling with B_z = 0.1 T: (*a*) velocity vectors, (*b*) streamlines, (*c*) isotherms, and (*d*) liquid isocomps

development of the mushy zone and of the solutally driven convection cell, Fig. 8(*b*), occurs sooner than without magnetic damping, Fig. 4. Although thermal stratification still occurs due to convection, Fig. 8(*c*), magnetic damping reduces the strength of the thermally driven recirculation, thereby decreasing heat transfer between the melt and the cooled mold wall. Hence, liquid near the outer mold wall cools more rapidly, and solidification commences earlier with magnetic damping. Furthermore, due to the decreased momentum associated with the thermally driven downflow along the outer mold wall, Sn-rich fluid from the mushy zone penetrates further into the melt, Fig. 8(*d*).

The mushy zone covers all of the outer mold wall at t = 170 s (Fig. 9), and radial liquid composition gradients, Fig. 9(*d*), induce a recirculation zone that encompasses much of the liquid and mushy zones, Fig. 9(*b*). Since the thermal convection cell is weakened by the magnetic field, it is less effective at opposing the discharge of Sn-rich liquid from the mushy zone, and the propensity for channel development is increased. A fully melted channel adjacent to the outer mold wall, Fig. 9(*a*), provides a preferred flow path for interdendritic fluid, Fig. 9(*b*), facilitating its transfer to the top of the mold cavity, where Sn-rich layers of liquid are forming, Fig. 9(*d*). Approximately 67 percent of the fluid exchange between the melt and mushy zones occurs through the channel.

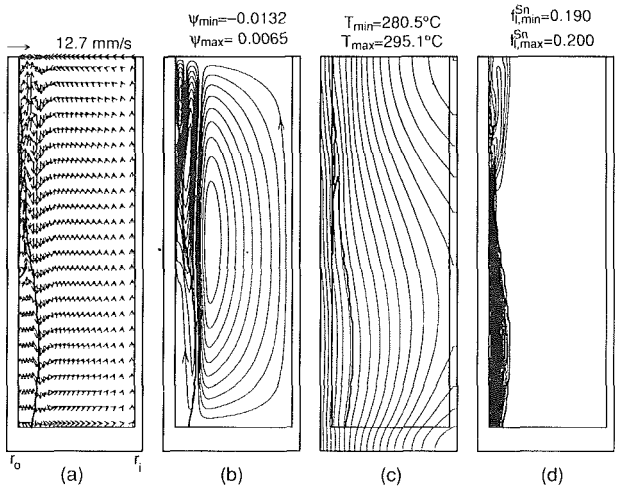

Fig. 11 Convection conditions after 140 s of cooling with B_z = 0.5 T: (*a*) velocity vectors, (*b*) streamlines, (*c*) isotherms, and (*d*) liquid isocomps

At t = 210 s, solutal buoyancy dominates convection in both the mush and fully melted zones, Figs. 10(*a*, *b*). Cool but Sn-rich layers have formed at the top of the cavity, Figs. 10(*c*, *d*), and the lower interior region of the melt is nearly isothermal. The small, counterclockwise thermal cell of Fig. 10(*b*) is quickly losing its momentum and will soon be extinct. The channel that formed earlier has turned radially inward near the top of the mushy zone and provides for transport of approximately 50 percent of the interdendritic liquid discharged from the mushy zone into the melt, Fig. 10(*b*), while the mushy zone is fed entirely by fluid of nominal composition, which crosses with the liquidus interface over the lower third of the cavity.

The macrosegregration that resulted from solidification with a 0.1 T induction field is shown in Fig. 7(*b*). The channel that existed at earlier times is manifested by a highly segregated zone among the pattern of A-segregates. Both positively (Sn rich) and negatively (Sn depleted) segregated region, immediately adjacent to each other, are associated with the channel. The channel itself was continually fed with Sn-rich fluid from adjacent regions, which were replenished by fluid of lower Sn concentration, Figs. 9(*b*, *d*). This channel segregate represents the main difference between the macrosegregation patterns of Figs. 7(*a*) and 7(*b*) for the base case and the 0.1 T case, respectively. The cone segregate in the top interior region of the ingot is unaffected by the magnetic field.

By increasing the induction field to 0.5 T, radial damping increases 25-fold over that caused by a 0.1 T field. Hence, thermal convection is significantly reduced during the initial cooling period, and because heat transfer is conduction dominated, thermal stratification is nearly eliminated. At t = 140 s (Fig. 11), a mushy zone covers nearly 90 percent of the vertical extent of the outer mold wall. The temperature gradient is primarily radial, Fig. 11(*c*), and the effects of thermal capacitance and conjugate heat transfer in the mold bottom are responsible for the maximum mushy zone thickness occurring at $z^* \approx 0.20$, rather than at the bottom of the mold. The Sn concentration gradient in the interdendritic liquid, Fig. 11(*d*), is responsible for a positive buoyancy force and the annular plume of Sn rich liquid rising from the mushy zone, Figs. 11(*a*, *b*). Since the magnetic field strongly damped thermal convection during the initial cooling period, the solutal upwelling is virtually unopposed. The ascending interdendritic fluid is also responsible for the channel that has formed along the mold wall, Figs. 11(*a*, *b*), where the local liquidus temperature is depressed. Also, the plume of fluid discharged from the channel is deflected radially inward at $z^* \approx 0.8$, bifurcating to

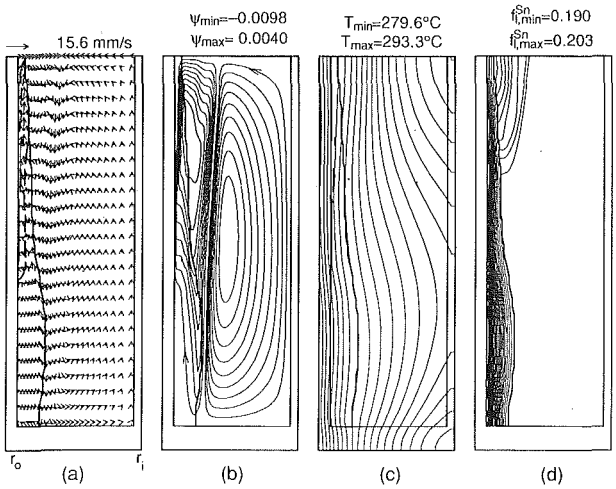

Fig. 12 Convection conditions after 155 s of cooling with B_z = 0.5 T: (*a*) velocity vectors, (*b*) streamlines, (*c*) isotherms, and (*d*) liquid isocomps

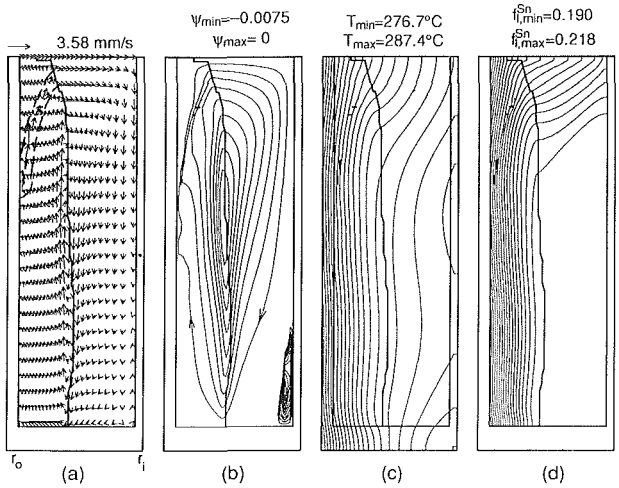

Fig. 13 Convection conditions after 210 s of cooling with B_z = 0.5 T: (*a*) velocity vectors, (*b*) streamlines, (*c*) isotherms, and (*d*) liquid isocomps

create a small, counterclockwise vortex near the top of the cavity and a large, clockwise solutal convection cell. Strong magnetic damping causes the thermal and solutal convection cells to be sharply divided by a hypothetical cylindrical surface whose radius corresponds closely with the liquidus interface, Fig. 11(*b*).

With time, the mushy zone and the vertical interface between thermal and solutal convection cells move radially inward, as indicated in Fig. 12(*b*) for t = 155 s. Since vertical motion is undamped, solutal buoyancy forces accelerate interdendritic fluid to relatively large velocities within the channel adjacent to the outer mold wall, Fig. 12(*a*), while magnetic damping has the effect of minimizing radial motion, Fig. 12(*b*). Hence, solutal stratification is inhibited during the early solidification period, Fig. 12(*d*). The thermal convection cell is large, but very weak, Figs. 12(*a*, *b*), despite a significant radial temperature gradient in the melt, Fig. 12(*c*).

The interface between the solutal and thermal convection cells continues to move inward as the mushy zone grows, until at approximately 210 s, the counterclockwise thermal convection cell is virtually extinct, Fig. 13(*b*). The radial Sn concentration gradient in the interdendritic liquid, Fig. 13(*d*), generates negative (clockwise) vorticity, which negates the generation of positive vorticity by the temperature gradient in the melt, Fig. 13(*c*). With dominance of solutal buoyancy, solutal stratification eventually occurs, Fig. 13(*d*), yielding the macrosegregation pattern of Fig. 7(*c*).

Although the channel in the outer, upper region of the cavity yields a zone of large segregation, the severity of this channel segregate, Fig. 7(*c*), is less than that for the reduced magnetic field, Fig. 7(*b*). Comparing Fig. 7(*c*) with Figs. 7(*a*) and 7(*b*), it is also apparent that the stronger magnetic field reduces that number of A-segregates that appear in the top half of the ingot. This reduction occurred because radial damping inhibited the development of small recirculation cells, as seen in Fig. 6(*b*), along the advancing liquidus interface. However, the magnetic field has virtually no effect on development of a cone of positive segregation, which extends downward from the top of the ingot.

4 Physical Considerations

To obtain a better appreciation for the effect of an applied magnetic field on convection and macrosegregation, it is instructive to examine pertinent dimensionless groups, such as the Hartmann number

$$M \equiv \left[\frac{\sigma_e B^2 L^2}{\mu}\right]^{1/2} \tag{11}$$

where M^2 is a measure of the relative strength of the Lorentz and viscous forces, and the Lykoudis number

$$\mathrm{Ly} \equiv \frac{\sigma_e B^2 L^{1/2}}{\rho (g \Delta\rho/\rho)^{1/2}} \tag{12}$$

which measures the relative strength of the Lorentz and buoyancy forces. Each of these groupings requires specification of an appropriate length scale, while Ly requires characterization of the buoyancy conditions. However, due to the evolutionary nature of the solidification process, unique values cannot be prescribed for these parameters. For example, an appropriate length scale for the melt could be its mean hydraulic diameter, which decreases with time as the liquidus interface advances. Within the mushy zone, the length scale could be associated with the dendrite arm spacing (10 to 100 μm) or the permeability, which also changes continuously as solidification progresses. Hence, length scales that differ by orders of magnitude can be chosen for the melt and mushy zones, each of which changes during the process. Similarly, the density difference $\Delta\rho$ depends on whether the melt or mushy zone is under consideration and on time during the process. During the initial cooling period, density gradients are influenced by temperature variations, while subsequently they are dominated by composition variations within the mushy zone.

The large differences in scaling parameters that exist between the melt and mushy zones can be partially reconciled by considering two additional groupings. The D'Arcy number is the ratio of permeability in the mushy zone to the square of a length scale characteristic of the mold

$$\mathrm{Da} \equiv \frac{K}{L^2} \tag{13}$$

and the buoyancy parameter is the ratio of solutal and thermal buoyancy effects within the mushy zone

$$\mathrm{N} \equiv \frac{\beta_S}{m\beta_T} \tag{14}$$

Estimating the permeability from the Blake–Kozeny equation with a liquid volume fraction of 0.70 and using the hydraulic diameter of the mold cavity for $L(L = 2(r_o - r_i))$ yields Da $= 1.2 \times 10^{-8}$ for the conditions in this study, which shows that viscous damping in the mushy zone (D'Arcy damping) is much stronger than large-scale viscous damping. Moreover, for hypoeutectic Pb–Sn alloys, $|N| = 14$, indicating that so-

lutal buoyancy dominates thermal buoyancy within the mushy zone.

During the initial cooling period, when solutal buoyancy and D'Arcy damping effects are small or nonexistent, it is appropriate to evaluate M^2 and Ly using a length scale of $2(r_o - r_i)$ and a density variation of $\Delta\rho/\rho = \beta_T \Delta T$, where $\Delta T \approx 5$ K. Thus, with $B = 0.1$ T, $M^2 = 6.1 \times 10^4$ and the *thermal* Lykoudis number is $\mathrm{Ly}_T = 6.6$, indicating that magnetic damping is significant during the initial period of solidification. Moreover, with $B = 0.5$ T, the magnetic damping effect is 25 times larger. However, during intermediate and later stages of solidification, when D'Arcy damping and solutal buoyancy are prominent, the appropriate groupings are $M^2 \cdot \mathrm{Da} = \sigma_e B^2 K/\mu$, for the ratio of Lorentz to D'Arcy (viscous) forces, and the *solutal* Lykoudis number, $\mathrm{Ly}_S = \mathrm{Ly}_T/N^{1/2}$, which is a measure of the ratio of magnetic damping to buoyancy. The D'Arcy number is not included in Ly_S, because the small length scale associated with the permeability does not influence the variation in buoyancy forces. With $B = 0.1$ and 0.5 T, Ly_S is 1.8 and 44, respectively. However, the values of $M^2 \cdot \mathrm{Da}$ are 7.2×10^{-4} and 1.8×10^{-2}, respectively, for induction fields of 0.1 and 0.5 T. It is therefore concluded that D'Arcy damping is the primary restriction to fluid flow during intermediate and later stages of the solidification, and that during this period, magnetic damping is negligible. The induction field would have to be increased by an order of magnitude (e.g., to approximately 5 T), before a significant change in macrosegregation can be expected for the interior of the ingot.

From the foregoing examination, it is concluded that, by damping thermal convection, a steady induction field changes the nature of thermosolutal interactions during the early stages of solidification, and hence the subsequent development of channels in the mushy zone and the formation of segregates near the outer mold wall. However, because magnetic damping is small in comparison to D'Arcy damping, the induction field does little to alter solutally driven natural convection through the mushy zone or to prevent cone segregates from forming on the top of the ingot.

5 Conclusions

Numerical simulations have been performed to assess the effects of moderately strong, steady induction fields on thermosolutal convection and macrosegregation during solidification of a metal alloy. The findings corroborate previous results (Prescott and Incropera, 1991), which indicate that convection during early and late stages of solidification is responsible for different, identifiable zones of macrosegregation. Channels and A-segregates in the outer region of the ingot are associated with thermosolutal interactions that follow the onset of solidification. In contrast, macrosegregration at the interior of the ingot is associated with large-scale fluid recirculation through the mushy zone, which is driven exclusively by solutal buoyancy.

Application of a magnetic field provides one means of altering convection in a liquid metal, and the results of this study reveal that thermosolutal interactions, which occur during early stages of solidification, are affected by a steady induction field. However, rather than inhibiting convection, which contributes to macrosegregation, a steady, axial induction field of reasonable (readily achievable) strength favors the development of a channel in the mushy zone and increases macrosegregation in outer regions of the ingot. The field also has little or no effect on the development of a large zone of positive segregation in the interior of an ingot. The inability of magnetic damping to reduce macrosegregation within the ingot is attributed to the fact that magnetic damping forces are negligible compared to D'Arcy damping, which ultimately limits the recirculation of interdendritic liquid during intermediate and later stages of solidification. It follows from the dimensionless product $M^2 \cdot \mathrm{Da}$ that magnetic damping would be most effective on materials with large electrical conductivity and those that freeze with relatively large dendrite arm spacings (i.e., with large permeability in the mushy zone), of which the Pb–Sn system is representative.

It is possible that channel formation might be more effectively controlled or eliminated by augmenting thermal convection, rather than by damping it. Increasing the strength of the thermally driven convection pattern that opposes solutal buoyancy will have the effect of inhibiting the development of channels and the penetration of interdendritic liquid into the melt. For the geometry of interest, thermal convection may be augmented by heating, perhaps intermittently, the center tube during solidification. Alternatively, a moderately strong magnetic field (e.g., 0.5 T) can be applied to preserve a radial temperature gradient in the melt until a time near the onset of solidification, when the field can be removed. Thermal convection will then be more effective during the crucial period in which the mushy zone develops along the outer mold wall.

Acknowledgments

The authors are grateful to the U.S. Department of Energy for providing financial support of this work through Award No. DE-FG02-87ER 13759.

References

Amberg, G., 1991, "Computation of Macrosegregation in an Iron–Carbon Cast," *Int. J. Heat Mass Transfer*, Vol. 34, pp. 217–227.

Beckermann, C., and Viskanta, R., 1988, "Double-Diffusive Convection During Dendritic Solidification of a Binary Mixture," *PhysicoChem. Hydrodyn.*, Vol. 10, pp. 195–213.

Beckermann, C., and Ni, J., 1992, "Modeling of Equiaxed Solidification With Convection," in: *Proc. First Int. Conf. Transport Phenomena in Processing*, Honolulu, HI, Mar.

Bennon, W. D., and Incropera, F. P., 1987a, "A Continuum Model for Momentum, Heat and Species Transport in Binary Solid–Liquid Phase Change Systems—I. Model Formulation," *Int. J. Heat Mass Transfer*, Vol. 30, pp. 2161–2170.

Bennon, W. D., and Incropera, F. P., 1987b, "A Continuum Model for Momentum, Heat and Species Transport in Binary Solid-Liquid Phase Change Systems—II. Application to Solidification in a Rectangular Cavity," *Int. J. Heat Mass Transfer*, Vol. 30, pp. 2171–2187.

Bennon, W. D., and Incropera, F. P., 1987c, "The Evolution of Macrosegregation in Statically Cast Binary Ingots," *Metall. Trans. B*, Vol. 18B, pp. 611–616.

Bennon, W. D,. and Incropera, F. P., 1988, "Numerical Analysis of Binary Solid–Liquid Phase Change Using a Continuum Model," *Numer. Heat Transfer*, Vol. 13, pp. 277–296.

Felicelli, S. D., Heinrich, J. C., and Poirier, D. R., 1991, "Simulation of Freckles During Vertical Solidification of Binary Alloys," *Metall. Trans. B*, Vol. 22B, pp. 847–859.

Fisher, K. M., 1981, "The Effects of Fluid Flow on the Solidification of Industrial Castings and Ingots," *PhysicoChem. Hydro*, Vol. 2, pp. 311–326.

Flemings, M. C., 1974, "Solidification Processing," *Metall. Trans.*, Vol. 5, pp. 2121–2134.

Ganesan, S., and Poirier, D. R., 1990, "Conservation of Mass and Momentum for the Flow of Interdendritic Liquid During Solidification," *Metall. Trans. B*, Vol. 21B, pp. 173–181.

Heinrich, J. C., Felicelli, S., and Poirier, D. R., 1991, "Vertical Solidification of Dendritic Binary Alloys," *Comp. Meth. Appl. Mech. Engrg.*, Vol. 89, pp. 435–461.

Hirata, H., and Inoue, N., 1985, "Macroscopic Axial Dopant Distribution in Czochralski Silicon Crystals Grown in a Vertical Magnetic Field," *Jap. J. Appl. Phys.*, Vol. 24, pp. 1399–1403.

Hoshikawa, K., Kohda, H., and Hirata, H., 1984, "Homogeneous Dopant Distribution of Silicon Crystal Grown by Vertical Magnetic Field-Applied Czochralski Method," *Jap. J. Appl. Phys. (Letters)*, Vol. 23, pp. L37–L39.

Kim, K. M., and Smetana, P., 1985, "Striations in CZ Silicon Crystals Grown Under Various Axial Magnetic Field Strength," *J. Appl. Phys.*, Vol. 58, pp. 2731–2735.

Kim, K. M., and Langlois, W. E., 1986, "Computer Simulation of Boron Transport in Magnetic Czochralski Growth of Silicon," *J. Electrochem. Soc.*, Vol. 133, pp. 2586–2590.

Langlois, W. E., 1984, "Computer Simulation of Czochralski Melt Convection in a Magnetic Field," *J. Crystal Growth*, Vol. 70, pp. 73–77.

Lee, K.-J., Langlois, W. E., and Kim, K. M., 1984, "Digital Simulation of Oxygen Transfer and Oxygen Segregation in Magnetic Czochralski Growth of Silicon," *PhysicoChem. Hydro.*, Vol. 5, pp. 135–141.

Mihelcic, M., and Wingerath, K., 1985, "Numerical Simulations of the Czochralski Bulk Flow in an Axial Magnetic Field: Effects on the Flow and Tem-

perature Oscillations in the Melt," *J. Crystal Growth*, Vol. 71, pp. 163–168.

Nasser-Rafi, R., Deshmukh, R., and Poirier, D. R., 1985, "Flow of Interdendritic Liquid and Permeability in Pb-20 wt pct Sn Alloys," *Metall. Trans A*, Vol. 16A, pp. 2263–2271.

Neilson, D. G., and Incropera, F. P., 1991, "Unidirectional Solidification of a Binary Alloy and the Effects of Induced Fluid Motion," *Int. J. Heat Mass Transfer*, Vol. 34, pp. 1717–1732.

Ni, J., and Beckermann, C., 1991, "A Volume-Averaged Two-Phase Model for Transport Phenomena During Solidification," *Metall. Trans. B*, Vol. 22B, pp. 349–361.

Oldenburg, C. M., and Spera, F. J., 1991, "Numerical Modeling of Solidification and Convection in a Viscous Pure Binary Eutectic System," *Int. J. Heat Mass Transfer*, Vol. 34, pp. 2107–2121.

Oreper, G. M., and Szekely, J., 1984, "The Effect of a Magnetic Field on Transport Phenomena in a Bridgeman-Stockbarger Crystal Growth," *J. Crystal Growth*, Vol. 67, pp. 405–419.

Organ, A. E., 1985, "Flow Patterns in a Magnetic Czochralski Crystal Growth System," *J. Crystal Growth*, Vol. 73, pp. 571–582.

Patankar, S. V., 1980, *Numerical Heat Transfer and Fluid Flow*, McGraw-Hill, New York.

Poirier, D. R., Nandapurkar, P. J., and Ganesan, S., 1991, "The Energy and Solute Conservation Equations for Dendritic Solidification," *Metall. Trans. B*, Vol. 22B, pp. 889–900.

Prakash, C., 1990a, "Two-Phase Model for Binary Solid–Liquid Phase Change, Part I: Governing Equations," *Numerical Heat Transfer, Part B*, Vol. 18, pp. 131–145.

Prakash, C., 1990b, "Two-Phase Model for Binary Solid-Liquid Phase Change, Part II: Some Illustrative Examples," *Numerical Heat Transfer, Part B*, Vol. 18, pp. 147–167.

Prescott, P. J., and Incropera, F. P., 1991, "Numerical Simulation of a Solidifying Pb–Sn Alloy: The Effects of Cooling Rate on Thermosolutal Convection and Macrosegregation," *Metall. Trans. B*, Vol. 22B, pp. 529–540.

Prescott, P. J., Incropera, F. P., and Bennon, W. D., 1991, "Modeling of Dendritic Solidification Systems: Reassessment of the Continuum Momentum Equation," *Int. J. Heat Mass Transfer*, Vol. 34, pp. 2351–2359.

Prescott, P. J., 1992, "Convective Transport Phenomena During Solidification of Binary Metal Alloys and the Effects of Magnetic Fields," Ph.D. thesis, Purdue University, West Lafayette, IN.

Rappaz, M., 1989, "Modeling of Microstructure Formation in Solidification Processes," *Int. Mater. Rev.*, Vol. 34, pp. 93–123.

Uhlmann, D. R., Seward, T. P., III, and Chalmers, B., 1966, "The Effect of Magnetic Fields on the Structure of Metal Alloy Castings," *TMS AIME*, Vol. 236, pp. 527–531.

Viskanta, R., and Beckermann, C., 1987, "Mathematical Modeling of Solidification," in: *Interdisciplinary Issues in Materials Processing and Manufacturing*, Samanta et al., eds., ASME, New York.

Viskanta, R., 1988, "Heat Transfer During Melting and Solidification of Metals," ASME JOURNAL OF HEAT TRANSFER, Vol. 110, pp. 1205–1219.

Viskanta, R., 1990, "Mathematical Modeling of Transport Processes During Solidification of Binary Systems," *JSME International Journal, Series II*, Vol. 33, pp. 409–423.

Vives, C., and Perry, C., 1987, "Effects of Magnetically Damped Convection During the Controlled Solidification of Metals and Alloys," *Int. J. Heat Mass Transfer*, Vol. 30, pp. 479–496.

Voller, V. R., and Prakash, C., 1987, "A Fixed Grid Numerical Modelling Methodology for Convection-Diffusion Mushy Region Phase-Change Problems," *Int. J. Heat Mass Transfer*, Vol. 30, pp. 1709–1719.

Voller, V. R., Brent, A. D., and Prakash, C., 1989, "The Modelling of Heat, Mass and Solute Transport in Solidification Systems," *Int. J. Heat Mass Transfer*, Vol. 32, pp. 1718–1731.

Evaluation of a Hue Capturing Based Transient Liquid Crystal Method for High-Resolution Mapping of Convective Heat Transfer on Curved Surfaces

C. Camci

K. Kim[1]

The Pennsylvania State University,
Aerospace Engineering Department,
University Park, PA 16802

S. A. Hippensteele

P. E. Poinsatte

NASA Lewis Research Center,
Internal Fluid Mechanics Division,
Cleveland, OH 44135

Accurate determination of convective heat transfer coefficients on complex curved surfaces is essential in the aerothermal design and analysis of propulsion system components. The heat transfer surfaces are geometrically very complex in most of the propulsion applications. This study focuses on the evaluation of a hue capturing technique for the heat transfer interpretation of liquid crystal images from a complex curved heat transfer surface. Impulsively starting heat transfer experiments in a square to rectangular transition duct are reported. The present technique is different from existing steady-state hue capturing studies. A real-time hue conversion process on a complex curved surface is adopted for a transient heat transfer technique with high spatial resolution. The study also focuses on the use of encapsulated liquid crystals with narrow color band in contrast to previous steady-state hue based techniques using wide band liquid crystals. Using a narrow band crystal improves the accuracy of the heat transfer technique. Estimated uncertainty for the heat transfer coefficient from the technique is about 5.9 percent. A complete heat transfer map of the bottom surface was possible using only seven liquid crystal image frames out of the 97 available frames during the transient experiment. Significant variations of heat transfer coefficients are quantitatively visualized on the curved surfaces of the transition duct.

Introduction

This study deals with the implementation of a recently developed transient hue capturing technique on complex curved surfaces. The specific emphasis is given to apply the technique on a liquid crystal sprayed curved surface to obtain two-dimensional heat transfer coefficient maps with high spatial resolution. Although there is a vast amount of information in the literature about line heat transfer distributions from liquid crystal measurements, there are a limited number of studies dealing with surface distributions, especially on complex curved surfaces. The present technique is different from the existing steady-state true color heat transfer approaches. A real-time hue conversion process is adopted for high-resolution heat transfer measurements using a transient heat transfer model.

The molecular structure, optical and thermal properties of cholesteric liquid crystals have been extensively reviewed by Fergason (1964, 1968). A general discussion on the use of liquid crystals for heat transfer purposes is given by Cooper et al. (1975), Simonich and Moffat (1984), Moffat (1990), Hippensteele et al. (1983, 1985, 1987), and Parsley (1991). Unencapsulated (neat) liquid crystals can be used to indicate shear stress and hence transition in wind tunnel tests and actual flight testing (Jones et al., 1992; Klein and Margozzi, 1970; Holmes and Gall, 1986; Holmes and Obara, 1987). However, encapsulated forms of cholesteric and chiral nematic liquid crystals show a very useful feature from a heat transfer point of view. They are relatively insensitive to normal and shearing stresses (Zharkova et al., 1980). The color response of liquid crystals to temperature is very fast and the response time is no more than a few milliseconds (Ireland and Jones, 1978).

Application of liquid crystals in transient heat transfer experiments is discussed by Ireland and Jones (1985) and Jones and Hippensteele (1988). In a transient experiment a complete heat transfer mapping of a complex surface can be obtained from a set of video images. However, in steady-state mode, multiple experiments with different heat flux settings are required to map the surface completely. Each new constant heat flux setting may also generate a new wall to free-stream temperature ratio. Transient experiments usually generate an approximately isothermal surface boundary condition. The deviation from an isothermal wall temperature is small most of the time when compared to the temperature difference between the wall and the free stream. Transient heat transfer techniques are also attractive from an operating cost point of view, especially when a large mass flow of heated air at high speed is required. Mechanical construction of a constant heat flux surface on a highly curved three-dimensional surface is considerably more difficult when compared to the simple liquid crystal spraying procedure for a typical transient experiment. Transient techniques used in the past employing discrete sensors or liquid crystal indicators never reached the spatial resolution (512 × 480 sensors per image) of the current method. The high spatial resolution of the present transient method having pixel by pixel processing capability is also applicable in unsteady heat transfer research for temperature fluctuation levels having a typical frequency of less than 60 Hz.

In most of the previous studies reviewed, a visual detection of yellow contour was the most quantitative description of a narrow isothermal band that could be captured from a specific image. Wang et al. (1990) used a technique to mark the pixels for the appearance of a light intensity peak. Bunker et al.

[1]Present address: Pusan National University, Korea.

Contributed by the Heat Transfer Division and presented at the ASME Winter Annual Meeting, Atlanta, Georgia, December 1-6, 1991. Manuscript received by the Heat Transfer Division November 1991; revision received October 1992. Keywords: Forced Convection, Instrumentation, Measurement Techniques. Associate Technical Editor: D. M. McEligot.

(1992) introduced another single color capturing technique using a chrominance-luminance technique developed by Hirsch (1987). Calibrating the hue from colors appearing on liquid crystal sprayed surface with respect to temperature has been frequently practiced in the past. The wavelength of the color from a liquid crystal covered surface was correlated with local temperature by Kuzniers et al. (1980). This study employed local temperature measurements in the field of plastic and restorative surgery. Buiko and Tsykalo (1980) used cholesteric liquid crystals for temperature mapping in the diagnosis of neoplasms of the human eye. The temperature dependency of the dominant wavelength of the light selectively reflected from the surface was obtained by a spectrophotometer. Hollingsworth et al. (1989) used a hue versus temperature relation in a steady-state convective heat transfer experiment for the first time. They could calculate the hue angle of a liquid crystal color starting from RGB attributes provided by standard video equipment. Their technique was useful for steady-state heat transfer measurements taken at several points on a heat transfer surface.

Most of the spectrum of colors appearing on liquid crystal sprayed surface can be used to obtain many isotherms simultaneously. A hue capturing technique based on the real-time determination of the dominant wavelength of each color appearing on a liquid crystal surface is described by Camci et al. (1992). An extensive experimental validation of this heat transfer mapping technique is presented by Kim (1991), for a well-documented test case of a round circular heated jet impinging on a flat plate, initially kept at ambient temperature. Liquid crystal based heat transfer distributions are compared with results from conventional surface mounted thermocouple based distributions. Additional comparisons are also made to other studies available in the literature. A detailed uncertainty analysis for the heat transfer technique is also presented. A complete numerical heat transfer simulation of the impinging jet heat transfer experiment is also provided by Kim (1991). Simulations include a differential solution for the transient energy equation in addition to momentum and continuity equations. As a result of a set of validation experiments and computations, it has been shown that the hue capturing method is an accurate and powerful heat transfer tool.

The current study deals with the implementation of the hue capturing technique developed by Camci et al. (1993) on a complex curved surface. The bottom surface of a square to rectangular transition duct is used for two-dimensional surface mapping of heat transfer coefficients. The current study combines a real-time hue conversion process with a transient heat transfer model developed for complex curved surfaces. The study also focuses on the use of narrow band, encapsulated liquid crystals for better accuracy in hue versus temperature calibration. The standard deviation of hue around a mean hue versus temperature line is about 1/10th of the bandwidth of the liquid crystal as reported by Camci et al. (1993), for an encapsulated chiral nematic liquid crystal.

Wind Tunnel and Transition Duct

A continuous flow wind tunnel is adapted such that flow can be switched suddenly through the test section. The wind tunnel and transition duct connected to a main laboratory vacuum system are shown in Fig. 1. Ambient temperature air is drawn from the laboratory through the test section. The transient experiment is started by opening a pneumatically controlled fast-acting valve 3 m downstream of the test section.

The model tested was a transition duct from (20.8 cm × 20.8 cm) square to a rectangular cross section of (32.2 cm × 10.7 cm). The heat transfer at the bottom wall of the transition duct was measured. Details of the duct geometry are given in Fig. 2. A microswitch on the valve sent a simultaneous trigger pulse for the start of the data acquisition sequence. A precision timer was also started at this specific time to time stamp the video frames. The chiral nematic liquid crystal images were recorded by a color video camera located in an approximately normal direction to the transition duct floor and transmitted to a high-resolution video recorder. Model illumination was provided by fluorescence lights located about 50 cm away from the duct floor.

The transition duct was preheated by using an electronically controlled electric heater chamber as two half cylinders. Blanket heaters as radiation heaters provided a sufficiently uniform model temperature after a five-hour initial heating period. The temperature uniformity was continuously monitored at ten discrete locations on the model surface. A standard initial temperature deviation of only $\mp$ 0.2°C was allowed. The transition duct model was precision machined from clear acrylic. A thermophysical triple product $(\rho c_p k)^{1/2}$ value of 569 $W(s)^{1/2}/(m^2K)$ was used in data reduction as reported by Baughn et al. (1988). Transient conduction analysis showed that the thermal wave did not reach the back end of the test wall during the heat transfer experiment (Jones and Hippensteele, 1985). A cross section of the heat transfer surface with liquid crystal coating is shown in Fig. 2.

Color Definition and Hue Capturing Process

Color may be defined as a psychophysical property of light, specifically, the combination of those characteristics of light that produce the sensations of hue, saturation, and intensity in a normal human observer. Color sensation from a liquid crystal covered surface is generated by several characteristics. A few of these characteristics can be summarized as the pitch of the helical arrangement of the crystal structure, the spectral characteristics of the light illuminating the liquid crystal cov-

Nomenclature

c = specific heat
h = convective heat transfer coefficient = $\dot{q}/(T_{o\infty} - T_w)$
HSI = hue, saturation, intensity (normalized)
k = thermal conductivity
L = one side of the square inlet section
Nu = Nusselt number
p = local pressure
$\dot{q}$ = heat flux
R = total error in uncertainty analysis
RGB = red, green, blue (normalized)
Re = local Reynolds number
t = time
T = temperature
TU = turbulence intensity
x, y, z = spatial coordinates
y = distance normal to the curved wall
α = thermal diffusivity of air = $k/(\rho/c_p)$
β = nondimensional time = $h(t/\rho c_p k)^{1/2}$
θ = nondimensional wall temperature = $(T_w - T_i)/(T_{o\infty} - T_i)$
λ = dominant wavelength of a color
ρ = density

Subscripts

i = initial
o = total condition
p = at constant pressure
rec = recovery
w = local wall condition
λ = spectral local value
∞ = free stream

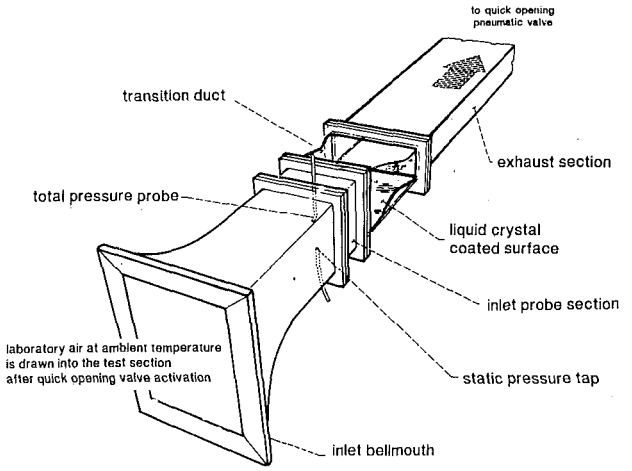

Fig. 1 Heat transfer tunnel and the transition duct

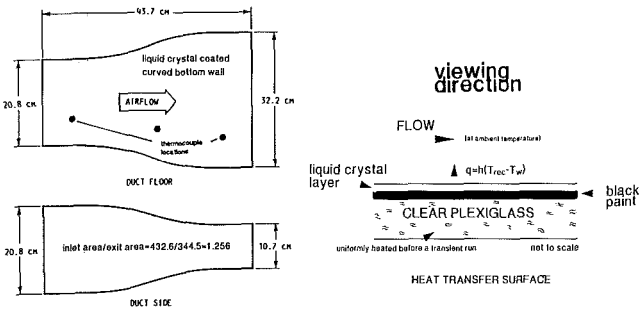

Fig. 2 Details of the duct geometry and the heat transfer surface

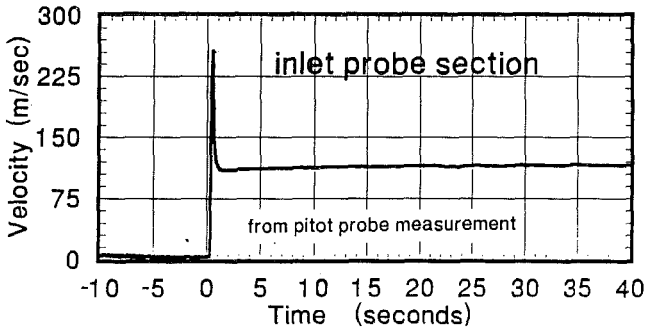

Fig. 3 Free-stream velocity at the inlet probe section

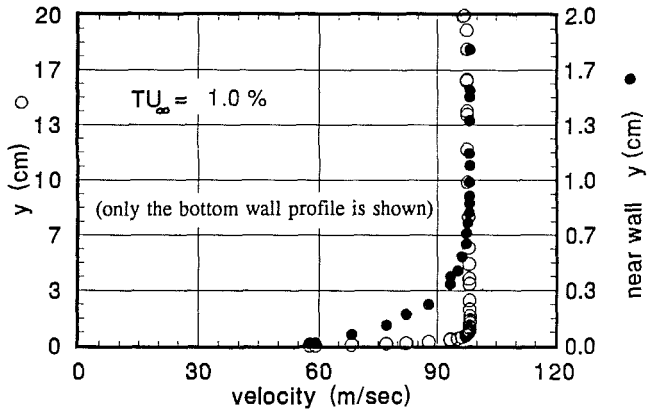

Fig. 4 Boundary layer profile at the inlet probe section

ered surface, and the spectral response of the color sensing component, which may be a human eye or an imaging sensor used in a color camera. The pitch of the helical arrangement in the liquid crystal structure is altered by local temperature on the heat transfer surface. The color recognition technique used in this study is further explained by Camci et al. (1993), Kim (1991), and Berns (1989). The present system uses three eight-bit video A/D converters. Each of the RGB attributes is scaled between 0 and 255. The real-time conversions from RGB attributes to HSI and the role of intensity and saturation in liquid crystal color interpretation are discussed by Camci et al. (1992).

Transient Heat Transfer Technique

The main assumption of the measurement technique is the small penetration depth of the thermal pulse into the plexiglass wall compared to the thickness of the wall. This assumption allows the use of a one-dimensional transient heat transfer theory developed for semi-infinite bodies. The local wall temperature rise for an impulsively starting heat transfer experiment can be related to time, thermophysical properties of the body, and the convective heat transfer coefficient h:

$$\theta = \frac{T_w - T_i}{T_{0\infty} - T_i} = 1 - \exp(\beta^2)\mathrm{erfc}(\beta) \qquad (1)$$

where θ and $\beta = h(t/\rho c_p k)^{1/2}$ are nondimensional temperature and time, respectively. A sixth-order spline fitting routine was developed for the variation of nondimensional time β with respect to the nondimensional wall temperature θ, using Eq. (1). Attention was paid to obtain an accurate representation for the first 15 seconds of a typical experiment.

$$\beta = (-0.01071) + (1.11390)\theta - (0.66474)\theta^2 + (2.22070)\theta^3 + (8.93390)\theta^4 - (24.57100)\theta^5 + (20.58600)\theta^6 \qquad (2)$$

Experimental Results and Discussion

Mainstream Flow and Thermal Boundary Conditions. A continuous recording of the tunnel inlet temperature, inlet velocity from a pitot probe, and fast valve initial transient behavior were obtained. Tunnel total temperature measured upstream of the inlet section was the same as the ambient temperature ($T_{0\infty}$ = 28.6°C). The inlet velocity measured at the inlet probe section by using a pitot probe was free of transients after the first second, measured from the valve opening time as shown in Fig. 3. However, additional inlet velocity measurements taken by a fast response hot wire showed that the actual start-up transients are confined to a 40 millisecond period after the valve opening.

The mean velocity component parallel to the tunnel axis measured at the free stream of the inlet probe section was about 97.5 m/s. Figure 4 shows a mean velocity traverse taken along the height of the duct centerline. The inlet boundary layer thickness at the bottom wall of the inlet probe section was measured to be 8.9 mm. It was also confirmed that the top wall boundary layer has a very similar distribution. The measured free-stream turbulence intensity in the mainstream of the inlet probe section was about 1.0 percent. The initial temperature for the liquid crystal covered bottom surface of the duct was about T_i = 55.7°C.

Three-dimensional mean flow in the duct was predicted by solving Navier–Stokes equations in a staggered grid (49 × 26 × 26) (Kim, 1991). Due to the symmetry of the duct, only one quadrant of the field was predicted in a generalized coordinate system as presented in Fig. 5. A kinetic energy-dissipation rate model was used for turbulent flow modeling. Turbulent kinetic energy at the inflow boundary was computed from measured root mean square values of the velocity fluctuation based on the isotropic field assumption. The inlet centerline velocity of 97.5 m/s is accelerated to 123 m/s at the exit section due to the overall area convergence of 0.716, Fig. 5(*a*). Two coun-

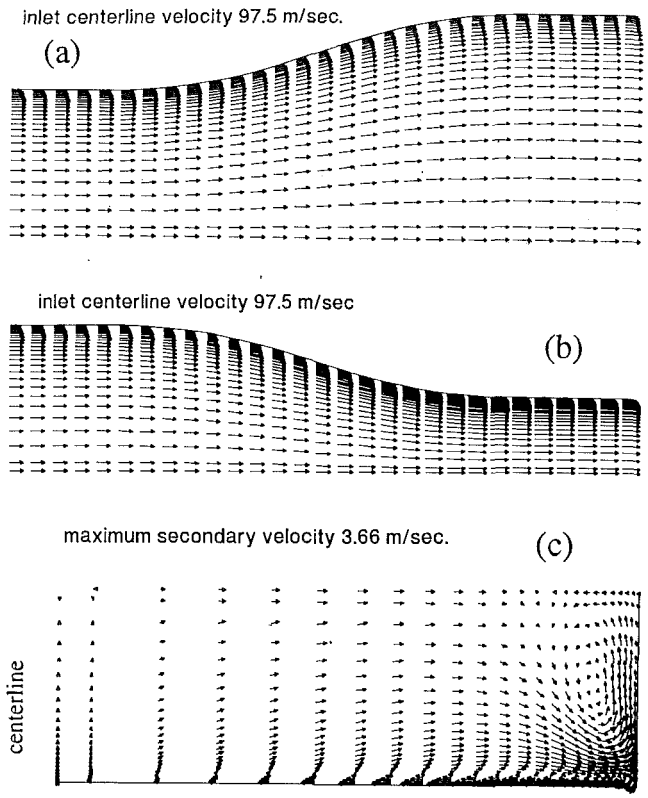

Fig. 5 Three-dimensional flow predictions in the duct: (*a*) horizontal plane; (*b*) vertical plane; (*c*) secondary velocities

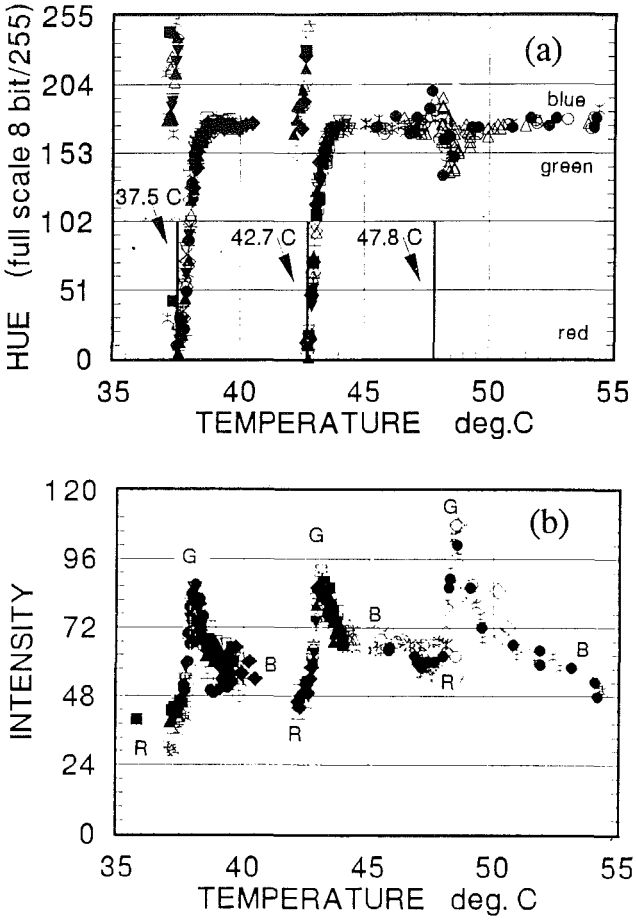

Fig. 6 Hue and intensity calibration with respect to temperature

terrotating vortices in the exit quadrant were identified. However, the absolute magnitude of the maximum secondary velocity (3.6 m/s) was found to be much smaller than that of the streamwise velocity, Fig. 5(*c*).

Liquid Crystal Calibration. Hue versus temperature calibrations were performed to find out the dependency of local liquid crystal hue to temperature. A mixture of three chiral nematic liquid crystals each having a color bandwidth of approximately 1°C was then sprayed simultaneously. The estimated thickness of the liquid crystal layer was on the order of 10 μm. The highest temperature crystal displayed red color at 47.8°C. The medium temperature and the lowest temperature crystal displayed red at 42.7°C and 37.5°C, respectively. The imaging camera was located on top of the duct in a direction almost normal to the bottom surface. The same illumination system of actual heat transfer runs was used. A heat gun with an approximate exit temperature of 85°C was directed to a *T*-type thin foil thermocouple with a typical time response of 1 millisecond. The thermocouple was flush mounted underneath the liquid crystal layer, at this specific pixel location. Figure 6(*a*) shows the variation of local temperature measured by the thermocouple with respect to liquid crystal hue as recorded by the hue capturing system. Different symbols in Fig. 6 suggest different hue capturing sequences performed at different times. The color information as hue shows an approximately linear variation with respect to local temperature between 37.7°C and 38.3°C. It is a known phenomenon that the perceived color especially from an unencapsulated (neat) liquid crystal is dependent on the angle at which it is viewed (Jones et al., 1992; Herald and Wiegel, 1980). However, our visual observations consistently showed that the viewing angle sensitivity of hue from micro-encapsulated chiral nematic liquid crystals is much less significant than that of the unencapsulated (neat) crystals.

Figure 6(*b*) shows the variation of local intensity with respect to local temperature for all three of the liquid crystals. A very distinct intensity peak for each liquid crystal range was always observed. After the peak, the intensities dropped continuously to a middle value between the lowest intensity and the peak intensity value. This final value corresponded to the dark blue color. For the highest temperature crystal, the total number of hue values captured was limited in comparison to the wide spectrum of colors obtained with the middle and lowest temperature crystals. Faded colors were attributed to the highest level of temperature gradient applied along a direction normal to the liquid crystal coated surface. However, the hue values between 130 and 160 provided a successful temperature calibration for the highest temperature liquid crystal.

High Resolution Heat Transfer Maps at the Bottom Surface of the Transition Duct. The experiment with an initally heated test section, T_i = 55.7°C, was started by suddenly connecting the test section to a large vacuum reservoir providing continuous steady flow at $T_{0\infty}$ = 28.6°C. The heat flow direction was from the wall to the free stream. The highest temperature liquid crystal responded between t = 3.38 and t = 6.25 seconds as shown in Fig. 7. The figure presents only eight of the 97 available video images and the associated quantitative heat transfer islands. The centerline of the duct is shown with a solid line in the figure.

Since hue determination at low intensity values is not a stable process (Berns, 1989), any hue value having an associated intensity value of 50 or less was discarded during the data reduction. Each pixel staying within the hue range between 140 and 150 was marked and its pixel coordinate was written into a computer file. A hue range 10 units wide corresponded to an approximate temperature interval of 0.31°C of the highest temperature crystal. The pixels marked with the criteria

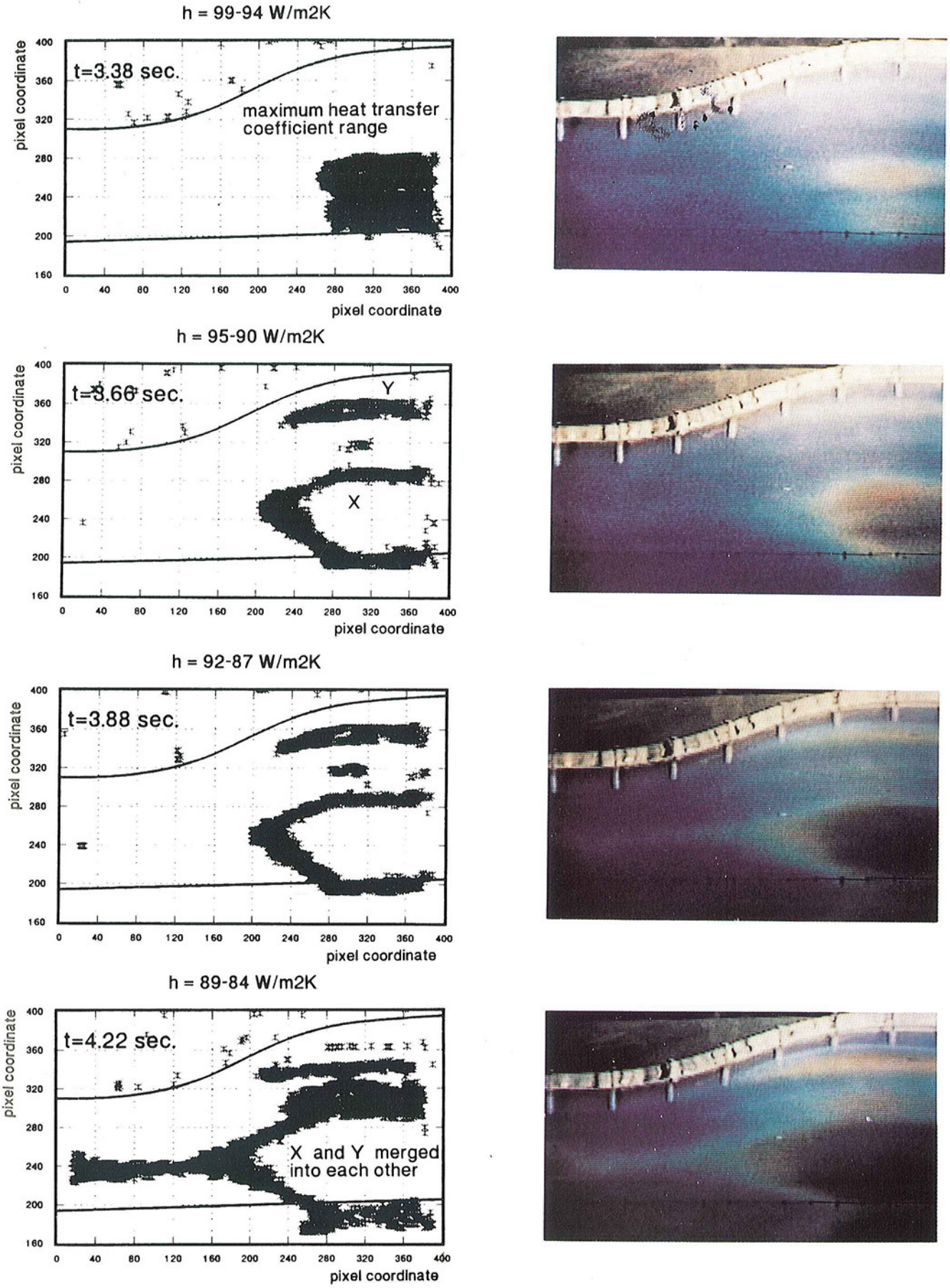

Fig. 7(*a*) Convective heat transfer coefficient distributions; t = 3.38, 3.66, 3.88, 4.22 s

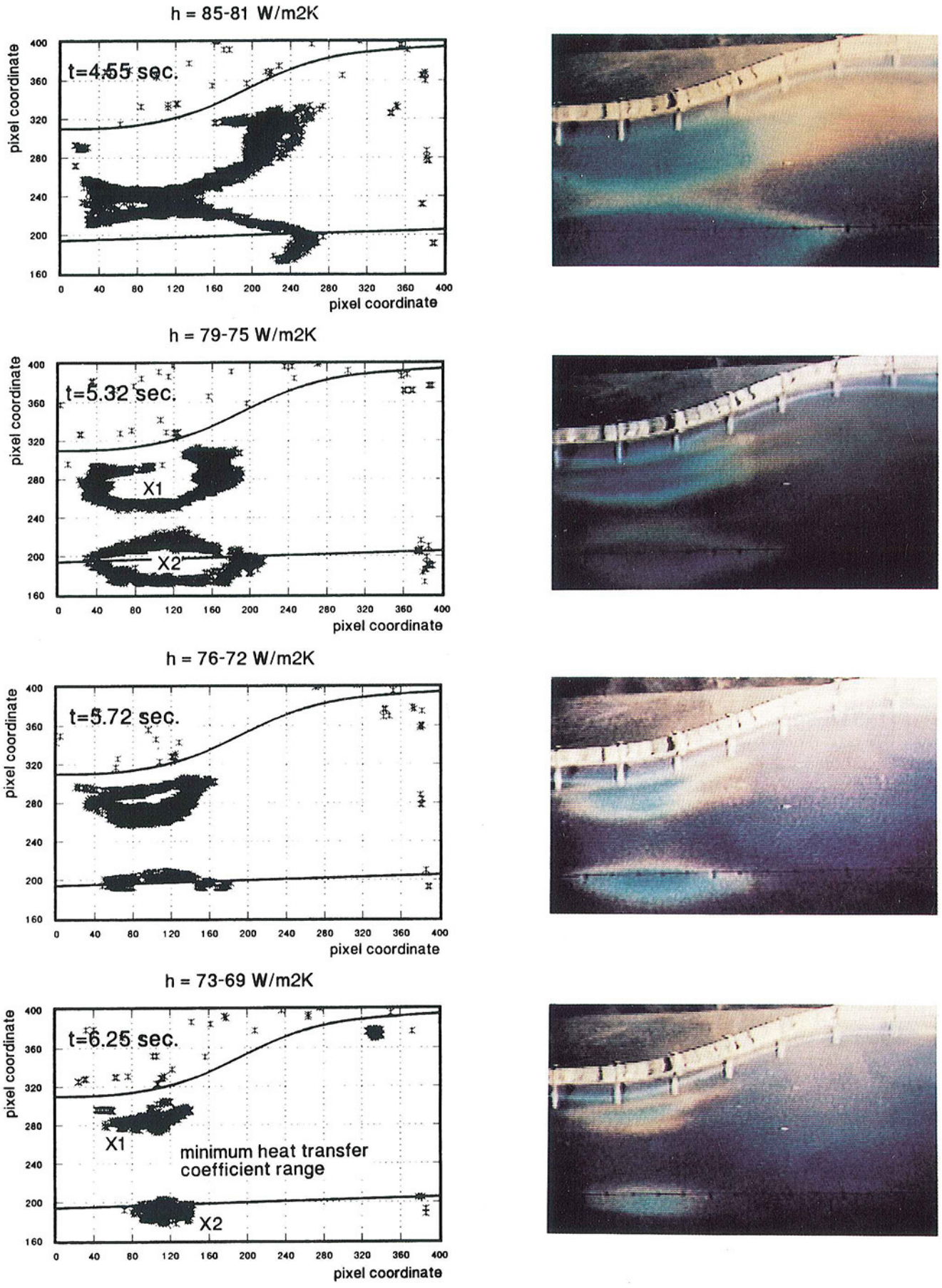

Fig. 7(*b*) Convective heat transfer coefficient distributions; t = 4.55, 5.32, 5.72, 6.25 s

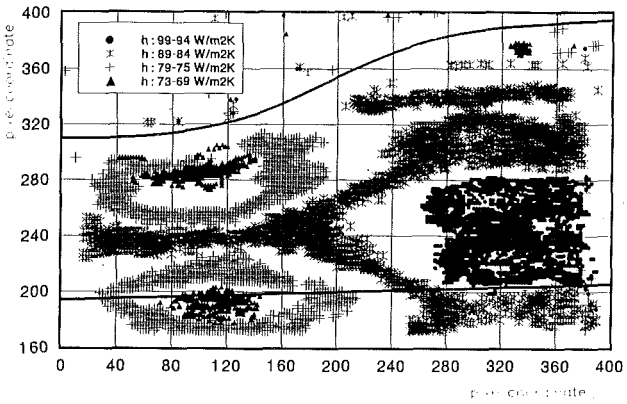

Fig. 8 Heat transfer map at the bottom surface of the transition duct

described above were also presented on the left-hand side of each color image. The temperature of each individual pixel was deduced from the calibration information shown in Fig. 6(*a*). The convective heat transfer coefficient was obtained by using the transient technique described in a previous section.

When the fast valve opened, the image from the bottom surface was completely dominated by black. The appearance of the first dark blue color was within the first second. The dark blue color was dominant almost uniformly all over the bottom surface. Blue content of the liquid crystal color did not change for a long period between $t = 0.0$ and $t = 3.30$ seconds due to a negligible hue-temperature slope around 49°C. The colors in this band could approximately be described by greenish-blue as shown for the image taken at $t = 3.38$ seconds in Fig. 7. This specific color band corresponded to the local temperatures between 48.25 and 48.56°C. The calculated heat transfer coefficient limits for the specific hue range at $t = 3.38$ s were between 99 and 94 W/m^{2}K. The specific heat transfer coefficient island shown at $t = 3.38$ s corresponded to the coldest zone of the duct bottom surface. This island generated the highest heat transfer coefficient. As the time passed, the cold front (48.25–48.56°C) diffused more into the inlet section of the duct. At $t = 3.43$ and $t = 3.56$ seconds the spread of the cold front was not very distinct due to small time steps on the order of 50 and 130 milliseconds. At $t = 3.66$ seconds, the cold front was no longer in the shape of a single closed island. The cold front was more diffused in a form that complemented the island representing the previous heat transfer distribution for $t = 3.38$ s. Besides this island, marked (X), a narrow band of the same cold front (Y) was apparent close to the upper right corner of the image. The images for $t = 3.66$, 3.88, and 4.22 seconds show the temporal growth of the islands marked as (X) and (Y). During this period, the region (Y) did not significantly alter its shape. However, (X) started to grow more into the inlet section of the duct. Regions (X) and (Y) gradually merged into each other at $t = 4.22$. Furthermore, the left-hand edge of the island (X) extended itself up to the square inlet section of the duct. The frames captured at $t = 4.55$ and 5/32 seconds showed the movement of the island (X) farther into the square inlet section. Gradual transition into smaller heat transfer coefficient islands with increasing time continued as shown in the image for $t = 5.32$ seconds. Islands ($X1$) and ($X2$) gradually reduced their areas as time passed. At $t = 6.25$ seconds, the island ($X2$) became a relatively small region near the symmetry line of the duct. The data density of useful heat transfer information from the highest temperature crystal was extremely high. A further combined presentation of data is shown in Fig. 8. As far as the h bandwidths are concerned, the corresponding heat transfer coefficient islands were distinctly marked without any significant overlapping. The blank areas that were not filled with symbols also automatically generated extra heat transfer coefficient islands between the marked areas.

As a general result, the highest convective heat transfer coefficients were observed near the exit section of the bottom surface. This area corresponded to a flow zone where the duct width was maximum in the horizontal plane and minimum in the vertical plane. The highest heat transfer coefficients appeared in an area where there was strong mainstream acceleration of the curved bottom surface. The entrance section of the duct resulted in the lowest level of convective heat transfer activity. As is shown in the images of $t = 5.32$, 5.72, and 6.25 seconds, the lowest heat transfer islands were organized along the first third of the duct length around the symmetry line, ($X1$ and $X2$). The flow and its corresponding convective heat transfer activity were symmetric in the transition duct. The corner flow regions near the curved duct boundary shown in Fig. 7 experienced minimal convective heat transfer coefficients.

Uncertainty Analysis

Typical uncertainties from the technique introduced, at better than 90 percent confidence level, are estimated as:

$$\delta(T_{o\infty} - T_i)/(T_{o\infty} - T_i) = \mp 1.5 \text{ percent}$$

$$\delta(T_w - T_i)/(T_w - T_i) = \mp 1.0 \text{ percent}$$

$$\delta((\rho c_p k)^{1/2})/(\rho c_p k)^{1/2} = \mp 5.0 \text{ percent} \quad \delta t/t = \mp 1.5 \text{ percent}$$

The uncertainty of heat transfer coefficient can be obtained from the combination of the listed errors (Kline and McClintock, 1953). The uncertainty of the nondimensional temperature $\theta = (T_w - T_i)/(T_{0\infty} - T_i)$ can be calculated as ($\delta\theta/\theta = 1.80$ percent). The uncertainty of the nondimensional time β is based on Eq. (1) ($\delta\beta/\beta = (1/\beta)(\delta\beta/\delta\theta)(\delta\theta) = 2.74$ percent). The combination rule results in final uncertainty estimate:

$$\delta h/h = \{[(\delta(\rho c_p k)^{1/2}/(\rho c_p k)^{1/2}]^2 + [\delta t/t]^2 + [\delta\beta/\beta]^2\}^{1/2} = 5.89 \text{ percent}$$

Conclusions

A recently developed digital image processing based real-time color capturing method was implemented to obtain convective heat transfer coefficients from liquid crystal coated surfaces in a transition duct with a complex geometry. The method, previously validated for simple geometries and line distributions, was successfully implemented on curved surfaces.

A real-time hue capturing technique was employed in a transient heat transfer experiment.

The high spatial resolution of the present transient method with pixel by pixel processing capability is also applicable in unsteady heat transfer research for wall temperature fluctuation levels having a typical frequency of less than 60 Hz.

A repeatable hue versus temperature calibration process for the crystal mixture provided an accurate heat transfer tool with an estimated uncertainly of ∓ 5.9 percent on convective heat transfer coefficient.

A complete heat transfer mapping of the bottom surface was possible with excellent spatial resolution, using only seven liquid crystal image frames out of 97 available from the passage of the highest temperature crystal colors.

An approximately three second long color passage period from a single crystal was adequate for the complete mapping effort. The reduced data as convective heat transfer coefficient islands on the surface were presented with their associated natural color image captured for each specific time. Consistency and repeatability of the method in terms of marking the pixels within a predetermined narrow temperature band were proven.

The highest convective heat transfer coefficients were induced near the exit section of the bottom surface, occupying a central region having one third of the duct length as a characteristic length. This area corresponded to a flow zone where the duct width was maximum in the horizontal plane and minimum in the vertical plane. This zone of the bottom wall was exposed to a flow with significant mainstream acceleration. The lowest level of convective heat transfer was observed near the entrance section of the duct along the first one third of the duct length around the symmetry line. There was also a second zone with relatively low convective heating activity near the upper curved boundary ($X1$, t = 6.25 second). The corner flow region experienced minimal convective heat transfer coefficient levels.

References

Baughn, J. W., Ireland, P. T., Jones, T. V., and Saniei, N., 1988, "A Comparison of the Transient and Heated Coating Methods for the Measurement of Local Heat Transfer Coefficients on a Pin Fin," ASME Paper No. 88-GT-180.

Berns, R. S., 1989, "Colorimetry for Electronic Imaging Devices," Tutorial Short Course Notes (T60), Center for Imaging Science/Rochester Institute of Technology, The International Society for Optical Engineering, OE/LASE '89.

Buiko, A. S., and Tsykalo, A. L., 1980, "Color Thermography of Liquid Crystals in Diagnosis of Neoplasms of Eye and Eye Socket," *Advances in Liquid Crystal Research and Applications*, Vol. 2, L. Bata, ed., Pergamon Press, Oxford, pp. 1301–1304.

Bunker, R. S., Metzger, D. E., and Wittig, S., 1992, "Local Heat Transfer in Turbine Disk Cavities. Part I: Rotor and Stator Cooling With Hub Injection of Coolant," ASME *Journal of Turbomachinery*, Vol. 114, pp. 211–220.

Camci, C., Kim, K., and Hippensteele, S. A., 1992, "A New Hue Capturing Technique for the Quantitative Interpretation of Liquid Crystal Images Used in Convective Heat Transfer Studies," ASME *Journal of Turbomachinery*, Vol. 114, pp. 512–518.

Camci, C., Kim, K., and Hippensteele, S. A., 1993, "An Image Processing Based Liquid Crystal Technique Using a New Hue Capturing Method for Convective Heat Transfer Studies," NASA Technical Memorandum, to be published.

Cooper, T. E., Field, R. J., and Meyer, J. F., 1975, "Liquid Crystal Thermography and Its Application to the Study of Convective Heat Transfer," ASME JOURNAL OF HEAT TRANSFER, Vol. 97, pp. 442–450.

Fergason, J. L., 1964, "Liquid Crystals," *Scientific American*, Vol. 211, No. 2, pp. 76–85.

Fergason, J. L., 1968, "Liquid Crystals in Nondestructive Testing," *Applied Optics*, Vol. 7, No. 9, pp. 1729–1737.

Herald, W., and Wiegel, D., 1980, "Problems of the Photographic Documentation of Liquid Crystalline Thermographs," *Advances in Liquid Crystal Research and Applications*, Vol. 2, L. Bata, ed., Pergamon Press, Oxford, pp. 1255–1259.

Hippensteele, S. A., Russell, L. M., and Stepka, F. S., 1983, "Evaluation of a Method for Heat Transfer Measurements and Thermal Visualization Using a Composite of a Heater Element and Liquid Crystals," ASME JOURNAL OF HEAT TRANSFER, Vol. 105, pp. 184–189.

Hippensteele, S. A., Russell, L. M., and Torres, F. J., 1985, "Local Heat Transfer Measurements on a Large Scale-Model Turbine Blade Airfoil Using a Composite of a Heater Element and Liquid-Crystals," ASME *Journal of Engineering for Gas Turbines and Power*, Vol. 107, pp. 953–960.

Hippensteele, S. A., Russell, L. M., and Torres, F. J., 1987, "Use of a Liquid-Crystal, Heater-Element Composite for Quantitative, High-Resolution Heat Transfer Coefficients on a Turbine Airfoil, Including Turbulence and Surface Roughness Effects," NASA TM 87355.

Hirsch, C., 1987, "Aufbau und Inbetriebnahme eines Versuchsstandes zur instätionaren Wärmeübergangsmessung an rotierenden Scheiben bei erzwungener Konvektion und Prallkühlung unter Nutzung thermochromer Flüssigkristalle als Temperaturindikatoren," Diplomarbeit No. 302, Institut für Thermische Strömungsmaschinen, Universität Karlsruhe, Germany.

Hollingsworth, D. K., Boehman, A. L., Smith, E. G., and Moffat, R. J., 1989, "Measurement of Temperature and Heat Transfer Coefficient Distribution in a Complex Flow Using Liquid Crystal Thermography and True-Color Image Processing," *Collected Papers in Heat Transfer*, ASME HTD-Vol. 123, pp. 35–42.

Holmes, B. J., and Gall, P. D., 1986, "Liquid Crystals for High Altitude in Flight Boundary Layer Flow Visualization," presented at the AIAA General Aviation Technology Conference, AIAA Paper No. 86-2592.

Holmes, B. J., and Obara, C. J., 1987, "Advances in Flow Visualization Using Liquid Crystal Coating," presented at the SAE General Aviation Aircraft Meeting, Wichita, SAE Paper No. 87-1017.

Ireland, P. T., and Jones, T. V., 1985, "The Measurement of Local Heat Transfer Coefficients in Blade Cooling Geometries," *AGARD Conference Proceedings on Heat Transfer and Cooling*, CP 390 Paper 28, Bergen, Norway.

Ireland, P. T., and Jones T. V., 1987, "The Response Time of a Surface Thermometer Employing Encapsulated Thermochromic Liquid Crystals," *J. Phys. E: Sci. Instrum.*, Vol. 20.

Jones, T. V., and Hippensteele, S. A., 1985, "High-Resolution Heat Transfer-Coefficient Maps Applicable to Compound-Curve Surfaces Using Liquid Crystals in a Transient Wind Tunnel," *Developments in Experimental Techniques in Heat Transfer and Combustion*, ASME HTD-Vol. 71.

Jones, T. V., and Hippensteele, S. A., 1988, "High-Resolution Heat Transfer-Coefficient Maps Applicable to Compound-Curve Surfaces Using Liquid Crystals in a Transient Wind Tunnel," NASA TM 89855.

Jones, T. V., Ireland, P. T., and Wang, Z., 1992, "Liquid Crystal Techniques," Keynote paper, *Proceedings of the International Symposium on Heat Transfer in Turbomachinery*, Athens, Greece, Aug. 24–28, 1992.

Kim, K., 1991, "A New Hue Capturing Technique for the Quantitative Interpretation of Liquid Crystal Images Used in Convective Heat Transfer Studies," Ph.D. Thesis, The Pennsylvania State University, Aerospace Engineering Department.

Klein, E. J., and Margozzi, A. P., 1970, *Review of Scientific Instruments*, Vol. 44, pp. 238–243.

Kline, S. J., and McClintock, F. A., 1953, "Describing Uncertainties in Single Sample Experiments," *Mechanical Engineering*, Vol. 75, Jan., pp. 3–8.

Kuzniers, J., Drzymala, A., Grossman, B., and Lipinski, A., 1980, "The Application of Liquid-Crystalline Temperature Indicators to Medical Diagnosis," *Advances in Liquid Crystal Research and Applications*, Vol. 2, L. Bata, ed., Pergamon Press, Oxford, pp. 1277–1281.

Moffat, R. J., 1990, "Experimental Heat Transfer," *Heat Transfer 1990, Proceedings of the Ninth International Heat Transfer Conference*, Keynote Paper 11, G. Hetsroni, ed., pp. 187–204.

Parsley, M., 1991, "The Use of the Thermochromic Liquid Crystals in Research Applications, Thermal Mapping and Nondestructive Testing," *Seventh IEEE SEMI-THERM Symposium*, pp. 53–58.

Simonich, J. C., and Moffat, R. J., 1984, "Liquid Crystal Visualization of Surface Heat Transfer on a Concavely Curved Turbulent Boundary Layer," ASME *Journal of Engineering for Gas Turbines and Power*, Vol. 106, pp. 619–627.

Wang, Z., Ireland, P. T., and Jones, T. V., 1990, "A Technique for Measuring Convective Heat-Transfer at Rough Surfaces," ASME Paper No. 90-GT-300.

Zharkova, G. M., Khachaturyan, V. M., Vostokov, L. A., and Alekseev, M. M., 1980, "Study of Liquid Thermoindicators," *Advances in Liquid Crystal Research and Applications*, Vol. 2, L. Bata, ed., Pergamon Press, Oxford, pp. 1221–1239.

J. von Wolfersdorf

R. Hoecker

T. Sattelmayer

ABB-Corporate Research Center,
Baden, Switzerland

A Hybrid Transient Step-Heating Heat Transfer Measurement Technique Using Heater Foils and Liquid-Crystal Thermography

A transient heat transfer technique using a heating foil and liquid crystals is described. The basic idea is a step-heating technique, eliminating the local heat flux and the surface temperature during the data reduction. Nonuniformities in the heating pattern are allowed and calibration of the liquid crystals is no longer necessary. They are used as an indicator of an isotherm only. The heat transfer coefficient is deduced from two time measurements. The laminar and turbulent boundary layer flows over a flat plate were tested to verify the applicability and accuracy of the method.

Introduction

Advanced cooling techniques in gas turbines are required to improve engine cycle performance by significantly increasing turbine inlet temperatures. Therefore, new and improved heat transfer measurement techniques with the capability of full surface heat transfer determination are required.

Transient heat transfer measurement techniques using liquid crystals, thermal paints, or melting point coatings are well known to be successful in high-resolution measurements on surfaces with complex shapes and film cooling geometries (Ireland and Jones, 1985; Clifford et al., 1983; Metzger and Larson, 1986; Jones and Hippensteele, 1988; Baughn et al., 1989; Blair et al., 1991; Vedula and Metzger, 1991).

If the model is of low thermal conductivity and the measurements are made in a short period of time, the model may be considered to be one dimensional and semi-infinite. This implies that the penetration depth of heat into the model is small compared to the model wall thickness. Usually, transient heat transfer techniques use an initial temperature difference between the flow and the model. Two possible methods are:

- Model initially at room temperature and the gas preheated (Ireland and Jones, 1985).
- Model preheated with a hot-air blower or by an external water jacket and the flow at room temperature (Jones and Hippensteele, 1988).

The model undergoes transient heating or cooling during the test. Under the assumptions of constant heat transfer coefficient as well as constant gas temperature with time and known model wall properties, the measurement of the wall temperature at a certain time enables the heat transfer coefficient to be found from the solution of the one-dimensional, transient heat conduction equation with the convection boundary condition if the gas and initial temperatures are also known (Carslaw and Jaeger, 1959, p. 72):

$$\frac{T_W - T_0}{T_G - T_0} = 1 - e^{\frac{\alpha^2 t}{k}} \operatorname{erfc}\left(\frac{\alpha\sqrt{t}}{\sqrt{k}}\right) \tag{1}$$

with

$$k = \lambda \rho c_p.$$

After calibrating the liquid crystals, the temperature ratio on the left-hand side of Eq. (1) is known. Using the measured temperature and time data pair at observed positions, heat transfer coefficients can be calculated from Eq. (1).

Liquid crystals are also used in steady-state experiments. The model walls are covered by thin electrically heated foils such as composite heater elements (Hippensteele et al., 1985), gold-coated plastic sheets (Baughn et al., 1985), or metal foils (Graziani et al., 1980).

In the case of a test flow at room temperature, a heater foil (heater input Q) produces the desired temperature difference for a transient test. An analogous solution of the one-dimensional, transient heat conduction equation with $q = Q/A$ can be derived (see following chapter for details):

$$\frac{T_W - T_0}{\frac{q}{\alpha} + T_G - T_0} = 1 - e^{\frac{\alpha^2 t}{k}} \operatorname{erfc}\left(\frac{\alpha\sqrt{t}}{\sqrt{k}}\right) \tag{2}$$

When the initial model temperature is equal to flow temperature ($T_0 = T_G$) Eq. (2) is reduced to:

$$\alpha \frac{T_W - T_0}{q} = 1 - e^{\frac{\alpha^2 t}{k}} \operatorname{erfc}\left(\frac{\alpha\sqrt{t}}{\sqrt{k}}\right). \tag{3}$$

After the measurement of the surface temperature at a certain time the heat transfer coefficient can be determined from the measured heater input. In this case it must be assumed that the heat dissipation in the foil is uniform over the entire surface, which may be hard to achieve in some cases. Possible errors are caused by nonuniformities in the resistance due to nonuniform heater thickness or temperature dependencies.

Metallic coatings can be applied instead of electrical heater sheets glued on the model surface. By using such a coating for complex geometries, nonuniformities in thickness are probable. Furthermore, some investigations show (Tarasuk and Castle, 1983) that the electrical power dissipation in a heated wide metallic foil of uniform thickness can be of the order of 30 percent higher near the center of the foil than near the foil edge.

Step-Heating Technique

Transient methods using step-heating techniques are known for measuring thermal transport properties of various materials (Bittle and Taylor, 1984; Rooke and Taylor, 1988). Most deal with a constant heat flux as a boundary condition for the heated surface.

Contributed by the Heat Transfer Division for publication in the JOURNAL OF HEAT TRANSFER. Manuscript received by the Heat Transfer Division April 1992; revision received October 1992. Keywords: Measurement Techniques, Transient and Unsteady Heat Transfer. Associate Technical Editor: J. M. McEligot.

An improved step-heating technique, which eliminates the local heat flux as well as the local surface temperature in the data reduction procedure, is given as follows: The model is assumed to be isotropic and covered with a surface heater of negligible thickness. Initially, the model has the same temperature as the test flow. At $t = 0$ the foil is heated with a predetermined power input. At each position on the model a local heat flux q is dissipated in the foil. The time-dependent pattern of isothermal contours on the model is monitored using a surface coated with thermochromic liquid crystals (TLC). The delay time t_1 from the start of the experiment taken for each position to reach a chosen temperature (color) is measured. After a period of time t_u, the power input is switched to a lower value, leading to a heat flux ϵq with $0 \le \epsilon < 1$. Now the isotherms move across the surface in the opposite direction. For each position the previous evaluated isotherm appears a second time at the delay time t_2. The governing equation is the heat conduction equation:

$$\rho c_p \frac{\partial T}{\partial t} = \lambda \frac{\partial^2 T}{\partial y^2} \quad 0 < y < \infty \tag{4}$$

with the initial condition:

$$T(y,\ t=0) = T_0 \tag{5}$$

and the boundary conditions:

$$-\lambda \frac{\partial T(y=0,\ t)}{\partial y} = q - \alpha (T_W - T_G) \quad 0 < t < t_u \tag{6}$$

$$-\lambda \frac{\partial T(y=0,\ t)}{\partial y} = \epsilon q - \alpha (T_W - T_G) \quad t_u < t. \tag{7}$$

The equation may be solved to give the surface temperature with $T_0 = T_G$ as (Carslaw and Jaeger, 1959, p. 74):

$$\alpha \frac{T_W - T_0}{q} = 1 - e^{\frac{\alpha^2 t}{k}} \operatorname{erfc}\left(\frac{\alpha\sqrt{t}}{\sqrt{k}}\right) \quad 0 < t < t_u \tag{8}$$

$$\alpha \frac{T_W - T_0}{q} = \epsilon - e^{\frac{\alpha^2 t}{k}} \operatorname{erfc}\left(\frac{\alpha\sqrt{t}}{\sqrt{k}}\right) + (1-\epsilon) e^{\frac{\alpha^2 (t-t_u)}{k}} \operatorname{erfc}\left(\frac{\alpha\sqrt{t-t_u}}{\sqrt{k}}\right) \quad t_u < t. \tag{9}$$

Measuring the times t_1 and t_2 with $0 < t_1 < t_u < t_2$ for an isotherm yields $T_W(t_1) = T_W(t_2)$ and therefore:

$$1 - e^{\frac{\alpha^2 t_1}{k}} \operatorname{erfc}\left(\frac{\alpha\sqrt{t_1}}{\sqrt{k}}\right) = \epsilon - e^{\frac{\alpha^2 t_2}{k}} \operatorname{erfc}\left(\frac{\alpha\sqrt{t_2}}{\sqrt{k}}\right) + (1-\epsilon) e^{\frac{\alpha^2 (t_2 - t_u)}{k}} \operatorname{erfc}\left(\frac{\alpha\sqrt{t_2 - t_u}}{\sqrt{k}}\right). \tag{10}$$

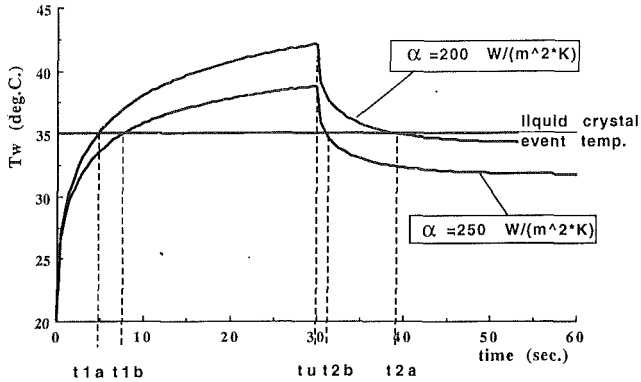

Fig. 1 Temperature histories for step-heating technique (t_u = 30 s, q = 6000 W/m^2, T_0 = 20°C, ϵ = 0.55, plexiglass)

For the calculation of the heat transfer coefficient only the two times t_1 and t_2 are required in addition to the heating ratio ϵ and the switchover time t_u. No information on the local heat flux at each position or the local surface temperature is necessary. In this case there is no need for a complicated calibration method for the liquid crystals (Akino et al., 1989).

In Fig. 1 temperature histories, using Eqs. (8) and (9) for two different heat transfer coefficients, are given. The time pairs t_{1a}, t_{2a}, and t_{1b}, t_{2b} are sufficient to obtain the heat transfer coefficients.

Influence of Heat Storage and Lateral Heat Conduction Effects

It is known from steady-state experiments using electrically heated foils that heat losses caused by lateral heat conduction occur, especially in the metallic foil (Baughn et al., 1985; Graziani et al., 1980). Using the described transient method, heat storage effects in the surface layers of the model must also be taken into account. For simplicity radiation effects are omitted in this discussion.

Figure 2 shows a sketch of the heat fluxes in the layers of TLC with paint, the heater foil and the glue. Compared to the plexiglas the temperature differences in the top three layers in the y direction are very small. Therefore, the vertical temperature gradient in these three layers are neglected.The heat flux q_1 into the model is obtained from the heat balance by ($q = \dot{e} dy_2$):

$$q_1 dx = \dot{e}\, dx dy_2 - q_2 dx - \beta \frac{dT_W}{dt} dx + (q_{L1} - q_{L2}) dy_2 \tag{11}$$

with

$$\beta = (\rho c_p)_1 dy_1 + (\rho c_p)_2 dy_2 + (\rho c_p)_3 dy_3.$$

The heat loss caused by lateral heat conduction can be expressed by (λ_1, $\lambda_3 \ll \lambda_2$):

Nomenclature

A = heat transfer surface area
C_f = skin friction coefficient
c_p = specific heat of the wall material
$\dot{e}$ = volumetric heat rate
$\dot{m}$ = mass flow rate
Nu = Nusselt number
Pr = Prandtl number
q = local surface heat flux
Q = electrical power input
Re = Reynolds number
t = time
t_u = switchover time
T = temperature
u = free-stream velocity
x = streamwise coordinate
y = vertical coordinate
α = heat transfer coefficient
Δ = difference
ϵ = heating ratio
λ = thermal conductivity of the wall material
ρ = density of the wall material

Subscripts

0 = initial state
f = fluid
G = gas
i = index of streamwise stations
L = losses
W = wall
x = quantities evaluated at streamwise positions

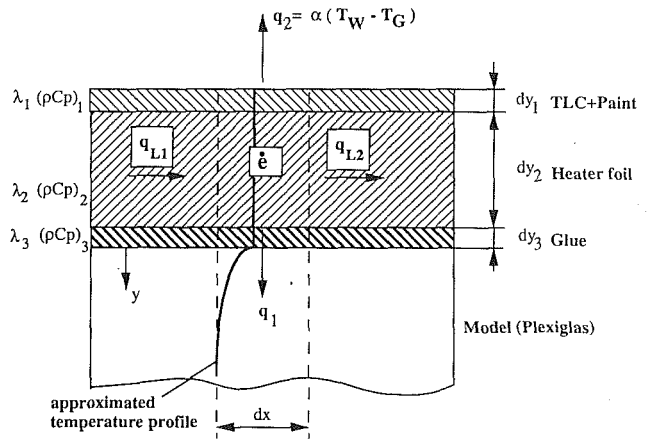

Fig. 2 Thermal model of the surface layers

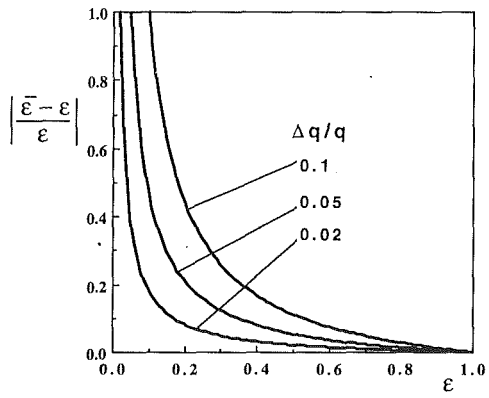

Fig. 3 Relative error for heating ratio

$$\Delta q = -\frac{q_{L1} - q_{L2}}{dx}\, dy_2 = -\lambda_2 \frac{\partial^2 T_W}{\partial x^2}\, dy_2. \tag{12}$$

It is assumed that the heat loss is almost constant with time for the heating as well as the cooling period. The following boundary conditions can be formulated:

$$-\lambda \frac{\partial T(y=0,\, t)}{\partial y} = q - \alpha(T_W - T_G) - \beta \frac{dT_W}{dt} - \Delta q_1 \qquad 0 < t < t_u \tag{13}$$

$$-\lambda \frac{\partial T(y=0,\, t)}{\partial y} = \epsilon q - \alpha(T_W - T_G) - \beta \frac{dT_W}{dt} - \Delta q_2 \qquad t_u < t. \tag{14}$$

The solution of Eq. (4) with these boundary conditions for the surface temperature T_W is found by taking Laplace transforms ($T_0 = T_G$):

$$\alpha \frac{T_W - T_0}{q - \Delta q_1} = 1 + \alpha\left(\frac{e^{A^2 t}\, \mathrm{erfc}(A\sqrt{t})}{\beta A(A-B)} - \frac{e^{B^2 t}\, \mathrm{erfc}(B\sqrt{t})}{\beta B(A-B)}\right) \qquad 0 < t < t_u \tag{15}$$

$$\alpha \frac{T_W - T_0}{q - \Delta q_1} = \bar{\epsilon} + \alpha\left(\frac{e^{A^2 t}\, \mathrm{erfc}(A\sqrt{t})}{\beta A(A-B)} - \frac{e^{B^2 t}\, \mathrm{erfc}(B\sqrt{t})}{\beta B(A-B)}\right) + (\bar{\epsilon} - 1)\alpha\left(\frac{e^{A^2(t-t_u)}\, \mathrm{erfc}(A\sqrt{t-t_u})}{\beta A(A-B)} - \frac{e^{B^2(t-t_u)}\, \mathrm{erfc}(B\sqrt{t-t_u})}{\beta B(A-B)}\right) \qquad t_u < t \tag{16}$$

with

$$A = \frac{\sqrt{\lambda \rho c_p}}{2\beta}\left(1 + \sqrt{1 - \frac{4\alpha\beta}{\lambda \rho c_p}}\right)$$

and

$$B = \frac{\sqrt{\lambda \rho c_p}}{2\beta}\left(1 - \sqrt{1 - \frac{4\alpha\beta}{\lambda \rho c_p}}\right).$$

After measuring the time pair t_1, t_2 with $T_W(t_1) = T_W(t_2)$ and eliminating the left-hand sides of Eqs. (15) and (16), we obtain a similar equation to Eq. (10) for the determination of the heat transfer coefficient α.

The influence of the lateral heat conduction is incorporated by using:

$$\bar{\epsilon} = \frac{\epsilon q - \Delta q_2}{q - \Delta q_1}. \tag{17}$$

For negligible lateral heat conduction losses (Δq_1, $\Delta q_2 \to 0$), the former heating ratio ϵ is obtained for $\bar{\epsilon}$. The influence of lateral heat conduction is estimated by the investigation of two limiting cases. Firstly, it is assumed that the heat loss is proportional to the dissipated heat:

$$\Delta q \sim q.$$

In this case $\Delta q_2 = \epsilon \Delta q_1$ and therefore $\bar{\epsilon} = \epsilon$.

Secondly, if $t_1 \to t_u$ and $t_2 \to t_u$, the heat losses are:

$$\Delta q_1 = \Delta q_2 = \Delta q$$

and the following condition for $\bar{\epsilon}$ is derived:

$$\bar{\epsilon} = \frac{\epsilon - \dfrac{\Delta q}{q}}{1 - \dfrac{\Delta q}{q}}. \tag{18}$$

For heat losses of the order of 0.02–0.1, which are realistic for steady-state experiments (Baughn et al., 1985), the relative error of $\bar{\epsilon}$ is shown in Fig. 3. If $\epsilon > 0.5$ this error is always less than the heat conduction loss error. For this reason, the experiments were only carried out in this range of ϵ.

In the case of rapid spatial variations of the heat transfer coefficients, lateral conduction smooths the surface temperature distribution and therefore the evaluated heat transfer coefficients. Numerical investigations using two-dimensional finite element computations showed that the influence of lateral conduction does not exceed that obtained in steady-state experiments. To overcome the difficulties in the case of large gradient changes of the wall temperature, very thin coatings, as well as very low conductive materials, have to be applied on the model surface to minimize the lateral heat conduction (see Eq. (12)). One method to achieve this would be to employ vapor or chemical deposition of conductive materials. In this case, coatings with a thickness of a few Angstroms can be achieved (Simonich and Moffat, 1984).

In the form given above, the heat transfer coefficients are based on the mixed mean inlet temperature ($T_G = T_0$). For internal flows, the heat transfer coefficients should be based instead on local mixed mean temperatures. The way to re-evaluating the heat transfer coefficients is given by Metzger and Larson (1986) using an energy balance in the streamwise direction:

$$\alpha = \alpha_x \Big/ \left(1 - \frac{1}{\dot{m} c_{pf}} \sum_{i=1}^{x-1} \bar{\alpha}_i A_i\right) \tag{19}$$

where α_i is the local heat transfer coefficient based on the mixed mean inlet temperature, the bar denotes averaged values, and the index i denotes measurement locations in the streamwise direction.

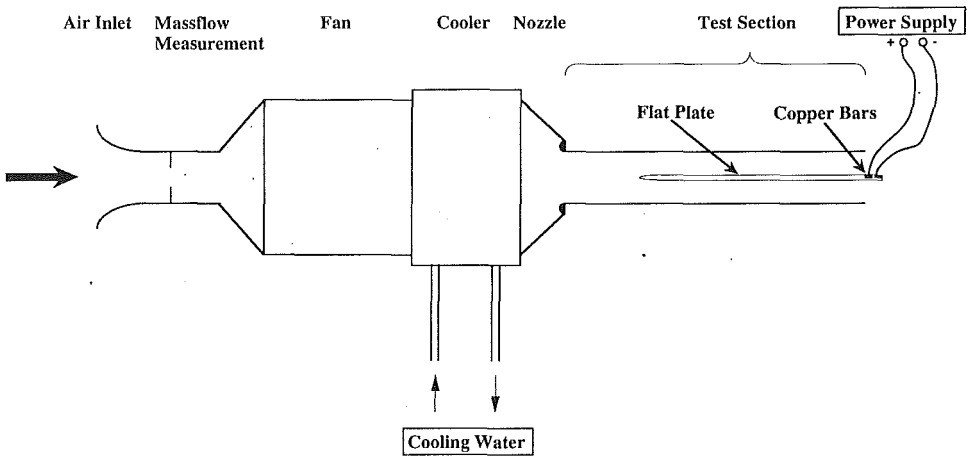

Fig. 4 Schematic drawing of experimental apparatus

Experimental Setup

As a well-documented test case, the flow over a flat plate was chosen to verify the proposed technique.

The experiments were carried out in an open wind tunnel. Since the proposed method needs a constant free-stream temperature, an air cooler was installed between the fan and the settling chamber. A constant free-stream temperature of 21 ± 0.3°C in the test section could be achieved. The test section has a cross-section of 90 mm × 90 mm and a total length of 600 mm. The plate (500 mm long and 10 mm thick) was mounted approximately two channel widths downstream of the square inlet nozzle in the middle of the test section. Velocity profiles could be measured at various locations along the centerline of the tunnel perpendicular to the plate (Fig. 4).

In order to obtain good optical access and low thermal conductivity, both the test section and the flat plate were made of plexiglass. The entire surface of the plate was covered with a thin Nichrome foil of 25 μm thickness. A precisely machined foil with uniform thickness and constant width was employed for reasons of verification in steady-state experiments. However, a uniform thickness (uniform heat dissipation) is not necessary for the transient method. At the trailing edge of the plate two copper bars are used for proper distribution of the power into the foil in the spanwise direction.

For better visibility of the TLC colors, the metal foil was sprayed with black paint before the liquid crystals were applied to the surface. In all cases narrow bandwidth liquid crystals (38.1°C. . .40.3°C) were employed. During the tests the color changes on the surface were observed and recorded by a commercial video camera and recorder.

Velocity profiles were measured by means of pitot and hot-wire probes to check the flow quality and to obtain skin friction factors from these profiles, which could be compared with the results from the heat transfer measurements using Colburn's analogy (Colburn, 1933).

During the heat transfer measurements, the timing of the heater input was controlled by a computer, which switched the heating power and recorded additional data such as plenum chamber pressure and temperature, mass flow, free-stream temperature, initial model temperature, and the voltage and current applied to the heater foil. Additionally, the time and the values of current and voltage were displayed in the video image to synchronize the evaluated data.

The experiments described above were carried out twice using plates with two different leading edges. The first one, with an elliptic shaped leading edge, was employed to obtain a laminar boundary layer with a subsequent transition zone and a turbulent boundary layer farther downstream. The other one, with a blunt leading edge, caused a separation bubble, a reattachment area, and a fully turbulent boundary layer.

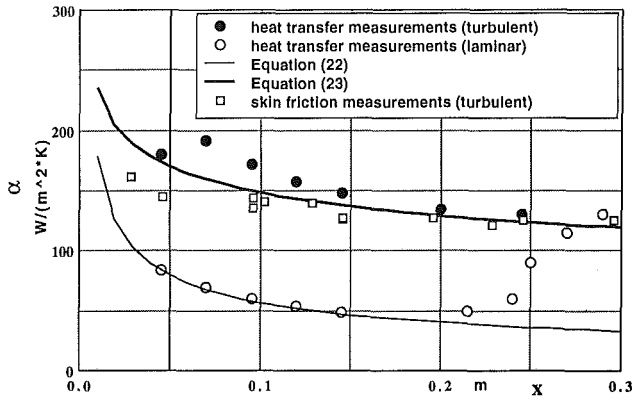

Fig. 5 Heat transfer distributions along the test plate

Both flow types were checked by the measurement of the velocity profiles as well as by the liquid crystal method. Compared to the information derived from the velocity profile measurements, that from the liquid crystal thermography is easier to understand and results are faster to obtain, especially in cases of two-dimensional flows.

Results and Discussion

The experimental results from the liquid crystal measurements at an upstream velocity of about 40 m/s are shown in Fig. 5 for both flows. Additionally, Fig. 5 includes values obtained from velocity profile measurements using Colburn's analogy:

$$\alpha = \frac{C_f}{2} \mathrm{Re}_x \mathrm{Pr}^{1/3} \frac{\lambda_f}{x}. \tag{20}$$

The wall skin friction coefficients for the turbulent case were inferred by fitting the velocity profile data in the near-wall region to the law-of-the-wall with $\kappa = 0.41$ and $C = 5.1$:

$$u^+ = \frac{u}{u_\tau} = \frac{1}{\kappa} \ln \frac{y u_\tau}{\nu} + C = \frac{1}{\kappa} \ln y^+ + C. \tag{21}$$

The measured data are compared to the analytical solutions for laminar boundary layers with uniform heat flux (Kays and Crawford, 1980, p. 151):

$$\alpha = 0.453 \ \mathrm{Re}_x^{0.5} \mathrm{Pr}^{1/3} \frac{\lambda_f}{x}. \tag{22}$$

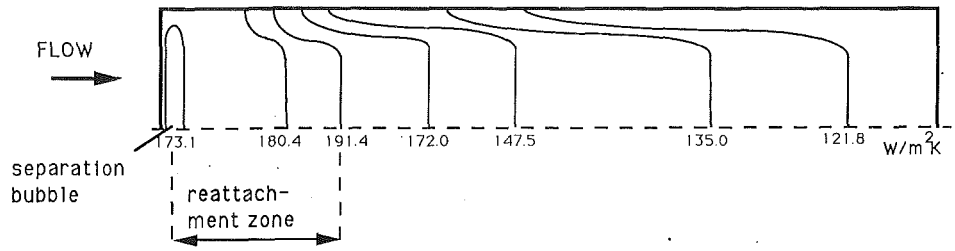

Fig. 6 Heat transfer contours on the test plate (turbulent)

as well as to turbulent boundary layers with uniform heat flux (Kays and Crawford, 1980, p. 217):

$$\alpha = 0.03\ \mathrm{Re}_x^{0.8}\mathrm{Pr}^{0.6}\frac{\lambda_f}{x}. \tag{23}$$

The measured heat transfer data of both cases agree very well with the analytical solutions.

In the first case the centerline transition region is located between positions $x_1 = 0.2$ m and $x_2 = 0.27$ m downstream of the leading edge, corresponding to Reynolds numbers $\mathrm{Re}_1 = 5 \times 10^5$ and $\mathrm{Re}_2 = 7 \times 10^5$, respectively. The measured free-stream turbulence level was less than 1 percent. Further downstream, the measured data indicate that the boundary layer has become fully turbulent.

The experimental results of the flat plate with blunt leading edge show a slight disagreement with the correlation in the first part of the plate. As mentioned above, in the case of the blunt plate, the flow separates at the leading edge and reattaches farther downstream. The distribution of the heat transfer coefficient shown in Fig. 5 is well known for this case of separated and reattached flow over a blunt flat plate (Ota and Kon, 1974, 1979). Near the reattachment point the heat transfer reaches its maximum and a turbulent boundary layer develops subsequently.

So far, the discussion has referred to centerline data, but the great advantage of the liquid crystal method is to produce two-dimensional data. Examples are given in Figs. 6 and 7, where heat transfer contours for both investigated cases are shown. Note that only one half of each plate is plotted due to the symmetric setup. Since the test section is of finite width, the influence of the side walls on the heat transfer can be seen clearly. It turns out that the heat transfer decreases toward the side walls.

In contrast to the fully turbulent case, the laminar boundary layer flow is much more interesting. In principal, for a flow over a plate of finite width, two different types of transition are possible. As shown by Elder (1960), the free-stream turbulence influences the transition. For a low turbulence level the transition regions from both side walls will have overlapped before normal transition occurs. Thus, the transition zone is cone shaped. With increasing turbulence level the normal transition region moves upstream and both types of transition are present. In this case the transition zone will have a trapezoidal shape. In our case, as Fig. 7 shows, both regions are approximately at the same location.

Accuracy

The great advantage of our novel method is that only the heat flux ratio ϵ and different time intervals Δt_i have to be measured. Since the electrical power input applied to the heater foil can be measured very precisely, the error of ϵ is less than 1 percent. The recording of the liquid crystal colors is limited to the video frequency of 50 Hz or 25 Hz for a full frame, respectively. Therefore, the lower limit of the absolute error of the time measurement is fixed to 0.04 seconds. This is much larger than the response time of the used TLC, for which

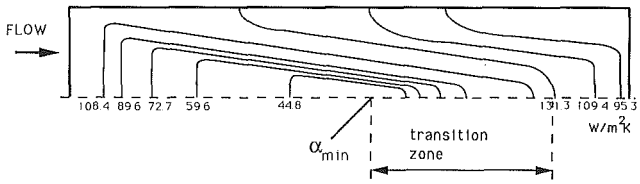

Fig. 7 Heat transfer contours on the test plate (laminar)

Ireland and Jones (1987) measured a time delay of 3 ms. In our cases, the shortest measured time interval was approximately one second, yielding a relative error in time of 4 percent.

The resulting overall error of 5 percent can be taken as the uppermost limit and can be decreased easily by redesigning the experiments and measuring longer time periods. This may be achieved by choosing liquid crystals with another temperature range and a suitable heat flux ratio.

Conclusions

The transient technique described has proved to be a very successful method for the measurement and visualization of heat transfer distributions. The basic tests on laminar as well as turbulent boundary layer flows showed good agreement with the analytical solutions. Only time measurements are required to evaluate heat transfer coefficients. The local surface heat flux and the surface temperature are eliminated during the data reduction. Nonuniform heating caused by nonuniform thickness of the heated material is allowed. This is important particularly for the use of coatings of very thin metallic materials on complex model shapes, where such nonuniformities are probable. Since the surface temperature is not required for the determination of the heat transfer coefficients, calibration of the liquid crystals is avoided.

It should be noted that this technique is not limited to liquid crystals but may be used also with any other surface temperature measurement technique. Furthermore, redundancy information can be obtained by applying more than one heat step. This may be the subject of future work. Additionally, the same experimental setup can be used for both transient and steady-state measurements.

References

Akino, N., Kunugi, T., Ichimiya, K., Mitsushiro,K., and Ueda, M., 1989, "Improved Liquid-Crystal Thermometry Excluding Human Color Sensation," ASME Journal of Heat Transfer, Vol. 111, pp. 558–565.

Baughn, J. W., Takahashi, R. K., Hoffman, M. A., and McKillop, A. A., 1985, "Local Heat Transfer Measurements Using an Electrically Heated Thin Gold-Coated Plastic Sheet," ASME Journal of Heat Transfer, Vol. 107, pp. 953–959.

Baughn, J. W., Ireland, P. T., Jones, T. V., and Saniei, N., 1989, "A Comparison of the Transient and Heated-Coating Methods for the Measurements of Local Heat Transfer Coefficients on a Pin Fin," ASME Journal of Heat Transfer, Vol. 111, pp. 877–881.

Bittle, R. R., and Taylor, R. E., 1984, "A Step Heating Technique for Thermal Diffusivity Measurements of Large-Grained Heterogeneous Materials," *J. of the American Ceramic Society*, Vol. 67, No. 3, pp. 186–190.

Blair, M. F., Wagner, J. H., and Steuber, G. D., 1991, "New Applications

of Liquid-Crystal Thermography in Rotating Turbomachinery Heat Transfer Research," ASME Paper No. 91-GT-354.

Carslaw, H. S., and Jaeger, J. C., 1959, *Conduction of Heat in Solids*, 2nd ed., Oxford University Press, London, United Kingdom.

Clifford, R. J., Jones, T. V., and Dunne, S. T., 1983, "Techniques for Obtaining Detailed Heat Transfer Coefficient Measurements Within Gas Turbine Blade and Vane Cooling Passages," ASME Paper No. 83-GT-58.

Colburn, A. P., 1933, "A Method of Correlating Forced Convection Heat Transfer Data and a Comparison With Fluid Friction," *Trans. AIChE*, Vol. 29, p. 174.

Elder, J. W., 1960, "The Flow Past a Flat Plate of Finite Width," *Journal of Fluid Mechanics*, Vol. 5, pp. 133–153.

Graziani, R. A., Blair, M. F., Taylor, J. R., and Mayle, R. E., 1980, "An Experimental Study of Endwall and Airfoil Surface Heat Transfer in a Large Scale Turbine Blade Cascade," ASME *Journal of Engineering for Power*, Vol. 102, pp. 257–267.

Hippensteele, S. A., Russel, L. M., and Torres, F. J., 1985, "Local Heat-Transfer Measurements on a Large Scale-Model Turbine Blade Airfoil Using a Composite of a Heater Element and Liquid Crystals," ASME *Journal of Engineering for Gas Turbines and Power*, Vol. 107, pp. 953–960.

Ireland, P. T., and Jones, T. V., 1985, "The Measurement of Local Heat Transfer Coefficients in Blade Cooling Geometries," presented at the AGARD Conference on Heat Transfer and Cooling in Gas Turbines, CP 390 Paper 28, Bergen.

Ireland, P. T., and Jones, T. V., 1987, "The Response Time of a Surface Thermometer Employing Encapsulated Thermochromic Liquid Crystals," *J. Phys. E: Sci. Instrum.*, Vol. 20, pp. 1195–1199.

Jones, T. V., and Hippensteele, S. A., 1988, "High-Resolution Heat-Transfer-Coefficient Maps Applicable to Compound-Curve Surfaces Using Liquid Crystals in a Transient Wind Tunnel," NASA TM 89855.

Kays, W. M., and Crawford, M. E., 1980, *Convective Heat and Mass Transfer*, 2nd ed., McGraw-Hill, New York.

Metzger, D. E., and Larson, D. E., 1986, "Use of Melting Point Surface Coatings for Local Convection Heat Transfer Measurements in Rectangular Channel Flows With 90-deg Turns," ASME JOURNAL OF HEAT TRANSFER, Vol. 108, pp. 48–54.

Ota, T., and Kon, N., 1974, "Heat Transfer in the Separated and Reattached Flow on a Blunt Flat Plate," ASME JOURNAL OF HEAT TRANSFER, Vol. 96, pp. 459–462.

Ota, T., and Kon, K., 1979, "Heat Transfer in the Separated and Reattached Flow Over Blunt Flat Plates—Effects of Nose Shape," *Int. J. Heat Mass Transfer*, Vol. 22, pp. 197–206.

Rook, S. P., and Taylor, R. E., 1988, "Transient Experimental Technique for the Determination of the Thermal Diffusivity of Fibrous Insulation," ASME JOURNAL OF HEAT TRANSFER, Vol. 110, pp. 270–273.

Simonich, J. C., and Moffat, R. J., 1984, "Liquid Crystal Visualization of Surface Heat Transfer on a Concavely Curved Turbulent Boundary Layer," ASME *Journal of Engineering for Gas Turbines and Power*, Vol. 106, pp. 619–627.

Tarasuk, J. D., and Castle, G. S. P., 1983, "Temperature Distribution in an Electrically Heated Wide Metallic Foil," ASME JOURNAL OF HEAT TRANSFER, Vol. 105, pp. 210–212.

Vedula, R. J., and Metzger, D. E., 1991, "A Method for the Simultaneous Determination of Local Effectiveness and Heat Transfer Distributions in Three-Temperature Convection Situations," ASME Paper No. 91-GT-345.

J. Zhang
Mem. ASME

L. A. Melton
Professor.

University of Texas at Dallas,
Department of Chemistry,
Richardson, TX 75083-0688

Potential Systematic Errors in Droplet Temperatures Obtained by Fluorescence Methods

Fluorescence methods have been used to measure droplet temperatures. In this work, a light scattering model is combined with a simplified heat transfer model in order to identify systematic errors that may be present in the inferred temperatures. Design of experiments that minimize these systematic errors is discussed.

1 Introduction

When liquid fuel is injected into a hot gas environment, heat is transferred to the fuel droplets. The temperature of an individual droplet is a key parameter in estimation of the heat and mass transfer rates as well as for prediction of the lifetime of the droplet. Recently droplet temperatures have been measured by two fluorescence methods, the exciplex (two-band) fluorescence method (Wells and Melton, 1990; Hanlon and Melton, 1992) and the one-band fluorescence method (Zhang, 1991). This work seeks to understand more clearly the limitations of these fluorescence thermometry methods.

In particular, the present work is motivated by a desire to understand the results obtained for falling 283-μm hexadecane droplets (Hanlon and Melton, 1992). In that experiment room temperature hexadecane droplets, which had been doped with an exciplex fluorescence thermometer (EFT), were allowed to fall into heated nitrogen. The droplets were irradiated with a laser and the resulting fluorescence was collected at 90 deg, focused onto the entrance slit of a monochromator, and dispersed onto a linear optical multichannel analyzer. The entire fluorescence spectrum could be obtained from a single droplet. The excitation and detection optics were fixed, but the droplet generator/fall tube could be raised and lowered; thus, they were able to obtain EFT data as a function of fall distance (time) in the heated zone. The inferred temperatures as a function of fall distance rose gently to about 40 deg, showed an abrupt rise of approximately 100 deg, and then rose gently. The reproducible, but anomalous, abrupt rise in the inferred temperatures spurred this work.

A simplified heat transfer model along with a light scattering model developed by Zhang et al. (1992) has been used to identify and analyze the potential systematic errors that may arise in such experiments. In this work, three major sources of systematic error have been identified. These effects appear when (1) the droplets are in the transient heating region, i.e., for droplets with significant temperature gradients, and (2) volume-averaged fluorescence measurements are used to infer droplet temperatures. First, the excitation laser beam as well as the fluorescence emissions are subject to refractions and reflections at the droplet surface. Thus, different points within the droplet may have different excitation intensities and also may have different scattering efficiencies (photons emitted from different points within the droplet have different probabilities of reaching the detector). The combination of the two effects imposes an uneven optical weighting on the temperature field inside the droplet. Second, nonlinearity of the calibration function (ratio of exciplex intensity to monomer intensity versus temperature) can lead to systematic bias in the inferred temperatures if volume integration of fluorescence is performed. In the two-band methods, if the inferred temperatures are obtained from ratios of volume-integrated intensities, rather than local intensity ratios, a third systematic error can be introduced. When a temperature gradient exists within a droplet, all these effects can introduce systematic errors in the volume-integrated temperature measurements; when the gradients are negligible, the above systematic errors become negligible.

As a final point, this analysis is applied to the design of effective and interpretable fluorescence thermometry experiments.

2 Analysis

The photophysics involved in the exciplex (two-band) fluorescence method has been discussed previously (Murray and Melton, 1985; Gossage and Melton, 1987; Wells and Melton, 1990) and can be expressed as

$$M^* + G(M) \Leftrightarrow E^* \tag{1}$$

where M^* is an excited state monomer; $G(M)$ is an appropriately chosen ground state molecule (which can be another M); and E^* is an excited state complex. The fluorescence emission from E^* is red-shifted with respect to that of M^*, and the populations of E^* and M^*, coupled by the above equation, can be strongly temperature dependent. After calibration, the temperatures can be deduced from the ratio of the emission intensity of the exciplex to that of the monomer. The one-band fluorescence method uses a fluorescent additive with one major spectral band. The quantum yield of the additive has a strong temperature dependence. With proper calibration, droplet temperature can be inferred from the measured absolute emission intensity.

Droplet temperatures can also be determined via a droplet-slicing-imaging method (Winter, 1990; Winter and Melton, 1990), which made use of the two-band method. A thin laser sheet was used to illuminate the central plane of a droplet, and the fluorescence patterns of that plane were recorded as two separate images (at two different colors). Temperatures were inferred from the intensity ratios of the two colors on a point by point basis. No volume integration is performed in this method, and the systematic errors discussed in this paper do not occur. In this paper, we only discuss the volume-integrated measurements.

In the volume-integrated measurements, the fluorescence intensity captured by a detector can be written as (Zhang et al., 1992)

$$P = \int\int\int_{\Omega} S(R)C(R)I(R)dv, \tag{2}$$

Contributed by the Heat Transfer Division for publication in the JOURNAL OF HEAT TRANSFER. Manuscript received by the Heat Transfer Division March 1992; revision received September 1992. Keywords: Direct-Contact Heat Transfer, Instrumentation, Sprays/Droplets. Associate Technical Editor: W. L. Grosshandler.

where $I(R)$ is the normalized excitation intensity, $S(R)$ is a scattering efficiency function, and $C(R)$ is a conversion function. The integration is carried out on the entire volume of the sphere, Ω. The product, $I(R) \times S(R)$, is defined as the optical weighting function, $W(R)$.

The conversion function C, obtainable from bulk sample calibration, converts a normalized excitation intensity to a fluorescence spectral intensity. In general, $C = C(\sigma, c, T)$, where σ is fluorescence yield, c is molecular concentration, and T is temperature. Ideally, for a specific experiment, C is a function of temperature only, $C = C(T)$, and carries local temperature information. In the exciplex fluorescence method, the ratio of intensities at two bands, $D(T) = C_e(T)/C_m(T)$, yields temperature information. To infer temperatures from the measured intensities or intensity ratios, the inversion function $T = T(C)$ or $T = T(D)$ is used.

In droplet temperature measurements, usually the volume-averaged temperature

$$\overline{T} = \frac{1}{V} \iiint_{\Omega} T(R)\, dv \tag{3}$$

is desirable. However, in experiments one actually measures

$$\overline{C}_3 = \frac{1}{V} \iiint_{\Omega} W(R) C[T(R)]\, dv \tag{4}$$

in the one-band fluorescence method (Zhang, 1991). In the exciplex (two-band) fluorescence method, the fluorescence emissions are volume integrated by the detectors at two bands and the ratio is taken afterward. Thus, one actually measures

$$D_3 = \frac{\iiint_{\Omega} W_e(R) C_e[T(R)]\, dv}{\iiint_{\Omega} W_m(R) C_m[T(R)]\, dv}. \tag{5}$$

Therefore, droplet temperature will be deduced from either

$$\overline{T} = T(\overline{C}_3) \tag{6}$$

in the one-band method or

$$\overline{T} = T(D_3) \tag{7}$$

in the two-band (exciplex) method, respectively. Note that in the absence of temperature gradients, i.e., $C[T]$ is independent of R and can be moved outside of the integral signs in Eqs. (3) and (4), the effects of optical weighting and volume integration disappear.

The model used for simulations has two major parts. The light propagation functions, $I(R)$ and $S(R)$, are computed with a hybrid method (Zhang et al., 1992). The heat transfer processes involved are approximated by a much simplified model. The spherical droplet has a uniform initial temperature T_0 when at $t \doteq 0$, its surface is suddenly exposed to an external environment characterized by a time-dependent ambient temperature T_∞ and a convective heat transfer coefficient h_c. Even though internal circulation may be important in the transient heating region (Prakash and Sirignano, 1978; Winter and Melton, 1990), for simplicity, only the conductive mode is considered inside the droplet. An evaporation rate proportional to the vapor pressure of the liquid at the surface temperature is assumed; the proportionality parameter is chosen to provide an approximate match to prior experimental results at 9 cm fall distance (Hanlon and Melton, 1992). With these assumptions and simplifications, the temperature distribution within the droplet is spherically symmetric.

The diameter of an evaporating droplet changes with time, and hence, so does the optical size parameter, α, and, in principle, the optical weighting function, $W(R)$. Rigorous treatment of this latter effect would require lengthy recalculation of $W(R)$ at each time step. However, for large droplets (in this work $\alpha > 2000$), the geometric optics approximation holds. For optically thin droplets, the distributions of $W(R)$ are independent of the absolute size of the droplet. In addition, in the prior experiments (Hanlon and Melton, 1992) video microscopy revealed that the droplet diameter changed very little during the observable fall. Thus, we kept the weighting function, $W(R)$, unchanged during the "time marching" process.

An implicit finite difference scheme similar to the Crank–Nicolson method (Anderson et al., 1984) was used to solve the one-dimensional transient heat transfer problem with time-dependent ambient temperature. When the ambient temperature was set to a constant value, excellent agreement between the numerical results obtained with the finite difference scheme and an analytical solution (White, 1988) was obtained.

Nomenclature

Bi = Biot number $= \mathrm{Nu}_D \times (k_\infty/k)$
$C(R)$ = local conversion function
$C(T)$ = temperature calibration function (one-band method)
$D(R)$ = local intensity ratio
d.o.d. = droplet optical density $= \epsilon cd$, where ϵ = molar absorptivity, c = concentration, and d = droplet diameter
$D(T)$ = temperature calibration function (two-band method)
E^* = excited state complex
$f/\#$ = f-number of receiving optics
$G(M)$ = ground state molecule
h_c = convective heat transfer coefficient
$I(R)$ = excitation intensity
k = thermal conductivity
M^* = excited state molecule (monomer)
n_1 = refractive index of the particle
Nu_D = Nusselt number (external)
P = radiation power reaching a detector
r_0 = droplet radius
R = denotes a point inside the sphere with Cartesian coordinates (x, y, z)
Re_D = Reynolds number
$S(R)$ = scattering efficiency function
t = time
T = temperature
$T(C)$ = inversion function of $C(T)$
$T(D)$ = inversion function of $D(T)$
ΔT_1 = error introduced by nonlinearity of $D(T)$
ΔT_2 = error introduced by using ratio of integrated intensities
ΔT_3 = total error
ΔT_{ow} = error introduced by optical weighting
V = volume of spherical droplet
$W(R)$ = optical weighting function $= I(R) \times S(R)$
α = optical size parameter $= 2\pi r_0/\lambda_0$
λ = emission wavelength
λ_0 = excitation wavelength
σ = fluorescence yield
Ω = spatial domain of sphere

Subscripts

e = exciplex emission band
m = monomer emission band
ow = value biased by optical weighting
1 = value biased by nonlinearity of $D(T)$
2 = value biased by using ratio of integrated intensities
3 = measurable value with all biases
∞ = gas phase parameter

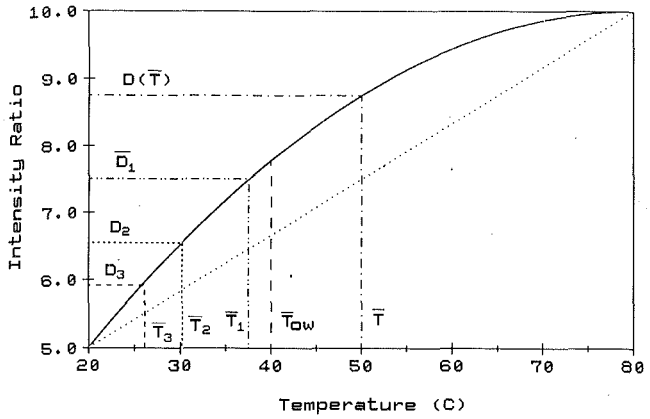

Fig. 1 Function *D(T)*. A two-node example illustrates the relationship between various relevant quantities and the systematic errors. (Values are given in Table 1.)

3 Results and Discussion

3.1 Origin of Systematic Errors. Before presenting the numerical results for droplets, it is worthwhile to examine an illustrative example with only two volume elements, Fig. 1. This unrealistic example gives the essence of the analysis of systematic errors and introduces the definitions and notations of various relevant quantities. Figure 1 presents graphically the results shown in Table 1.

In the example, the volume-averaged temperature $\overline{T}=50°\text{C}$, whereas the inferred temperature $\overline{T}_3=26.1°\text{C}$. The error results from three effects: optical weighting, nonlinearity of the calibration function (see Fig. 1), and use of a ratio of volume-integrated intensities to replace local intensity ratios. First, in order to show the latter two effects, we assume uniform optical weighting. In the two-band method, for estimation of the volume-averaged temperature, $\overline{T}$, $D(\overline{T})$ should be known; however, it is not experimentally measurable. An alternative quantity would be $\overline{D}_1$, which is the volume-averaged value of local intensity ratio, $D(R)$. From $\overline{D}_1$, an estimation of $\overline{T}_1=37.5°$ is obtained. However, $\overline{D}_1$ is not experimentally measurable either. What one measures in experiments is the ratio of the volume-integrated intensities, i.e., D_2. Thus, $\overline{T}_2=30.2°$ is obtained.

An analysis of the sign of nonlinearity error, $\Delta T_1=\overline{T}-\overline{T}_1$, reveals that

$$\Delta T_1 \propto \frac{\Delta D}{D'(\overline{T})}, \tag{8}$$

where $\Delta D=\overline{D}_1-D(\overline{T})$ and $D'(\overline{T})$ is the derivative of D with respect to T at $\overline{T}$. The sign of ΔT_1 can be determined as follows. For the case of $D(T)$ concave (downward), as in Fig. 2,

$$\Delta D=\overline{D}_1-D(\overline{T})\le 0, \tag{9}$$

where the $\le$ sign is from Jensen's inequality (Feller, 1971). From Eqs. (8) and (9), it follows that for $D'(\overline{T})>0$, $\Delta T_1<0$ and for $D'(\overline{T})<0$, $\Delta T_1>0$. That is for a concave (downward) calibration function, in the region where $D(T)$ increases with T, the systematic error, ΔT_1, is negative; whereas in the region where $D(T)$ decreases, ΔT_1 is positive. In Eq. (9), the equal sign holds when $D(T)$ is linear. Therefore, in the region, where $D(T)$ is linear, the systematic error, ΔT_1, is absent.

The error due to nonlinearity is probably increased by the use of the ratio of the volume-integrated intensities, i.e., D_2. We have found no general rule to determine the sign of $\Delta T_2=\overline{T}_1-\overline{T}_2$. However, empirical analysis shows that in a region of T where both $C_e(T)$ and $C_m(T)$ are monotonic, the sign of $\overline{D}_1-D_2$ is consistent throughout the region. Thus the sign of ΔT_2 is consistent in that region provided that $D(T)$ is monotonic.

Table 1

Node	1	2	Avg.
T	$20°C$	$80°C$	
Vol. Element Δv	1	1	
Optical Weight W	2	1	
C_e	10	9	
C_m	2	0.9	
$D=\frac{C_e}{C_m}$	5	10	
$D(\overline{T})$			8.75
$\overline{D}_1=\overline{\left(\frac{C_e}{C_m}\right)}$			7.5
$D_2=\frac{\iiint_\Omega C_e dv}{\iiint_\Omega C_m dv}$			6.55
$D_3=\frac{\iiint_\Omega WC_e dv}{\iiint_\Omega WC_m dv}$			5.92
$\overline{T}=\frac{1}{V}\iiint_\Omega T dv$			$50.0°C$
$\overline{T}_{ow}=\frac{\iiint_\Omega WT dv}{\iiint_\Omega W dv}$			$40.0°C$
$\overline{T}_1=T\left(\overline{D}_1\right)$			$37.5°C$
$\overline{T}_2=T(D_2)$			$30.2°C$
$\overline{T}_3=T(D_3)$			$26.1°C$

The introduction of optical weighting causes bias in the inferred temperatures; different volume elements in the droplet contribute disproportionately to the accumulated intensities. In the example shown, optical weighting introduces additional systematic error: $\overline{T}_{ow}=40°\text{C}$, whereas the volume-averaged temperature $\overline{T}=50°\text{C}$. In general, optical weighting may increase or decrease the total systematic error. This effect will be discussed later using optical weights calculated for droplets.

In the one-band fluorescence method, droplet temperature is inferred from absolute fluorescence intensity; no ratio is taken. Thus, the errors due to ratios of integrated intensities are not present. Otherwise the analysis is the same.

3.2 Numerical Results. In this section, numerical examples simulating different experimental conditions are presented. In the computations, the Nusselt number, Nu_D, and the convective heat transfer coefficient, h_c, were estimated using the equations proposed by Whitaker (1972). The Biot number used in the computations is defined as $\text{Bi}=\text{Nu}_D\times(k_\infty/k)$, where k and k_∞ are the thermal conductivities of the liquid

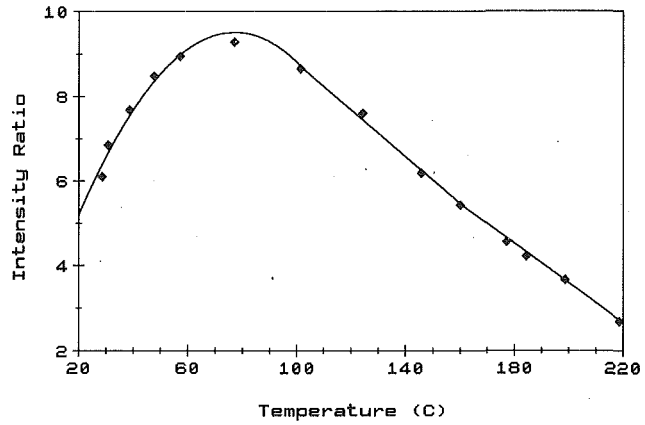

Fig. 2 Temperature calibration function, $D(T)$ (Hanlon and Melton, 1992). Scattered data are experimental results. The continuous lines show sectional curve fit of the experimental data.

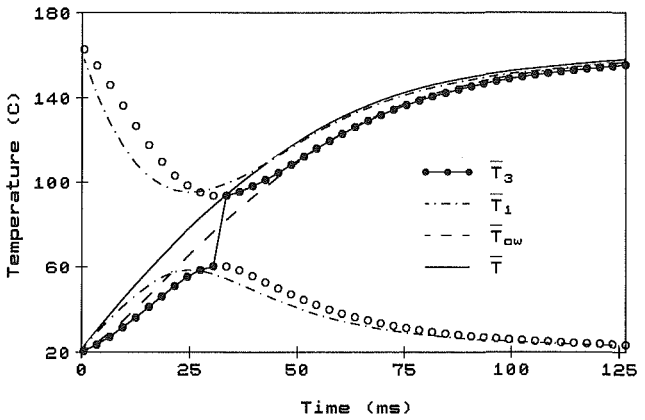

Fig. 3 Droplet heating. Various average temperatures as functions of time. Bi = 0.55.

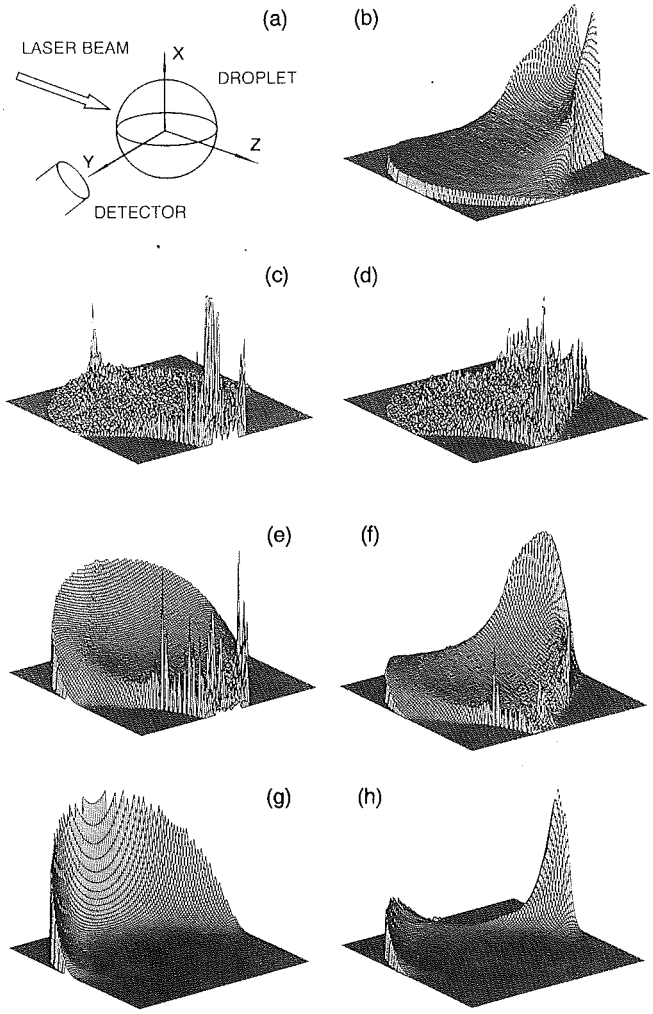

Fig. 4 Scattering function (*b*), excitation intensity (*c, e, g*), and weighting function (*d, f, h*) on *Y–Z* plane. (*c–d*) d.o.d. = 0.0458; (*e, f*) d.o.d. = 2.40; (*g, h*) d.o.d. = 9.16. (*a*) shows the incident and observation angles.

and gas phase, respectively. The temperature calibration function $D(T)$, the conversion functions, $C_e(T)$ and $C_m(T)$, and the time-dependent ambient temperature, $T_\infty(t)$, were obtained from curve fitting of the experimental data (Hanlon and Melton, 1992). For every value of D, the inversion function, $T = T(D)$, has two roots; see Fig. 2. Both roots have been shown in the figures (a lower branch and a higher branch). With knowledge of specific experiments, e.g., the droplet temperature increases monotonically with time, it is not difficult to choose the correct roots (indicated by solid circles) from the two branches. It should be noticed that the numerical and experimental data presented in the following examples are comparable only qualitatively, because the heat transfer model used was greatly simplified.

In the computational examples displayed (Figs. 3, 6–9), the volume-averaged temperature $\overline{T}$ and the optically weighted temperature $\overline{T}_{ow}$ are displayed along with the temperatures $\overline{T}_1$, $\overline{T}_2$, and $\overline{T}_3$, which are inferred using the experimental $D(T)$ (Hanlon and Melton, 1992). The most important issues these figures address are (1) the extent of bias due to optical weighting, i.e., the difference between $\overline{T}$ and $\overline{T}_{ow}$, and (2) the deviations from $\overline{T}_{ow}$ caused by the nonlinearity of $D(T)$ and the use of ratios of integrated intensities.

A droplet heating example is given in Fig. 3, which simulates the experiments conducted by Hanlon and Melton (1992). An optically thin 283-μm-dia hexadecane droplet is illuminated by a laser beam at 337 nm wavelength ($\alpha = 2638$, $n_1 = 1.4345 + 1.0 \times 10^{-5} i$, d.o.d. = 0.0458 and $f/2.9$). The computed scattering function, $S(R)$, excitation intensity, $I(R)$, and the weighting function, $W(R)$ in the Y–Z plane are given in Fig. 4(*b, c, d*). The Reynolds number ($\mathrm{Re}_D = 5.9$), Biot number ($\mathrm{Bi} = 0.55$), and the fluid properties used in the computations were kept constant at values estimated from average experimental conditions.

In Fig. 3, $\overline{T}_{ow}$ is lower than $\overline{T}$ during the entire droplet history shown. To understand the effects of optical weighting, it is necessary to examine the radial distributions of optical weights, Fig. 5(*a*). In Fig. 5, the radius of the spherical droplet is divided into eight equal segments. Figure 5(*a*) shows that for an optically thin droplet, while 58 percent of the volume is in the two outermost (seventh and eighth) layers, optical weighting puts 50 percent of the weighting on the fifth and sixth layers. For droplet heating, temperature T increases with radius. Thus, the volume-averaged temperature, $\overline{T}$, is obtained by putting most of the weight on the highest temperature region, whereas $\overline{T}_{ow}$ is obtained by putting the major weight on a relatively lower temperature inner region. Therefore, $\overline{T}_{ow}$ is consistently lower than $\overline{T}$ ($\Delta T_{ow} < 0$).

In the region from 20°C to 77°C, the calculated $\overline{T}_3$ (lower branch) is consistently lower than the optically weighted temperature $\overline{T}_{ow}$. This is because $D(T)$ is concave (downward) and increasing with T in this region; as shown in the previous analysis, the systematic error ΔT_1 is negative in this case. In the next region (77°C–110°C), $D(T)$ is concave (downward) but decreasing with T. Accordingly, ΔT_1 becomes positive (up-

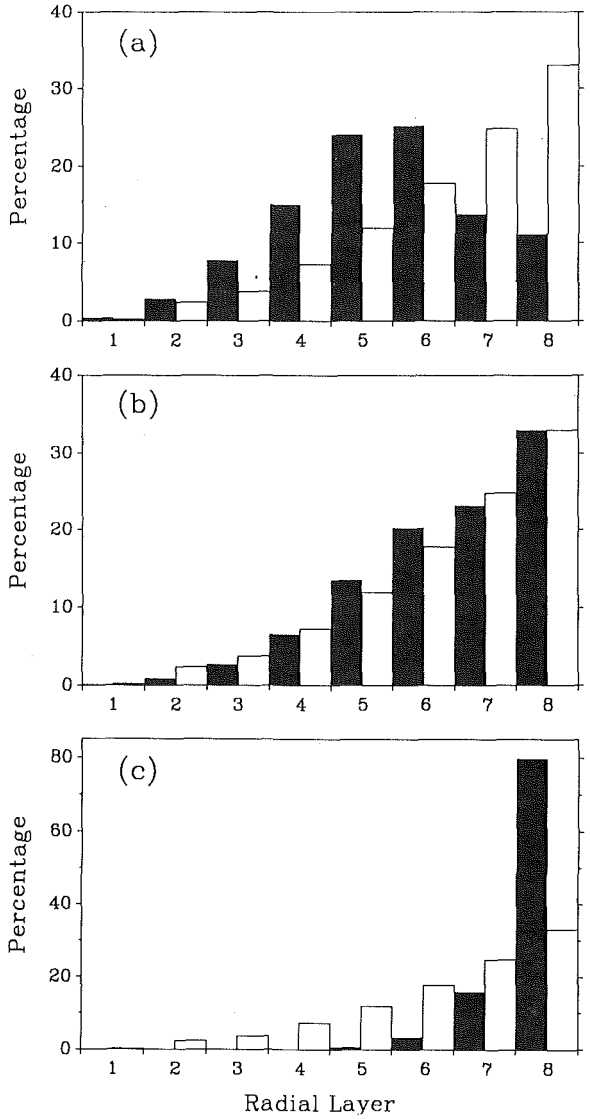

Fig. 5 Optical weight (filled bar) and volume weight (blank bar) on eight concentric layers having equal radial thickness. The central layer is labeled 1 and the outermost layer is labeled 8. The droplet optical densities (d.o.d.) are (*a*) 0.0458, (*b*) 2.40, and (*c*) 9.16.

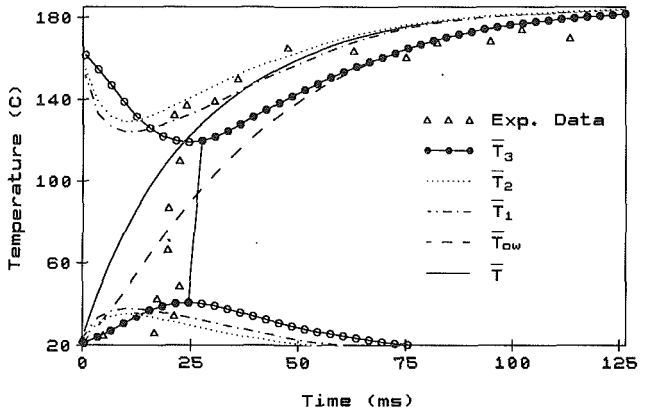

Fig. 6 Droplet heating. Same as Fig. 3, except Bi = 2.49. ΔT_2 can be seen clearly in this example. Open triangles show experimental data (Hanlon and Melton, 1992).

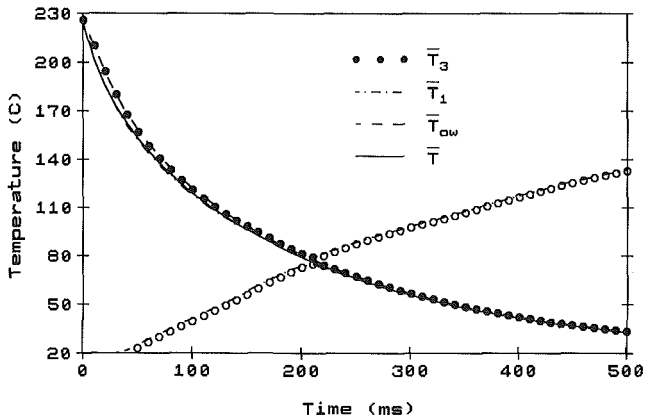

Fig. 7 Droplet cooling. Same as Fig. 3, except the initial temperature was changed to 227°C and the ambient temperature was kept at 20°C (Bi = 0.33).

per branch). An abrupt rise in $\overline{T}_3$ is observed as the temperature rises across the transition point at 77°C. In the last region, from 110°C to 220°C, $D(T)$ is nearly linear. $\overline{T}_3$ (upper branch) is almost coincident with $\overline{T}_{ow}$; ΔT_1 is negligible. (In this example the effects due to ratios of integrated intensities, ΔT_2, are small; $\overline{T}_3$ is virtually unaffected.)

At early times ($t < 30$ ms), the temperature differences inside the droplet are large. So $\overline{T}_3 << \overline{T}$. In the region (77°C–110°C), ΔT_1 and ΔT_{ow} have opposite signs and nearly cancel each other out; the total systematic error, ΔT_3, is greatly reduced. In the near-linear region of $D(T)$ ($T > 110$°C), the total error, ΔT_3, is mainly from optical weighting.

Figure 6 gives results obtained for droplet heating with a larger Biot number (Bi = 2.49). With larger Bi, the temperature differences inside the droplet are greater than those obtained with a small Bi. Consequently, the systematic errors are greater than those in the first example, although the basic trends stay the same. The size of the abrupt rise in the inferred temperature $\overline{T}_3$ is dramatically increased and a better fit to the experimental results (Hanlon and Melton, 1992) is obtained.

An immediate implication of this observation is that the empirical equation used for estimation of the Nusselt number, Nu_D, may not be valid for a liquid droplet with possible internal circulation. Further, since the numerical examples show that the size of the abrupt rise in the inferred temperature is sensitive to Bi, this suggests a possible application, i.e., to fit inferred temperatures obtained in similar experiments and thereby to determine the Biot number directly and further to estimate an "effective thermal conductivity" (Talley and Tao, 1986; Jin and Borman, 1985). At least two issues must be addressed prior to use of such fits. First, the temperature profiles would have to be calculated using a more sophisticated heat transfer model. Second, preliminary experimental work in our laboratory has shown that the PYPYP exciplex fluorescence is quenched by molecular oxygen more efficiently than the monomer fluorescence. Thus the presence of stray oxygen will reduce the ratio of exciplex intensity to monomer intensity, i.e., enhance the effects assigned to the concave nonlinearity of $D(T)$. Experiments intended to obtain the Biot number directly would have to exclude oxygen rigorously.

A further example is given in Fig. 7, in which the same droplet as in Fig. 3 is undergoing a cooling process. The droplet has an initial uniform temperature of 227°C and is suddenly exposed to room temperature. For a cooling droplet, the temperature decreases with radius. Accordingly, $\overline{T}_{ow}$ is consistently higher than $\overline{T}$, which can be observed in Fig. 7. The systematic error ΔT_1 is dramatically reduced in this cooling process. At the initial stage ($t < 120$ ms), although the temperature gradients inside the droplet are significant, the temperatures are within the near-linear region (> 110°C) of the calibration func-

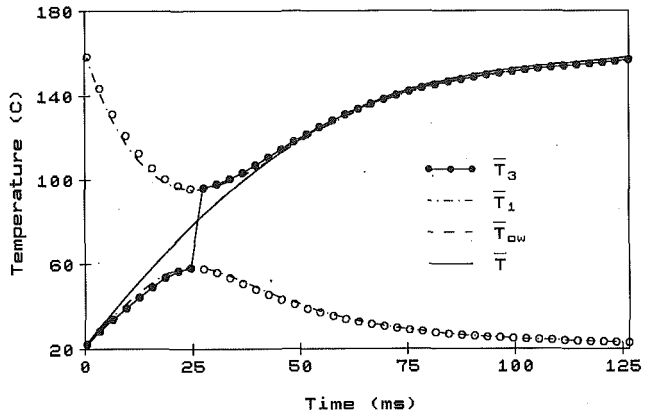

Fig. 8 Droplet heating. Same as Fig. 3, except the absorptivity was chosen such that the optical weights matched the volume weights ($\overline{T}_{ow}$ almost coincides with $\overline{T}$).

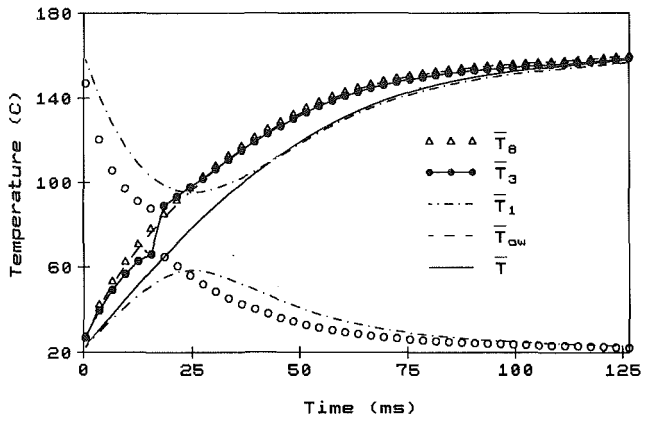

Fig. 9 Droplet heating. Same as Fig. 3, except the absorptivity was so high that the inferred temperature, $\overline{T}_3$, reflected a "skin" temperature. ($\overline{T}_8$ is the volume-averaged temperature of the eighth layer.)

tion $D(T)$, Fig. 2. Accordingly, ΔT_1 is minimized in this region. As the temperatures cool down to the highly nonlinear region of $D(T)$, the gradients have become much smaller and hence, ΔT_1 becomes smaller, the abrupt break in the inferred temperature (a fall in this case) is virtually negligible.

Figure 8 shows that the systematic error due to optical weighting can be substantially reduced by appropriate choice of the droplet optical density. The conditions are identical to those for the droplet heating as shown in Fig. 3; however the absorptivity of the solution is properly chosen ($n_1 = 1.4345 + 5.4 \times 10^{-4} i$, d.o.d. = 2.4) such that the radial distributions of optical weights in the eight concentric layers of the sphere are a good match to the corresponding volume weights, Fig. 5(*b*). The calculated $I(R)$ and $W(R)$ are given in Figs. 4(*e*) and 4(*f*), respectively. This "optical matching" technique is strictly valid only for a spherical symmetric temperature distribution inside the droplet. However, it can probably be used for a temperature distribution that is axially symmetric with some sacrifice of effectiveness. Another limiting consideration is that "optical matching" can only be valid at a certain range of the droplet diameters, i.e., it is not possible to impose "optical matching" throughout the entire history of an evaporating droplet.

Finally, results for a highly absorbing droplet ($n_1 = 1.4345 + 2.0 \times 10^{-3} i$, d.o.d. = 9.16) are shown in Fig. 9. This d.o.d. matches that used in earlier experiments (Wells and Melton, 1990). The calculated $I(R)$ and $W(R)$ are given in Figs. 4(*g*) and 4(*h*), respectively. The radial distributions of optical weights are given in Fig. 5(*c*). It is seen that about 80 percent of the optical weight is given to the outermost layer. The seven other layers have only 20 percent of the weight. In this case, temperature, $\overline{T}_3$, actually reflects a "skin" temperature of the droplet. As shown in Fig. 9, the inferred temperature matches closely the averaged eighth layer temperature, $\overline{T}_8$.

3.3 Implications for Design of Experiments. For fluorescence thermometry measurements in which the detector integrates signals from the entire droplet, the analysis of the experimental results must take into account the optically weighted averaging of the temperature field over the entire droplet. Further, if the fluorescence thermometry system $D(T)$ (or $C(T)$ for one band systems) used is nearly linear with T, the inferred temperature should be interpreted as $\overline{T}_{ow}$, the optically weighted temperature, rather than $\overline{T}$, the volume-averaged temperature. If $D(T)$ (or $C(T)$) is concave downward (a rather common occurrence), the inferred temperature will show systematic negative biases from $\overline{T}_{ow}$ in the region where $D(T)$ is increasing with T, and positive biases from $\overline{T}_{ow}$ in the region where $D(T)$ is decreasing. If the droplet temperature is virtually uniform, the systematic errors discussed here are negligible.

If oxygen is rigorously excluded from the thermometry system and if an adequate heat transfer model is used, the temperatures computed from the numerical model should be directly comparable with the experimental results provided that all the systematic biases have been taken into account. With the numerical model it may be possible to fit the inferred temperature curve to obtain directly the convective gas-to-liquid heat transfer coefficient. These measurements will be valid for evaporating droplets as long as the droplet remains optically thin.

For measurements on sufficiently optically thick droplets, it should be possible to obtain "skin temperatures." The systematic errors described in this paper are minimized in this case. These techniques will be valid for evaporating droplets provided that the accumulation of the (relatively concentrated) fluorescent dopant does not affect the evaporation processes for the droplet.

It is possible to produce optically matched droplets, in which the d.o.d. is adjusted so that $\overline{T}_{ow}$ approaches $\overline{T}$. However, the optically matched condition can only be maintained within a certain range of droplet diameter and will be destroyed as the droplet evaporates.

Because droplet-slicing-imaging measurements are not subject to the systematic errors described in this paper, i.e., pointwise rather than volume-averaged fluorescence measurements are possible in droplet-slicing-image measurements, more incisive results on the temperature field within droplets will probably come from the maturation of this technique.

4 Conclusions

Systematic errors have been identified in fluorescence droplet thermometry measurements that use the volume integration method. These errors arise from optical weighting, nonlinearity of the calibration function, and use of the ratio of volume-integrated fluorescence intensities to replace local intensity ratios.

Acknowledgments

This work was supported by the Army Research Office under contract No. DAAL03-91-G-0033.

References

Anderson, D. A., Tannehill, J. C., and Pletcher, R. H., 1984, *Computational Fluid Mechanics and Heat Transfer*, Hemisphere Pub. Corp., Washington, DC, pp. 55–57.

Feller, W., 1971, *An Introduction to Probability Theory and Its Applications*, Wiley, New York, pp. 153–154.

Gossage, H. E., and Melton, L. A., 1987, "Fluorescence Thermometers Using Intramolecular Exciplexes," *Appl. Opt.*, Vol. 26, pp. 2256–2259.

Hanlon, T. R., and Melton, L. A., 1992, "Exciplex Fluorescence Thermometry of Falling Hexadecane Droplets," ASME JOURNAL OF HEAT TRANSFER, Vol. 114, No. 2, pp. 450–457.

Jin, J. D., and Borman, G. L., 1985, "A Model for Multicomponent Droplet Vaporization at High Ambient Pressures," *Combustion Emission and Analysis*, SAE, Inc., P-162, pp. 213–223.

Murray, A. M., and Melton, L. A., 1985, "Fluorescence Methods for Determination of Temperature in Fuel Sprays," *Appl. Opt.*, Vol. 24, pp. 2783–2787.

Prakash, S., and Sirignano, W. A., 1978, "Liquid Fuel Droplet Heating With Internal Circulation," *Int. J. Heat Mass Transfer*, Vol. 21, pp. 885–895.

Talley, D. G., and Tao, S. C., 1986, "A Semi-empirical Approach to Thermal and Composition Transients Inside Vaporizing Fuel Droplets," *21st Symposium (International) on Combustion*, Munich, West Germany, pp. 609–616.

Wells, M. R., and Melton, L. A., 1990, "Temperature Measurements of Falling Droplets," ASME JOURNAL OF HEAT TRANSFER, Vol. 112, pp. 1008–1013.

Whitaker, S., 1972, "Forced Convection Heat Transfer Correlations for Flow in Pipes, Past Flat Plates, Single Cylinders, Single Spheres, and Flow in Packed Beds and Tube Bundles," *AIChE J.*, Vol. 18, pp. 361–371.

White, F. M., 1988, *Heat and Mass Transfer*, Addison-Wesley, New York, pp. 207–208.

Winter, M., 1990, "Measurement of the Temperature Field Inside a Falling Droplet," ILASS-AMERICAS, 4th annual conference, Extended Abstracts, Hartford, CT.

Winter, M., and Melton, L. A., 1990, "Measurement of Internal Circulation in Droplets Using Laser-Induced Fluorescence," *Appl. Opt.*, Vol. 29, pp. 4574–4577.

Zhang, J., 1991, "Fluorescence Methods for Determination of Temperature in Aerosol Particles," Ph.D. dissertation, Mech. Eng. Dept., UNL, Nebraska, pp. 56–79; submitted to Univ. Microfilm Inc.

Zhang, J., Alexander, D. R., and Barton, J. P., 1992, "Hybrid Inelastic Scattering Models for Particle Thermometry: Unpolarized Emissions," *Appl. Opt.*, Vol. 31, pp. 7132–7139.

A. Gopinath
Postdoctoral Student.
Student Mem. ASME

A. F. Mills
Professor.
Assoc. Mem. ASME

Department of Mechanical, Aerospace, and Nuclear Engineering,
University of California at Los Angeles,
Los Angeles, CA 90024-1597

Convective Heat Transfer From a Sphere Due to Acoustic Streaming

Convective heat transfer from a sphere due to acoustic streaming is examined for large streaming Reynolds numbers. Analytical and numerical solution techniques are used to obtain Nusselt number correlations for a wide range of Prandtl numbers with particular emphasis on the case of $Pr \sim 1$. A simple experiment performed to confirm some of the predictions is described. The results obtained can be used for the thermal analysis of containerless materials processing in space using acoustic levitation.

1 Introduction

The purpose of this study is to investigate the flow-field and convective heat transfer rates due to acoustic streaming from an isolated sphere in a standing sound field. The work is motivated by a series of basic science experiments planned for a Space Shuttle flight, for which there is a need to design and control the thermal features of a suitable cell for the containerless processing of materials at near zero gravity. The objective of some of the experiments is to isolate and study, in the absence of buoyancy, the effects of thermocapillary-dominated phenomena on the structure and properties of metal alloys. The alloy samples (usually spheres) are acoustically levitated to avoid physical contact with the container walls and thereby reduce contamination and other related surface effects. The levitated samples are positioned in a furnace in order to obtain controlled heating/cooling conditions in an inert gas environment. The use of a sound field (versus a magnetic field) to levitate and position the samples is considered especially attractive since it prevents directional effects from being introduced into the properties. However, the required sound fields, of the order of 155–165 dB at 1000–2000 Hz, give rise to strong (steady) acoustic streaming flows around the samples and on the walls of the test cells. The associated convective heat transfer rates are instrumental in determining heating/cooling rates (as recognized, for example, by Rey et al., 1991) and hence the material structure and thermophysical properties of heat alloys. A proper knowledge of the transport processes between the samples and the chamber walls is thus important to the successful design and execution of the experiments.

The treatment here is based on the foundation laid by Riley (1966) in his study of the flow around an oscillating sphere and also closely follows the work by Davidson (1973) on the heat transfer from a vibrating circular cylinder. The study by Riley (1966) is augmented by extending his results to obtain a more complete description of the steady streaming flow around the sphere for large streaming Reynolds number, R_s. This result is then used to examine the problem of transport of heat between an isothermal sphere and an isothermal ambient fluid for a wide range of Prandtl numbers. Only small temperature differences are considered, to allow the constant property assumption and thereby to concentrate on obtaining a basic understanding of the physics of the transport processes involved. It must be emphasized that the interaction of the acoustic and thermal fields through the properties of the medium can be properly explained only by a suitable high-temperature theory and has thus been neglected as a first approximation in the present study. The solution technique used combines the method of matched asymptotic expansions and the numerical solution of nonlinear partial differential equations. Results are obtained in the form of correlations for the average Nusselt number, Nu, and compared to those of Davidson (1973) for a vibrating circular cylinder. Particular attention is given to the boundary layer structure of the flow for large streaming Reynolds numbers, R_s, when the surrounding fluid is a gas with $Pr = O(1)$, which corresponds to the flow around an acoustically levitated alloy sample under normal operating conditions. These analytical predictions of the heat transfer are verified by conducting a simple experiment using a small spherical thermistor bead in an acoustic levitation test cell apparatus operated at normal gravity. Measurements of heat transfer from the thermistor show excellent agreement with the correlations for large values of R_s.

2 Governing Equations

This section is devoted to the development of the governing equations for the velocity and temperature distributions associated with the flow generated by a standing transverse sound field at the rigid boundaries of an isothermal solid sphere immersed in an infinite fluid domain maintained at a different temperature.

Fluid flows induced by sound fields are characterized by a large number of independent length scales. For a sphere in a plane standing sound wave with a velocity distribution of the form $U_\infty \cos(\omega\tau^*) \sin(2\pi z^*/\lambda)$ these length scales are the sphere radius, a, the displacement amplitude of the fluid particle in the sound field, $A = U_\infty/\omega$, the wavelength of the sound wave, $\lambda = 2\pi c/\omega$, and the viscous diffusive thickness of the Stokes layer, $\delta \sim \sqrt{\nu/\omega}$. Some important deductions are made from a comparison of these primary length scales, which allow the governing equations to be presented in a considerably simplified form. Foremost among these is the restriction to sound fields with wavelengths large compared to the radius of the sphere, i.e., those that satisfy $ak \ll 1$ where $k = 2\pi/\lambda$ is the wave number. This condition has been derived using order of magnitude arguments by Lighthill (1963, pp. 11–13), as the condition for the negligible radiation of acoustic energy by an obstacle in a sound field and satisfies one of the requirements for incompressibility. Under such a restriction, the sphere (typically located at a velocity antinode of the sound field) does not experience any appreciable changes in the sound wave characteristics over its surface. It should be noted that with this assumption, the wavelength no longer appears explicitly as a length scale representative of the flow around the sphere.

The length scale ratio, $\epsilon = A/a$, has some very important implications for the physical nature of the flow and the methods used to describe the flow. In this application ϵ is found to take on values small with respect to 1, implying that the oscillatory fluid particles traverse very short distances (on the scale of the sphere radius) before reversing their direction of

Contributed by the Heat Transfer Division for publication in the JOURNAL OF HEAT TRANSFER. Manuscript received by the Heat Transfer Division February 1992; revision received July 1992. Keywords: Forced Convection, Materials Processing and Manufacturing Processes, Microgravity Heat Transfer. Associate Technical Editor: Y. Bayazitoglu.

motion. The condition $\epsilon << 1$ thus ensures that separation does not arise and the flow instead remains attached and laminar. Another important consequence is that for this range of values of ϵ, the governing equations are rendered analytically tractable by the method of matched asymptotic expansions with ϵ playing the role of a small perturbation parameter. This feature was exploited by Riley (1966) who developed a consistent theory to describe the flow analytically. Similar techniques are used in this study. From the above arguments for the range of values covered by each of the two length-scale ratios, ak and A/a, it follows that their product Ak is also small compared to unity. This ensures that the Mach number defined as U_∞/c is also small and allows compressibility effects to be ignored.

The diffusive thickness of the Stokes layer, $\delta \sim \sqrt{\nu/\omega}$, the sphere radius, a, and the displacement amplitude of the sound wave, A, completely determine the essential characteristics of *isothermal* flow around the sphere. These three length scales yield two dimensionless parameters: the amplitude parameter, $\epsilon = A/a$, defined earlier, and the frequency parameter, $M = a/\delta$. The frequency parameter, M, is a measure of the extent of penetration of the viscous diffusive effects of the oscillatory sound field on the scale of the sphere radius. For small values of M the retarding effects of the stationary sphere on the oscillatory sound field permeate to large distances from the surface of the sphere. On the other hand, for large values of M treated in this study, the fluid velocities are rapidly brought up to their oscillatory free-stream values across narrow Stokes boundary layers present close to the surface of the sphere. It is later shown that the product of these independent parameters ϵ and M results in a length-scale ratio (A/δ) that is of primary importance in determining the behavior of the steady streaming flow. When a temperature difference is also present between the sphere and the fluid, the thermal diffusive thickness, $\delta_T \sim \sqrt{\alpha/\omega}$, is an additional length scale giving $\delta/\delta_T = \mathrm{Pr}^{1/2}$ as a corresponding dimensionless parameter.

The above assumptions establish the parameter range of interest and satisfy the conditions for solenoidality and thereby render major simplifications to the governing equations. The equations are formulated with the isolated solid sphere located at the velocity antinode of a plane standing sound wave (with a velocity distribution of the form $U_\infty \cos(\omega\tau^*)\sin(2\pi z^*/\lambda)$) in an infinite fluid domain. For this axisymmetric problem a spherical polar coordinate system is chosen, fixed in the sphere, with radial distance r and the polar directions $\theta = 0$, π coinciding with the axis of oscillation of the sound field external to the sphere. It is also convenient in such problems to recast the governing equations for velocity and pressure into a single higher-order equation, formulated in terms of only one dependent variable, the Stokes stream function. The axisymmetric stream function is chosen so as to satisfy the equation of continuity and its variation is governed by the equation of vorticity in the fluid. The energy equation is formulated for the temperature with the solid sphere taken to be at a uniform temperature, T_s, different from the temperature, T_∞, of the ambient fluid.

Following Riley (1966), with the time, radial distance, velocity, and stream function scaled with respect to their nominal values ω^{-1}, a, U_∞, and $U_\infty a^2$, respectively, and the temperature difference in the fluid $(T - T_\infty)$ normalized with respect to $(T_s - T_\infty)$, the governing equations of motion and energy in dimensionless form are

$$\frac{\partial}{\partial\tau}(D^2\psi) + \frac{\epsilon}{r^2}\left[\frac{\partial(\psi, D^2\psi)}{\partial(r, \mu)} + 2D^2\psi L\psi\right] = \frac{1}{M^2} D^4\psi \tag{1}$$

$$\frac{\partial\phi}{\partial\tau} + \frac{\epsilon}{r^2}\left[\frac{\partial(\psi, \phi)}{\partial(r, \mu)}\right] = \frac{1}{\mathrm{Pr}\cdot M^2}\nabla^2\phi \tag{2}$$

together with the boundary conditions

$$\phi = 1 \text{ and } \psi = \frac{\partial\psi}{\partial r} = 0 \text{ on } r = 1 \tag{3}$$

$$\left.\begin{aligned}\psi &\to (1/2)r^2(1-\mu^2)\cos\tau \\ \phi &\to 0\end{aligned}\right\} \text{as } r \to \infty \tag{4}$$

where in the above equations $\mu = \cos\theta$ and $\phi = (T - T_\infty)/(T_s - T_\infty)$ along with the operators,

Nomenclature

α = radius of the sphere
A = oscillation amplitude of the sound wave = U_∞/ω
c = velocity of propagation of sound in the fluid = ω/k
d = diameter of thermistor bead described in Appendix B
h = average heat transfer coefficient
I = intensity of the sound field
I_0 = reference intensity, 10^{-12} Wm^{-2}
k = wave number = $2\pi/\lambda$
M^2 = frequency parameter = $a^2\omega/\nu$
Nu = average Nusselt number
Pr = Prandtl number = ν/α
Q = heat transfer rate
r = radial coordinate
R_s = streaming Reynolds number = $U_\infty^2/\omega\nu = \epsilon^2 M^2$
SPL = Sound Pressure Level (in decibels)
t = dimensionless temperature defined in Section 4.2
T = temperature of the fluid
T_s = temperature of the sphere
T_∞ = temperature of the ambient
u, v = artificial velocities defined in Section 4.1
u_θ, u_r = angular, radial velocity components
U_∞ = velocity amplitude in the sound wave = $A\omega$
x = streamwise boundary layer coordinates used in Section 4.1
y = normal boundary layer coordinate used in Section 4.1
z = coordinate in the axial direction
α = thermal diffusivity of the fluid
δ = Stokes layer thickness = $\sqrt{\nu/\omega}$
δ_0 = (outer) streaming boundary layer thickness in Section 4.1
δ_T = thermal boundary layer thickness
ϵ = amplitude parameter = A/a
$\bar{\eta}, \hat{\eta}, \tilde{\eta}$ = normal boundary layer coordinates
θ = angular coordinate in spherical geometry
κ = thermal conductivity of the fluid
λ = wavelength of the sound field
μ = angular coordinate in spherical geometry = $\cos\theta$
ν = kinematic viscosity of the fluid
ρ = density of the fluid
τ = dimensionless time = $\omega\tau^*$
ϕ = dimensionless temperature difference = $(T - T_\infty)/(T_s - T_\infty)$
ψ = dimensionless stream function = $\psi^*/U_\infty a^2$
ω = angular frequency
ω_0 = dimensionless angular frequency defined in Section 3

Superscripts

* = represents dimensional quantities

$$D^2=\frac{\partial^2}{\partial r^2}+\frac{(1-\mu^2)}{r^2}\frac{\partial^2}{\partial \mu^2},\quad L=\frac{\mu}{(1-\mu^2)}\frac{\partial}{\partial r}+\frac{1}{r}\frac{\partial}{\partial \mu} \tag{5}$$

$$\nabla^2=\frac{1}{r^2}\frac{\partial}{\partial r}\left[r^2\frac{\partial}{\partial r}\right]+\frac{1}{r^2}\frac{\partial}{\partial \mu}\left[(1-\mu^2)\frac{\partial}{\partial \mu}\right] \tag{6}$$

and the velocity components defined by

$$u_r=-\frac{1}{r^2}\frac{\partial \psi}{\partial \mu}\text{ and }u_\theta=\frac{(1-\mu^2)^{-1/2}}{r}\frac{\partial \psi}{\partial r} \tag{7}$$

3 The Streaming Flow

It is appropriate at this stage to outline the solution technique and briefly examine the origin of the steady streaming terms. As mentioned earlier, this study is concerned with cases of $\epsilon \ll 1$ and $M \gg 1$. This parameter range has been treated by Riley (1966) to develop a solution for the basic flow field in terms of two complementary perturbation series in powers of ϵ and $1/M$. It is well known that a governing equation of motion of this type does not permit a uniformly valid solution in the entire domain and the matched asymptotic technique must be used. This requires independent solutions to be developed in different regions of the flow in terms of variables appropriate to each region. These independent solutions are made to satisfy the boundary conditions pertinent to their respective domains and are also suitably coupled in the zone of overlap. Similar methods are also used to determine the temperature distribution in the fluid. The focus in this study is on the steady transport due to the acoustic streaming motion. The details of the analysis describing the origin and nature of the mechanism giving rise to such a steady flow can be found in the paper by Riley (1966). Here only the salient features are summarized to provide a proper perspective to the complete problem.

It is clear from Eq. (1) that in the limit of $\epsilon \to 0$ the inertial terms become vanishingly small; Riley (1966, p. 463) has given an exact $O(1)$ solution, $\psi_0(r, \mu, \tau; M)$, of the resulting linear equation for the stream function, which satisfies the boundary condition on the surface of the sphere and also has a $\cos \tau$ variation to satisfy the far-field velocity behavior of the harmonic sound wave. It therefore follows that all subsequent corrections to this basic linear solution satisfy homogeneous boundary conditions. These corrections include contributions from the nonlinear inertial terms and result in the generation of higher order harmonics in the flow. In particular, when considering the $O(\epsilon)$ correction to the stream function it becomes clear from Eq. (1) that the basic linear solution contributes to the forcing function via the nonlinear inertia terms. This gives rise to terms with a time dependence of the form $\sim \cos^2 \tau$, which from a simple trigonometric identity is $1/2(1+\cos 2\tau)$. Then for this $O(\epsilon)$ contribution to the stream function, a time-independent term is created along with the second harmonic. It is this dominant $O(\epsilon)$ component of the steady flow, termed acoustic streaming, and its transport effects, which are of prime concern in this study. From the need to satisfy homogeneous boundary conditions, it can be seen that with increasing radial distance, the magnitude of this steady velocity increases from zero at the sphere surface and reaches a peak in the fluid, beyond which it decays once again to adjust to the conditions of the stationary fluid at large distances from the sphere.

The steady streaming motion itself arises due to viscous Reynolds-like stresses in a narrow inner Stokes layer region with thickness of $O(M^{-1})$. The origin of the stress can be viewed as the average effect of the nonlinear inertial interaction of the first harmonic (streamwise and normal) velocities in the Stokes boundary layers. The phase difference in these velocities gives rise to a nonzero average over one cycle and allows a net transfer of momentum. This steady motion in the inner region takes the form of a hemispherically symmetric recirculatory

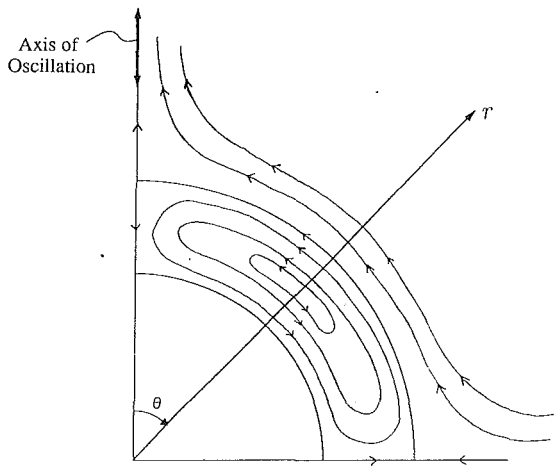

Fig. 1 Schematic of the recirculatory streamlines of steady flow in the inner Stokes layer region (proportions exaggerated for clarity)

flow pattern with closed streamlines (see Fig. 1), though its precise behavior emerges only from a solution of the governing equations in terms of suitable Stokes boundary layer variables (Riley, 1966). The details of the behavior are not included and it suffices to note that a steady drift velocity of $O(\epsilon)$ persists at a larger radial distance from the surface of the sphere corresponding to the outer edge of the Stokes layer region. This steady drift plays the role of a slip velocity in driving the outer flow and is directed from the equatorial plane to the polar axes. A noteworthy feature of the steady drift velocity is that despite being generated by viscous Reynolds-like stresses, its magnitude of $\sim \epsilon U_\infty = U_\infty^2/a\omega$ is independent of the viscosity of the fluid. A Reynolds number defined on the basis of this velocity scale and the sphere radius (Stuart, 1966)

$$\mathrm{R}_s=\epsilon U_\infty \frac{a}{\nu}=\frac{U_\infty^2}{\omega \nu} \tag{8}$$

is called the streaming Reynolds number and plays a fundamental role in determining the nature of the steady transport in the outer region. This new measure, R_s, is not an independent parameter and can be expressed as $\mathrm{R}_s=\epsilon^2 M^2$. Having been defined in this manner as the product of a large parameter (M^2) and a small parameter (ϵ^2), the magnitude of the streaming Reynolds number, R_s, is yet unspecified. In terms of the length scales defined earlier, the measure R_s represents the square of the ratio of the amplitude of the sound wave, A, and the Stokes layer thickness, δ, i.e., $\mathrm{R}_s=A^2/\delta^2$ and is independent of the characteristic length scale of the sphere.

For the associated transfer problem it can be shown from Eq. (2) that the leading order temperature contribution, ϕ_0, is time independent and that the transport of heat across the narrow inner layer is essentially diffusive for fluids with Prandtl number of $\sim O(1)$. The resistance to heat transfer is negligible in this region and the fluid remains essentially isothermal across the inner Stokes layer. This does not provide any information on the driving temperature gradient and attention is now turned to the convective transport effects in the outer region responsible for the heat transfer.

Based on the above deductions, it requires some manipulation of the original form of the governing Eqs. (1)–(4) of *unsteady* transport, to arrive at the governing equations of *steady* transport (Riley, 1966); details are omitted here for brevity. It can be shown that the variations of the steady component of the $O(\epsilon)$ contribution to the stream function, ψ_{1s}, and the $O(1)$ temperature, ϕ_0, are governed by

$$\frac{1}{r^2}\left[\frac{\partial(\psi_{1s}, D^2\psi_{1s})}{\partial(r, \mu)}+2D^2\psi_{1s}L\psi_{1s}\right]=\frac{1}{\mathrm{R}_s}D^4\psi_{1s} \tag{9}$$

$$\frac{1}{r^2}\left[\frac{\partial(\psi_{1s},\,\phi_0)}{\partial(r,\,\mu)}\right]=\frac{1}{\mathrm{Pr}\cdot \mathrm{R}_s}\,\nabla^2\phi_0 \tag{10}$$

which can be recognized as the complete governing equations of motion and energy for the steady viscous and laminar axisymmetric flow around a sphere with Reynolds number R_s. The above equations satisfy inner conditions from matching with the Stokes layer solution (Riley, 1966)

$$\left.\begin{array}{l}\psi_{1s}\to 45/16\;(r-1)\mu(1-\mu^2)\\ \phi_0\to 1\end{array}\right\}\ \text{as } r\to 1 \tag{11}$$

and the decaying conditions in the far field,

$$\left.\begin{array}{l}\psi_{1s}\to o(r^2)\\ \phi_0\to 0\end{array}\right\}\ \text{as } r\to\infty \tag{12}$$

Due to their decoupled nature, once the flow field is determined from Eq. (9), the temperature distribution can be ascertained from Eq. (10) for a given Prandtl number. Before proceeding to solve these equations it is important to be able to estimate the magnitude of the streaming Reynolds number, R_s, in a given situation and thereby be able to predict the dominant mechanism of this steady transport. This is done by starting with the definition of $\mathrm{R}_s = U_\infty^2/\omega\nu$ from which it was shown that the streaming Reynolds number is independent of any typical dimension of the sphere and is completely determined by the characteristics of the sound wave and the properties of the medium through which it propagates. The strength of the acoustic signal, measured by the Sound Pressure Level (SPL) in decibels (dB), is first given in terms of intensity as

$$\mathrm{SPL}=10\,\log_{10}\frac{I}{I_0} \tag{13}$$

where I_0 is a reference intensity equal to $10^{-12}\ \mathrm{Wm}^{-2}$ and I is the intensity, which, for a plane standing wave with a velocity distribution of the form $U_\infty\cos(\omega\tau^*)\sin(2\pi z^*/\lambda)$ typically used in the levitation process, is defined as

$$I=\frac{1}{2}\,\rho c U_\infty^2 \tag{14}$$

The above two Eqs. (13) and (14) are used to redefine the SPL in terms of the streaming Reynolds number, R_s, as

$$\mathrm{SPL}=10\,\log_{10}(\omega_0\,\mathrm{R}_s) \tag{15}$$

where ω_0 is a conveniently defined dimensionless angular frequency given by

$$\omega_0=\frac{\rho c\nu\omega}{2I_0} \tag{16}$$

Then the streaming Reynolds number, R_s, can be determined for a given acoustic signal usually specified in terms of the SPL (in dB) and the frequency (in Hz). Typical values of the acoustic signal used for acoustic levitation range in SPLs from 150 dB–180 dB for frequencies of 1–2 kHz. The corresponding values of R_s are ~ 100 at the lower end of the spectrum and could be as large as $O(10^4)$ for the strongest acoustic signals used. Thus convection is the predominant mechanism of steady momentum and energy transport for the range of parameters employed and these strong streaming effects are considered in detail in the following section. A treatment of the weaker effects of the streaming motion in the predominantly diffusive limit ($\mathrm{R}_s \ll 1$) can be found elsewhere (Gopinath, 1992). For the case of $\mathrm{R}_s \sim 1$ it is not possible to identify a single dominant mechanism of the steady transport and full-scale numerical solutions of the governing equations of motion are required to determine the steady velocity distribution completely.

4 Case of $\mathrm{R}_s \gg 1$

For large values for R_s encountered in this study, Stuart (1966) first predicted the presence of an outer boundary layer structure associated with the steady flow. He was able to show that the streaming velocity generated within the inner Stokes layer region decays to match the quiescent free stream across an outer streaming boundary layer, which is thin on the scale of the sphere radius but thick with respect to the inner Stokes region. This concept is used to develop a detailed description of this outer boundary layer structure for the streaming flow around the sphere and subsequently determine the resulting heat transfer rates for different Prandtl numbers.

4.1 The Flow Field. Starting with Eq. (9) the boundary layer velocity and length scales are first established. For the boundary layer thickness, δ_0, an order of magnitude analysis requiring a balance of the inertial and diffusive terms shows that $\delta_0/a \sim \mathrm{R}_s^{-1/2}$. In contrast the Stokes boundary layer thickness is such that $\delta/a \sim M^{-1}$. It is clear then that though both boundary layers are thin on the scale of the sphere radius, the ratio $\delta_0/\delta \sim 1/\epsilon$ indicates that for $\epsilon \ll 1$ the outer boundary layer is much thicker than the inner Stokes layer that remains embedded within it. The steady velocities also scale accordingly, and as in conventional laminar boundary layer theory the steady tangential (meridional) velocity remains of $O(\epsilon)$ where as the steady normal (radial) velocity is an $O(\epsilon \mathrm{R}_s^{-1/2})$ quantity in this region.

The boundary layer variables are defined in the usual manner as

$$\bar\eta=(r-1)\sqrt{\mathrm{R}_s}\ \text{and}\ \bar\psi_{1s}\,(\bar\eta,\,\mu)=\psi_{1s}\,(r,\,\mu)\sqrt{\mathrm{R}_s} \tag{17}$$

and Eq. (9) is modified to a form in which all the terms are of comparable magnitude:

$$\bar D^4\bar\psi_{1s}=\left[\frac{\partial(\bar\psi_{1s},\,\bar D^2\bar\psi_{1s})}{\partial(\bar\eta,\,\mu)}+2\bar D^2\bar\psi_{1s}\bar L\,\bar\psi_{1s}\right] \tag{18}$$

where now

$$\bar D^2=\frac{\partial^2}{\partial\bar\eta^2},\quad \bar L=\frac{\mu}{(1-\mu^2)}\frac{\partial}{\partial\bar\eta},\ \text{and}\ \bar\phi_0\,(\bar\eta,\,\mu)\equiv\phi_0(r,\mu)$$

The equation is subject to a far-field condition on the decaying velocity obtained from Eq. (12),

$$\frac{\partial\bar\psi_{1s}}{\partial\bar\eta}\to 0\ \text{as}\ \bar\eta\to\infty \tag{19}$$

and an inner matching condition from Eq. (11),

$$\bar\psi_{1s}\to\frac{45}{16}\,\bar\eta\,\mu(1-\mu^2)\ \text{as}\ \bar\eta\to 0 \tag{20}$$

It is easier to work with a simplified form of the above governing equation obtained by integrating once with respect to $\bar\eta$. Assuming continuity of the partial derivatives and applying the condition in Eq. (19) for the velocity in the far field, the integration results in,

$$\frac{\partial\bar\psi_{1s}}{\partial\bar\eta}\frac{\partial^2\bar\psi_{1s}}{\partial\bar\eta\partial\mu}-\frac{\partial\bar\psi_{1s}}{\partial\mu}\frac{\partial^2\bar\psi_{1s}}{\partial\bar\eta^2}+\frac{\mu}{(1-\mu^2)}\left(\frac{\partial\bar\psi_{1s}}{\partial\bar\eta}\right)^2=\frac{\partial^3\bar\psi_{1s}}{\partial\bar\eta^3} \tag{21}$$

This can be expressed in the form of a familiar set of boundary layer equations with the variables redefined for convenience in terms of commonly used symbols for the coordinates and suitably defined (artificial) velocities as

$$y\equiv\bar\eta,\quad x\equiv\mu\ \text{and}\ u=\frac{\partial\bar\psi_{1s}}{\partial\bar\eta},\quad v=-\frac{\partial\bar\psi_{1s}}{\partial\mu} \tag{22}$$

to give to leading order,

$$\frac{\partial u}{\partial x}+\frac{\partial v}{\partial y}=0 \tag{23}$$

$$u\frac{\partial u}{\partial x}+v\frac{\partial u}{\partial y}+\frac{xu^2}{(1-x^2)}=\frac{\partial^2 u}{\partial y^2} \tag{24}$$

The boundary conditions in Eqs. (19) and (20) are appropriately modified to

$$u=\frac{45}{16}x(1-x^2),\ v=0 \text{ at } y=0 \tag{25}$$

$$u\to 0 \text{ as } y\to\infty \tag{26}$$

The artificial velocities introduced above are related to the true velocity components, and from their definitions in Eq. (7), it is clear that the true steady tangential component is $-u(1-\mu^2)^{-1/2}$ to $O(\epsilon)$ accuracy whereas the true steady radial component is just v to $O(\epsilon R_s^{-1/2})$ accuracy. A suitable initial condition is required at $x=0$ to start the solution process for the above equations. It is clear from the boundary conditions that the steady flow is purely radial along $x=0$, which forms a plane of symmetry. This radial velocity can be described by an exact solution obtained from a limiting form of the governing equations of motion by following the procedure commonly adopted for studying the limiting form of the velocity near the point of attachement in natural convection flows. In this limit (as $x\to 0$) the tangential velocity is assumed to have a behavior given by $u\to xf'(y)$, which requires that $v\to -f(y)$ in order to satisfy Eq. (23). Substitution into Eq. (24) shows that to leading order $f(y)$ satisfies the nonlinear ordinary differential equation

$$f'''+ff''-f'^2=0 \tag{27}$$

with boundary conditions obtained from Eqs. (25) and (26) as,

$$f(0)=0,\ f'(0)=\frac{45}{16} \text{ and } f'\to 0 \text{ as } y\to\infty \tag{28}$$

It can be shown that Eqs. (27) and (28) yield an exponentially decaying exact solution:

$$f(y)=\sqrt{\frac{45}{16}}\,(1-e^{-y\sqrt{45/16}}) \tag{29}$$

It is worthwhile to note that the function $f(y) > 0$, whereby the normal velocity, $u_r\sim v=-f(y)$, reveals a purely radially inward flow along the equator in the outer boundary layer and indicates that $x=0$ corresponds to a stagnation plane of attachment.

The equation of motion itself has been considered independently by Riley (1965) and Stuart (1966) for the case of an oscillating circular cylinder. They used different methods (both involving series solutions in powers of the angular coordinate) to characterize the velocity boundary layer around the stagnation plane of attachment. The procedure they adopted involves a considerable amount of manipulative labor, and though it provides an accurate description of the mechanics of the flow in the local region around the stagnation plane, it does not explain the behavior of the flow over the complete periphery from the plane of attachment to the axis of oscillation. Consequently a numerical finite-difference scheme is used in a manner similar to that used by Davidson (1973) for the cylinder, to obtain an accurate description of the outer streaming boundary layer flow on the sphere.

The coupled set of nonlinear partial differential Eqs. (23) and (24) for u and v are solved using an implicit finite-difference scheme with marching from $x=0$ to $x=1$. All the derivatives are approximated by central differences and the nonlinearity is handled by quasi-linearization and iteration at each x location along the surface. The symmetry in the problem about the stagnation plane $x=0$ is utilized to carry out the solution procedure over only one half of the sphere. The computational domain along with the mesh star used in the numerical procedure is shown in Fig. 2. A typical node (m, n) represents a point (x_m, y_n) that is $(m-1)\,\Delta x$ distant from the stagnation plane, $x=0$ (corresponding to $m=1$), and $(n-1)\Delta y$ distant from the surface of the sphere, $y=0$ (corresponding to

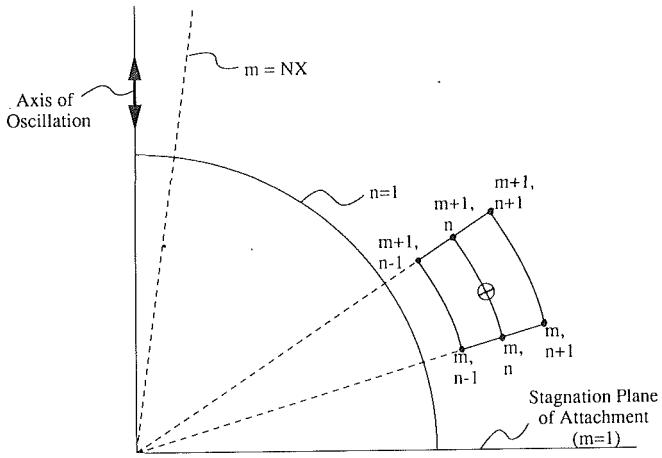

Fig. 2 The computational domain showing the mesh star

$n=1$). The edge of the boundary layer is chosen to correspond to a value of $n=NY$. In the x direction the computations are terminated at a value of $m=NX$ before encountering the expected singularity at the pole. A double-suffix notation is used to represent the nodal values of the artificial velocities as $u_{m,n}$, and $v_{m,n}$. Derivatives with respect to both x and y are approximated by central differences based on the halfway point (marked with a $\otimes$ in Fig. 2) and are achieved by using the average value of the neighboring nodes.

For the flow field, the implicit scheme enables us to evaluate the *array* of velocities, $\mathbf{u}_{m+1,n}^{(j+1)}$ and $\mathbf{v}_{m+1,n}^{(j+1)}$, $(2\le n\le NY)$ at the $(m+1)$th x location. This is done in terms of the array of values of the previous iteration, $\mathbf{u}_{m+1,n}^{(j)}$ and $\mathbf{v}_{m+1,n}^{(j)}$, $(2\le n\le NY)$ and the converged values, $\mathbf{u}_{m,n}$ and $\mathbf{v}_{m,n}$, $(2\le n\le NY)$ at the previous x location. The superscript represents the iteration number in the converging computational cycle. The details of the differencing and the quasi-linearization process are omitted here and it can be shown that after grouping together corresponding terms, the nodal relations of Eq. (24) can be represented in the familiar tridiagonal form as

$$a_n^{(j)}\,[u_{m+1,n+1}^{(j+1)}]+b_n^{(j)}\,[u_{m+1,n}^{(j+1)}]+c_n^{(j)}\,[u_{m+1,n-1}^{(j+1)}]=d_n^{(j)} \tag{30}$$

where the coefficients of the u terms in the matrix are given by

$$a_n^{(j)}=\frac{1}{4}v_{m+1/2,n}^{(j)}-\frac{1}{2\Delta y}$$

$$b_n^{(j)}=\Delta y u_{m+1,n}^{(j)}\left(\frac{1}{\Delta x}+w(x_{m+1/2})\right)+\frac{1}{\Delta y}$$

$$c_n^{(j)}=-\frac{1}{4}v_{m+1/2,n}^{(j)}-\frac{1}{2\Delta y}$$

$$d_n^{(j)}=\frac{\Delta y}{2\Delta x}\,(u_{m+1,n}^{(j)2}+u_{m,n}^2)-\frac{1}{4}\,v_{m+1/2,n}^{(j)}\,(u_{m,n+1}-u_{m,n-1})$$
$$+\frac{1}{2\Delta y}\,(u_{m,n+1}-2u_{m,n}+u_{m,n-1})$$
$$-\frac{1}{2}\Delta y w(x_{m+1/2})\,(u_{m+1,n}^{(j)2}-u_{m,n}^2) \tag{31}$$

in which the function $w(x_m)$ is defined as

$$w(x_m)=\frac{x_m}{1-x_m^2} \tag{32}$$

and $v_{m+1/2,n}^{(j)}$ is obtained from a numerical integration of Eq. (23) as,

$$v^{(j)}_{m+1/2,\,n} = v^{(j)}_{m+1/2,\,n-1} - \frac{\Delta y}{\Delta x}\left[\frac{1}{2}\left(u^{(j)}_{m+1,\,n} + u^{(j)}_{m+1,\,n-1}\right) - \frac{1}{2}\left(u_{m,\,n} + u_{m,\,n-1}\right)\right] \quad (33)$$

The appropriate boundary conditions corresponding to Eqs. (25) and (26) specified at the surface ($n=1$) and in the far field ($n=NY$) along with the initial condition on the stagnation plane ($m=1$) are

$$\begin{aligned} u_{m,\,1} &= (45/16)x_m\,(1-x_m^2) && \text{for } 1 \le m \le NX \\ u_{m,\,NY} &= 0 && \text{for } 1 \le m \le NX \\ u_{1,\,n} &= 0 && \text{for } 1 \le n \le NY \end{aligned} \quad (34)$$

At any general x location, the solution procedure is initiated by approximating the radial distribution of the artificial velocity, u, at that x location to be the same as that at the previous x location. (For the very first x location, $m=1$, it follows from the last of the boundary conditions in Eq. (34) that $u=0$.) This is then used in Eq. (33) to obtain an estimate for the artificial velocity, v, at the halfway point (marked $\otimes$ in Fig. 2) between the current and next x locations. This is in turn substituted in Eq. (31) to determine the coefficients of the tridiagonal system in Eq. (30) used to solve for u at the next x location. This cycle of calculations is repeated at each x location until the sum of the absolute differences between the current and previous iterates for u at all the y locations falls below a certain prescribed tolerance. At this juncture the iterative scheme is deemed to have converged at that x location and the whole process is advanced to the next x location, in this manner covering the entire periphery of the sphere from the equator ($x=0$) to the pole ($x=1$). The results of the computations for this steady flow field are probably best represented by the boundary layer velocity profiles in Fig. 3 showing the radial variation of u_θ at different angular locations along the periphery of the sphere.

For the case of the oscillating cylinder, Davidson and Riley (1972) were able to show that this streaming boundary layer flow on each half of the cylinder converges from the two quadrants to collide at the axis of oscillation. They found that the momentum in the boundary layers is turned smoothly and the fluid is ejected outward along the axis in the form of planar jets on each half of the cylinder. For the streaming flow around the sphere this collision process is more complex and may be compared to large Grashof number free convective flow on a heated sphere in the presence of a normal gravitational field as treated for example by Potter and Riley (1980). For the latter case the free convective flow in the upper hemisphere sweeps over the surface and converges at the upper pole to form a buoyant plume. For the streaming flow too, the fluid in the outer boundary layer exhibits such as sweeping motion. However, from the equatorial plane of symmetry, the flow is expected to be directed toward both the upper and lower poles in the case of the streaming flow. Then it is expected that the boundary layers converge and collide at both the poles, and in this case the fluid is ejected outward from the sphere along the axis of oscillation in the form of round inertial jets. A detailed discussion of the mechanics of formation of these jets is beyond the scope of this paper and may be found elsewhere; Lee and Wang (1988) have made simplistic scaling arguments of the length scales in the collision zone, though a more rigorous treatment is available in recent independent studies by Amin and Riley (1990) and Gopinath (1992).

4.2 The Temperature Field, Pr ~ 1. The energy equation is first considered for moderate Prandtl numbers, Pr ~ 1. This Prandtl number range is appropriate for gases and determines the heat transfer rates required in this study. It also helps establish some primary results, which are later used to determine the temperature distribution in the asymptotic limits of small and large Prandtl numbers. In this case for $R_s \gg 1$ and Pr ~ 1 it is well known that the temperature gradients are confined to a thermal boundary layer which attains a full structure on the scale of the hydrodynamic boundary layer. Under these conditions both the convective and diffusive modes of heat transfer are equally important and the governing energy equation has to be solved numerically using the results for the velocities obtained earlier. The details of this procedure are described next.

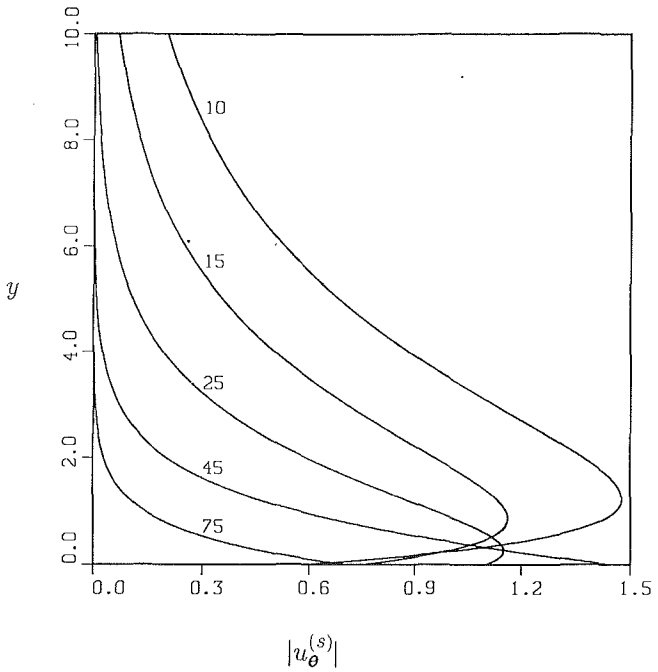

Fig. 3 Boundary layer velocity profiles for the streaming flow on a sphere for large Re_s (the corresponding angular locations, θ, in deg are shown on the figure)

In terms of the boundary layer variables defined in Eq. (17), the governing energy equation is

$$\frac{\partial^2 \bar{\phi}_0}{\partial \bar{\eta}^2} = \mathrm{Pr}\left[\frac{\partial(\bar{\psi}_{1s},\,\bar{\phi}_0)}{\partial(\bar{\eta},\,\mu)}\right] + O(\mathrm{R}_s^{-1/2}) \quad (35)$$

subject to an inner matching condition and a far-field condition on the temperature,

$$\begin{aligned} \bar{\phi}_0 &\to 1 \text{ as } r \to 1 \\ \bar{\phi}_0 &\to 0 \text{ as } r \to \infty \end{aligned} \quad (36)$$

The definitions in Eq. (22) along with $t(x, y) \equiv \bar{\phi}_0(\mu, \bar{\eta})$ are used to express Eq. (35) to leading order in the familiar form,

$$u\frac{\partial t}{\partial x} + v\frac{\partial t}{\partial y} = \frac{1}{\mathrm{Pr}}\frac{\partial^2 t}{\partial y^2} \quad (37)$$

subject to

$$\begin{aligned} t &= 1 \text{ on } y = 0 \\ t &\to 0 \text{ as } y \to \infty \end{aligned} \quad (38)$$

The limiting form of the radial variation of temperature at $x=0$ can also be established in a manner similar to that leading up to Eq. (29). If this variation of $t(x \to 0, y)$ is denoted by $g(y)$, then from the expected limiting behavior of $u(x \to 0, y)$ and $v(x \to 0, y)$, it follows from Eq. (37) that $g(y)$ satisfies the ordinary differential equation:

$$g'' + \mathrm{Pr} f g' = 0 \quad (39)$$

In view of the boundary conditions in Eq. (38)

$$g(0) = 1 \text{ and } g \to 0 \text{ as } y \to \infty \quad (40)$$

Using Eq. (29) for $f(y)$ it can be shown that $g(y)$ has an exact solution, which can be expressed in a compact form given by,

$$g(y) = \frac{\gamma(\mathrm{Pr},\ \mathrm{Pr}e^{-y\sqrt{45/16}})}{\gamma(\mathrm{Pr},\ \mathrm{Pr})} \tag{41}$$

where $\gamma(a, c)$ is the Incomplete Gamma Function defined as (Abramowitz and Stegun, 1965, §6.5.2)

$$\gamma(a, c) = \int_0^c e^{-s} s^{a-1} ds \tag{42}$$

The energy equation, Eq. (37), is now completely defined, and for the numerical solution it is discretized on the basis of the same mesh-star used for the flow field. A double suffix notation, $t_{m,n}$, is also adopted here and represents the temperature at a typical node, (m, n), corresponding to the location (x_m, y_n). The nodal equations for the temperature are generated in a manner analogous to that used for the artificial velocities and the derivatives are once again approximated by central-differencing about the halfway point between nodes. The actual details of the discretization procedure are not given here and it can be shown that the resulting form of the linear energy equation for the temperature, t, can be represented in the familiar tridiagonal form as,

$$A_n t_{m+1,n-1} + B_n t_{m+1,n} + C_n t_{m+1,n-1} = D_n \tag{43}$$

where the coefficients of the t terms in the matrix are given by

$$A_n = \frac{1}{4} v_{m+1/2,n} + \frac{1}{2\mathrm{Pr}\Delta y}$$

$$B_n = \frac{-\Delta y}{2\Delta x}(u_{m,n} + u_{m+1,n}) - \frac{1}{\mathrm{Pr}\Delta y}$$

$$C_n = -\frac{1}{4} v_{m+1/2,n} + \frac{1}{2\mathrm{Pr}\Delta y} \tag{44}$$

$$D_n = -t_{m,n-1} A_n + t_{m,n}(2A_n + B_n + 2C_n) - t_{m,n+1} C_n$$

Once again the appropriate boundary conditions corresponding to Eq. (38) specified at the surface ($n = 1$) and in the far field ($n = NY$) are

$$\left.\begin{aligned} t_{m,1} &= 1 \\ t_{n,NY} &= 0 \end{aligned}\right\} \text{ for } 1 \le m \le NX \tag{45}$$

For the starting condition $t_{1,n}$, $1 \le n \le NY$, the temperature profile specified by the function $g(y)$ in Eq. (41) is evaluated to sufficient accuracy from the series representations for the Incomplete Gamma function by Abramowitz and Stegun (1965, §6.5.4, 29) and used to initialize the temperature distribution along the stagnation plane. Using the known velocity distribution from §4.1, the transverse variation of temperature in the fluid at each angular location along the periphery is determined from Eqs. (37) and (38). This can be done in a relatively straightforward and noniterative manner involving triangular resolution and backward substitution.

Before carrying out this procedure, it is important to establish a proper set of grid parameters, and after some numerical experimentation it was found that a step length, $\Delta y = 0.05$, would be appropriate in the y direction for the entire domain. This was confirmed by repeating the calculations with a smaller step size $\Delta y = 0.025$ and ensuring that the improvement in accuracy obtained with the finer mesh was not significant enough to merit the additional computational time and cost for the prescribed accuracy. In the streamwise direction, a node-spacing of $\Delta x = 0.05$ was used along with an edge specification of $y = 20$ ($NY = 400$) in the normal direction, which was found to be sufficiently thick to capture the boundary layer effects. However, to account for the increasing x derivatives as the solution procedure was advanced toward the pole at $x = 1$, the mesh was refined by reducing Δx to 0.01, and to accommodate the thickening boundary layer the grid was enlarged in the y direction to 100 ($NY = 2000$). Both these changes were made past a chosen intermediate value of $x_0 = 0.80$ beyond which the effects of the growing boundary layer were found to be significant. To avoid the singularity at the pole, the marching procedure was advanced only up to a certain maximum value of $x_{\max} = 0.99$. Beyond this the flow was considered to be too close to the collision zone around the axis, $x = 1$, for the boundary layer form of the governing equations to be valid.

Table 1 Numerical results for the average Nusselt number as a function of the Prandtl number

Pr	$Nu/\sqrt{R_s}$	Pr	$Nu/\sqrt{R_s}$
0.1	0.2378	1.0	1.4108
0.2	0.4146	2.0	2.2046
0.3	0.5790	3.0	2.8186
0.4	0.7270	4.0	3.3388
0.5	0.8620	5.0	3.7994
0.6	0.9864	6.0	4.2180
0.7	1.1022	7.0	4.6058
0.8	1.2108	8.0	4.9706
0.9	1.3134	9.0	5.3122
1.0	1.4108	10.0	5.6418

The total heat transfer between the sphere and the fluid is characterized by the average Nusselt number (based on the sphere diameter), which from the symmetry of the problem can be expressed as

$$\frac{\mathrm{Nu}}{\sqrt{\mathrm{R}_s}} = -2\int_0^1 \left(\frac{\partial t}{\partial y}\right)_{y=0} dx \tag{46}$$

where the dependence on the Prandtl number is implicit in the temperature gradient at the surface of the sphere. Once the temperature profiles at the different x locations are determined for a given Prandtl number, Pr, the numerical integration in Eq. (46) is carried out using Simpson's rule to fourth-order accuracy. The derivative in the integrand representing the temperature gradient at the surface of the sphere is approximated from the numerical results for the temperature field by a forward differencing scheme, which is of second-order accuracy.

The numerical scheme was used to generate values of the average Nusselt number for Pr varying from 0.1 to 1.0 in steps of 0.1 and from 1.0 to 10.0 in steps of 1.0. These results are presented in Table 1. The implicit assumption that the thicknesses of the velocity and thermal boundary layers are of the same order of magnitude was considered invalid outside this range of Prandtl numbers. A plot of the boundary layer temperature profiles for air ($\mathrm{Pr} = 0.7$) has been presented in Fig. 4 as a representative result of the temperature gradients driving the heat transfer in gases.

A least-squares fit of the values of $\mathrm{Nu}/\sqrt{\mathrm{R}_s}$ in Table 1 with the Prandtl number, Pr, gives a correlation to determine the heat transfer in this large R_s case as,

$$\frac{\mathrm{Nu}}{\sqrt{\mathrm{R}_s}} = 1.314\ \mathrm{Pr}^{0.665} \text{ for } 0.1 \le \mathrm{Pr} \le 10.0 \tag{47}$$

In the Prandtl number range for gases a more appropriate fit is given by

$$\frac{\mathrm{Nu}}{\sqrt{\mathrm{R}_s}} = 1.413\ \mathrm{Pr}^{0.7} \text{ for } 0.6 \le \mathrm{Pr} \le 1.0 \tag{48}$$

A similar curve fit for the average Nusselt number (based on

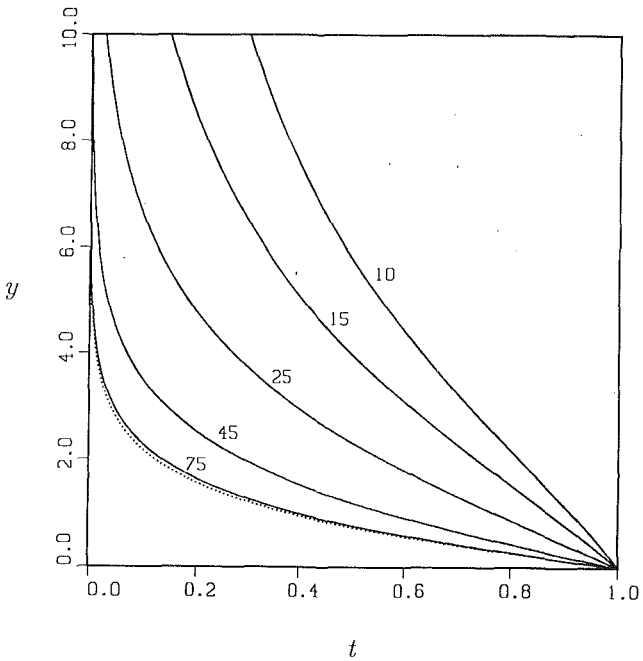

Fig. 4 Boundary layer temperature profiles (Pr = 0.7) for the streaming flow on a sphere for large R_s. The dotted line from Eq. (41) represents the starting profile at $\theta = 90$ deg (for the remaining curves, the corresponding angular locations, θ, in deg are shown on the figure)

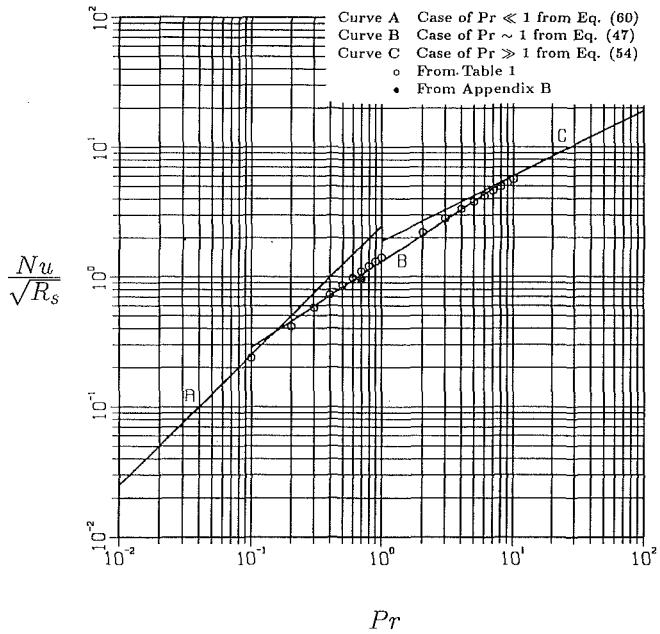

Fig. 5 Variation of the average Nusselt number as a function of the Prandtl number for large R_s

the diameter) of a circular cylinder has been extracted from the results of Davidson (1973, Fig. 9) for comparison as

$$\frac{\mathrm{Nu}}{\sqrt{\mathrm{R}_s}} = 1.388\ \mathrm{Pr}^{0.731} \text{ for } 0.2 \le \mathrm{Pr} \le 1.5 \qquad (49)$$

and gives Nu values about 2 to 3 percent lower than Eq. (48).

5 Closure

The convective heat transfer rates due to acoustic streaming were determined for an isolated sphere in a standing sound field. After a comparison of the length scales involved in the problem, the governing equations of motion and energy were stated in Section 2. Based on the study by Riley (1966), some deductions and basic results for the time-periodic and time-independent parts of the flow field were presented in Section 3. The steady transport problem was treated for large streaming Reynolds numbers, R_s, in Section 4 and Nusselt number correlations were developed for the case of $\mathrm{Pr} \sim 1$. These are supplemented by brief analyses for the limiting cases of small and large Prandtl numbers in Appendix A. Where relevant, comparisons were made with the results obtained by Davidson (1973). A simple experiment is described in Appendix B and its results were found to confirm some of the predictions made earlier. The results of this work have been summarized in Fig. 5. The details behind the results reported here may be found in a recent study by Gopinath (1992) wherein a scale analysis has also been performed to examine the role played by buoyancy and viscous dissipation in influencing the heat transfer.

Acknowledgments

This work was supported by the National Science Foundation on Grant No. CTS-8918777. The experiment described in Appendix B was conducted at the facilities of Loral Electro-Optical Systems Inc. in Pasadena, CA, as a part of a joint effort to study convective heat transfer rates to/from acoustically levitated samples. The authors would like to thank Mr. Scott Lee, their resident mechanical engineer, for collecting the data.

References

Abramowitz, M., and Stegun, I. A., eds., 1965, *Handbook of Mathematical Functions*, Dover, NY.

Amin, N., and Riley, N., 1990, "Streaming From a Sphere Due to a Pulsating Source," *J. Fluid Mech.*, Vol. 210, pp. 459–473.

Davidson, B. J., and Riley, N., 1972, "Jets Induced by Oscillatory Motion," *J. Fluid Mech.*, Vol. 53, pp. 287–303.

Davidson, B. J., 1973, "Heat Transfer From a Vibrating Circular Cylinder," *Int. J. Heat Mass Transfer*, Vol. 16, pp. 1703–1727.

Gopinath, A., 1992, "Convective Heat Transfer in Acoustic Streaming Flows," Ph.D. Dissertation, School of Engineering and Applied Science, University of California at Los Angeles, Los Angeles, CA.

Lee, C. P., and Wang, T. G., 1988, "Acoustic Radiation Force on a Heated Sphere Including Effects of Heat Transfer and Acoustic Streaming," *J. Acoust. Soc. Am.*, Vol. 83, pp. 1324–1331.

Lighthill, M. J., 1963, "Introduction. Real and Ideal Fluids," *Laminar Boundary Layers*, L. Rosenhead, ed., Clarendon Press, Oxford, pp. 1–45.

Potter, J. M., and Riley, N., 1980, "Free Convection From a Heated Sphere at Large Grashof Number," *J. Fluid Mech.*, Vol. 100, pp. 769–783.

Rey, C. A., Merkley, D. R., Hampton, S., DeVos, J., Mapes-Riordan, D., and Zatarski, M., 1991, "Containerless Processing at High Temperatures Using Acoustic Levitation," *Advances in Space Research*, Vol. 11, pp. 769–777.

Richardson, P. D., 1967, "Heat Transfer From a Circular Cylinder by Acoustic Streaming," *J. Fluid Mech.*, Vol. 30, pp. 337–355.

Riley, N., 1965, "Oscillating Viscous Flows," *Mathematika*, Vol. 12, pp. 161–175.

Riley, N., 1966, "On a Sphere Oscillating in a Viscous Fluid," *Quart. J. Mech. Appl. Math.*, Vol. 19, pp. 461–472.

Stuart, J. T., 1966, "Double Boundary Layers in Oscillatory Viscous Flows," *J. Fluid Mech.*, Vol. 24, pp. 673–687.

APPENDIX A

Limiting Prandtl Numbers

A.1 Case of $\mathrm{Pr} \gg 1$. For large Prandtl numbers, the thermal boundary layer is very thin on the scale of the hydrodynamic boundary layer. The scale of the thermal boundary layer thickness, δ_T, can be established by ensuring a balance of the diffusive and convective terms in the governing energy equation, Eq. (35), in which distances have been scaled with respect to δ_0. An order of magnitude analysis shows that a new balance is possible only if $\delta_T/\delta_0 \sim \mathrm{Pr}^{-1/2}$ and for $\delta_0/a \sim \mathrm{R}_s^{-1/2}$, it follows that $\delta_T/a \sim \mathrm{Pr}^{-1/2}\ \mathrm{R}_s^{-1/2}$. Based on the above scalings the boundary layer variables appropriate to this region are

$\tilde{\eta} = \bar{\eta}\sqrt{\mathrm{Pr}}$ and $\tilde{\psi}_{1s}(\tilde{\eta}, \mu)$
$= \sqrt{\mathrm{Pr}}\ \bar{\psi}_{1s}(\tilde{\eta}, \mu)$ with $\tilde{\phi}_0(\tilde{\eta}, \mu) \equiv \bar{\phi}_0(\bar{\eta}, \mu)$ (50)

With the thermal boundary layer embedded within the velocity boundary layer the dominant contribution to the heat transfer comes from the streaming velocity present at the outer edge of the Stokes region. The velocity profile is linear to leading order in this inner thermal region and the structure of the transport is sought in expansions of the form

$$\tilde{\psi}_{1s} \sim \tilde{\psi}_{1s}^{(0)} + O(\mathrm{Pr}^{-1/2}) \text{ and } \tilde{\phi}_0 \sim \tilde{\phi}_{00} + O(\mathrm{Pr}^{-1/2}) \quad (51)$$

It follows from the governing equations, Eqs. (9)–(12), that $\tilde{\psi}_{1s}^{(0)} = 45/16\ \tilde{\eta}\,\mu(1-\mu^2)$ and $\tilde{\phi}_{00}$ satisfies

$$\frac{\partial^2 \tilde{\phi}_{00}}{\partial \tilde{\eta}^2} = \left[\frac{\partial(\tilde{\psi}_{1s}^{(0)}, \tilde{\phi}_{00})}{\partial(\tilde{\eta}, \mu)}\right] \quad (52)$$

subject to the conditions: $\tilde{\phi}_{00} = 1$ at $\tilde{\eta} = 0$ and $\tilde{\phi}_{00} \to 0$ as $\tilde{\eta} \to \infty$. The above equation has an exact solution,

$$\tilde{\phi}_{00} = \mathrm{erfc}\left[\frac{3\sqrt{5}}{4}\,\tilde{\eta}\,\frac{(1-\mu^2)}{\sqrt{2-\mu^2}}\right] \quad (53)$$

from which the average Nusselt number can be obtained as

$$\frac{\mathrm{Nu}}{\sqrt{\mathrm{R}_s}} = \frac{3}{2}\sqrt{\frac{5}{\pi}}\sqrt{\mathrm{Pr}} + O(1) \quad (54)$$

A similar dependence had been obtained earlier by Davidson (1973, Eq. 78) and Richardson (1967, Eq. 13) as

$$\frac{\mathrm{Nu}}{\sqrt{\mathrm{R}_s}} = \frac{4}{\pi}\sqrt{\frac{6}{\pi}}\sqrt{\mathrm{Pr}} + O(1) \quad (55)$$

for the heat transfer from a circular cylinder in this asymptotic limit of $\mathrm{Pr} \gg 1$. It should be noted that the above analysis is restricted to thicknesses $\delta_T \gg \delta$ (i.e., $\mathrm{Pr} \ll \epsilon^{-2}$) whereby the complex transport effects of the recirculatory Stokes region can be ignored.

A.2 Case of $\mathrm{Pr} \ll 1$. For very small Prandtl numbers the changes in the temperature are more gradual and extend into a region beyond the scale of the velocity boundary layers. In this region, the steady tangential velocity is essentially nonexistent (exponentially small) and there is only an $O(\epsilon \mathrm{R}_s^{-1/2})$ radially inward steady drift velocity typical of boundary layer flows. It is only the convective effects due to this entrainment velocity that could possibly balance the diffusive effects in an outer thermal region external to the velocity boundary layer. An order-of-magnitude analysis shows that this outer thermal boundary layer region has a thickness $\delta_T \sim \delta_0\ \mathrm{Pr}^{-1}$, which is large in comparison with δ_0 and yet small on the scale of the sphere radius, provided that $\mathrm{Pr} \gg \mathrm{R}_s^{-1/2}$. The appropriate "slow" variable for this outer region is

$$\hat{\eta} = \bar{\eta}\mathrm{Pr} \text{ with } \hat{\phi}_0(\hat{\eta}, \mu) = \bar{\phi}_0(\bar{\eta}, \mu) \quad (56)$$

However, in an inner thermal region on the scale of the velocity boundary layer, thermal diffusive effects dominate and the variables originally defined in Eq. (17) are retained for this region.

It can be shown that matching between the inner and outer thermal regions requires that an inner linear solution,

$$\bar{\phi}_0 = 1 + \bar{\eta}\mathrm{Pr}\ v_\infty(\mu) + O(\mathrm{Pr}^2) \quad (57)$$

couple with an outer exponentially decaying solution of the form

$$\hat{\phi}_0 = e^{\hat{\eta} v_\infty}\ [1 + O(\mathrm{Pr}^2)] \quad (58)$$

where $v_\infty(\mu) = -\partial\bar{\psi}_{1s}/\partial\mu < 0$ is a function describing the angular distribution of the $O(\epsilon \mathrm{R}_s^{-1/2})$ steady radial entrainment velocity as $\bar{\eta} \to \infty$ in the outer reaches of the streaming velocity boundary layer. The average Nusselt number can now be determined from the temperature gradient in the inner thermal region according to

$$\frac{\mathrm{Nu}}{\sqrt{\mathrm{R}_s}} = 2\mathrm{Pr}\int_0^1 -v_\infty(\mu)\,d\mu + O(\mathrm{Pr}^2) \quad (59)$$

wherein the value of the function $v_\infty(\mu)$ (at each angular location) is simply equal to v at the outermost radial node $n = NY$ in the computational grid used to obtain the velocity field as described in Section 4.1. The integral in Eq. (59) above is subsequently evaluated numerically using Simpson's rule to fourth-order accuracy to yield

$$\frac{\mathrm{Nu}}{\sqrt{\mathrm{R}_s}} = 2.50\mathrm{Pr} + O(\mathrm{Pr}^2) \quad (60)$$

which can be compared to the result obtained by Davidson (1973, Eq. 91),

$$\frac{\mathrm{Nu}}{\sqrt{\mathrm{R}_s}} = 2.71\mathrm{Pr} + O(\mathrm{Pr}^2) \quad (61)$$

for a circular cylinder in this asymptotic limit of $\mathrm{Pr} \ll 1$. It should be noted that the above thermal boundary layer analysis is possible only for $\mathrm{Pr} \gg \mathrm{R}_s^{-1/2}$; for smaller Prandtl numbers diffusive effects dominate the heat transport.

APPENDIX B

A Simple Experiment

In this section an experiment is described that was conceived to verify the prediction for the heat transfer rate from an isolated sphere in the presence of an acoustic signal typically used in the levitation process. With a voltage source connected to a thermistor bead, the objective of the experiment is to measure the convective heat transfer rate when the power dissipated within the thermistor is balanced by the cooling action of the steady streaming motion induced by the standing sound field around the thermistor. A sufficiently small bead is chosen to ensure that buoyancy effects are negligible as per the criterion identified by Gopinath (1992). At equilibrium, measurements of voltage and current give the power being dissipated in the thermistor and transferred to the ambient. Assuming the bead to be isothermal at the temperature recorded by the thermistor, the average heat transfer coefficient and the average Nusselt number over the surface of the bead can be calculated from

$$h = \frac{Q}{\pi d^2\ (T_s - T_\infty)}, \quad \mathrm{Nu} = \frac{hd}{\kappa} \quad (62)$$

In the experiment, a thermistor bead was physically suspended (by its lead wire) along the centerline of an acoustic levitation test cell of length 50.8 cm and of square cross section, 6.35 cm on its side. The bead was held in place at an axial location (roughly equidistant from the end walls of the test cell) corresponding to the observed stable position of an acoustically levitated sample. This position corresponds (approximately) to the location of the velocity antinode (peak) of the plane standing sound field excited across the ends of the test cell. The bottom portion of the test cell comprising the acoustic drivers and transducers was fixed to the ground and connected to the appropriate controls. The test cell itself was completely covered by a well-lined and sound-proofed acoustic chamber to provide shielding from the loud acoustic signals used in the experiment.

The experiment was conducted with a plane standing sound wave for one typical setting of the acoustic signal given by an SPL of 155 dB and a frequency of 1018 Hz. Equation (15) readily shows that this corresponds to a streaming Reynolds

Table 2 Experimental results along with their uncertainty values

$\mathcal{I}$ [mA]	$T_s - T_\infty$ [K]	h [W/m² K]	Δ_h [W/m² K]	Nu	Δ_{Nu}
3.50	10.0	159.40	23.17	14.02	2.04
3.60	10.8	151.54	20.48	13.32	1.80
12.0	42.8	125.59	5.56	11.04	0.49
4.23	14.5	131.69	13.54	11.58	1.19
4.06	13.5	136.04	14.93	11.96	1.31
5.60	21.8	115.03	8.29	10.11	0.73

number, R_s, of 157.8 for properties of air taken at an ambient temperature measured to be 22°C. The other fixed parameters in this experiment were the thermistor bead diameter (2.286 mm) and the output of the voltage source (7.76 V). However, different power dissipation rates were tried in many runs of the experiment by allowing the thermistor to draw different amounts of current. Between each such run the test cell was flushed to dispel any accumulated hot air and introduce fresh air from the ambient. For each run the heat transfer rate, the heat transfer coefficient, and the Nusselt number were calculated. The calculations accounted for radiative losses and power losses in the lead wire connecting the thermistor to the voltage source. These corrections were found to be minor and at worst resulted in a 5 percent reduction in the Nusselt number. Finally an estimate was made of the random errors in the measurements that propagated through to the final results. Uncertainties in the measurement of current, voltage, and temperature were used to calculate the absolute uncertainties in the heat transfer coefficient and the Nusselt number. The results of this experiment are summarized in Table 2. The measured quantities in this table are the current and the temperature of the thermistor. The remaining values are the results of the calculations outlined above and include the estimated uncertainties in these results. The other important parameters relevant to this experiment are the frequency parameter, $M^2 = 532.3$, and the amplitude parameter, $\epsilon = 0.54$.

It is appropriate to compare the results from this experiment with the predictions made from the corresponding theory for the case of $R_s \gg 1$, $Pr \sim 1$ in Section 4.2. If the experimental result for the average Nusselt number from Table 2 were to be correlated in the form $Nu/\sqrt{R_s} = C$ then it is a simple matter to show that corresponding to $R_s = 157.8$ the constant $C = 0.96$ for air. Comparing this with the computational results in Table 1 against the Prandtl number for air, $Pr = 0.7$, the constant C is found to be 1.10. The good agreement is perhaps fortuitous and more detailed experiments with a better spread of data are required before being able to make any firm conclusions. However, the agreement is encouraging and further supports the correctness of the analysis in the previous sections.

Development of Oscillatory Asymmetric Recirculating Flow in Transient Laminar Opposing Mixed Convection in a Symmetrically Heated Vertical Channel

Tsing-Fa Lin
Professor.
Assoc. Mem. ASME

Tsai-Shou Chang
Graduate Student.

Yu-Feng Chen
Graduate Student.

Department of Mechanical Engineering, Manufacturing and Thermal-Fluid Engineering Research Center, National Chiao Tung University, Hsinchu, Taiwan

Detailed flow and thermal characteristics in transient laminar opposing mixed convection in a vertical plane channel subject to a symmetric heat input are numerically investigated. First, a linear stability analysis was employed to evidence the occurrence of flow bifurcation. Then, the unsteady Navier–Stokes equations along with the continuity and energy equations were respectively integrated by a third-order upwind and power-law finite-difference scheme with the resulting matrices inverted by the Fast Fourier Transform and conjugated gradient methods. Reverse flow in the form of symmetric, elongated recirculating cells is initiated earlier and is stronger in a lower Prandtl number fluid with higher opposing buoyancy and Reynolds number and longer heated section length. At a high opposing buoyancy, sudden flow asymmetry and oscillation occur simultaneously in a nearly steady flow after the initial transient. Periodic flow and thermal evolution are noted in space and time. An empirical equation for the condition for inducing flow oscillation is proposed.

Introduction

Fundamental understanding of buoyancy-induced laminar–turbulent flow transition is important in the basic study of fluid dynamics and in the optimal design of thermal-fluid devices in various engineering systems. The study of the laminar–turbulent transition in pressure-driven flow, extensively explored in the past, indicates that in the early stage of the transition, two-dimensional waves appear and later spanwise variations become important. In the meantime the flow exhibits changes from periodic to aperiodic and later to chaotic fluctuations. In an initial attempt to elucidate the buoyancy-induced transitional flow, this study investigates the detailed unsteady, two-dimensional flow and thermal characteristics in a symmetrically heated vertical channel flow through a rigorous numerical simulation.

It has long been known that buoyancy can have significant effects on the forced fluid flow and heat transfer in a vertical plane channel. Specifically, recirculating flow occurs when the opposing buoyancy force is strong enough to reverse the direction of the forced flow. In aiding flow at a high Gr/Re^2, the flow near the walls is accelerated to a very high speed, causing the flow reversal in the central portion to maintain the mass conservation at every cross section of the channel. In general, an opposing buoyancy is more likely to induce flow reversal. Due to the existence of inflection points in the velocity profiles, the recirculating flow is very unstable according to the theory of the boundary layer flow stability (White, 1974). The flow is then prone to instability and becomes transitional. In fact, velocity and temperature oscillation are rapidly amplified at a large τ when the opposing buoyancy is high. The flow soon becomes unstable and transitional, and it is essentially three dimensional. Experimental investigations on the instability and transition of the mixed convection in vertical tube were conducted by Scheele et al. (1960), Scheele and Hanratty (1962, 1963), Lawrence and Chato (1966), and Zeldin and Schmidt (1972). Interestingly, Scheele and Hanratty observed unsteady and asymmetric flow shortly after the appearance of the flow reversal at a high opposing buoyancy. However, the detailed flow and thermal characteristics in this unsteady three-dimensional flow are still poorly understood.

Up-to-date reviews on the internal mixed convection were recently conducted by Incropera (1986), Aung (1987), and Gebhart et al. (1988). In what follows the relevant literature on the recirculating mixed convection is briefly reviewed.

Steady fully developed and developing mixed convection was treated by Tao (1960) and Quintiere and Mueller (1973). The numerical solution for aiding mixed convection of air from Habchi and Acharya (1986) shows that the air temperature increases with Gr/Re^2 and the Nusselt number decreases monotonically. A similar study was carried out by Aung and Worku (1986a), showing that buoyancy force can cause a severe distortion in the velocity profiles especially under asymmetric wall heat condition. An investigation for flow with unequal wall heat fluxes (Aung and Worku, 1987) indicates that flow reversal is prone to occur in uniform wall temperature situation. In particular, no flow reversal is predicted for Gr/Re up to 500. Low Peclet number mixed convection in a short channel was examined by Chow et al. (1984). Various axial length scales to distinguish regions of different convective mechanisms were discussed by Yao (1983).

Recirculating flow and heat transfer in steady laminar opposing mixed convection in a vertical flat duct were examined by Cebeci et al. (1982). Criteria for the presence of reverse flow have been derived for mixed convection in vertical ducts (Aung and Worku, 1986b) and in inclined ducts (Lavine, 1988). Through detailed numerical simulation, Ingham et al. (1988a, b) noted that poor heat transfer results for flow retarded by an opposing buoyancy force, but for a large and negative Gr/Re^2 heat transfer is rather effective. In fact, heat transfer is greatly improved over the section containing strong reverse flow.

Contributed by the Heat Transfer Division for publication in the JOURNAL OF HEAT TRANSFER. Manuscript received by the Heat Transfer Division November 1990; revision received October 1992. Keywords: Flow Instability, Mixed Convection, Transient and Unsteady Heat Transfer. Associate Technical Editor: F. P. Incropera.

Visualization of recirculating flow in steady aiding and opposing mixed convection in vertical or inclined ducts was recently conducted by Morton et al. (1989), Lavine et al. (1989), and Ingham et al. (1990). The corresponding numerical analysis was performed by Heggs et al. (1990) including heat conduction in the wall.

Regarding the unsteady mixed convection in a vertical tube, Shadday (1986) numerically predicted the flow reversal for $\mathrm{Re}=100$ and $\mathrm{Gr}\geq 10^5$ and unstable flow at $\mathrm{Re}=100$ and $\mathrm{Gr}=10^6$. In the analysis the heat capacity of the wall is not included. This is inappropriate, especially during the transient stage, as evident from the studies of transient pure natural convection (Joshi, 1988) and forced convection (Sucec and Sawant, 1984; Sucec, 1987; Lin and Kuo, 1988) in the channel. In an attempt to delineate the transient internal mixed convection, Lin et al. (1991) investigated the unsteady laminar mixed convection of air in a vertical flat duct with a low Gr/Re so that no flow reversal occurs.

Despite the extensive study on steady mixed convection in vertical channels that has been carried out in the past, relatively little attention has been paid to investigating transient unstable thermal and flow characteristics in internal mixed convection flow, especially during the process of flow reversal. Through a detailed numerical simulation, we aim to examine these characteristics in a forced flow under strong opposing buoyancy.

The physical model under consideration and the coordinates chosen are depicted in Fig. 1. As shown in the figure, a parallel plane channel of wall thickness δ and interplate spacing b is oriented along the gravitational direction. The dimension of the channel walls perpendicular to the x-y plane is very large, so that the flow can be considered as two dimensional. A downward flow enters the channel at temperature T_e in the far upstream region, $x\rightarrow -\infty$. Initially, the flow and the confining walls are at the same uniform temperature T_e. At time $t=0$, uniform and equal heat fluxes are respectively imposed on the left and right walls over the finite length ($0\leq x\leq \ell$) and maintained at these levels thereafter. Upstream and downstream of the heated section ($x\leq 0$ or $x\geq \ell$) the channel is well insulated. Flow is assumed to reach the fully developed state prior to moving into the region of significant heat transfer. Only buoyancy-opposing flows will be examined since flow reversal frequently appears under this situation. Particular attention is paid to examining the unsteady oscillatory flow and heat transfer characteristics during the development of recirculating flow.

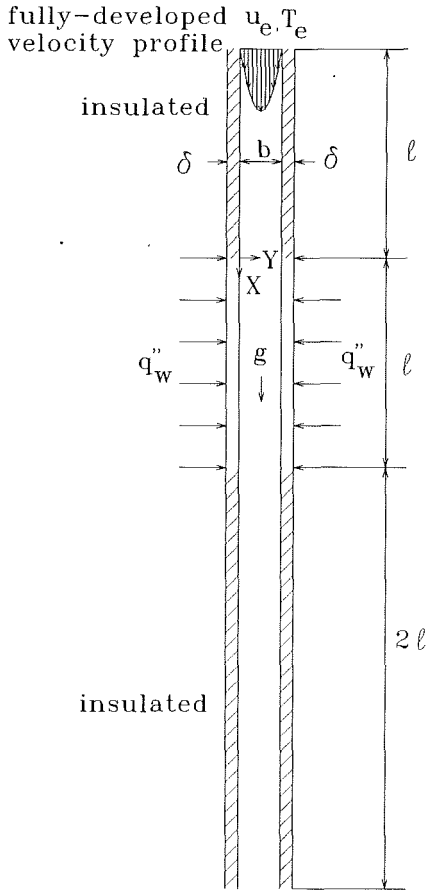

Fig. 1 Schematic diagram of the physical system

Mathematical Formulation

Basic nondimensional equations of the unsteady two-dimensional combined convection of a Boussinesq fluid through a vertical channel with the possible presence of flow recirculation are

$$\frac{\partial U}{\partial X}+\frac{\partial V}{\partial Y}=0 \tag{1}$$

Nomenclature

A = wall-to-fluid heat capacity ratio
b = channel width
$\mathbf{B}$ = body force
c = complex speed of wave
c_p = specific heat at constant pressure
g = gravitational acceleration
Gr = Grashof number
h = convection heat transfer coefficient
k = thermal conductivity of fluid
k_1 = wave number
ℓ, L = dimensional and dimensionless length of the directly heated section
Nu, $\overline{\mathrm{Nu}}$ = local and average Nussselt numbers
p, P = dimensional and dimensionless pressure
p_m = dynamic (motion) pressure
Pe = Peclet number = Re·Pr
Pr = Prandtl number
q'' = heat flux
Re = Reynolds number
t, τ = dimensional and dimensionless time
T, θ = dimensional and dimensionless temperatures
u, v = velocity components in x and y directions
U, V = dimensionless velocity components in X and Y directions
$\mathbf{V}$ = velocity vector
$\hat{V}$ = dimensionless velocity disturbance in Y direction
x, y = Cartesian coordinates
X, Y = dimensionless Cartesian coordinates
α = thermal diffusivity
β = coefficient of volumetric thermal expansion
ΔX = grid size in X direction
$\Delta\tau$ = time interval
δ = thickness of the channel wall
$\hat{\theta}$ = dimensionless temperature disturbance
ν = kinematic viscosity
ρ = density

Subscripts

b = quantity of basic flow
e = entrance plane
i, j = indices in x and y directions
l = on the left wall
r = on the right wall
w = on wall
x = local quantity

Superscripts

n = time step
$*$ = predicted value

$$\frac{\partial U}{\partial \tau}+U\frac{\partial U}{\partial X}+V\frac{\partial U}{\partial Y}=-\frac{\partial P}{\partial X}+\frac{\mathrm{Gr}}{\mathrm{Re}^2}\theta+\frac{1}{\mathrm{Re}}\left[\frac{\partial^2 U}{\partial X^2}+\frac{\partial^2 U}{\partial Y^2}\right] \quad (2)$$

$$\frac{\partial V}{\partial \tau}+U\frac{\partial V}{\partial X}+V\frac{\partial V}{\partial Y}=-\frac{\partial P}{\partial Y}+\frac{1}{\mathrm{Re}}\left[\frac{\partial^2 V}{\partial X^2}+\frac{\partial^2 V}{\partial Y^2}\right] \quad (3)$$

$$\frac{\partial \theta}{\partial \tau}+U\frac{\partial \theta}{\partial X}+V\frac{\partial \theta}{\partial Y}=\frac{1}{\mathrm{Re}\cdot\mathrm{Pr}}\left[\frac{\partial^2 \theta}{\partial X^2}+\frac{\partial^2 \theta}{\partial Y^2}\right] \quad (4)$$

and the associated initial and boundary conditions are

for $\tau=0$

$$\text{at } X\to-\infty,\quad U=6(Y-Y^2),\ V=0,\ \theta=0 \quad (5)$$

for $\tau>0$

$$\text{at } X\to-\infty,\quad U=6(Y-Y^2),\ V=0,\ \theta=0 \quad (6)$$

$$\text{at } X\to\infty,\quad \frac{\partial U}{\partial X}=0,\ V=0,\ \frac{\partial \theta}{\partial X}=0 \quad (7)$$

$$\text{at } Y=0,\ U=V=0,\ A\frac{\partial \theta}{\partial \tau}-\frac{\partial \theta}{\partial Y}=\begin{cases}1 & \text{for } 0\le X\le L\\ 0 & \text{otherwise}\end{cases} \quad (8)$$

$$\text{at } Y=1,\ U=V=0,\ A\frac{\partial \theta}{\partial \tau}+\frac{\partial \theta}{\partial Y}=\begin{cases}1 & \text{for } 0\le X\le L\\ 0 & \text{otherwise}\end{cases} \quad (9)$$

Note that in the opposing mixed convection the parameter $\mathrm{Gr}/\mathrm{Re}^2$, which signifies the relative strength of the buoyancy to inertia forces, is negative. The effects of the wall heat capacity are accounted for in Eqs. (8) and (9). The above equations are written in terms of the following nondimensional variables:

$$\begin{gathered}X=x/b,\quad Y=y/b,\quad L=\ell/b\\ U=u/\bar{u}_e,\quad V=v/\bar{u}_e,\quad \tau=t/(b/\bar{u}_e)\\ \theta=(T-T_e)/(q_w'' b/k),\quad P=p/\rho\bar{u}_e^2\\ \mathrm{Re}=\bar{u}_e b/\nu,\quad \mathrm{Gr}=g\beta q_w'' b^4/(k\nu^2),\\ \mathrm{Pr}=\nu/\alpha,\quad A=\frac{\rho_w c_{pw}\delta}{\rho c_p b}\mathrm{Re}\cdot\mathrm{Pr}\end{gathered} \quad (10)$$

The local and space-averaged Nusselt numbers on the left and right channel walls can be evaluated from the equations

$$\mathrm{Nu}_1=\frac{h_1\cdot b}{k}=\frac{-k\left.\frac{\partial T}{\partial y}\right|_{y=0}}{T_w-T_e}\cdot\frac{b}{k}=-\frac{1}{\theta}\left.\frac{\partial \theta}{\partial Y}\right|_{Y=0}, \quad (11)$$

$$\mathrm{Nu}_1=\frac{h_r\cdot b}{k}=\frac{k\left.\frac{\partial T}{\partial y}\right|_{y=b}}{T_w-T_e}\cdot\frac{b}{k}=-\frac{1}{\theta}\left.\frac{\partial \theta}{\partial Y}\right|_{Y=1}, \quad (12)$$

and

$$\overline{\mathrm{Nu}}=\frac{1}{L}\int_0^L \mathrm{Nu}\,dX \quad (13)$$

Solution Method

To simulate the complicated oscillatory flow accurately, a higher order numerical scheme is needed. After testing a number of schemes such as SIMPLE, SIMPLER, QUICK, MAC, etc., the projection method developed by Chorin (1968) and Temam (1968) was chosen to solve the time-dependent governing equations in their primitive form with three interlacing staggered grids, respectively, for the horizontal and vertical velocity components and all scalar variables. The positions of the grid points and their spacings are chosen such that the fluid boundaries lie on the nodes for the velocity components. This fractional step method consists of two steps. First, a provisional value $\mathbf{V}^*$ is explicitly computed for velocity field ignoring the pressure gradient,

$$\frac{\mathbf{V}^*-\mathbf{V}^n}{\Delta\tau}+A\cdot(\mathbf{V}^n)-\frac{1}{\mathrm{Re}}\cdot\nabla^2\mathbf{V}^n-\mathbf{B}=0 \quad (14)$$

where $A\cdot(\mathbf{V}^n)$ is the convective term, $A\cdot(\mathbf{V})=(\mathbf{V}\cdot\nabla)\mathbf{V}$, Re is the Reynolds number of the flow, and $\mathbf{B}$ is the buoyancy force. Then, the provisional velocity field $\mathbf{V}$ is corrected by including the pressure effect and by enforcing the mass conservation at time step $n+1$,

$$\frac{\mathbf{V}^{n+1}-\mathbf{V}^*}{\Delta\tau}+\nabla P^{n+1}=0 \quad (15)$$

and

$$\nabla\cdot\mathbf{V}^{n+1}=0 \quad (16)$$

Substituting Eq. (16) into Eq. (15) yields the Poisson equation for pressure,

$$\nabla^2 P^{n+1}=\frac{1}{\Delta\tau}\nabla\cdot\mathbf{V}^* \quad (17)$$

In discretizing the above equations, centered difference is used to approximate all the derivatives except the convective terms. To enhance numerical stability and to yield accurate results for the complicate flow and thermal evolution studied here, a third-order upwind scheme developed by Kawamura et al. (1985) is employed to discretize these convective terms. For instance, in the X-direction momentum equation one of the nonlinear term is written as

$$f\left.\frac{\partial U}{\partial X}\right|_i=f_i\frac{-U_{i+2}+8U_{i+1}-8U_{i-1}+U_{i-2}}{12\Delta X}+|f_i|\frac{U_{i+2}-4U_{i+1}+6U_i-4U_{i-1}+U_{i-2}}{4\Delta X} \quad (18)$$

Time advancement may be done either implicitly or explicitly. The first-order Euler explicit scheme was employed since it was easy to implement. It has a much lower computational cost per time step, and requires much less computer memory allocation than any equivalent implicit implementation. We also found that the first-order scheme was sufficiently accurate to resolve the smallest physical time scale. The stability of the scheme limited by the requirement that the Courant number be less than unity (Anderson et al., 1984) was found to be governed by the grid spacing normal to the confined walls. The step selected to comply with the above stability limitation was smaller than that required to resolve the largest frequency appears in the flow considered. The sequence of numerical operation is as follows:

1 Explicitly calculate $\mathbf{V}^*$ from Eq. (14).
2 Solve the pressure Eq. (17) for P^{n+1} by the Fast Fourier Transform (FFT) method (Wilhelmson and Erichsen, 1977). This direct solution method is relatively accurate and, in fact, it was noted that the mass imbalance for every computational cell compared with the inlet mass flow rate is all below 10^{-7}. Furthermore, the residual for each discretized equation of each node is found to be less than 10^{-7}.
3 Explicitly calculate the desired velocity field at the new time step, $\mathbf{V}^{n+1}$, from Eq. (15).

Various schemes were used to discretize the energy equation. The power-law scheme developed by Patankar (1980) was found to be most satisfactory with the time derivative treated implicitly. The FFT method was not used to invert the discrete energy equations due to the presence of the Gibbs phenomenon (Canuto et al., 1988) associated with the step change in the boundary conditions for the energy equation, Eqs. (8) and (9). By employing the Conjugate Gradient Squared method (Sonneveld, 1989) to solve the resulting finite-difference equations, the temperature field at every time step can be calculated to a very high accuracy. In fact, the convergence criteria that the relative error in temperature between two consecutive in-

Table 1 Comparison of U and θ for various grid arrangements for $Re = 500$, $Pr = 0.72$, $Gr/Re^2 = -1.2$, $L = 10$, and $A = 0$ at various time instants

Grid		X=5			X=10			
		τ			τ			
		10	20	30	10	20	30	100
U	280x24	0.5853 0.9219	0.5314 0.9014	0.5263 0.9003	0.5656 0.9006	0.3997 0.7906	0.3274 0.7485	0.2803 0.7181
	280x32	0.5840 0.9239	0.5294 0.9033	0.5244 0.9023	0.5642 0.9022	0.3964 0.7898	0.3234 0.7440	0.2763 0.7166
	280x40	0.5836 0.9223	0.5291 0.9017	0.5242 0.9006	0.5637 0.9009	0.3967 0.7891	0.3241 0.7437	0.2775 0.7167
	320x32	0.5839 0.9238	0.5294 0.9034	0.5245 0.9025	0.5643 0.9021	0.3963 0.7896	0.3232 0.7437	0.2762 0.7164
θ	280x24	0.07700 0.04555	0.1124 0.06686	0.1181 0.06953	0.07914 0.05086	0.1408 0.1014	0.1724 0.1291	0.1931 0.1494
	280x32	0.07680 0.04510	0.1123 0.06633	0.1179 0.06888	0.07938 0.05036	0.1409 0.1012	0.1730 0.1292	0.1943 0.1500
	280x40	0.07691 0.04531	0.1125 0.06666	0.1180 0.06923	0.07945 0.05051	0.1410 0.1014	0.1731 0.1294	0.1944 0.1499
	320x32	0.07685 0.04514	0.1123 0.06620	0.1176 0.06863	0.07939 0.05038	0.1409 0.1013	0.1729 0.1293	0.1939 0.1500

Note: The upper and lower rows are respectively for Y=0.14 and 0.2.

teractions is set below 10^{-8} and the residual of the discretized energy equation is set below 10^{-5} are enforced for every node at every time step. This method of solving the energy equation is further supported by noting that the overall energy balance for the channel is satisfied within 0.1 percent.

Due to the elliptical nature of the flow, an extended computational domain was employed, including the directly heated section ($0 \le X \le L$) and the insulated sections immediately upstream and downstream of it, as depicted in Fig. 1. The extended domains in the insulated sections must be long enough so that the obtained solution is independent of their sizes. In the program test it was observed that over the ranges of the governing parameters to be considered, the upstream and downstream extended regions should each have length L and $2L$. In view of the symmetry in the flow and thermal conditions with respect to the center plane at $Y = 1/2$, only the left or right half domain should be used. The experimental measurement from Scheele and Hanratty (1962), however, indicates that in the transitional stage the flow is no longer symmetric. Thus the entire domain is used to allow for the possible presence of asymmetric flow. A uniform grid system is placed in the whole computational domain. In the X-direction 280 grid lines are used, while in the Y direction 32 grid lines are employed. Meanwhile, a uniform time step limited by the requirement that the Courant number be less than unity is used. Computation is started immediately after the sudden imposition of the heat fluxes on the channel wall at $\tau = 0$. It is terminated when the steady state is reached, which is detected by the relative changes in U, V, and θ over 1000 time steps being less than 10^{-5}. For the cases without steady state at high Gr/Re^2, the basic equations are integrated until we obtain periodic solution.

Considering the complicated fluid flow to be simulated here, a stringent program test is conducted. First, the predicted velocity profile at the exit of the computational domain ($X = 3L$) where the buoyancy exhibits negligible effects agrees with the exact fully developed velocity profile $U = 6(Y - Y^2)$ to six digits after the decimal point. Next, excellent agreement with the results of Aung and Worku (1987) is noted for the wall temperature distributions for the cases without flow reversal for low Gr/Re^2. Then, it is observed that the predicted steady fully developed velocity profiles for a long heated section ($L \ge 70$) differ from the exact solution of Lavine (1988) by less than 1 percent. Finally, a grid test is carried out. A comparison of the result for some flow and thermal characteristics from such a test for the case with $Re = 500$, $Pr = 0.72$, $Gr/Re^2 = -1.2$, $L = 10$, and $A = 0$ is shown in Table 1 for the entire transient. Furthermore, we compare in Table 2 the periodic flow and thermal characteristics at large τ for the case with higher opposing buoyancy at $Gr/Re^2 = -4$ in which the flow does not approach steady state. Reasonable agreement between the results from various grids is noted. Further comparison is made by directly comparing the predicted periodic temperature variations with time at a given location at large τ. It is noted that the phase difference between the results from the 280×32 and 320×40 grids is small. The 280×32 grid is therefore considered to be suitable for the present study and will be used in the subsequent computation. The above program test indicates that the adopted solution procedures are suitable for the present study.

Table 2 Comparison of θ and U fluctuation for various grid arrangements at (5, 0.2) for $Re = 500$, $Pr = 0.7$, $Gr/Re^2 = -4.0$, $L = 10$, and $A = 0$

Grid	frequency	magnitude			
		temperature		velocity	
		max.	min.	max.	min.
280x24	0.02248	0.2827	0.07327	1.0909	-0.8270
280x32	0.02169	0.2860	0.07442	0.9088	-0.9150
280x40	0.02111	0.2922	0.07766	0.9256	-0.9209
320x32	0.02089	0.2887	0.07458	0.9230	-0.9267
280x32[a]	0.02183	0.2864	0.07430	0.9051	-0.9119

Note
[a] time step is reduced by half

Onset of Instability

To investigate the flow stability mentioned earlier, a linear

stability analysis was carried out for the limiting case of the heated section being relatively long. In this limiting case the analytic fully developed velocity and temperature distributions given by Lavine (1988) can be used for the basic flow (U_b, V_b, θ_b). The procedures adopted here resemble those described by White (1974). The disturbance equation is obtained by subtracting the equations for the basic flow from the instantaneous flow equations, and then eliminating the pressure from the resulting equations. Neglecting the nonlinear terms and assuming the disturbances as two dimensional with the general from

$$\phi' = \hat{\phi}(Y) \cdot \exp(ik_1(X - c\tau)) \tag{19}$$

where i, k_1 and c are, respectively, the square root of -1, the wave number, and the complex wave speed, one arrives at the equations governing the amplitudes of the Y component disturbed velocity $\hat{V}$ and temperature $\hat{\theta}$

$$\frac{d^4\hat{V}}{dY^4} - 2k_1^2\frac{d^2\hat{V}}{dY^2} + k_1^4\,\hat{V} + ik_1\,\mathrm{Re}\left(\left(k_1^2\,U_b + \frac{d^2U_b}{dY^2}\right)\hat{V} - U_b\frac{d^2\hat{V}}{dY^2} - \frac{\mathrm{Gr}}{\mathrm{Re}^2}\hat{\theta}\right) = ick_1\,\mathrm{Re}\left(k_1^2\,\hat{V} - \frac{d^2\hat{V}}{dY^2}\right) \tag{20}$$

$$\hat{V}\,\mathrm{Pe}\frac{d\theta_b}{dY} + i\frac{\mathrm{Pe}}{k_1}\frac{d\theta_b}{dX} - \frac{d^2\hat{\theta}}{dY^2} + k_1^2\,\hat{\theta} + ik_1\,U_b\,\mathrm{Pe}\,\hat{\theta} = ik_1\,c\,\mathrm{Pe}\,\hat{\theta} \tag{21}$$

subject to the boundary conditions

$$\hat{V}(0) = \hat{V}(1) = \frac{d\hat{V}(0)}{dY} = \frac{d\hat{V}(1)}{dY} = 0,\quad \frac{d\hat{\theta}(0)}{dY} = \frac{d\hat{\theta}(1)}{dY} = 0 \tag{22}$$

The above eigenvalue problem was solved by expressing $\hat{V}$ and $\hat{\theta}$ as the Nth degree Chebychev polynomials and then discretize the equations by the collocation method (Canuto et al., 1988). The resulting eigenmatrix is solved by the IMSL subroutine EIGZC. The above procedure was first tested for the limiting case of the Orr-Sommerfeld equation (Orszag, 1971). Excellent agreement is noted.

The predicted neutral stability curves are shown in Fig. 2 for air and water flowing in a long heated channel with Re ranging from 100 to 500. Note that the region on the left of a given curve is unstable for that case. The results indicate that the critical $|\mathrm{Gr}/\mathrm{Re}^2|$ decreases with increasing Reynolds number. Besides, the critical $|\mathrm{Gr}/\mathrm{Re}^2|$ increases rapidly at high and low wave numbers especially for air. These critical values are much smaller than the value of the critical $|\mathrm{Gr}/\mathrm{Re}^2|$ for the appearance of flow oscillations from directly solving Eqs. (1)–(4), as will become clear later. These differences can be attributed to the finite heated section length in the direct numerical simulation and to the fact that the lower bound is predicted in the linear stability analysis (White, 1974).

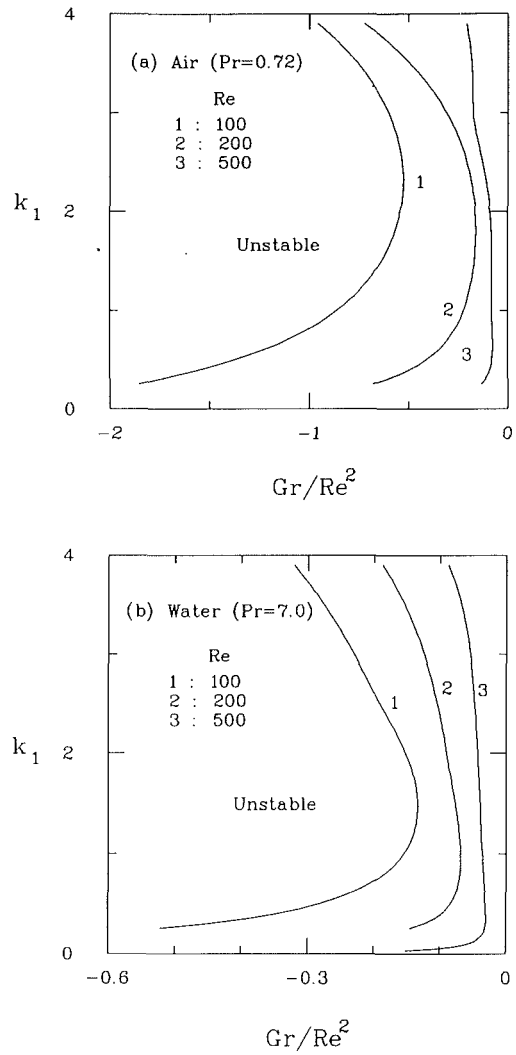

Fig. 2 Neutral stability curves for (*a*) air (Pr = 0.72) and (*b*) water (Pr = 7.0)

Results and Discussion

The foregoing problem formulation indicates that the transient mixed convection in the vertical channel is governed by five nondimensional parameters: Prandtl number Pr, Reynolds number Re, ratio of buoyancy to inertia force $\mathrm{Gr}/\mathrm{Re}^2$, wall-to-fluid heat capacity ratio A, and length of the heated section L. Computations will be carried out over wide ranges of these parameters. Particularly, both air ($\mathrm{Pr} = 0.72$) and water ($\mathrm{Pr} = 7.0$) will be considered with Re varying from 250 to 1000, $\mathrm{Gr}/\mathrm{Re}^2$ from 0 to -4, A from 0 to 100, and L from 10 to 15. Although many computations have been performed, in what follows only a sample of results will be presented to illustrate the detailed flow and thermal characteristics during the evolution of the unsteady recirculating flow at high $\mathrm{Gr}/\mathrm{Re}^2$.

Effects of $\mathrm{Gr}/\mathrm{Re}^2$ are examined first. Results for the cases with $\mathrm{Pr} = 0.72$, $\mathrm{Re} = 500$, $L = 10$, and $A = 0$ with various $\mathrm{Gr}/\mathrm{Re}^2$ indicate that at a low opposing buoyancy ($|\mathrm{Gr}/\mathrm{Re}^2| \le 1$) the flow is unidirectional and no reverse flow exists in the channel. The flow and heat transfer in it are simple and quickly reach steady state, as observed in our previous study (Lin et al., 1991) for transient mixed convection in a boundry layer flow. When $\mathrm{Gr}/\mathrm{Re}^2$ is raised to -1.2, weak recirculating flow is seen. A pair of elongated cells appear near the exit of the directly heated section at $\tau = 30$, which grow gradually and are symmetric with respect to the centerline $Y = 1/2$. At $\tau = 100$, steady state is reached. It is of interest to note that increasing $\mathrm{Gr}/\mathrm{Re}^2$ slightly to -1.25 causes the flow to become oscillatory at large τ.

To delineate the formation of reverse flow and the occurrence of the oscillatory flow at large τ, we present the results for a typical case with $\mathrm{Gr}/\mathrm{Re}^2 = -2$ in great detail. Figure 3 shows the predicted temporal evolution of the streamlines and temperature contours in the flow for $\mathrm{Gr}/\mathrm{Re}^2 = -2$, $\mathrm{Pr} = 0.72$, $\mathrm{Re} = 500$, $L = 10$, and $A = 0$ from the initiation of the transient at $\tau = 0$ to the final periodic oscillatory state. These results clearly indicate that at this higher opposing buoyancy, the reverse flow appears earlier and is much stronger. At $\tau = 40$, a symmetric pair of large and strong recirculating cells is already seen in the lower half of the heated section (Fig. 3(*a*)). These cells grow slowly. It is of interest to note that at $\tau = 210$ the cells become asymmetric. They move back and forth in the longitudinal direction. This change from a symmetric to an asymmetric flow was suggested in the experiment of Scheele and Hanratty (1962). Later at $\tau \ge 230$, a new cell is induced and the flow stream in the central region is sinuous. Finally,

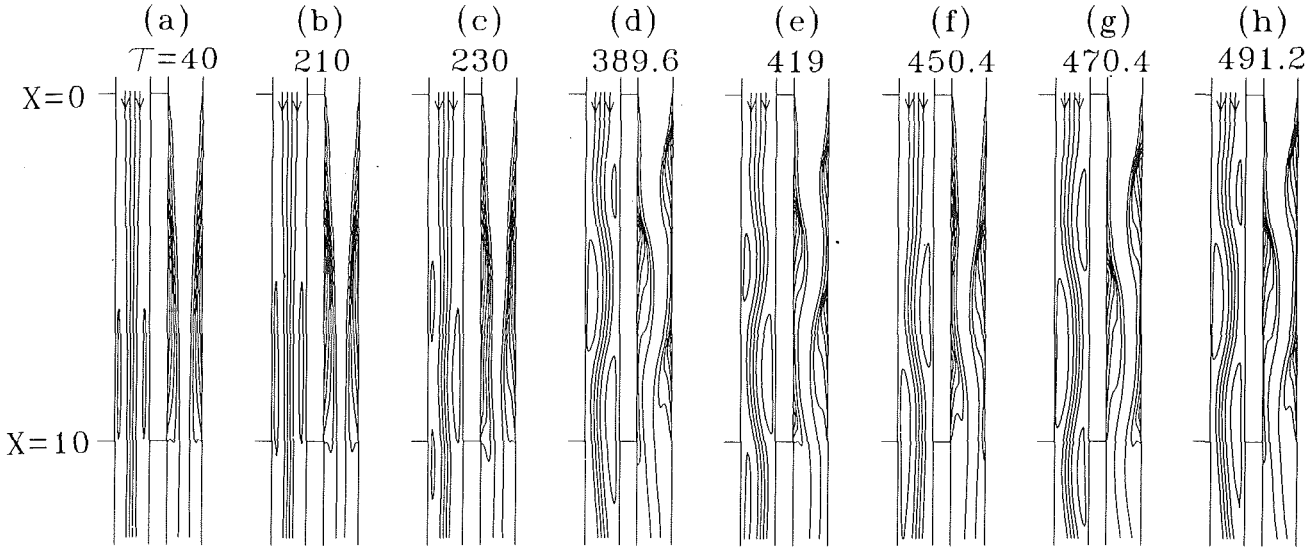

Fig. 3 Streamlines and isotherms in the flow for Re = 500, Pr = 0.72, $Gr/Re^2 = -2$, $L = 10$, and $A = 0$ at various time instants. The values of stream-function contours are in the set {−0.02, 0.2, 0.4, 0.6. 0.8, 1.02} and the increment is 0.058 thereafter without noting.

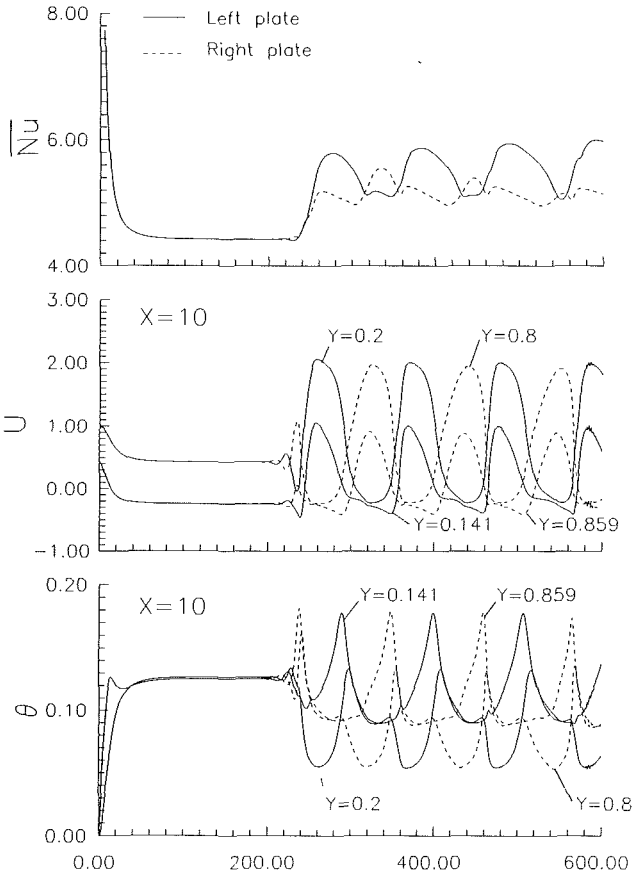

Fig. 4 Time samples of $\overline{Nu}$ for left and right plates, θ and U at selective locations for Re = 500, Pr = 0.72, $Gr/Re^2 = -2$, $L = 10$, and $A = 0$

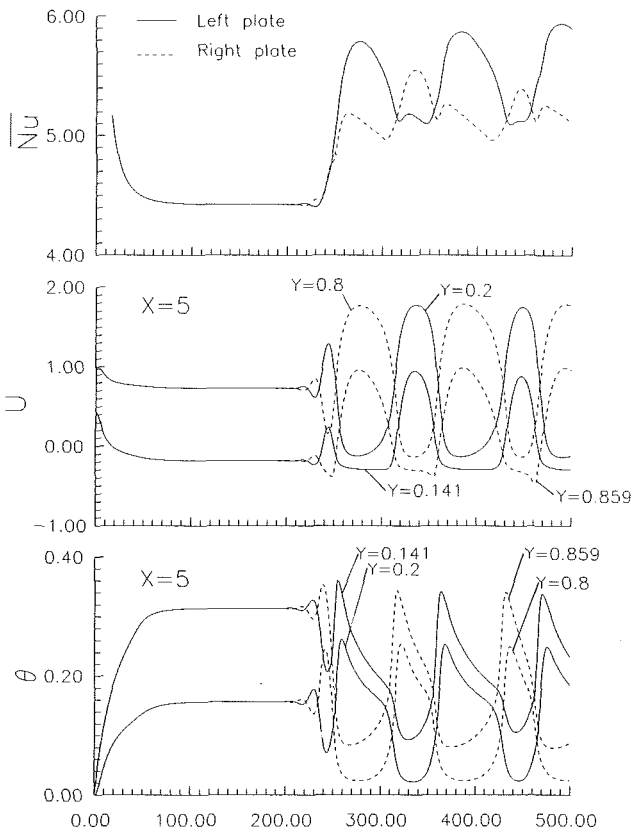

Fig. 5 Time samples of $\overline{Nu}$, U and θ for the four locations at $X = 5$ for the same case as those in Fig. 4

the flow reaches a periodic state. This periodic flow evolution is illustrated in Figs. 3(*d–h*). To examine the flow asymmetry and oscillation in more detail, Fig. 4 displays the time traces of the vertical velocity and temperature at two sets of symmetric points with respect to the center plane ($Y = 1/2$) at the exit plane of the heated section ($X = 10$) along with the transient average Nusselt number distributions at the left and right plates. These results clearly reveal that for $\tau \leq 200$ the flow and heat transfer are symmetric. Flow and thermal asymmetry is clearly seen around $\tau = 205$ at all these detection points. It is important to point out that at the onset of flow asymmetry we also note the inception of flow and thermal fluctuations. Immediately after the fluctuations are initiated, they become rather significant. This sudden change from a nearly steady to an unsteady

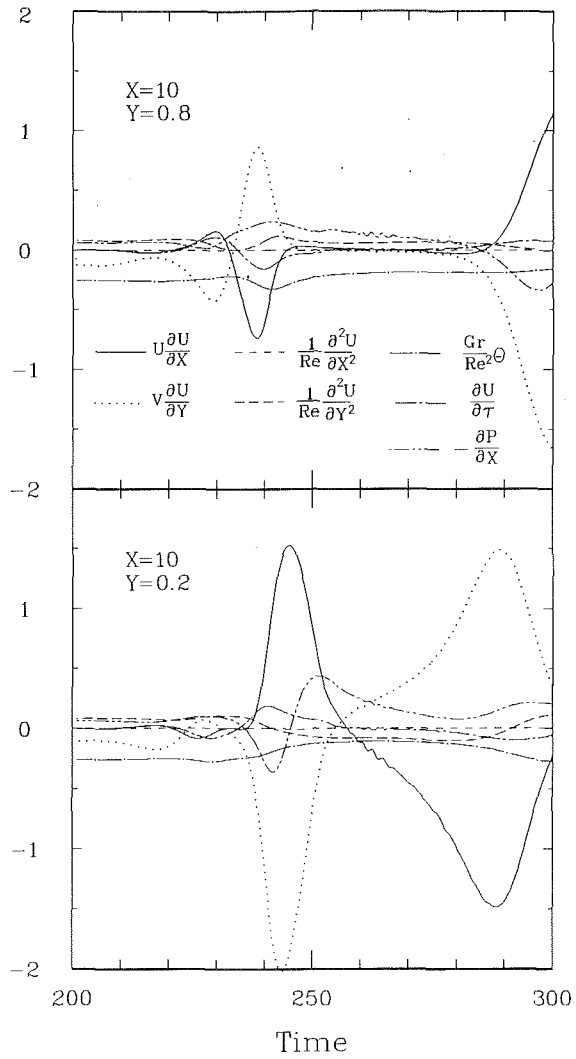

Fig. 6 Temporal force balance at the two symmetric locations for Re = 500, Pr = 0.72, Gr/Re^2 = 2, L = 10, and A = 0

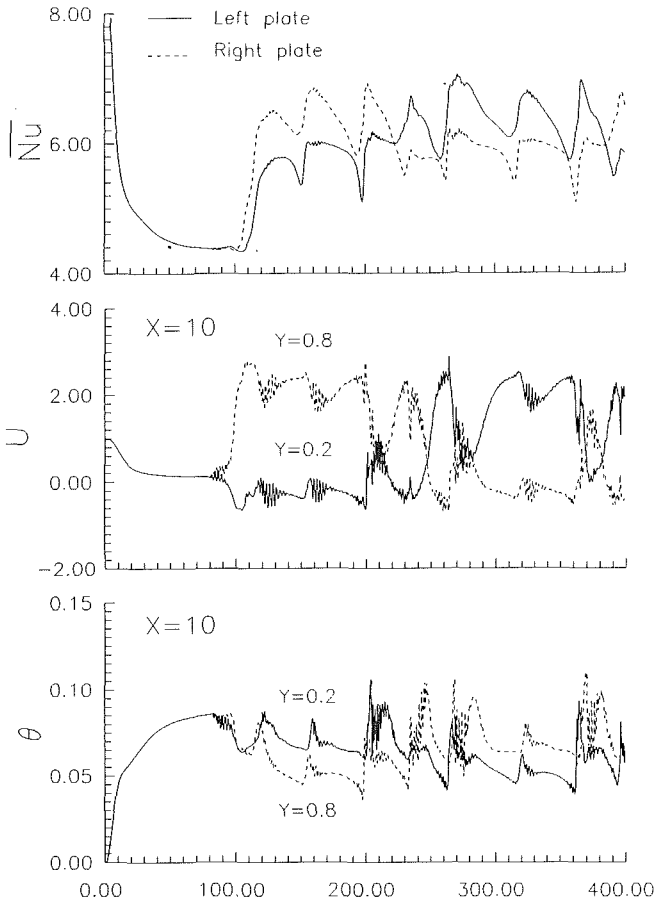

Fig. 7 Time traces of $\overline{Nu}$, U and θ for Re = 500, Pr = 0.72, Gr/Re^2 = −4, L = 10, and A = 0

flow, a characteristic of subcritical transition, is consistent with the observation of Scheele and Hanratty (1962). Note that when U is at a peak at one point, at the corresponding symmetric point U is nearly at a valley, implying that U is almost out of phase at the symmetric points. However, U is in phase for the points at the same side of the center plane at $Y = 1/2$. Similar results are noted for the temperature signals. Similar time traces are given in Fig. 5 for locations at the midheight ($X = 5$). The U and θ oscillations at these locations have the same frequency as those at $X = 10$. Again, both U and θ at the symmetric points show a phase angle of approximately 180 deg. Inspecting the results for $\tau \leq 200$ discloses that the flow is relatively steady except in the initial transient due to sudden heat flux input at $\tau = 0$. But, in fact, these curves possess small fluctuations for $\tau \leq 200$ by checking with the numerical data. However, for $|\mathrm{Gr/Re^2}| \leq 1.2$ no fluctuation is found in these curves even at large τ.

It is essential to understand the reason why a nearly steady flow over a long period of time can evolve into an asymmetric oscillatory flow. To provide the clue, we scrutinize the force balance during the transient. Figure 6 shows the temporal variations of all the forces in the X-direction momentum equation at the corresponding symmetric points (10, 0.2) and (10, 0.8). First, we note that at these locations the flow is dominated by the pressure, buoyancy, and inertia forces, which have invisible variation with time, and they balance each other to a good degree to result in a nearly steady flow ($\partial U/\partial \tau \to 0$) for $60 \leq \tau \leq 200$. Secondly, focusing the results around $\tau = 205$, we observe slight deviation in the inertia forces, $U(\partial U/\partial X)$ and $V(\partial U/\partial Y)$, from their respective nearly steady values. These deviations then cause the deviations in the pressure and buoyancy forces, $-\partial P/\partial X$ and $-\mathrm{Gr/Re^2}\cdot\theta$. A little later larger variations in these forces ensue. Around $\tau = 220$ these forces cannot balance each other, causing the unsteady term $\partial U/\partial \tau$ to deviate significantly from zero and obviously resulting an unsteady flow. Besides, the viscous force $(\partial^2 U/\partial Y^2)/\mathrm{Re}$ begins to fluctuate at this instant. From now on all the forces except $(\partial^2 U/\partial X^2)/\mathrm{Re}$ start to exhibit substantial changes with time by comparing the corresponding curves in Figs. 6(*a*) and 6(*b*).

The results in Fig. 6 seem to suggest the following processes for the flow instability. At a high opposing buoyancy, the velocity profiles are highly distorted due to the presence of strong reverse flow. According to the stability theory (White, 1974), these velocity profiles are very unstable. Through the nonlinear interactions in the inertia terms, $U(\partial U/\partial X)$ and $V(\partial U/\partial Y)$, significant fluctuations are induced. The flow asymmetry, intimately accompanying the flow oscillation, appears to result from the symmetry-breaking process (Crawford and Knoblock, 1991). The details of the process are not clear, but it is normally attributed to the nonlinear interaction processes in the flow and occurs in the early stage of the transition from laminar to turbulent flows (Paolucci and Chenoweth, 1989). More innovative research is need in this area.

Raising the opposing buoyancy further to $\mathrm{Gr/Re^2} = -4$, we note, by contrasting the time samples of U, θ, and $\overline{Nu}$ in Fig. 7 with those of Fig. 4, that the flow is reversed earlier, the reverse flow is stronger, and the cells are larger, extending further upstream and downstream. Moreover, the flow asym-

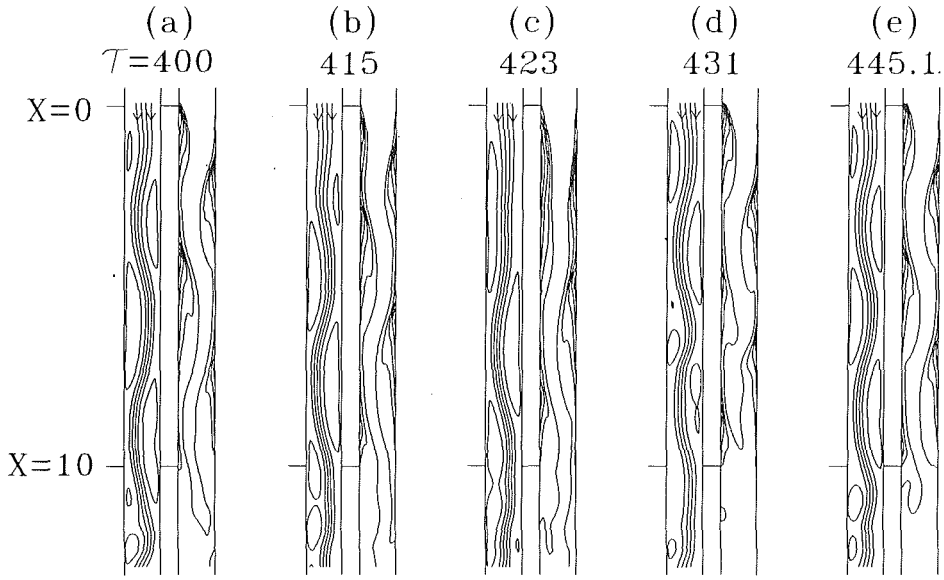

Fig. 8 Streamlines and temperature contours in the flow for Re = 500, Pr = 0.72, $Gr/Re^2 = -4$, $L = 10$, and $A = 0$

metry and oscillation are initiated earlier. The oscillatory flow has higher amplitude and frequency. A number of high-frequency wave packets exist in the low-frequency cycles in the time histories of U and θ. These fluctuating flow and thermal characteristics clearly indicate that under the strong action of the opposing buoyancy, the flow has become rather unstable although it is still laminar. Also note that the flow becomes quasi-periodic. Intense wave activity takes place in the flow. Comparing the flow and thermal fields for a complete quasi-periodic cycle in Fig. 8 with those in Fig. 3 for $Gr/Re^2 = -2$ reveals that at a higher opposing buoyancy more recirculating cells are induced and the flow stream in the core region swings intensively in the Y direction, as the oscillatory wake behind a circular cylinder.

Next, the effects of the Reynolds number are studied. Results for a higher Reynolds number (Re = 1000) with other parameters fixed ($Gr/Re^2 = -2$, Pr = 0.72, $L = 10$, and $A = 0$) are illustrated in Fig. 9 for the time records of U, θ, and $\overline{Nu}$ again for two pairs of symmetric points. Comparing these results with those in Fig. 4 for Re = 500 indicates that increasing the Reynolds number to 1000 causes a slightly earlier appearance of the flow asymmetry and oscillation at $\tau = 178$. Besides, it is noted that after a number of oscillatory cycles the flow gradually approaches steady state but it remains asymmetric. Therefore we have steady asymmetric flow in the channel at large τ, reflecting that an asymmetric solution is possible for the flow equations subject to symmetric initial and boundary conditions in a symmetric domain. This situation is unusual. Inspecting the flow field evolution reveals that the reverse flow is stronger in the initial stage of the transient before the oscillation occurs. As the flow begins to oscillate, more secondary cells are induced. Some of these cells disappear with time elapsed.

The length of the heated section is expected to have important effects since the flow acted by the buoyancy over a longer distance would be modified to a greater degree. The computed results, when collated with those in Fig. 4 for $L = 10$, suggest that an increase in the heated section length causes earlier appearance of the reverse flow and flow asymmetry and fluctuation. Additionally, the oscillation frequency is higher. A comparison of the periodic flow patterns at large τ shown in Fig. 10 with those in Fig. 3 for $L = 10$ indicates that similar patterns are noted for different L except that more secondary cells exist in a channel with a longer heated section.

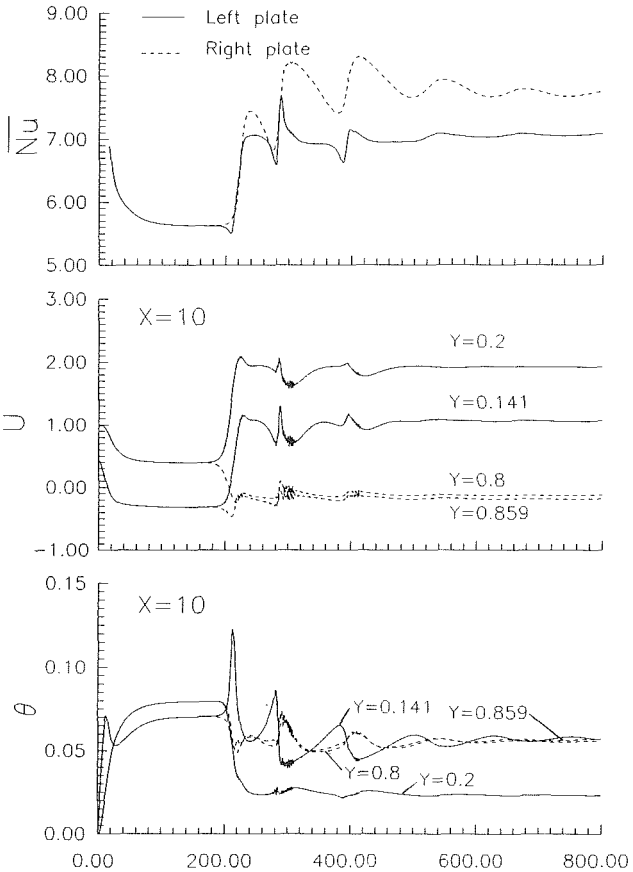

Fig. 9 Time traces of $\overline{Nu}$, U, and θ for Re = 1000, Pr = 0.72, $Gr/Re^2 = -2$, $L = 10$, and $A = 0$

Buoyancy effects in water flow are of interest since it is a common coolant in various heat transfer devices. Computations have been carried out for water (Pr = 7.0) with various Gr/Re^2 at fixed Re (= 500), L (= 10), and A (= 0). It is noted that for $|Gr/Re^2| \leq 2.5$ no flow fluctuation is detected and the flow approach a steady state. Figure 11 presents the time records of U and θ at locations (10, 0.141), (10, 0.2), (10, 0.8),

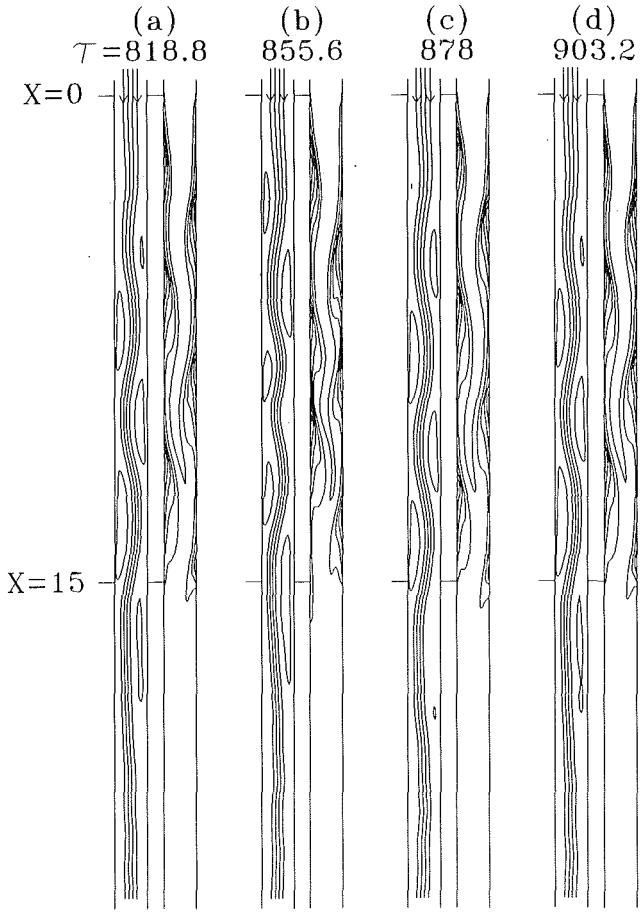

Fig. 10 Streamlines and isotherms in the flow over a complete period for Re = 500, Pr = 0.72, $Gr/Re^2 = -2$, $L = 15$, and $A = 0$

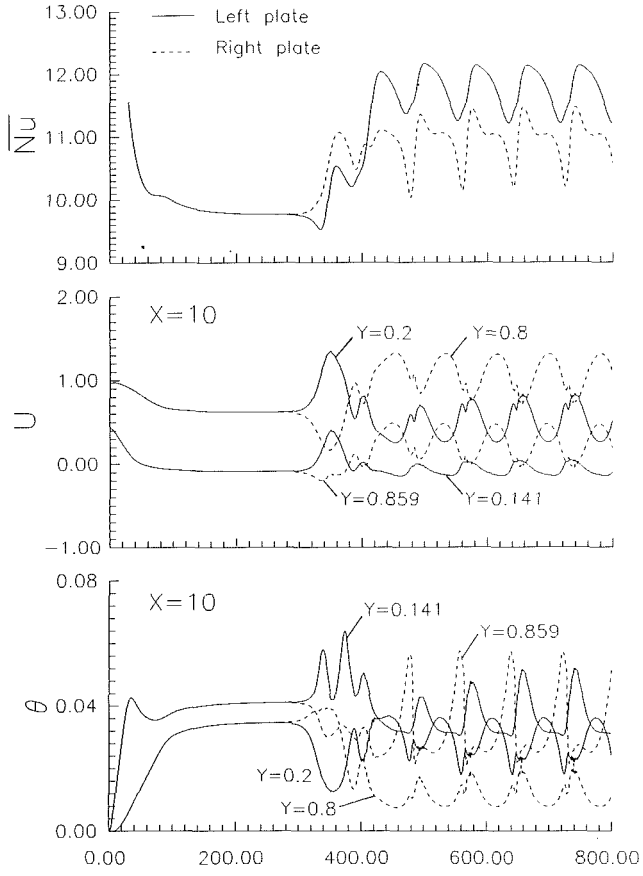

Fig. 11 Time records of $\overline{Nu}$, U, and θ for Re = 500, Pr = 7.0, $Gr/Re^2 = -4$, $L = 0$, and $A = 0$

and (10, 0.859) and $\overline{Nu}$ at the channel walls for $Gr/Re^2 = -4$. Contrasting these results with those in Fig. 7 for air (Pr = 0.72) discloses that in a higher Prandtl fluid the reverse flow is weaker and its appearance is delayed. In addition, the flow asymmetry and oscillation appear at a later time and the oscillation amplitude and frequency are smaller. A careful inspection of the onset of flow oscillation at different locations indicates that flow near the central region starts to fluctuate at an earlier time. Besides, the flow and thermal asymmetry is less significant. The temporal evolution of the corresponding flow and thermal fields indicates that the flow is only slightly affected by the small recirculating cells, but the distortion of the isotherms by these cells is clearly seen.

Finally, the effects of the wall heat capacity are investigated. An increase in the wall-to-fluid heat capacity ratio primarily causes the whole momentum and heat transfer processes to slow down with slight modification in the detailed flow and thermal characteristics. In particular, at a higher A the forced flow is reversed at a later time and the oscillation frequency is lower with the same oscillation amplitude. However, the overall flow evolution is similar for various A.

In addition to the above detailed flow and thermal characteristics, results for the time variations of the local Nusselt number over the heated section at the channel walls for various parameters are important in thermal system design. Some of these results are presented in Fig. 12 for a selected instants of time. Note that for a given τ the local Nusselt number decreases sharply in the entry portion due to entrance effect and then shows wavy variation with the longitudinal distance, which obviously results from the presence of the buoyancy-driven recirculating cells in the channel. For a given location Nu

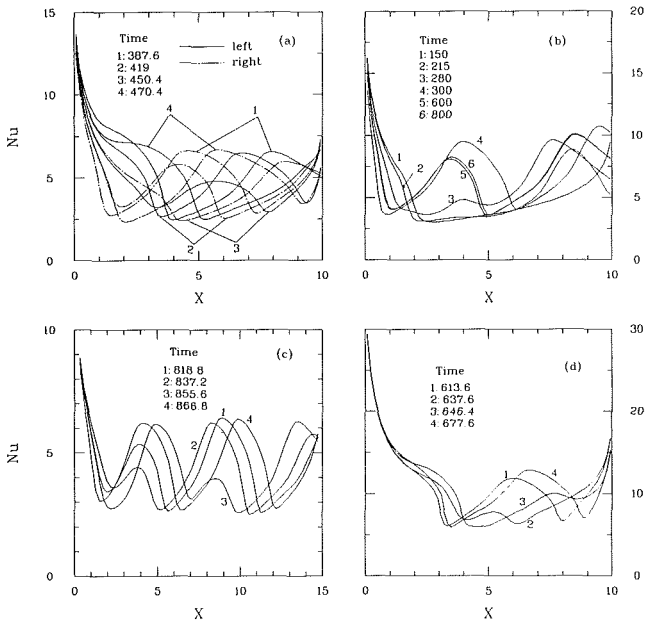

Fig. 12 Temporal development of Nu for various Re, Pr, and L: (*a*) Re = 500, Pr = 0.72, $Gr/Re^2 = -2$, $L = 10$, and $A = 0$, (*b*) Re = 1000, Pr = 0.72, $Gr/Re^2 = -2$, $L = 10$ and $A = 0$, (*c*) Re = 500, Pr = 0.72, $Gr/Re^2 = -2$, $L = 15$ and $A = 0$. (*d*) Re = 500, Pr = 7.0, $Gr/Re^2 = -4$, $L = 10$ and $A = 50$. A complete period is presented except for (*b*), which reaches a steady state.

fluctuates periodically at large τ (except in Fig. 12(*b*)), as for the average Nusselt number presented above. Phase differences exist between the local Nusselt numbers at the left and right plates, reflecting the existence of the asymmetric flow. Severe

Table 3 Fluctuation frequency at $X=10$ and steady or statistically average Nusselt numbers for various cases

Re	Pr	Gr/Re^2	L	A	$f(\times 10^3)$	$\overline{Nu}$
500	0.72	-0.5	10	0	- *	5.28 **
500	0.72	-1.0	10	0	-	4.97
500	0.72	-1.2	10	0	-	4.82
500	0.72	-2.0	10	0	9.4	5.52,5.10 ***
1000	0.72	-0.6	10	0	-	6.47
1000	0.72	-1.0	10	0	-	5.90
1000	0.72	-1.5	10	0	-	7.54,6.25
1000	0.72	-2.0	10	0	-	7.70,7.05
1000	0.72	-2.5	10	0	13.12	7.77,7.46
250	0.72	-1.5	10	0	-	3.90
250	0.72	-1.75	10	0	-	3.81
250	0.72	-2.0	10	0	5.6	4.02,4.00
250	0.72	-2.4	10	0	7.7	3.85,4.25
250	0.72	-4.0	10	0	19.8	4.45,4.22
500	0.72	-0.8	15	0	-	3.60
500	0.72	-0.9	15	0	-	4.25
500	0.72	-0.95	15	0	3.1	4.42,4.34
500	0.72	-1.0	15	0	4.1	4.50,4.31
500	0.72	-1.33	15	0	7.6	4.65,4.49
500	0.72	-2.0	15	0	11.5	5.24,4.72
500	7.0	-2.0	10	0	-	10.62
500	7.0	-2.5	10	0	-	10.14
500	7.0	-2.75	10	0	6.7	10.98,10.47
500	7.0	-3.0	10	0	7.8	10.49,11.28
500	7.0	-3.53	10	0	10.2	11.59,11.71
500	7.0	-4.0	10	0	12.1	11.74,10.97
500	0.72	-2.0	10	50	6.3	5.75,5.07
500	0.72	-4.0	10	50	14.0	6.36,5.87
500	0.72	-2.0	10	100	4.4	5.33,5.41
500	0.72	-4.0	10	100	5.4	5.86,6.29

* Symbol '-' indicates that the flow approaches steady state.
** Values of steady or time averaged Nusselt number at large τ.
*** Values for the left and right plates when different.

spatial variation in Nu is noted for a lower Prandtl number fluid flowing at a lower Reynolds number in a channel with a longer heated section under a higher heat input.

The computed oscillation frequency at location (10, 0.2) and space and/or time-averaged Nusselt number at steady state or statistically periodic state for various cases studied in this investigation are summarized in Table 3. Focusing on the results for $\overline{Nu}$, we note that at a low opposing buoyancy, heat transfer is poor with an increasing buoyancy. But at a high opposing buoyancy the reverse flow is strong enough to reverse the trend. Additionally, different Nusselt numbers at the walls resulted for the flow approaching fluctuating state at large τ. This was also observed for the two cases ($Gr/Re^2 = -1.5$ and -2) at a higher Reynolds number ($Re = 1000$) although the flow reaches steady state. The difference in the Nusselt number between the two plates can be as high as 17 percent for the case with $Re = 1000$, $Pr = 0.72$, $Gr/Re^2 = -1.5$, $L = 10$, and $A = 0$. Results for the oscillation frequency indicate that it increases with the magnitude of the opposing buoyancy and heated section length but decreases with the Prandtl number and wall-to-fluid heat capacity ratio. However, the effect of the Reynolds number is nonmonotonic.

Based on the results in Table 3, a criterion to distinguish the state of flow at long time is proposed here:

$$\text{for } (Gr/Re^2)\cdot Re^{3/5}\cdot L^{2/3}\cdot Pr^{-1/3} < 258.3, \text{ steady flow} \quad (23)$$

$$\text{for } (Gr/Re^2)\cdot Re^{3/5}\cdot L^{2/3}\cdot Pr^{-1/3} > 258.3, \text{ oscillatory unsymmetric flow} \quad (24)$$

Concluding Remarks

Through a detailed numerical simulation transient laminar opposing mixed convection in a downward vertical channel flow subject to a sudden imposition of the equal wall heat fluxes over a finite portion of the channel walls is investigated. Computations have been carried out over wide ranges of the governing parameters. Results obtained can be briefly summarized as follows:

1 Earlier inception of the reverse flow occurs for the flow with higher opposing buoyancy, higher Reynolds number, longer heated section length, lower Prandtl number, and smaller wall heat capacity. Under these conditions the reverse flow is stronger.

2 As the opposing buoyancy is high enough, the flow and temperature begin to oscillate at a certain instant of time with the accompanying presence of the flow asymmetry. The oscillations become relatively significant in a short period of time. The flow is prone to fluctuate at higher Gr/Re^2, longer L, and lower Re and Pr. With a raise in the opposing buoyancy, the flow undergoes a transition from a periodic to quasi-periodic state.

3 Significant asymmetry in the flow and heat transfer happens as long as the flow start to oscillate. However, at high Reynolds number unsymmetric flow is noted even at steady state.

4 The increase in the wall heat capacity primarily causes the slowdown of the whole transport process.

In spite of the great endeavor devoted in the present study, a number of relevant studies need to be pursued in near future. These include extending the present work to the flow in a relatively short or long heated section length, at a very low or high Reynolds number ($Re < 100$ or $Re > 2000$), in liquid metal ($Pr \le 0.02$) and at a very high opposing buoyancy ($|Gr/Re^2| \ge 8$) where the flow is expected to be nonperiodic and even chaotic. Flow is essentially three dimensional and unsteady for a higher Reynolds number and buoyancy. The investigation of these complicated mixed convection flows poses a great challenge at the present time.

Acknowledgments

The financial support of this study by the engineering division of National Science Council of Taiwan through contract No. NSC78-0401-E009-11 is greatly appreciated.

References

Anderson, D. A., Tannehill, J. C., and Pletcher, R. H., 1984, *Computational Fluid Mechanics and Heat Transfer*, Hemisphere, Washington, DC, Chap. 4.

Aung, W., and Worku, G., 1986a, "Developing Flow and Flow Reversal in a Vertical Channel With Asymmetric Wall Temperature," ASME JOURNAL OF HEAT TRANSFER, Vol. 108, pp. 299-304.

Aung, W., and Worku, G., 1986b, "Theory of Fully Developed Combined Convection Including Flow Reversal," ASME JOURNAL OF HEAT TRANSFER, Vol. 108, pp. 485-488.

Aung, W., 1987, "Mixed Convection in Internal Flow," in: *Handbook of Single-Phase Convective Heat Transfer*, S. Kakac, R. K. Shah, and W. Aung, eds., Wiley, New York, Chap. 15.

Aung, W., and Worku, G., 1987, "Mixed Convection in Ducts With Asymmetric Wall Heat Flux," ASME JOURNAL OF HEAT TRANSFER, Vol. 109, pp. 947-951.

Canuto, C., Hussaini, M. Y., Quarteroni, A., and Zang, T. A., 1988, *Spectral Methods in Fluid Dynamics*, Springer-Verlag, New York, Chap. 2.

Cebeci, T., Khattab, A. A., and LaMont, R., 1982, "Combined Natural and Forced Convection in Vertical Ducts," *Proc. 7th Int. Heat Transfer Conference*, U. Grigull, E. Hahne, K. Stephan, and J. Straub, eds., Vol. 3, pp. 419-424.

Chorin, A. J., 1968, "Numerical Solution of the Navier-Stokes Equations," *Math Comput.*, Vol. 22, pp. 745-762.

Chow, L. C., Husain, S. R., and Campo, A., 1984, "Effects of Free Convection and Axial Conduction on Forced Convection Heat Transfer Inside a Vertical Channel at Low Peclet Numbers," ASME JOURNAL OF HEAT TRANSFER, Vol. 106, pp. 297-303.

Crawford, J. D., and Knobloch, E., 1991, "Symmetry and Symmetry-Breaking Bifurcations in Fluid Dynamics," *Ann. Rev. Fluid Mech.*, Vol. 23, pp. 341-387.

Gebhart, B., Jaluria, Y., Mahajan, R. L., and Sammarkia, 1988, *Buoyancy-Induced Flows and Transport*, Hemisphere, Washington, DC, Chap. 10.

Habchi, S., and Acharya, S., 1986, "Laminar Mixed Convection in a Symmetrically or Asymmetrically Heated Vertical Channel," *Numerical Heat Transfer*, Vol. 9, pp. 605–618.

Heggs, P. J., Ingham, D. B., and Keen, D. J., 1990, "The Effects of Heat Conduction in the Wall on the Development of Recirculating Combined Convection Flows in Vertical Tubes," *International Journal of Heat and Mass Heat Transfer*, Vol. 33, pp. 517–528.

Incropera, F. P., 1986, "Buoyancy Effects in Double-Diffusive and Mixed Convection Flows," *Proc. 8th Int. Heat Transfer Conference*, C. L. Tien, V. P. Carey, and J. K. Ferrel, eds., Vol. 1, pp. 121–130.

Ingham, D. B., Keen, D. J., and Heggs, P. J., 1988a, "Two Dimensional Combined Convection in Vertical Parallel Plate Ducts, Including Situations of Flow Reversal," *International Journal for Numerical Methods in Engineering*, Vol. 26, pp. 1645–1664.

Ingham, D. B., Keen, D. J., and Heggs, P. J., 1988b, "Flows in Vertical Channels With Asymmetric Wall Temperatures and Including Situations Where Reversal Flows Occur," ASME JOURNAL OF HEAT TRANSFER, Vol. 110, pp. 910–917.

Ingham, D. B., Keen, D. J., Heggs, P. J., and Morton, B. R., 1990, "Recirculating Pipe Flows," *J. Fluid Mech.*, Vol. 213, pp. 443–464.

Joshi, H. M., 1988, "Transient Effect in Natural Convection Cooling of Vertical Parallel Channels," *International Communications in Heat and Mass Transfer*, Vol. 15, pp. 227–238.

Kawamura, T., Takami, H., and Kawahara, K., 1985, "New Higher-Order Upwind Scheme for Impressible Navier–Stokes Equations," *Proc. 9th Int. Conf. Num. Meth. Fluid Dyn.*, Springer-Verlag, pp. 291–295.

Lavine, A. S., 1988, "Analysis of Fully Developed Opposing Mixed Convection Between Inclined Parallel Plates," *Warme- und Stoffubertragung*, Vol. 23, pp. 249–257.

Lavine, A. S., Kim, M. Y., and Shores, C. N., 1989, "Flow Reversal in Opposing Mixed Convection Flow in Inclined Pipes," ASME JOURNAL OF HEAT TRANSFER, Vol. 111, pp. 114–120.

Lawrence, W. T., and Chato, J. C., 1966, "Heat Transfer Effects on the Developing Laminar Flow Inside Vertical Tubes," ASME JOURNAL OF HEAT TRANSFER, Vol. 88, pp. 214–222.

Lin, T. F., and Kuo, J. C., 1988, "Transient Conjugated Heat Transfer in Fully Developed Laminar Pipe Flows," *International Journal of Heat and Mass Transfer*, Vol. 31, pp. 1093–1102.

Lin, T. F., Yin, C. P., and Yan, W. M., 1991, "Transient Laminar Mixed Convection Heat Transfer in a Vertical Flat Duct," ASME JOURNAL OF HEAT TRANSFER, Vol. 113, pp. 384–390.

Morton, B. R., Ingham, D. B., Keen, D. J., and Heggs, P. J., 1989, "Recirculating Combined Convection in Laminar Pipe Flow," ASME JOURNAL OF HEAT TRANSFER, Vol. 111, pp. 106–113.

Orszag, S. A., 1971, "Accurate Solution of the Orr–Sommerfeld Stability Equation," *J. Fluid Mech.*, Vol. 50, pp. 689–703.

Paolucci, S., and Chenoweth, D. R., 1989, "Transition to Chaos in a Differentially Heated Vertical Cavity," *J. Fluid Mech.*, Vol. 201, pp. 379–410.

Patankar, S. V., 1980, *Numerical Heat Transfer and Fluid Flow*, McGraw-Hill, New York.

Quintiere, J., and Mueller, W. K., 1973, "An Analysis of Laminar Free and Forced Convection Between Finite Vertical Parallel Plates," ASME JOURNAL OF HEAT TRANSFER, Vol. 95, pp. 53–59.

Scheele, G. F., Rosen, E. M., and Hanratty, T. J., 1960, "Effect of Natural Convection on Transition to Turbulence in Vertical Pipes," *The Canadian Journal of Chemical Engineering*, Vol. 38, pp. 67–73.

Scheele, G. F., and Hanratty, T. J., 1962, "Effect of Natural Convection on Stability of Flow in a Vertical Pipe," *J. Fluid Mech.*, Vol. 14, pp. 244–256.

Scheele, G. F., and Hanratty, T. J., 1963, "Effect of Natural Convection Instabilities on Rates of Heat Transfer at Low Reynolds Numbers," *AIChE Journal*, Vol. 9, pp. 183–185.

Shadday, M. A., Jr., 1986, "Combined Forced/Free Convection Through Vertical Tubes at High Grashof Numbers," *Proc. 8th International Heat Transfer Conference*, C. L. Tien, V. P. Carey, and J. K. Ferrel, eds., Vol. 3, pp. 1433–1437.

Sonneveld, P., 1989, "CGS, A Fast Lanczos-Type Solver for Nonsymmetric Linear Systems," *SIAM Journal of Sci. Stat. Comput.*, Vol. 10, pp. 36–52.

Sucec, J., and Sawant, A., 1984, "Unsteady, Conjugated, Forced Convection Heat Transfer in a Parallel Plate Duct," *International Journal of Heat and Mass Transfer*, Vol. 27, pp. 95–101.

Sucec, J., 1987, "Unsteady Conjugated Forced Convective Heat Transfer in a Duct With Convection From the Ambient," *International Journal of Heat and Mass Transfer*, Vol. 30, pp. 1963–1970.

Tao, L. N., 1960, "On Combined Free and Forced Convection in Channels," ASME JOURNAL OF HEAT TRANSFER, Vol. 82, pp. 233–238.

Temam, R., 1968, "On an Approximation Solution of the Navier–Stokes Equations by the Method of Fractional Step: Part 1," *Archiv. Ration. Math. Anal.*, Vol. 32, pp. 135–153.

White, F. M., 1974, *Viscous Fluid Flow*, McGraw-Hill, New York, Chap. 5.

Wilhelmson, R. B., and Ericksen, J. H., 1977, "Direct Solution for Poisson's Equations in Three Dimensions," *J. Comp. Phys.*, Vol. 25, pp. 315–331.

Yao, L. S., 1983, "Free and Forced Convection in the Entry Region of a Heated Vertical Channel," *International Journal of Heat and Mass Transfer*, Vol. 26, pp. 65–72.

Zeldin, B., and Schmidt, F. W., 1972, "Developing Flow With Combined Forced-Free Convection in an Isothermal Vertical Tube," ASME JOURNAL OF HEAT TRANSFER, Vol. 94, pp. 211–223.

Thermal Analysis of Complex Crossflow Exchangers in Terms of Standard Configurations

R. K. Shah
Harrison Division,
General Motors Corporation,
Lockport, NY 14094

A. Pignotti
Industrial Research Center,
FUDETEC,
Leandro Alem 1067
1001 Buenos Aires, Argentina

An attempt is made in this paper to examine very complicated heat exchanger flow arrangements and relate them to simple forms for which either a solution exists or an approximate solution can be obtained. This is shown by an example of a tubular crossflow exchanger having seven possible flow arrangements that can be manufactured from the same six-row tube bundle. All but one are shown to be equivalent to standard crossflow configurations that have been solved in the literature, or to assemblies of such configurations. The remaining case can be bracketed between two such geometries. Values for the thermal effectiveness are obtained, and a comparative analysis is performed.

Introduction

One of the standard procedures to evaluate the thermal performance of a heat exchanger is the calculation of the exchanger temperature effectiveness P as a function of the heat capacity rates ratio R and the number of heat transfer units NTU. This relationship is a function of the geometry/configuration of the exchanger. Many different geometries have been analyzed in the literature, with the simplifying idealizations of constant physical properties, no phase change, no longitudinal conduction, and various fluid mixing hypotheses for each fluid side.

Even if we restrict the analysis to crossflow exchangers, there is a large number of configurations that can be studied, which differ from each other in the number of passes involved, the fluid mixing hypotheses, and the other in which the fluids meet in successive passes. These idealized geometries are usually characterized by a schematic two-dimensional diagram, and the results of the thermal analysis are available to the designer. See Bowman et al. (1940), Stevens et al. (1957), Braun (1975), Roetzel and Neubert (1979), Bačlić and Gvozdenac (1983), and Pignotti and Cordero (1983). What is not always easy to establish is the correspondence between these standard ideal geometries and real-life three-dimensional tube bundles, which are interconnected to each other through headers in a complicated way. In this context, even the commonplace word "pass" does not have a unique meaning, because, as will be apparent from the following discussion, whether two passes are located "side-by-side" or "over-and-under" makes a significant difference in the overall thermal performance of the exchanger. The side-by-side and over-and-under passes, also referred to as parallel-coupled and series-coupled passes, respectively, are further defined in Appendix 1 of Shah and Pignotti (1991).

When an engineer needs to design an air-conditioning coil, he/she has a question: Which is better (or best) refrigerant circuit out of many possible combinations for a given number of tubes in a tube-fin coil? As mentioned in the following paragraph, we have taken one example idealized as having a single phase on each fluid side, analyzed its very complicated possible flow arrangements by relating them to simple forms (for which either a solution already exists in the literature or an approximate solution can be presented), and showed quantitatively what type of differences one would expect in the exchanger effectiveness (which in turn can be related to the heat transfer performance of a coil). Once quantitative heat transfer performance is known for various circuiting alternatives, a designer can take into account other design considerations to arrive at proper trade-offs for the optimum design. We hope the present methodology is applied to many industrial complicated heat exchanger flow arrangements for which no explicit ϵ-NTU solution exists in the literature.

In the following, we select a well-defined standard ideal six-row tube bundle with 60 tubes, and use it for the analysis of seven different crossflow exchangers that can be manufactured from it. The purpose of this work is twofold: first, to show how actual flow arrangements can be reduced to combinations of standard idealized flow arrangements (geometries); this may not always be straightforward. Second, to perform a comparative analysis of alternative arrangements so that the designer could select the optimum geometries based on thermal performance and other design criteria. Some of the modern techniques of analysis, as briefly summarized by Pignotti and Shah (1992), are used to derive the ϵ-NTU relationship of the exchangers with complicated flow arrangements.

Definition of the Geometry

We consider a tube bundle of 60 tubes, arranged in six rows of ten tubes each. In order to specify how the fluid flows, we draw transverse cross sections of the tube, as shown in Figs. 1(a), 2(a), ..., 7(a). Within each tube section, "$-$" and "$+$" signs indicate that the fluid flows out of or into the paper, respectively.

In addition, the complete specification of the flow arrangement requires the description of the headers. They are indicated by solid lines if they are located at the front end of the exchanger (closest to the reader), and by broken lines when they are at the back. These lines encompass the cross sections of the tubes through which the fluid flows into or out of the header. By convention, the inlet header is assumed to be located at the front end of the exchanger, and the outlet header is therefore either at the front or the rear end, depending on whether the number of passes is even or odd. In addition, there are "intermediate" headers, which direct the flow from one pass to the following one. In some cases, they allow streams from different rows to mix, and whether this happens is also relevant to the full characterization of the exchanger geometry.

In the following, the out-of-tube fluid is called the "external" fluid. It is assumed to flow normal to the tube bundle. By convention, the figures are drawn such that the fluid flows from the lower to the upper side of the diagrams as shown by arrows.

Contributed by the Heat Transfer Division for publication in the JOURNAL OF HEAT TRANSFER. Manuscript received by the Heat Transfer Division August 1991; revision received November 1992. Keywords: Augmentation and Enhancement, Heat Exchangers. Associate Technical Editor: W. A. Fiveland.

With regard to the mixing idealizations for the external fluid, two separate points should be made. For the actual heat transfer on the tube surfaces, the external fluid should be considered not to mix in the transverse direction. But, as the external fluid proceeds from one row to the following one, a certain amount of transverse mixing is likely to occur, depending on the geometry, turbulence generated, and thermal conductivity of the external fluid. Nonetheless, the idealization of no mixing between rows is generally more realistic than the one of perfect mixing, and is adopted here, even though it is much harder from the analysis point of view. A quantitative assessment of the differences between these two limiting cases is given by Pignotti and Cordero (1983).

Standard Configurations

In the case-by-case analysis of the following section, we examine each one of the proposed configurations and relate them to standard geometries, which are characterized by the following specifications:

- Number of passes (actual, "true," or "over-and-under" passes, as opposed to apparent, or "side-by-side" passes).
- Number of rows per pass. This amounts to different mixing hypotheses for the tube fluid. This is because even though this fluid is assumed to be perfectly mixed within each tube, it becomes partially unmixed when it is split into streams that proceed through different rows.

In the notation for the effectiveness, two subscripts are used to represent the number of passes and rows per pass, in that order. Thus, $P_{2,3}$ denotes the temperature effectiveness of a six-row exchanger, having two passes and three rows per pass.

In order to define the standard configurations fully, two more specifications have to be provided when more than one pass is involved:

- *The relative order in which the external fluid meets the tube passes.* If the inlet external fluid first meets the inlet tube fluid, the configuration is called overall cross-parallel flow, and the effectiveness bears the superscript "*p*." Conversely, if the inlet external fluid first meets the last tube pass, the superscript "*c*" is used for overall cross-counterflow.
- *The connection between rows belonging to neighboring passes for the case having more than one tube row per pass.* In such a case, three types of connection may occur at the intermediate header:
  - (*a*) the fluid from different rows of the same pass may be mixed before proceeding to the following pass; or
  - (*b*) fluid from the first row of one pass is connected to the first row of the following pass, and the same pattern is followed for the subsequent rows. This type of connection is denoted by adding the superscript "*so*," for same order; or
  - (*c*) same as in (*b*), but with fluid from the first row of one pass proceeding to the last row of the following one; from the second into the one before the last, etc. This is denoted by the superscript "*io*," for inverted order.

With these conventions, the effectiveness of the geometries of Figs. 3(*b*), 4(*b*), and 7(*b*) is denoted by $P^{c}_{3,2}$, $P^{c,so}_{3,2}$, and $P^{c}_{6,1}$, respectively.

Case-by-Case Analysis

As mentioned earlier, a total of seven different crossflow exchangers, as shown in Figs. 1–7, are analyzed in this paper. The temperature effectiveness-NTU formulas for each one are presented separately below in Eqs. (1)–(7) in terms of standard crossflow configurations. Since the *P*-NTU formulas or results are available for standard crossflow configurations through the recursive algorithms of Pignotti and Cordero (1983), the effectiveness of the present configurations is denoted in terms of the effectiveness of the standard configurations in Eqs. (1)–(7).

It should be emphasized that we have opted to present the results in terms of the *P*-NTU-*R* approach (based on the out-of-tube fluid), which is a variant of the conventional ϵ-NTU-C^* approach (based on the $C_{\min}$ fluid). When a heat exchanger is stream unsymmetric, there will be two different formulas for ϵ depending upon whether the tube fluid or the out-of-tube fluid is the $C_{\min}$ fluid, while the *P*-NTU formula remains the same for the complete range of R from 0 to ∞. The heat exchanger configurations analyzed in this paper are all stream unsymmetric.

Case 1. We begin by analyzing the exchanger of Fig. 1(*a*). Here the tube fluid enters the exchanger through the front inlet header, drawn on the right-hand side, which encompasses 20 tubes distributed as uniformly as possible among the six rows. At the back side intermediate header, the fluid is mixed and transferred to 20 tubes in the central bundle section. Similarly, at the front immediate header the tube fluid is again mixed and sent back through the remaining 20 tubes on the left-hand side.

At first sight, this configuration would be called a three-pass geometry, because each tube fluid particle travels three times the full length of the exchanger. However, these are side-by-side passes with each having different streams of the external fluid flowing over (see Fig. 1*b*). As a result, the thermal effectiveness is much closer to that of a single-pass exchanger than to a three-pass one. Indeed, if the exchanger is "stretched out" and the three side-by-side passes are aligned, it becomes clear that the effectiveness is equivalent to that of a new six-row single-pass exchanger, with tubes three times as long, except for the occurrence of mixing of the tube fluid at the two intermediate header locations. This equivalent geometry

Nomenclature

A = exchanger surface area, m^2
C_1 = out-of-tube fluid heat capacity rate, W/K
C_2 = tube fluid heat capacity rate, W/K
NTU = UA/C_1 = number of heat transfer units
P = $(t_o - t_i)/(T_i - t_i)$ = out-of-tube fluid temperature effectiveness
R = C_1/C_2 = heat capacity rates ratio
t_i = out-of-tube fluid inlet temperature, °C
t_o = out-of-tube fluid outlet temperature, °C
T_i = tube fluid inlet temperature, °C
T_o = tube fluid outlet temperature, °C
U = overall heat transfer coefficient, W/m^2K
ϵ = conventional heat exchanger effectiveness

Subscripts

1, 2 = the first digit is the number of passes of the exchanger; the second is the number of tube rows per pass

Superscripts

c = overall cross-counterflow connection
io = inverted order connection between tube passes
p = overall cross-parallel flow connection
so = same order connection between tube passes

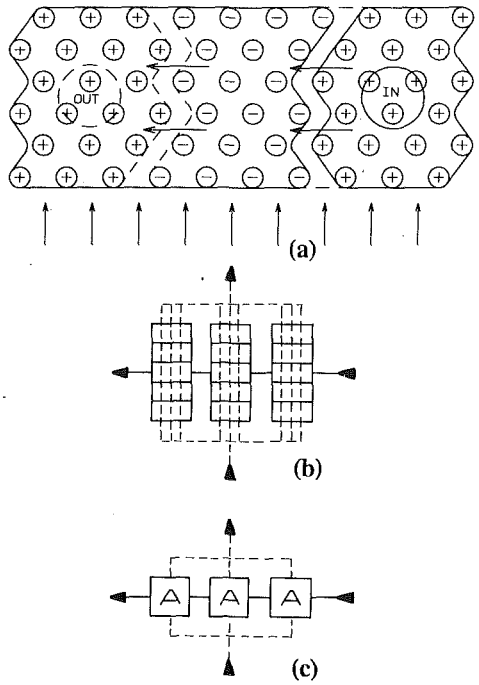

Fig. 1 Case 1: (*a*) tube bundle and headers cross section; (*b*) equivalent two-dimensional geometry; (*c*) equivalent assembly of heat exchangers

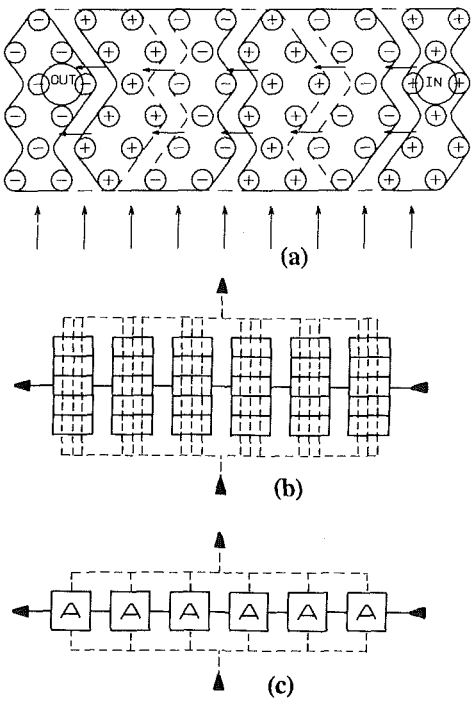

Fig. 2 Case 2: (*a*) tube bundle and headers cross section; (*b*) equivalent two-dimensional geometry; (*c*) equivalent assembly of heat exchangers

is schematically indicated in Fig. 1(*b*). Here only one of the 3 or 4 tubes in a given row is shown by a horizontal solid line, because the other ones are assumed to undergo the same thermal history. This is clearly not rigorously true, because among other things the number of tubes per row is not strictly the same for every row in a given pass. However, this is still a reasonable approximation, and the best that can be done without going into a full-fledged numerical calculation.

A close look at Fig. 1(*b*) reveals that it is just an assembly of three exchangers as shown in Fig. 1(*c*). Here each exchanger

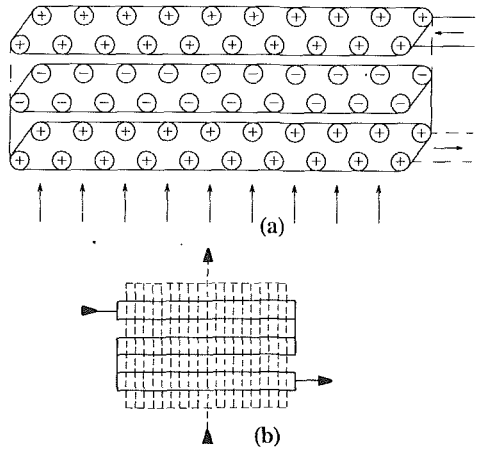

Fig. 3 Case 3: (*a*) tube bundle and headers cross section; (*b*) equivalent two-dimensional geometry

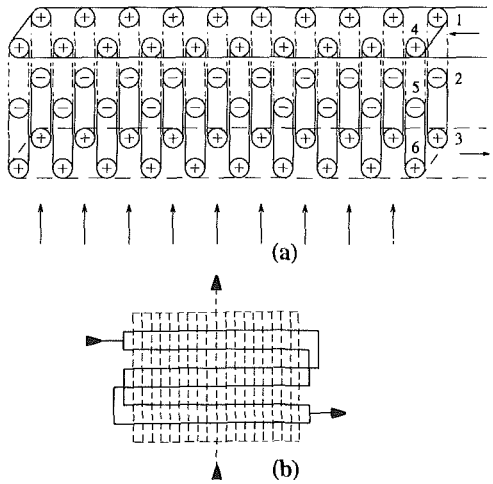

Fig. 4 Case 4: (*a*) tube bundle and headers cross section; (*b*) equivalent two-dimensional geometry

denoted by the letter A is a single-pass, six-row exchanger having one third of the total exchanger surface area, one third of the external fluid flow rate, and the full tube fluid flow rate. Therefore, using Domingos' (1969) formula for the temperature effectiveness of this assembly of heat exchangers, we can write

$$P(R, \text{NTU}) = \{1 - [-R\, P_{1,3}(R/3, \text{NTU})/3]^3\}/R \quad (1)$$

Case 2. The configuration of Fig. 2(*a*) can be analyzed in the same style as that of Fig. 1(*a*), with the only difference that the number of side-by-side tube passes is six, each one constituted by 10 tubes. As a result, the overall effectiveness is given by

$$P(R, \text{NTU}) = \{1 - [1 - R\, P_{1,6}(R/6, \text{NTU})/6]^6\}/R \quad (2)$$

Case 3. This case, as shown in Fig. 3(*a*), is a fairly standard configuration, in which the tube fluid undergoes three consecutive passes, each one with two tube rows. These are true over-and-under passes, such that all of them are met by each stream of the external fluid, in contrast to what happens with the side-by-side passes of Cases 1 and 2. Observing that it is a cross-counterflow arrangement with mixing at the intermediate headers (i.e., between passes), the effectiveness can be written as

$$P(R, \text{NTU}) = P^c_{3,2}(R, \text{NTU}) \quad (3)$$

Case 4. This case is shown in Fig. 4(*a*), and differs from

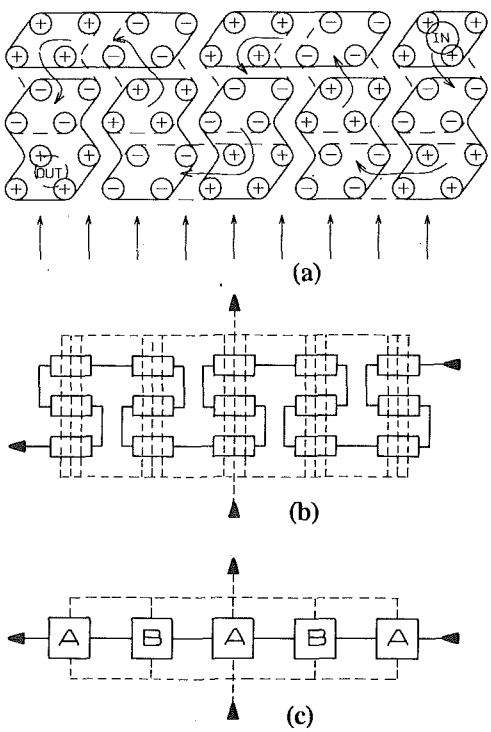

Fig. 5 Case 5: (*a*) tube bundle and headers cross section; (*b*) equivalent two-dimensional geometry; (*c*) equivalent assembly of heat exchangers

Case 3 in that there is no mixing at the intermediate headers, and the tube rows are connected in a "same-order" sequence. For example, the fluid going in tube 1 goes through tubes 2 and 3 subsequently without mixing with the fluid from other tubes; the case for the fluid going in tubes 4, 5 and 6 is similar. Therefore, we have, for this case,

$$P(R, \text{NTU}) = P^{c,so}_{3,2}(R, \text{NTU}) \tag{4}$$

Case 5. This configuration, as shown in Fig. 5(*a*), requires a more detailed analysis. Each tube fluid particle proceeds 15 times from one to the opposite end of the exchanger, sometimes in an over-and-under fashion, others in a side-by-side sequence. This complicated three-dimensional layout is clarified when the equivalent two-dimensional diagram of Fig. 5(*b*) is considered. Just as in the previous cases, only a fraction (in this case 1/2) of the total number of tubes is shown. The remaining tubes need not be considered because they follow an entirely equivalent pattern of heat exchange with the external fluid.

From Fig. 5(*b*), it is clear that the whole exchanger can be reduced to the equivalent assembly of exchangers of Fig. 5(*c*). These exchangers are of two kinds: those labeled by the letter *A* are cross-counterflow, three-pass, two-rows-per-pass exchangers, whereas those labeled *B* are similar but of the cross-parallel flow type. As a result, we can write for this case, using Domingos' method,

$$P(R, \text{NTU}) = \{1 - [1 - R\,P^{c}_{3,2}(R/5, \text{NTU})/5]^3 \times [1 - R\,P^{p}_{3,2}(R/5, \text{NTU})/5]^2\}/R \tag{5}$$

Case 6. At first sight, this case, as shown in Fig. 6(*a*), is fairly similar to the previous one. However, the difference is the tube fluid in Fig. 6(*a*) flows effectively in the "horizontal" direction in contrast to the effective vertical direction for Fig. 5(*a*). Again, each particle of tube fluid goes 15 times from end to end of the exchanger. Figure 6(*c*) shows the equivalent two-dimensional layer, and this time it cannot be broken down into a simple assembly of standard configurations. More complicated coupling schemes involving 4 × 4 matrices or matrix

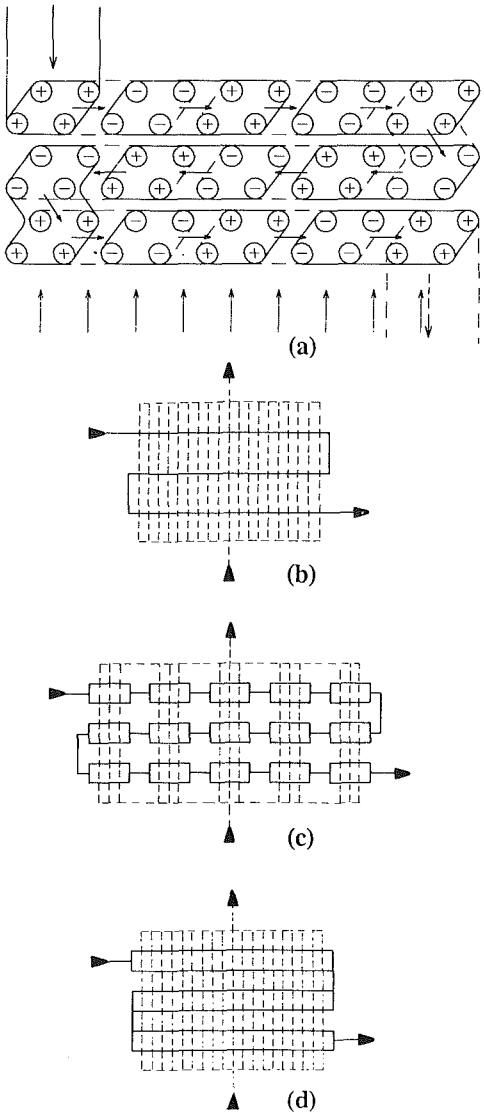

Fig. 6 Case 6: (*a*) tube bundle and headers cross section; (*b*) geometry that provides a lower bound for the effectiveness; (*c*) equivalent two-dimensional geometry for this case; (*d*) geometry that provides an upper bound for the effectiveness

operators can be used to handle this problem exactly (Pignotti, 1989). However, given the underlying approximations used to formulate the problem in the first place, it is equally meaningful to provide approximate solutions, or better still, close upper and lower bounds that bracket the exact solution. Such bounds can be found by observing that Fig. 6(*c*) is equivalent to a three-pass, two-rows-per-pass overall counterflow exchanger in which the fluids from the intervening rows are mixed at four locations within each pass. This situation is clearly an intermediate one between the case in which this additional mixing does not occur (see Fig. 6*d* or Fig. 3*b*), and that in which it occurs all the time, i.e., in which there is only one row per pass (see Fig. 6*b*). Alternately, one can see that the tube fluid is unmixed in each module (of four tubes, see Fig. 6*a*) and mixed between modules as shown in Fig. 6(*c*). This situation is between the cases of the tube fluid completely mixed (Fig. 6*b*) and completely unmixed (Fig. 6*d*). From the previous analysis (Pignotti and Cordero, 1983), it is known that the effectiveness of the Fig. 6(*b*) case is slightly lower than that of the Fig. 6(*d*) or 3(*b*) case. Hence, we can write

$$P^{c}_{3,1}(R, \text{NTU}) < P(R, \text{NTU}) < P^{c}_{3,2}(R, \text{NTU}) \tag{6}$$

Fig. 6(*b*) Fig. 6(*c*) Fig. 6(*d*)/3(*b*)

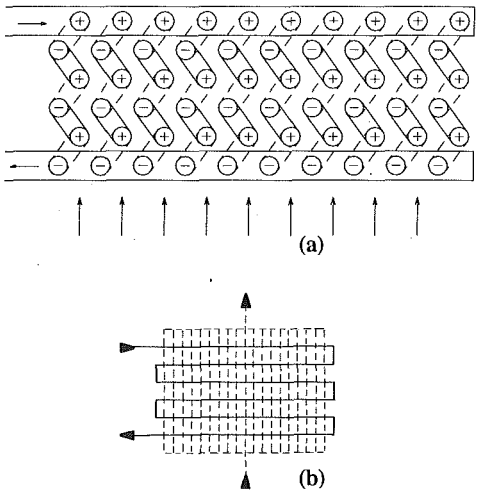

Fig. 7 Case 7: (*a*) tube bundle and headers cross section; (*b*) equivalent two-dimensional geometry

Case 7. The last case considered is that of Fig. 7, which is just the standard six-pass, one-row-per-pass cross-counterflow exchanger, for which

$$P(R, \text{NTU}) = P^{c}_{6,1}(R, \text{NTU}) \tag{7}$$

Results and Discussion

Table 1 shows the results obtained for the seven geometries considered, in order of decreasing effectiveness, for selected values of R and NTU. For reference, the values for a pure counterflow exchanger are tabulated as well as values for a mixed-unmixed ($P_{1,1}$), six tube row-unmixed ($P_{1,6}$) and unmixed-unmixed ($P_{1,\infty}$) crossflow exchangers. The values of the standard configurations have been calculated using the recursive algorithms of Pignotti and Cordero (1983). No graphic results are presented since the differences among P's at given NTU and R are too small in general. Probably, the number of tabulated values is too high in Table 1, but they have been included for closer interpolation as well as for future applications that may require a wider range of NTU and R.

Table 1 Thermal effectiveness for selected values of R and NTU, for overall counterflow geometry and for the seven cases discussed in the text. For Case 6 of Fig. 6(*c*), the lower bound is tabulated under Case 6 and the upper bound is the neighboring Case 3.

R	NTU	P										
		COUNTF	CASE 7	CASE 4	CASE 3	CASE 6	CASE 1	CASE 2	CASE 5	$P_{1,1}$	$P_{1,6}$	$P_{1,\infty}$
0.2	0.2	0.1782	0.1782	0.1782	0.1782	0.1782	0.1780	0.1780	0.1780	0.1780	0.1780	0.1780
0.2	0.3	0.2532	0.2532	0.2531	0.2531	0.2531	0.2526	0.2526	0.2526	0.2526	0.2526	0.2526
0.2	0.5	0.3807	0.3807	0.3805	0.3805	0.3805	0.3785	0.3784	0.3785	0.3784	0.3787	0.3787
0.2	0.7	0.4841	0.4839	0.4836	0.4835	0.4835	0.4792	0.4790	0.4791	0.4789	0.4798	0.4798
0.2	1.0	0.6050	0.6047	0.6039	0.6038	0.6038	0.5947	0.5942	0.5942	0.5938	0.5965	0.5965
0.2	1.5	0.7436	0.7429	0.7414	0.7411	0.7409	0.7223	0.7209	0.7204	0.7195	0.7277	0.7280
0.2	2.0	0.8317	0.8306	0.8285	0.8280	0.8275	0.7996	0.7968	0.7955	0.7940	0.8103	0.8108
0.2	3.0	0.9261	0.9246	0.9217	0.9210	0.9199	0.8775	0.8715	0.8677	0.8654	0.9007	0.9016
0.2	5.0	0.9853	0.9839	0.9814	0.9808	0.9788	0.9229	0.9119	0.9042	0.9008	0.9665	0.9680
0.2	7.0	0.9970	0.9962	0.9947	0.9944	0.9922	0.9319	0.9187	0.9092	0.9056	0.9864	0.9880
---	---	---	---	---	---	---	---	---	---	---	---	---
0.3	0.2	0.1767	0.1767	0.1767	0.1767	0.1767	0.1764	0.1764	0.1764	0.1764	0.1764	0.1764
0.3	0.3	0.2503	0.2503	0.2502	0.2502	0.2502	0.2494	0.2494	0.2494	0.2494	0.2494	0.2494
0.3	0.5	0.3745	0.3744	0.3741	0.3741	0.3741	0.3713	0.3712	0.3713	0.3711	0.3715	0.3716
0.3	0.7	0.4746	0.4744	0.4738	0.4738	0.4737	0.4677	0.4675	0.4675	0.4672	0.4685	0.4685
0.3	1.0	0.5915	0.5911	0.5900	0.5898	0.5897	0.5771	0.5764	0.5764	0.5758	0.5795	0.5796
0.3	1.5	0.7263	0.7253	0.7231	0.7227	0.7223	0.6968	0.6949	0.6942	0.6930	0.7042	0.7045
0.3	2.0	0.8136	0.8120	0.8088	0.8081	0.8073	0.7692	0.7655	0.7636	0.7616	0.7836	0.7842
0.3	3.0	0.9110	0.9086	0.9040	0.9029	0.9011	0.8432	0.8351	0.8301	0.8268	0.8738	0.8751
0.3	5.0	0.9787	0.9759	0.9714	0.9702	0.9666	0.8888	0.8739	0.8636	0.8589	0.9468	0.9492
0.3	7.0	0.9948	0.9928	0.9894	0.9887	0.9841	0.8991	0.8810	0.8684	0.8633	0.9733	0.9764
---	---	---	---	---	---	---	---	---	---	---	---	---
0.5	0.2	0.1738	0.1738	0.1737	0.1737	0.1737	0.1733	0.1733	0.1733	0.1733	0.1733	0.1733
0.5	0.3	0.2445	0.2445	0.2444	0.2444	0.2444	0.2431	0.2431	0.2431	0.2431	0.2432	0.2432
0.5	0.5	0.3623	0.3621	0.3617	0.3617	0.3617	0.3574	0.3573	0.3574	0.3572	0.3578	0.3578
0.5	0.7	0.4560	0.4556	0.4548	0.4547	0.4547	0.4457	0.4454	0.4455	0.4451	0.4469	0.4470
0.5	1.0	0.5647	0.5640	0.5623	0.5621	0.5619	0.5438	0.5429	0.5428	0.5420	0.5473	0.5475
0.5	1.5	0.6908	0.6892	0.6858	0.6852	0.6846	0.6492	0.6465	0.6455	0.6438	0.6593	0.6597
0.5	2.0	0.7746	0.7721	0.7669	0.7658	0.7646	0.7125	0.7074	0.7048	0.7020	0.7316	0.7324
0.5	3.0	0.8744	0.8700	0.8621	0.8602	0.8571	0.7785	0.7677	0.7610	0.7564	0.8178	0.8197
0.5	5.0	0.9572	0.9506	0.9404	0.9380	0.9303	0.8231	0.8032	0.7897	0.7828	0.8974	0.9017
0.5	7.0	0.9847	0.9779	0.9681	0.9661	0.9543	0.8354	0.8107	0.7940	0.7864	0.9329	0.9394
---	---	---	---	---	---	---	---	---	---	---	---	---
0.7	0.2	0.1709	0.1709	0.1708	0.1708	0.1708	0.1703	0.1702	0.1703	0.1702	0.1703	0.1703
0.7	0.3	0.2389	0.2389	0.2387	0.2387	0.2387	0.2371	0.2371	0.2371	0.2370	0.2372	0.2372
0.7	0.5	0.3504	0.3502	0.3497	0.3497	0.3496	0.3442	0.3441	0.3442	0.3439	0.3447	0.3448
0.7	0.7	0.4379	0.4374	0.4363	0.4362	0.4362	0.4251	0.4247	0.4248	0.4243	0.4266	0.4267
0.7	1.0	0.5384	0.5374	0.5352	0.5349	0.5347	0.5131	0.5119	0.5118	0.5108	0.5173	0.5175
0.7	1.5	0.6545	0.6525	0.6481	0.6473	0.6466	0.6057	0.6025	0.6013	0.5992	0.6173	0.6178
0.7	2.0	0.7326	0.7293	0.7227	0.7213	0.7197	0.6609	0.6549	0.6520	0.6487	0.6820	0.6830
0.7	3.0	0.8295	0.8233	0.8127	0.8102	0.8061	0.7191	0.7070	0.6995	0.6940	0.7611	0.7634
0.7	5.0	0.9207	0.9094	0.8936	0.8900	0.8788	0.7612	0.7390	0.7241	0.7158	0.8390	0.8445
0.7	7.0	0.9598	0.9452	0.9274	0.9240	0.9054	0.7745	0.7465	0.7282	0.7187	0.8773	0.8864
---	---	---	---	---	---	---	---	---	---	---	---	---
1.0	0.2	0.1667	0.1666	0.1666	0.1666	0.1666	0.1658	0.1658	0.1658	0.1658	0.1658	0.1658
1.0	0.3	0.2308	0.2307	0.2305	0.2305	0.2305	0.2284	0.2283	0.2284	0.2283	0.2285	0.2285
1.0	0.5	0.3333	0.3331	0.3324	0.3324	0.3323	0.3256	0.3255	0.3256	0.3253	0.3263	0.3263
1.0	0.7	0.4118	0.4112	0.4099	0.4097	0.4096	0.3965	0.3960	0.3961	0.3955	0.3983	0.3984
1.0	1.0	0.5000	0.4988	0.4962	0.4958	0.4955	0.4712	0.4699	0.4697	0.4685	0.4760	0.4762
1.0	1.5	0.6000	0.5975	0.5923	0.5914	0.5905	0.5473	0.5438	0.5425	0.5402	0.5596	0.5602
1.0	2.0	0.6667	0.6626	0.6549	0.6533	0.6514	0.5919	0.5856	0.5824	0.5788	0.6132	0.6142
1.0	3.0	0.7500	0.7424	0.7301	0.7272	0.7225	0.6394	0.6270	0.6194	0.6133	0.6789	0.6813
1.0	5.0	0.8333	0.8183	0.7995	0.7955	0.7827	0.6759	0.6537	0.6392	0.6296	0.7450	0.7509
1.0	7.0	0.8750	0.8528	0.8306	0.8267	0.8054	0.6892	0.6610	0.6430	0.6318	0.7786	0.7887

Table 1 (cont'd)

R	NTU	P										
		COUNTF	CASE 7	CASE 4	CASE 3	CASE 6	CASE 1	CASE 2	CASE 5	$P_{1,1}$	$P_{1,6}$	$P_{1,\infty}$
1.5	0.2	0.1599	0.1599	0.1598	0.1598	0.1598	0.1587	0.1587	0.1588	0.1587	0.1588	0.1588
1.5	0.3	0.2179	0.2178	0.2175	0.2175	0.2175	0.2148	0.2148	0.2149	0.2147	0.2150	0.2150
1.5	0.5	0.3067	0.3064	0.3055	0.3055	0.3054	0.2976	0.2974	0.2975	0.2972	0.2984	0.2985
1.5	0.7	0.3713	0.3707	0.3690	0.3689	0.3688	0.3545	0.3539	0.3540	0.3534	0.3566	0.3566
1.5	1.0	0.4404	0.4391	0.4361	0.4357	0.4354	0.4112	0.4098	0.4096	0.4084	0.4162	0.4164
1.5	1.5	0.5134	0.5109	0.5057	0.5047	0.5038	0.4658	0.4625	0.4611	0.4588	0.4770	0.4775
1.5	2.0	0.5584	0.5545	0.5474	0.5459	0.5442	0.4966	0.4909	0.4880	0.4844	0.5142	0.5152
1.5	3.0	0.6084	0.6023	0.5929	0.5907	0.5869	0.5290	0.5186	0.5124	0.5064	0.5577	0.5597
1.5	5.0	0.6474	0.6390	0.6287	0.6264	0.6184	0.5550	0.5375	0.5261	0.5164	0.5981	0.6024
1.5	7.0	0.6598	0.6514	0.6420	0.6403	0.6288	0.5654	0.5433	0.5295	0.5177	0.6166	0.6232
2.0	0.2	0.1535	0.1534	0.1533	0.1533	0.1533	0.1521	0.1521	0.1521	0.1520	0.1521	0.1521
2.0	0.3	0.2058	0.2057	0.2054	0.2054	0.2054	0.2023	0.2023	0.2024	0.2023	0.2025	0.2025
2.0	0.5	0.2824	0.2820	0.2811	0.2810	0.2810	0.2728	0.2726	0.2727	0.2724	0.2737	0.2737
2.0	0.7	0.3348	0.3342	0.3325	0.3323	0.3322	0.3185	0.3179	0.3180	0.3173	0.3205	0.3206
2.0	1.0	0.3873	0.3860	0.3832	0.3828	0.3825	0.3615	0.3602	0.3599	0.3588	0.3660	0.3662
2.0	1.5	0.4372	0.4351	0.4308	0.4301	0.4293	0.4004	0.3975	0.3963	0.3943	0.4094	0.4099
2.0	2.0	0.4637	0.4609	0.4560	0.4550	0.4537	0.4213	0.4167	0.4143	0.4113	0.4341	0.4348
2.0	3.0	0.4872	0.4841	0.4793	0.4781	0.4759	0.4425	0.4350	0.4304	0.4252	0.4605	0.4618
2.0	5.0	0.4983	0.4962	0.4930	0.4922	0.4889	0.4592	0.4475	0.4400	0.4314	0.4813	0.4835
2.0	7.0	0.4998	0.4986	0.4966	0.4962	0.4925	0.4659	0.4517	0.4427	0.4322	0.4891	0.4918
3.0	0.2	0.1415	0.1415	0.1413	0.1413	0.1413	0.1399	0.1398	0.1399	0.1398	0.1399	0.1399
3.0	0.3	0.1841	0.1839	0.1836	0.1835	0.1835	0.1803	0.1802	0.1803	0.1802	0.1805	0.1805
3.0	0.5	0.2402	0.2398	0.2389	0.2388	0.2388	0.2314	0.2312	0.2313	0.2309	0.2322	0.2323
3.0	0.7	0.2736	0.2730	0.2716	0.2714	0.2713	0.2607	0.2602	0.2602	0.2597	0.2625	0.2626
3.0	1.0	0.3018	0.3009	0.2990	0.2987	0.2985	0.2854	0.2844	0.2841	0.2833	0.2885	0.2887
3.0	1.5	0.3221	0.3210	0.3191	0.3187	0.3183	0.3049	0.3031	0.3022	0.3009	0.3097	0.3099
3.0	2.0	0.3292	0.3284	0.3268	0.3264	0.3260	0.3140	0.3116	0.3103	0.3084	0.3196	0.3200
3.0	3.0	0.3328	0.3323	0.3316	0.3314	0.3309	0.3223	0.3191	0.3172	0.3141	0.3279	0.3283
3.0	5.0	0.3333	0.3333	0.3331	0.3330	0.3327	0.3278	0.3240	0.3215	0.3164	0.3320	0.3324
3.0	7.0	0.3333	0.3333	0.3333	0.3333	0.3330	0.3297	0.3256	0.3230	0.3167	0.3329	0.3331
5.0	0.2	0.1210	0.1209	0.1208	0.1208	0.1208	0.1192	0.1192	0.1193	0.1192	0.1193	0.1193
5.0	0.3	0.1487	0.1486	0.1482	0.1482	0.1482	0.1454	0.1453	0.1454	0.1453	0.1456	0.1456
5.0	0.5	0.1777	0.1775	0.1769	0.1768	0.1768	0.1724	0.1722	0.1722	0.1720	0.1730	0.1730
5.0	0.7	0.1902	0.1898	0.1892	0.1891	0.1890	0.1845	0.1842	0.1841	0.1839	0.1854	0.1854
5.0	1.0	0.1971	0.1968	0.1963	0.1962	0.1961	0.1924	0.1920	0.1918	0.1915	0.1935	0.1936
5.0	1.5	0.1996	0.1995	0.1993	0.1992	0.1991	0.1971	0.1966	0.1963	0.1959	0.1980	0.1981
5.0	2.0	0.1999	0.1999	0.1998	0.1998	0.1998	0.1986	0.1982	0.1979	0.1973	0.1993	0.1994
5.0	3.0	0.2000	0.2000	0.2000	0.2000	0.2000	0.1996	0.1992	0.1990	0.1983	0.1999	0.1999
5.0	5.0	0.2000	0.2000	0.2000	0.2000	0.2000	0.1999	0.1997	0.1996	0.1986	0.2000	0.2000
5.0	7.0	0.2000	0.2000	0.2000	0.2000	0.2000	0.2000	0.1998	0.1998	0.1986	0.2000	0.2000
7.0	0.2	0.1043	0.1043	0.1041	0.1041	0.1041	0.1027	0.1027	0.1027	0.1027	0.1028	0.1028
7.0	0.3	0.1221	0.1220	0.1217	0.1217	0.1217	0.1197	0.1197	0.1197	0.1196	0.1198	0.1198
7.0	0.5	0.1367	0.1366	0.1362	0.1362	0.1362	0.1340	0.1339	0.1339	0.1338	0.1343	0.1343
7.0	0.7	0.1410	0.1409	0.1406	0.1406	0.1406	0.1389	0.1388	0.1387	0.1386	0.1393	0.1394
7.0	1.0	0.1426	0.1425	0.1424	0.1424	0.1424	0.1415	0.1413	0.1412	0.1411	0.1418	0.1418
7.0	1.5	0.1428	0.1428	0.1428	0.1428	0.1428	0.1425	0.1424	0.1423	0.1422	0.1427	0.1427
7.0	2.0	0.1429	0.1429	0.1429	0.1429	0.1428	0.1428	0.1427	0.1426	0.1425	0.1428	0.1428
7.0	3.0	0.1429	0.1429	0.1429	0.1429	0.1429	0.1428	0.1428	0.1428	0.1427	0.1429	0.1429
7.0	5.0	0.1429	0.1429	0.1429	0.1429	0.1429	0.1429	0.1429	0.1428	0.1427	0.1429	0.1429
7.0	7.0	0.1429	0.1429	0.1429	0.1429	0.1429	0.1429	0.1429	0.1429	0.1427	0.1429	0.1429

It should be emphasized that the effectiveness results for all cases except for Case 6 are exact; only the lower and upper bounds for P are given for Case 6 since a closed-form formula is not easy to derive, but is possible by the chain rule methodology of second-order loops (Pignotti, 1989).

Even if the flow rates, surface areas, and inlet conditions for each tube bundle remain the same, the overall heat transfer coefficient and tube side pressure drop will vary with the cases considered. For example, given the total tube fluid flow rate W, the actual flow rate w in any single tube varies depending on the case considered. In Cases 1, 3, and 4, we have $w = W/20$; in Cases 2 and 7, $w = W/10$; and in Cases 5 and 6, $w = W/4$. Thus, these tube bundles will not have identical NTUs and ΔP's for specified A and W, i.e., for a given application. With this in mind, we can proceed to compare the values obtained for the effectiveness for the same values of R and NTU for the whole exchanger. Note that the same NTU will require different A's since U's will be different due to different amount of tube fluid flow rate per tube in different cases.

Bearing in mind that the cross-counterflow exchangers approach the pure counterflow geometry as the number of passes increases, it is not surprising to find that Case 7 is the one with the highest effectiveness. Next come Cases 4 and 3, which are both three-pass, two-rows-per-pass exchangers, and differ from each other in the mixing (or lack of mixing) of the tube fluid at the intermediate headers. It turns out that the Case 4 of not mixing with "same order" (in the sense described in the section Standard Configurations) slightly enhances the effectiveness compared to the mixed case (Case 3) whereas an "inverted order" would lead to a slightly lower effectiveness.

Next we find Case 6, which is also a cross-counterflow three-pass case. The occurrence of mixing of the tube fluid at intermediate points within each pass decreases the effectiveness slightly as compared to Cases 4 and 3. The value tabulated corresponds to the conservative lower bound in Eq. (6) corresponding to Fig. 6(*b*). The upper bound is given by the neighboring Case 3.

Cases 1 and 2 are clearly single-pass. The only difference is that Case 2, having a higher degree of tube fluid mixing than Case 1, has correspondingly a slightly lower effectiveness. If there had been only one six tube row exchanger instead of three side-by-side six tube row exchangers of Case 1, it would represent a lower degree of mixing and the corresponding effectiveness $P_{1,6}$ would be slightly higher as listed in Table 1. When the number of tube rows is increased from six to infinity for one six tube row exchanger, it represents an unmixed-unmixed exchanger with $P_{1,\infty}$ as listed in Table 1. On the other side, if six side-by-side exchangers of Case 2 have been increased to infinity, it would represent the tubeside fluid as mixed and the other fluid as unmixed; the corresponding effectiveness is listed in Table 1 as $P_{1,1}$. Indeed, for the one-pass arrangements, one can write (and also find from Table 1) that

$$P_{1,1} < P_{\text{Case 2}} < P_{\text{Case 1}} < P_{1,6} < P_{1,\infty} \tag{8}$$

Finally, Case 5, which looks similar to Case 6, is actually not a three-pass case. A common feature of cross-counterflow three-pass exchangers is the fact that only after having traveled two thirds of the way through the exchanger, the tube fluid meets the inlet external fluid. Instead, in this case, this meeting occurs already after having traveled 2/15 of the way through the exchanger, can easily be seen from Fig. 5(*b*). Indeed, Fig. 5(*c*) shows that the coarse structure of the exchanger is that of a single-pass case, independent of the details in the boxes labeled A and B. In formulas, this can be argued in the following way. It is well known that the limiting value of the effectiveness for small values of R regardless of the details (configurations) of the exchanger is given by

$$P_o = 1 - \exp(-\text{NTU}) \tag{9}$$

In Fig. 5(*c*), the value of the heat capacity rates ratio for each one of the component exchangers is 1/5 of the total R, i.e., $R_A = R_B = R/5$. Therefore, using the small-R approximation for each one of the components, we can approximate the effectiveness of the whole exchanger, using Domingos' formula (1969), as

$$P = \{1 - [1 - RP_o/5]^5\}/R \tag{10}$$

Using the well-known formula

$$\lim_{N\to\infty} [1 - x/N]^N = \exp(-x), \tag{11}$$

we obtain

$$P = [1 - \exp(-RP_o)]/R, \tag{12}$$

which is precisely the formula for the effectiveness of a single-pass crossflow exchanger, with mixed tube fluid and unmixed external fluid. Of course, this argument breaks down for large values of R, for which the approximations made are not valid; but it helps understanding why Case 5 is a single-pass case. Indeed, as can be seen from Table 1, the effectiveness of Case 5 is almost equal to that of mixed tube fluid and unmixed external fluid ($P_{1,1}$) except for high values of NTU.

From the foregoing discussion, it appears that Case 7 provides the highest effectiveness and Case 5 the lowest for the same NTU and R. If we consider air or gas as the out-of-tube fluid and liquid or phase-change fluid as the tube fluid, the typical value of R will be 0.2 (or lower), and the difference in P between Cases 7 and 5 is 1.7 and 4.1 percent at NTU = 1 and 2, respectively. In contrast, the maximum difference in P for a gas-to-gas exchanger with $R = 1$ will be 6 and 12 percent at NTU = 1 and 2, respectively, for the foregoing two cases. Now, the tube fluid velocity will be higher for Case 5 compared to that for Case 7 since the number of tubes in a given pass is 4 and 10, respectively, for these cases. This will result in a higher heat transfer coefficient (and ΔP) for Case 5 yielding higher NTU and ΔP, and the difference in P for the same A and W will be smaller than indicated above. In the actual selection of a specific configuration, one also needs to consider the tubeside pressure drops as well as manufacturing and durability aspects before a design is finalized. However, the analysis presented here first shows which arrangements are better from the heat transfer point of view and how much better before other design criteria are considered.

Conclusions

We have shown how a number of widely different arrangements obtained from a given tube bundle (6 rows, 60 tubes) can be described as far as the exchanger thermal effectiveness is concerned, in terms of standard configurations of known solutions. The expression of the actual configurations in terms of the standard ones is straightforward in some cases, whereas in others it requires a careful analysis and leads to results that are not evident at first sight, such as those of Cases 5 and 6. Of course, many more configurations can be obtained from the same tube bundle and analyzed in a similar way. In particular, inversion of the tube fluid direction of flow in Cases 3, 4, 6, and 7 leads to cross-parallel flow geometries, which can be analyzed following exactly the same methods as here, but of course will yield lower values for the thermal effectiveness.

Specifically, out of seven configurations considered from the same tube bundle, Case 7 provides the highest effectiveness and Case 5 the lowest for the same NTU and R.

In addition to the complex crossflow configurations presented here, there are many other complex heat exchanger configurations possible. Many of which are now possible to analyze in closed form using the chain rule methodology outlined by Pignotti (1989) and Pignotti and Shah (1992).

References

Bačlić, B., and Gvozdenac, D. D., 1983, "ϵ-NTU-ω Relationships for Inverted Order Flow Arrangements of Two-Pass Crossflow Heat Exchangers," in: *Regenerative and Recuperative Heat Exchangers*, R. K. Shah and D. E. Metzger, eds., ASME HTD-Vol. 21, pp. 27–41.

Bowman, R. A., Mueller, A. C., and Nagle, W. M., 1940, "Mean Temperature Difference in Design," *Trans. ASME*, Vol. 62, pp. 283–294.

Braun, B., 1975, "Wärmeübergang und Temperaturverlauf in Querstrom-Rohrbundeln bei beliebiger Schaltung der Rohrreihen," *Forsch. Ing. Wes.*, Vol. 41, No. 6, pp. 181–191.

Domingos, J. D., 1969, "Analysis of Complex Assemblies of Heat Exchangers," *Int. J. Heat Mass Transfer*, Vol. 12, pp. 537–548.

Pignotti, A., and Cordero, G., 1983, "Mean Temperature Difference in Multipass Crossflow," ASME JOURNAL OF HEAT TRANSFER, Vol. 105, pp. 584–591.

Pignotti, A., 1989, "Coupling Rules for Basic Thermal Analysis of Complex Heat Exchangers," in: *Compact Heat Exchangers: A Festschrift for A. L. London*, R. K. Shah, A. D. Kraus, and D. Metzger, eds., Hemisphere Publishing Co., Washington, DC, pp. 13–30.

Pignotti, A., and Shah, R. K., 1992, "Effectiveness-Number of Transfer Units Relationships for Heat Exchanger Complex Flow Arrangements," *Int. J. Heat Mass Transfer*, Vol. 35, pp. 1275–1291.

Roetzel, W., and Neubert, J., 1979, "Calculation of Mean Temperature Difference in Air Cooled Crossflow Heat Exchangers," ASME JOURNAL OF HEAT TRANSFER, Vol. 101, pp. 511–513.

Shah, R. K., and Pignotti, A., 1991, "Thermal Analysis of Complex Crossflow Exchangers in Terms of Standard Configurations," in: *Advances in Heat Exchanger Design, Radiation and Combustion*, ASME HTD-Vol. 182, pp. 11–18.

Stevens, R. A., Fernandez, J., and Woolf, J. R., 1957, "Mean Temperature Difference in One, Two, and Three-Pass Crossflow Heat Exchangers," *Trans. ASME*, Vol. 79, pp. 287–297.

Rayleigh-Bénard Convection in a Small Aspect Ratio Enclosure: Part I—Bifurcation to Oscillatory Convection

D. Mukutmoni

K. T. Yang

Department of Aerospace and Mechanical Engineering, University of Notre Dame, Notre Dame, IN 46556

The present numerical study documents bifurcation sequences for Rayleigh-Bénard convection in a rectangular enclosure with insulated sidewalls. The aspect ratios are 3.5 and 2.1 and the Boussinesq fluid is water (average temperature of 70°C) with a Prandtl number of 2.5. Two transitions are documented numerically. The first transition is from steady-state to oscillatory flow and the second is a subharmonic bifurcation as the Rayleigh number is increased further. The dynamics of the flow and temperature field is analyzed in detail for the subcritical steady convection and the supercritical oscillatory convection. The numerical results compared well with experiments, both qualitatively and quantitatively.

Introduction

The Rayleigh-Bénard system has been studied over the past century by a large number of researchers, who form a diverse group. This is not surprising. The Rayleigh-Bénard system has applications to fields such as astrophysics, geophysics, and atmospheric sciences, as well as in engineering. There are strong theoretical reasons to study the system as well. The governing equations are a set of coupled nonlinear partial differential equations. It is now generally recognized that time dependence in the Rayleigh-Bénard system offers clues to the transition from laminar to turbulent flow.

The aim of this investigation is to document and examine flow transitions or bifurcations by direct numerical simulation as the control parameter, the Rayleigh number, is varied. The Rayleigh-Bénard (henceforth referred to as RB) system is a convenient vehicle for studying the transition process, since the transition sequence is more well defined and stretched out in certain cases (Yang, 1988). Not surprisingly, the transition process has been a subject of much experimental work in the past (Busse, 1978).

When the Rayleigh number is increased beyond a certain critical value, RB convection becomes oscillatory. Experimentally (Behringer, 1985), it was shown that when the Rayleigh number is increased further, flow becomes turbulent soon after in large aspect ratio enclosures. It is only in small aspect ratio enclosures (less than 5) that RB convection evolves according to a distinct set of bifurcations, ultimately leading to turbulence. This has been documented experimentally (Gollub and Benson, 1980; Maurer and Libchaber, 1979; Berge et al., 1982). The experiments suggest that in small aspect ratio boxes the dynamic behavior is simpler due to the restricting and pervasive influence of the side walls. Also significant is that the dynamic behavior is highly degenerate and nonunique. It is a strong function of the aspect ratios, Prandtl number, and the time-averaged mean flow. Many sequences of bifurcation (or scenarios) are possible for RB convection in small aspect ratio enclosures.

In this paper the focus is on the period-doubling route to chaos for RB convection, theoretically described for the first time in iterated one-dimensional maps (Feigenbaum, 1978). The set of experiments that documented this is from Gollub and Benson (1980) and Gollub et al. (1980). The experiments performed with water as the fluid used LDV techniques. The cell had a 3.5:2.1:1 geometry with a height of 7.90 mm. The strong temperature dependence on the viscosity of water made it possible to vary the Prandtl number by changing the mean temperature. Experiments were reported for a Prandtl number of 2.5. The mean flow observed consisted to two symmetric rolls oriented with axes parallel to the short side of the cell.

Although these experiments (Gollub et al., 1980; Gollub and Benson, 1980) were comprehensive, many important issues couldn't be addressed. Due to experimental constraints, temperature and flow field details were seldom known. Most of the data were local measurements of velocities. If numerical simulations can be made to correlate strongly with these experiments, new insights can be garnered due to the greater degree of details available to the numerical analyst. The first part of the study looks into transition from steady-state to oscillatory convection. A second companion paper documents the transition from oscillatory flow to chaos (Mukutmoni and Yang, 1993).

The paper begins with a discussion on the formulation of the problem and validation of the code. This is followed by a study of the initial condition and a grid refinement study. The next sections deal with oscillatory convection and its mechanism. Subsequent bifurcations are then briefly documented followed by a summary of the conclusions.

Formulation

The formulation is made consistent with the experiments of Gollub et al. (1980) (henceforth referred to as GBS). The geometry of the enclosure is shown in Fig. 1. The vertical walls are adiabatic. The bottom wall is heated and the top wall is cooled, both isothermally. The fluid is Boussinesq, i.e., all transport properties are assumed constant with the exception of the buoyancy term in the momentum equations, which is linearized. The maximum temperature difference in the experiments of GBS was 0.7 K. The Boussinesq approximation is justified according to the criteria set by Gray and Giorgini (1976). The aspect ratios are 3.5 and 2.1, and the Prandtl number is 2.5 as dictated by the experiments. The governing equations are nondimensionalized by suitable scales of the dependent and independent variables. The x, y, and z coordinates were scaled by L, the enclosure height, the velocities were scaled by α/L, the time by L^2/α, and the pressure dif-

Contributed by the Heat Transfer Division for publication in the JOURNAL OF HEAT TRANSFER. Manuscript received by the Heat Transfer Division August 1991; revision received October 1992. Keywords: Enclosure Flows, Flow Instability, Natural Convection. Associate Technical Editor: J. R. Lloyd.

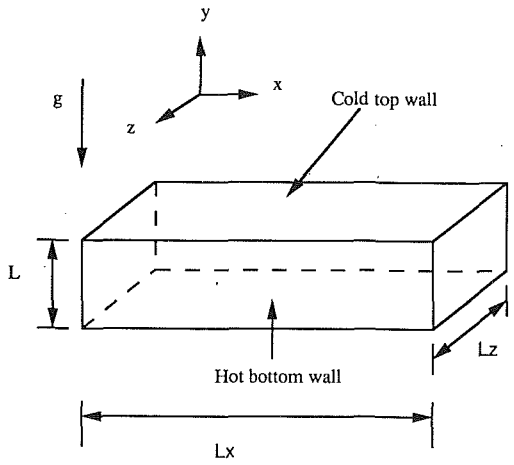

Fig. 1 Geometry of enclosure

ference between the total pressure and the equilibrium hydrostatic pressure in the absence of a temperature gradient was scaled by $\rho\alpha^2/L^2$. The temperature was nondimensionalized by $(T-T_m)/\Delta T$, $\Delta T = T_H - T_C$, and $T_m = (T_H + T_C)/2$, α is the thermal diffusivity, and ρ is the fluid density. The nondimensionalized governing equations for the Boussinesq fluid are (Yang, 1988):

$$\nabla \cdot \mathbf{U} = 0 \tag{1}$$

$$\frac{\partial u}{\partial t} + \nabla \cdot (u\mathbf{U}) = -\frac{\partial p}{\partial x} + \mathrm{Pr}\,\nabla^2 u \tag{2}$$

$$\frac{\partial v}{\partial t} + \nabla \cdot (v\mathbf{U}) = -\frac{\partial p}{\partial y} + \mathrm{Pr}\,\nabla^2 v + \mathrm{RaPr}T \tag{3}$$

$$\frac{\partial w}{\partial t} + \nabla \cdot (w\mathbf{U}) = -\frac{\partial p}{\partial z} + \mathrm{Pr}\,\nabla^2 w \tag{4}$$

$$\frac{\partial T}{\partial t} + \nabla \cdot (T\mathbf{U}) = \nabla^2 T \tag{5}$$

The boundary conditions consistent with the adiabatic and isothermal walls in a nondimensional form are the following:

$$x = 0, A_x;\ 0 \le z \le A_z,\ 0 \le y \le 1\ \ u = v = w = 0\ \ \frac{\partial T}{\partial x} = 0 \tag{6}$$

$$z = 0, A_z;\ 0 \le x \le A_x,\ 0 \le y \le 1\ \ u = v = w = 0\ \ \frac{\partial T}{\partial z} = 0 \tag{7}$$

$$y = 0,1;\ 0 \le x \le A_x,\ 0 \le z \le A_z\ \ u = v = w = 0\ \ T = 0.5 - y \tag{8}$$

Note that the pressure defined is actually the pressure difference between the total pressure and the hydrostatic pressure under isothermal and quiescent conditions nondimensionalized by the pressure scale $\rho\alpha^2/L^2$.

The governing equations were solved in primitive variables in a uniform, three-dimensional staggered grid based on the control volume method (Patankar, 1980). The QUICK scheme was used in the finite difference formulation of the convective terms to minimize numerical diffusion effects (Leonard, 1983). The SIMPLEX algorithm (Van Doormaal and Raithby, 1984) was used to solve the coupled heat transfer and fluid flow problem, which is essentially a more implicit variant of SIMPLE. Time stepping was done by an implicit Backward-Euler scheme. The time step was typically 0.0002 for the unsteady calculations and 0.001 when only the final steady-state solution was required. The time stepping error was quite minimal.

Table 1 Comparison between experimental (Farhadieh and Tankin, 1974) and numerical Nusselt numbers as a function of the Rayleigh number

Ra	Present work	Farhadieh and Tankin (1974)	Percentage difference	Rolls Prescribed
2410	1.45	1.45	< 0.5	29
3740	1.82	1.82	< 0.5	27
4600	1.98	1.96	1.02	26
6460	2.15	2.18	1.38	22

Validation

The code was validated with the experimental results of Farhadieh and Tankin (1974). This was necessary, since no analytical solutions are available for three-dimensional RB convection in a box for even limiting cases. Experiments were performed in a large aspect ratio box of dimensions 32:12:1. Fluid used was distilled water (Pr = 6.8). The experimentally observed wave-numbers were prescribed by starting the computations with sinusoidal perturbations. We refer the reader to Mukutmoni and Yang (1993) for additional details. Table 1 compares the Nusselt numbers of the experiments with those of Farhadieh and Tankin (1974). Figure 2(*a*) is the interferogram of the experiments for a Rayleigh number of 6460. The isotherms from the calculation (Fig. 2(*b*)) are compared with the actual fringe patterns, which are essentially isotherms. The computations have exploited the fourfold symmetry in the flow and temperature fields (for an even number of rolls) in the horizontal plane. A $160 \times 20 \times 5$ grid used gives a resolution of 0.05 in the vertical y direction and 0.1 in the x direction. Figure 2(*c*) shows only half the number of rolls, the other half being symmetric about the left wall.

The results show that there is good agreement with experiments for both the average and local values. Note that exact adiabatic and isothermal boundary conditions cannot be maintained experimentally and some differences are to be expected

Nomenclature

A_x = L_x/L = aspect ratio in the x direction
A_z = L_z/L = aspect ratio in the z direction
g = acceleration due to gravity, m^2/s
L = height of the enclosure, m
L_x = dimension of enclosure in x direction, m
L_z = dimension of enclosure in z direction, m
Nu = Nusselt number averaged over a horizontal cross section
p = nondimensional pressure
Pr = ν/α = Prandtl number
Ra = $g\beta\Delta TL^3/\nu\alpha$ = Rayleigh number
t = nondimensional time
T = nondimensional temperature
T_C = cold wall temperature, °C
T_H = hot wall temperature, °C
ΔT = temperature difference = $T_H - T_C$, °C
u = nondimensional x-direction velocity
v = nondimensional y-direction velocity
w = nondimensional z-direction velocity
x = nondimensional horizontal spatial coordinate
y = nondimensional vertical spatial coordinate
z = nondimensional spatial coordinate in the direction of depth
α = thermal diffusivity, m^2/s
β = coefficient of volume expansion, 1/K
ν = dynamic viscosity, m^2/s
ρ = density, kg/m^3

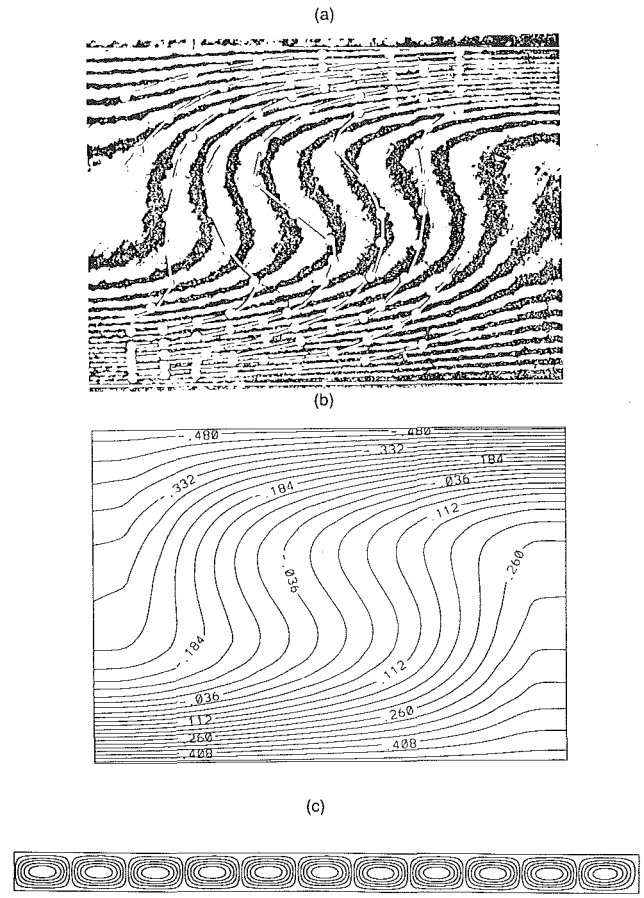

Fig. 2 (*a*)Interferogram for Ra = 6460 and Pr = 6.8 (Farhadieh and Tankin, 1974); (*b*) numerically computed isotherms for Ra = 6460, Pr = 6.8, and grid size of 160 x 20 x 5; (*c*) computed streamlines for Ra = 6460, Pr = 6.8, and a 32:12:1 geometry

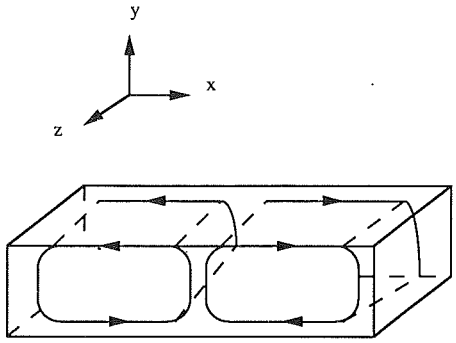

Fig. 3 Schematic diagram of two-roll Rayleigh-Bénard convection

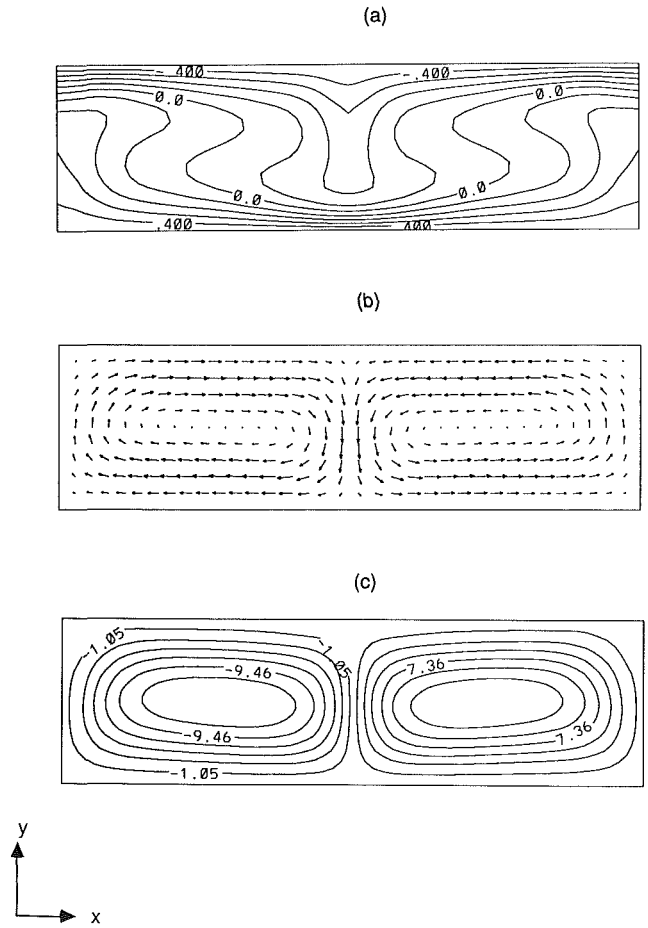

Fig. 4 (*a*) Sectional streamlines, (*b*) velocity vectors, and (*c*) isotherms at vertical section $z = 1.7$; Ra = 20,000; grid size equals 30 x 20 x 30.

due to uncertainties in the boundary conditions. Table 1 shows that the difference between experimental and numerical Nusselt numbers is less than 2 percent for all cases.

Internal checks on the accuracy and consistencies show that the average Nusselt number at the cold and hot wall, which is a test of global energy balance, were equal to within machine precision when steady state was reached. The average mass flux across sections in the cavity was also checked. In most cases it was 10^{-6} or less (should be exactly zero for overall mass balance).

Initial Conditions and Grid Refinement Studies

The flow and temperature fields are complex functions of the governing parameters: the Rayleigh number, Prandtl number, and the aspect ratios. Due to the nonlinearity of the governing equations, multiple solutions are possible for a given point in the parameter space. The solutions depend on the initial conditions. Hence, to get a reproducible and unique set of bifurcations, it is necessary to specify the initial conditions very precisely. In the experiments of GBS and in this paper, the subcritical flow consisting of two symmetric and counter-rotating rolls parallel to the short side shown schematically in Fig. 3 is imposed by prescribing the required wavenumber. The two-cell pattern shown in Fig. 4 is for a Rayleigh number of 20,000. Some more details of the subcritical flow will now be described.

Figures 5 shows the w-velocity contours (z direction) at different vertical planes perpendicular to the roll axis. The w velocity is larger as we move away from the midplane and toward the endwalls. The three dimensionality of the flow is quite self-evident in the form of a weak spiraling motion along the roll axis (Fig. 6). Physically, this is caused by the rigid endwalls interacting with the rotating rolls. This induces an axial flow away from the wall. The same phenomenon was reported by Kessler (1987). Also, the rolls are no longer confined to the vertical plane near the walls (Fig. 6). More details were reported by Mukutmoni and Yang (1991b).

Computations shown are on a $20 \times 20 \times 20$ uniform grid. A grid refinement study (summarized in Table 2) was carried out to gage the adequacy of the grid. The average Nusselt number as well as the maximum velocities and their locations are shown. The fourth column shows near grid-independent values as a result of Richardson extrapolation. These have a sixth-order truncation error. The final column compares the extrapolated numbers with the $20 \times 20 \times 20$ grid calculations.

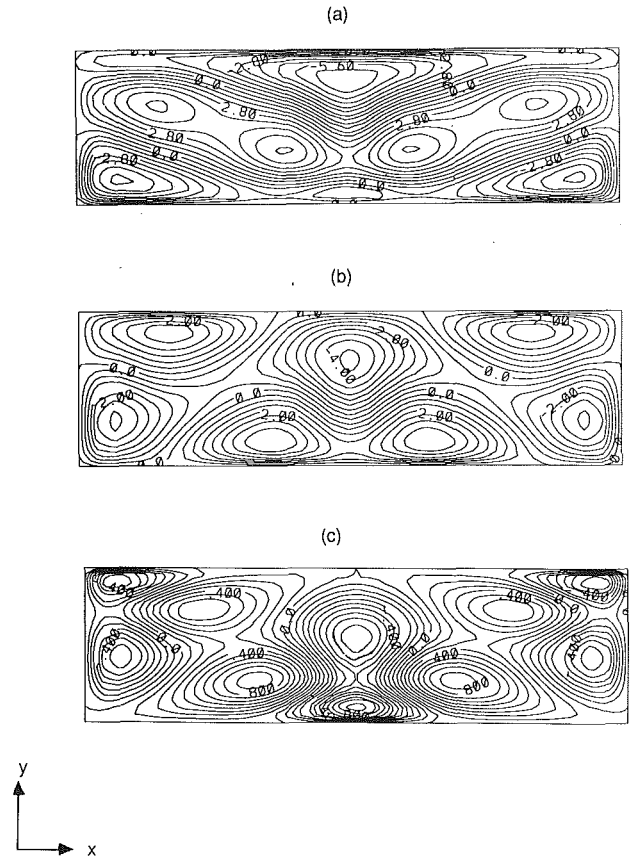

Fig. 5 *w*-velocity contours for Ra = 20,000 and a grid size of 20 × 20 × 20 for different vertical sections: (*a*) $z = 0.24$, (*b*) $z = 0.6$, and (*c*) $z = 0.94$

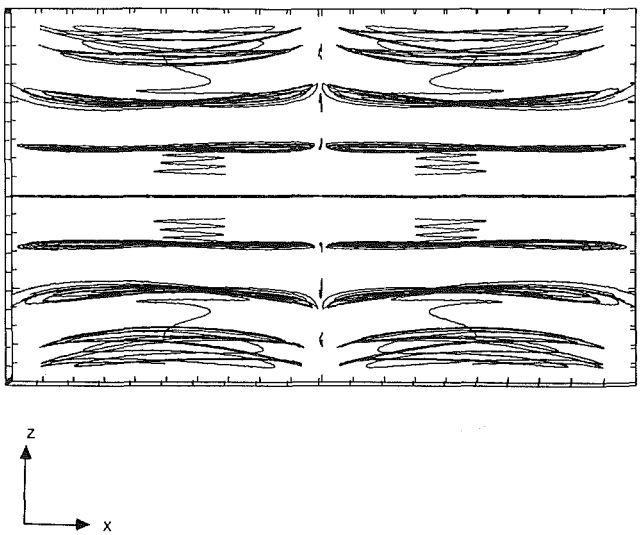

Fig. 6 Top view of pathlines for Ra = 20,000 and a grid size of 20 × 20 × 20

From the grid refinement study it is seen that quantitatively the average Nusselt number differs from the grid-independent value by about 3 percent for a $20 \times 20 \times 20$ grid (Table 2). The most serious resolution problem is with the velocity boundary layer along the vertical walls parallel to the roll axes. Even then, the maximum vertical velocities differ by less than 11 percent from the grid-independent value. As a compromise between computing resources and accuracy, the $20 \times 20 \times 20$ grid was chosen for most of the computations. The flow and temperature fields do have a fourfold symmetry in the horizontal plane (Figs. 4 and 6). These symmetries might not be sustained in the supercritical regime. Symmetry conditions (which would reduce computational expenses considerably) were used a posteriori, i.e., when direct calculations revealed such a symmetry.

Table 2 A grid refinement study for average and local values for subcritical steady two-roll convection ($A_x = 3.5$, $A_z = 2.1$, Pr = 2.5, Ra = 20,000)

Grid size	20×20 ×20	40×40 ×40	80×80 ×80	Projected estimate	Percentage difference
Nu	2.646	2.586	2.571	2.566	3.12
U_{max}	42.75	42.97	43.01	43.02	0.63
x (U_{max})	0.70	0.61	0.66	0.677	-
y (U_{max})	0.82	0.81	0.81	0.804	-
z (U_{max})	0.47	0.50	0.51	0.517	-
V_{max}	46.67	51.05	51.95	52.23	10.64
x (V_{max})	0.09	0.04	0.02	0.014	-
y (V_{max})	0.55	0.52	0.52	0.514	-
z (V_{max})	1.0	1.02	1.04	1.042	-
W_{max}	7.81	8.13	8.18	8.200	4.76
x (W_{max})	0.09	0.04	0.02	0.014	-
y (W_{max})	0.22	0.21	0.21	0.204	-
z (W_{max})	0.315	0.315	0.315	0.315	-

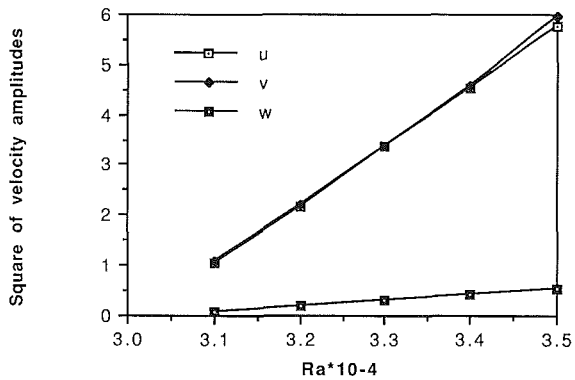

Fig. 7 The square of the amplitude of oscillation of the *u*, *v*, and *w* velocity as a function of the Rayleigh number for a 20 × 20 × 20 grid for the grid location (7, 7, 7)

Oscillatory Convection

With an initial flow configuration consisting of two symmetric rolls, it is now possible to proceed with the calculations in the supercritical region. Unless otherwise stated, all calculations are restricted to a $20 \times 20 \times 20$ grid. The flow field undergoes a bifurcation from steady flow to oscillatory convection. The critical Rayleigh number was estimated by extrapolation. It is almost computationally intractable to calculate it directly, since the transients get larger and larger as one approaches the critical point.

The square of the amplitude of oscillation of the u, v, and w velocity as a function of the Rayleigh number shows a linear variation (Figs. 7 and 9) for two different grids, respectively. This functional dependence is consistent with stability theory (Behringer, 1985), which was derived for RB convection without sidewalls. It is surprising that this is valid even for small boxes. The amplitude of the velocities corresponds to the grid

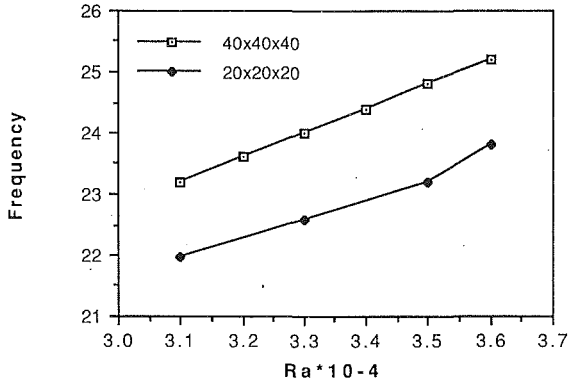

Fig. 8 The fundamental frequency as a function of the Rayleigh number for 20 × 20 × 20 and 40 × 40 × 40 grids

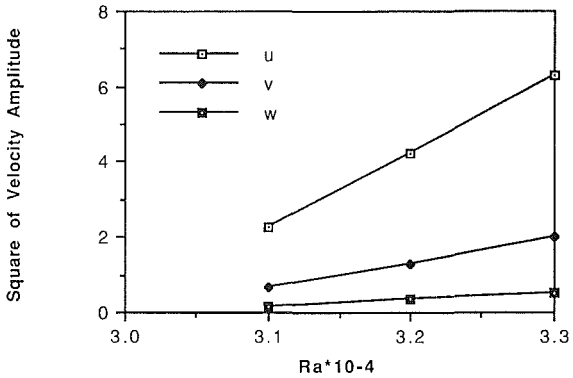

Fig. 9 The square of the amplitude of oscillation of the *u*, *v*, and *w* velocity as a function of the Rayleigh number for a 40 × 40 × 40 grid for the grid location (13, 13, 13)

location (6, 6, 6), which was quite arbitrarily chosen. Since the grid is staggered, *u*, *v*, and *w* locations do not correspond to the same point. Extrapolation to zero velocity amplitude of oscillation (using Figs. 7 and 9) shows that the critical Rayleigh number is around 30,000 (consistent with the experimental results of GBS).

The frequency of oscillation is a weak function of the Rayleigh number (Fig. 8). As the Rayleigh number is increased, the frequency of oscillation also increases (also confirmed by GBS). Figure 8 shows the frequency as a function of the Rayleigh number for two different grids. In both cases, the results of the simulation are consistent with experiments and show the same qualitative behavior. Table 3 compares the numerical and experimental (GBS) frequencies of oscillation for a Rayleigh number of 35,000. The quantitative agreement is quite encouraging (less than 5 percent difference for the fine grid).

In the time-dependent domain the dynamic behavior of the flow field can be conveniently depicted in terms of phase trajectories and the power spectra. The phase trajectory plots the *u* and *v* velocities at a fixed grid location (at (6, 6, 6)). The power spectrum was computed by the fast Fourier transform using the standard Cooley–Tukey algorithm. For most cases, at least 8192 points were sampled for estimating the amplitudes in the frequency domain. The *u*-velocity time series was chosen for calculating the power spectra.

In the experiments that document bifurcations, the Rayleigh number is progressively increased by increasing the temperature difference between the horizontal walls. For a highly nonlinear problem such as this, the bifurcation not only depends on the mean flow but also on the thermal history (Busse, 1978). It is important to known in what steps the Rayleigh number was increased between successive runs. Unfortunately, this

Table 3 Comparison of experimental and numerical frequencies for Ra = 35,000

Grid Size	Non-dimensional Frequency	Dimensional Frequency (Hz)	GBS (Hz)	Percentage Difference
20×20×20	23.8	0.062	0.067	7.46
40×40×40	24.4	0.064	0.067	4.48

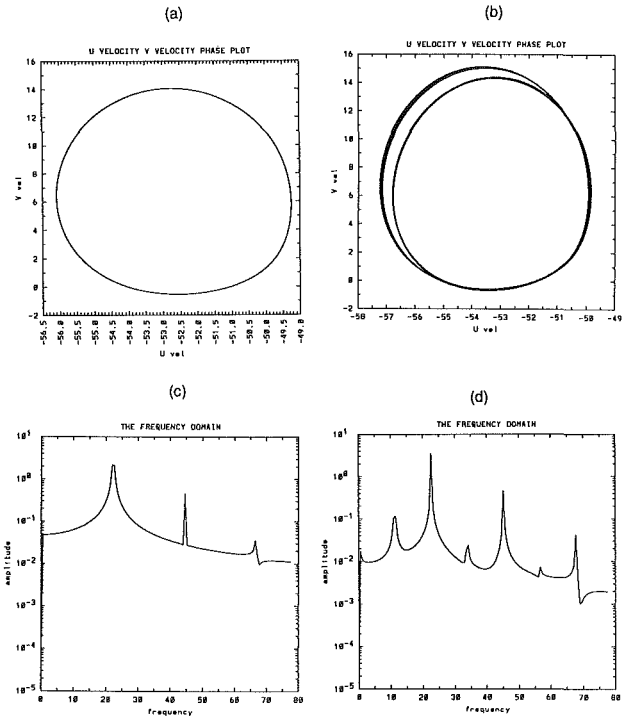

Fig. 10 Phase trajectory for (*a*) Ra = 35,000, (*b*) Ra = 36,000; power spectra for (*c*) Ra = 35,000, (*d*) Ra = 36,000

information was not explicitly stated by GBS. In the set of simulations, Rayleigh number was increased in steps of 2000 or 1000. In some cases sensitivity to step size (or thermal history) was observed. Further details are given by Mukutmoni (1991). The results of the runs for the Rayleigh numbers of 3.5×10^4 and 3.6×10^4 are shown in Fig. 10. The period-doubling bifurcation is clearly shown to occur between 35,000 and 36,000, most probably very close to 36,000, since the subharmonic component is weak and the transients long.

The experimental and numerical bifurcations thus far, summarized in Table 4 show complete qualitative agreement. The critical Rayleigh numbers show good agreement as well (Table 4).

Flow Mechanism

The oscillating temperature field (at Ra = 35,000) as a function of time was looked into by taking eight "snapshots" than span one complete oscillation cycle (Fig. 11). The isotherms are taken in a horizontal plane above the plane of symmetry. Figure 11 indicates that oscillations consist of standing waves propagating along the roll axis. This is consistent with the stability results of Clever and Busse (1974). Accordingly, time dependence is in the form of traveling waves propagating along the axis of the rolls for RB convection with no lateral boundaries. The standing wave observed in the numerical simulation

Table 4 Experimental and computed critical Rayleigh numbers

	First Bifurcation	Second Bifurcation
GBS	29,000	36,700
Present work	30,000	36,000

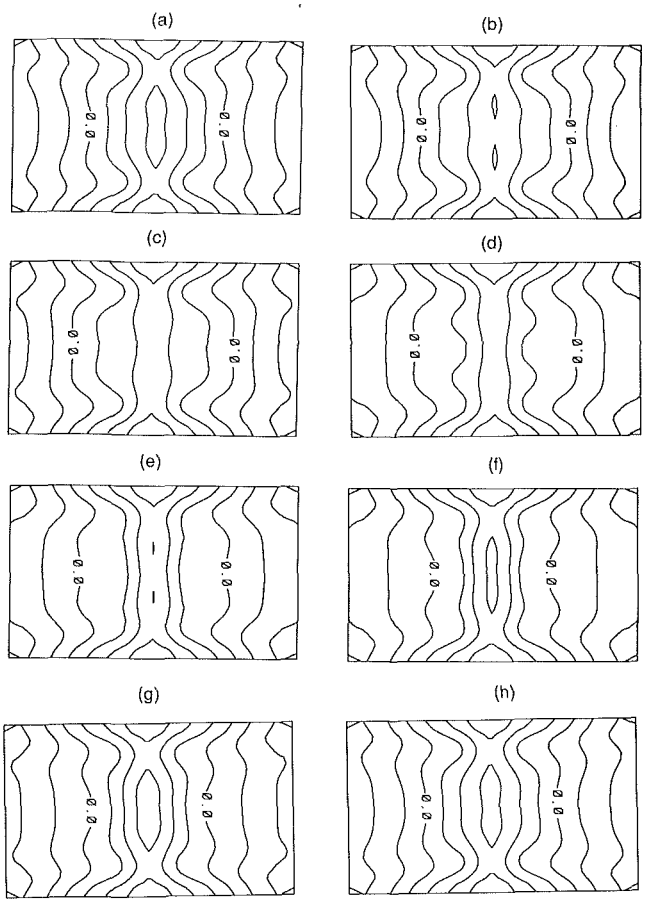

Fig. 11 Instantaneous isotherms over a complete oscillation cycle; Ra = 35,000 at the horizontal section $y = 0.78$

is an obvious extension of their results. As a result of reflection off the walls, a standing wave pattern is created instead of traveling waves in a horizontally unbounded domain.

Contour maps of the amplitude of the subharmonic and fundamental frequency of the temperature oscillations are shown in Figs. 12(*a*) and 12(*b*). The Rayleigh number is 36,000, just beyond the subharmonic bifurcation. The contours correspond to the same horizontal location shown in Fig. 11. The contours show that maximum temperature oscillations occur on either side of the line of symmetry near the core of the cavity away from the walls. A fourfold symmetry is seen in the oscillation amplitude contours for both the fundamental and the subharmonic. This fourfold symmetry is a crucial feature and will be discussed at length in the companion paper. A strict standing wave pattern is not observed. If that was the case, the contours would be horizontal lines and no closed contours would occur.

Structurally, the fundamental and subharmonic share similar features. The maximum amplitude for the subharmonic is close to the spatial location of the fundamental frequency. The same was concluded by GBS in their experiments. The simulation results of Kessler (1987) for RB convection with conducting sidewalls was physically different. In such a case, strong corner eddies develop. Kessler (1987) found that the spatial structure of the subharmonic oscillations was markedly different from the oscillations of the fundamental frequency. The subharmonic component was found to be strongest in those corner eddies.

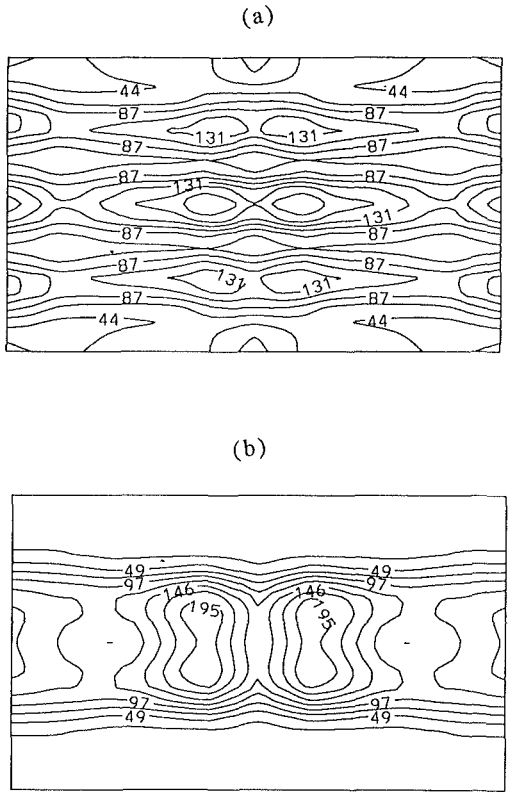

Fig. 12 Temperature oscillation contours at $y = 0.78$ for Ra = 36,000: (*a*) subharmonic; (*b*) harmonic

Subsequent Bifurcations

According to GBS, as the Rayleigh number is increased further a second subharmonic bifurcation was recorded at 46,000. This is shortly followed by a periodic flow at 48,000. Between 46,000 and 48,000 the flow was found to show evidence of quasi-periodicity with a low-frequency component. In contrast, a bifurcation observed in the simulations was somewhat different. The details of the differences and the reason for these observed differences and a complete documentation of the bifurcation sequence until the onset of chaos is described in detail in the companion paper (Mukutmoni and Yang, 1993). It will be shown that the period-doubling route to chaos can indeed be faithfully reproduced if certain symmetry conditions are imposed.

Conclusions

The numerical experiments have shown that RB convection in a small aspect ratio box undergoes a sequence of bifurcation from steady state to oscillatory convection. The code was validated with the experimental results of Farhedieh and Tankin (1974) and good agreement between the two was observed. A grid refinement study revealed that a $20 \times 20 \times 20$ uniform grid was sufficient for our needs. The steady subcritical RB convection consisted of two symmetric counterrotating rolls. The flow field was found to be completely three dimensional, es-

pecially near the end-walls. A weak spiraling motion was observed along the roll axis.

In the time-dependent domain, the qualitative behavior of oscillation amplitudes near the critical Rayleigh number (from steady to unsteady convection) was identical to results from stability theory. The bifurcation sequence observed ($SS \Rightarrow P_1 \Rightarrow P_2$) is identical to the experiments (GBS) until this point. The critical Rayleigh numbers for the two bifurcations and the frequencies of oscillation were in good quantitative agreement with experiments (GBS). The frequency as a function of the Rayleigh number showed the same qualitative behavior as the experiments (GBS).

The nature of the oscillations was determined and found to consist of an approximate standing wave pattern. The maximum temperature oscillations were found to occur around the symmetry line separating the two rolls. The fourfold symmetry in the horizontal plane of the flow and temperature fields was preserved for the temperature oscillation amplitudes as well.

In the second part of the paper, we note that beyond the first subharmonic bifurcation there are qualitative differences between experiments and numerics and probe into the reasons behind these differences.

Acknowledgments

The computations were done on a CONVEX C240 supercomputer and IBM RS/6000 workstation. The support of the Office of University Computing of the University of Notre Dame is greatly appreciated. Some of the calculations were carried out in the Cray Y/MP at the National Center for Supercomputing Applications. Their support under grant No. ATM89007n is graciously acknowledged.

References

Behringer, R. P., 1985, "Rayleigh-Bénard Convection and Turbulence in Liquid Helium," *Reviews of Modern Physics*, Vol. 57, pp. 657-687.

Berge, P., Dubois, M., and Croquette, V., 1982, "Approach to Rayleigh-Bénard Turbulent Convection in Different Geometries," *Convective Transport and Instability Phenomenon*, J. Zierep and H. Oertel, Jr., eds., G. Braun, Karlsruhe, Germany, pp. 123-148.

Busse, F. H., 1978, "Nonlinear Properties of Thermal Convection," *Reports on Progress in Physics*, Vol. 41, pp. 1929-1976.

Clever, R. M., and Busse, F. H., 1974, "Transition to Time Dependent Convection," *Journal of Fluid Mechanics*, Vol. 65, pp. 625-645.

Farhadieh, R., and Tankin, R. S., 1974, "Interferometric Study of Two-Dimensional Bénard Convection Cells," *Journal of Fluid Mechanics*, Vol. 66, pp. 739-752.

Feigenbaum, M. J., 1978, "Quantitative Universality for a Class of Nonlinear Transformations," *Journal of Statistical Physics*, Vol. 19, pp. 25-52.

Gollub, J. P., and Benson, S. V., 1980, "Many Routes to Turbulent Convection," *Journal of Fluid Mechanics*, Vol. 100, pp. 449-470.

Gollub, J. P., Benson, S. V., and Steinman, J. F., 1980, "A Subharmonic Route to Turbulent Convection," *Nonlinear Dynamics*, H. G. Helleman, ed., New York Academy of Sciences, pp. 22-27.

Gray, D. D., and Giorgini, A., 1976, "The Validity of the Boussinesq Approximation for Liquids and Gases," *International Journal of Heat and Mass Transfer*, Vol. 19, pp. 545-551.

Kessler, R., 1987, "Nonlinear Transition in Three-Dimensional Convection," *Journal of Fluid Mechanics*, Vol. 174, pp. 357-379.

Leonard, B. P., 1983, "A Convectively Stable, Third-Order Accurate Finite-Difference Method for Steady Two-Dimensional Flow and Heat Transfer," *Numerical Properties and Methodologies in Heat Transfer*, T. M. Shih, ed., Hemisphere Publishing Corporation, Washington, DC, pp. 211-226.

Maurer, J., and Libchaber, A., 1979, "Rayleigh-Bénard Experiment in Liquid Helium: Frequency Locking and the Onset of Turbulence," *Journal of Physics Letters*, Vol. 40, pp. L419-423.

Mukutmoni, D., 1991, "Transitions and Bifurcations in Rayleigh-Bénard Convection in a Small Aspect Ratio Box," Ph.D. dissertation, Department of Aerospace and Mechanical Engineering, University of Notre Dame, Notre Dame, IN.

Mukutmoni, D., and Yang, K. T., 1991a, "Flow Transitions in a Three-Dimensional Rectangular Enclosure Heated From Below," *ASME/JSME Thermal Engineering Proceedings*, Vol. 1, pp. 77-82.

Mukutmoni, D., and Yang, K. T., 1991b, "Transition to Oscillatory Flow in Rayleigh-Bénard Convection in a Three-Dimensional Box," ASME Paper No. 91-HT-10.

Mukutmoni, D., and Yang, K. T., 1993, "Rayleigh-Bénard Convection in a Small Aspect Ratio Enclosure: Part II—Bifurcation to Chaos," ASME JOURNAL OF HEAT TRANSFER, Vol. 115, this issue, pp. 367-376.

Patankar, S. V., 1980, *Numerical Heat Transfer and Fluid Flow*, Hemisphere Publishing Corporation, Washington, DC.

Van Doormaal, J. P., and Raithby, G. D., 1984, "Enhancements of the Simple Method for Predicting Incompressible Fluid Flows," *Numerical Heat Transfer*, Vol. 17, pp. 147-163.

Yang, K. T., 1988, "Transitions and Bifurcations in Laminar Buoyant Flows in Confined Enclosures," ASME JOURNAL OF HEAT TRANSFER, Vol. 110, pp. 1191-1204.

Rayleigh-Bénard Convection in a Small Aspect Ratio Enclosure: Part II—Bifurcation to Chaos

D. Mukutmoni

K. T. Yang

Department of Aerospace and Mechanical Engineering, University of Notre Dame, Notre Dame, IN 46556

The present numerical study documents bifurcation sequences for Rayleigh-Bénard convection in a rectangular enclosure with insulated sidewalls. The aspect ratios are 3.5 and 2.1 and the Boussinesq fluid is water (average temperature of 70°C) with a Prandtl number of 2.5. The transition to chaos observed in the simulations and experiments is similar to the period-doubling (Feigenbaum) route to chaos. However, special symmetry conditions must be imposed numerically, otherwise the route to chaos is different (Ruelle-Takens-Newhouse). In particular, the Feigenbaum route to chaos can be realized only if the oscillating velocity and temperature field preserves the fourfold symmetry that is observed in the mean flow in the horizontal plane.

Introduction

In recent years there has been mounting evidence from various disciplines that all nonlinear dynamic systems share some very universal features; namely that when some control parameter is varied the system undergoes a series of bifurcations that ultimately leads to chaos. One such system that is governed by coupled nonlinear partial differential equations, Rayleigh-Bénard convection, is the subject of the present paper.

The Rayleigh-Bénard (henceforth called RB) system has been of particular interest to researchers because of its relevance to the problem of transition, i.e., the mechanism by which laminar flow becomes turbulent. The RB system has been studied in the past to see whether it behaves like other simpler dynamic systems. The hope is that additional insights could be obtained of this complicated phenomenon by linking it to the advances that have already been made in dynamic system theory and chaos. One such dynamic behavior, the period-doubling (Feigenbaum) route to chaos that occurs in simple dynamic systems, has been found to occur in RB convection as well (Gollub et al., 1980) and in particular for small aspect ratio boxes.

First, it must be noted that the period-doubling route to chaos documented experimentally does not exactly match the sequence of bifurcations observed in iterated noninvertible maps (Feigenbaum, 1978). In the case of the iterated maps the bifurcation sequence consists of an infinite sequence of subharmonic bifurcations until the onset of chaos. This is followed by windows of periodicity beyond chaos. The experimental documentations have been somewhat different. Gollub et al. (1980) (henceforth referred to as GBS) recorded two subharmonic bifurcations before chaos set in. Chaos was preceded by quasi-periodic flow consisting of a low-frequency component.

Libchaber and Maurer (1981) in their experiments with liquid helium observed four successive period-doubling bifurcations. This was followed by a low-frequency component in the spectrum and chaos soon after. Windows of periodicity after the onset of chaos was observed for higher Rayleigh numbers. Nevertheless, the bifurcations sometimes did not result in halving of the frequency. The frequency observed at times was one-third or one-fifth.

In an experiment with mercury, Libchaber et al. (1982) observed a period-doubling sequence for a four-roll pattern. Five period-doubling bifurcations were recorded. The inverse cascade after chaos was observed.The low-frequency quasi-periodic flow observed by others did not occur. Experimentally, it was necessary to stabilize the rolls by subjecting the fluid to a magnetic field parallel to the roll axis.

It is therefore clear that the period-doubling route to chaos

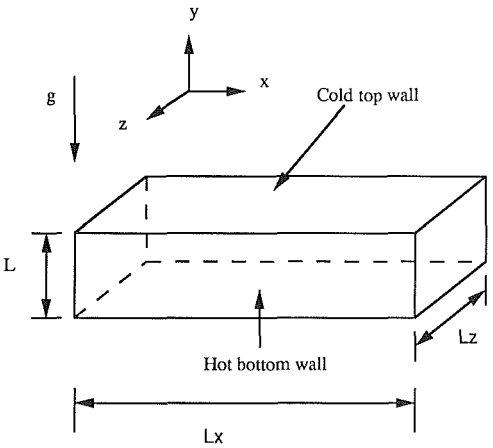

Fig. 1 Geometry of the enclosure

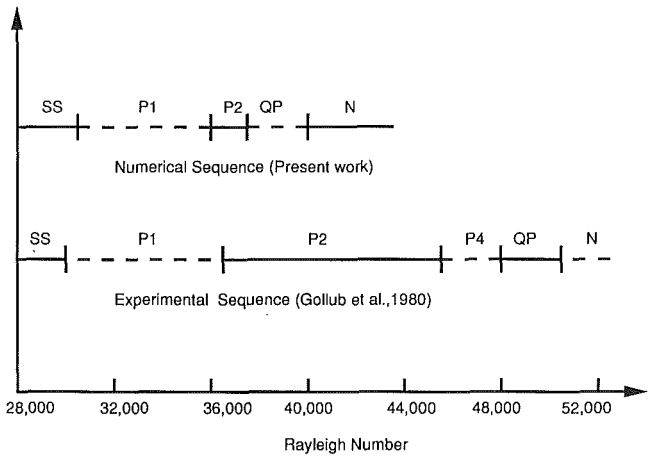

Fig. 2 Bifurcation sequence observed experimentally and numerically. The parameters are $A_x = 3.5$, $A_z = 2.1$, and $Pr = 2.5$. SS = steady state; P_1 = periodic; P_2 = periodic after one period-doubling; P_4 = periodic after two period-doublings; N = chaotic; QP = quasi-periodic

Contributed by the Heat Transfer Division for publication in the JOURNAL OF HEAT TRANSFER. Manuscript received by the Heat Transfer Division August 1991; revision received October 1992. Keywords: Enclosure Flows, Flow Instability, Natural Convection. Associate Technical Editor: J. R. Lloyd.

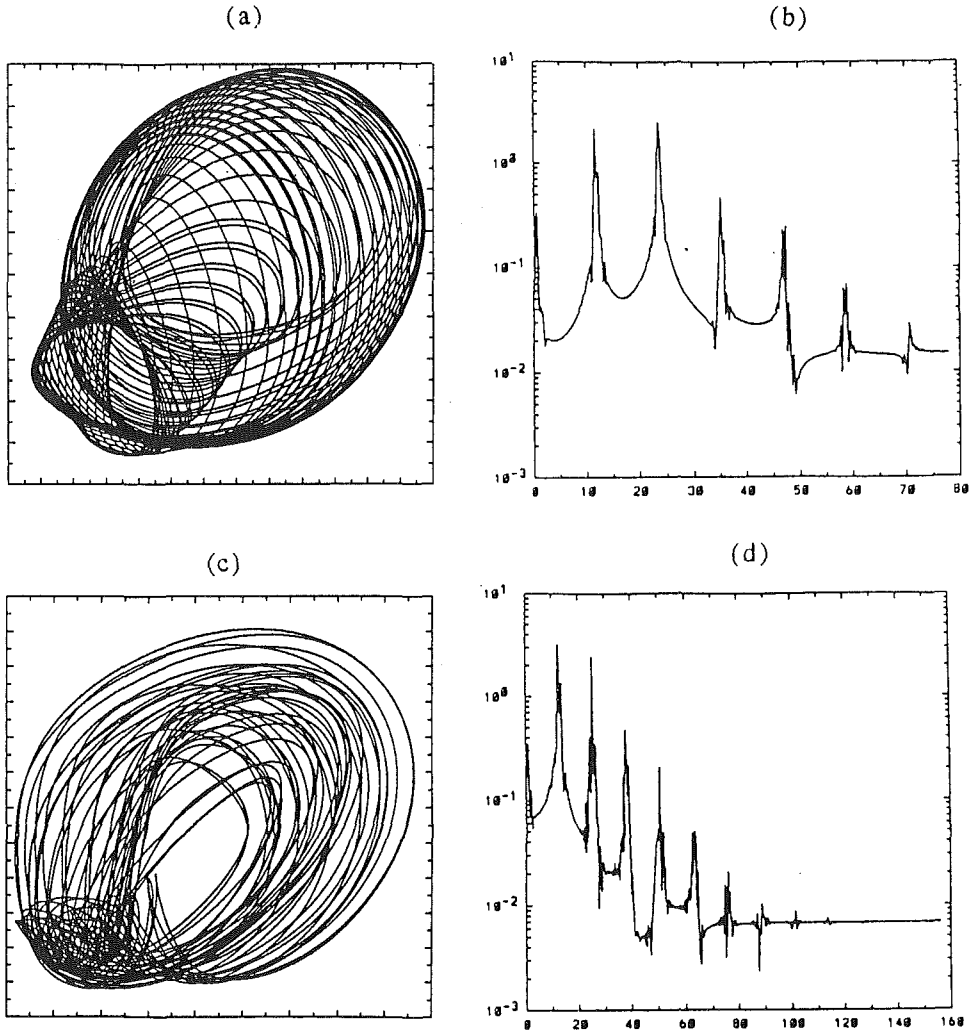

Fig. 3 Ra = 39,000: (*a*) phase trajectory, (*b*) spectral amplitudes; Ra = 41,000; (*c*) phase trajectory, (*d*) spectral amplitudes

is not quite faithfully reproduced. Even such a limited agreement is quite remarkable. It is seen that the RB system with its potentially infinite number of degrees of freedom behaves similar to a one-dimensional iterated map system. The principal difference is the presence of low-frequency quasi-periodicity in the spectrum that terminates the period-doubling cascade.

The numerical investigation of the companion paper (Mukutmoni and Yang, 1993) is continued here. The paper begins with a brief description of the formulation (same as the companion paper). This is followed by a study of the bifurcation sequence until the onset of chaos. The formulation is then changed to one where a fourfold symmetry is imposed. The bifurcation sequence is then studied. The main conclusions are then stated.

Nomenclature

A_x = L_x/L = aspect ratio in the x direction
A_z = L_z/L = aspect ratio in the z direction
g = acceleration due to gravity, m^2/s
L = height of the enclosure, m
L_x = dimension of enclosure in x direction, m
L_z = dimension of enclosure in z direction, m
Nu = Nusselt number averaged over a horizontal cross section
Pr = ν/α = Prandtl number
Ra = $g\beta\Delta TL^3/\nu\alpha$ = Rayleigh number
t = nondimensional time
T = nondimensional temperature
T_C = cold wall temperature, °C
T_H = hot wall temperature, °C
ΔT = temperature difference = $T_H - T_C$, °C
u = nondimensional x-direction velocity
v = nondimensional y-direction velocity
w = nondimensional z-direction velocity
x = nondimensional horizontal spatial coordinate
y = nondimensional vertical spatial coordinate
z = nondimensional spatial coordinate in the direction of depth
α = thermal diffusivity, m^2/s
β = coefficient of volume expansion, 1/K
λ = bifurcation parameter
ν = dynamic viscosity, m^2/s
ρ = density, kg/m^3

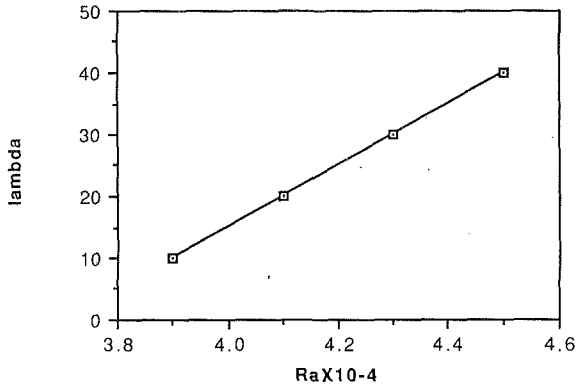

Fig. 4 Maximum Lyapunov exponent as a function of the Rayleigh number

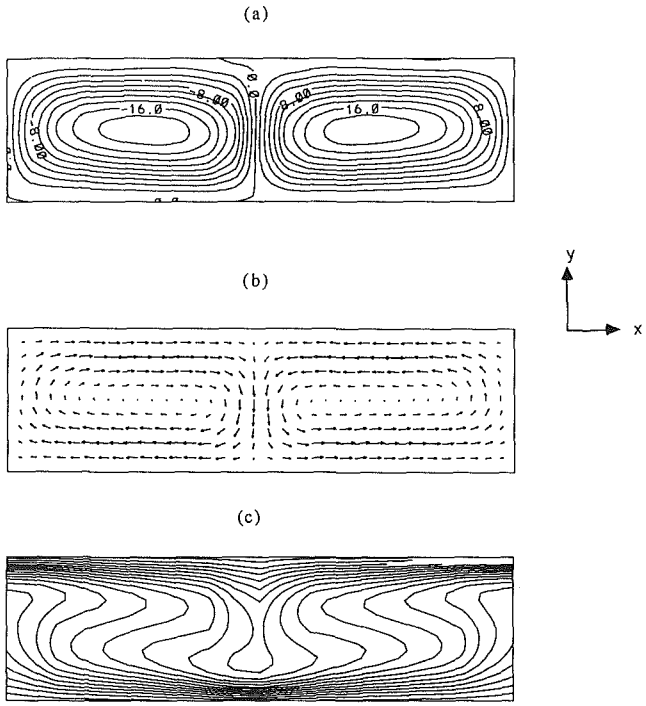

Fig. 5 Mean velocity and temperature fields for Ra = 37,000: (*a*) streamlines, (*b*) velocity vectors, (*c*) isotherms

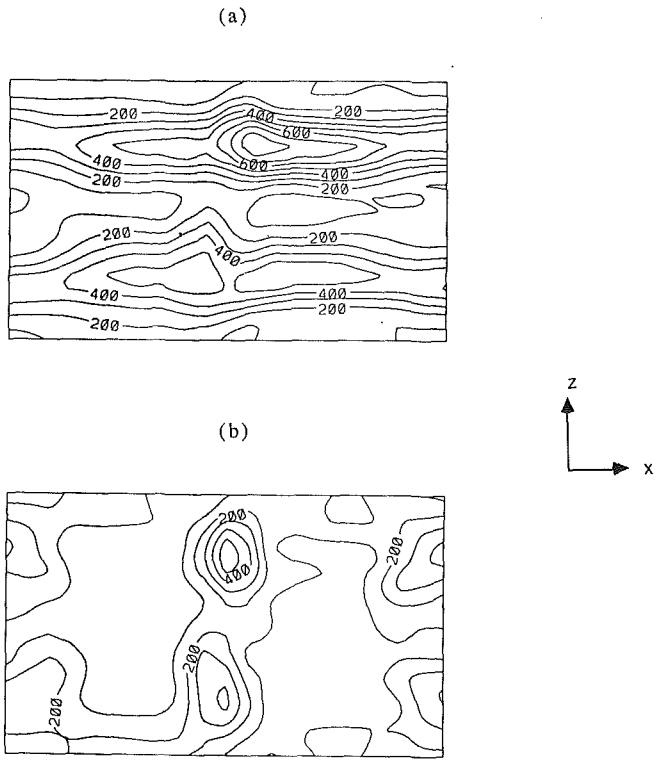

Fig. 6 Contours for temperature oscillation amplitudes in a horizontal section: (*a*) $y = 0.78$, (*b*) $y = 0.6$

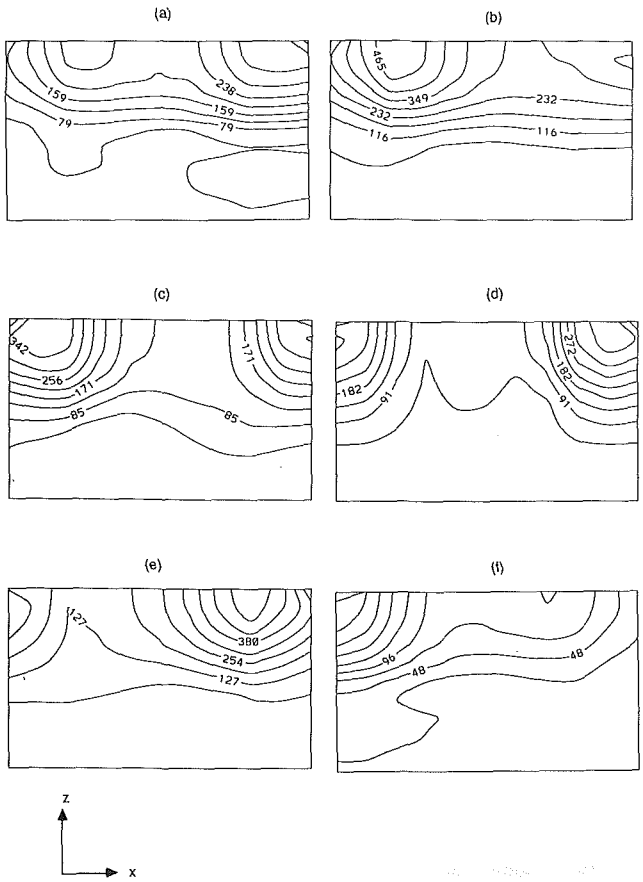

Fig. 7 Spectral amplitudes for different horizontal sections: (*a*) $y = 0.075$, (*b*) $y = 0.225$, (*c*) $y = 0.3$, (*d*) $y = 0.375$, (*e*) $y = 0.45$, (*f*) $y = 0.525$

Formulation

The geometry of the enclosure is shown in Fig. 1. The vertical walls are all adiabatic. The bottom wall is heated and the top wall is cooled, both isothermally. The fluid is Boussinesq, i.e., all transport properties of the fluid are constant with the exception of the buoyancy term in the momentum equations, which is linearized. The aspect ratios of 3.5 and 2.1 and the Prandtl number of 2.5 are the same as the parameters given by GBS. The rest of the details on the formulation, validation, and grid refinement are given in the companion paper (Mukutmoni and Yang, 1993) and will not be repeated. All simulations were done on a $20 \times 20 \times 20$ uniform grid unless otherwise stated.

Bifurcation Sequence

The bifurcation sequence observed numerically and documented experimentally until the onset of chaos is shown in Fig. 2. Experimentally (GBS), a second subharmonic bifurcation was observed close to Ra = 46,000. The flow becomes quasi-periodic (with a low-frequency component) soon after and chaotic at Ra = 48,000. The bifurcation observed in the

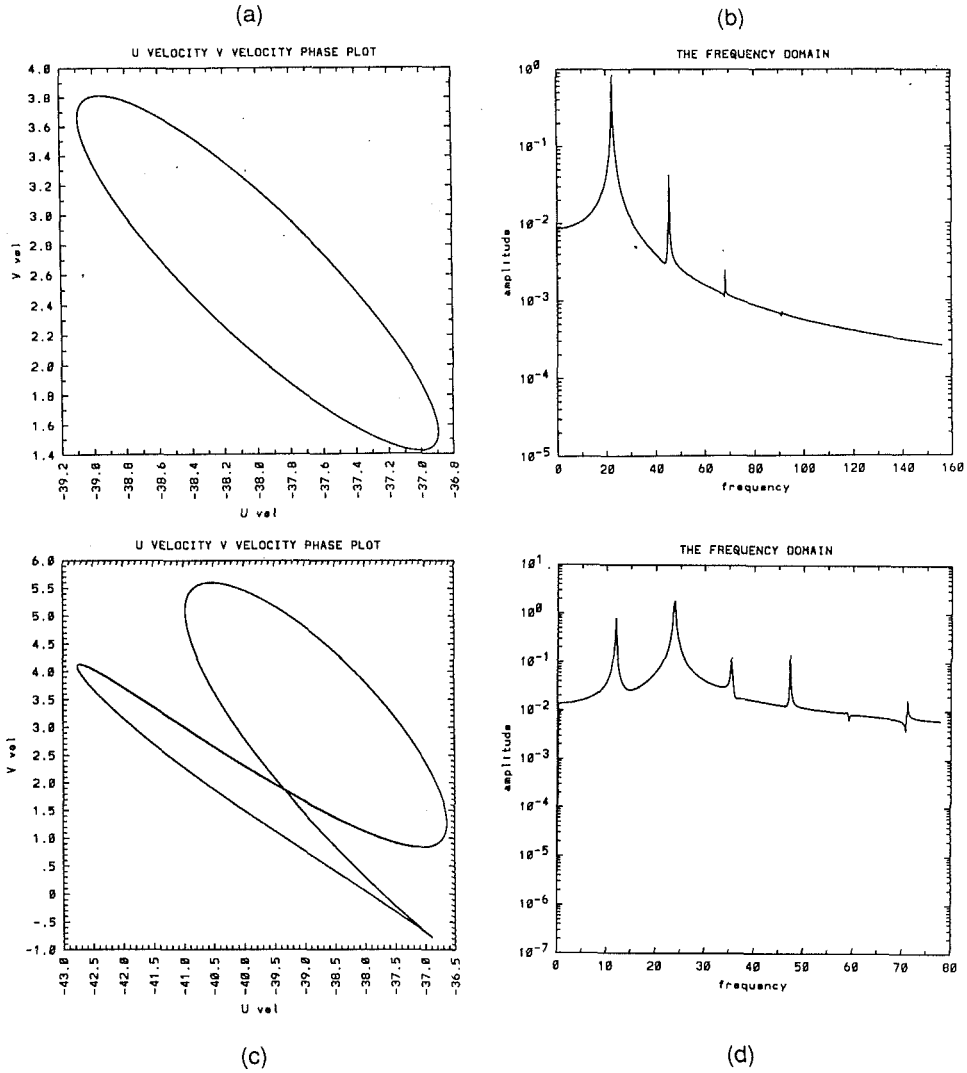

Fig. 8 (*a*) Phase trajectory, (*b*) spectral amplitudes for Ra = 35,000; (*c*) phase trajectory, (*d*) spectral amplitudes for Ra = 36,000

simulations (Fig. 2) did not record any further subharmonic bifurcation. Flow was quasi-periodic between 36,000 and 37,000 and chaotic between 39,000 and 41,000 (Fig. 3).

Chaos was determined by calculating the largest Liapunov exponent. The largest Liapunov exponent was estimated using a one-dimensional time series. The algorithm and implementation details are given by Wolf et al. (1985). In this case, the u-velocity signal was used as the time series. A positive Liapunov exponent implies chaos.

The largest exponents calculated (Fig. 4) were all positive and were found to increase with an increase in Rayleigh number. Unfortunately, the exponents themselves cannot be estimated very accurately using this technique. Errors up to 40 percent are not unusual (Wolf et al., 1985). A positive exponent could very well be zero, in which case the flow is not chaotic. Additional information is necessary to interpret the exponents. An inspection of the phase trajectory for Ra = 39,000 (Fig. 3(*a*)) shows that it is a projection of a torus, implying that the dynamics is quasi-periodic. On the other hand, the dynamics for Ra = 41,000 (Fig. 3(*c*)) is irregular. The Liapunov exponents must then be "calibrated" accordingly. Any positive value for the exponent greater than the one corresponding to 39,000 is taken to be positive and hence chaotic.

Thus, it is estimated that flow became chaotic between 39,000 and 41,000. The route to chaos is the Ruelle–Takens–Newhouse scenario ($P \Rightarrow QP \Rightarrow N$).

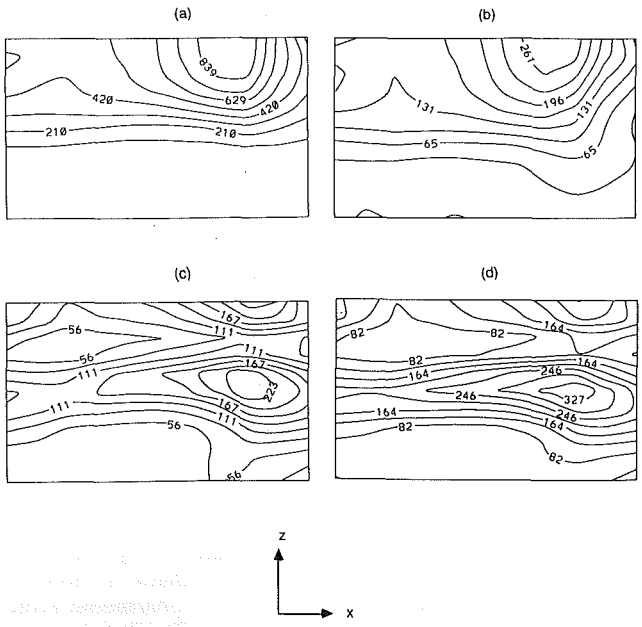

Fig. 9 Oscillation contours for the fundamental frequency: (*a*) Ra = 36,000, (*b*) Ra = 42,000; oscillation contours for the subharmonic: (*c*) Ra = 36,000, (*d*) Ra = 42,000

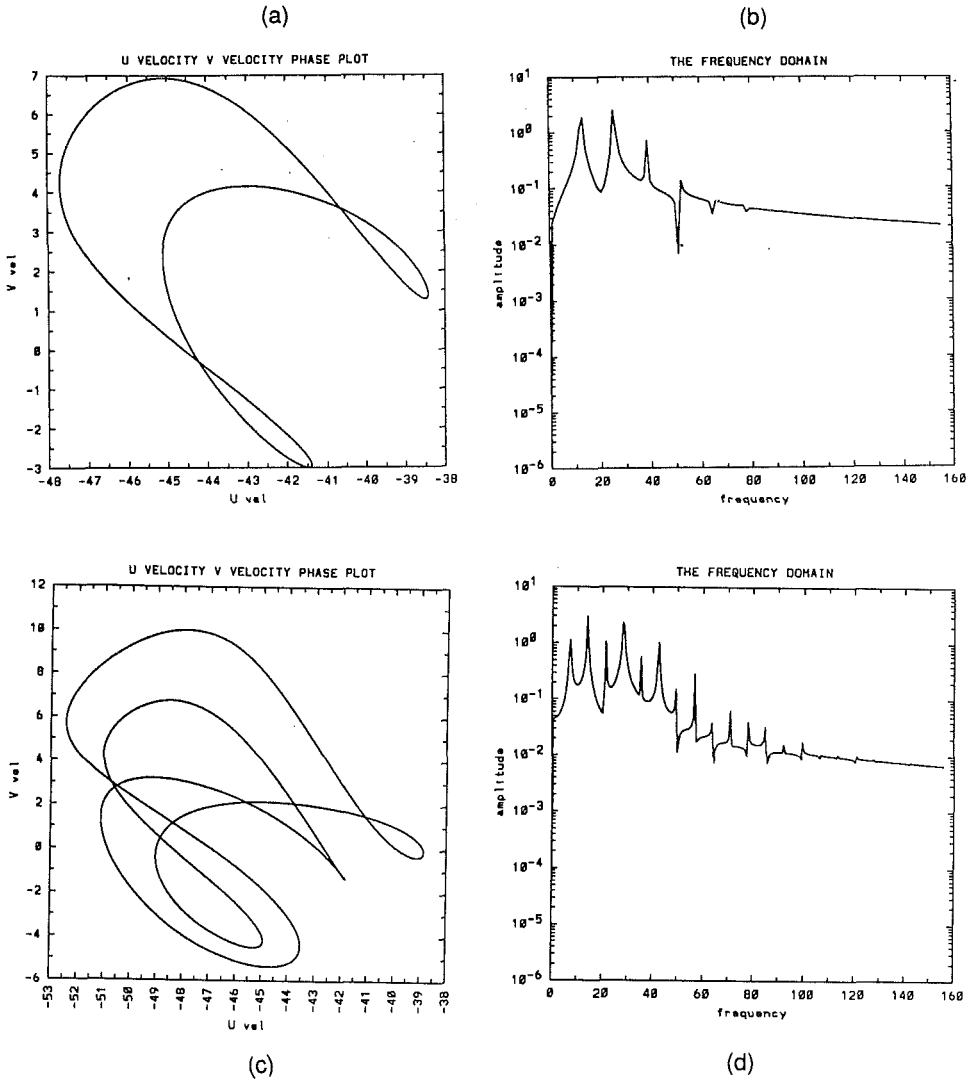

Fig. 10 (*a*) Phase trajectory, (*b*) spectral amplitudes for Ra = 47,000; (*c*) phase trajectory, (*d*) spectral amplitudes for Ra = 48,000

The sequence of bifurcations observed in the simulations was not unique. They were sensitive to the step changes in the Rayleigh number. If the Rayleigh number was increased in steps of 2000, the sequence observed was different. The bifurcation sequence presented in this and the companion paper is for a step change of 1000. Further details of this sensitivity are given by Mukutmoni (1991). The low-frequency noise in some cases was found to occur immediately after bifurcation to periodic flow for other step changes.

The premature incidence of the low frequency is not entirely unexpected. This has been noted in experiments. GBS observed, "Relatively small variations in the geometry, Prandtl number, or mean flow caused a second incommensurate frequency to appear after at most one subharmonic bifurcation. It thus seems probable that the subharmonic route to turbulence is but one of several distinct paths, and may not even be the most common one." The low-frequency case at a Rayleigh number of 37,000 merits a more detailed study.

Accordingly, the mean velocity and temperature field was looked into (Fig. 5). Note that in contrast to the perfectly symmetric counterrotating rolls of the subcritical regime, some degree of asymmetry was observed. The roll on the left is a little shorter than the roll on the right (Fig. 5(*c*)). The spatial distribution of the low-frequency temperature oscillations for the same case was looked into at two different horizontal sections (Fig. 6). Figure 6 shows that the maximum oscillations of the low frequency occur near the plane of symmetry separating the rolls. The low frequency is thus associated with the slow expansion and contraction of the rolls themselves.

From the results of the simulation it appears that the introduction of this low frequency, which physically corresponds to the slight mismatch between the rolls, can be delayed if the increase in heating (or Rayleigh number) is done quasi-statically or in infinitesimal steps. However, it cannot be avoided.

Simulations With Symmetry

The reasons for the observed differences between the results of the simulation and experiments will now be discussed. To reiterate, GBS reported that the low frequency in the flow showed up after two subharmonic bifurcations as the Rayleigh number was progressively increased. Also, when the sequence was traversed backwards, by starting from the maximum and reducing the temperature difference, the low-frequency noise appeared quite abruptly at 46,000. In the companion paper (Mukutmoni and Yang, 1993) it was noted that the subcritical steady convection showed a fourfold symmetry in the horizontal plane. The temperature oscillation amplitudes were also found to share the same symmetry. It is this very symmetry that is lost when the low-frequency noise sets in. It therefore

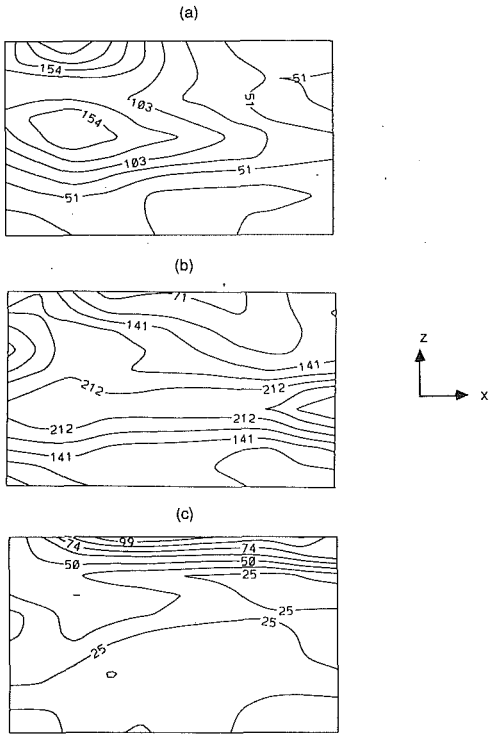

Fig. 11 Oscillation contours for Ra = 50,000: (*a*) fundamental frequency (*f*), (*b*) frequency of *f*/2, (*c*) frequency of *f*/4

seems reasonable that if this symmetry is imposed by any means, the low-frequency modulation can be avoided altogether. In the next section, the formulation and results of the calculation when such a symmetry is imposed are presented.

Formulation With Symmetry

The formulation is identical to the case without symmetry except for the boundary conditions given below:

$$x=\frac{A_x}{2},\quad 0\le z\le\frac{A_z}{2},\quad 0\le y\le 1\quad u=v=w=0,\ \frac{\partial T}{\partial x}=0 \tag{1}$$

$$x=0;\quad 0\le z\le\frac{A_z}{2},\quad 0\le y\le 1\quad u=\frac{\partial v}{\partial x}=\frac{\partial w}{\partial x}=0,\ \frac{\partial T}{\partial x}=0 \tag{2}$$

$$z=\frac{A_z}{2};\quad 0\le x\le\frac{A_x}{2};\quad 0\le y\le 1\quad u=v=w=0,\ \frac{\partial T}{\partial z}=0 \tag{3}$$

$$z=0;\quad 0\le x\le\frac{A_x}{2};\quad 0\le y\le 1\quad \frac{\partial u}{\partial z}=\frac{\partial v}{\partial z}=w=0,\ \frac{\partial T}{\partial z}=0 \tag{4}$$

$$y=0,\ 1;\quad 0\le x\le\frac{A_x}{2};\ 0\le z\le\frac{A_z}{2};\ u=v=w=0,$$

$$T=0.5-y \tag{5}$$

The computational domain is now reduced by a factor of four as a result of the symmetry imposed on two vertical walls. The grid used for these calculations with symmetry is $10\times20\times10$. The resolution is the same as a $20\times20\times20$ grid, which was judged adequate from a grid refinement analysis carried out by Mukutmoni and Yang (1993). The experiments of Libchaber

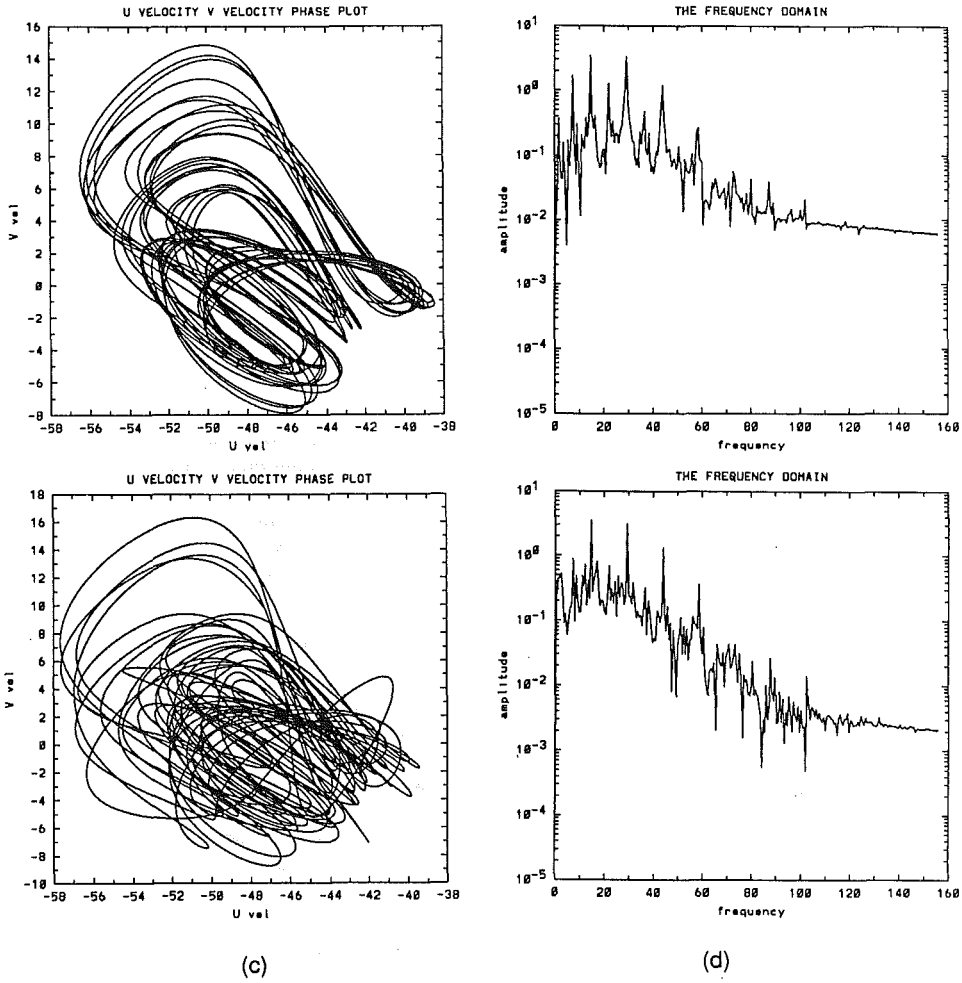

Fig. 12 (*a*) Phase trajectory, (*b*) spectral amplitudes for Ra = 51,500; (*c*) phase trajectory, (*d*) spectral amplitudes for Ra = 52,000

et al. (1982) are quite suggestive. By forcibly aligning the rolls using magnetic fields, the low-frequency noise was eliminated and this made the Feigenbaum scenario possible. The following looks into this possibility with the help of numerically imposed symmetries.

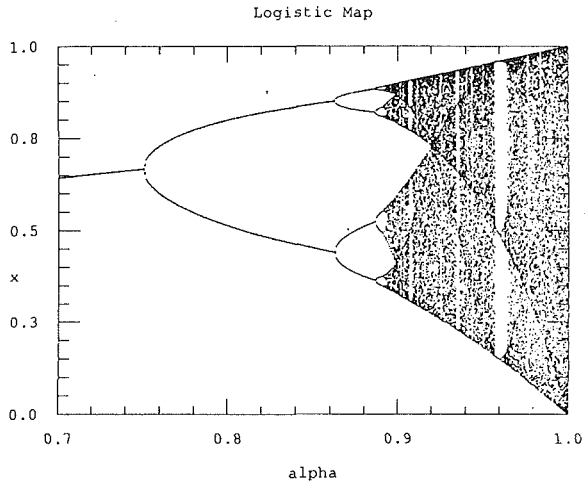

Fig. 13 Bifurcation diagram for the quadratic map as given by Parker and Chua (1988)

Results and Discussion

The results of the simulation show that the bifurcation sequence is unchanged until the first subharmonic bifurcation. The first bifurcation to time-dependent flow occurred at a Rayleigh number of 30,000 (by extrapolation). The first period-doubling bifurcation occurred between 35,000 and 36,000. Unlike the case without symmetry, no sensitivity to step size was observed.

Unless otherwise stated, the phase trajectories are between the u and v velocity at the grid location (2, 5, 2). This corresponds to the spatial location of (0.35, 0.225, 0.158) for the u velocity and (0.52, 0.2, 0.158) for the v velocity due to the staggered nature of the grid. The oscillation contours are for the horizontal section $y = 0.78$ and correspond to the temperature field. The spectral amplitudes correspond to the u velocity.

Figure 7 shows the spectral amplitude of the fundamental frequency (about 23 in nondimensional units) for different horizontal sections. Figure 7(a) corresponds to the horizontal section $y = 0.075$. The other sections are in intervals of 0.15 in increasing order. The contours have been scaled by a factor of 10^4. The section shown represents only one-fourth of the geometry. The plane of symmetry is represented by the top and left line of the rectangle. The oscillations have the following features:

1 The oscillations are the highest in the core region and decays toward the walls. The nature of the oscillations are not

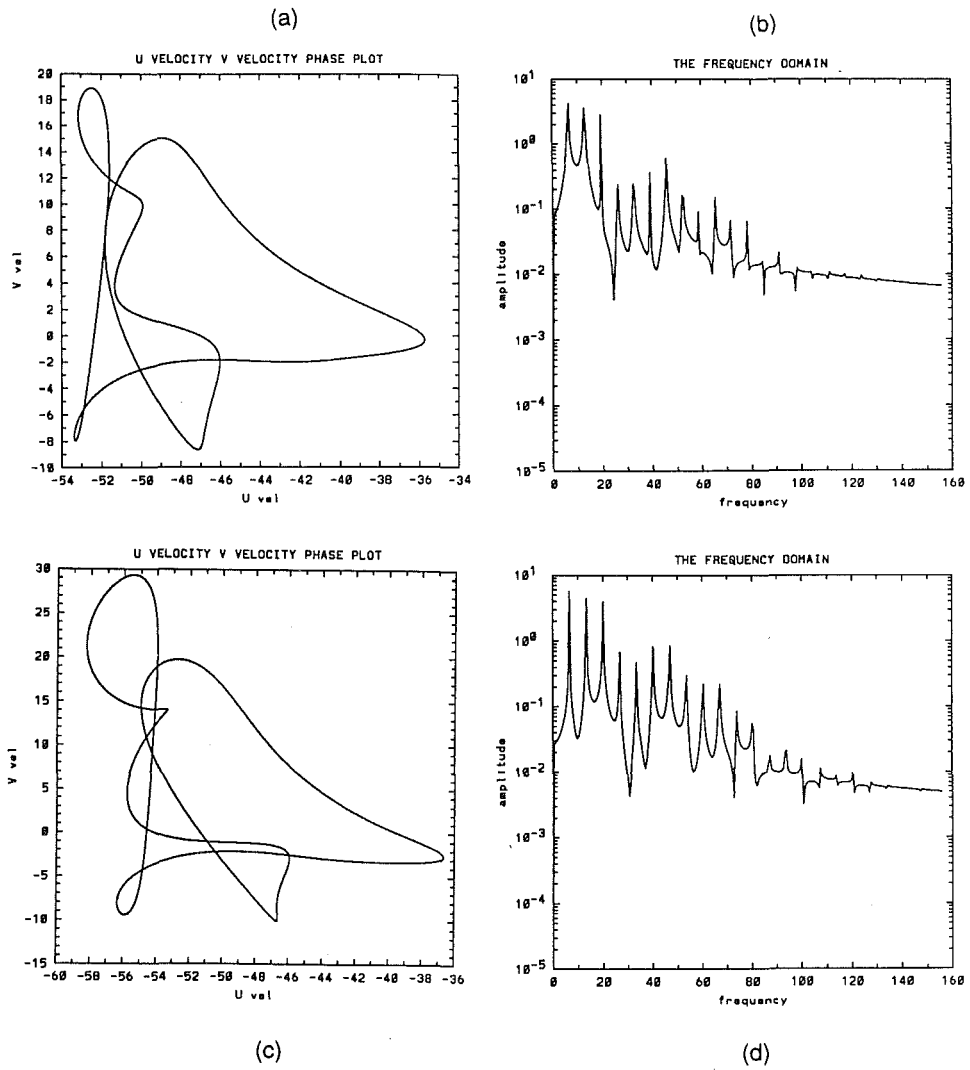

Fig. 14 (a) Phase trajectory, (b) spectral amplitudes for Ra = 52,500; (c) phase trajectory, (d) spectral amplitudes for Ra = 57,000

exactly standing waves. If that was so, the oscillation contours would have been parallel horizontal lines. The oscillating temperature field is more complicated. The horizontal lines are superposed with closed contours, which can be described as sources or focal points of oscillation.

2 The maximum oscillations or focal points are close to the vertical line of symmetry near the middle of the cell where the flow is descending and far from or near the walls depending on the horizontal cross section.

First Subharmonic Bifurcation. Between Rayleigh numbers of 35,000 and 36,000, a period-doubling bifurcation occurs (Fig. 8). As a result, a frequency with half the fundamental is added to the spectrum. Linear combinations of the fundamental and its subharmonic (Fig. 8(*d*)) were observed. The phase trajectory is typically folded as well after the bifurcation (Fig. 8(*c*)). Note that the experimentally observed bifurcation occurred between 36,000 and 37,000 (GBS).

As a result of the bifurcation, the spatial distribution of the fundamental is almost unchanged (Fig. 9(*a*)). The spatial distribution of the subharmonic is more complicated. The maximum of the subharmonic at the given section ($y=0.78$) is neither near the core nor near the walls, but rather somewhere in between (Fig. 9(*c*)). As the Rayleigh number is increased, the subharmonics get stronger at the expense of the harmonic, but the spatial structure of the harmonic and the subharmonic is unchanged (Figs. 9(*b*) and 9(*d*)).

Subsequent Bifurcations. The second subharmonic bifurcation was found to occur between a Rayleigh number of 47,000 and 48,000. This is close to the experimentally determined critical Rayleigh number of 46,000 for the second subharmonic bifurcation (GBS). A second folding is observed in the trajectories (Fig. 10(*c*)) accompanied by another subharmonic frequency (Fig. 10(*d*)).

Unlike the previous bifurcations, the spatial structure of the fundamental (*f*) undergoes dramatic changes. The maximum amplitude is now localized near the plane of symmetry on the left (Fig. 11(*a*)). The oscillations are lower near the vertical walls perpendicular to the roll axis (horizontal lower line in Fig. 11(*b*)), thus preserving the essential standing wave pattern. The first subharmonic ($f/2$) has its maximum near the walls, in contrast to the fundamental. The second subharmonic (Fig. 11(*c*)) is the weakest of the three. These oscillations are closest to the standing wave pattern, with the maximum occurring at the vertical plane of symmetry perpendicular to the rolls and gradually tapering off near the walls (Fig. 11(*c*)).

Subsequent period-doubling bifurcations were also documented. Qualitatively, the interval between subsequent period-doubling bifurcations decreased. This is exactly what was observed in the one-dimensional quadratic map. Feigenbaum (1978) determined that $(\lambda_n-\lambda_{n-1})/(\lambda_{n+1}-\lambda_n)=4.669201\ldots$ in the limit when n tends to infinity. It becomes increasingly difficult to pinpoint subsequent bifurcations since the bifurcation points get closer and closer. The

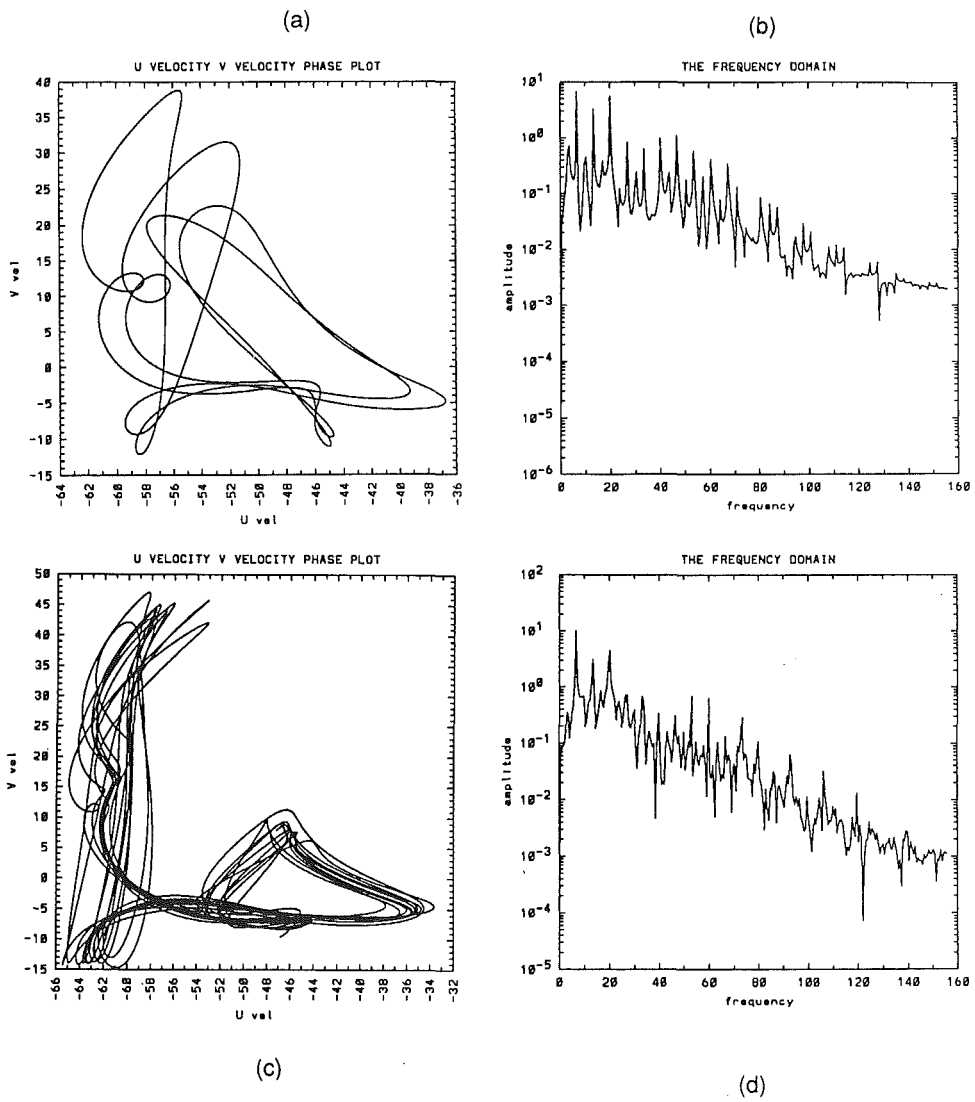

Fig. 15 (*a*) Phase trajectory, (*b*) spectral amplitudes for Ra = 60,000; (*c*) phase trajectory, (*d*) spectral amplitudes for Ra = 65,000

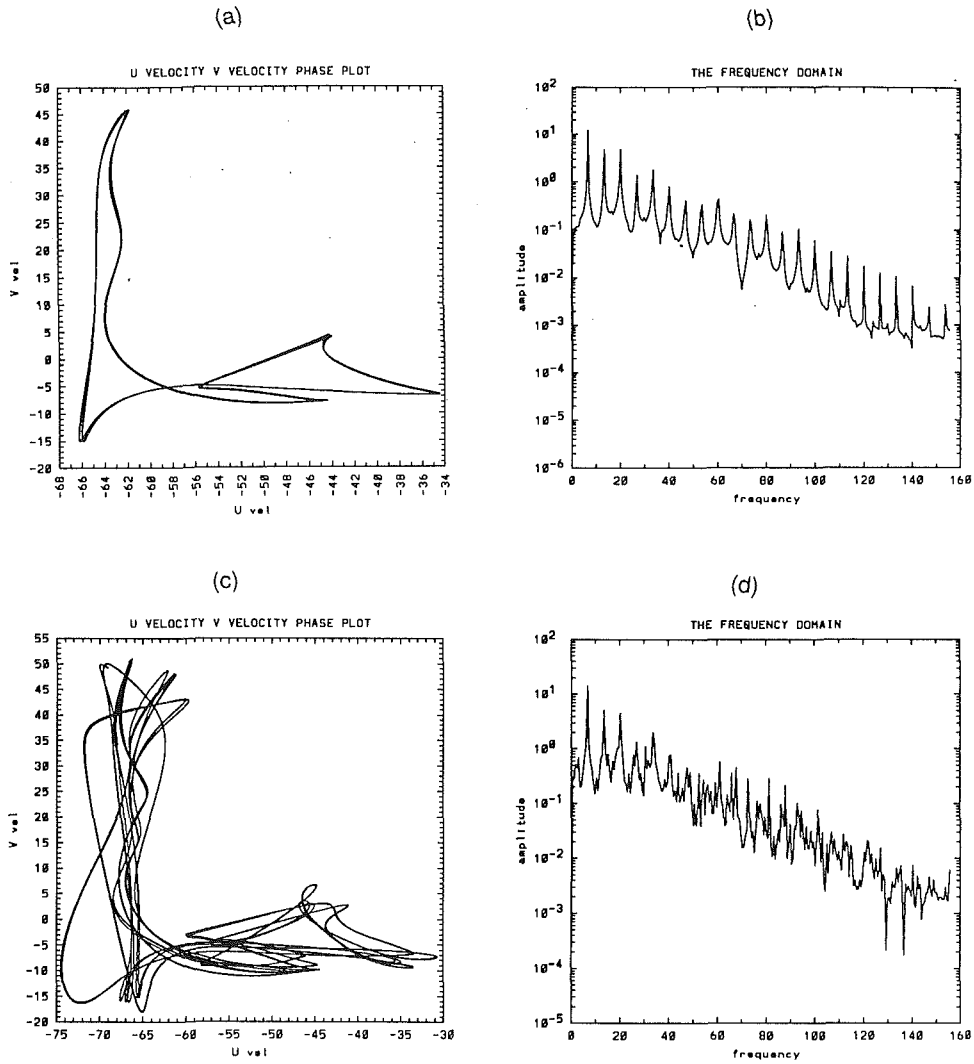

Fig. 16 (*a*) Phase trajectory, (*b*) spectral amplitudes for Ra = 70,000; (*c*) phase trajectory, (*d*) spectral amplitudes for Ra = 75,000

third subharmonic bifurcation was observed between 51,000 and 51,500. Since the frequencies are getting lower and lower, more points need to be sampled to resolve the frequencies. Figures 12(*a*) and (*b*) show the fourth period-doubling in the spectra. At 52,000 (Figs. 12(*c*) and (*d*)) the flow is probably chaotic, but the time series is not long enough to determine that for certain. In all these cases, the time step was taken to be 0.0001, and 16,384 points were sampled in each case.

The Feigenbaum number for the first three subharmonic bifurcations is approximately 3.2. This is markedly different from the universal constant in quadratic maps since the constant is valid only in the limit of a large number of bifurcations. The determination of subsequent bifurcations by brute force numerical simulation is too time consuming and was not attempted. It is quite clear that by imposing numerical symmetry, the low frequency was "filtered out." The scenario observed in the absence of the low frequency is almost certainly the Feigenbaum route to chaos, which is an infinite sequence of subharmonic bifurcations ($P_1 \Rightarrow P_2 \Rightarrow P_4 \ldots N$). This is consistent with the qualitative observations of Libchaber et al. (1982).

Windows of Periodicity. The one-dimensional quadratic map shows a surprisingly complicated dynamic behavior. Not only does it exhibit a sequence of period-doubling bifurcation, but as shown in Fig. 13, there are regions of periodic behavior between regions of chaotic behavior (Parker and Chua, 1988). This has been documented in the experiments of Libchaber et al. (1982) and also was found to occur in the simulations. At a Rayleigh number of 52,500 the flow is again periodic (Figs. 14(*a*) and 14(*b*)).

The next period-doubling bifurcation occurs between 57,000 and 60,000. The dynamics at 57,000 is no different from the 53,000 case (Figs. 14(*c*) and 14(*d*)). At 60,000 the subharmonic is visible, but somewhat weak (Fig. 15(*b*)). The folding of the trajectory is obvious (Fig. 15(*a*)). This is the beginning of yet another period-doubling cascade.

A further increase in the bifurcation parameter (the Rayleigh number) to 70,000 reveals a second window of periodicity as seen in Figs. 16(*a*) and 16(*b*). In fact, if the behavior of the quadratic map is any indication there should be an infinite number of such windows. Naturally, it is an impossible task to locate all the windows. Figures 16(*c*) and 16(*d*) show the flow after perhaps several period-doublings at a Rayleigh number of 75,000. This is the highest Rayleigh number simulated. Since the grid refinement study reported by Mukutmoni and Yang (1993) was for much lower Rayleigh numbers, it was felt that it would not be reasonable to continue further. The fact that such a complex system qualitatively reproduces the dynamics of a one-dimensional map is itself very surprising, since the spatial distribution of the oscillations was found to be so complex.

Conclusions

In an attempt to understand the physics of the bifurcations in Rayleigh–Bénard convection, direct numerical simulation was carried out for the case experimentally documented by Gollub et al. (1980). There was good agreement between the computations and experiments for the 3.5:2.1:1 box and $Pr = 2.5$ case (for water) for the first two bifurcations. Further down, computations revealed a low-frequency noise in the spectra, which was physically associated with the asymmetry in the rolls. This was followed by chaos.

Although the experiments documented a second subharmonic bifurcation before encountering the low frequency and subsequent chaos, the calculations are consistent with the observation by GBS that this route is atypical and can be realized only with difficulty. The computations indicate that the route observed in experiments is possible only if the Rayleigh number is increased in small steps or quasi-statically. Numerically it was found that the only feasible way of traversing this bifurcation path was by imposing a perfect fourfold symmetry in the horizontal plane.

In such a run, it was found that the Feigenbaum scenario was observed, and no low-frequency quasi-periodicity was encountered. This makes it quite clear that it is the asymmetry between the rolls that terminates the Feigenbaum sequence and the introduced quasi-periodicity. The bifurcation sequence for the set of parameters is therefore non-unique. The most common scenario, it seems, is a finite cascade of period-doubling followed by quasi-periodicity (with a low frequency) and subsequent chaos.

This generic bifurcation path was avoided numerically by imposing symmetry. The scenario observed as a result is strikingly similar to that observed in one-dimensional maps. There appears to be an unending sequence of period-doubling bifurcations until chaos. There were at least two windows of periodicity between chaos, as in quadratic maps.

Acknowledgments

The computations were done on a CONVEX C240 supercomputer and IBM RS/6000 workstation. The support of the Office of University Computing of the University of Notre Dame is greatly appreciated. Some of the calculations were carried out on the Cray Y/MP at the National Center for Supercomputing Applications. Their support under grant ATM89007n is graciously acknowledged.

References

Feigenbaum, M. J., 1978, "Quantitative Universality for a Class of Nonlinear Transformations," *Journal of Statistical Physics*, Vol. 19, pp. 25–52.

Gollub, J. P., Benson, S. V., and Steinman, J. F., 1980, "A Subharmonic Route to Turbulent Convection," *Nonlinear Dynamics*, H. G. Helleman, ed., New York Academy of Sciences, pp. 22–27.

Libchaber, A., and Maurer, J., 1981, "A Rayleigh Bénard Experiment: Helium in a Small Box," *Nonlinear Phenomena at Phase Transitions and Instabilities*, T. Riste, ed., Plenum Press, New York, pp. 259–286.

Libchaber, A., Larouche, C., and Fauve, L., 1982, "Period Doubling Cascade in Mercury, a Quantitative Measurement," *Le Journal de Physique-lettres*, Vol. 43, pp. L-211–L-216.

Mukutmoni, D., 1991, "Transitions and Bifurcations in Rayleigh–Bénard Convection in a Small Aspect Ratio Box," Ph.D. Dissertation, Department of Aerospace and Mechanical Engineering, University of Notre Dame, Notre Dame, IN 46556.

Mukutmoni, D., and Yang, K. T., 1993, "Rayleigh–Bénard Convection in a Small Aspect Ratio Enclosure: Part I—Bifurcation to Oscillatory Convection," ASME JOURNAL OF HEAT TRANSFER, Vol. 115, this issue, pp. 360–366.

Parker, T. S., and Chua, L. O., 1988, *Practical Numerical Algorithms for Chaotic Systems*, Springer-Verlag, New York.

Wolf, A., Swift, J. B., Swinney, H. L., and Vastano, J. A., 1985, "Determining Lyapunov Exponents From a Time Series," *Physica 16D*, pp. 285–317.

Natural Convective Heat Transfer in a Divided Vertical Channel: Part I—Numerical Study

D. Naylor
Postdoctoral Fellow,
Department of Mechanical Engineering,
Queen's University,
Kingston, Ontario, Canada

J. D. Tarasuk
Professor,
The University of Western Ontario,
London, Ontario, Canada

This is a two-part study of two-dimensional laminar natural convection heat transfer in a divided vertical channel. The divided channel consists of an isothermal dividing plate located on the center line of a vertical channel formed by two isothermal walls. The study examines the effect of Rayleigh number, plate-to-channel length ratio, vertical plate position, and plate thickness on the heat transfer rate from the channel walls, the dividing plate, and the channel as a whole. In Part I, solutions to both the full elliptic and parabolic forms of the Navier–Stokes and energy equations are obtained for Prandtl number Pr = 0.7 (air). Positioning the plate at the bottom of the channel was found to give the highest average Nusselt numbers for the plate and channel. Dividing plate average Nusselt numbers as much as two times higher than the isolated plate Nusselt number were predicted numerically. Experimental measurements and data correlations for the divided channel are presented in Part II of this paper.

Introduction

At present there is a resurgence of interest in natural convection heat transfer from parallel plates because of modern applications to the cooling of electronic equipment. Although limited to low power density applications, natural convective cooling is inexpensive, highly reliable, and free of electromagnetic and acoustic noise.

Studies of natural convective heat from cylinders have shown that the presence of confining walls can enhance the heat transfer because of the "chimney" effect. Marsters (1975) found that the presence of unheated confining walls can enhance the heat transfer rate from a horizontal cylinder by up to 50 percent. In a similar study of a finned tube confined by adiabatic walls, Sparrow et al. (1986) measured average heat transfer coefficients 2.5 times higher than for free-space positioning.

Sparrow et al. (1983) have also performed experiments on free convective heat transfer from a short horizontal cylinder mounted in an asymmetrically heated duct. In this study, the cylinder was attached to the heated wall and partially spanned the channel gap width. Both the heated wall and the attached cylinder were isothermal and maintained at the same temperature. They found that the heat transfer rate from the cylinder could be enhanced by up to 60 percent compared to the external flow situation (cylinder mounted on an isolated vertical isothermal plate) when the cylinder was located near the bottom of the channel.

The present study examines the heat transfer enhancements that can be obtained for parallel plate configurations utilizing the "chimney" effect. The model geometry is shown in Fig. 1. A plate of length L_p and thickness $2t$ is positioned on the centerline of a vertical channel formed by parallel walls of length L_c, spaced $2b$ apart. The dividing plate is located a distance L_i from the channel inlet. Both the confining walls and the dividing plate are at the same surface temperature T_s above the ambient temperature T_o.

The objective of the present study is to determine whether significant heat transfer enhancements, particularly for the center plate, can be obtained from the careful choice of geometric parameters. In addition, it is desired to obtain an understanding of the interactions between the dividing plate and the confining channel walls over a wide range of Rayleigh number and geometric parameters. Calculations were performed for a Prandtl number Pr = 0.7 (air).

Problem Formulation

The flow is assumed to be steady, laminar, incompressible, and two dimensional. Viscous dissipation is neglected and all thermophysical properties are assumed to be constant, except for density in the buoyancy term of the y-momentum equation, i.e., the Boussinesq approximation. With these assumptions, the governing equations become:

$$\partial u/\partial x + \partial v/\partial y = 0 \tag{1}$$

$$\rho(u\partial u/\partial x + v\partial u/\partial y) = -\partial p'/\partial x + \mu(\partial^2 u/\partial x^2 + \partial^2 u/\partial y^2) \tag{2}$$

$$\rho(u\partial v/\partial x + v\partial v/\partial y) = -\partial p'/\partial y + g\rho\beta(T - T_o) + \mu(\partial^2 v/\partial x^2 + \partial^2 v/\partial y^2) \tag{3}$$

$$u\partial T/\partial x + v\partial T/\partial y = \alpha(\partial^2 T/\partial x^2 + \partial^2 T/\partial y^2) \tag{4}$$

where the pressure defect p' is the difference between the channel pressure and the ambient pressure at the same elevation.

Equations (1)–(4) have been solved both with and without the boundary-layer approximations. Solution of the boundary-layer equations requires much fewer computational resources than the full elliptic problem. Furthermore, in previous studies of channel geometries, boundary-layer solutions have been in good agreement with experimental data. However, there is some concern about the accuracy of boundary-layer solutions, particularly for predicting local quantities, because of the arbitrary inlet boundary conditions. In addition, the present parabolic solution is restricted to dividing plates with zero thickness ($t = 0$). For these reasons, the full elliptic problem has also been solved. The solution to the full equations will be referred to as the *elliptic solution* and the approximate boundary-layer solution will be referred to as the *parabolic solution*.

Numerical Solutions

1 Elliptic Solution. The full elliptic equations were solved using the finite element code FIDAP (Fluid Dynamics International, 1989). The computational domain for the elliptic

Contributed by the Heat Transfer Division for publication in the JOURNAL OF HEAT TRANSFER. Manuscript received by the Heat Transfer Division January 1992; revision received September 1992. Keywords: Electronic Equipment, Natural Convection. Associate Technical Editor: J. R. Lloyd.

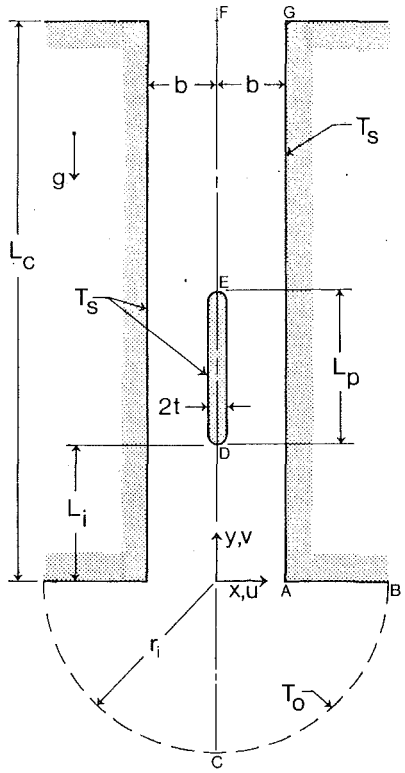

Fig. 1 The model heat transfer geometry

solution is shown in Fig. 1. For $t > 0$, the dividing plate has rounded leading and trailing edges with radii equal to the plate half-thickness. The flow was assumed to be symmetric about the channel center line. Hence, only the right half of the flow field was solved. In dimensional form, the boundary conditions are:

$$\partial T/\partial x = \partial v/\partial x = u = 0, \text{ for } -r_i \le y < L_i,\ x = 0 \quad \text{(CD)} \quad (5)$$

$$\partial T/\partial x = \partial v/\partial x = u = 0, \text{ for } (L_i + L_p) < y \le L_c, x = 0 \quad \text{(EF)} \quad (6)$$

$$T = T_s,\ u = v = 0, \text{ for } L_i \le y \le (L_i + L_P),$$
$$0 \le x \le t \text{ on plate surface} \quad \text{(DE)} \quad (7)$$

$$T = T_s,\ u = v = 0, \text{ for } 0 \le y \le L_c,\ x = b \quad \text{(AG)} \quad (8)$$

$$\partial T/\partial y = u = v = 0, \text{ for } b \le x \le r_i,\ y = 0 \quad \text{(AB)} \quad (9)$$

$$\partial T/\partial y = \partial u/\partial y = \partial v/\partial y = 0,$$
$$\text{for } 0 \le x \le b,\ y = L_c \quad \text{(FG)} \quad (10)$$

$$v_\theta = \sigma_{rr} = 0,\ T = T_o, \text{ on semicircular boundary} \quad \text{(BC)} \quad (11)$$

The derivative boundary conditions applied to the upper boundary (FG) are not entirely realistic. Although these conditions could affect the flow in the channel, it was the best assumption available short of extending the domain to consider the plume region. However, for a sufficiently long channel, streamwise conduction at the channel exit can be reasonably neglected except at very low Rayleigh number.

The inlet boundary conditions (11) of zero tangential velocity ($v_\theta = 0$) and zero normal stress ($\sigma_{rr} = -p + 2\mu\partial v_r/\partial r = 0$) are based on Jeffrey-Hamel flow. Jeffrey-Hamel flow is a similarity solution of isothermal flow caused by the presence of a source or sink at the point of intersection of two walls. For a sufficiently large inlet domain radius (r_i) the flow at the boundary (BC) will approach that produced by a point sink. A more detailed discussion of the rationale for the inlet boundary conditions is given by Naylor et al. (1991).

Now for the elliptic solution we introduce the following dimensionless quantities:

$$X = x/b, \quad Y = y/b, \quad R = r/b \quad (12)$$

$$U = u/U_{\text{ref}}, \quad V = v/U_{\text{ref}} \quad (13)$$

$$T^* = (T - T_o)/(T_s - T_o), \quad P = (p'b)/(\mu U_{\text{ref}}) \quad (14)$$

where

$$U_{\text{ref}} = (\alpha \text{PrGr}^{1/2})/b, \text{ and } \text{Gr} = (g\beta(T_s - T_o)b^3\rho^2)/\mu^2 \quad (15)$$

Nomenclature

b = half channel width
C_p = constant pressure specific heat
g = gravitational acceleration
Gr = Grashof number = $g\beta(T_s - T_o)b^3\rho^2/\mu^2$
h_c = channel average heat transfer coefficient
h_p, $h_{p,y}$ = average and local plate heat transfer coefficient
h_w, $h_{w,y}$ = average and local wall heat transfer coefficient
H_c = total rate of heat transfer from the entire half channel
k = thermal conductivity
K = constant in Eq. (55)
L_c = channel (and wall) length
L_i = length of the channel that is undivided at the channel inlet
L_p = dividing plate length
$L_{p,\text{wet}}$ = wetted length of the dividing plate
Nu_c = channel average Nusselt number
Nu_p, $\text{Nu}_{p,y}$ = average and local dividing plate Nusselt number
Nu_w, $\text{Nu}_{w,y}$ = average and local wall Nusselt number
p' = pressure defect = $p - p_o$
P = dimensionless pressure
Pr = Prandtl number
q = half channel flow rate
Q_e = dimensionless half channel flow rate for the elliptic solution
r, R = radius and dimensionless radius
r_i, R_i = dimensional and dimensionless inlet domain radius
Ra_c^* = channel Rayleigh number = $\text{GrPr}(b/L_c)$
Ra_p^* = plate Rayleigh number = $\text{GrPr}(b/L_p)$
t = dividing plate half thickness
T, T^* = temperature and dimensionless temperature
T_s = surface temperature
T_o = ambient temperature
u, U = dimensional and dimensionless x velocity component
U_{ref} = reference velocity scale = $\alpha\text{Pr}(\text{Gr})^{1/2}/b$
v, V = dimensional and dimensionless y velocity component
v_r, v_θ = radial and tangential component of velocity
V_r, V_θ = dimensionless radial and tangential velocity components
x, y = Cartesian coordinates
X, Y = dimensionless Cartesian coordinates
α = thermal diffusivity
β = volumetric expansion coefficient
μ = dynamic viscosity
ρ = density
σ_{rr} = radial stress component
ψ = dimensionless stream function ($U = \partial\psi/\partial Y$, $V = -\partial\psi/\partial X$)

Using the above quantities, the dimensionless governing equations become:

$$\partial U/\partial X + \partial V/\partial Y = 0 \tag{16}$$

$$\mathrm{Gr}^{1/2}(U\partial U/\partial X + V\partial U/\partial Y) = -\partial P/\partial X + \partial^2 U/\partial X^2 + \partial^2 U/\partial Y^2 \tag{17}$$

$$\mathrm{Gr}^{1/2}(U\partial V/\partial X + V\partial V/\partial Y) = -\partial P/\partial Y + \mathrm{Gr}^{1/2}T^* + \partial^2 V/\partial X^2 + \partial^2 V/\partial Y^2 \tag{18}$$

$$\mathrm{Gr}^{1/2}\mathrm{Pr}(U\partial T^*/\partial X + V\partial T^*/\partial Y) = \partial^2 T^*/\partial X^2 + \partial^2 T^*/\partial Y^2 \tag{19}$$

The dimensionless boundary conditions are:

$$\partial T^*/\partial X = \partial V/\partial X = U = 0, \text{ for } -R_i \le Y < L_i/b, \quad X = 0 \quad \text{(CD)} \tag{20}$$

$$\partial T^*/\partial X = \partial V/\partial X = U = 0, \text{ for } (L_i + L_p)/b < Y \le L_c/b, \quad X = 0 \quad \text{(EF)} \tag{21}$$

$$T^* = 1,\ U = V = 0, \text{ for } L_i/b \le Y \le (L_i + L_p)/b, \quad 0 \le X \le t/b, \text{ on plate surface} \quad \text{(DE)} \tag{22}$$

$$T^* = 1, \quad U = V = 0, \text{ for } 0 \le Y \le L_c/b, \quad X = 1 \quad \text{(AG)} \tag{23}$$

$$\partial T^*/\partial Y = U = V = 0, \text{ for } 1 \le X \le R_i, \quad Y = 0 \quad \text{(AB)} \tag{24}$$

$$\partial T^*/\partial Y = \partial U/\partial Y = \partial V/\partial Y = 0, \quad \text{for } 0 \le X \le 1,\ Y = L_c/b \quad \text{(FG)} \tag{25}$$

and

$$V_\theta = 0,\ -P + 2\partial V_r/\partial R = 0,\ T^* = 0, \quad \text{on the semicircular boundary} \quad \text{(BC)} \tag{26}$$

where

$$V_r = v_r/U_{\mathrm{ref}},\ V_\theta = v_\theta/U_{\mathrm{ref}} \tag{27}$$

The inlet boundary conditions are not valid for low Rayleigh number; at low Rayleigh number the fluid is heated by conduction far upstream from the channel inlet. For this reason, the lower limit of the calculations for the elliptic solution was $\mathrm{Ra}_c^* = 5$ (see Figs. 3(*a*, *c*)).

The local heat transfer coefficient and local Nusselt numbers for the wall and dividing plate are defined as:

$$h_{w,y} = \frac{k\left.\dfrac{\partial T}{\partial x}\right|_{y=b}}{(T_s - T_o)}, \quad h_{p,y} = \frac{-k\left.\dfrac{\partial T}{\partial n}\right|_{\mathrm{surface}}}{(T_s - T_o)} \tag{28}$$

$$\mathrm{Nu}_{w,y} = \frac{h_{w,y}b}{k} = \left.\frac{\partial T^*}{\partial X}\right|_{X=1}, \quad \mathrm{Nu}_{p,y} = \frac{h_{p,y}b}{k} = \left.\frac{-\partial T^*}{\partial N}\right|_{\mathrm{surface}} \tag{29}$$

where n and N are dimensional and dimensionless unit vectors normal to the plate surface. The average wall and plate Nusselt numbers were calculated by integrating the local Nusselt number distributions:

$$\mathrm{Nu}_w = \frac{b}{L_c}\int_0^{L_c/b}\left.\frac{\partial T^*}{\partial X}\right|_{X=1} dY, \quad \mathrm{Nu}_p = \frac{b}{L_{p,\mathrm{wet}}}\int_0^{L_{p,\mathrm{wet}}/b}\left.\frac{-\partial T^*}{\partial N}\right|_{\mathrm{surface}} dS \tag{30}$$

where dS is an incremental dimensionless distance around the wetted perimeter of the plate. Note that the wetted length of the dividing plate ($L_{p,\mathrm{wet}}$) is slightly greater than the linear length in the y direction (L_p) when the plate has finite thickness.

The overall channel Nusselt number Nu_c is defined as:

$$\mathrm{Nu}_c = \frac{h_c b}{k} = \frac{H_c b}{(L_{p,\mathrm{wet}} + L_c)(T_s - T_o)k} \tag{31}$$

where H_c is the total heat transfer rate from the half channel (plate and wall combined). Nu_c was calculated using two different methods. One method was a heat balance:

$$\mathrm{Nu}_c = \mathrm{Gr}^{1/2}\mathrm{Pr}\left(\frac{b}{L_c + L_{p,\mathrm{wet}}}\right)\left(\int_0^1 VT^* dX\Big|_{Y=\frac{L_c}{b}} - \int_0^1 VT^* dX\Big|_{Y=0}\right) + \int_0^1 \left.\frac{\partial T^*}{\partial Y}\right|_{Y=0} dX \tag{32}$$

The first, second, and third integrals in Eq. (32) correspond to the heat convected out of the top of the channel, the heat convected back into the channel entrance, and heat conducted out of the channel entrance. For the lowest Rayleigh number considered ($\mathrm{Ra}_c^* = 5$), it was found that the heat conducted out of the channel entrance was equal to the heat convected back into the channel. Hence, in all cases, Nu_c was computed by:

$$\mathrm{Nu}_c = \mathrm{Gr}^{1/2}\mathrm{Pr}\left(\frac{b}{L_c + L_{p,\mathrm{wet}}}\right)\int_0^1 VT^* dX|_{Y=L_c/b} \tag{33}$$

The channel average Nusselt number (Nu_{c2}) was also calculated from the average wall and plate Nusselt numbers (Eq. (30)) as:

$$\mathrm{Nu}_{c2} = \frac{\mathrm{Nu}_p L_{p,\mathrm{wet}} + \mathrm{Nu}_w L_c}{L_{p,\mathrm{wet}} + L_c} \tag{34}$$

Calculations for the elliptic solution were done on five different grid structures. For these grids, the plate was located on the channel centerline and the length ratios were fixed at $L_c/b = 15$ and $L_p/b = 5$ ($L_p/L_c = 1/3$). This relatively large channel aspect ratio was chosen so that the heat conducted out of the channel exit could be reasonably neglected in the numerical calculations (see Ramanathan and Kumar, 1991). Calculations were made for a zero thickness dividing plate ($t/b = 0$) located at the bottom ($L_i/L_c = 0$), middle ($L_i/L_c = (1 - L_p/L_c)/2 = 1/3$), and top ($L_i/L_c = 1 - L_p/L_c = 2/3$) of the channel. Additional calculations were done for a finite thickness dividing plate located at the bottom of the channel ($L_i/L_c = 0$) with blockage ratios of $t/b = 0.1, 0.2$. A course grid for $t/b = 0.2$ and $L_i/L_c = 0$ is shown in Fig. 2 to illustrate the finite element grid structure. Nine-node quadrilateral elements were used. Local interpolation functions for these elements are quadratic for velocity and temperature. The penalty formulation was used for pressure.

Grid tests were conducted to ensure that the results were independent of both the grid density and the size of the inlet computational domain (R_i). For all cases the data were most grid dependent at the upper limit of Rayleigh number, $\mathrm{Ra}_c^* = 10^4$. Table 1 shows partial results from the tests for $t/b = 0$, $L_i/L_c = 0$. For cases A and B, the grid density remains roughly constant and the inlet domain radius R_i is varied. Case C shows the effect of increasing the grid density with $R_i = 5$. The channel and wall average Nusselt numbers for cases A and C differ by less than 1 percent. However, the flow rate and plate average Nusselt number are somewhat more grid sensitive; the results from cases A and C differ by slightly greater than 1 percent. For all cases, Nu_c was 2–3 percent lower than Nu_{c2}. Also, Nu_c showed less grid dependence than Nu_{c2}. The local Nusselt number distributions along the channel wall for cases A and C had a maximum difference of about 5 percent near the leading edge; the plate local Nusselt number distributions had a maximum difference of about 3 percent near the leading edge. Toward the top of the plate and wall, the differences in the local Nusselt number distributions became negligible.

Based on the results of grid testing, the finite element grids used for all the elliptic calculations had an inlet domain radius of $R_i = 5$ and about 14,500 nodes (3600 elements). The convergence criteria were set such that the calculations were carried to four-digit accuracy. A more detailed description of the grid testing is given in the thesis by Naylor (1991).

2 Parabolic Solution. The parabolic form of the governing equations is obtained by applying the boundary-layer approximations to Eqs. (1)–(4). Specifically, diffusion of momentum and heat in the streamwise (y) direction is neglected and the pressure is assumed to depend only on the y coordinate ($\partial p/\partial x = 0$). With these simplifications, the governing equations become:

$$\partial u/\partial x + \partial v/\partial y = 0 \tag{35}$$

$$\rho(u\partial v/\partial x + v\partial v/\partial y) = -dp'/dy + g\rho\beta(T - T_o) + \mu\partial^2 v/\partial x^2 \tag{36}$$

$$u\partial T/\partial x + v\partial T/\partial y = \alpha\partial^2 T/\partial x^2 \tag{37}$$

Because of symmetry about the channel centerline, only half of the flow field was solved. The boundary conditions are:

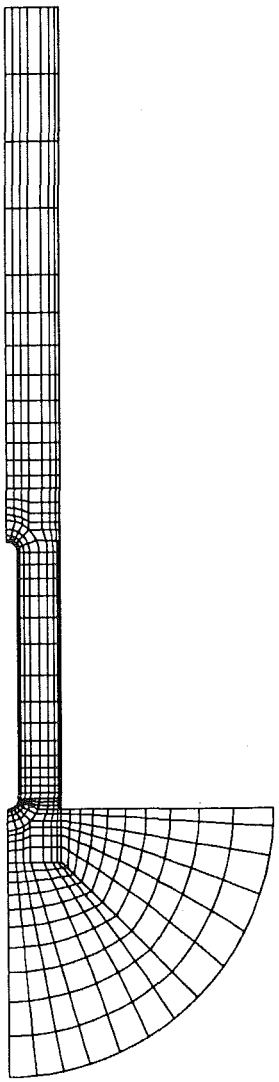

Fig. 2 A coarse finite element grid ($t/b = 0.2$, $L_p/L_c = 1/3$, $L_i/L_c = 0$)

$$v = v_o, \quad u = 0, \quad T = T_o \text{ for } y = 0, \quad 0 < x < b \tag{38}$$

$$u = v = 0, \quad T = T_s \text{ for } x = b, \quad 0 \le y \le L_c \tag{39}$$

$$\partial v/\partial x = \partial T/\partial x = u = 0 \text{ for } x = 0, \quad 0 \le y < L_i, \quad (L_i + L_p) < y \le L_c \tag{40}$$

$$T = T_s, \quad u = v = 0, \quad \text{for } x = 0, \quad L_i \le y \le (L_i + L_p) \tag{41}$$

The channel inlet and exit pressures are:

$$p' = -\rho v_o^2/2 \quad \text{for } y = 0, \quad p' = 0 \quad \text{for } y = L_c \tag{42}$$

A forward marching finite difference procedure, as described by Aung et al. (1972), was used to solve Eqs. (35)–(37). In the forward marching solution the computations start at the channel inlet where uniform temperature ($T = T_o$) and velocity profiles ($v = v_o$) are assumed. The dividing plate location is specified by a change in boundary conditions on the channel centerline as the calculations proceed up the channel. Thus, the parabolic solution is restricted to modeling a dividing plate with no thickness ($t = 0$). A similar technique of changing boundary conditions during the forward marching procedure has been used successfully by Sparrow and Prakash (1980) and Oosthuizen (1984) to solve developing free convection in other channel configurations. Solution procedures for this problem are very well documented in the literature and need not be described here; in addition to Aung et al. (1972), the reader is referred to Aihara (1973) and Miyatake and Fujii (1972).

Extensive grid testing was conducted for the parabolic solution. In the X direction, 200 evenly spaced mesh points were used. In the Y direction between 650 and 1100 steps were used, depending upon the values of L_p/L_c and Ra_c^*. Test runs were made (with double the total number of nodes) at the lowest, intermediate, and highest values of Rayleigh number for each value of L_p/L_c and L_i/L_c studied. In all cases, the local and overall Nusselt number data from these calculations differed by less than 1 percent. Comparisons of local and average Nusselt numbers, induced flow rates, and pressure distributions were made with the parabolic solutions of Aung et al. (1972) and Aihara (1973) for the undivided isothermal channel. In all cases, the present calculations gave identical results. Also, it was confirmed that calculations for the fully divided channel ($L_p/L_c = 1$) gave results identical to the undivided channel ($L_p/L_c = 0$) after rescaling the data to account for the different half channel width.

The Fully Developed Limit

For channels with large aspect ratios (L_c/b), the flow in the channel approaches fully developed conditions at low Rayleigh number. Recently, Ramanathan and Kumar (1991) have shown (for constant heat flux boundary conditions) that at low Rayleigh number, the channel average Nusselt number is independent of aspect ratio for $L_c/b \ge 10$. In other words, for $L_c/b \ge 10$ the inclusion of vertical conduction terms does not significantly increase the overall heat transfer rate.

For the divided channel it is assumed that the flow is thermally fully developed and the velocity field is fully developed. Also, it is assumed that the "redeveloping" lengths for the

Table 1 Partial results from the elliptic solution grid tests (for $\mathrm{Ra}_c^* = 10^4$, $t/b = 0$, $L_i/L_c = 0$, $L_p/L_c = 1/3$)

Case	Number of nodes	Inlet radius, R_i	Average Nusselt numbers: Channel Nu_c	Channel Nu_{c2}	Wall Nu_w	Plate Nu_p	Flow rate, Q_e
A	9003	3	6.389	6.262	5.257	9.278	1.527
B	10,143	5	6.386	6.256	5.258	9.250	1.511
C	14,479	5	6.382	6.234	5.259	9.158	1.511

velocity profile at the beginning and end of the dividing plate are small compared to the plate and channel lengths, such that:

$$v = v_1(x) \quad \text{for} \quad 0 \le y \le L_i^- \tag{43}$$

$$v = v_2(x) \quad \text{for} \quad L_i^+ \le y \le (L_i + L_p)^- \tag{44}$$

$$v = v_1(x) \quad \text{for} \quad (L_i + L_p)^+ \le y \le L_c \tag{45}$$

In the fully developed limit, it is assumed that $T(x, y) = T_s$. With these assumptions the governing equations reduce to:

$$-\frac{dp'}{dy} + \mu \frac{d^2v}{dx^2} + g\beta\rho(T_s - T_o) = 0 \tag{46}$$

The buoyancy term in Eq. (46) is a constant and dp'/dy can be at most a constant since $v = v(x)$. Hence, it is evident from Eq. (46) that the velocity profiles in both the divided and undivided sections are parabolic. Applying the boundary conditions gives:

$$v_1(x) = \frac{3q}{2b}\left(1 - \frac{x^2}{b^2}\right),$$

$$v_2(x) = \frac{-6q}{(b-t)^3}(x^2 - bx - tx + bt) \tag{47}$$

where q is the half channel volume flow rate.

Substituting the appropriate velocity profile and integrating Eq. (46) with respect to y over each section of the channel gives:

$$-p'|_{L_i} - \frac{3q\mu L_i}{b^3} + g\beta\rho(T_s - T_o)L_i = 0, \quad 0 \le y \le L_i^- \tag{48}$$

$$p'|_{L_i} - p'|_{L_i + L_p} - \frac{12q\mu L_p}{(b-t)^3} + g\beta\rho(T_s - T_o)L_p = 0,$$

$$L_i^+ \le y \le (L_i + L_p)^- \tag{49}$$

$$p'|_{L_i + L_p} - \frac{3q\mu(L_c - L_i - L_p)}{b^3}$$

$$+ g\beta\rho(T_s - T_o)(L_c - L_i - L_p) = 0, (L_i + L_p)^+ \le y \le L_c \tag{50}$$

Note that the pressure is assumed to be equal to the ambient pressure at the channel inlet and outlet. Equations (48), (49), and (50) can be solved for the half channel flow rate:

$$q = \frac{g\beta\rho(T_s - T_o)L_c}{3\mu\left(\frac{4L_p}{(b-t)^3} + \frac{L_c - L_p}{b^3}\right)} = \frac{\mu \mathrm{Gr}_b L_c}{3\rho b^3\left(\frac{4L_p}{(b-t)^3} + \frac{L_c - L_p}{b^3}\right)} \tag{51}$$

The total heat transfer rate from the half channel is:

$$H_c = \rho q C_p (T_s - T_c) \tag{52}$$

Neglecting the small additional area at the leading and trailing edges of the dividing plate (i.e., $L_{p,\mathrm{wet}} = L_p$), and substituting Eqs. (51) and (52) into Eq. (31) gives:

$$\mathrm{Nu}_c = \frac{\mathrm{Ra}_c^*}{3\left(4\left(\frac{L_p}{L_c}\right)^2\left(\frac{b}{b-t}\right)^3 + 4\frac{L_p}{L_c}\left(\frac{b}{b-t}\right)^3 - \left(\frac{L_p}{L_c}\right)^2 + 1\right)} \tag{53}$$

For $L_p = 0$, Eq. (53) gives the well-known relation for the undivided channel: $\mathrm{Nu}_c = \mathrm{Ra}_c^*/3$. For $L_p = L_c$ and $t = 0$, Eq. (53) gives an equivalent expression for the undivided channel (with b corresponding to the wall spacing): $\mathrm{Nu}_c = \mathrm{Ra}_c^*/24$. Note that in the fully developed limit, Nu_c is independent of the dividing plate location (L_i).

For $L_i = 0$, the flow is divided by the plate at the channel inlet. In this case, half of the total heat transfer may be assumed to come from the dividing plate because of symmetry. With this assumption, the fully developed average plate Nusselt number is:

$$\mathrm{Nu}_p = \frac{\mathrm{Ra}_p^*}{6\left(4\frac{L_p}{L_c}\left(\frac{b}{b-t}\right)^3 - \frac{L_p}{L_c} + 1\right)} \quad \text{for } L_i = 0 \tag{54}$$

If the flow is thermally fully developed when it reaches the plate, the plate Nusselt number will be zero. Hence, in the fully developed limit, $\mathrm{Nu}_p = 0$ for $L_i > 0$.

Applying the same procedure to the channel walls gives the fully developed average wall Nusselt number:

$$\mathrm{Nu}_w = \frac{\mathrm{Ra}_c^*}{K\left(4\frac{L_p}{L_c}\left(\frac{b}{b-t}\right)^3 - \frac{L_p}{L_c} + 1\right)} \tag{55}$$

For $L_i = 0$, $K = 6$ in Eq. (55). For $L_i = 0$, Eq. (55) is not valid for $L_p = 0$ since it is assumed that one half of the total heat transfer is contributed by the dividing plate. For $L_i > 0$, the heat transferred from the plate is assumed to be zero. With this assumption, $K = 3$ in Eq. (55) for $L_i > 0$.

The Isolated Plate Limit

The similarity solution by Ostrach (1953) for a single isolated plate of length L gives:

$$\mathrm{Nu} = \frac{hb}{k} = C\left(\mathrm{Gr}_b \mathrm{Pr}\frac{b}{L}\right)^{1/4} \tag{56}$$

where $C = 0.515$ for a Prandtl number of $\mathrm{Pr} = 0.7$. At high Rayleigh number the divided channel will behave like three isolated flat plates: two isolated plates of length L_c and one isolated plate of length L_p. Using Eq. (56), the total heat transfer rate (H_c) from channel wall and plate in the half channel is:

$$H_c = \frac{Ck(T_s - T_o)}{b}(\mathrm{Ra}_p^{*1/4}L_p + \mathrm{Ra}_c^{*1/4}L_c) \tag{57}$$

Again, to simplify the expression it is assumed that $L_{p,\mathrm{wet}} = L_p$. Substituting Eq. (57) into Eq. (31) gives:

$$\mathrm{Nu}_c = C\mathrm{Ra}_c^{*1/4}\left(\frac{\left(\frac{L_p}{L_c}\right)^{3/4} + 1}{\frac{L_p}{L_c} + 1}\right) \tag{58}$$

Hence, for the divided channel the isolated plate limit for Nu_c is a function of the plate length ratio. Equation (58) has a maximum with respect to L_p/L_c at $L_p/L_c \approx 0.23$. The maximum is caused by the fact that the short isolated dividing plate has a greater average heat transfer coefficient than the longer channel walls.

Presentation of Results

The heat transfer rate from the dividing plate and the overall channel was found to be the highest when the plate was located at the bottom of the channel ($L_i/L_c = 0$). For this reason, the data for this geometry are likely of most practical interest and are presented in more detail. To show the effect of L_i/L_c, the results for each vertical plate position are compared for one fixed plate length ratio $L_p/L_c = 1/3$ ($t/b = 0$). From the behavior of the zero-thickness dividing plate, most of the geometric influences on heat transfer are delineated. Finally, the effect of blockage caused by a finite thickness dividing plate ($t/b \le 0.2$) is shown.

Streamline and isotherm contours from the elliptic solution for a divided channel with a plate length ratio $L_p/L_c = 1/3$ are shown in Fig. 3. In Fig. 3, a plate with zero thickness ($t/b = 0$) is located at the bottom ($L_i/L_c = 0$) and top ($L_i/L_c = 2/3$) of the channel. At low Rayleigh number ($\mathrm{Ra}_c^* = 5$, Figs. 3(a, c)) the flow enters the channel smoothly, whereas separation occurs at the channel inlet for high Rayleigh number ($\mathrm{Ra}_c^* = 10^4$, Figs. 3(b, d)). For $L_p/L_c = 1/3$, $L_c/b = 15$,

$L_i/L_c = 0$, the elliptic solution predicts that separation occurs between $100 < Ra_c^* < 200$, as determined from the wall shear stress distributions. At $Ra_c^* = 10^4$, the thermal boundary layers look similar to those of isolated flat plates; however, the boundary layers merge before the channel exit. Also, the adverse effect of separation on the wall local heat transfer rate near the channel inlet can be seen from the isotherm contours. This will be discussed further when the local Nusselt number distributions are presented.

Effect of Plate Length Ratio (L_p/L_c). The variation of average plate Nusselt number with plate Rayleigh number for several length ratios is shown in Fig. 4 for $L_i/L_c = 0$ and $t/b = 0$. The close agreement of the parabolic and elliptic solutions for $L_p/L_c = 1/3$ gives confidence in both numerical results. At low Rayleigh number, the plate average Nusselt number approaches the expression for the fully developed Nusselt number (Eq. (54)). With increasing Rayleigh number, average plate Nusselt numbers well above those for a single isolated plate are predicted. For example, Nu_p for $L_p/L_c = 1/10$ is about two times higher than the isolated plate Nusselt number at $Ra_p^* = 100$.

In Fig. 4 it can be seen that the length of the confining channel walls strongly influences the heat transfer rate from

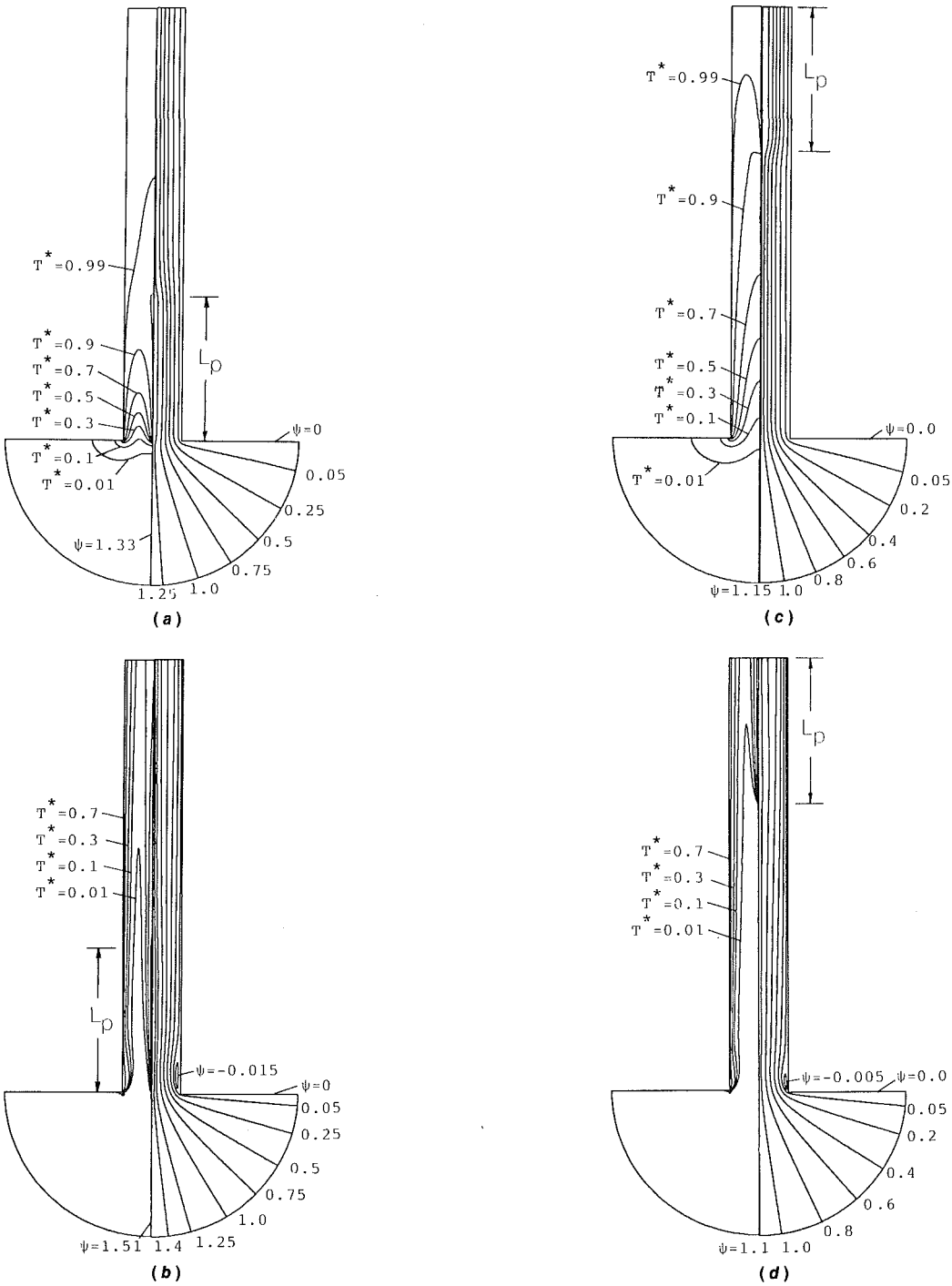

Fig. 3 Streamline and isotherm contours for the divided channel with $t/b = 0$ and $L_p/L_c = 1/3$, (*a*) $Ra_c^* = 5$, $L_i/L_c = 0$, (*b*) $Ra_c^* = 10^4$, $L_i/L_c = 0$, (*c*) $Ra_c^* = 5$, $L_i/L_c = 2/3$, (*d*) $Ra_c^* = 10^4$, $L_i/L_c = 2/3$.

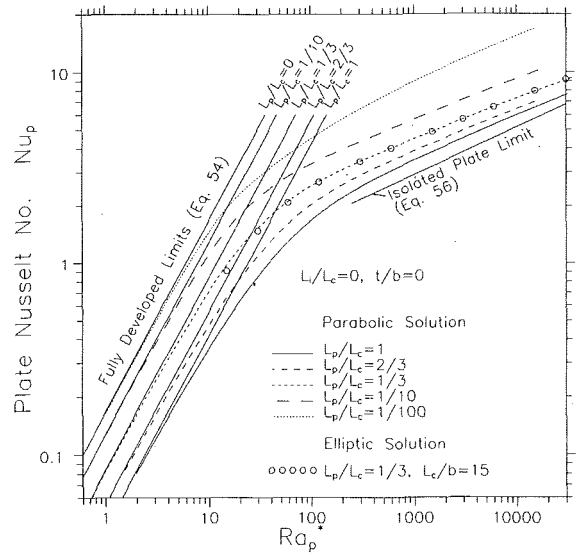

Fig. 4 Effect of plate length ratio (L_p/L_c) on the average plate Nusselt number ($t/b = 0$, $L_i/L_c = 0$)

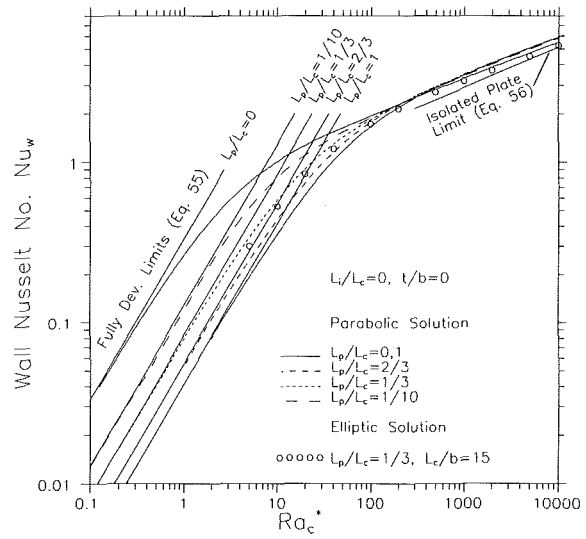

Fig. 5 Effect of plate length ratio (L_p/L_c) on the average wall Nusselt number ($t/b = 0$, $L_i/L_c = 0$)

the plate. Consider a channel with a dividing plate of fixed length. For this channel, Fig. 4 shows that extending the channel walls above the plate (decreasing L_p/L_c while holding Ra_p^* constant), gives substantial heat transfer enhancement for the plate over the full range of Rayleigh number. For $L_p/L_c = 1/10$, at low Rayleigh number there is about a 300 percent increase in Nu_p compared to $L_p/L_c = 1$; at $Ra_p^* = 10^4$ there is approximately a 55 percent enhancement for $L_p/L_c = 1/10$ compared to $L_p/L_c = 1$. Extension of the channel walls beyond $L_p/L_c = 1/10$ is of little practical significance. However, calculations were made for $L_p/L_c = 1/100$ to confirm that the numerical results approach a fully developed limit close to that for $L_p/L_c = 0$ at small plate length ratios.

Figure 5 shows the behavior of the average wall Nusselt number with channel Rayleigh number for several plate length ratios and for $L_i/L_c = 0$, $t/b = 0$. The average wall Nusselt number predicted by the elliptic solution (for $L_p/L_c = 1/3$) is in fair agreement with the parabolic solution data. Both sets of data have the same trend. However, the elliptic solution gives wall Nusselt numbers about 10 percent lower than the parabolic solution.

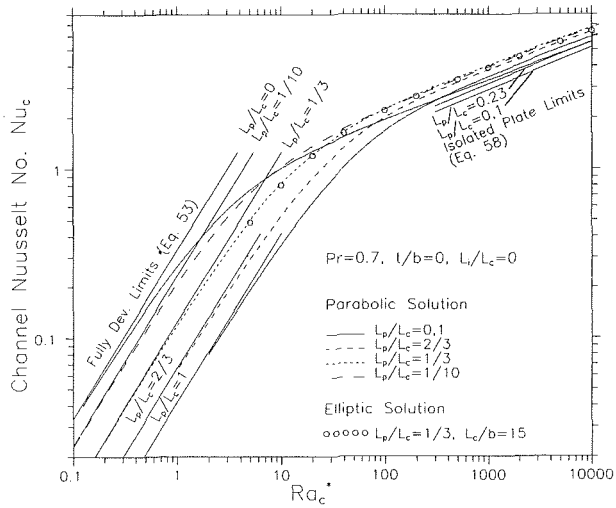

Fig. 6 Effect of plate length ratio (L_p/L_c) on the channel average Nusselt number ($t/b = 0$, $L_i/L_c = 0$)

An important feature shown in Fig. 5 is the large reduction at low Rayleigh number of the average wall Nusselt number for $L_p/L_c = 1/10$ compared to the undivided channel ($L_p/L_c = 0$). At low Rayleigh number the flow becomes thermally fully developed within a short distance from the channel inlet. As a result, even a short dividing plate will contribute about one half of the total heat transfer and cause the average wall Nusselt number to be reduced by about a factor of two. Increasing the length of the dividing plate (larger values of L_p/L_c) causes a further reduction in Nu_w at low Rayleigh number because of the additional viscous resistance of the dividing plate. In contrast, at high Rayleigh number Nu_w is almost independent of the plate length ratio. So, for $Ra_c^* > 200$, average plate Nusselt numbers well above the isolated plate limit can be achieved (see Fig. 4) without adversely affecting the heat transfer rate from the confining walls.

The effect of plate length ratio (L_p/L_c) on the channel average Nusselt number is shown in Fig. 6 (for $L_i/L_c = 0$, $t/b = 0$). Consider a channel of fixed length L_c. Figure 6 shows that at low Ra_c^*, increasing the length of the dividing plate (larger values of L_p/L_c) causes Nu_c to decrease. Nu_c decreases because of the higher viscous resistance in the divided section of the channel. Also, the additional surface area of the dividing plate causes a further reduction in the channel average Nusselt number. In contrast to the low Rayleigh number behavior, at $Ra_c^* = 10^4$ the undivided channel ($L_p/L_c = 0$) gives the lowest Nusselt number. At high Rayleigh number, the addition of a dividing plate increases the bulk fluid temperature in the channel. The higher fluid temperature increases the induced flow and heat transfer rate. Note also that the isolated plate Nusselt number for the divided channel is a function of the plate length ratio (Eq. (58)).

Effect of Vertical Plate Position (L_i/L_c). Figure 3 shows that there are only minor differences in the streamline patterns for the plate located in the bottom and top of the channel. However, the effect of vertical plate position on the temperature field is more pronounced. Comparing Figs. 3(a, b) with Figs. 3(c, d) shows that the average fluid temperature at any elevation in the channel is higher when the plate is located at the bottom of the channel. Hence, it could be expected that the buoyancy-induced flow and overall heat transfer rate will be higher when the plate is located at the bottom of the channel.

Figure 7 shows the average plate Nusselt number versus the plate Rayleigh number for the plate in the bottom, middle, and top of the channel with the plate length ratio fixed at $L_p/L_c = 1/3$ ($t/b = 0$). At low Rayleigh number the vertical

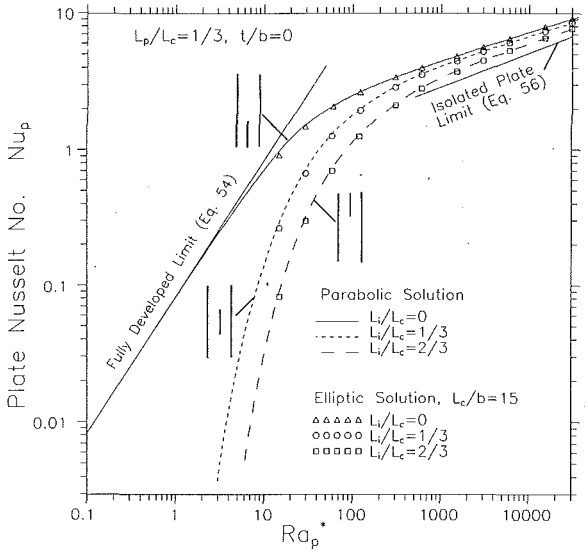

Fig. 7 Effect of plate position (L_i/L_c) on the average plate Nusselt number (t/b = 0, L_p/L_c = 1/3)

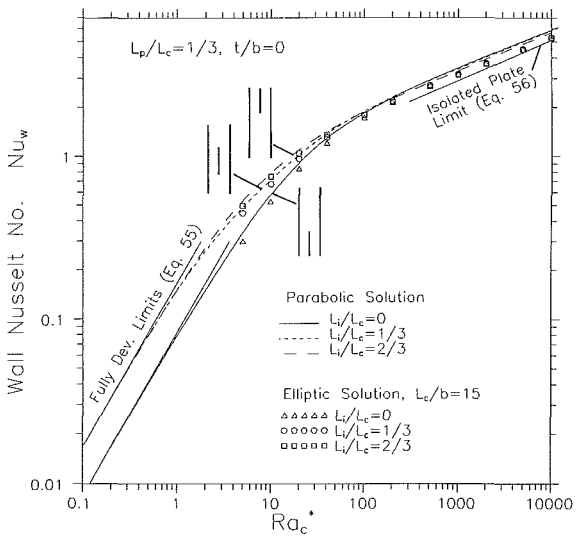

Fig. 8 Effect of plate position (L_i/L_c) on the average wall Nusselt number (t/b = 0, L_p/L_c = 1/3)

position of the plate has a strong influence on the average plate Nusselt number. For $L_i/L_c > 0$, Nu_p drops off very rapidly with decreasing Rayleigh number because of the shortening thermal developing length; with decreasing Rayleigh number the flow eventually becomes thermally fully developed upstream of the plate. At high Rayleigh number, Nu_p is much less dependent on the vertical location of the plate. At $Ra_p^* = 3 \times 10^4$, the average Nusselt number for the plate located at the bottom of the channel ($L_i/L_c = 0$) is only about 20 percent higher than for the plate located at the top of the channel ($L_i/L_c = 2/3$).

The behavior of the average wall Nusselt number for each plate position with $L_p/L_c = 1/3$ ($t/b = 0$) is shown in Fig. 8. At low Rayleigh number the average wall Nusselt number for $L_i/L_c = 0$ is one half the value for $L_i/L_c > 0$ for reasons previously discussed. However, the lack of dependence on plate location at high Ra_c^* is very interesting. Although the induced flow rate is larger when the plate is in the bottom of the channel (which would tend to increase the wall heat transfer rate), the bulk fluid temperature is also higher (which tends to decrease the wall heat transfer rate). These effects counteract each other at about $Ra_c^* > 200$, causing the wall Nusselt number to be almost independent of the plate position.

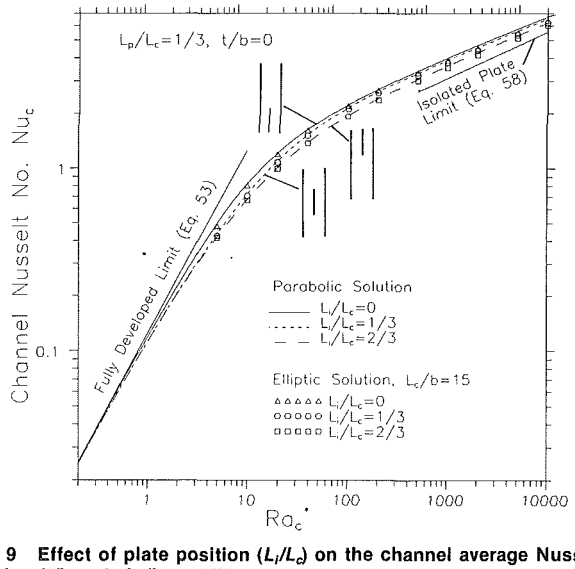

Fig. 9 Effect of plate position (L_i/L_c) on the channel average Nusselt number (t/b = 0, L_p/L_c = 1/3)

The effect of the plate position on the channel average Nusselt number is shown in Fig. 9 with $L_p/L_c = 1/3$, $t/b = 0$. Positioning the plate at the bottom of the channel ($L_i/L_c = 0$) produces the greatest heat transfer rate over the entire range of Rayleigh number. However, the channel average Nusselt number is only moderately dependent upon the plate's vertical position; at $Ra_c^* = 10^4$, the channel average Nusselt number for $L_i/L_c = 0$ is only 7 percent higher than for $L_i/L_c = 2/3$. Since the average wall Nusselt number is almost independent of the plate position at high Ra_c^* (see Fig. 8), this increase in Nu_c can be attributed solely to the additional heat transfer from the plate.

Figure 10 shows the plate local Nusselt number distributions from the elliptic and parabolic solutions for $L_p/L_c = 1/3$ with the plate located in the bottom ($L_i/L_c = 0$) and middle ($L_i/L_c = 1/3$) of the channel ($t/b = 0$). At low Rayleigh number, the distributions predicted by both numerical methods are in good agreement for the plate in either vertical position. For $L_i/L_c = 0$ (Fig. 10(a)), at high Rayleigh number the results from the parabolic solution differ substantially from those of the elliptic solution because of flow separation at the channel inlet. For the elliptic solution, there is a separated flow region next to the wall at the channel inlet (see Fig. 3(b)). The separated flow reduces the effective cross section for the flow at the entrance, causing the fluid velocity near the leading edge of the plate to be higher than in the absence of separation. Hence, the elliptic solution predicts a higher local heat transfer rate near the leading edge of the plate. Although there are large differences in the local distributions, the average Nusselt numbers from both numerical schemes are nearly the same. For $L_i/L_c = 1/3$ (Fig. 10(b)) the local Nusselt number distributions from both methods are in agreement because the plate is sufficiently far downstream from the separated flow region.

Although a minor effect, it is noteworthy that the elliptic solution predicts an increase in the plate local Nusselt number near the trailing edge of the plate (see Fig. 10). Upstream of the trailing edge of the plate the streamlines start to bend toward the channel centerline. As the fluid moves toward the centerline, it brings cooler fluid closer to the plate surface, causing the plate local Nusselt number to increase slightly. The parabolic solution cannot predict this phenomena; by the na-

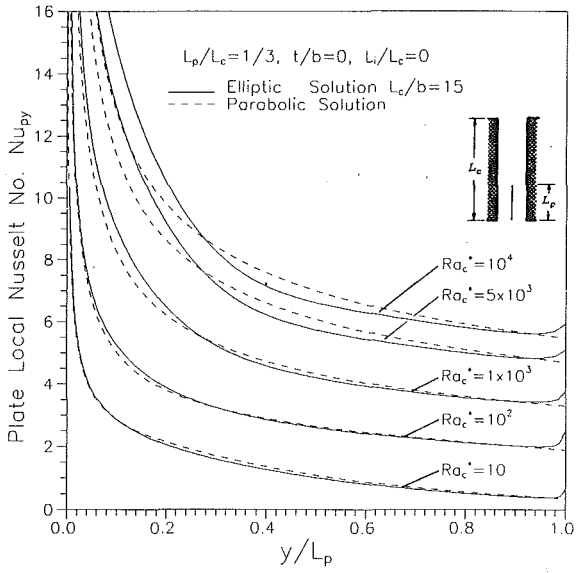

(a)

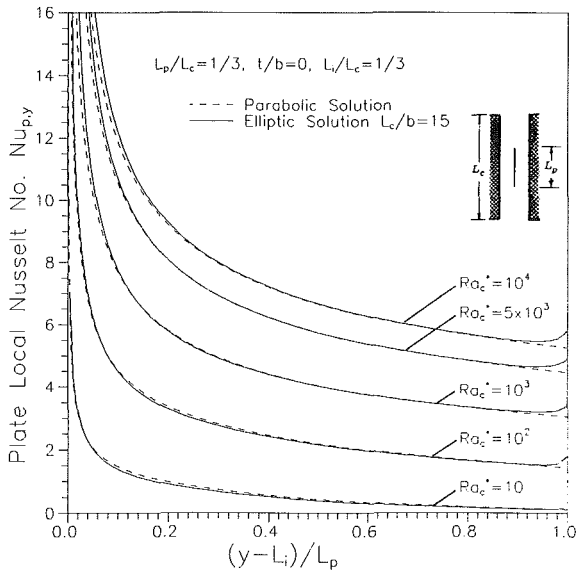

(b)

Fig. 10 Plate local Nusselt number distributions for L_p/L_c = 1/3, t/b = 0: (a) L_i/L_c = 0, (b) L_i/L_c = 1/3

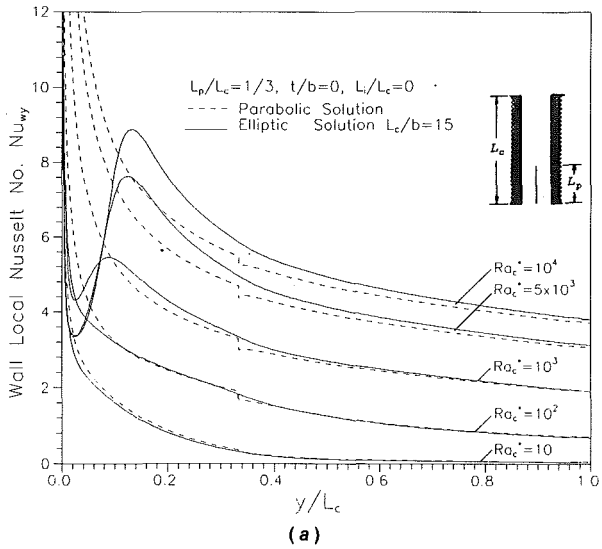

(a)

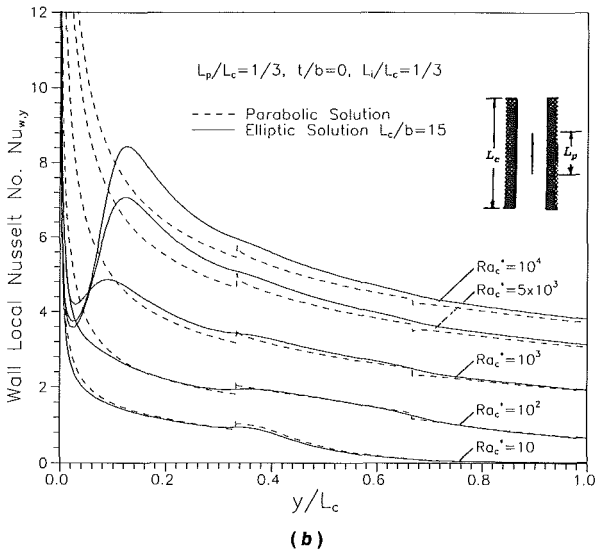

(b)

Fig. 11 Wall local Nusselt number distributions for L_p/L_c = 1/3, t/b = 0: (a) L_i/L_c = 0, (b) L_i/L_c = 1/3

ture of the approximate equations, downstream changes cannot affect the upstream solution.

Figure 11 shows the wall local Nusselt number distributions from the elliptic and parabolic solutions for the plate located at the bottom (L_i/L_c = 0) and middle (L_i/L_c = 1/3) with L_p/L_c = 1/3. At low Rayleigh number the flow does not separate at the inlet and both numerical predictions are in close agreement. As found in a previous study of the undivided channel (Naylor et al., 1991), the flow separation in the divided channel has an adverse effect on the wall local heat transfer rate. For $Ra_c^* \geq 10^3$, there is a pronounced minimum in the local heat transfer rate distribution near the channel inlet. With increasing Rayleigh number, the separated flow gets stronger and larger, causing the local minimum value of Nusselt number to decrease. At $Ra_c^* = 10^4$, the local Nusselt number is about four times lower than predicted by the parabolic solution. Despite the large differences in the local distributions, the average Nusselt numbers from both numerical methods differ by only about 10 percent.

Figure 11 also shows that the wall heat transfer rate rises slightly near the location of the leading edge of the plate and falls slightly near the trailing edge of the plate. At the leading edge of the plate a momentum boundary layer begins to develop on the dividing plate; accordingly, the x component of velocity (u) is positive across the entire channel. This traverse component of velocity brings cooler fluid from the center regions of the channel closer to the wall, causing the heat transfer rate to increase slightly. Similarly, at the trailing edge of the dividing plate, the transverse component of velocity is negative across the entire channel. Hence, cooler fluid moves away from the wall, causing the wall heat transfer rate to decrease slightly.

In Fig. 11 (a, b), each wall local Nusselt number distribution predicted by the parabolic solution has discontinuities at the location of the leading and trailing edges of the plate, y/L_c = 1/3, 2/3. The discontinuities are caused by the singularity at the leading and trailing edges of the plate and the nature of the approximate parabolic equations. The parabolic equations are solved using a forward marching method. During the forward marching procedure the boundary conditions on the channel centerline are changed at the leading and trailing edges of the dividing plate. This instantaneous change in boundary conditions causes the numerical discontinuity in local heat

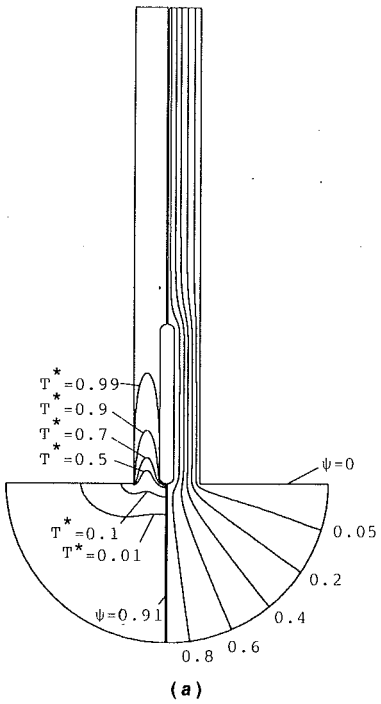

(a)

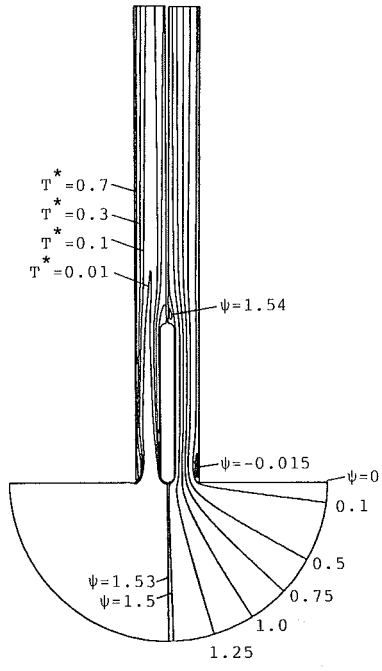

(b)

Fig. 12 Streamline and isotherm contours for the divided channel with t/b = 0.2, L_p/L_c = 1/3, L_i/L_c = 0: (a) Ra_c^* = 5, (b) Ra_c^* = 10^4

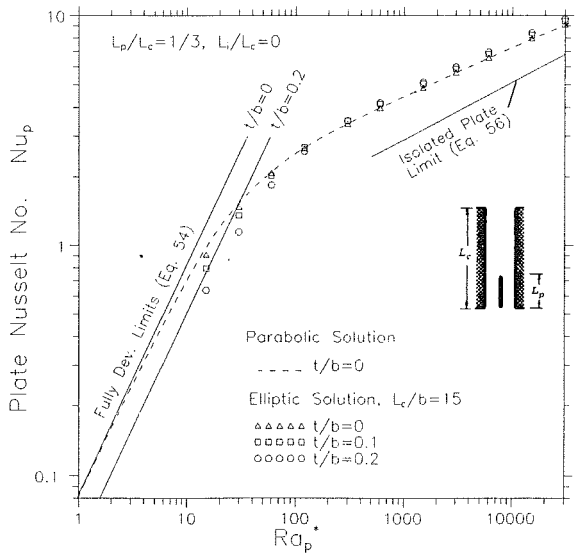

Fig. 13 Effect of plate thickness (t/b) on the average plate Nusselt number (L_p/L_c = 1/3, L_i/L_c = 0)

transfer rate. Within about two steps in the y direction from the end of the plate, the numerical solution rapidly adjusts for the newly imposed boundary conditions. Although the numerical results from the parabolic solution are not accurate close to the singularity points, the results downstream recover the correct flow and temperature field characteristics. This was confirmed by comparing the temperature and velocity profiles from the parabolic solution with those from the elliptic solution.

An important point that may not be readily apparent from Figs. 10(a) and 11(a) is that at low Rayleigh number for L_i/L_c = 0, the plate and wall local Nusselt numbers from the elliptic solution are almost the same in the entrance region of the channel. That is, for $0 \le y \le L_p$ at a fixed value of GrPr, the different entrance flow conditions for the plate and the wall have little influence on the local heat transfer distributions. Of course, for the parabolic solution the plate and wall local heat transfer distributions are identical for $y \le L_p (L_i/L_c$ = 0) even at high GrPr because the inlet velocity profile is assumed to be uniform.

Effect of Plate Thickness (t/b). Figure 12 shows streamline and isotherm contours from the elliptic solution for a divided channel with a plate length ratio L_p/L_c = 1/3 and thickness t/b = 0.2 (L_i/L_c = 0). The behavior is similar to that of the divided channel with t/b = 0 (Figs. 3(a, b)). At low Rayleigh number the flow enters the channel smoothly. Separation occurs on the wall at the channel inlet at higher Rayleigh number. The elliptic solution predicts that increasing the plate thickness delays the onset of separation at the channel inlet. With 20 percent blockage separation occurs between 200 < Ra_c^* < 500, as compared to 100 < Ra_c^* < 200 for zero blockage (t/b = 0). Separation is delayed because blockage reduces the induced flow rate in this range of Rayleigh number. For finite thickness dividing plates, flow separation also occurs at the top of the dividing plate; for L_p/L_c = 1/3, L_p/b = 5, L_i/L_c = 0, and t/b = 0.2, the elliptic solution predicts that separation occurs in the range 10 < Ra_c^* < 20, as determined from the plate shear stress distribution.

The behavior of the average plate Nusselt number for 0, 10, and 20 percent channel blockage is shown in Fig. 13 (L_p/L_c = 1/3, L_i/L_c = 0). Only the graph for Nu_p is presented since the effect of blockage on the wall and overall channel average Nusselt numbers is very similar. At low Rayleigh number, blockage caused by a finite thickness plate reduces the overall induced flow rate and the average Nusselt numbers. Note that the data from the elliptic solution for t/b > 0 appear to be approaching the fully developed asymptotes (Eq. (54)). At Ra_c^* = 5, for L_p/L_c = 1/3 and L_i/L_c = 0, 20 percent blockage of the channel cross section causes a 30 percent reduction in the plate average Nusselt number. In the fully developed limit, the maximum reduction is predicted to be 38.8 percent.

At high Rayleigh number, small plate thicknesses have almost no effect on the channel's thermal behavior, since the dividing plate and walls tend toward isolated plates. There is, however, a small secondary effect to be considered. A dividing

plate with finite plate thickness has a slightly larger wetted length than a plate of zero thickness with the same length in the y direction. For example, the plate with thickness $t/b = 0.2$ has 4.6 percent more wetted length than the zero thickness plate. This extra wetted length tends to increase the bulk fluid temperature. Consequently, at high Rayleigh number, the channel with 20 percent blockage ($t/b = 0.2$) has a slightly higher induced flow and heat transfer rate than the channel with $t/b = 0$ and $t/b = 0.1$. However, the extra wetted length is a minor effect for $t/b \leq 0.2$. At $Ra_c^* = 10^4$, the plate, wall, and overall channel average Nusselt numbers for $t/b = 0.2$ are only about 3 to 5 percent higher than for $t/b = 0$.

Summary

A numerical study has been conducted on natural convection in a divided vertical isothermal channel. Solutions to both the full elliptic and boundary-layer forms of the Navier-Stokes and energy equations have been obtained for Pr = 0.7 (air). In addition, expressions were derived for the limiting case of fully developed flow in the divided channel.

The numerical solutions predict that the heat transfer rate from the dividing plate can be significantly enhanced by the presence of the confining walls. For example, for $L_p/L_c = 1/10$ and $L_i/L_c = 0$, at $Ra_p^* = 100$ the average plate Nusselt number is about two times higher than the isolated plate Nusselt number. Positioning the plate at the bottom of the channel ($L_i/L_c = 0$) gave the highest average Nusselt number for the plate and channel as a whole.

The wall average Nusselt number is highly dependent upon the vertical location of the plate at low Rayleigh number. However, with increasing Rayleigh number, the average wall Nusselt number becomes almost independent of both the vertical plate position (L_i/L_c) and the plate length ratio (L_p/L_c). This is a significant result: Above $Ra_c^* \approx 200$ the heat transfer rate from the dividing plate is enhanced by the confining walls without reducing the heat transfer rate from the walls. Below $Ra_c^* \approx 200$ there is a trade-off between the dividing plate and the channel walls.

The effect of blockage caused by a finite thickness dividing plate ($t/b \leq 0.2$) is largest at low Rayleigh number. With increasing Rayleigh number blockage effects diminish.

Acknowledgments

The authors wish to acknowledge the support received from NSERC of Canada.

References

Aihara, T., 1973, "Effects of Inlet Boundary-Conditions on Numerical Solutions of Free Convection Between Vertical Parallel Plates," Report of the Institute of High Speed Mechanics, Tohoku University, Sendai, Japan, Vol. 28, No. 256, pp. 1-27.

Aung, W., Fletcher, L. S., and Sernas, V., 1972, "Developing Laminar Free Convection Between Vertical Flat Plates With Asymmetric Heating," *Int. J. Heat Mass Transfer*, Vol. 15, pp. 2293-2308.

Fluid Dynamic International, 1989, Evanston, IL, FIDAP version 4.51.

Marsters, G. F., 1975, "Natural Convective Heat Transfer From a Horizontal Cylinder in the Presence of Nearby Walls," *The Canadian Journal of Chemical Engineering*, Vol. 53, pp. 144-149.

Miyatake, O., and Fujii, T., 1972, "Free Convection Heat Transfer Between Vertical Parallel Plates—One Plate Isothermally Heated and the Other Thermally Insulated," *Heat Transfer: Japanese Research*, Vol. 1, pp. 30-38.

Naylor, D., Floryan, J. M., and Tarasuk, J. D., 1991, "A Numerical Study of Developing Free Convection Between Isothermal Vertical Plates," ASME JOURNAL OF HEAT TRANSFER, Vol. 113, pp. 620-626.

Naylor, D., 1991, "A Numerical and Interferometric Study of Natural Convective Heat Transfer From Divided and Undivided Vertical Channels," Ph.D. Thesis, The University of Western Ontario, London, Ontario, Canada.

Oosthuizen, P. H., 1984, "A Numerical Study of Laminar Free Convective Flow Through a Vertical Open Partially Heated Plane Duct," *Fundamentals of Natural Convection—Electronic Equipment Cooling*, ASME HTD-Vol. 32, pp. 41-48.

Ostrach, S., 1953, "An Analysis of Laminar Free-Convection Flow and Heat Transfer About a Flat Plate Parallel to the Direction of the Generating Body Force," NACA Technical Report #1111.

Ramanathan, S., and Kumar, R., 1991, "Correlations for Natural Convection Between Heated Vertical Plates," ASME JOURNAL OF HEAT TRANSFER, Vol. 113, pp. 97-107.

Sparrow, E. M., and Prakash, C., 1980, "Enhancement of Natural Convection Heat Transfer by a Staggered Array of Discrete Vertical Plates," ASME JOURNAL OF HEAT TRANSFER, Vol. 102, pp. 215-220.

Sparrow, E. M., Souza Mendes, P., Ansari, M. A., and Prata, A. T., 1983, "Duct-Flow Versus External-Flow Natural Convection at a Short, Wall-Attached Horizontal Cylinder," *Int. J. Heat Mass Transfer*, Vol. 26, pp. 881-889.

Sparrow, E. M., Ansari, M. A., Stryker, P. C., and Ruiz, R., 1986, "Enhanced Heat Transfer From a Horizontal Finned Tube Situated in Vertical Channel," ASME JOURNAL OF HEAT TRANSFER, Vol. 108, pp. 62-69.

Natural Convective Heat Transfer in a Divided Vertical Channel: Part II—Experimental Study

D. Naylor
Postdoctoral Fellow,
Department of Mechanical Engineering,
Queen's University,
Kingston, Ontario, Canada

J. D. Tarasuk
Professor,
The University of Western Ontario,
London, Ontario, Canada

An interferometric study has been conducted on two-dimensional laminar natural convection heat transfer in an isothermal vertical divided channel. Interferograms were obtained for air and a plate-to-channel length ratio of $L_p/L_c = 1/3$. Data are presented for the dividing plate located at the bottom ($L_i/L_c = 0$) and top of the channel ($L_i/L_c = 2/3$). Comparisons of local and average Nusselt numbers are made with the numerical predictions from Part I. Although the experimental average Nusselt numbers are typically about 10 percent lower than the numerical results, the general trends of the data are in good agreement. Average Nusselt number correlation equations are presented.

Introduction

In this paper experimental data are obtained for air using a Mach-Zehnder interferometer. Comparisons are made with the numerical predictions from Part I. In addition, average Nusselt number correlation equations are presented for the dividing plate, the confining walls, and the overall channel. These correlation equations include the effects of Rayleigh number (Ra^*), plate length ratio (L_p/L_c), plate position (L_i/L_c), and plate thickness (t/b).

Experimental Apparatus and Procedure

A cross-sectional diagram of the divided channel test section is shown in Fig. 1. The height of the channel ($L_c = 120.0 \pm 0.05$ mm) and the dividing plate length ($L_p = 40.0 \pm 0.05$ mm) were selected such that $L_p/L_c = 1/3$; this plate length ratio was used for most of the numerical calculations. The length of the test section in the direction of the interferometer light beam was 25.91 ± 0.01 cm. For this length and air as the test fluid, each full fringe shift corresponds to a temperature difference of $\Delta T \approx 3°C$.

The construction of each channel wall assembly was identical (see Fig. 1). The main component of each wall assembly was a 1.27-cm-thick precision machined aluminum plate (item 1). The aluminum plate was insulated on the back surface by a layer of polystyrene (2.54 cm thick) and sheet of plywood (1.27 cm thick). The polystyrene, wood, and aluminum plates were held together by six nylon rods (item 6) that were threaded into the back surface of the aluminum plate. To support the assembly, a 37-cm length of $5 \times 5 \times 0.48$ cm angle aluminum was attached to the back of both ends of each wall. Four nylon threaded rods were used to connect the two wall assemblies at the top and bottom of each angle bracket. The thread rods held the walls at a fixed distance apart and allowed the spacing ($2b$) to be adjusted.

Each channel wall was heated by four electric strip heaters affixed to the back surface of the aluminum plate. Each heater had dimensions $25.5 \times 2 \times 0.04$ cm and a resistance of about 60 ohm. The approximate location of each strip heater is shown in Fig. 1 (item 11). Nine copper-constantan (40 gage) thermocouples were installed in each wall of the channel. Holes were drilled into the back of each aluminum plate such that the tips were within 2 mm of the outer surface. The thermocouples were located in an array of three evenly spaced columns on the centerline and 13 mm from each end of the wall. The bottom row of three thermocouples was located within 8 mm of the leading edge. For all experiments, the nine thermocouples read the same to within 0.5°C, which is about 2.4 percent of the overall temperature difference ($T_s - T_o \approx 18 - 25°C$).

Preliminary tests showed that there was significant heating of the horizontal surfaces near the channel inlet. To cool the phenolic board near the channel inlet, small single-pass heat exchangers, fabricated from soldered copper sheet, were installed in each wall assembly (see items 9, 10).

The dividing plate (item 5) was machined from two pieces of $259.1 \times 40.0 \times 1.59$ mm copper plate. Both the top and the bottom of the plate were machined to have a radius equal to the plate half thickness. Four thin foil electric heaters were "sandwiched" lengthwise between the two halves of the copper plate. Each heating element had dimensions $260 \times 6 \times 0.16$ mm

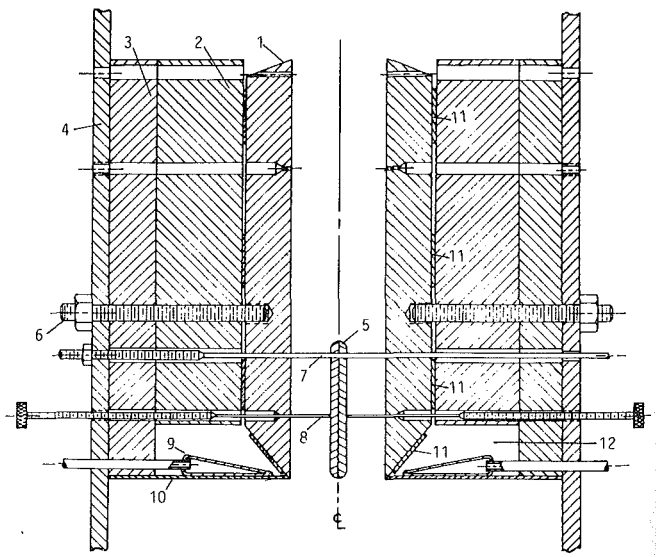

1. aluminum plate 1.27cm thick
2. polystyrene insulation 2.54cm thick
3. plywood 1.27cm thick
4. 5x5x0.48cm aluminum angle
5. copper divider plate
6. nylon threaded rod 6.35mm dia.
7. plate support wire 1.2mm dia.
8. plate locating pin 0.53mm dia.
9. heat exchanger
10. phenolic sheet 0.8mm thick
11. electric heaters (4 per wall)
12. air gap

Fig. 1 Cross-sectional view of the divided channel test section

Contributed by the Heat Transfer Division for publication in the JOURNAL OF HEAT TRANSFER. Manuscript received by the Heat Transfer Division January 1992; revision received September 1992. Keywords: Electronic Equipment, Natural Convection. Associate Technical Editor: J. R. Lloyd.

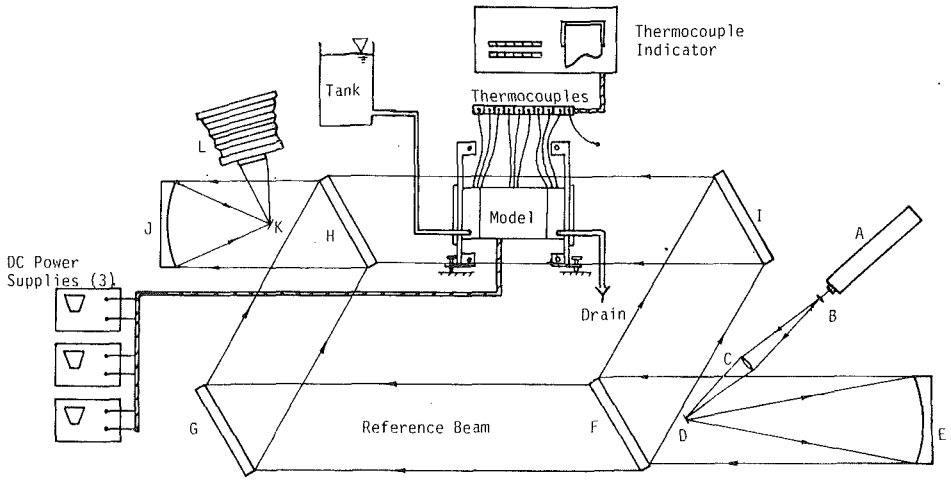

Fig. 2 Schematic diagram of the experimental apparatus

and a resistance of about 50 ohm. Three shallow vertical grooves (0.5 mm deep) for thermocouples were machined on the inside surface of one half of the dividing plate. The grooves were located 15 mm from each end and in the middle of the plate. Nine copper-constantan (24 gage) thermocouples were positioned in three rows at the top, middle, and bottom of the grooves. Care was taken to ensure that the thermocouple tips were not directly beneath the heating elements. For all experiments, the plate was isothermal to within 0.4°C. Ten countersunk flat head screws were used to assemble the two halves of the dividing plate. After assembly, the plate thickness was measured to be $2t = 3.50 \pm 0.04$ mm.

As shown in Fig. 1, the dividing plate was supported in the channel at each end by steel music wire (1.2 mm dia). The wire (item 7) was attached to a piece of threaded steel rod so that the plate position could be finely adjusted. At each end of the channel, fine positioning pins (0.53 mm dia) were provided on both sides of the plate. These pins (item 8) were used to align the dividing plate in the center of the channel. The dividing plate could be installed at both the bottom ($L_i/L_c = 0$) and the top ($L_i/L_c = 2/3$) of the channel. After assembly, each end of the test section was sealed off with a 15.2-cm-dia optical window.

The test section and associated instrumentation were integrated with a Mach-Zehnder interferometer. A schematic layout of the experimental apparatus is shown in Fig. 2. The model surface temperatures, as well as the ambient and cooling water temperatures, were recorded by a data logger. The thermocouple readings, checked at the freezing point of distilled water, were correct within ± 0.1°C. The power input to each wall and the center dividing plate was controlled separately from three d-c power supplies. For all experiments, the average surface temperatures of both walls and the dividing plate were within 0.5°C. Two shielded thermocouples located near the channel entrance were used to measure the ambient air temperature (T_o). A 15 liter tank supplied room temperature cooling water (at ≈ 0.3 liters/min) by gravity feed to the heat exchangers installed in the channel walls.

Eleven experiments were performed covering the following range of variables:

$$L_p/L_c = 1/3, \quad L_i L_c = 0, 2/3$$

$$0.069 \le t/b \le 0.2, \quad 4.73 \le L_c/b \le 13.68$$

$$81.4 \le \mathrm{Ra}_c^* \le 5{,}930$$

For these experiments, the channel-to-ambient temperature

Nomenclature

b = half channel width
C, C_1, C_2 = constants in correlation Eqs. (8) and (9)
C_p = constant pressure specific heat
g = gravitational acceleration
Gr = Grashof number = $g\beta(T_s - T_o)b^3\rho^2/\mu^2$
h_p, $h_{p,y}$ = average and local plate heat transfer coefficient
h_w, $h_{w,y}$ = average and local wall heat transfer coefficient
k = thermal conductivity
L_c = channel (and wall) length
L_i = length of the channel undivided at the channel inlet
L_p = dividing plate length
$L_{p,\mathrm{wet}}$ = wetted length of the dividing plate
n = exponent in correlation equations
Nu_c = channel average Nusselt number
Nu_p, $\mathrm{Nu}_{p,y}$ = average and local dividing plate Nusselt number
Nu_w, $\mathrm{Nu}_{w,y}$ = average and local wall Nusselt number
Pr = Prandtl number
r = radius
Ra_c^* = channel Rayleigh number = Gr Pr(b/L_c)
Ra_p^* = plate Rayleigh number = Gr Pr(b/L_p)
t = dividing plate half thickness
T, T^* = temperature and dimensionless temperature
T_s = surface temperature (wall or dividing plate)
T_o = ambient temperature
T_f = film temperature $= (T_s + T_o)/2$
x, y = Cartesian coordinates
β = volumetric expansion coefficient
μ = dynamic velocity
ρ = density

difference was held roughly constant ($T_s - T_o \approx 18$ to 25°C) and Rayleigh number was increased by widening the channel wall spacing ($2b$). Spacers made from aluminum and brass bar stock were used to set the channel wall spacing. The following wall spacings were used: $2b = 17.55$ mm, 25.4 mm, 31.95 mm, 38.15 mm, and 50.7 mm (±0.05 mm).

The experimental channel Rayleigh number was calculated as:

$$\mathrm{Ra}_c^* = \mathrm{Gr}\ \mathrm{Pr}\ \frac{b}{L_c} = \frac{g\beta(T_s - T_o)b^4\rho^2 C_p}{\mu L_c k} \tag{1}$$

In Eq. (1), the temperature difference ($T_s - T_o$) was calculated from the averaged thermocouple readings and the air properties were evaluated at the film temperature, $T_f = (T_s + T_o)/2$.

Interference patterns were recorded using Polaroid 10 cm × 12.5 cm Land film, type 55 (positive/negative). Interferograms were analyzed using a digital imaging system. The film negatives were viewed by a charged coupled device camera mounted onto a variable magnification microscope. The camera supplied a video signal to a frame grabber board in an IBM-PC (80286) computer. Rather than capturing the entire interferogram at once, it was stored as many separate images. Each image was digitized and stored in 640 × 480 × 8 bit frame memory (256 grey levels). In this way, high image resolution was achieved. The sole function of the imaging system was to determine the location of interference fringe centers at scans perpendicular to the model surface. Only the right-hand half of the channel was scanned because of symmetry. The fringe temperatures were calculated using a standard two-dimensional interferometric analysis (Eckert and Goldstein, 1976).

Finite fringe interferograms were analyzed to determine the wall local heat transfer coefficients. Equating the heat transferred by convection to the heat transferred by conduction at the wall gives an expression for the local heat transfer coefficient:

$$h_{w,y} = \frac{k_s \left.\frac{dT}{dx}\right|_{x=b}}{T_s - T_o} \tag{2}$$

where k_s is the thermal conductivity of air evaluated at the wall temperature (T_s). The wall local Nusselt number is defined by:

$$\mathrm{Nu}_{w,y} = \frac{h_{w,y}b}{k_f} = \frac{k_s \left.\frac{dT}{dx}\right|_{x=b} b}{(T_s - T_o)k_f} \tag{3}$$

where k_f is the thermal conductivity of air evaluated at the film temperature, $T_f = (T_s + T_o)/2$. Equation (3) was used to calculate the wall local Nusselt number distributions. The temperature difference ($T_s - T_o$) was calculated from the averaged wall and ambient thermocouples readings. The temperature gradients at the surface were evaluated by linearly extrapolating the optically determined temperature profiles obtained from scans perpendicular to the wall. That is, only the two destructive fringes closest to the wall were used to estimate the surface gradients.

Local convective coefficients were measured at about 70 to 80 locations along the wall. The distance between measurements was decreased toward the channel inlet because of the rapid increase in the local heat transfer rate. Accurate fringe center locations could not be obtained from the interferogram at the inlet corner ($y = 0$), so the leading edge heat transfer had to be estimated based on linear extrapolation using the two measurements closest to the leading edge. After linearly extrapolating the local Nusselt number distribution to $y = 0$, the local coefficients were integrated using the trapezoidal rule to give the average wall Nusselt number. The contribution of the extrapolated portion of the local heat transfer distribution was typically about 2–3 percent of the total heat transfer rate from the wall.

The plate local Nusselt number is calculated as:

$$\mathrm{Nu}_{p,y} = \frac{h_{p,y}b}{k_f} = \frac{-k_s \left.\frac{dT}{dn}\right|_s b}{(T_s - T_o)k_f} \tag{4}$$

where $dT/dn|_s$ = the surface temperature gradient normal to the plate surface. The plate was analyzed in three separate sections to determine the local heat transfer distribution. The curved leading edge, the straight middle section, and the upper curved trailing edge were each scanned separately. For the straight middle section of the plate, the analysis method was the same as for the channel wall. The local Nusselt number was calculated using linear extrapolation based on the first two destructive interference fringe centers.

The bottom curved section of the plate was scanned at 15-deg increments for local heat transfer coefficients. However, the radius of curvature of the bottom section of the plate is small. Eckert and Soehngen (1948) recommend logarithmic extrapolation when the radius of curvature is low; since the fluid velocity is low near the surface, the temperature field is conduction dominated and logarithmic extrapolation reflects the nature of conduction in a cylindrical layer. So, the surface gradients ($dT/dr|_s$) were obtained using a straight line fit to the first two fringe temperatures versus the logarithm of radius:

$$\left.\frac{dT}{dr}\right|_s = \frac{(T_2 - T_1)}{R_o \ln\left(\frac{r_2}{r_1}\right)} \tag{5}$$

where R_o = radius of curvature of the bottom of the plate, T_1, T_2 = temperatures of the first and second fringe centers from the plate surface, and r_1, r_2 = first and second fringe radii.

The local heat transfer rate from the curved top portion of the plate was calculated differently from the bottom surface (AB). Although the surface has a low radius of curvature, logarithmic extrapolation did not give reliable local heat transfer data because the fringes were too far from the surface and well outside the conduction dominated region. For this reason, linear extrapolation based on the first two fringe temperatures was used. It should be noted that in this region the fringes are widely spaced and the accuracy of the experimental local coefficients is expected to be poor. However, the contribution to the total plate heat transfer rate is small, so the accuracy of the average plate Nusselt number is not greatly affected.

The average plate Nusselt number was calculated by integrating the local Nusselt number distribution (using trapezoidal rule) over the wetted length of one side of the plate. The wetted length of one side of the plate is $L_{p,\mathrm{wet}} = 42.0$ mm; the plate length in the y direction is $L_p = 40.0$ mm.

The channel average Nusselt (Nu_c) was calculated using the experimental average wall and plate Nusselt numbers as:

$$\mathrm{Nu}_c = \frac{L_{p,\mathrm{wet}}\ \mathrm{Nu}_p + L_c Nu_w}{L_{p,\mathrm{wet}} + L_c} = \frac{42.0\mathrm{Nu}_p + 120.0\mathrm{Nu}_w}{162.0} \tag{6}$$

Error estimates for the local Nusselt numbers have been made using the single-sample uncertainty analysis of Kline and McClintock (1953). The largest single source of error was the uncertainty in the fringe center location due to noise in the interferogram. The scatter in the fringe location data due to optical imperfections, bench vibrations, surface diffraction fringes, imperfections in the film, etc. was about ±5 percent. In addition, the uncertainty in the measured local Nusselt number associated with the thermocouple readings was approximately ±2 percent. Combining these uncertainties with other lesser sources of error (see Naylor, 1991, for details), the total

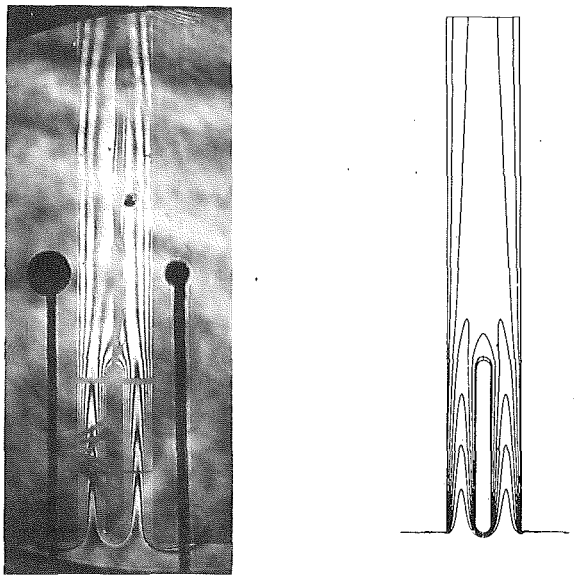

(a) infinite fringe interferogram

(b) numerical isotherm contours (elliptic)

Fig. 3 Comparison of an infinite fringe interferogram and numerical isotherm contours for $Ra_c^* = 97.6$, $L_i/L_c = 0$, $L_p/L_c = 1/3$, $L_c/b = 13.68$, $t/b = 0.2$

uncertainty in the local Nusselt numbers was found to be about ±8 percent. Integration averages the noise in the local Nusselt numbers. Hence, the average Nusselt number data are likely to be more accurate than the local Nusselt number data. In a repeated experiment the avearge Nusselt number data were found to be reproductible to within 3 percent.

An error estimate was also made for the experimental Rayleigh number (Ra_p^* or Ra_c^*). The fluid properties and their uncertainties were taken from Touloukian et al. (1970, 1975). Combining these fluid property errors with the uncertainties in the other measured quantities gave an uncertainty in the Rayleigh number of about ±3 percent.

Further details about the experimental apparatus, test procedure, and data reduction are given in the thesis by Naylor (1991).

Discussion of Results

Figure 3 shows the comparison of an infinite fringe interferogram and the numerical isotherms at $Ra_c^* = 97.6$, $L_i/L_c = 0$, $t/b = 0.2$. It can be seen in Fig. 3 that the temperature fields are qualitatively similar, although some differences exist, especially in the plume region above the plate.

Figure 4 shows the comparison of the numerical and experimental local heat transfer distributions on the dividing plate and channel walls for the case shown in Fig. 3. The largest differences occur near the leading edge of both the wall and plate. At the tip of the plate, the experimental local Nusselt number is about 20 percent lower than the numerical prediction. The comparison of average Nusselt numbers is shown in Table 1. The experimental average heat transfer rate results are about 11 percent lower than the numerical predictions. The experimental results may, in part, be lower than the numerical predictions because of the low-order extrapolation method used to determine the experimental temperature gradient. Also, despite the presence of the heat exchangers, the local heat transfer coefficient on the wall near the leading edge will be reduced because of the slight preheating of the air at the channel inlet.

In Fig. 4 it should be noted that the experimental wall and plate local Nusselt number distributions are almost the same in the range $0 < y < L_p$, except on the curved leading and trailing

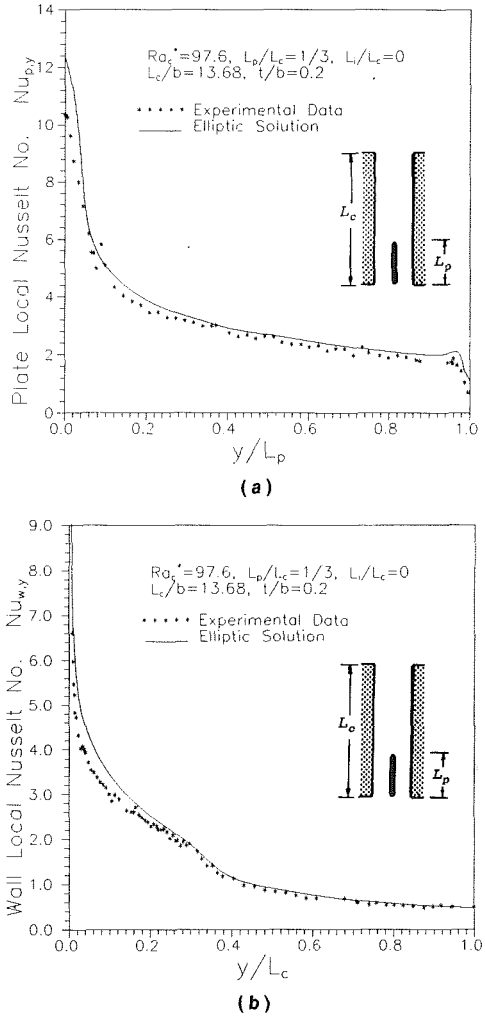

Fig. 4 Experimental and numerical (elliptic) local Nusselt number distributions for (*a*) the dividing plate and (*b*) the wall

Table 1 Experimental and numerical average Nusselt numbers for $Ra_c^* = 97.6$, $L_p/L_c = 1/3$, $t/b = 0.2$, $L_c/b = 13.68$

	Experiment	Elliptic Solution	% diff.
Wall Nusselt Number, Nu_w	1.44	1.60	11.1
Plate Nusselt Number, Nu_p	3.13	3.48	11.2

edges of the plate. As found in Part I for the elliptic solution, at low Rayleigh numbers the difference in inflow conditions for the wall and plate has very little effect on the local Nusselt number distributions.

It is interesting that both the numerical and experimental data in Fig. 4(*b*) show a subtle change in the slope of the wall local Nusselt number distribution at the end of the dividing plate. At $y/L_c \approx 1/3$, the wall local Nusselt number decreases at a slightly greater rate as the flow adjusts to the undivided portion of the channel. The effect was also seen and discussed in Part I for a zero thickness plate.

Infinite fringe interferograms showing the effect of vertical plate location and Rayleigh number on the temperature field are given in Fig. 5. For $L_i/L_c = 0$, the thermal boundary layers of the plate and wall merge close to the channel inlet at low Rayleigh number. With increasing Rayleigh number the boundary layers on the walls and plate gradually tend toward

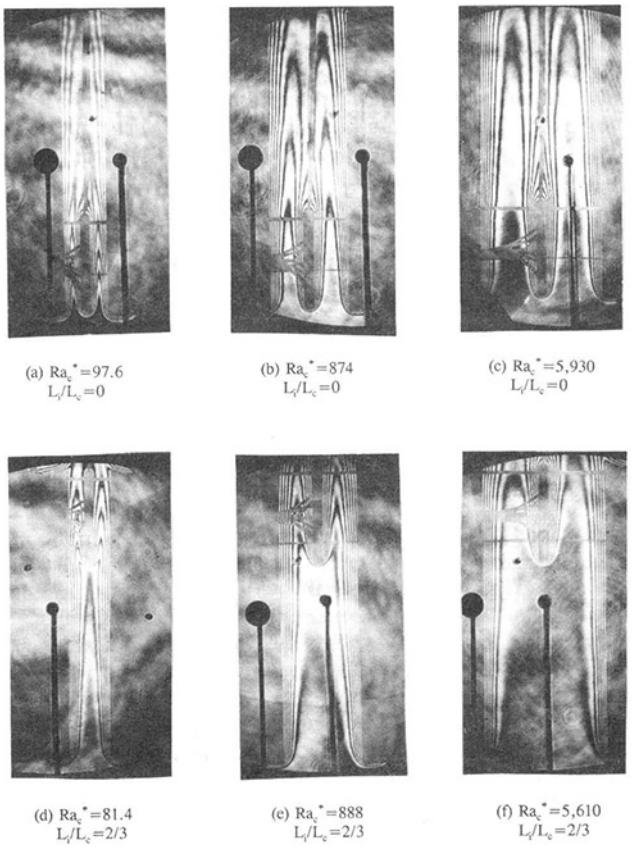

Fig. 5 Infinite fringe interferograms of the divided channel

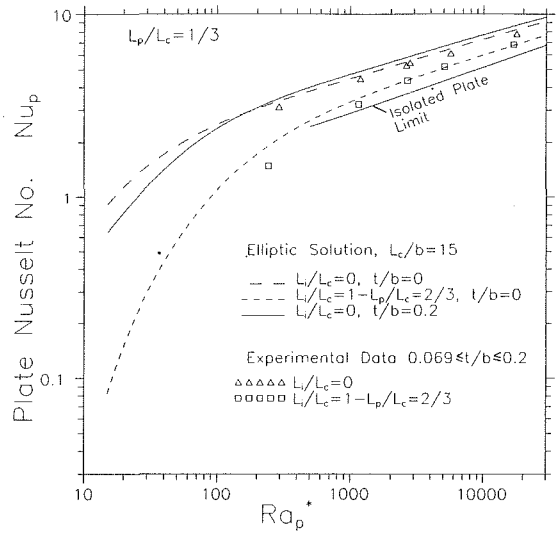

Fig. 6 Comparison of the experimental and numerical average plate Nusselt numbers (L_p/L_c = 1/3)

Table 2(*a*) Experimental average Nusselt number data for L_p/L_c = 1/3, L_i/L_c = 0 (bottom)

Ra_c^*	Ra_p^*	L_c/b	t/b	Pr	Nu_p	Nu_w	Nu_c
97.6	293	13.68	0.200	0.712	3.13	1.44	1.88
395	1,185	9.45	0.138	0.713	4.43	2.55	3.04
874	2,620	7.51	0.110	0.713	5.26	2.89	3.50
931	2,790	7.51	0.110	0.713	5.43	2.86	3.53
1,890	5,660	6.29	0.0917	0.713	6.11	3.48	4.16
5,930	17,790	4.73	0.069	0.713	7.80	4.79	5.57

Table 2(*b*) Experimental average Nusselt number data for L_p/L_c = 1/3, L_i/L_c = 1 − L_p/L_c = 2/3 (top)

Ra_c^*	Ra_p^*	L_c/b	t/b	Pr	Nu_p	Nu_w	Nu_c
81.4	244	13.68	0.200	0.713	1.48	1.44	1.45
383	1,150	9.45	0.138	0.713	3.23	2.37	2.59
888	2,660	7.51	0.110	0.713	4.34	2.97	3.33
1,690	5,670	6.29	0.0917	0.713	5.18	3.25	3.75
5,610	16,800	4.73	0.069	0.713	6.82	4.48	5.09

the appearance of boundary layers on isolated plates. The influence of dividing plate's vertical position on the temperature field is most striking at the lowest Rayleigh number. Comparing Figs. 5(*a*) and 5(*d*) shows that the plate heat transfer rate is reduced when the plate is in the top of the channel largely because air is warmed by the walls before reaching the plate. Also, it is evident that the bulk air temperature in the middle and top portions of the channel is much higher when the plate is at the bottom. As discussed in Part I, this causes additional heat transfer because of the chimney effect.

Some of the interferograms shown in Fig. 5 show slight asymmetry of the fringe patterns about the channel centerline. It should be noted that such minor asymmetry may result from an imperfect infinite fringe setting and cannot be interpreted as actual asymmetries in the temperature field.

Unfortunately, it was not feasible to verify leading edge separation and its effect on the wall local heat transfer rate using the current experimental apparatus. In the present experiment, the Rayleigh number was increased by widening the channel wall spacing 2(*b*). The channel length was fixed at L_c = 12 cm because the working height of the interferometer test beam was about 13 cm. For this reason, the experimental data at high Rayleigh number were obtained for channel aspect ratios much lower than the numerical data. Naylor et al. (1991) have shown that the critical Rayleigh number for the onset of separation is strongly dependent on channel aspect ratio. Channels with low aspect ratios (L_c/b) require much higher Rayleigh numbers to induce sufficient flow to cause fluid separation. Hence, at high Rayleigh number the channel aspect ratio was too low for the experimental wall local Nusselt number distribution to have a local minimum near the leading edge.

Figures 6 and 7 show comparisons of the experimental average wall and plate Nusselt numbers with the numerical predictions. The average Nusselt number data are given in Table 2. When comparing the results it is important to realize that the blockage ratio for the experiments decreases from t/b = 0.2 at the lowest Rayleigh number to t/b = 0.069 at the highest Rayleigh number. So, at the lowest Rayleigh number the experimental data can be compared to the numerical data for t/b = 0.2. At high Rayleigh number the experimental data can be compared to the numerical results for t/b = 0, since the effect of blockage was predicted to be small in Part I.

In Fig. 6 it can be seen that the experimental average plate Nusselt number trends are very similar to the numerical predictions. When the plate is at the top of the channel (L_i/L_c = 2/3), the data are in close agreement with the numerical results (for t/b = 0) at high Rayleigh number. At low Rayleigh number the experimental data (for L_i/L_c = 2/3, t/b = 0.2) are slightly below the numerical results for t/b = 0. The experimental results are likely lower, at least to some extent, because of the higher blockage effects. When the plate is located in the bottom of the channel, the experimental data are about 10 percent lower than the numerical data at lowest Rayleigh number and about 6 percent lower at the highest Rayleigh number. For most practical purposes the experimental results confirm the

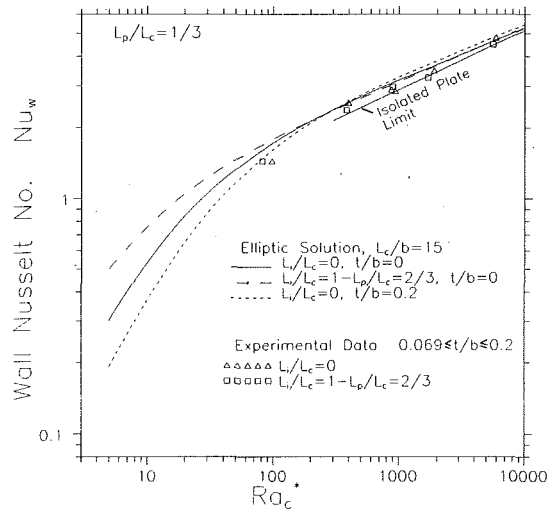

Fig. 7 Comparison of the experimental and numerical average wall Nusselt numbers ($L_p/L_c = 1/3$)

Table 3 Constants and statistics for the channel Nusselt number correlation Eq. (8)

Plate Position L_i/L_c	C	n	Number of Data	Standard Deviation	Maximum Error
0	0.626	1.63	116	4.6%	±12.1%
$(1-L_p/L_c)/2$	0.618	1.45	89	4.4%	±10.9%
$1-L_p/L_c$	0.595	1.42	95	5.0%	±15.0%

Table 4 Constants and statistics for the wall Nusselt number correlation Eq. (9)

Plate Position L_i/L_c	C_1	C_2	n	Number of Data	Standard Deviation	Maximum Error
0	0.588	6	1.48	84	6.2%	±17.0%
$(1-L_p/L_c)/2$	0.595	3	1.37	76	6.0%	±17.9%
$1-L_p/L_c$	0.583	3	1.53	82	4.9%	±13.0%

numerical prediction regarding the effect of plate position on average plate Nusselt number. Positioning the plate higher in the channel reduces the heat transfer rate from the plate. This effect is most severe at lower Rayleigh numbers. For $L_p/L_c = 1/3$, moving the plate from the top to the bottom of the channel approximately doubles the average plate Nusselt number at $Ra_p^* \approx 300$.

Figure 7 shows the comparison of numerical and experimental data for the average wall Nusselt number. Again, the trends of the experimental and numerical data are in fair agreement. In general, the experimental data are slightly lower than the numerical results. Nevertheless, the experimental data confirm that the average wall Nusselt number is relatively insensitive to the plate position at moderate and high Rayleigh number.

Data Correlation

The data from the numerical solutions (Part I) and the experimental data have been correlated using the method of Churchill and Usagi (1972). Using this method, the upper and lower limiting expressions are combined as follows:

$$\mathrm{Nu} = [(\mathrm{Nu}_{\text{Fully Dev.}})^{-n} + (\mathrm{Nu}_{\text{Isol. Plate}})^{-n}]^{-\frac{1}{n}} \tag{7}$$

where $\mathrm{Nu}_{\text{Fully Dev.}}$ is the expression for fully developed conditions ($\mathrm{Ra}^* \to 0$) and $\mathrm{Nu}_{\text{Isol. Plate}}$ is the expression for the isolated plate limit ($\mathrm{Ra}^* \to \infty$).

Channel Average Nusselt Number Nu_c: There are three separate correlations for the channel average Nusselt number: one for the plate in the bottom $L_i/L_c = 0$, middle $L_i/L_c = (1 - L_p/L_c)/2$, and top $L_i/L_c = 1 - L_p/L_c$ of the channel. The general form of the correlations for Nu_c is:

$$\mathrm{Nu}_c = \left(\left(\frac{\mathrm{Ra}_c^*}{3\left(4\left(\frac{L_p}{L_c}\right)^2\left(\frac{b}{b-t}\right)^3 + 4\frac{L_p}{L_c}\left(\frac{b}{b-t}\right)^3 - \left(\frac{L_p}{L_c}\right)^2 + 1\right)} \right)^{-n} + \left(C\,\mathrm{Ra}_c^{*\frac{1}{4}} \frac{\left(\frac{L_p}{L_c}\right)^{\frac{3}{4}} + 1}{\frac{L_p}{L_c} + 1} \right)^{-n} \right)^{-\frac{1}{n}} \tag{8}$$

The constant C was treated as an arbitrary constant in Eq. (8) to compensate for the fact that the upper asymptotic limit is approached from above. For each vertical plate position, both the constant C and the exponent n were determined numerically by minimizing the rms percent error between the correlation and the data. Table 3 gives the values of C and n for each vertical plate position and the correlation statistics. Equation (8) fits the numerical and experimental data with a maximum error of ±15 percent.

Average Wall Nusselt Number Nu_w. Correlations for the average wall Nusselt number were calculated using the same method as for the channel average Nusselt number. The general form of the correlations for Nu_w is:

$$\mathrm{Nu}_w = \left(\left(\frac{\mathrm{Ra}_c^*}{C_2\left(4\left(\frac{L_p}{L_c}\right)\left(\frac{b}{b-t}\right)^3 - \frac{L_p}{L_c} + 1\right)} \right)^{-n} + \left(C_1\,\mathrm{Ra}_c^{*\frac{1}{4}} \right)^{-n} \right)^{-\frac{1}{n}} \tag{9}$$

Table 4 gives the values of the constants C_1, C_2, the exponent n and the correlation statistics for each vertical plate position. The lower limiting asymptotic value of Nu_w depends upon the plate's vertical position: $C_2 = 6$ for $L_i/L_c = 0$, and $C_2 = 3$ for $L_i/L_c > 0$. Note that Eq. (9) should not be used for plate length ratios much less than $L_p/L_c = 1/10$ when the plate is at the bottom of the channel; as discussed in Part I, the expression for the fully developed average wall Nusselt number is not valid as $L_p/L_c \to 0$ for $L_i/L_c = 0$. Similarly, the correlation should not be used for plate length ratios much larger than $L_p/L_c = 2/3$ when the plate is not located at the channel inlet; for $L_i/L_c > 0$ the expression for fully developed average wall Nusselt number is not valid as $L_p/L_c \to 1$.

It can be seen from Table 4 that the Nu_w data do not correlate as well as the Nu_c data. The main reason for the poorer correlation is the larger difference between the data from the parabolic and elliptic solutions.

Average Plate Nusselt Number Nu_p. For $L_i/L_c > 0$, a closed-form expression is not available for the lower limiting behavior ($\mathrm{Ra}_p^* \to 0$) of the average plate Nusselt number. Hence, a cor-

relation for Nu_p is presented only for $L_i/L_c=0$. Fortunately, this is the channel configuration of most practical interest.

The correlation for the average plate Nusselt number for $L_i/L_c=0$ is:

$$Nu_p=\left(\left(\frac{Ra_p^*}{6\left(4\left(\frac{L_p}{L_c}\right)\left(\frac{b}{b-t}\right)^3-\frac{L_p}{L_c}+1\right)}\right)^{-2.0}+\left(0.632\left(\frac{L_p}{L_c}\right)^{-0.19}Ra_p^{*\frac{1}{4}}\right)^{-2.0}\right)^{-\frac{1}{2.0}} \quad (10)$$

Notice that the upper asymptotic limit has been modified to include the effect of the plate length ratio L_p/L_c. The numerical results presented in Part I show that Nu_p depends strongly on plate length ratio (L_p/L_c) even at the highest Rayleigh number considered in this study. The factor $(L_p/L_c)^{-0.19}$, included in Eq. (10), was derived from this numerical data. Equation (10) fits the experimental and numerical data with a maximum error of ± 13 percent and a standard deviation of 6.2 percent. This correlation should not be used for plate length ratios much less than $L_p/L_c=1/10$ because the expression for the fully developed average plate Nusselt number is not valid as $L_p/L_c \to 0$.

Summary

The results of an interferometric study of laminar natural convection in a vertical divided channel have been presented. Interferograms were obtained for air and for $L_p/L_c=1/3$ with the dividing plate located at both the bottom $(L_i/L_c=0)$ and top of the channel $(L_i/L_c=2/3)$. Comparisons of local and average Nusselt numbers were made with the numerical predictions from Part I. The experimentally measured average Nusselt numbers were typically about 10 percent lower than the numerical results. However, the general trends of the numerical and experimental data were in good agreement. The experimental results confirm that positioning the plate at the bottom of the channel $(L_i/L_c=0)$ gives the maximum heat transfer rate, and the average wall Nusselt number is almost independent of the plate's vertical position (L_i/L_c) at moderate and high Rayleigh number. Average Nusselt number correlation equations for the dividing plate, the channel walls, and the overall channel were also presented.

Acknowledgments

The authors wish to acknowledge the support received from NSERC of Canada.

References

Churchill, S. W., and Usagi, R., 1972, "A General Expression for the Correlation of Rates of Transfer and Other Phenomena," *AIChE Journal*, Vol. 18, No. 6, pp. 1121–1128.

Eckert, E. R. G., and Soehngen, E. E., 1948, "Studies on Heat Transfer in Laminar Free Convection With the Zehnder-Mach Interferometer," United States Air Force, AF Technical Report 5747.

Eckert, E. R. G., and Goldstein, R. J., 1976, *Measurements in Heat Transfer*, Hemisphere Publishing Corp., pp. 264–293.

Kline, S. J., and McClintock, F. A., 1953, "Describing Uncertainties in Single-Sample Experiments," *Mechanical Engineering*, Vol. 75, Jan., pp. 3–8.

Naylor, D., 1991, "A Numerical and Interferometric Study of Natural Convective Heat Transfer From Divided and Undivided Vertical Channels," Ph.D. Thesis, The University of Western Ontario, London, Ontario, Canada.

Naylor, D., Floryan, J. M., and Tarasuk, J. D., 1991, "A Numerical Study of Developing Free Convection Between Isothermal Vertical Plates," ASME JOURNAL OF HEAT TRANSFER, Vol. 113, pp. 620–626.

Touloukian, Y. S., Liley, P. E., and Saxena, S. C., 1970, "Thermal Conductivity: Nonmetallic Liquids and Gases," in: *Thermophysical Properties of Matter*, Vol. 3, Thermophysical Properties Research Center (TPRC), Purdue University, Plenum Publishing Corp.

Touloukian, Y. S., and Makita, T., 1970, "Specific Heat: Nonmetallic Liquids and Gases," in: *Thermophysical Properties of Matter*, Vol. 6, Thermophysical Properties Research Center (TPRC), Purdue University, Plenum Publishing Corp.

Touloukian, Y. S., Saxena, S. C., and Hestermans, P., 1975, "Viscosity," in: *Thermophysical Properties of Matter*, Vol. 11, Thermophysical Properties Research Center (TPRC), Purdue University, Plenum Publishing Corp.

A. G. Straatman
Graduate Student.

J. D. Tarasuk
Professor of Mechanical Engineering.

J. M. Floryan
Professor of Mechanical Engineering.

The University of Western Ontario,
London, Ontario, Canada

Heat Transfer Enhancement From a Vertical, Isothermal Channel Generated by the Chimney Effect

A numerical and experimental investigation of free convection from vertical, isothermal, parallel-walled channels has been undertaken to explore the heat transfer enhancement obtained by adding adiabatic extensions of various sizes and shapes. Investigations were carried out for air ($Pr = 0.7$) over a wide range of wall heating conditions. In all cases, the adiabatic extensions were able to increase heat transfer. The increase varied from 2.5 at low Ra to 1.5 at high Ra*. The experimental and numerical results are in excellent agreement. A single correlation accounting for the channel aspect ratio* L_h/b, *expansion ratio,* B/b, *modified Rayleigh number, Ra* and heated length ratio,* L_h/L *is presented.*

Introduction

Natural convection is an energy transport process which takes place as a result of buoyancy-induced fluid motion occurring in the presence of a body force field. The heated, parallel-walled channel is an archetypal configuration where natural convection heat transfer has been studied extensively. Continued research is of considerable value in the electronics industry since waste heat from printed circuit boards and board-mounted chips is still commonly extracted in this manner. The first comprehensive study of the parallel-walled channel was by Elenbaas (1942), who established overall heat transfer correlations for isothermal channels over a wide range of thermal and geometric parameters. Since this pioneering work, many authors (Bodoia and Osterle, 1962; Kettleborough, 1972; Nakamura et al., 1982; Bar-Cohen and Rohsenow, 1984) have undertaken studies to improve our understanding of the mechanisms involved and to provide more information necessary for use in engineering design. For a detailed literature review on channel convection, see Naylor et al. (1991). The most recent refinements to the analysis of isothermal parallel-walled channels were studies by Naylor et al. (1991) and Martin et al. (1991). Naylor et al. (1991) presented new information exhibiting secondary flow near the channel entrance and its resulting effect on local heat transfer. Upstream conduction at low Ra* was discussed in detail by Martin et al. (1991).

In general, there is good agreement as to the overall heat transfer one can expect from a parallel-walled channel due to natural convection. To enhance the heat transfer from such a channel, more fluid must be forced through it so that additional energy can be convected away. The well-known "chimney" effect, first treated in a paper by Haaland and Sparrow (1983), is a method of naturally inducing a higher flow of fluid through a confined, open-ended enclosure. Oosthuizen (1984) numerically calculated the heat transfer enhancement from isothermal parallel-walled channels caused by the addition of straight adiabatic extensions at the exit. The approach he used was a fully implicit forward marching procedure to solve the parabolic form of the governing equations. He found that enhancements in heat transfer of up to 50 percent occurred, but enormous unheated lengths were required to bring about the change (i.e., $L_h/L < 10^{-2}$). Very small enhancements were reported for short extensions. Asako et al. (1990) studied heat transfer enhancement gained by attaching unheated tubes of greater diameter to the exit of a vertical isothermal tube. Their approach was also numerical, but the full elliptic form of the governing equations was solved using finite element discretization. Increases in heat transfer of up to 250 percent were reported for low Rayleigh numbers and modest chimney sizes, which contradicts Oosthuizen's results. Flow field plots show the formation of standing vortices below the tube inlet which questions the validity of the inflow boundary conditions (see Naylor et al., 1991, for discussion).

In both of the aforementioned works, the main focus was on the overall increases in heat transfer that could be obtained by exploiting the "chimney" effect in a specific situation. No studies were made in either case to explore the local changes that must occur, nor were the changes experimentally verified. The intent of the present study is to provide a complete and systematic analysis of heat transfer enhancement gained by adding adiabatic extensions of various width to an isothermal parallel-walled channel, and specifically to remove contradictions existing in the available literature. Attention is given to the global as well as local changes of the convection process within the channel that are brought about by the addition of the extension. Experiments using a Mach-Zehnder interferometer provide verification for both the local and global changes in heat transfer. A general correlation will be formulated to make the result useful for engineering design considerations.

Formulation of Problem

The geometry under investigation is shown in Fig. 1. The heated portion of the channel, formed by two plates of length L_h and separation $2b$, is maintained at a constant temperature T_w above the ambient T_o. Fluid travels through the channel and then through an adiabatic extension before returning to the ambient. Flow in both the channel and the chimney is assumed to be two-dimensional, laminar, steady and incompressible with negligible viscous dissipation. All thermophysical properties of the fluid (ρ, C_p, μ, k, Pr) are assumed constant except for the variation in density with temperature (Boussinesq approximation) giving rise to the buoyancy forces.

Numerical Solution

Since the problem is symmetric, only half of the flow field needs to be solved. The boundary conditions for the half channel and extension are (refer to Fig. 1):

$$T = T_w, \quad u = v = 0 \quad \text{for} \quad x = b, \quad 0 \le y \le L_h \tag{1}$$

$$\partial T/\partial y = \partial u/\partial y = \partial v/\partial y = 0 \quad \text{for} \quad 0 < x < B, \quad y = L \tag{2}$$

Contributed by the Heat Transfer Division for publication in the JOURNAL OF HEAT TRANSFER. Manuscript received by the Heat Transfer Division May 1992; revision received October 1992. Keywords: Augmentation and Enhancement, Natural Convection. Associate Technical Editor: J. R. Lloyd.

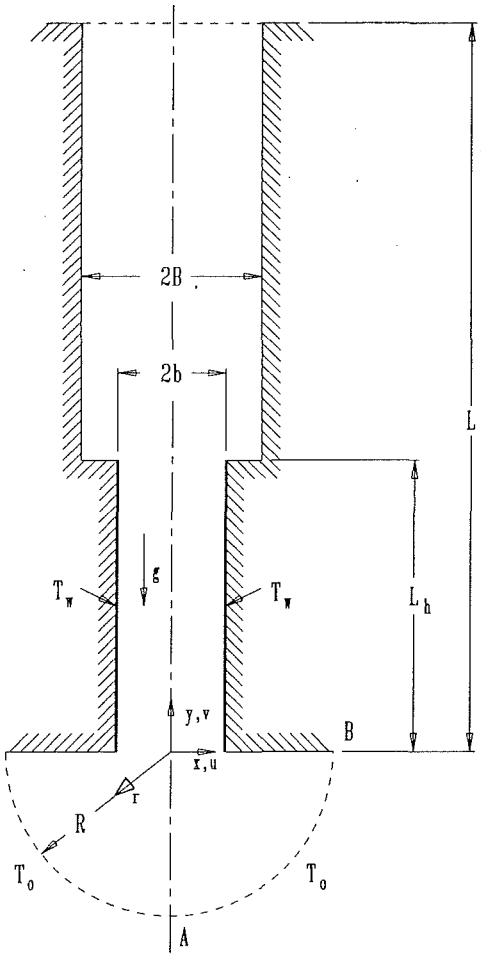

Fig. 1 Geometry under investigation showing dimensions and coordinate system

$$\partial T/\partial x = \partial v/\partial x = u = 0 \quad \text{for} \quad x = 0, \quad -R \le y \le L \tag{3}$$

$$\partial T/\partial y = u = v = 0 \quad \text{for} \quad b < x \le R, \quad y = 0 \quad \text{for} \quad b < x \le B, \quad y = L_h \tag{4}$$

$$\partial T/\partial x = u = v = 0 \quad \text{for} \quad x = B, \quad L_h < y \le L \tag{5}$$

$$v_\theta = \sigma_{rr} = 0, \quad T = T_o \quad \text{on the circular inlet } AB \tag{6}$$

The inlet boundary conditions are based on Jeffrey-Hamel flow, a similarity solution for isothermal flow caused by the presence of a source or sink located at the intersection of two walls. The inlet conditions were imposed as described by Naylor et al. (1991).

By introducing the following nondimensional quantities:

$$U = u/U^*, \quad V = v/U^*, \quad X = x/b, \quad Y = y/b, \quad V_\theta = v_\theta/U^*,$$

$$V_r = v_r/U^*, \quad T^* = (T - T_o)/(T_w - T_o), \quad P = p^* b/\mu U^* \tag{7}$$

where

$$U^* = \alpha \mathrm{PrGr}^{1/2}/b, \quad \mathrm{Gr} = g\beta(T_w - T_o)b^3/\nu^2 \tag{8}$$

the governing equations are transformed to:

$$\mathrm{Gr}^{1/2}\left(U\frac{\partial U}{\partial X} + V\frac{\partial U}{\partial Y}\right) = -\frac{\partial P}{\partial X} + \left(\frac{\partial^2 U}{\partial X^2} + \frac{\partial^2 U}{\partial Y^2}\right) \tag{9}$$

$$\mathrm{Gr}^{1/2}\left(U\frac{\partial V}{\partial X} + V\frac{\partial V}{\partial Y}\right) = -\frac{\partial P}{\partial Y} + \left(\frac{\partial^2 V}{\partial X^2} + \frac{\partial^2 V}{\partial Y^2}\right) + \mathrm{Gr}^{1/2}T^* \tag{10}$$

$$\mathrm{PrGr}^{1/2}\left(U\frac{\partial T^*}{\partial X} + V\frac{\partial T^*}{\partial Y}\right) = \left(\frac{\partial^2 T^*}{\partial X^2} + \frac{\partial^2 T^*}{\partial Y^2}\right) \tag{11}$$

$$\frac{\partial U}{\partial X} + \frac{\partial V}{\partial Y} = 0 \tag{12}$$

subject to the boundary conditions:

$$T^* = 1, \quad U = V = 0 \quad \text{for} \quad X = 1, \quad 0 \le Y \le L_h/b \tag{13}$$

$$\partial T^*/\partial Y = \partial U/\partial Y = \partial V/\partial Y = 0 \quad \text{for} \quad 0 < X < B/b, \quad Y = L/b \tag{14}$$

$$\partial T^*/\partial X = \partial V/\partial X = U = 0 \quad \text{for} \quad X = 0, \quad -R/b \le Y \le L/b \tag{15}$$

$$\partial T^*/\partial Y = U = V = 0 \quad \text{for} \quad 1 < X \le R/b, \quad Y = 0 \quad \text{for} \quad 1 < X \le B/b, \quad Y = L_h/b \tag{16}$$

$$\partial T^*/\partial X = U = V = 0 \quad \text{for} \quad X = B/b, \quad L_h/b < Y \le L/b \tag{17}$$

$$V_\theta = 0, \quad -P + 2\partial V_r/\partial r = 0, \quad T^* = 0 \quad \text{on the circular boundary} \tag{18}$$

The local Nusselt number is given by:

$$\mathrm{Nu}_y = \frac{h_y b}{k} = \left[-\frac{\partial T^*}{\partial X}\right]_{X=1} \tag{19}$$

Nomenclature

- b = half channel width
- B = half extension width
- C_p = specific heat at constant pressure
- g = acceleration due to gravity
- Gr = Grashof number = $g\beta(T_w - T_o)b^3/\nu^2$
- h_y = local heat transfer coefficient
- k = thermal conductivity of fluid
- L = total length of channel and extension
- L_h = length of heated channel
- Nu_{mo} = average Nusselt number for channel without extension
- Nu_m = average Nusselt number
- Nu_y = local Nusselt number
- p = pressure
- P = dimensionless pressure deficit
- Pr = Prandtl number
- Q^* = dimensionless induced flow rate
- r = radial coordinate in semicircular inlet region
- R = inlet radius
- Ra^* = modified Rayleigh number = $\mathrm{GrPr}(b/L_h)$
- T = temperature
- T^* = dimensionless temperature = $(T - T_o)/(T_w - T_o)$
- T_o = ambient fluid temperature
- T_w = wall temperature
- u, v = velocity components in x and y direction
- U, V = dimensionless velocity components
- U^* = velocity scale
- v_r, v_θ = radial and tangential velocity components
- V_r, V_θ = dimensionless radial and tangential velocity components
- x, y = Cartesian coordinates
- X, Y = dimensionless Cartesian coordinates
- α = thermal diffusivity
- β = volumetric expansion coefficient
- μ = dynamic viscosity
- ν = kinematic viscosity
- ρ = density
- σ_{rr} = radial stress tensor

Subscripts

- h = heated
- m = mean (average)
- o = ambient
- r = radial
- w = wall
- y = local
- θ = tangential

Table 1 Results of testing for grid density and location of inlet boundary performed at $L_h/L = 1/3$ and $L_h/b = 17$

# Elements	Gr	R	B/b	Expansion	Nu_m	Q^*
1848	100	5	2.75	Diffused	1.1682	4.0977
3800	100	5	2.75	Diffused	1.1716	4.0968
1848	1000	5	2.75	Diffused	2.0616	4.6280
3800	1000	5	2.75	Diffused	2.0699	4.6287
1848	10000	5	2.75	Diffused	3.1958	4.7808
3800	10000	5	2.75	Diffused	3.2256	4.7856
3800	10000	5	2.75	Diffused	3.1958	4.7808
3800	10000	7	2.75	Diffused	3.2176	4.7558
4540	100	7	2.00	Abrupt	1.1811	4.1717
4984	100	7	2.00	Abrupt	1.1810	4.1711
4540	1000	7	2.00	Abrupt	2.0268	4.3774
4984	1000	7	2.00	Abrupt	2.0268	4.3771
4540	10000	7	2.00	Abrupt	3.1366	4.2472
4984	10000	7	2.00	Abrupt	3.1366	4.2469

The overall channel Nusselt number was computed as:

$$Nu_m = \left[Gr^{1/2} Pr \frac{b}{L_h} \int_0^{B/b} VT^* dX \right]_{Y=L/b} \quad (20)$$

and the dimensionless flow rate was calculated from:

$$Q^* = \left[\int_0^{B/b} V dX \right]_{Y=L/b} \quad (21)$$

The numerical solution employs finite element discretization. Computations were carried out using the commercial software FIDAP (Fluid Dynamics International 1989). The mesh was constructed with nine-node quadrilateral elements for which velocity and temperature are approximated using biquadratic interpolation functions and the pressure with discontinuous linear functions. The "penalty function" approach for pressure was used in the calculations. Accuracy of results was determined by a sequence of calculations carried out at low, intermediate, and high heating with an increasing grid density. Similarly, the location of the inlet boundary was determined on the basis of calculations with an increasing radius, R. Table 1 summarizes the results from the grid density and boundary location study. The overall Nusselt number and dimensionless flow rate were both numerically accurate to better than 1 percent. Local Nusselt numbers along the channel wall were most sensitive at high heating where differences of ≈ 2 percent occurred near the channel inlet tapering off to much less than 1 percent for the remainder of the wall. An example of the final mesh is shown in Fig. 2. The inlet radius is $R = 7$ and 18577 nodes were used. The diagram is divided into three parts to make the element distribution in the critical areas more clear.

The analysis was carried out for the following classes of geometry: heated channel without extension, channels with straight adiabatic extensions (i.e., $B/b = 1$), channels with abrupt expansions (i.e., $B/b \geq 1$), and channels with diffused expansions. Solutions were obtained for air ($Pr = 0.7$) and covered the range: $10 \leq L_h/b \leq 24$, $1/4 \leq L_h/L \leq 1$, $1 \leq B/b \leq 5$ and $1 \leq Ra^* \leq 500$.

Experimental Apparatus and Measurements

Experiments were performed with ambient air using a Mach-Zehnder interferometer. The light source for the interferometer was a 5 mW red Helium-neon Laser beam ($\lambda = 632.8$ nm). The technique used to align the interferometer was that described by Tarasuk (1968).

A detailed view of the test-section is shown in Fig. 3. The heated channel consisted of two precision machined aluminum

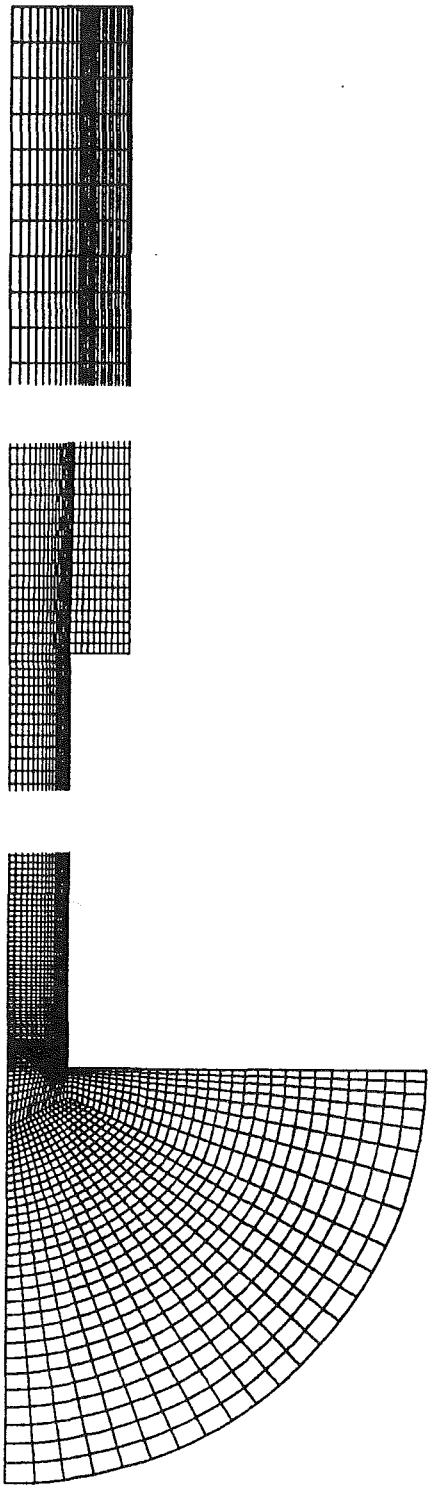

Fig. 2 Finite element mesh for entire flow domain

plates 12 ± 0.005 cm high, 25.91 ± 0.01 cm long and 1.2 cm thick, bevelled along the upper and lower edges (item 1). The plates were flat to within 0.0025 cm over the described dimensions and the exposed surfaces were brought to a highly polished finish to minimize radiant heat transfer. Each plate had nine holes drilled to within 2 mm of the exposed surface for the placement of copper-constantan thermal couples (item 3) to monitor the wall temperature. The holes were drilled in a three-by-three array with the bottom row 0.8 cm from the leading edge and the outermost columns 1.3 cm from the ends of the plates. Electrical strip heaters (item 7, four per plate)

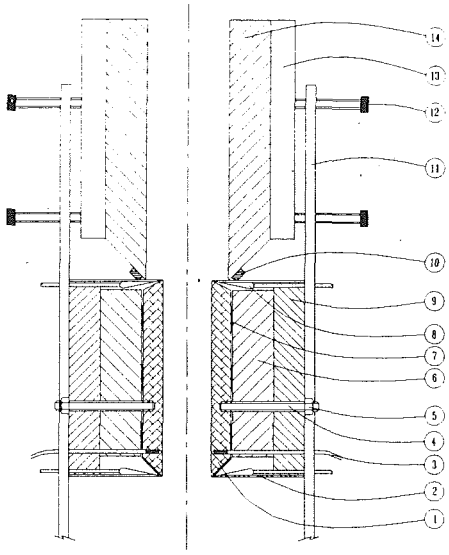

1 - Precision machined aluminum plate
2 - Phenolic board
3 - 40 gauge Copper-constantan thermocouple
4 - Nylon threaded rod
5 - Nylon nut
6 - Polystyrene, 2.54 cm thick
7 - Electric strip heater ($\approx 60\ \Omega$)
8 - Single pass heat Exchanger
9 - Plywood, 1.2 cm thick
10 - Adhesive weather seal
11 - Aluminum frame assy
12 - Nylon adjusting pin
13 - Wood strip 1.9 x 1.9 cm
14 - Polystyrene, 2.54 cm thick

Fig. 3 Detailed cross-section of the experimental model

were pasted to the back surface of each plate to supply the heating. The back surfaces were insulated from the surroundings with 2.54-cm-thick polystyrene insulating material (item 6) and 1.2 cm of spruce plywood (item 9). Each plate assembly was held together using four threaded nylon rods (item 4) extending 0.5 cm into the aluminum wall, through the insulation and the plywood and secured with nylon nuts (item 10). The horizontal surfaces at the entrance and exit of the heated channel were fabricated from 1-mm-thick phenolic boards (item 2). Adjacent to each board, a semiflattened copper tube (item 8) was "glued" using a conducting compound and silicon adhesive. The tubes were installed so that water at ambient temperature could be circulated through them to ensure that the upper and lower surfaces would function adiabatically. This adiabatic condition was maintained during each experiment by adjusting the water flow to each of the separately controlled tubes until the interference fringes (isotherms) penetrated the surfaces normally. A tiny bead of silicon adhesive was used to seal the interface between the aluminum plates and the phenolic boards.

The chimney was constructed using various heights of 2.54-cm-thick, 26-cm-long polystyrene insulating material (item 14). The polystyrene walls were made flat by gluing 1.9×2.5 cm wood strips (item 13, five per wall) on the back surfaces. The interface between the upper surface of the channel and the extension was sealed off with adhesive weather stripping (item 10) to eliminate ambient air from being entrained through the gap.

The entire channel assembly and extension was mounted into an adjustable frame (item 11) constructed from four sections of aluminum angle ($3.8 \times 3.8 \times .6$ cm). The aspect ratio of the heated channel was adjustable from $10 \le L_h/b \le 24$. The width of the chimney was adjustable from $1 \le B/b \le 4$ at a channel aspect ratio of $L_h/b = 17$. The ends of the heated channel were closed off using 3.0-cm-thick, 15-cm-dia optical flats to prevent ambient air from being entrained at the edges, thus reinforcing the two dimensionality of the model. The ends of the extension were closed off for the same reason, using additional sections of 2.54-cm-thick, polystyrene insulating material. Several experiments were performed at $L_h/b = 17$, $L_h/L = 1/3$, $1 \le B/b \le 2.5$ and $\mathrm{Ra}^* \approx 20$, 40 to check whether radiation heat transfer or boundary layer growth on the end caps had a significant effect on the convection results. The boundary layer growth on the end caps (three-dimensional effects) was checked by performing experiments with and without diffused end caps. The amount that the ends were diffused was calculated from elementary boundary layer theory for flow along a flat plate. The effects of radiation were checked in separate experiments with and without a radiation shield. The radiation shield, consisting of four sections of polystyrene insulating sheet, was arranged over the exit of the extension in a manner which would isolate the inner walls of the extension from the surroundings without obstructing the exiting flow. Since the exiting flow contacted the shield before reaching the surroundings, the shield took on the temperature of the extension and their radiative exchange was minimized. The boundary layer was found to have no measurable effect, while the radiation losses at large B/b warranted the use of a radiation shield at the exit for all subsequent experiments.

A typical experiment was initiated by obtaining an infinite fringe setting on the interferometer across the aligned, unheated model, using the procedure outlined by Tarasuk (1968). After a scale photograph was taken, direct current was applied to the heaters and the walls were brought up to the required temperature. The model was assumed to have reached steady-state when the temperatures obtained from the 18 separate thermal couples were within 0.5°C (usually 30–40 min). An infinite fringe photograph was then taken for observation of the temperature field. The interferometer setting was changed to observe finite fringes and a photograph was obtained for analysis purposes. Finite fringes were chosen for analysis since ambient reference fringes were visible on all photographs obtained at this setting. Local fringe shift gradients were extracted from the finite fringe photographs using a digital imaging system. Fifty to seventy scans were taken along the height of a wall with more scans concentrated near the inlet. Local and overall Nusselt numbers were calculated from the experimental fringe shift gradients for comparison with the numerical results. The estimated experimental error in the local heat transfer coefficients was ±8 percent and for the overall channel heat transfer, about ±4 percent. Two similar tests at $L_h/b = 17$, $L_h/L = 1/3$, $B/b = 2.5$ and $\mathrm{Ra}^* \approx 40$ demonstrated that the measurements were reproducible to within 2.5 percent. For a detailed treatment of the experimental error, refer to Straatman (1992).

Results and Discussion

The primary aim of the present study was to quantify the local and overall changes in heat transfer that could be brought about by exploiting the "chimney" effect. To make the changes more apparent, the overall results for heat transfer and mass flow obtained from heated channels with extensions are presented as a ratio of those obtained from heated channels without extensions. Figure 4 shows the results for the reference case of the overall Nusselt number, Nu_{mo} versus the Rayleigh number, Ra^* $(= g\beta(T_w - T_o)b^4/\nu\alpha L_h)$, for an isothermal channel (without extension) obtained as a part of the present study and by Naylor et al. (1991) and Elenbaas (1942).

Effects of Geometry

Part I Straight Extensions. The case of heated channels with straight adiabatic extensions is considered first. Figure 5 shows the present numerical results for relative overall heat transfer and flow rate as a function of Rayleigh number, Ra^*, for different values of L_h/L. Channel aspect ratios of $L_h/b = 10$, 17, 24 were used in the calculations. The relative quantities were consistently greater than one and increased as L_h/L decreased (i.e., as the unheated extension increased in length). By following a line of constant Ra^*, it is seen that

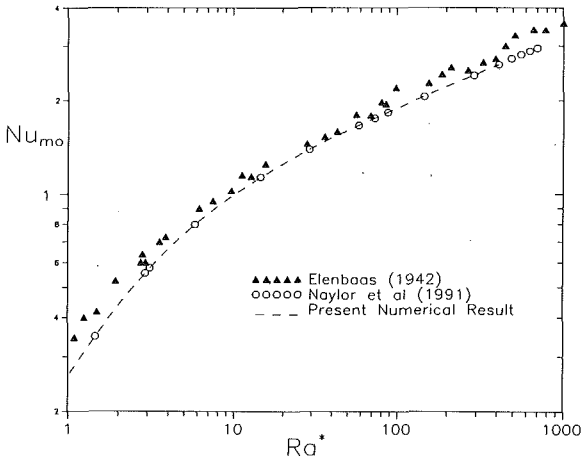

Fig. 4 Comparison of existing experimental and numerical data to the present solution for fully heated isothermal channels over applicable range

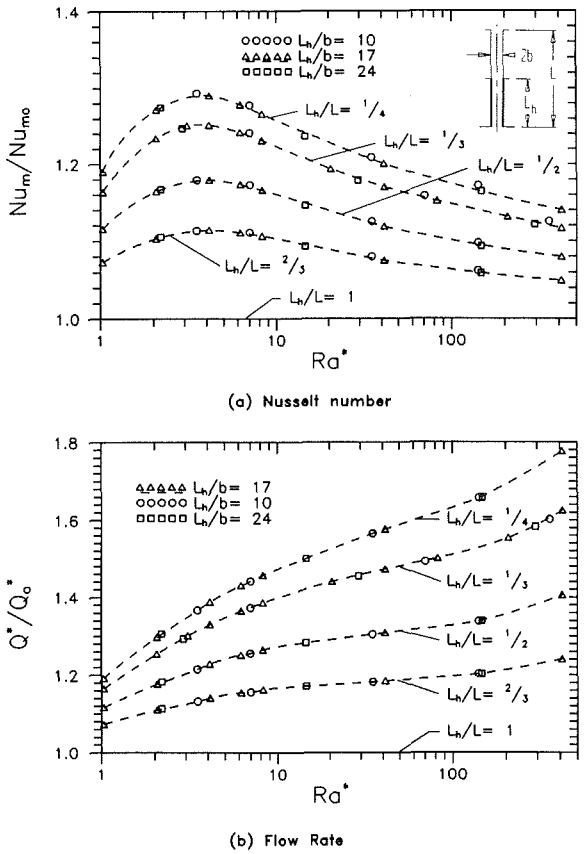

Fig. 5 Ratios of heat transfer (*a*) and dimensionless flow rate (*b*) for straight extensions (*B/b* = 1)

enhancements in heat transfer do not increase linearly as the unheated extension is increased. Based on the length ratios studied, each subsequent unheated length (i.e., $L_h/L = 1/L$ where: $L = 1, 2, 3, 4$) produced an enhancement equal to ≈ 50 percent of the previous unheated length. If this trend were to continue beyond $L_h/L = 1/4$, 99 percent of the maximum possible enhancement would be obtained using $L_h/L = 1/8$. Calculations were not carried out beyond $L_h/L = 1/4$ because it is not likely that such long extensions can be used in actual applications.

Figure 5(*a*) shows a local maximum occurring in relative overall heat transfer at $Ra^* \approx 4$ ($Gr \approx 100$) indicating the region where the "chimney effect" is most pronounced. Some discussion regarding heated channels without extensions will aid

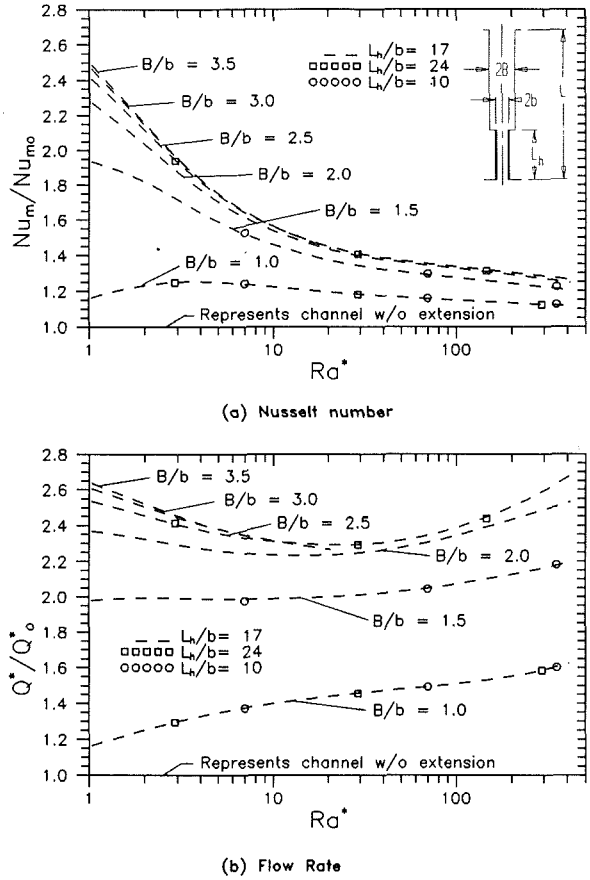

Fig. 6 Ratios of heat transfer (*a*) and dimensionless flow rate (*b*) for an abrupt expansion over the heating range studied. The curves represent $L_h/L = 1/3$.

the rationalization. For the limiting case of $Ra^* \to 0$ (Martin et al., 1991), no convective motion exists and the addition of an unheated extension can bring about no changes, i.e., the function of the extension is to allow a heated plume to increase its momentum. As Ra* increases, convection heat transfer starts to dominate and induced mass flow in the form of a heated plume begins to move up the channel. For moderately low Ra* ($1 < Ra^* < 10$), the induced flow within the channel is balanced by frictional resistance from the walls and fully (hydrodynamically and thermally) developed flow occurs. The addition of an extension in this region allows the warm plume to gain momentum and cause the flow in the heated channel to exist as undeveloped, giving rise to significantly higher heat transfer. When Ra* is much larger ($Ra^* > 40$) the flow in the unaugmented channel already exists as undeveloped, and further increases in flow can only bring about modest increases in overall heat transfer.

The relative flow rate shown in Fig. 5(*b*) increases fairly consistently with increased Ra*. For the cases where $Ra^* \to 0$ and $Ra^* \to \infty$, insufficient data was obtained to make a prediction on the behavior of Q^*/Q_o^*. The flow behavior was not pursued since it is of secondary interest in the present study.

Part II Abrupt Expansions. As the ratio of widths of the chimney and channel, B/b, is increased, the frictional resistance in the chimney decreases. This allows the plume to gain greater momentum leading to an increase in flow rate and, more importantly, heat transfer. Figure 6 shows the present numerical results for the relative overall heat transfer and flow rate as a function of Ra* for a fixed value of $L_h/L = 1/3$ and $1 \le B/b \le 3.5$. The curves for increasing values of B/b in part (*a*) share the same general characteristics as any one curve from Fig. 5(*a*). One notable difference is that as B/b increases,

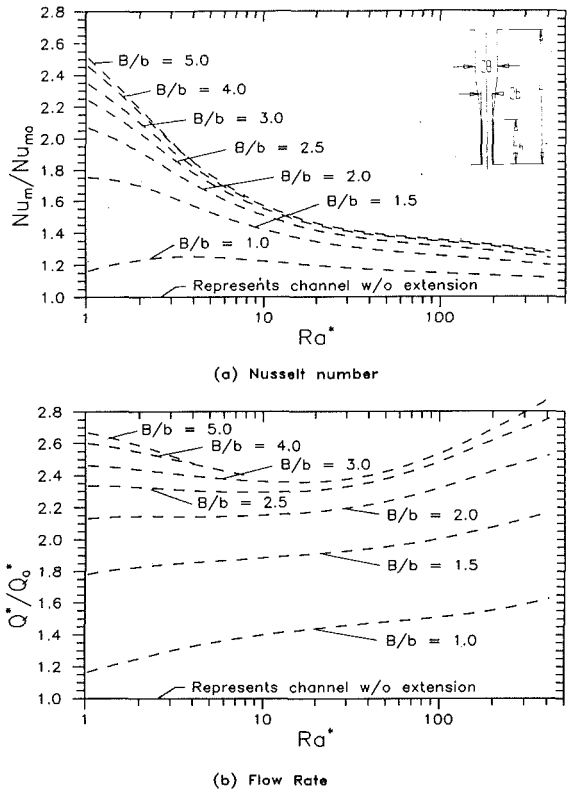

Fig. 7 Ratios of heat transfer (*a*) and dimensionless flow rate (*b*) for a diffused expansion over the heating range studied. The curves represent $L_h/L = 1/3$, $L_h/b = 17$.

the local maximum shifts to a lower value of Ra*. This suggests that in the absence of wall friction (from the extension), even very weak motion associated with small Ra* is augmented, resulting in enormous relative increases in heat transfer.

For low Ra* (≈ 1), enhancements of up to 2.5 were observed in overall heat transfer owing to enhancements of 2.6 in mass flow. In the intermediate range, $5 < \text{Ra}^* < 100$, enhancements were in the order of 1.5 for overall heat transfer and 2.4 for mass flow and in the upper range, $\text{Ra}^* > 100$, enhancement of overall heat transfer was 1.3, owing to increases of 2.5 in mass flow. In comparison, the straight extension brought about relative increases in heat transfer of $1.1 \rightarrow 1.25$ in the same overall range. This compares qualitatively with the work of Oosthuizen (1984). A detailed comparison could not be made because of the large unheated lengths that he considered. It is, however, doubtful, based on the present results, that enormous extensions are required to reach the maximum possible enhancement as reported by Oosthuizen (1984).

Part III Diffused Expansions. A channel with a diffused expansion was considered to examine the relevance of the hydrodynamic loss caused by the sudden expansion at the inlet of the extension. The diffuser was formed by allowing the first segment (of length L_h) of the unheated extension to open gradually as the extension was expanded (see diagram in Fig. 7). Figure 7 shows the present numerical results for relative overall heat transfer and flow rate as a function of Ra* for $L_h/L = 1/3$ and $1 \le B/b \le 5$. There are no apparent differences between the results from Figs. 6(*a*),(*b*) and 7(*a*),(*b*). Figure 8 demonstrates how the overall heat transfer for the diffused expansion compares to those from the abrupt expansion. For very large values of B/b, the diffused expansion offers modestly higher enhancements in heat transfer, but, for the most part, the abrupt expansion is more effective and thus the loss at the entry is of no consequence. In the rest of the paper, the emphasis is directed towards the straight extensions and abrupt expansions only.

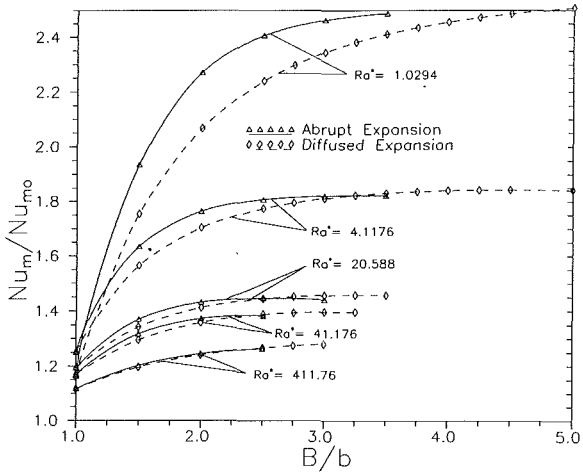

Fig. 8 Ratio of Nusselt numbers versus expansion ratio, *B/b*, for selected constant Rayleigh numbers, Ra*

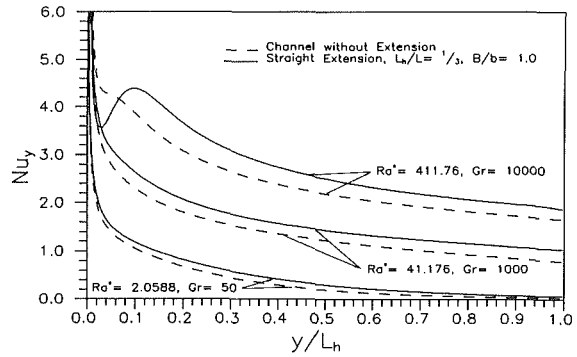

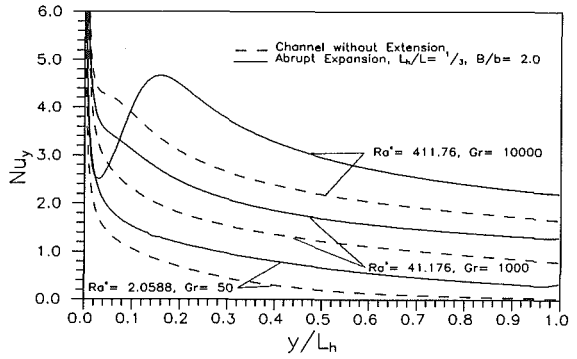

Fig. 9 Local Nusselt number distributions (*a*) for the channel with a straight extension, $B/b = 1.0$ and (*b*) for the channel with an abrupt expansion, $B/b = 2.0$

Local Heat Transfer. The local changes in heat transfer are analyzed in detail to order to determine how the heat flux is distributed along the channel. Figure 9 gives the present numerical results for local Nusselt number in the case of (*a*) a channel with a straight extension and (*b*) a channel with an abrupt expansion ($B/b = 2$). For low and intermediate heating, the increase in heat transfer occurs over the entire channel length in both cases. When the heating (Ra*) is high, there is a sharp decrease in the local heat transfer just beyond the channel inlet. This is caused by flow separation resulting in a small recirculating eddy adjacent to each wall just above the channel inlet when the induced flow rate exceeds a certain critical value. Figure 10 shows the changes in the flow pattern near the inlet occurring due to the increased flow rate generated by the "chimney" effect. This flow separation has been first

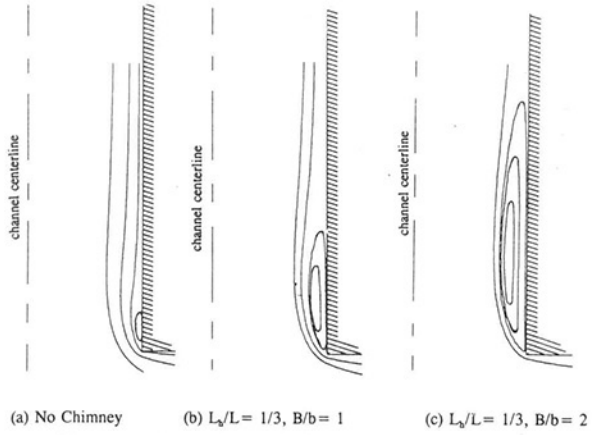

Fig. 10 Comparison of recirculating regions at the channel inlet for various types of extensions at $Ra^* = 411.76$

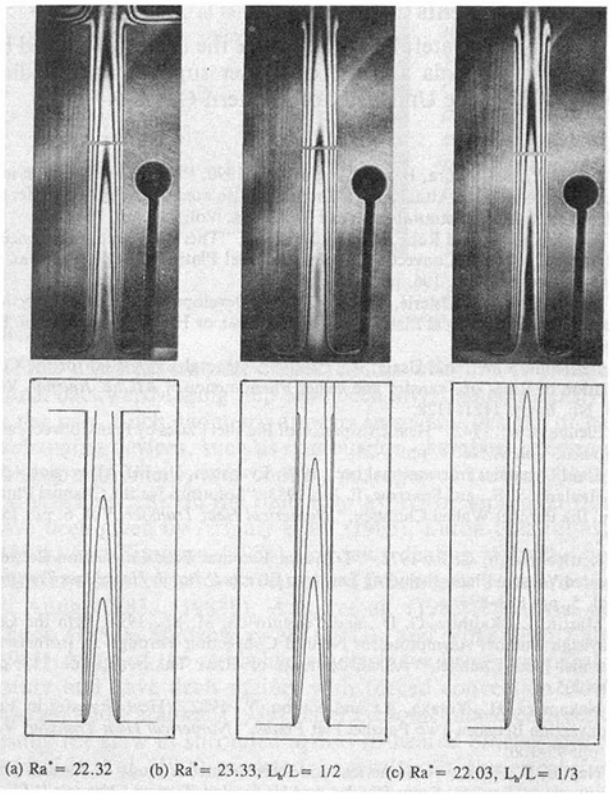

Fig. 11 Experimentally and numerically determined isotherms for $L_h/b = 17$, $B/b = 1$

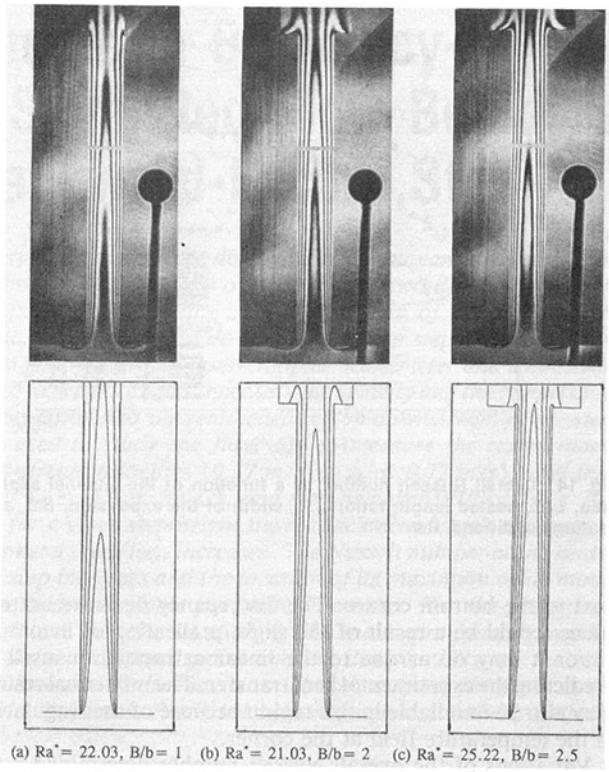

Fig. 12 Experimentally and numerically determined isotherms for $L_h/L = 1/3$ and various B/b

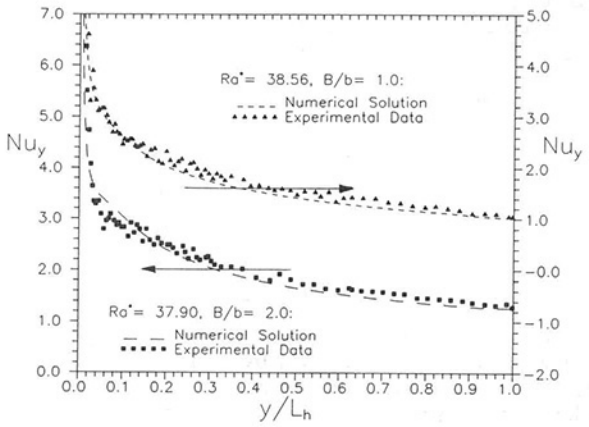

Fig. 13 Comparison of experimental and theoretical local Nusselt numbers for $L_h/b = 17$, $L_h/L = 1/3$

documented by Naylor et al. (1991). The resulting eddies effectively "insulate" the wall from the incoming air stream and cause local decreases in heat transfer. An attempt was made by Naylor et al. (1991) to correlate the onset of separation with the flow rate. They found that the channel aspect ratio, L_h/b, had a strong effect on it. The present results confirm this finding and suggest that such a correlation can be established for any constant aspect ratio L_h/b. Details are omitted due to space limitation.

Experimental Results. A Mach-Zehnder interferometer was used to perform experiments to validate the present numerical findings. Figure 11 gives a comparison of experimentally and numerically determined isotherms for (a) channel without an extension, (b) channel with straight extension equal to the length of the channel ($L_h/L = 1/2$) and (c) channel with straight extension equal to twice the length of the channel ($L_h/L = 1/3$).

Figure 12 gives a comparison of experimentally and numerically determined isotherms for an extension of $L_h/L = 1/3$ and (a) no expansion ($B/b = 1.0$), (b) abrupt expansion $B/b = 2.0$ and (c) abrupt expansion $B/b = 2.5$. Note that in all of the photographs, ambient air is represented by darkness so that the isotherms are represented by successive bright fringes. In all cases, the numerical and experimental isotherms are in excellent agreement, with slight differences occurring only at the inlet. Care was taken, through the installation of heat exchangers (see Fig. 3), to minimize the amount by which the ambient air might have been preheated by the lower surfaces before entering the channel, but the possibility of a very small energy transfer near the bottom corner could not be excluded. Figure 13 shows the comparison of local Nusselt numbers obtained numerically and experimentally for $L_h/L = 1/3$ and (a) a straight extension ($B/b = 1.0$) and (b) an abrupt expansion of $B/b = 2.0$. The agreement is good in both cases with average scatter of ± 3 percent and a maximum of 12 percent occurring

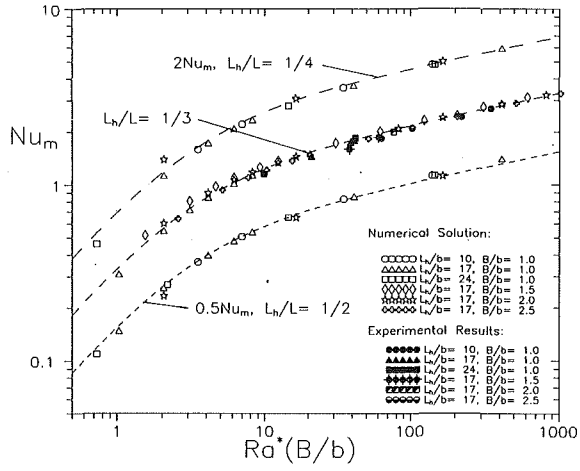

Fig. 14 Overall Nusselt number as a function of the channel aspect ratio, L_h/b, heated length ratio, L_h/L, width of the expansion, B/b, and heating conditions, Ra*

next to the bottom corner. The discrepancy near the bottom corner could be a result of the slight preheating of incoming air or it may occur due to the linear extrapolation used in predicting the experimental heat transfer. The numerical results may also be unreliable in this region because of the singularity in the temperature field at the corner.

Variations of the overall Nusselt number determined both numerically and experimentally are shown on Fig. 14. These results show that it is possible to scale out the effects of aspect ratio of the heated channel, L_h/b, and expansion ratio of the extension, B/b, for a given length of the extension, L_h/L. The method described by Churchill and Usagi (1972) was used to produce the following correlation for Nu_m:

$$\mathrm{Nu}_m = \left(\frac{L}{L_h}\right)^{0.16}\left[\left(\frac{1}{3}\mathrm{Ra}^*(B/b)\right)^{-1.4} + \left(\frac{4}{5}(\mathrm{Ra}^*(B/b))^{0.18}\right)^{-1.4}\right]^{-1/1.4} \quad (22)$$

valid over the range:

$$1/4 \le L_h/L \le 1, \quad 1 \le B/b \le 2.5, \quad 1 \le \mathrm{Ra}^* \le 400$$

At low $\mathrm{Ra}^*(B/b)$, the result approximates the fully developed channel limit ($\mathrm{Ra}^*/3$) proposed by Bodoia et al. (1962). At high $\mathrm{Ra}^*(B/b)$, the result approaches the curve for a channel without an extension rather than the isolated plate limit. Although the correlation for a channel with no extension does approach the isolated plate limit as $\mathrm{Ra}^* \to \infty$, this does not occur in the range of parameters studied. The upper asymptote was approximated using a sequence of calculations to minimize the scatter using all of the present numerical data. The exponent in the correlation equation was found in a similar manner after the asymptote was set. The largest deviation between the correlation (Eq. (22)) and the data is evident at low Ra^* ($\mathrm{Ra}^* \le 4$) where differences of up to 15 percent occur. For $\mathrm{Ra}^* > 4$, the correlation (Eq. (22)) is accurate to better than 8 percent, which is acceptable for most design considerations. Figure 14 shows curves generated by Eq. (22) for $L_h/L = 1/2$, 1/3, and 1/4. Note that the curve and the data for $L_h/L = 1/2$ is multiplied by 0.5 and the curve and the data for $L_h/L = 1/4$ is multiplied by 2 to avoid overlap. This simple correlation should be of enormous help in a design process.

Conclusions

The addition of an adiabatic extension enhances the heat transfer from an isothermal channel for all geometric configurations considered in the present analysis. Straight adiabatic extensions ranging in length from $1/4 \le L_h/L \le 2/3$ resulted in overall heat transfer enhancements of 1.1 to 1.3. Abrupt expansions in the range of $1 \le B/b \le 3.5$ offered enhancements of 1.3 to 2.5. The extension was most effective at low Rayleigh numbers for which the flow in the channel without an extension is fully developed. The experimental and numerical results are in excellent agreement both locally and globally. A single correlation accounting for the channel aspect ratio, L_h/b, expansion ratio, B/b, modified Rayleigh number, Ra*, and heated length ratio, L_h/L, is presented.

Acknowledgments

The authors gratefully acknowledge the funding received by NSERC of Canada and the computer support and funding received from the University of Western Ontario.

References

Asako, Y., Nakamura, H., and Faghri, M., 1990, "Natural Convection in a Vertical Heated Tube Attached to a Thermally Insulated Chimney of a Different Diameter," ASME JOURNAL OF HEAT TRANSFER, Vol. 112, pp. 790-793.

Bar-Cohen, A., and Rohsenow, W. M., 1984, "Thermally Optimum Spacing of Vertical, Natural Convection Cooled, Parallel Plates," ASME JOURNAL OF HEAT TRANSFER, Vol. 106, pp. 116-123.

Bodoia, J. R., and Osterle, J. F., 1962, "The Development of Free Convection Between Heated Vertical Plates," ASME JOURNAL OF HEAT TRANSFER, Vol. 84, pp. 40-44.

Churchill, S. W., and Usagi, R., 1972, "A General Expression for the Correlation of Rates of Transfer and Other Phenomenon," *AIChE Journal*, Vol. 18, No. 6, pp. 1121-1128.

Elenbaas, W., 1942, "Heat Dissipation of Parallel Plates by Free Convection," *Physica*, Vol. 9, No. 1, pp. 1-28.

Fluid Dynamics International Inc., 1989, Evanston, IL, FIDAP version 4.51.

Haaland, S. E., and Sparrow, E. M., 1983, "Solutions for the Channel Plume and the Parallel-Walled Chimney," *Numerical Heat Transfer*, Vol. 6, pp. 155-172.

Kettleborough, C. F., 1972, "Transient Laminar Free Convection Between Heated Vertical Plates Including Entrance Effects," *Int. J. Heat Mass Transfer*, Vol. 5, pp. 883-896.

Martin, L., Raithby, G. D., and Yovanovich, M. M., 1991, "On the Low Rayleigh Number Asymptote for Natural Convection Through an Isothermal, Parallel Plate Channel," ASME JOURNAL OF HEAT TRANSFER, Vol. 113, pp. 899-905.

Nakamura, H., Yutaka, A., and Naitou, T., 1982, "Heat Transfer by Free Convection Between Two Parallel Flat Plates," *Numerical Heat Transfer*, Vol. 5, pp. 95-106.

Naylor, D., 1991, "A Numerical and Interferometric Study of Natural Convective Heat Transfer From Divided and Undivided Vertical Channels," Ph.D. Thesis, University of Western Ontario, London, Ontario, Canada.

Naylor, D., Floryan, J. M., and Tarasuk, J. D., 1991, "A Numerical Study of Developing Free Convection Between Isothermal Vertical Plates," ASME JOURNAL OF HEAT TRANSFER, Vol. 113, pp. 620-626.

Oosthuizen, P. H., 1984, "A Numerical Study of Laminar Free Convective Flow Through a Vertical Open Partially Heated Plane Duct," *Fundamentals of Natural Convection—Electronic Equipment Cooling*, ASME HTD-Vol. 32, pp. 41-48.

Straatman, A. G., 1992, "Heat Transfer Enhancement From a Vertical, Isothermal Channel Generated by the Chimney Effect," M.E.Sc. Thesis, University of Western Ontario, London, Ontario, Canada.

Tarasuk, J. D., 1968, "The Theory, Design and Operation of the University of Saskatchewan 8-inch Mirror Mach-Zehnder Interferometer," Technical Report C-3, Mechanical Engineering Department, University of Saskatchewan, June.

Measurements in Buoyancy-Assisting Separated Flow Behind a Vertical Backward-Facing Step

B. J. Baek

B. F. Armaly
Fellow ASME

T. S. Chen
Fellow ASME

Department of Mechanical and Aerospace Engineering and Engineering Mechanics, University of Missouri—Rolla, Rolla, MO 65401

Measurements of velocity and temperature distributions in buoyancy-assisting laminar mixed convection boundary-layer flow over a vertical, two-dimensional backward-facing step are reported. The leading surface upstream of the step and the step itself were adiabatic, and the surface downstream of the step was heated and maintained at a uniform temperature. A laser-Doppler velocimeter and a cold-wire anemometer were utilized to measure simultaneously the velocity and the temperature distributions in the recirculation and the reattached region downstream of the step. Flow visualization was used to study the flow and to measure the reattachment length for different free-stream velocities ($0.37\ m/s \le u_0 \le 0.72\ m/s$), wall temperature differences ($10°C \le \Delta T \le 30°C$), and step heights ($0.38\ cm \le s \le 1\ cm$). Results show that for a given step height the reattachment length decreases as the buoyancy force parameter, Gr_s/Re_s^2, increases. The Nusselt number at the heated wall downstream of the step increases and the location of its maximum value moves closer to the step as the buoyancy force parameter increases. For the present experimental range, it is found that the location of the maximum Nusselt number occurs downstream of the reattachment point and the distance between the reattachment point and the location of the maximum Nusselt number increases as the buoyancy force parameter increases. Predicted behavior agrees favorably with the measured results.

Introduction

Flow and heat transfer characteristics behind a two-dimensional backward-facing step have been investigated extensively in the past. Such geometry appears in several designs of heat exchanging devices, such as combustion chambers, electronic cooling equipment, and cooling passages of turbine blades. Extensive reviews on the fluid flow aspect of separated flows have been given by Armaly et al. (1983), Eaton and Johnson (1981), and Simpson (1981). Reviews dealing with the heat transfer characteristics of separated flows have been provided by Aung (1983a, 1983b), Aung et al. (1985), Sparrow and Chuck (1987), Sparrow et al. (1987), and Vogel and Eaton (1985). Most of the published studies have been numerical in nature and have dealt mainly with forced convection flows. Braaten and Patankar (1985) reported some mixed convection results for flow in shrouded arrays of heated blocks, and recently Lin et al. (1990) reported the results of a numerical study dealing with the effects of buoyancy in a vertical backward-facing step flow in a duct. Experimental results for heat transfer in separated flows are lacking, and measurements of the buoyancy effects on separated flows do not seem to have appeared in the literature. This has motivated the present study, which explores experimentally and numerically the effects of buoyancy on the flow and heat transfer characteristics in separated boundary layer flow downstream of a two dimensional backward-facing step.

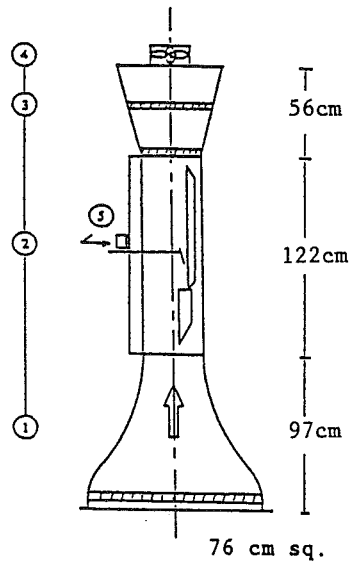

1. Mixing Chamber 2. Test Section 3. Diffuser
4. Fan Assembly 5. Probe Traversing Unit

Fig. 1 Schematic diagram of air tunnel

Experimental Facilities and Procedure

The experimental investigation was performed in a low-turbulence, open circuit wind tunnel that was oriented vertically, with air flowing in the upward direction. This tunnel was described in detail by Ramachandran et al. (1985) and a schematic diagram of the tunnel is shown in Fig. 1. The test section of the tunnel (30.48 cm × 30.48 cm × 91.44 cm) was instrumented with a cold-wire anemometer system for measuring the air temperature and with a traverse mechanism for moving the measuring boundary layer probe to any desired location in the flow domain. The normal motion of the probe (relative to the plane of the heated surface) was controlled by a stepper motor and by a sweep drive unit capable of moving the probe to within 0.02 mm of a desired location. The movement of the probe along the other two directions (along the plate length and width) were manually controlled by a lead screw to an accuracy level of 1 mm.

Contributed by the Heat Transfer Division for publication in the JOURNAL OF HEAT TRANSFER. Manuscript received by the Heat Transfer Division October 7, 1991; revision received June 26, 1992. Keywords: Flow Separation, Measurement Techniques, Mixed Convection. Associate Technical Editor: D. M. McEligot.

The heated backward-facing step geometry was supported in the test section of the tunnel and spanned its entire width (30.48 cm). A cross section of 20.32 cm × 30.48 cm was provided adjacent to the test surface for air flow. The test surface was constructed to provide an adiabatic upstream section, an adiabatic (backward-facing) step, and a downstream section behind the step that was heated to maintain uniform surface temperature. The height of the step could be changed and the temperature level of the downstream section could be maintained at any desired uniform value between 22°C and 80°C. The upstream section of the backward facing step was 30.48 cm long and was constructed from plexiglass. The front edge of this upstream section was chamfered to provide a good starting edge for the boundary layer flow, and the back edge was squared to form the adiabatic step. The heated section downstream of the backward-facing step was constructed from three layers, which were held together by screws and instrumented to provide an isothermal heated test surface. The upper layer (test surface) was an aluminum plate (30.48 cm wide, 79 cm long, and 1.27 cm thick) instrumented with 11 calibrated copper-constantan thermocouples that were distributed in both the axial and the transverse directions. Each thermocouple was inserted into a small hole on the backside of the plate and its measuring junction was flush with the test surface. The middle layer consisted of six heating pads, which were backed by insulation tiles. The power input to each of the six heating pads was controlled by individual microprocessor-based temperature controllers, which maintained the entire length of the heated surface at a specified uniform temperature. An aluminum plate, 1.27 cm thick, served as the bottom layer and as a support to keep the three-layered structure together. The front edge of this structure was chamfered (45 deg) and pressed to the back edge of the upstream section to form the backward-facing step, as shown in Fig. 1. This arrangement minimized the conduction between the heated plate and the adiabatic step. Flow visualizations indicated the presence of a developing two-dimensional laminar boundary layer flow adjacent to the upstream adiabatic section, and a two-dimensional laminar separation and reattachment region behind the step. The two dimensionality of the flow and thermal fields was also verified from the measurements of velocity and temperature across the width of the flow region, and the heated plate could be maintained at a specified uniform temperature to within 0.2°C by controlling the input power to the individual heaters.

The velocity measurement was performed by using a three-beam, backward scattering, two-component laser-Doppler velocimeter (LDV) that utilizes two counters to process the Doppler signal. The measuring point of the LDV system could be moved to within 0.1 mm from any desired location in the flow field by a three-dimensional traverse mechanism that was located adjacent to the tunnel. The traverse mechanism and the processing of the Doppler signals were controlled by an IBM-AT personal computer. Glycerin vapor was mixed with the inlet air flow to provide the scattering particles (0.2–0.5 μm in diameter) for the LDV measuring system. A cold-wire boundary layer probe with a constant-current bridge/anemometer and a traverse system were used to measure the temperature in the flow domain. Temperature and velocity in the flow domain were measured simultaneously by placing the cold wire probe 2 mm behind the measuring volume of the LDV system. It was verified experimentally that the presence of the cold wire probe behind the LDV measuring volume did not influence significantly the magnitude of the measured velocity (less than one percent) in the experimental range. The repeatability (under steady-state conditions) of the temperature measurements was determined to be within 0.2°C, and that of the free-stream velocity measurements was within 3 percent.

Numerical Analysis

The experimental geometry and the boundary conditions were modeled by numerically solving the governing elliptic partial differential equations for the temperature and the velocity fields. The backward-facing step and the upstream section were considered as adiabatic surfaces, and the downstream section was considered as heated to a uniform temperature T_w corresponding to the measured value. The flow was considered to be steady, two-dimensional, and laminar, and the properties were considered to be constant but evaluated at the film temperature $T_f = (T_o + T_w)/2$. By utilizing the Boussinesq approximation ($\beta\Delta T$ is smaller than 0.1 in the experimental range), the governing conservation equations can be written as follows:

$$\frac{\partial u}{\partial x}+\frac{\partial v}{\partial y}=0 \tag{1}$$

$$\frac{\partial(uu)}{\partial x}+\frac{\partial(uv)}{\partial y}=-\frac{1}{\rho}\frac{\partial P}{\partial x}+\nu\left(\frac{\partial^2 u}{\partial x^2}+\frac{\partial^2 u}{\partial y^2}\right)+g\beta(T-T_o) \tag{2}$$

$$\frac{\partial(uv)}{\partial x}+\frac{\partial(vv)}{\partial y}=-\frac{1}{\rho}\frac{\partial P}{\partial y}+\nu\left(\frac{\partial^2 v}{\partial x^2}+\frac{\partial^2 v}{\partial y^2}\right) \tag{3}$$

$$\frac{\partial(uT)}{\partial x}+\frac{\partial(vT)}{\partial y}=\alpha\left(\frac{\partial^2 T}{\partial x^2}+\frac{\partial^2 T}{\partial y^2}\right) \tag{4}$$

The boundary conditions are given by

$s<y<H$, $x=0$;

$u=u_o$, $v=0$, and $T=T_o$, or measured values at inlet (5)

$0<y<H$, $x=L_i+L_e$;

u, v, and T = measured values (at exit) (6)

Nomenclature

g = gravitational acceleration
Gr_s = Grashof number $= g\beta\,(T_w-T_o)s^3/\nu^2$
h = local heat transfer coefficient $= -k(\partial T/\partial y)_{y=0}/(T_w-T_o)$
H = height of computational domain
k = thermal conductivity
Nu_s = local Nusselt number $= hs/k$
L_i = length upstream of the step in the calculation domain
L_e = length downstream of the step in the calculation domain
p = pressure
Re_s = Reynolds number $= u_o s/\nu$
s = step height
T = fluid temperature
T_o = inlet and free-stream air temperature
T_w = heated wall temperature
u = streamwise velocity component
u_o = inlet and free-stream velocity
v = transverse velocity component
x, y = streamwise and transverse coordinates
x_n = location of peak Nusselt number
x_r = location of reattachment
X = $(x-L_i)/s$
X_n = $(x_n-L_i)/s$
X_r = $(x_r-L_i)/s$
Y = $(y-s)/s$
α = thermal diffusivity
β = volumetric expansion coefficient
θ = dimensionless temperature $= (T-T_o)/(T_w-T_o)$
ν = kinematic viscosity
ξ = buoyancy parameter $= \mathrm{Gr}_s/\mathrm{Re}_s^2$
ρ = density

$y = H$, $0 < x < L_i + L_e$;

$$u = u_o,\ \partial v/\partial y = 0,\ T = T_o \text{ (free stream)} \quad (7)$$

$y = 0$, $L_i < x < L_e$

$$u = v = 0,\ T = T_w \text{ (downstream heated wall)} \quad (8)$$

$y = s$, $0 < x < L_i$;

$$u = v = 0,\ \partial T/\partial y = 0 \text{ (upstream adiabatic wall)} \quad (9)$$

$0 < y < s$, $x = L_i$;

$$u = v = 0,\ \partial T/\partial x = 0 \text{ (adiabatic step wall)} \quad (10)$$

The downstream length L_e, the upstream length L_i, and the height H of the computational domain were selected to be 21 steps long ($L_e/s = 21$), 5 steps long ($L_i/s = 5$), and 10 steps high ($H/s = 10$), respectively. Measured velocity and temperature distributions at the start and at the end of the calculation domain were used as inlet and exit boundary conditions for the numerical simulation. Linear interpolation between two measured points was used to establish values at each mesh point. The solution to the governing set of coupled partial differential equations was obtained by using a finite difference scheme, embodied in the computer code TEACH using the SIMPLE algorithm, as described by Patankar (1980). The solution procedure started by supplying initial estimates for the velocity, temperature, and pressure fields, along with the physical boundary conditions, and iterations were continued until a converged solution was obtained. The momentum equations were solved first in the iteration process, using estimated temperature for the buoyancy force calculations, and then the energy equation was solved to upgrade the temperature. This process was repeated for each iteration step until a converged solution was reached. Convergence of the solution was considered satisfactory when the sum of the normalized (relative to inlet conditions) residuals, (mass, momentum, and energy) over the whole calculation domain was less than 0.01.

The grid distribution in the calculation domain was nonuniform in both the streamwise and transverse coordinate directions. A large number of grid points were placed in the area where steep variations of velocities were observed from measurements, i.e., near the corner of the step and adjacent to the walls. Various grid densities and and grid numbers were tested, and the resulting velocity distributions from these tests were compared, to determine a grid-independent solution. It was found that for the range of parameters examined in this study, a grid density of $N_x \times N_y = 90 \times 60$ is sufficient for providing a grid-independent solution (for the two mesh sizes of 70×35 and 90×60 the maximum change in the predicted velocity is less than 3 percent, in the predicted Nusselt number it is less than 1.5 percent, and in the reattachment length it is less than 1 percent). The computations were performed on an IBM 4381 Model Group 14 computer system and a Floating Point System FPS-164 located at the University of Missouri-Rolla. About 600 to 1000 iterations were needed to obtain a converged solution.

Discussion of Results

The two-dimensional nature of the flow in the experimental geometry was verified by measuring the axial velocity at $y = 0.64$ cm (equivalent to the step height) across the width of the plate at various streamwise locations downstream from the step. These results verified that there is a large region in the center of the tunnel (80 percent of its width) where the flow can be approximated (to within 5 percent) as being two dimensional. All the reported velocity and temperature measurements were taken along the midplane ($z = 0$) of the plate and only after the system had reached steady-state conditions.

The results from the numerical solution to the governing equations (for the case of a step height $s = 0.64$ cm) were used to develop the contour plots of the dimensionless stream function. These results are presented in Fig. 2 to illustrate the qualitative nature of the buoyancy force effects on the flow field. Only a portion (the relevant region) of the calculation domain is presented in the individual figures. It should be noted that the X and Y coordinates in these figures are not presented to the same scale (the Y coordinate is stretched relative to the X coordinate) in order to show more clearly what happens in the recirculation region. As expected, the flow separates behind the step and reattaches to the wall downstream of the step, forming a recirculation region between the step and the reattachment point. The results show that for a fixed inlet velocity (Fig. 2*a*, $u = 0.55$ m/s), the reattachment length, X_r, decreases as the wall temperature (buoyancy force) increases. Fluid properties are evaluated at the film temperatures, $T_f = (T_w + T_o)/2$, and are used to calculate the reported Reynolds and Grashof numbers for temperature differences, $\Delta T = T_w - T_o$, of 0, 10 and 30°C. The difference in the magnitudes of the Reynolds numbers reported in Fig. 2(*a*) is due only to the changes in the magnitude of the kinematic viscosity due to changes in film temperature. Similarly, as the inlet velocity decreases for a fixed temperature difference (Fig. 2*b* for $\Delta T = 10$°C, $Gr_s = 362$, and $u_o = 0.72$, 0.55, and 0.37 m/s), the reattachment length and the volume of the recirculation region decrease. The rate of change of momentum in the streamwise direction, in the recirculation region adjacent to the heated wall, generates a force that is opposed by the buoyancy-assisting force that results from the heating of the wall. When the resulting total force is negative the velocity component in that region is negative, and vice versa. Thus, an increase in the buoyancy force causes a decrease in the negative streamwise velocity compo-

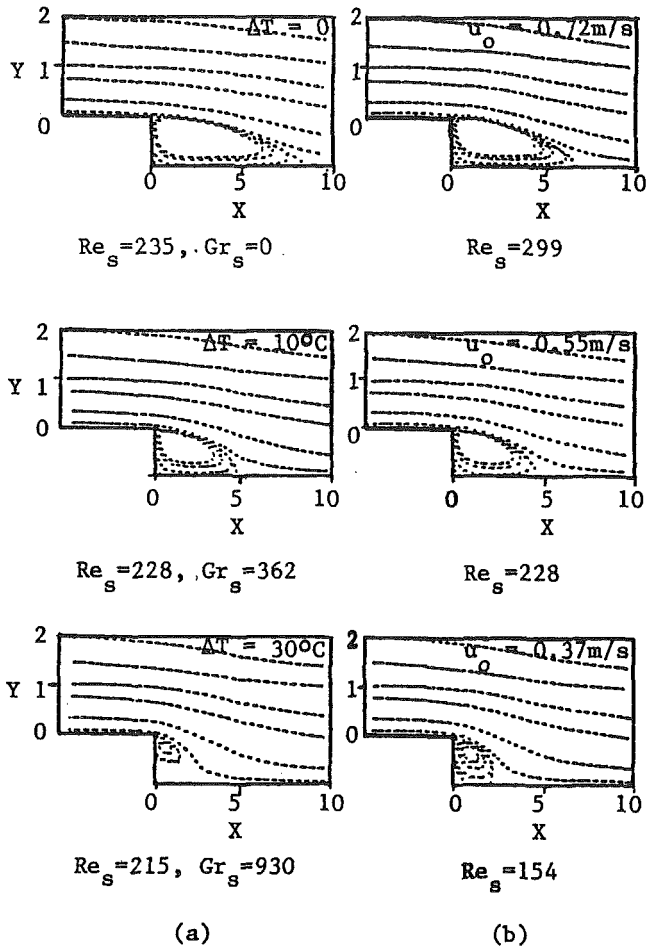

Fig. 2 Effects of wall temperature and inlet velocity on streamlines, $s = 0.64$ cm: (*a*) $u_o = 0.55$ m/s; (*b*) $\Delta T = 10$°C and $Gr_s = 362$

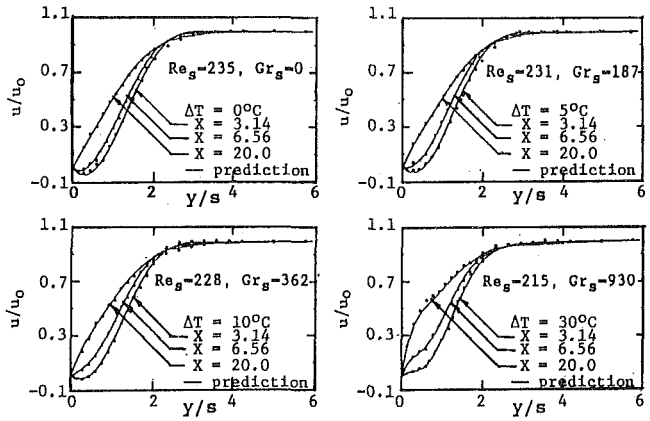

Fig. 3 Streamwise velocity distributions (u_o = 0.55 m/s and s = 0.64 cm); uncertainty in u/u_o is ± 0.014 and in y/s ± 0.022

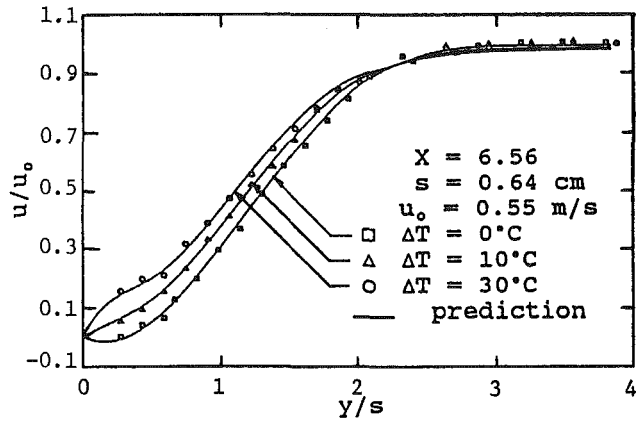

Fig. 4 Effects of wall temperature on the velocity distribution (uncertainty in u/u_o is ± 0.014 and in y/s ± 0.022)

nent in the recirculation region adjacent to the heated wall, and that results in decreasing the reattachment length. As the buoyancy force component continues to increase and exceeds a critical value, the total force in the streamwise direction becomes positive everywhere close to the heated plate, thus causing the streamwise velocity component in that region to become positive. This positive velocity forces the recirculation region to detach from the heated wall and attaches only to the adiabatic step, as shown in Fig. 2. Measurements of velocities in this region verified these observations.

The measured and predicted streamwise velocity distributions u/u_o for the case of a step height of s = 0.64 cm are presented in Fig. 3. The solid lines in the figure represent the predicted results and the points that are represented by various symbols are the measured values. It is clear from the individual figures that the buoyancy effects on the flow characteristics in the recirculation region are significant. The numerical predictions of the velocity distribution agree favorably (within 5 percent) with measurements. The significant effect of the buoyancy force on the streamwise velocity distribution is better illustrated in Fig. 4 where the recirculation region at that location is eliminated by increasing the wall temperature. It is also interesting to note from the results in Fig. 5, that higher free-stream velocities could produce lower streamwise velocities in the recirculation region close to the heated wall due to the resulting decrease in the magnitude of the assisting buoyancy force.

The measured and predicted temperature distributions for the case of a step height of s = 0.64 cm, at three representative streamwise locations, are presented in Fig. 6. As can be seen from the figure, good agreement exists between the predicted

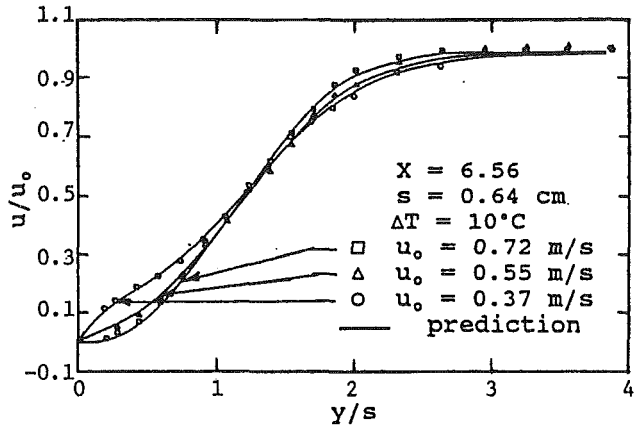

Fig. 5 Effects of inlet velocity on the velocity distribution (uncertainty in u/u_o is ± 0.014 and in y/s ± 0.022)

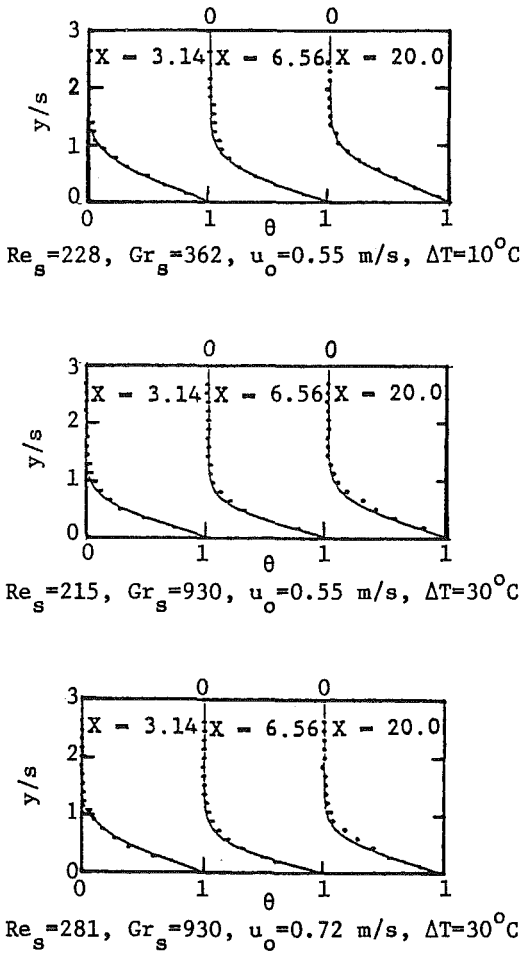

Fig. 6 Dimensionless temperature distributions (s = 0.64 cm); uncertainty in y/s is ± 0.022 and in θ ± 0.025

(solid lines) and the measured values. The temperature gradients at the wall (i.e., the heat transfer rate) is seen to increase as the temperature difference increases. The actual difference between the measured and predicted temperature was less than 0.5°C, which is less than 5 percent of the free-stream temperature. The predicted results indicate that the fluid temperature in the recirculation region behind the step ($X < X_r$) is considerably higher than the temperature downstream of the reattachment point ($X > X_r$). This is due to the fact that a more active dispersion of the heated layer by the cooler main

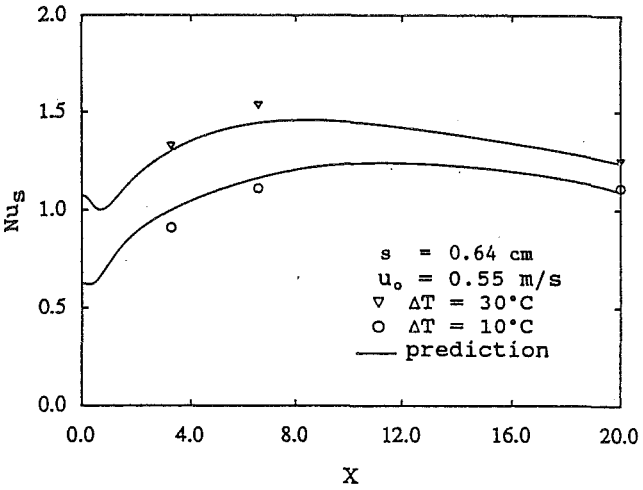

Fig. 7 Effects of buoyancy force on the local Nusselt number (uncertainty in Nu_s is ± 0.05 and in X ± 0.05)

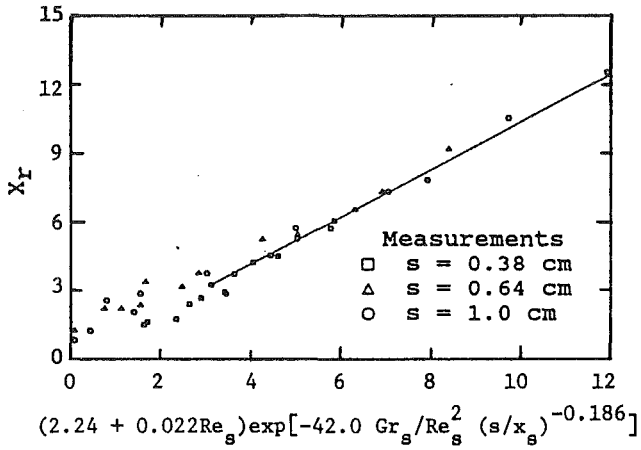

Fig. 8 Correlation for the reattachment length (uncertainty in X_r is ± 0.05)

stream occurs outside and downstream from the recirculation region.

The local Nusselt number, defined in terms of the step height, wall temperature gradient, and the temperature difference between the heated wall and the free stream ($T_w - T_o$), is given by

$$Nu_s = hs/k = -[(\partial T/\partial y)_{y=0}]\, s/(T_w - T_o) \qquad (11)$$

This temperature gradient at the wall was deduced from the measured temperature distribution, through a cubic spline fit of the measured temperatures (four points) near the heated wall, and the resulting Nusselt numbers at three streamwise locations are compared with predicted results in Fig. 7 for the case of a step height of 0.64 cm. It can be seen from the figure that the local Nusselt number has a finite nonzero value at the edge of the heated plate ($X = 0$), which is characteristic of an adiabatic step in this geometry (Lin et al., 1990). The results for the higher buoyancy case ($\Delta T = 30°C$) reveal the development of a different minimum value in the Nusselt number distribution, which is caused by the development and growth of the secondary recirculation region close to the lower corner of the step. A higher buoyancy force, resulting from the increase in wall temperature, increases the magnitude of the Nusselt number and moves the location of its peak closer to the step. The Nusselt number distribution in the experimental geometry (large H/s) does not have the sharp peak that is associated with separated flow in ducts having small H/s values. This is in agreement with the work of Sparrow et al. (1987), which shows that the Nusselt number distribution becomes flatter as the H/s increases. Results presented in Fig. 2–7 are associated only with a step height of $s = 0.64$ cm. Results for the other step heights exhibit similar trends but different magnitudes and, due to space limitations, are not presented in this paper.

The reattachment length was measured from flow visualization for different step heights (0.38 cm, 0.64 cm, 1.0 cm), inlet velocities ($u_o = 0.37$, 0.55, and 0.72 m/s), and temperature differences ($\Delta T = 0$, 10, 30°C). Flow visualization was carried out by using a 15 W collimated white light beam, 2.5 cm in diameter, with glycerin particles seeding the flow. The reported reattachment length measurements represent the average for the many readings that were taken under a fixed condition in order to reduce visualization errors. The uncertainty in these measurements is ±1 mm, which is less than 5 percent of the smallest measured reattachment length. An effort is made in this study to modify the existing empirical correlation for the reattachment length in laminar forced convection flow, as given by Goldstein et al. (1970), to reflect also the influence of step height and buoyancy parameter. The developed empirical correlation should be viewed as applicable only to the range of parameters covered in this experiment, and is given by

$$X_r = (2.24 + 0.022\mathrm{Re}_s)\exp[-42(\mathrm{Gr}_s/\mathrm{Re}_s^2)(s/x)_s^{-0.186}] \qquad (12)$$

where x_s is the adiabatic inlet length upstream of the step, which for this experiment was fixed at a value of 30.48 cm. This length, which influences the boundary layer thickness at the edge of the step, was used to express the relation in dimensionless form. Equation (12) is presented along with the measured values in Fig. 8, and it predicts favorably the measured reattachment length to within 7 percent for low buoyancy levels. The measured values, however, start to deviate from the correlation equation at high buoyancy levels, i.e., when $X_r < 3.5$. This deviation is due to the fact that secondary recirculation region starts to develop and grow at the corner of the step as the buoyancy level increases, casing the reattachment length behavior to change.

Predicted reattachment length, X_r, and the length where the maximum local Nusselt number occurs, X_n, decrease as the buoyancy level increases. The peak Nusselt number occurs downstream of the reattachment length (i.e., $X_n > X_r$) and the spacing ($X_n - X_r$) increases slowly as the buoyancy level increases. Similar behavior was reported by Lin et al. (1990) for buoyancy-affected separated flow behind a backward-facing step in a duct.

Conclusion

Measurements of velocity and temperature distributions are reported for buoyancy-assisting laminar mixed convection boundary layer flow adjacent to a two-dimensional, heated (uniform wall temperature) vertical backward-facing step. Heat transfer (Nusselt number) and reattachment length behaviors as a function of the buoyancy level were deduced from these measurements. Predicted results agree favorably (within 5 percent) with measured values and show the significant influence of the buoyancy force on the flow and heat transfer characteristics in the recirculation region behind the step. An increase in the buoyancy force causes a decrease in the size of the recirculation region behind the step and a decrease in the reattachment length. The local Nusselt number increases and the location of its maximum value moves closer to the step as the buoyancy force increases. The location of the maximum Nus-

selt number, X_n, and the reattachment length, X_r, decreases as the buoyancy force increases.

Acknowledgments

The present study was supported in part by the National Science Foundation under the grant No. NSF CTS-8923010.

References

Armaly, B. F., Durst, F., Pereira, J. C. F., and Schonung, B., 1983, "Experimental and Theoretical Investigation of Backward-Facing Step Flow," *Journal of Fluid Mech.*, Vol. 127, pp. 473–496.

Aung, W., 1983a, "Separated Forced Convection," *Proceedings of the ASME/JSME Thermal Engineering Joint Conference*, Vol. 2, pp. 499–515.

Aung, W., 1983b, "An Experimental Study of Laminar Heat Transfer Downstream of Backstep," ASME JOURNAL OF HEAT TRANSFER, Vol. 105, pp. 823–829.

Aung, W., Baron, A., and Tsou, F. K., 1985, "Wall Independency and Effect of Initial Shear-Layer Thickness in Separated Flow and Heat Transfer," *International Journal of Heat and Mass Transfer*, Vol. 28, pp. 1757–1771.

Braaten, M. E., and Patankar, S. V., 1985, "Analysis of Laminar Mixed Convection in Shrouded Arrays of Heated Rectangular Blocks," *International Journal of Heat and Mass Transfer*, Vol. 28, pp. 1699–1709.

Eaton, J. K., and Johnson, J. P., 1981, "A Review of Research on Subsonic Turbulent Flow Reattachment," *AIAA Journal*, Vol. 10, pp. 1093–1100.

Goldstein, R. J., Eriksen, V. L., Olson, R. M., and Eckert, E. R. G., 1970, "Laminar Separation, Reattachment, and Transition of the Flow Over a Downstream-Facing Step," ASME *Journal of Basic Engineering*, Vol. 92, pp. 732–741.

Lin, J. T., Armaly, B. F., and Chen, T. S., 1990, "Mixed Convection in Buoyancy-Assisting Vertical Backward-Facing Step Flows," *International Journal of Heat and Mass Transfer*, Vol. 33, No. 10, pp. 2121–2132.

Patankar, S. V., 1980, *Numerical Heat Transfer and Fluid Flow*, Hemisphere Publishing Co., Washington, DC.

Ramachandran, N., Armaly, B. F., and Chen, T. S., 1985, "Measurements and Predictions of Laminar Mixed Convection Flow Adjacent to a Vertical Surface," ASME JOURNAL OF HEAT TRANSFER, Vol. 107, pp. 636–641.

Simpson, R. L., 1981, "A Review of Some Phenomena in Turbulent Flow Separation," ASME *Journal of Fluids Engineering*, Vol. 103, pp. 520–530.

Sparrow, E. M., and Chuck, W, 1987, "PC Solutions for Heat Transfer and Fluid Flow Downstream of an Abrupt, Asymmetric Enlargement in a Channel," *Numerical Heat Transfer*, Vol. 12, pp. 19–40.

Sparrow, E. M., Kang, S. S., and Chuck, W., 1987, "Relation Between the Points of Flow Reattachment and Maximum Heat Transfer For Regions of Flow Separation," *International Journal of Heat and Mass Transfer*, Vol. 30, pp. 1237–1246.

Vogel, J. C., and Eaton, J. K., 1985, "Combined Heat Transfer and Fluid Dynamic Measurements Downstream of a Backward-Facing Step," ASME JOURNAL OF HEAT TRANSFER, Vol. 107, pp. 922–929.

Radiative Properties of Flame-Generated Soot

Ü. Ö. Köylü
Graduate Student Research Assistant.

G. M. Faeth
Professor.
Fellow ASME

Department of Aerospace Engineering,
The University of Michigan,
Ann Arbor, MI 48109-2140

Approximate methods for estimating the optical properties of flame-generated soot aggregates were evaluated using existing computer simulations and measurements in the visible and near-infrared portions of the spectrum. The following approximate methods were evaluated for both individual aggregates and polydisperse aggregate populations: the Rayleigh scattering approximation, Mie scattering for an equivalent sphere, and Rayleigh–Debye–Gans (R–D–G) scattering for both given and fractal aggregates. Results of computer simulations involved both prescribed aggregate geometry and numerically generated aggregates by cluster–cluster aggregation; multiple scattering was considered exactly, considered using the mean-field approximation, and ignored using the R–D–G approximation. Measurements involved the angular scattering properties of soot in the postflame regions of both premixed and nonpremixed flames. The results show that available computer simulations and measurements of soot aggregate optical properties are not adequate to provide a definitive evaluation of the approximate prediction methods. The simulations involve either exact solutions for small aggregates where effects of multiple scattering are small, or approximate solutions of uncertain accuracy for the large aggregates of interest for practical flames. The measurements are limited to conditions where soot aggregate structure is not known, and for relatively large scattering angles where the various approximations yield similar results. Within these limitations (for aggregates larger than the Rayleigh scattering regime) the approximate theories performed as follows: Rayleigh scattering generally understimated scattering, Mie scattering for an equivalent sphere yielded unreliable results, while basic and fractal aggregate R–D–G scattering yielded best results for given and fractal aggregates, respectively. However, existing simulations suggest significant effects of multiple scattering for soot aggregates (except near soot inception conditions) that are not included in R–D–G scattering so that improved approximate optical theories for soot aggregates should be sought.

Introduction

Most practical hydrocarbon-fueled flames contain and emit soot. This has important implications concerning their radiation and pollutant emission properties: Continuum radiation from soot generally is much stronger than radiation from infrared gas bands for flames (Tien and Lee, 1982; Viskanta and Mengüc, 1987; Gore and Faeth, 1986, 1988); and the emission of carbon monoxide from buoyant turbulent diffusion flames is correlated strongly with the emission of soot (roughly 0.37 kg CO per kg of soot emitted) (Köylü and Faeth, 1991). These observations motivate interest in the optical properties of flame-generated soot both to estimate the continuum radiation properties of flames and to develop nonintrusive laser-based methods for measuring soot properties within flames.

Early work concerning the optical and radiative properties of soot in flames is reviewed by Tien and Lee (1982) and Viskanta and Mengüc (1987). It was generally agreed that soot particles were small enough so that their optical properties could be obtained based on the small-particle Rayleigh scattering limit for wavelengths in the visible of interest for laser scattering measurements ($\lambda \geq 488$ nm). Thus, numerous studies of the properties of soot in flames have exploited the Rayleigh scattering approximation; see Gore and Faeth (1986, 1988), Köylü and Faeth (1991), Sivathanu and Faeth (1990), Tien and Lee (1982), and references cited therein. Nevertheless, even early measurements, involving sampling and analysis using transmission electron microscopy (TEM), showed that soot in the fuel-lean (overfire) region of diffusion flames involved large aggregates of small primary soot particles, suggesting that their optical properties differed from the Rayleigh scattering limit (Dalzell et al., 1970; Erickson et al., 1964; Magnussen, 1974; Martin and Hurd, 1987; Medalia and Heckman, 1969; Wersborg et al., 1973). Furthermore, Dalzell et al. (1970) found that approximating soot aggregates as equivalent spherical Mie scattering particles (having the same volume), in order to avoid the small particle approximation of Rayleigh scattering theory, was not very promising either.

More recently, Dobbins and Megaridis (1987) developed a thermophoretic sampling probe that provided a means of sampling soot aggregates from flames environments for subsequent analysis using TEM. This approach has been applied to laminar ethylene/air flames (Megaridis and Dobbins, 1989, 1990; Samson et al., 1987) and the fuel-lean (overfire) region of turbulent flames for various hydrocarbon fuels burning in air (Köylü and Faeth, 1992). These measurements showed that flame-generated soot ranged from small aggregates (dimensions on the order of 10 nm) observable near the start of soot formation at fuel-rich conditions in laminar flames, to large aggregates (dimensions on the order of 1 μm) emitted from turbulent flames — the latter clearly being too large for application of the Rayleigh scattering approximation. A useful property of soot aggregates, however, is that they approximate mass fractals (Köylü and Faeth, 1992; Jullien and Botet, 1987; Megaridis and Dobbins, 1989, 1990; Samson et al., 1987). Thus, Dobbins and Megaridis (1992) formalized an optical theory for polydisperse fractal soot aggregates, based on earlier work in the carbon black literature using the Rayleigh–Debye–Gans (R–D–G) scattering approximation (Jullien and Botet, 1987; Martin and Hurd, 1987). This approach yielded reasonably good predictions of soot aggregate optical properties found

Contributed by the Heat Transfer Division and presented at the ASME Winter Annual Meeting, Anaheim, California, November 8–13, 1992. Manuscript received by the Heat Transfer Division May 1992; revision received September 1992. Keywords: Combustion, Fire/Flames, Radiation. Associate Technical Editor: W. L. Grosshandler.

by Mountain and Mulholland (1988) from computations based on R-D-G scattering theory for computer-simulated aggregates. Subsequently, fractal aggregate optical theory was applied to interpret laser scattering measurements from the fuel-rich region of laminar ethylene/air flames, yielding reasonable results (Dobbins et al., 1990); and to estimate the laser extinction properties of aggregates in the fuel-lean region of turbulent flames, finding extinction cross sections as much as 100 percent larger than Rayleigh scattering estimates for heavily sooting fuels (Köylü and Faeth, 1992). Nevertheless, the fractal aggregate optical theory has not been experimentally evaluated as yet.

Use of the R-D-G scattering approximation implies that the refractive index of the scattering medium is near unity and that effects of multiple scattering within each aggregate are small (Bohren and Huffman, 1983; Kerker, 1969). These approximations are questionable for soot aggregates due to the relatively large refractive index of soot, while recent computational studies suggest significant effects of multiple scattering for soot aggregates (Berry and Percival, 1986; Borghese et al., 1984; Chen et al., 1988, 1990, 1991; Iskander et al., 1989; Nelson, 1989a, 1989b). Thus, no approximate theory—Rayleigh scattering, Mie scattering for an equivalent sphere, basic R-D-G scattering (for a given aggregate) and fractal aggregate R-D-G scattering (for a fractal aggregate)—has been established as a reliable method for estimating soot aggregate optical properties over the range of interest for practical flames. Thus, the objective of the present investigation was to evaluate the predictions of these various approximations using available computational and experimental results for soot aggregates in the literature.

The paper begins with a summary of the measured structure of flame-generated soot aggregates and a discussion of existing methods for computing soot aggregate optical properties. Approximate predications are then evaluated, considering computational and experimental results, in turn.

Soot Aggregate Structure

Numerous TEM photographs of soot aggregates for various flame conditions have appeared in the literature (Dalzell et al., 1970; Dobbins and Megaridis, 1987; Köylü and Faeth, 1992; Medalia and Heckman, 1969; Nelson, 1989b; Samson et al., 1987; Wersborg et al., 1973). They show that soot consists of spherical primary particles having nearly constant diameters (generally less than 60 nm) that are aggregated into branched structures having a large range of primary particles per aggregate. A number of experimental studies have shown that flame-generated soot aggregates exhibit mass fractal-like behavior with a Hausdorf or fractal dimension, $D_f < 2$, even when the number of primary particles in an aggregate is small (Jullien and Botet, 1987; Megaridis and Dobbins, 1989, 1990; Köylü and Faeth, 1992; Samson et al., 1987). The fractal dimension has important implications for soot optical properties because the scattering per primary particle continues to grow as the size of the aggregate increases if $D_f > 2$ but reaches a constant saturated value if $D_f < 2$ (Berry and Percival, 1986; Dobbins and Megaridis, 1992; Nelson, 1989b).

Recent measurements of soot aggregate properties in flame environments, largely using TEM, include the findings of Dobbins and co-workers in the fuel-rich region of laminar ethylene/air flames (Dobbins and Megaridis, 1987; Megaridis and Dobbins, 1990; Dobbins et al., 1990), and the results of Köylü and Faeth (1992) in the overfire region of turbulent flames at long residence times where soot structure is independent of position and residence time. These results show that primary particle diameters are nearly monodisperse and are less than 51 nm, yielding size parameters, $x_i < 0.300$ for $\lambda > 500$ nm, so that it is reasonable to assume they behave like Rayleigh scatterers, i.e., total scattering and absorption cross sections are within 1 and 5 percent, respectively, of estimates based on the Rayleigh scattering approximation for $m = 1.57 + 0.56i$, which is a typical value for soot (Dalzell et al., 1970). Soot aggregates are small near the soot inception point but they aggregate rapidly to reach $\bar{N}$ in the range 200–600 in the overfire region, with broad (log normal) size distribution functions (e.g., 30–1800 primary particles per aggregate). Fractal dimensions are generally in the range 1.7–1.8, even for small aggregates (Megaridis and Dobbins, 1990; Köylü and Faeth, 1992).

Nomenclature

C = optical cross section
d_p = primary particle diameter
d_e = equivalent sphere diameter
D_f = mass fractal dimension
D_{30} = volume-averaged equivalent aggregate diameter
$E(m)$ = refractive index function, Eq. (6)
$f(k,\theta, R_g)$ = aggregate form factor, Eq. (13)
f_n = moment ratio = $\overline{N^2}/(\bar{N})^2$
$F_d(\theta)$ = differential scattering enhancement factor, Eq. (27)
$F(m)$ = refractive index function, Eq. (7)
$g(k, R_g)$ = aggregate scattering factor, Eq. (13)
i = $(-1)^{1/2}$
k = wave number = $2\pi/\lambda$
k_f = fractal prefactor, Eq. (24)
m = refractive index of soot = $n + \kappa i$
n = real part of refractive index of soot
N = number of primary particles in an aggregate
$P(N)$ = probability density function of aggregate size
q = modulus of scattering vector, Eq. (17)
r_i = distance of each primary particle from the center of mass of the aggregate
R_g = radius of gyration of an aggregate
R_{ge} = radius of gyration of an equivalent sphere
w = aggregate size parameter, Eq. (16)
x_a = effective aggregate size parameter = $2\pi R_g/\lambda$
x_i = primary size parameter of particle i = $\pi d_{pi}/\lambda$
ϵ = dielectric constant, m^2
θ = angle of scattering from forward direction
κ = imaginary part of refractive index of soot
λ = wavelength of radiation
ρ_{sa} = ratio of scattering to absorption cross section of an aggregate

Subscripts

a = absorption
d = differential
e = extinction
hh, vv = scattering for horizontally (vertically) polarized incident and scattering directions
pp = either hh or vv
s = total scattering

Superscripts

a = aggregate property
p = primary particle property
$\bar{(\ )}$ = mean value over a polydisperse aggregate population

Table 1 Existing computations of soot aggregate optical properties

Aggregate Structure	Multiple Scattering	m	x_i	maximum N
Iskander et al. (1989):				
Prescribed	Exact[a]	1.33+0.11i 1.75+0.29i	0.013,0.25	125
Ku and Shim (1992a,b):				
Prescribed	Exact[a]	1.38+0.275i 1.7+0.1i 1.33	0.01-0.15	136
Chen et al. (1990, 1991):				
Simulated	Exact[a]	1.33+0.11i 1.75+0.29i	0.013,0.25	372
Nelson (1989a,b):				
Simulated	Exact[a]	1.75+0.5i	0.05,0.25	50
Simulated	Mean Field	1.75+0.5i	0.05,0.25	50 (vector), 256 (scalar)
Prescribed PDF	Mean Vector Field	1.75+0.5i	0.05,0.25	4000
Berry and Percival (1986):				
Prescribed PDF	Mean Scalar Field	---	0.111	10^6
Prescribed PDF	Mean Vector Field	---	0.111	10^6
Mountain and Mulholland (1988):				
Simulated	Rayleigh-Debye-Gans	---	0.065-0.25	687

[a]Exact implies touching spherical constant diameter primary particles, having uniform refractive indices and individually satisfying the Rayleigh scattering approximation, accounting for multiple scattering up to second order.

Scattering Predictions

Fundamental Methods. A variety of methods have been used for fundamental predictions of soot aggregate optical properties, as summarized in Table 1. Three approaches have been used with respect to aggregate structure, all limited to round primary particles having constant diameters that touch one another: (1) prescribed arrays of primary particles, (2) computer simulations to construct aggregates from an array of individual primary particles, and (3) prescribed probability density functions (PDF) of the separation distances of randomly chosen pairs of primary particles for fractal aggregates. Prescribed aggregates include straight chains, clusters, branched clusters, strips, etc.; see Iskander et al. (1989), Ku and Shim (1992a, 1992b), and Kumar and Tien (1989) for examples. Computer simulations involve random walk calculations where colliding particles stick together; models involving cluster-cluster aggregation yield aggregates most like flame-generated soot (Mountain and Mulholland, 1988; Nelson, 1989a, 1989b). Finally, PDF approximations of particle/pair correlations simplify calculations of aggregate orientation effects; they are found from either structure measurements or simulations (Berry and Percival, 1986; Nelson, 1989a, 1989b).

Borghese et al. (1984, 1987) describe an exact solution for the optical properties of clusters of spheres; however, the approach requires extensive computations and has only been applied to small clusters, $N = 20$, of nonabsorbing spheres, with questionable accuracy due to truncation of series. Thus, existing fundamental computations are limited to small primary particles, individually satisfying the Rayleigh scattering approximation, while only accounting for multiple scattering to second order. The general formulation is similar to Jones (1979a, 1979b), after correction for the proper sign of the imaginary part of the refractive index of soot as pointed out by Kumar and Tien (1989), and to include a self-interaction term needed to satisfy the optical theorem, as pointed out by Ku (1991). The Iskander-Chen-Penner (I-C-P) approach of Iskander et al. 1989) is the most accurate and has also been used by Ku and Shim (1992a, 1992b), Chen et al. (1990, 1991), and Nelson (1989a, 1989b). The bulk of the results of Nelson (1989a, 1989b) and Berry and Percival (1986), however, involve use of the mean field approximation (considering both scalar and vector wave fields), which implies that the internal field of all primary particles is the same. Finally, Mountain and Mulholland (1988) adopt the R-D-G approximation, where multiple- and self-scattering are ignored and the electrical field of each primary particle is the same as the incident field. Berry and Percival (1986) evaluate the adequacy of R-D-G theory for fractal aggregates, using mean-field theory, and argue that effects of multiple scattering are negligible for $D_f < 2$ when:

$$N \ll x_i^{-D_f} \tag{1}$$

or if this criterion is not satisfied, when

$$x_i \ll \left[\frac{|\epsilon - 1|^2 {}^{1-D_f}(D_f(D_f+1))^{D_f/2}}{3(D_f-1)(2-D_f)} \right]^{1/(D_f-3)} \tag{2}$$

The first condition is rarely satisfied for soot aggregates, while the second requires $x_i \ll 0.15$, which is not satisfied for a very wide range of conditions for soot aggregates—particularly in the visible portion of the spectrum use for optical measurements of soot structure. Thus, results based on R-D-G scattering do not serve as a reliable basis for judging more approximate methods.

Approximate Methods. A variety of approximate methods have been proposed to treat soot aggregate optical properties: Rayleigh scattering, Mie scattering for an equivalent sphere, and R-D-G scattering for both particular aggregates and populations of fractal aggregates. The Rayleigh scattering approximation only rigorously applies for individual particles and $x_i \ll 1$. Within this regime, expressions for the absorption, total scattering, and vertical (horizontal) polarized incident and scattering cross sections of individual primary particles are as follows (Bohren and Hoffman, 1983; Kerker, 1969; Van de Hulst, 1981):

$$C_a^p = 4\pi x_i^3 E(m)/k^2 \tag{3}$$

$$C_s^p = 8\pi x_i^6 F(m)/(3k^2) \tag{4}$$

$$C_{vv}^p = C_{hh}^p/\cos^2\theta = x_i^6 F(m)/k^2 \tag{5}$$

where θ is the scattering angle from the forward-scattering direction, while $C_e^p = C_a^p + C_s^p \approx C_a^p$ and

$$E(m) = -Im((\epsilon-1)/(\epsilon+2)) \tag{6}$$

$$F(m) = |(\epsilon-1)/(\epsilon+2)|^2 \tag{7}$$

Then applying the Rayleigh scattering approximation to an aggregate, assuming that the individual primary particles act independently and that all particles have the same diameter and refractive indices, yields:

$$C_a^a = N C_a^p, \quad C_s^a = N C_s^p, \quad C_{pp}^a(\theta) = N C_{pp}^p(\theta) \tag{8}$$

where *pp* denotes either *vv* or *hh* polarizations. At these conditions, it is easily shown that extinction is proportional to the volume fraction of soot (Tien and Lee, 1982; Viskanta and Mengüc, 1987), a property that has been widely used to measure soot concentrations in flame environments.

Another widely used approximation is to assume that the optical properties of aggregates can be found from Mie scattering calculations for a single sphere having the same volume as the aggregates. For monodisperse primary particles, the effective diameter of the equivalent sphere becomes:

$$d_e/d_p = N^{1/3} \tag{9}$$

Various modifications of this approach exist, involving corrections of the Mie scattering results for various assumed aggregate geometries, or use of corrected refractive indices under the porous sphere or Maxwell-Garnett approximations; see Dobbins and Megaridis (1992), Ku and Shim (1992b), Kumar and Tien (1989), and references cited therein. This approach is appealing due to the availability of efficient algorithms to compute Mie scattering functions (Bohren and Huffman, 1983).

More realistic approximations of soot aggregate optical properties seek to account directly for closely spaced primary particles in aggregates. If the aggregates involve small primary particles with negligible multiple scattering and self interaction (R-D-G scattering), and if the aggregates are small enough so that the phase differences of scattered radiation from various primary particles are small as well, the aggregate cross sections become (Bohren and Hoffman, 1983):

$$C_a^a = NC_a^p, \quad C_s^a = N^2 C_s^p, \quad C_{pp}^a(\theta) = N^2 C_{pp}^p(\theta) \tag{10}$$

For this approximation, absorption is the same as for independently scattering particles; however, total scattering from an aggregate is N times larger than scattering from an aggregate at the Rayleigh limit (compare Eqs. (8) and (10)). This implies enhanced extinction from scattering when N is large, which causes overestimation of soot volume fractions from extinction measurements interpreted using Rayleigh scattering theory. However, the approximations leading to Eqs. (10) are rarely satisfied by soot aggregates in flames, so alternative behavior is expected. In particular, Eqs. (10) indicate that the ratio of scattering-to-absorption cross sections, $\rho_{sa} = C_s^a/C_a^a = N(C_s^p/C_a^p)$, increases without bound as N increases, rather than saturating at large N for $D_f < 2$ as found from more exact methods (Berry and Percival, 1968; Nelson, 1989a, 1989d).

A further improvement of approximate theories can be obtained by applying correction factors for the phase and multiple scattering effects of real aggregates to the expressions for cross sections of Eqs. (10). Methods reported thus far have been based on R-D-G scattering, yielding (Jullien and Botet, 1987; Martin and Hurd, 1987):

$$C_a^a = NC_a^p \tag{11}$$

$$C_s^a = N^2 C_s^p g(k, R_g) \tag{12}$$

$$C_{pp}^a(\theta) = N^2 C_{pp}^p(\theta) f(k, \theta, R_g) \tag{13}$$

where the form factor, $f(k, \theta, R_g) \to 1$ as $\theta \to 0$, which follows from R-D-G theory, and R_g is the radius of gyration of the aggregate. Assuming monodisperse primary particle diameters as before, R_g can be found from:

$$R_g^2 = \sum_{i=1}^{N} r_i^2/N \tag{14}$$

where r_i is the distance of the center of each primary particle from the center of mass of the aggregate. Debye derived an expression for the form factor of aggregates of any shape and size, as follows (Kerker, 1969):

$$f(w) = 2(\exp(-w) + w - 1)/w^2 \tag{15}$$

where w is an aggregate size parameter

$$w = q^2 R_g^2 \tag{16}$$

and q is the modulus of the scattering vector

$$q = 2k \sin(\theta/2) \tag{17}$$

Equation (15) implies $f(w) \to 1 - w/3$ for small angles (small w) and $f(w) \to 2/w$ for large angles (large w). Applying the same approach to mass fractal aggregates then yields (Jullien and Botet, 1987; Martin and Hurd, 1987):

$$f(w) \approx 1 - w/3, \quad w \ll 1 \tag{18}$$

$$f(w) \approx w^{-D_f/2}, \quad w \gg 1 \tag{19}$$

Equation (18) properly yields $C_{pp}^a(\theta) \approx N^2 C_{pp}^p(\theta)$ as $w \sim \theta \to 0$ while Eq. (19) provides a means of finding D_f for mass fractals from scattering measurements if the range of w where this behavior is observed is large enough (Martin and Hurd, 1987). Another variant of this approach for fractal aggregates has been developed by Kuman and Tien (1989).

More recently, Dobbins and Megaridis (1992) applied R-D-G scattering to polydisperse aggregates, each consisting of primary particles having the same diameter and refractive index and individually in the Rayleigh scattering regime. Upon matching predictions at the Rayleigh scattering limit for small aggregates, and the R-D-G scattering computations for simulated aggregates from Mountain and Mulholland (1988) for large aggregates, they find:

$$g(k, R_g) = (1 + 4k^2 \overline{R}_g^2/(3D_f))^{-D_f/2} \tag{20}$$

$$f(w) = \exp(-w/3), \quad w \le 1.5D_f \tag{21}$$

$$f(w) = (3D_f/(2w \exp(1)))^{D_f/2}, \quad w > 1.5D_f \tag{22}$$

where $w = q^2 \overline{R}_g^2$. Computations of $f(w)$ for a given w from Eqs. (21) and (22) are essentially identical to Eqs. (18) and (19). Based on the fundamental scattering behavior of Eq. (10), Dobbins and Megaridis (1992) recommend finding the mean square radius of gyration of the polydisperse population of aggregates as follows:

$$\overline{R}_g^2 = \int_1^\infty N^2 R_g^2(N) P(N) dN / \int_1^\infty N^2 P(N) dN \tag{23}$$

where $R_g^2(N)$ is an average over all aggregates of size N in the population. Finally, R_g and N for particular aggregates are related through the following equation for fractal aggregates (Samson et al., 1987; Jullien and Botet, 1987):

$$N = k_f (R_g/d_p)^{D_f} \tag{24}$$

Values of the prefactor k_f in Eq. (24) are in the range 5.8–9.4; see the discussions of Megaridis and Dobbins (1990) and Köylü and Faeth (1992). The mean ratio of the scattering-to-absorption cross sections for this formulation is

$$\overline{\rho}_{sa} = (2F(m)/3E(m)) x_i^3 \overline{N} f_n (1 + 4k^2 \overline{R}_g^2/(3D_f))^{-D_f/2} \tag{25}$$

where $f_n = \overline{N^2}/(\overline{N})^2$ is the moment ratio for the aggregate size distribution. The moment ratio is in the range 2–4 for soot aggregates, being largest when aggregates are large, i.e., the overfire region of strongly sooting fuels (Köylü and Faeth, 1992). Equation (25) correctly represents the fact that R-D-G scattering from fractal aggregates saturates when $\overline{N}$ is large for $D_f < 2$, rather than continuing to increase according to Eq. (10); see Berry and Percival (1986) and Nelson (1989a, 1989b). For example, if the aggregates are assumed to be large and monodisperse, relating N and R_g^2 through Eq. (24) in Eq. (25), yields the following limiting behavior at large N:

$$\overline{\rho}_{sa} = (2F(m)/3(E(m)) x_i^3 k_f (3D_f/(16x_i^2))^{D_f/2}, \quad N \gg 1 \tag{26}$$

which implies that ρ_{sa} clearly is independent of N at large N. In spite of this correct trend, however, the fractal aggregate optical theory is based on the R-D-G scattering approximation, which is questionable for soot aggregates as discussed earlier. Thus, the value of the approximate theories rests on their capabilities to match behavior predicted by more exact methods and measurements, which will be taken up next.

Results and Discussion

Prescribed Aggregates. The approximate aggregate optical property theories will be evaluated considering theoretical results for prescribed and simulated aggregates, and measurements in flame environments, in turn. Figure 1 is an illustration of the differential scattering enhancement factor,

$$F_d(\theta) = C_d^a(\theta)/(NC_d^p(\theta)) \tag{27}$$

where

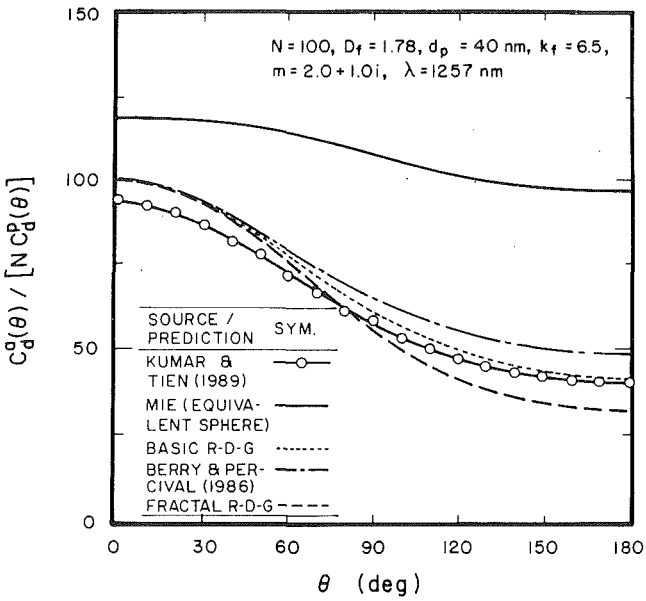

Fig. 1 Differential scattering enhancement factors as a function of scattering angle: conditions of Kumar and Tien (1989)

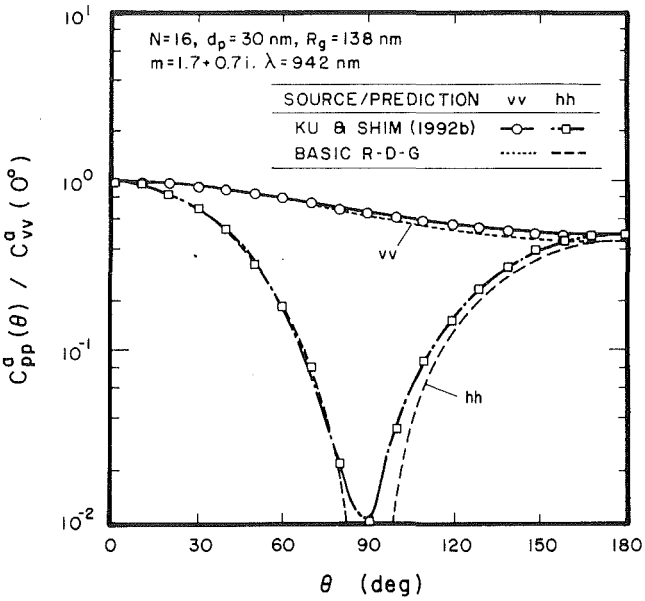

Fig. 2 Angular scattering pattern of a straight chain aggregate: conditions of Ku and Shim (1992b)

$$C_d^i(\theta) = (C_{vv}^i(\theta) + C_{hh}^i(\theta))/2, \; i = a \text{ or } p \qquad (28)$$

plotted as a function of θ for a prescribed fractal cluster considered by Kumar and Tien (1989). These results have been made specific to allow comparisons between a variety of approximate predictions for aggregate optical properties: N = 100, d_p = 40 nm, λ = 1257 nm, $m = 2+i$, D_f = 1.78, and k_f = 6.5. In addition to the predictions of Kumar and Tien (1989), the following approximate predictions are shown: Mie scattering for an equivalent sphere, basic R-D-G theory from Eq. (15), and fractal aggregate R-D-G theory based on Eqs. (18) and (19) (or equivalently, Eqs. (21) and (22)). The scalar-wave predictions of Berry and Percival (1986) can be applied to these results and are shown on the figure as well. The two R-D-G theories and the results of Berry and Percival (1986) yield the correct result (under the R-D-G approximation) that $F_d(\theta) \to N$ = 100 as $\theta \to 0$ while the prediction of Kumar and Tien (1989) is low and the Mie scattering approach is high. Use of Mie scattering for an equivalent sphere overestimates scattering at all angles and is not very satisfactory. There is little to choose between results for the approximate R-D-G theories; nevertheless, the Kumar and Tien (1989) approach will not be considered subsequently because it offers no particular advantages, is less satisfactory for $\theta \to 0$, is less widely used, and is more complex to compute than the basic and fractal aggregate R-D-G methods.

Figure 2 is an illustration of angular scattering patterns for a small straight chain aggregate, N = 16, from the results of Ku and Shim (1992b) using the I-C-P method. For these conditions, an effective size parameter for the aggregate, $x_a = 2\pi R_g/\lambda$, is 0.92 and some departures from Rayleigh scattering behavior ($C_{vv}^a(\theta)/(C_{vv}^a(0 \text{ deg}) = 1$ and $C_{hh}^a(\theta)/C_{vv}^a(0 \text{ deg}) = \cos^2\theta$) are anticipated. Departures are observed due to the significant reduction of $C_{vv}^a(\theta)/C_{vv}^a(0 \text{ deg})$ from unity as θ increases and the finite values of $C_{hh}^a(\theta)/C_{vv}^a(0 \text{ deg})$ near θ = 90 deg. Ku and Shim (1992b) show that Mie scattering from an equivalent sphere yields poor results for these conditions; thus only the basic R-D-G approach (the object is not a mass fractal) is illustrated. The approximate predictions are reasonably good except for *hh* scattering near θ = 90 deg—this is always the case for R-D-G estimates of *hh* scattering near 90 deg for aggregates larger than the Rayleigh scattering regime. Nevertheless, this deficiency of R-D-G scattering does not have a large effect on total scattering properties because the discrepancy only occurs over a narrow range of angles. Finally, the small size and straight chain configuration is not very typical of soot aggregates and is a particularly adverse geometry for R-D-G theory. More realistic results can be obtained with the larger simulated aggregates that are considered next.

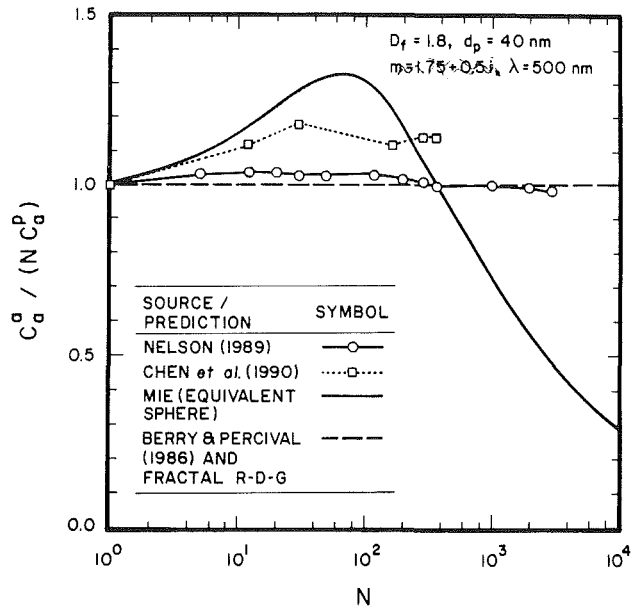

Fig. 3 Absorption enhancement factors as a function of aggregate size: conditions of Nelson (1989a), m = 1.75 + 0.5i except for Chen et al. (1990) where m = 1.33 + 0.11i

Simulated Aggregates. Figure 3 is an illustration of the absorption properties of fractal aggregates for conditions considered by Nelson (1989a). Predictions shown on the figure include I-C-P results from Chen et al. (1990), mean-scalar field results from Nelson (1989a) and Berry and Percival (1986), Mie scattering for an equivalent sphere, and fractal aggregate R-D-G theory. The computations of Chen et al. (1990) involve smaller refractive indices, m = 1.33 + 0.11i, than the other

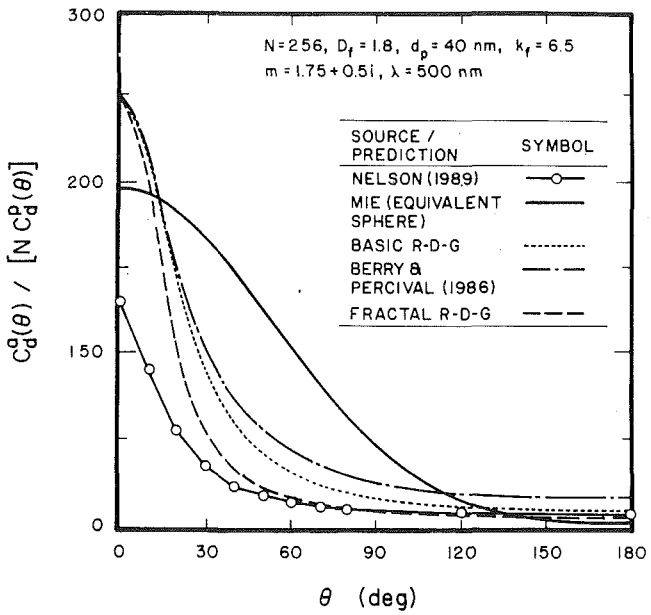

Fig. 4 Differential scattering enhancement factors as a function of scattering angle: conditions of Nelson (1989a)

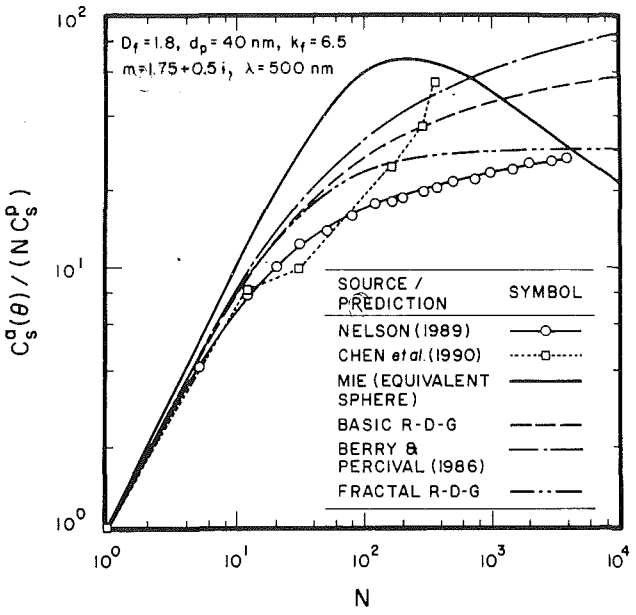

Fig. 5 Scattering enhancement factors as a function of aggregate size: conditions of Nelson (1989a), m = 1.75 + 0.5i except for Chen et al. (1990) where m = 1.33 + 0.11i

results on the figure where $m = 1.75 + 0.5i$. The results of Berry and Percival(1986) are consistent with R-D-G estimates of Eq. (11), which implies that $C_a^a/(NC_p^a) = 1$ at all N, due to their selection of the particle-pair separation distance PDF. Nelson (1989a) criticizes their PDF and develops improved mean-scalar field predictions based on a PDF method matched to exact predictions for small aggregates. The mean-scalar-field predictions of Nelson (1989a) yield aggregate absorption roughly 5 percent greater than R-D-G estimates for $N > 5$, suggesting significant effects of multiple scattering. The I-C-P results of Chen et al. (1990) are not very smooth because only one simulated aggregate was considered at each value of N, which is not sufficient for statistically significant results. Nevertheless, the I-C-P predictions exhibit absorption values 15-20 percent larger than R-D-G for $N > 10$, while absorption would be even larger if the m used for these calculations was the same as the rest; see Chen et al. (1990). This effect is due to the departure of the aggregates from R-D-G behavior because the refractive indices are relatively large. The enhanced absorption for I-C-P predictions in Fig. 3 is comparable to enhanced scattering, raising questions about whether effects of multiple scattering can be ignored for soot aggregates. Finally, the equivalent sphere results overestimate absorption for small aggregates, $N < 100$, and underestimate absorption for large aggregates, $N > 300$, because a compact spherical structure is not realistic for fractal aggregates with $D_f < 2$.

Figure 4 is an illustration of differential scattering enhancement factors for conditions considered by Nelson (1989a). Results shown on the figure include mean scalar field theory from Nelson (1989a) and Berry and Percival (1986), Mie scattering for an equivalent sphere, and basic and fractal aggregate R-D-G theory. The differences between the two sets of mean-scalar field predictions are due to problems with the PDF for primary pair separation distances chosen by Berry and Percival (1986) mentioned earlier: The Nelson (1989a) predictions are felt to be the most accurate solution illustrated in Fig. 4, because they have been matched to more exact methods and account for the modified field within primary particles. At small θ, approximate R-D-G based theories yield differential enhancement factors that approach N as expected. The mean-scalar field result of Nelson (1989a) is much lower at this condition, which implies significant effects of multiple scattering for aggregates that are typical of those found in flames.

Predictions of the fractal aggregate theory are reasonably good at larger angles, while results from basic R-D-G theory indicate slightly larger values of scattering in the same region. These results also raise questions about the use of fractal aggregate R-D-G theory to estimate soot structure from differential scattering measurements. The Mie scattering predictions for an equivalent sphere are the worst of the approximate theories; unfortunately, the errors of this approach are particularly large for θ near 45 deg, which is often used for soot structure measurements.

Total scattering enhancement factors for aggregates, $C_s^a/(NC_s^p)$, are plotted as a function of N in Fig. 5 for the conditions considered by Nelson (1989a), which are typical of laser scattering measurements of soot concentrations. Fundamental predictions shown on the plot include the I-C-P results of Chen et al. (1990) and the mean-scalar-field results of Nelson (1989a) and Berry and Percival (1986); approximate theories include Mie scattering for an equivalent sphere, and basic and fractal aggregate R-D-G theory (both using Eq. (24) to relate N and R_g). Similar to Fig. 3, the computations involve $m = 1.75 + 0.5i$ except for the I-C-P results of Chen et al. (1990) where $m = 1.33 + 0.11i$. The I-C-P results are fundamentally the most accurate but they are not smooth due to the limited number of aggregates considered; notably, these results do not suggest approach to a saturated condition at large N like the other theories. Because of uncertainties about mean-scalar-field and R-D-G predictions for large aggregates, where they indicate saturated behavior, this issue merits additional study. The mean-scalar-field results of Nelson (1989a) are lower than the rest of the fundamental theories at large N, which is consistent with Nelson's (1989a) view that this approach provides a lower bound for scattering properties as discussed earlier. The higher values for the mean-scalar-field results of Berry and Percival (1986) are caused by their less satisfactory choice of the PDF of particle pair separation distance within the mean-scalar-field approximation. Results for basic R-D-G theory are higher than those of fractal aggregate theory and provide the best agreement with I-C-P on the whole. Mie scattering predictions for an equivalent sphere are reasonably good for small aggregates, $N < 10$; however, trends of this approach are unreliable for large aggregates that are not very representative of compact spheres. The large en-

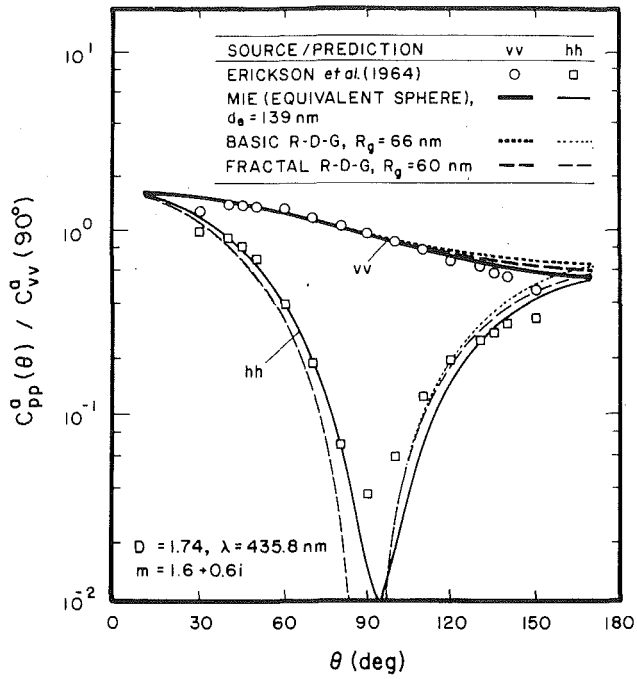

Fig. 6 Angular scattering pattern for soot aggregates in the postflame region of a premixed benzene-air flame: conditions of Erickson et al. (1964)

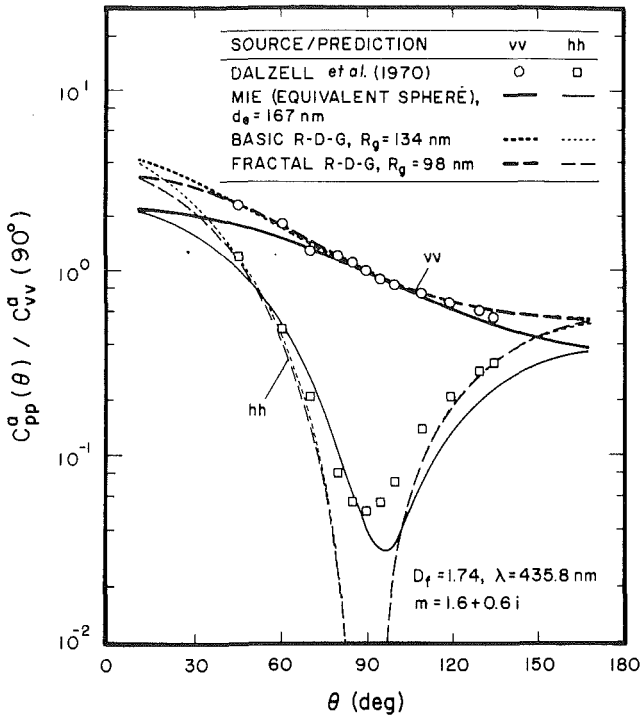

Fig. 7 Angular scattering pattern for soot aggregates in the overfire region of a nonpremixed propane-air flame: conditions of Dalzell et al. (1970)

hancement of scattering from Rayleigh scattering predictions is quite evident, highlighting the need for realistic optical models for aggregates in order to evaluate soot concentrations from laser scattering measurements in the visible portion of the spectrum. Effects of enhanced scattering of aggregates are smaller in the infrared where flame radiation effects are most significant; unfortunately, this difference still affects radiation predictions through overestimation of soot concentrations (Gore and Faeth, 1986, 1988; Köylü and Faeth, 1992).

Flame-Generated Aggregates. The final results to be considered include the measurements of angular scattering patterns for soot aggregates in the postflame region of premixed benzene–air flames due to Erickson et al. (1964) and in the overfire region of nonpremixed propane–air flames due to Dalzell et al. (1970). None of these measurements provide an adequate evaluation of optical theories for soot aggregates because the structure of the soot aggregates is not known. However, the exercise is useful because it highlights features about laser scattering measurements of soot structure.

Figure 6 is an illustration of the angular scattering, $C^a_{pp}(\theta)/C^a_{vv}(90 \text{ deg})$ pattern measurements of Erickson et al. (1964) at a wavelength of 435.8 nm, along with the approximate predictions of basic and fractal aggregate R–D–G theory and Mie scattering for an equivalent sphere. The approximate theories have been computed using m from Dalzell et al. (1970) and $D_f = 1.74$ for the fractal aggregate method, which is a reasonable value from existing measurements for soot aggregates (Köylü and Faeth, 1992). Best fits of the measurements and the approximate theories were sought by adjusting the values of R_g for the R–D–G theories and d_e for the equivalent sphere method. The measurements indicate significant departures from Rayleigh scattering theory, which implies $C^a_{vv}(\theta)/C^a_{vv}$ (90 deg) = 1, for these measurements; thus, aggregate scattering properties clearly are important. All the approximate theories are somewhat unsatisfactory for $C^a_{vv}(\theta)$ in the forward and backward scattering directions, and for C^a_{hh} (θ) near 90 deg and larger, with the fractal aggregate approach providing the best overall fit. Noting that the radius of gyration of a sphere (the mass-weighted root mean square radius about the center of mass of the sphere) is 0.39 d_e, the radius of gyration for the equivalent sphere is 54 nm; this is smaller than the results for the two R–D–G predictions, which are nearly the same, 66 and 60 nm for basic and fractal aggregate predictions, respectively. This difference is caused by overestimation of scattering using the Mie scattering approximation, except for very large aggregates, which yields a smaller diameter equivalent sphere when fitted to data, see Figs. 1 and 5. Erickson et al. (1964) conclude that Mie scattering theory does not adequately fit their data; fractal aggregate theory is the best of the rest but no approximate theory is very satisfactory for these results.

The angular scattering pattern of soot aggregates from the diffusion flame measurements of Dalzell et al. (1970) is illustrated in Fig. 7. Departures from Rayleigh scattering behavior are greater in this case than in Fig. 6 because larger aggregates generally are produced by diffusion flames than premixed flames. The three approximate theories have been fitted to the measurements in the same manner as for Fig. 6. All three approximate theories yield poor results for C^a_{hh} (90 deg) as before, with the best overall fit aside from this region provided by the R–D–G predictions. The results indicate that the forward and back scattering directions would provide greatest sensitivity to distinguish between predictions; unfortunately, the measurements do not extend into this region. The basic R–D–G approach yields a larger value of R_g than the fractal aggregate approach because it tends to overestimate scattering at large angles; see Fig. 4. Similar to Fig. 6, the equivalent sphere approach yields the smallest particles, with the radius of gyration of the equivalent sphere being 65 nm, rather than 134 and 98 nm for the basic and fractal aggregate R–D–G predictions. The difference between the R_g estimates from the R–D–G and Mie scattering methods is greater here than for the Erickson et al. (1964) data because the soot aggregates obviously are larger; see Figs. 1 and 5.

Other fits of the Dalzell et al. (1970) measurements were considered in order to examine the sensitivity of scattering measurements for determining soot aggregate sizes (Köylü, 1992). Computed results using basic and fractal-aggregate

R-D-G theory for $N = 100$ and 1000, over the range of angles of the measurements (45–135 deg), showed that predictions from both R-D-G theories, and both values of N, are essentially the same, implying very poor sensitivity for discriminating between approximate theories or aggregate sizes for these aggregates. In contrast, effects of aggregate size were far more evident for small scattering angles ($\theta < 45$ deg), which also provided greater discrimination between the two approximate theories. It is concluded that measurements of angular scattering patterns should place greater emphasis on the forward scattering region, unless the aggregates are relatively small where the variation of $C_{vv}^{a}(\theta)$ with θ near 90 deg provides some discrimination of particle size; see Figs. 2, 6, 7.

Conclusions

Major conclusions of the study are as follows:

1 Available computer simulations of flame-generated soot optical properties do not provide an adequate basis for evaluating approximate theories because they involve either fundamentally accurate solutions for small aggregates where effects of multiple and self-induced scattering are small, or approximate solutions having uncertain accuracy for the large soot aggregates of interest in practical flames. Additionally, even the more accurate existing solutions are questionable because issues of numerical closure with respect to truncation of series expansions in the solution, and statistically significant samples of simulated soot aggregates, have not been resolved.

2 Similarly, available measurements of the optical properties of flame-generated soot do not provide an adequate basis for evaluating approximate theories because the soot structure is unknown and the various theories yield similar results for the relatively large scattering angles (> 45 deg) that were considered. Measurements involving soot aggregates having known structure with more emphasis on results at small (forward) scattering angles, where the various theories can be distinguished, are needed.

3 Within the limitations of the present evaluation over the full range of soot aggregate sizes and wavelengths of interest in flames, the performance of various approximate theories for soot optical properties was as follows: Rayleigh scattering generally underestimates scattering and extinction, Mie scattering for an equivalent sphere yields unreliable results because a compact sphere is not a good model of the open wispy structure of soot aggregates, while best results were obtained using basic and fractal aggregate R-D-G scattering for given and fractal aggregates, respectively. However, due to the large refractive indices and sizes of flame-generated soot aggregates, the reliability of R-D-G scattering for their optical properties is questionable due to effects of multiple and self-induced scattering that were apparent from more exact predictions. Thus, both the basis for evaluation and the approximate methods themselves deserve additional attention.

Acknowledgments

This research was supported by the Building and Fire Research Laboratory of the National Institute of Standards and Technology, Grant No. 60NANB8D033, with H. R. Baum serving as Scientific Officer.

References

Berry, M. V., and Percival, I. C., 1986, "Optics of Fractal Clusters Such as Smoke," *Optica Acta*, Vol. 33, pp. 577–591.

Bohren, C. F., and Huffman, D. R., 1983, *Absorption and Scattering of Light by Small Particles*, Wiley, New York, pp. 477–482.

Borghese, F., Denti, P., Saija, R., Toscano, G., and Sindoni, O. I., 1984, "Multiple Electromagnetic Scattering From a Cluster of Spheres. I. Theory," *Aero Sci. Tech.*, Vol. 3, pp. 227–235.

Borghese, F., Denti, P., Saija, R., Toscano, G., and Sindoni, O. I., 1987, "Multiple Electromagnetic Scattering From a Cluster of Spheres. II. Symmetrization," *Aerosol Sci. Tech.*, Vol. 7, pp. 173–196.

Chen, H. Y., Iskander, M. F., and Penner, J. E., 1990, "Light Scattering and Absorption by Fractal Agglomerates and Coagulations of Smoke Aerosols," *J. Modern Optics*, Vol. 2, pp. 171–181.

Chen, H. Y., Iskander, M. F., and Penner, J. E., 1991, "Empirical Formula for Optical Absorption by Fractal Aerosol Aggregates," *Appl. Optics*, Vol. 30, pp. 1547–1551.

Chen, Z., Sheng, P., Weitz, D. A., Lindsay, H. H., and Lin, M. Y., 1988, "Optical Properties of Aggregate Clusters," *Phys. Rev. B.*, Vol. 34, pp. 5232–5235.

Dalzell, W. H., Williams, G. C., and Hottel, H. C., 1970, "A Light Scattering Method for Soot Concentration Measurements," *Combust. Flame*, Vol. 14, pp. 161–170.

Dobbins, R. A., and Megaridis, C. M., 1987, "Morphology of Flame-Generated Soot as Determined by Thermophoretic Sampling," *Langmuir*, Vol. 3, pp. 254–259.

Dobbins, S. A., and Megaridis, C. M., 1992, "Absorption and Scattering Light by Polydisperse Aggregates," *Appl. Optics*, Vol. 30, pp. 4747–4754.

Dobbins, R. A., Santoro, R. J., and Semerjian, H. G., 1990, "Analysis of Light Scattering From Soot Using Optical Cross Sections for Aggregates," *Twenty-Third Symposium (International) on Combustion*, The Combustion Institute, Pittsburgh, pp. 1525–1532.

Erickson, W. D., Williams, G. C., and Hottel, H. C., 1964, "Light Scattering Measurements on Soot in a Benzene–Air Flame," *Combust. Flame*, Vol. 8, pp. 127–132.

Gore, J. P., and Faeth, G. M., 1986, "Structure and Spectral Radiation Properties of Turbulent Ethylene/Air Diffusion Flames," *Twenty-First Symposium (International) on Combustion*, The Combustion Institute, Pittsburgh, pp. 1521–1531.

Gore, J. P., and Faeth, G. M., 1988, "The Structure and Radiation Properties of Luminous Turbulent Acetylene/Air Diffusion Flames," ASME JOURNAL OF HEAT TRANSFER, Vol. 110, pp. 173–181.

Iskander, M. F., Chen, H. Y., and Penner, J. E., 1989, "Optical Scattering and Absorption by Branches Chains of Aerosols," *Appl. Optics*, Vol. 28, pp. 3083–3091.

Jones, A. R., 1979a, "Electromagnetic Wave Scattering by Assemblies of Particles in the Rayleigh Approximation," *Proc. Roy. Soc. London A*, Vol. 366, pp. 111–127.

Jones, A. R., 1979b, "Scattering Efficiency Factors for Agglomerates of Small Spheres," *J. Phys. D: Appl. Phys.*, Vol. 12, pp. 1661–1672.

Jullien, R., and Botet, R., 1987, *Aggregation and Fractal Aggregates*, World Scientific Publishing Co., Singapore, pp. 46–50.

Kerker, M., 1969, *The Scattering of Light*, Academic Press, New York, pp. 414–486.

Köylü, Ü. Ö., and Faeth, G. M., 1991, "Carbon Monoxide and Soot Emissions From Liquid-Fueled Buoyant Turbulent Diffusion Flames," *Combust. Flame*, Vol. 87, pp. 61–67.

Köylü, Ü. Ö., 1992, "Emission, Structure and Optical Properties of Overfire Soot From Buoyant Turbulent Diffusion Flames," Ph.D. Thesis, The University of Michigan, Ann Arbor, MI.

Köylü, Ü. Ö., and Faeth, G. M., 1992, "Structure of Overfire Soot in Buoyant Turbulent Diffusion Flames at Long Residence Times," *Combust. Flame*, Vol. 89, pp. 140–156.

Ku, J. C., 1991, "Correction for the Extinction Efficiency Factors Given in the Jones Solution for Electromagnetic Scattering by Agglomerates of Small Spheres," *J. Phys. D. Appl. Phys.*, Vol. 24, pp. 71–75.

Ku, J. C., and Shim, K.-H., 1992a, "Optical Diagnostics and Radiative Properties of Simulated Soot Agglomerates," ASME JOURNAL OF HEAT TRANSFER, Vol. 113, pp. 953–958.

Ku, J. C., and Shim, K.-H., 1992b, "A Comparison of Solutions for Light Scattering and Absorption by Agglomerated or Arbitrarily-Shaped Particles," *J. Quant. Spect. and Rad. Trans.*, in press.

Kumar, S., and Tien, C. L., 1989, "Effective Diameter of Agglomerates for Radiative Extinction and Scattering," *Combust. Sci. Tech.*, Vol. 66, pp. 199–216.

Magnussen, B. F., 1974, "An Investigation Into the Behavior of Soot in a Turbulent Free Jet C_2-H_2-Flame," *Fifteenth Symposium (International) on Combustion*, The Combustion Institute, Pittsburgh, pp. 1415–1425.

Martin, J. E., and Hurd, A. J., 1987, "Scattering From Fractals," *J. Appl. Cryst.*, Vol. 20, pp. 61–78.

Medalia, A. I., and Heckman, F. A., 1969, "Morphology of Aggregates—II. Size and Shape Factors of Carbon Black Aggregates From Electron Microscopy," *Carbon*, Vol. 7, pp. 567–582.

Megaridis, C. M., and Dobbins, R. A., 1989, "Comparison of Soot Growth and Oxidation in Smoking and Non-smoking Ethylene Diffusion Flames," *Comb. Sci. Tech.*, Vol. 66, pp. 1–16.

Megaridis, C. M., and Dobbins, R. A., 1990, "Morphological Description of Flame-Generated Materials," *Comb. Sci. Tech.*, Vol. 77, pp. 95–109.

Mountain, R. D., and Mulholland, G. W., 1988, "Light Scattering From Simulated Smoke Agglomerates," *Langmuir*, Vol. 4, pp. 1321–1326.

Nelson, J., 1989a, "Test of a Mean Field Theory for the Optics of Fractal Clusters," *J. Modern Optics*, Vol. 36, pp. 1031–1057.

Nelson, J., 1989b, "Fracticality of Sooty Smoke: Implications for the Severity of Nuclear Winter," *Nature*, Vol. 339, pp. 611–613.

Samson, R. J., Mulholland, G. W., and Gentry, J. W., 1987, "Structural Analysis of Soot Agglomerates," *Langmuir*, Vol. 3, pp. 272–281.

Sivathanu, Y. R., and Faeth, G. M., 1990, "Soot Volume Fractions in the Overfire Region of Turbulent Diffusion Flames," *Combust. Flame*, Vol. 81, pp. 133–149.

Tien, C. L., and Lee, S. C., 1982, "Flame Radiation," *Prog. Energy Combust. Sci.*, Vol. 8, pp. 41–59.

Van de Hulst, H. C., 1981, *Light Scattering by Small Particles*, Dover Publications, New York.

Viskanta, R., and Mengüc, M. P., 1987, "Radiation Heat Transfer in Combustion Systems," *Prog. Energy Combust. Sci.*, Vol. 13, pp. 97–160.

Wersborg, B. L, Howard, J. B., and Williams, G. C., 1973, "Physical Mechanisms in Carbon Formation in Flames," *Fourteenth Symposium (International) on Combustion*, The Combustion Institute, Pittsburgh, pp. 929–940.

Heat Transfer From Radiatively Heated Material in a Low Reynolds Number Microgravity Environment

H. Yamashita[1]

H. R. Baum

G. Kushida[1]

K. Nakabe[2]

T. Kashiwagi

Building and Fire Research Laboratory,
National Institute of Standards and Technology,
Gaithersburg, MD 20899

A mathematical model of the transient three-dimensional heat transfer between a slowly moving ambient gas stream and a thermally thick or thin flat surface heated by external radiation in a microgravity environment is presented. The problem is motivated in part by fire safety issues in spacecraft. The gas phase is represented by variable property convection-diffusion energy and mass conservation equations valid at low Reynolds numbers. The absence of gravity and low Reynolds number together permit the flow to be represented by a self-consistent velocity potential determined by the ambient velocity and the thermal expansion in the gas. The solid exchanges energy with the gas by conduction/convection and with the surroundings by surface absorption and re-emission of radiation. Heat conduction in the solid is assumed to be one dimensional at each point on the surface as a consequence of the limited times (of order of 10 seconds) of interest in these simulations. Despite the apparent simplicity of the model, the results show a complex thermally induced flow near the heated surface. The thermal exchange between the gas and solid produces an outward sourcelike flow upstream of the center of the irradiated area and a sinklike flow downstream. The responses of the temperature fields and the associated flows to changes in the intensity of the external radiation and the ambient velocity are discussed.

1 Introduction

This paper is a continuation of our analysis of heat transfer phenomena associated with the radiative ignition of cellulosic materials in a microgravity environment. The objective of this work is both scientific understanding and the development of a potential hazard analysis capability for spacecraft fire safety studies. The use of a microgravity environment to study radiative ignition eliminates the need to study simultaneously the starting buoyant plume, which is itself a major task requiring a time-dependent solution to multidimensional Navier–Stokes equations. Previous radiative auto-ignition models avoided this problem by limiting the analysis to one dimension (Kashiwagi, 1974; Kindelan and Williams, 1977; Baek and Kim, 1991), or at a stagnation point (Amos and Fernandez-Pello, 1988). Almost any scenario of interest in a spacecraft potential hazard analysis is both multidimensional and time dependent. Thus, one of the goals of the present work is a formulation of a computationally tractable model of the thermal transport that can be used in transient three-dimensional ignition studies.

In a microgravity environment, the dominant vorticity creation mechanism in the bulk of the gas is absent. Vorticity is still generated at the surface by the non-slip condition. However, at low Reynolds numbers the tangential velocity profile near the surface is not important in the convective transport of mass, momentum, or energy. Thus, the no-slip condition was relaxed in our earlier study of radiatively induced degradation of a thermally thin solid in a quiescent gas (Kushida et al., 1992). This permitted the flow in this axially symmetric configuration to be represented by a velocity potential. In the present work, this approximation is used to investigate two major extensions; the incorporation of a slow ambient flow generalizing the analysis to three dimensions, and coupling this to both thermally thick and thermally thin solid samples. These extensions are motivated by the experimentally observed strong effects of ambient flow velocity on flame spread rate in a microgravity environment (Olson et al., 1988; Olson, 1991). It appears that a ventilation flow in a spacecraft should have a strong effect on the flame spread rate. In the present study only the coupled heat transfer processes are studied. Later papers will describe the effects of the condensed phase degradation reactions and gas phase oxidation.

2 Theory

2.1 Gas Phase. The study of radiative heating or ignition of solid fuels in a microgravity environment requires a description of time-dependent coupled processes in both the gas and solid phases. The mathematical and computational complexity inherent in such a study suggests that the simplifications permitted by the microgravity environment and the small physical scale of the idealized experiment be built into the mathematical model. These simplifications principally affect the gas phase processes. The absence of gravity removes the buoyancy-induced vorticity generation mechanism. The small radiatively heated surface area in the scenarios of interest together with the slow externally imposed velocity implies a low Reynolds number flow domain. Classical analyses of low Reynolds number flows have demonstrated that using the Oseen approximation to the convective terms in the equations of motion "constitutes an ad-hoc uniformization" (Van Dyke, 1964) of the first approximation to the rigorous calculation of the flow past isolated bodies. The central point that emerges from these analyses is that diffusion dominates convection near the surface, so the fact that the Oseen flow does not satisfy the no-slip boundary condition is irrelevant at lowest order in the theory. When the gasification of condensed fuels is included in our future studies, the thermally induced surface blowing velocity must be taken into account, even at low Reynolds numbers. The generalization to a flow past an arbitrarily shaped body with a prescribed surface blowing distribution can also be accommodated by a potential flow, if vorticity generated in the interior of the flow is not significant.

The potential flow description of the velocity field greatly simplifies both the formulation and subsequent computation

[1]Guest researcher from Nagoya University, Nagoya, Japan.

[1]Guest researcher from Osaka University, Osaka, Japan.

Contributed by the Heat Transfer Division for publication in the JOURNAL OF HEAT TRANSFER. Manuscript received by the Heat Transfer Division March 1992; revision received November 1992. Keywords: Microgravity Heat Transfer, Transient and Unsteady Heat Transfer. Associate Technical Editor: L. S. Fletcher.

of a wide variety of low Reynolds number microgravity heat transfer and combustion problems. Accordingly, the formulation will be developed in a fairly general context and then specialized to the specific case of the radiative heating of a thermally thick solid. The starting point is the conservation of mass and energy in the gas. Under low Mach number heat transfer conditions, generalized governing equations including gas phase oxidation reactions and radiative heat transfer can be written as:

$$\frac{D\rho}{Dt}+\rho\nabla\cdot\mathbf{v}=0 \tag{1}$$

$$\rho c_p\frac{DT}{Dt}-\nabla\cdot(k\nabla T)=\dot{q}_R(\mathbf{r},\,t) \tag{2}$$

Here, $\dot{q}_R(\mathbf{r},\,t)$ is the net chemical and radiative heat release per unit volume into the gas of density ρ, temperature T, and velocity $\mathbf{v}$. The gas was assumed to be air. The specific heat c_p and thermal conductivity k are in general functions of T, and they are fitted by the fifth-order polynomial expression. These equations are supplemented by an equation of state, taken in a form appropriate for low Mach number flows:

$$\rho h=\rho_\infty h_\infty \tag{3}$$

The subscript ∞ refers to suitable ambient or reference conditions:

$$h=\int_0^T c_p(T)dT \tag{4}$$

Now multiply Eq. (1) by h and add it to Eq. (2). The result, after using Eqs. (3) and (4), is:

$$\rho_\infty h_\infty\nabla\cdot\mathbf{v}-\nabla\cdot(k\nabla T)=\dot{q}_R(\mathbf{r},\,t) \tag{5}$$

Equation (5) is the fundamental equation for determing the velocity field $\mathbf{v}$. Since $\mathbf{v}$ is a vector field, it can be decomposed into the gradient of a potential ϕ and a solenoidal field $\mathbf{u}$:

$$\mathbf{v}=\nabla\phi+\mathbf{u} \tag{6}$$

$$\nabla\cdot\mathbf{u}=0 \tag{7}$$

Substitution of Eqs. (6) and (7) into Eq. (5) yields:

$$\nabla^2\phi=\frac{1}{\rho_\infty h_\infty}\,(\dot{q}_R(\mathbf{r},\,t)+\nabla^2\psi) \tag{8}$$

$$\psi=\int_{T_\infty}^T k(T)dT \tag{9}$$

Note that the second term on the right-hand side of Eq. (8) can be eliminated by introducing a particular solution ϕ_p as:

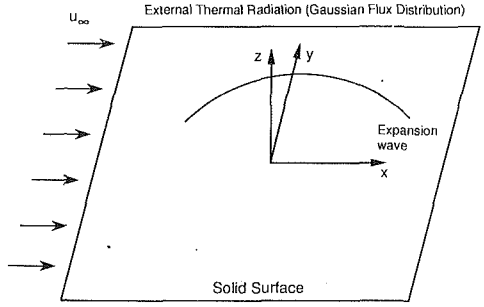

Fig. 1 A schematic illustration of coordinates and the flow field near the heated surface area by external radiation

$$\phi_p=\frac{\psi}{\rho_\infty h_\infty} \tag{10}$$

Furthermore, it is convenient to introduce another particular potential $\phi_{p\infty}$ representing the effect of the ambient wind velocity u_∞. Then, introducing a remainder of potential $\Phi(\mathbf{r},\,t)$, ϕ may be expressed in the form:

$$\phi=\phi_p+\phi_{p\infty}+\Phi(\mathbf{r},\,t) \tag{11}$$

$$\nabla^2\Phi=\frac{\dot{q}_R(\mathbf{r},\,t)}{\rho_\infty h_\infty} \tag{12}$$

Equations (10), (11), and (12) relate the potential field to the temperature distributions in the gas phase. Since it is necessary to determine this quantity in any event, solution of Eq. (12) represents the minimum additional work required to obtain a self-consistent velocity field. Implied in this statement is the assumption that the solenoidal velocity field $\mathbf{u}$ is not of interest in its own right. If $\mathbf{u}$ is of interest, then there is no alternative to solving the Navier–Stokes equations. However, a large portion of both the combustion and heat transfer literature consists of calculations in which the details of the velocity field are approximated, often crudely, in order to understand the thermophysical phenomenon of direct interest. In the present circumstances, the approximations have been justified in simple geometries by detailed analyses, and interest will be confined to temperature fields induced by radiative heating.

Now consider the specific problem of heat transfer from radiative heating of thermally thick solid with a slow flow along the surface in microgravity environment. The geometry is shown in Fig. 1. Let x, y, and z be the streamwise, spanwise, and transverse coordinates in a three-dimensional Cartesian coordinate system as shown in the figure. The center of the

Nomenclature

c, c_p = specific heat
G = Green's function
h = enthalpy
k = thermal conductivity
Pe = Peclet number
Pe_l = 1/Pe
$\dot{q}$ = heat flux
$\dot{q}_N$ = net heat flux at solid surface
$\dot{q}_R$ = net chemical and radiative heat release in the gas phase
r, $\mathbf{r}$ = distance from origin, position vector
r_0 = width of Gaussian distribution of external radiation
T = temperature
t = time
$\mathbf{u}$ = solenoidal velocity vector
u_∞ = ambient velocity
$\mathbf{v}$ = velocity vector
x, y, z = Cartesian coordinates (streamwise, spanwise, transverse)
α = thermal diffusivity
δ = thickness of thin solid sheet
ϵ = emissivity
Δt = time interval
Δx, Δy, Δz = grid spacing
ρ = density
σ = Stefan–Boltzmann constant
Φ = remainder potential function
ϕ = potential function
ϕ_p = particular solution of potential function
ψ = potential function related with heat conduction

Subscripts

N = net
rad = solid surface re-radiation
s = solid phase
∞ = ambient or reference condition

concentrated external radiant flux with a Gaussian distribution impinging on the solid surface is set up at the origin of coordinates. The ambient flow is parallel to the solid surface and then $\phi_{P\infty} = u_\infty x$. The gas is assumed to be transparent to the radiation. Under these circumstances, the term $\dot{q}_R(\mathrm{r}, t)$ in Eq. (2) can be ignored. The gas phase energy conservation equation takes the form:

$$\rho c_p\left(\frac{\partial T}{\partial t}+\mathbf{v}\cdot\nabla T\right)=\nabla\cdot(k\nabla T) \tag{13}$$

This equation is to be solved together with Eqs. (10), (11), and (12), subject to boundary and initial conditions.

At time $t = 0$, the entire system is assumed to have uniform flow at ambient temperature T_∞. Hence:

$$\begin{aligned}\Phi(x, y, z, 0)&=0\\ T(x, y, z, 0)&=T_\infty\end{aligned} \tag{14}$$

Once the heating process has started, the temperature at the solid surface $T_s(x, y, 0, t)$ rises above ambient, and the temperatures at the flow inlet and open boundaries remain at T_∞. The gas phase boundary conditions for temperature and Φ must be provided at the flow inlet $x = -\infty$ and the flow exit $x = +\infty$, at the symmetric boundary $y = 0$, at the open boundary $y = \infty$ and $z = \infty$, and at the solid surface $z = 0$. The boundary conditions for temperature T can be expressed as follows:

$$\begin{aligned}T(\pm\infty, y, z, t)&=T_\infty\\ \frac{\partial T(x, 0, z, t)}{\partial y}&=0\\ T(x, \infty, z, t)&=T_\infty\\ T(x, y, 0, t)&=T_s(x, y, 0, t)\\ T(x, y, \infty, t)&=T_\infty\end{aligned} \tag{15}$$

The boundary conditions for Φ are:

$$\begin{aligned}\Phi(-\infty, y, z, t)&=\Phi_{x_{-\infty}}\\ \Phi(\infty, y, z, t)&=\Phi_{x_\infty}\\ \frac{\partial\Phi(x, 0, z, t)}{\partial y}&=0\\ \Phi(x, \infty, z, t)&=\Phi_{y_\infty}\\ \rho_\infty h_\infty\frac{\partial\Phi(x, y, 0, t)}{\partial z}&=-k\frac{\partial T(x, y, 0, t)}{\partial z}\\ \Phi(x, y, \infty, t)&=\Phi_{z_\infty}\end{aligned} \tag{16}$$

where $\Phi_{x-\infty}$, $\Phi_{x\infty}$, $\Phi_{y\infty}$, and $\Phi_{z\infty}$ are the values at positions far away from the solid surface. Far from the surface, Φ and T must decay to their ambient values. Translating this into boundary conditions suitable for numerical computation, however, requires some care. Numerical boundary conditions are applied at the sides of a rectangular box shaped computational domain. Since T decays exponentially to its ambient value, using Eq. (14) is permissible until the first calculated non-ambient contours of these quantities approach the computational boundary. However, the potential field decays slowly away from the heated region, i.e., $\Phi\sim(x^2+y^2+z^2)^{-1}$. Thus, putting Φ or its gradient equal to zero at the computational boundary would introduce unacceptable errors into the calculation. These errors can be avoided by using Eq. (17) shown below, that is, the solution to Eq. (12) subject to the boundary condition given by Eq. (16).

$$\rho_\infty h_\infty\Phi=\int_{-\infty}^{\infty}dx_0\int_{-\infty}^{\infty}dy_0\int_0^{\infty}dz_0\dot{q}_R(x_0,y_0,z_0)G(x,y,z,x_0,y_0,z_0)$$
$$+\rho_\infty h_\infty\int_{-\infty}^{\infty}dx_0\int_{-\infty}^{\infty}dy_0\frac{\partial\Phi(x_0,y_0,0,t)}{\partial z}G(x,y,z,x_0,y_0,0)$$

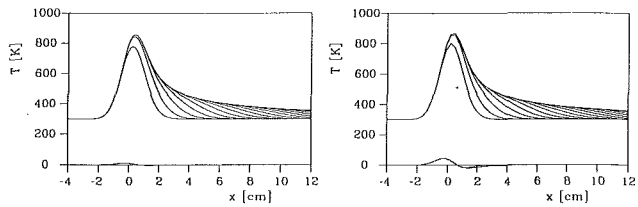

Fig. 2 Time history of surface temperature distribution at $y = 0$ and at the interval of 0.5 s for the case of linear problem ($u_\infty = 2$ cm/s, $\ddot{q}_0 = 4$ W/cm^2) and difference between the analytical solution and the numerically calculated results at 10 s: (*a*) grid size 128 × 32 × 32; (*b*) grid size 64 × 16 × 16

$$G(x,y,z,x_0,y_0,z_0)=-\frac{1}{4\pi}\left(\frac{1}{[(x-x_0)^2+(y-y_0)^2+(z-z_0)^2]^{1/2}}\right.$$
$$\left.+\frac{1}{[(x-x_0)^2+(y-y_0)^2+(z+z_0)^2]^{1/2}}\right) \tag{17}$$

G is a Green's function satisfying Neumann boundary conditions. Now $\partial\Phi(x, y, 0, t)/\partial z$ is given by Eq. (16) at any instant of time, and the temperature is an exponentially decaying function of the radial integration variable in Eq. (17). Hence, the use of Eq. (17) to evaluate Φ around the computational boundary provides a fast and highly accurate means of applying computational boundary conditions to Φ.

2.2 Condensed Phase Model. In much of the present paper the sample is thermally thick. Since it is expected that the ignition event would occur within a relatively short time (less than 10 seconds) after the beginning of external irradiation, only heat conduction normal to the surface is important and conduction along the y and x coordinates is assumed to be negligible. Also, it is assumed that the condensed material is opaque and there is no radiative transfer in the sample. Thermal properties of the sample are assumed to be independent of temperature. Then, the governing energy equations for the condensed phase are given as follows:

$$\frac{\partial T_s}{\partial t}=\alpha_s\frac{\partial^2 T_s}{\partial z^2} \tag{18}$$

where α_s is the thermal diffusivity of the solid. The initial condition and the boundary condition are as follows:

$$\begin{aligned}T_s(x,y,z,0)&=T_\infty\\ T_s(x,y,-\infty,t)&=T_\infty\\ T_s(x,y,0,t)=T(x,y,0,t),\qquad k_s\frac{\partial T_s(x,y,0,t)}{\partial z}&=\ddot{q}_N\end{aligned} \tag{19}$$

Then, the solution for the surface temperature yields the following relation:

$$k_s[T_s(x,y,0,t)-T_\infty]=\int_0^t\left(\frac{\alpha_s}{\pi(t-\tau)}\right)^{1/2}\ddot{q}_N(x,y,\tau)d\tau \tag{20}$$

The subscript s refers to properties of the condensed phase, and $\ddot{q}_N$ is the net heat flux to the solid surface.

The net heat flux at the material surface is

$$\ddot{q}_N=\ddot{q}_{ex}-\ddot{q}_{\mathrm{rad}}+k\frac{\partial T(x,y,0,t)}{\partial z} \tag{21}$$

where $\ddot{q}_{ex}$ is external radiant flux and its distribution is defined to be Gaussian. In the calculation reported here,

$$\ddot{q}_{ex}=\ddot{q}_0\exp\left[-\left(\frac{r}{r_0}\right)^2\right] \tag{22}$$

where $r = (x^2+y^2)^{1/2}$, $r_0 = 1$ cm and $\ddot{q}_0$ is a peak external radiant flux. $\ddot{q}_{\mathrm{rad}}$ is the re-radiation flux from the material surface and is given by the following expression:

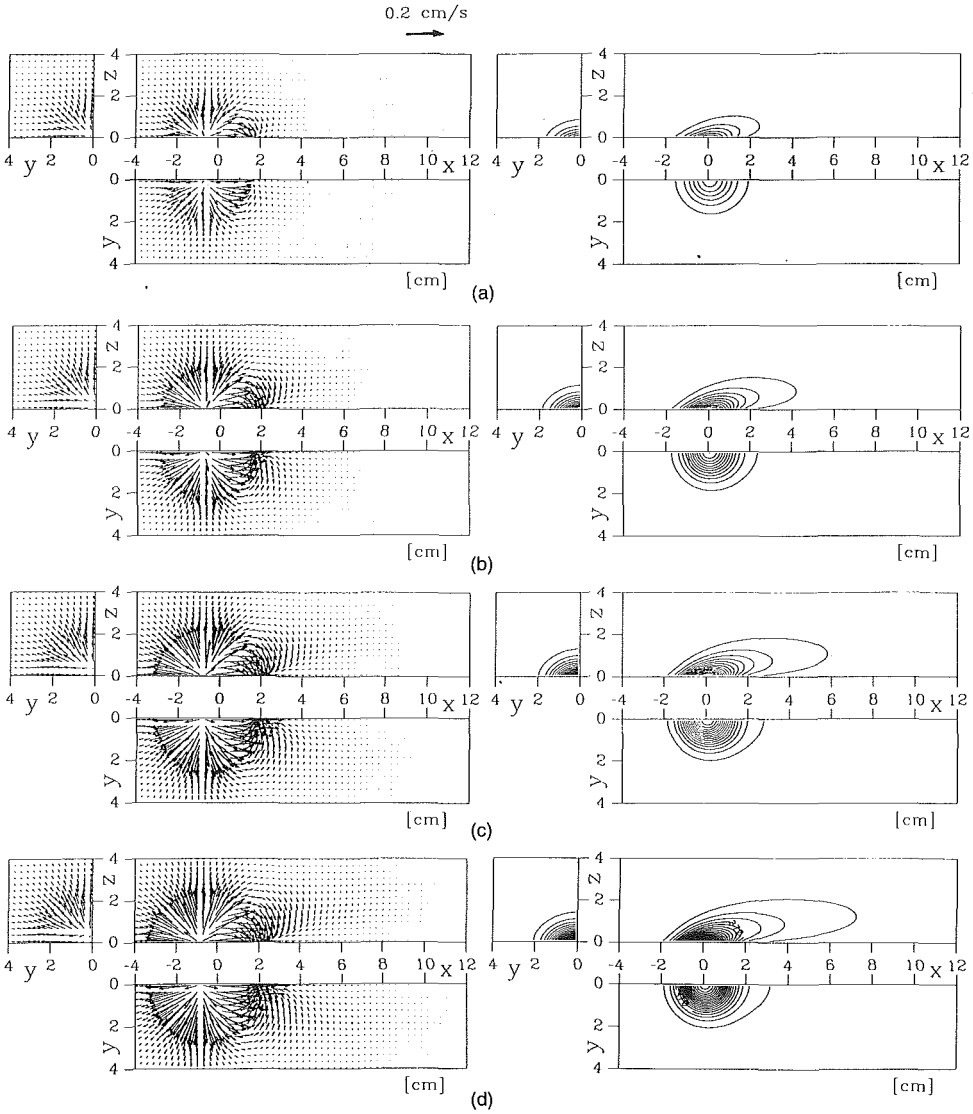

Fig. 3 The distributions of velocity vectors relative to ambient flow and the temperature contours (from 310 K at the interval of 20 K) for u_∞ = 2 cm/s and $\ddot{q}_0$ = 4 W/cm^2. (*a*) t = 2 s; (*b*) t = 4 s; (*c*) t = 6 s; (*d*) t = 8 s

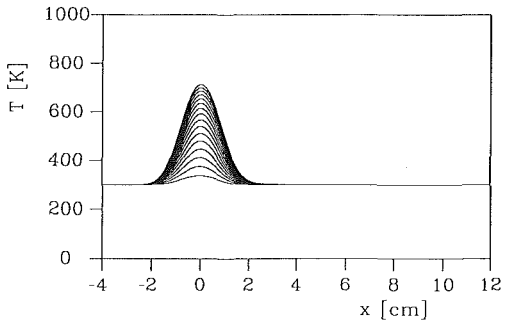

Fig. 4 Time history of the surface temperature distribution at y = 0 for u_∞ = 2 cm/s and $\ddot{q}_0$ = 4 W/cm^2 at the interval of 0.5 s

$$\ddot{q}_{\text{rad}} = \epsilon\sigma[T_s^4(x,y,0,t) - T_\infty^4] \tag{23}$$

where the Stefan-Boltzmann constant $\sigma = 56.7 \times 10^{-13}$ W/(cm^2•K^4). The surface re-radiation is quite important when the surface temperature becomes high. Therefore, the surface temperature can rise to the value at which re-radiation flux becomes equal to external radiant flux. The surface temperature reaches as high as 919 K or 1091 K for q_0 = 4 or 8 W/cm^2 with ϵ = 1.0 and T_∞ = 300 K, respectively.

Two other limiting cases of this heat transfer problem have been studied for comparison purposes; the thermally thin solid with the same gas phase description, and a simplified gas phase heat transfer problem for which an analytical solution can be derived to examine the accuracy of the numerical code. For a thermally thin material, the governing energy equation, Eq. (18), does not need to be solved and the following boundary equation is used:

$$\rho_s c_s \frac{\partial T_s(x,y,0,t)}{\partial t} \cdot \delta = \ddot{q}_{ex} - \ddot{q}_{\text{rad}} + k \frac{\partial T(x,y,0,t)}{\partial z} \tag{24}$$

where δ is the thickness of the thermally thin sheet. Since a cellulosic paper has been used for the thermally thin material in our previous studies (Kushida et al., 1991), the same thermal properties of the cellulosic paper are used.

Heat transfer with an Oseen flow problem is selected to obtain the analytical solution to test the numerical code. The flow field is uniform with u_∞ and only the energy equation in the gas phase is involved as described in the appendix. Heat is transferred by conduction and convection from the specified energy flux at the surface. The analytical solution is derived and expressed as

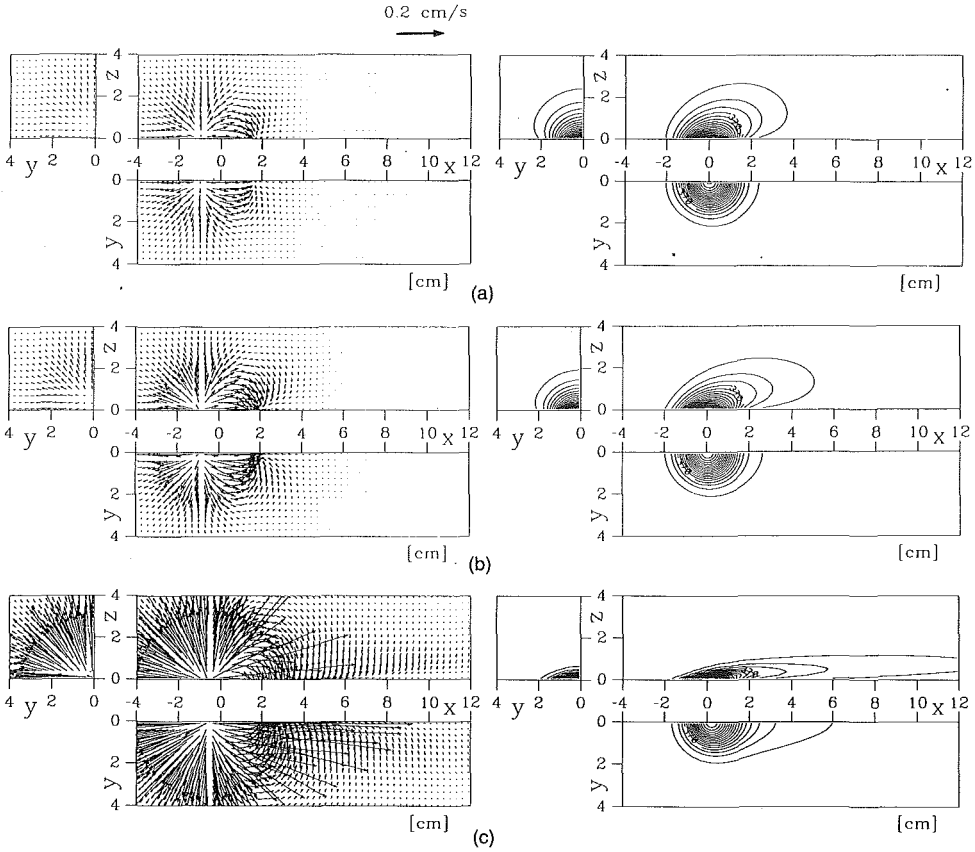

Fig. 5 Effects of ambient flow velocity on the distributions of velocity vectors relative to the ambient flow and the temperature contours (from 310 K at the interval of 20 K) at t = 8 s for $\ddot{q}_0$ = 4 W/cm^2. (*a*) u_∞ = 0.5 cm/s (Pe = 2.27); (*b*) u_∞ = 1.0 cm/s (Pe = 4.55); (*c*) u_∞ = 10 cm/s (Pe = 45.5)

$$\theta = \frac{\int_0^{\tilde{t}} \sqrt{\mathrm{Pe}_i}\exp\{-(\tilde{x}-\tau)^2+(\tilde{y})^2]/(1+4\mathrm{Pe}_i\tau)-(\tilde{z})^2/4\mathrm{Pe}_i\tau\}d\tau}{\pi^{3/2}\sqrt{\tau}(1+4\mathrm{Pe}_i\tau)} \tag{25}$$

where θ, $\tilde{x}$, $\tilde{y}$, $\tilde{z}$, $\tilde{t}$ are nondimensionalized temperature, three coordinates, and time as defined in the appendix. Pe_i is a reciprocal of a Peclet number, which is $k/(\rho C_p u_\infty r_0)$. The integral in Eq. (25) is calculated numerically and the results are compared with those calculated by a finite difference method. The comparison is shown in the next section.

2.3 Numerical Methods. For the gas phase, the numerical calculation is performed by using a finite difference method. The Gaussian external radiant flux radius r_0 is fixed at 1.0 cm. The computational domain is taken to be x = −4.8–14.4 cm, y = 0–4.8 cm, and z = 0–4.8 cm. Two different grid sizes were used: 128 × 32 × 32 corresponding to a grid spacing $\Delta x = \Delta y = \Delta z$ = 0.15 cm and 64 × 16 × 16 with cell size $\Delta x = \Delta y = \Delta z$ = 0.3 cm. The equations to be solved for the gas phase are those for the potential function Φ and the temperature T.

The equation for Φ is calculated using the FISHPAK direct solver of the Poisson equation in Cartesian coordinates using the standard seven-point finite difference approximation on a staggered grid (VHS3 package, HS3CRT subroutine). The boundary conditions for Φ are specified at the open boundary by evaluating Eq. (17) at each time step. In the present problem, since there are no volumetric source terms, only the surface integral remains. This can be efficiently handled by "coarse graining" the integrals into clusters of 8 × 8 cells for the 128 × 32 × 32 grid and 4 × 4 cells for the 64 × 16 × 16 grid. Each subintegral is then estimated by using the average value over that portion of the surface, but with the source points of the Green's function evaluated at the centroid of the integrand. This is formally equivalent to the first two terms of the asymptotic expansion of each "coarse graining" subintegral. The errors introduced by this procedure are negligible compared with the discretization errors. The equation for temperature is solved using a second-order central difference scheme for both convection and diffusion terms. The time advance is made by using the DuFort Frankel method with a time interval Δt = 0.01 s (for Grid 64 × 16 × 16) or Δt = 0.005 s (for Grid 128 × 32 × 32). These values of time intervals are sufficiently small to ensure that the Courant condition is satisfied.

For the solid phase, the equations of the temperature T also have to be solved. Equation (20) was reduced to nonlinear algebraic equations with the integral being converted to a summation. These nonlinear algebraic equations were solved by using the Newton–Raphson method. In the case of a thin solid, Eq. (24) is solved by using the Euler explicit method. The computation time for the thermally thick case was about 17 seconds per time step on IBM RS6000/550 computer with 128 × 32 × 32 grids.

3 Results and Discussion

3.1 Comparison With the Linear Analytical Solution. The numerically calculated results for the simplified heat transfer model were compared with the analytically calculated results of Eq. (25) for the case of u_∞ = 2 cm/s (Peclet number $\mathrm{Pe} = u_\infty r_0/(k/\rho c_p)$ = 9.1), $\ddot{q}_0$ = 4 W/cm^2 to examine the accuracy of the numerical method. The results in Figs. 2(*a*) and 2(*b*) show the time history of the surface temperature distribution along the x coordinate at the y = 0 plane calculated numerically with the two different grid sizes, 128 × 32 × 32 and 64 × 16 × 16, respectively. The bottom of the figures

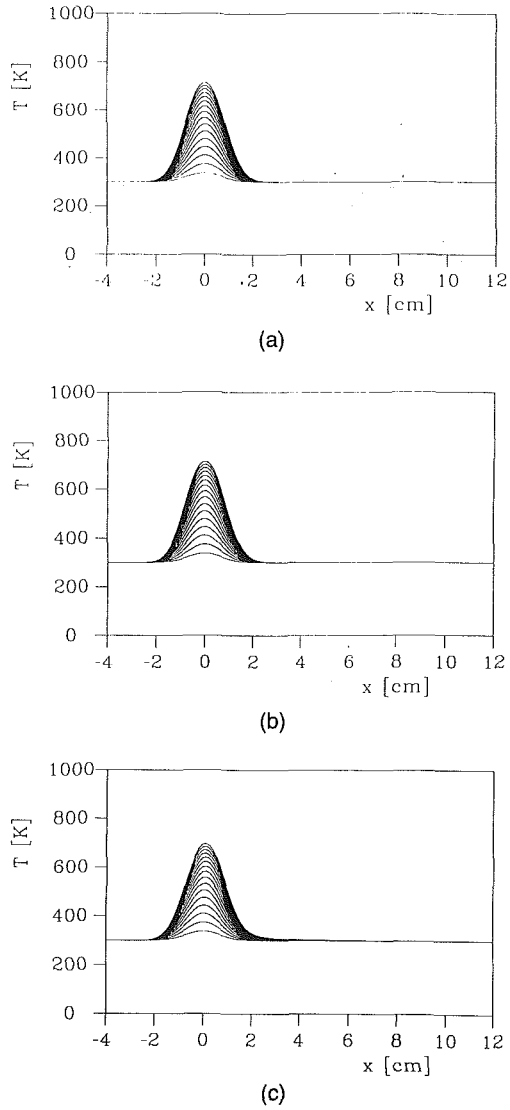

Fig. 6 Time history of surface temperature distributions at $y = 0$ at the interval of 0.5 s for $\ddot{q}_0 = 4$ W/cm^2: (*a*) $u_\infty = 0.5$ cm/s; (*b*) $u_\infty = 1.0$ cm/s; (*c*) $u_\infty = 10$ cm/s

indicates the difference in surface temperature between the analytical calculation and the numerical calculation. These two figures show that the errors in the numerical calculations are within 1.5 percent for the finer grid size calculation and within 5 percent for the coarser grid size calculation. The rest of the results shown in this paper were obtained using the finer grid size.

3.2 Fluid Flow and Heat Transfer Characteristics. Typical examples of the distributions of velocity vectors relative to ambient flow and temperature contours in the gas phase are shown in Fig. 3 and surface temperature distributions are shown in Fig. 4 for $u_\infty = 2$ cm/s (Pe = 9.1), $\ddot{q}_0 = 4$ W/cm^2, $\epsilon = 1.0$, and the thermally thick solid. Typical values of thermal properties for a plastic (Brandrup and Immergut, 1975) are used for the calculation: $c_s = 1.3$ J/(g•K), $\rho_s = 1.2$ g/cm^3, and $k_s = 2.1 \times 10^{-3}$ W/(cm•K). The arrow indicates the vector projected on each cross section. The length of arrow indicates the magnitude of velocity with the reference value of 0.2 cm/s, and the starting point of arrow indicates the location of velocity vector. The left corner figure in Fig. 3 represents the flow vector distribution in the half of the y plane at $x = 0.075$ cm. The top rectangular figure represents the distribution in the x-z plane at $y = 0.075$ cm. The lower rectangular figure represents the distribution in the x-y plane at $z = 0.075$ cm.

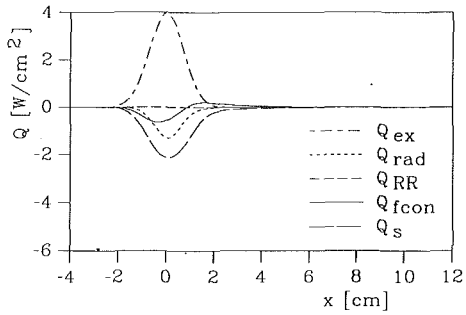

Fig. 7 Energy balance at the surface along $y = 0$ for $u_\infty = 10$ cm/s and $\ddot{q}_0 = 4$ W/cm^2

The temperature contours are indicated at intervals of 20 K from 310 K. Figures 3(*a*), 3(*b*), 3(*c*), and 3(*d*) show the results of time $t = 2$, 4, 6, and 8 s after the irradiation, respectively. The distribution of velocity vectors represents the flow component generated by heat addition from the irradiated surface. This flow is much smaller than the ambient flow of 2 cm/s. There is an upward slow flow generated by the steep temperature gradient due to heat addition. Its center is located a short distance upstream from the center of the external irradiation ($x = 0$). This indicates that the steepest temperature gradient occurs at the upstream location due to downward pushing of the heated layer by the ambient flow. At a short distance downstream from $x = 0$, there is a sink of flow due to the steep temperature gradient resulting from heat loss from the hot gas stream to the cold surface. Since the temperature gradient drives the flow, the flow generated by the external irradiation is limited to a region near the irradiated surface area at an early time. As time increases, the flow velocity gradually increases, but the magnitude of velocity remains at most 0.2 cm/s due to the absence of combustion and buoyancy induced flow. The heated region in the gas phase increases as time increases. The heat in the gas phase is convected radially and downstream by the gas flow due to expansion and ambient flow.

Figure 4 shows the time history of the solid surface temperature distribution $T_s(x, 0, 0, t)$ in the x direction at $t = 0.5$ s intervals. This distribution corresponds to the Gaussian flux distribution of external radiation expressed by Eq. (22) with slight modification by the ambient flow. However, the modification by convective heating is not significant for the results because the ambient flow velocity is small for this case. The temperature increase slows down gradually because of the heat balance between external radiation and the re-radiation loss from the high temperature surface.

3.3 Effects of Parameters on Fluid Flow and Heat Transfer Characteristics. The effects of several parameters, such as ambient flow velocity, external radiant flux, condensed phase thickness, and others, on distributions of velocity vector and temperature in the gas phase were studied. The results are discussed in this section.

3.3.1 Effect of Ambient Flow Velocity, u_∞. Figures 5(*a*), 5(*b*), and 5(*c*) show the distributions of velocity vectors relative to ambient flow and the temperature contours for the three different ambient flow velocities of $u_\infty = 0.5$ cm/s (Pe = 2.27), 1.0 cm/s (4.55), and 10.0 cm/s (45.5), respectively. These results are at 8 seconds after the irradiation. The temperature contours are plotted at intervals of 20 K from 310 K. As the ambient flow velocity increases, the heated area is pushed toward the surface and temperature gradients in the gas phase near the surface become steeper. Steeper temperature gradients generate larger flow velocities, as shown in Fig. 5. The center of the heat-generated flow near the surface moves closer to the center of the irradiated area with an increase in the ambient flow velocity. The distributions of surface temperature along

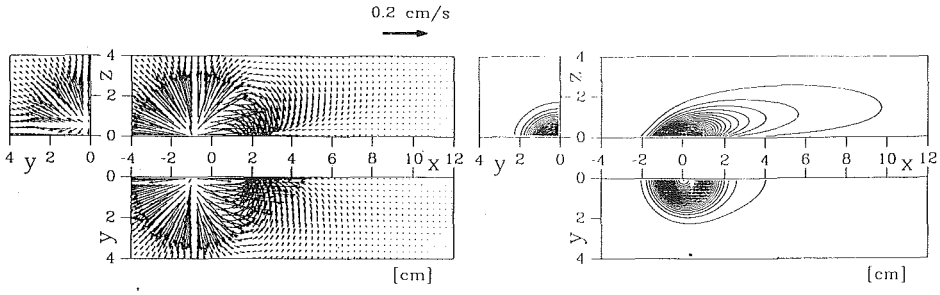

Fig. 8 *(a)* **The distributions of velocity vectors relative to ambient flow, and (*b*) the temperature contours (from 310 K at the interval of 20 K) for $\ddot{q}_0$ = 8 W/cm^2 and u_∞ = 2 cm/s at 8 s**

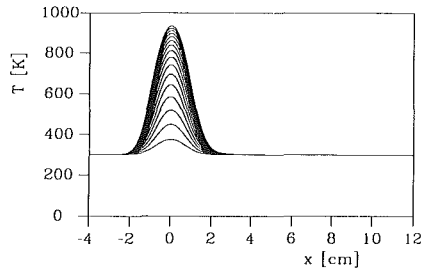

Fig. 9 Time history of surface temperature distribution at y = 0 for $\ddot{q}$ = 8 W/cm^2 and u_∞ = 2 cm/s at the interval of 0.5 s

$y = 0$ corresponding to the above three cases are shown in Fig. 6. There is no significant difference in surface temperature in the upstream part ($x \leq 0$). The difference occurs only in the downstream region, particularly, where the distribution of surface temperature becomes close to the ambient such as around 2 cm in the case of u_∞ = 10.0 cm/s.

The energy balance at the surface along $y = 0$ is calculated at 8 seconds and the results are plotted in Fig. 7. The term Q_{ex} is external radiant flux, which is a Guassian shape as described previously. Q_{rad} is re-radiation loss from the surface, Q_{RR} is the net of thermal degradation reactions that are not included in this study, Q_{fcon} is convective heating to the surface, and Q_s is heat conduction loss to the interior of the material. The largest heat loss term at this time is the heat conduction loss followed by re-radiation loss. The convection term is negative in the region about -2 cm $< x <$ 0.8 cm due to higher surface temperatures than gas temperatures. However, in the region about 0.8 cm $< x <$ 4 cm the convective heating term becomes positive due to higher gas temperatures than surface temperatures. This transition in convective heating is caused by the ambient flow. The amount of heat convection increases with an increase in the ambient flow velocity. This could be important for the case from the transition from ignition to flame spread with the ambient flow.

3.3.2 Effects of External Radiation Flux. Figure 8 shows the distribution of velocity vector relative to the ambient flow (u_∞ = 2 cm/s) and of temperature in the gas phase with external radial flux of 8 W/cm^2 at 8 seconds after the irradiation. It is clear that the heated gas region is larger than that at 4 W/cm^2 shown in Fig. 3(*d*). Subsequently, the flow field generated by the gas heating for 8 W/cm^2 is larger than that for 4 W/cm^2. The flow toward the surface and toward the y = 0 plane in the immediate downstream region of the irradiated area (almost like a flow toward a sink) shown in Fig. 8 is more distinct than that for 4 W/cm^2. The maximum surface temperature shown in Fig. 9 is about 950 K, which is slightly higher than about 900 K for 4 W/cm^2. This small increase in surface temperature from 4 W/cm^2 to 8 W/cm^2 is due to an increase in re-radiation loss from the surface as shown in the energy balance at the surface.

3.3.3 Effects of Solid Thickness. Figure 10 shows the velocity distribution and temperature contours at 8 seconds after irradiation of external radiant flux of 4 W/cm^4 with a thermally thin solid with ρ_s = 0.6 g/cm^3, c_s = 1.26 J/(g•K), and δ = 0.025 cm. The ambient flow velocity is 2 cm/s. Figure 11 shows the history of the surface temperature distribution. The comparison of these results with those shown in Fig. 3(*d*) indicates the effects of the solid thickness. Since heat loss to the interior of the solid by heat conduction is not included for the thermally thin material, the surface temperature rises rapidly and reaches about 920 K compared to roughly 700 K for the thermally thick material. After 7.5 seconds the surface temperature distribution does not change significantly with time. Therefore, more heat is transferred from the surface to the gas phase and the heated region in the gas phase for the thermally thin material is much larger than the thermally thick material. The corresponding flow velocity induced by the heat addition from the thin material is larger than that for the thick material.

4 Conclusion

A time-dependent three-dimensional heat transfer model describing the flow field generated by the surface heated by an external radiation was developed. This model is applicable to the low Reynolds number flow in a microgravity environment. The results show a complex flow field generated by temperature gradients in the gas phase near the irradiated hot surface area. The induced flow appears like a source of flow slightly upstream from the center of the external radiation beam. Then, there is a sink of flow downstream when the hot gas stream cools by heat loss to the solid surface. Higher external radiant flux and a thermally thin solid enhance the induced flow and enlarge the heated gas region due to larger temperature gradients in the gas phase. Higher ambient flow velocity also generates more vigorous induced flow due to an increase in temperature gradient by compressing the heated flow stream toward the solid surface. Therefore, the heated gas region becomes smaller than that for lower ambient flow velocities, although the induced flow is increased.

Acknowledgments

This study is supported by the NASA Microgravity Science Program under Inter-Agency Agreement No. C-32000-R.

References

Akita, K., 1978, "Ignition of Polymers and Flame Propagation on Polymer Surface," in: *Aspects of Degradation and Stabilization of Polymers*, H. H. G. Jellinek, ed., Elsevier Scientific, Chap. 10.

Amos, B., and Fernandez-Pello, A. C., 1988, "Model of the Ignition and Flame Development on a Vaporizing Combustible Surface in a Stagnation Point Flow: Ignition by Vapor Fuel Radiation Absorption," *Combust. Sci. Tech.*, Vol. 62, pp. 331–343.

Baek, S. W., and Kim, J. S., 1991, "Ignition of a Pyrolyzing Solid With Radiatively Active Fuel Vapor," *Combust. Sci. Tech.*, Vol. 75, pp. 89–102.

Brandrup, J., and Immergut, E. H., eds., 1975, *Polymer Handbook*, Wiley-Interscience, New York, Chap. 5.

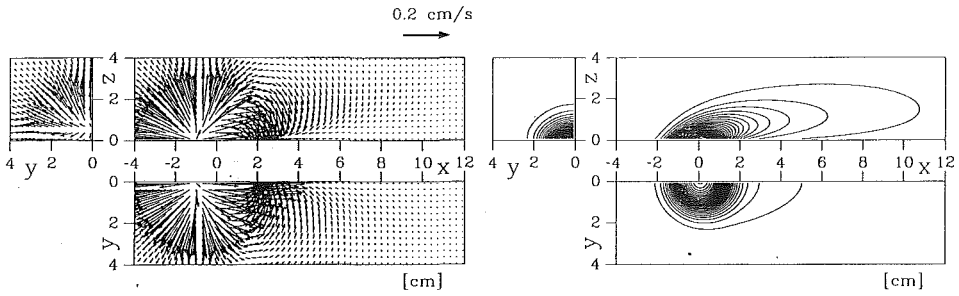

Fig. 10 (*a*) The distributions of velocity vector relative to ambient flow and (*b*) the temperature contours (from 310 K at the interval of 20 K) for the thermally thin solid ($\ddot{q}_0$ = 4 W/cm^2 and u_∞ = 2 cm/s)

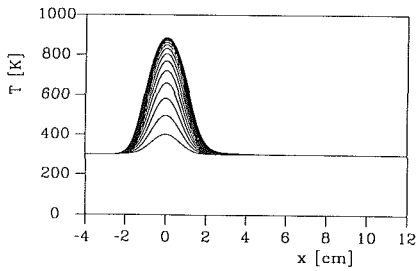

Fig. 11 Time history of the surface temperature distribution for the thermally thin solid at the interval of 0.5 s ($\ddot{q}_0$ = 4 W/cm^2 and u_∞ = 2 cm/s)

Kashiwagi, T., 1974, "A Radiative Ignition Model of a Solid Fuel," *Combust. Sci. Tech.*, Vol. 8, pp. 225–236.

Kindelan, M., and Williams, F., 1977, "Gas-Phase Ignition of a Solid With In-Depth Absorption of Radiation," *Combust. Sci. Tech.*, Vol. 16, pp. 47–58.

Kushida, G., Baum, H. R., Kashiwagi, T., and di Blasi, C., 1992, "Heat and Mass Transport From Thermally Degrading Thin Cellulosic Materials in a Microgravity Environment," ASME JOURNAL OF HEAT TRANSFER, Vol. 114, pp. 494–502.

Mutoh, N., Hirano, T., and Akita, K., 1978, "Experimental Study on Radiative Ignition of Polymethylmethacrylate," *Seventeenth Symposium (International) on Combustion*, The Combustion Institute, Pittsburgh, PA, pp. 1183–1190.

Olson, S. L., Ferkul, P. V., and Tien, J. S., 1988, "Near-Limit Flame Spread Over a Thin Solid Fuel in Microgravity," *Twenty-Second Symposium (International) on Combustion*, The Combustion Institute, Pittsburgh, PA, pp. 1213–1222.

Olson, S. L., 1991, "Mechanisms of Microgravity Flame Spread Over a Thin Solid Fuel: Oxygen and Opposed Flow Effects," *Combust. Sci. Tech.*, Vol. 76, pp. 233–249.

Van Dyke, M., 1964, *Perturbation Methods in Fluid Mechanics*, Academic Press, New York, pp. 149–158.

APPENDIX

A three-dimensional time-dependent heat transfer problem similar to the problem of interest is solved analytically to examine the accuracy of the numerical code used in this study. This problem is based on the Oseen flow. Then, the linearized energy equation is

$$\rho C_p\left\{\frac{\partial T}{\partial t}+u_\infty\frac{\partial T}{\partial x}\right\}=k\Delta T \tag{A1}$$

where T is the relative temperature with respect to an ambient temperature.

The initial condition is

$$\text{At } t=0, \qquad T=T_\infty$$

and boundary conditions are

$$\text{At } z=0, \qquad k\partial T/\partial z=-\ddot{q}(x,y)$$
$$\text{At } \mathbf{r}=\infty, \qquad T=T_\infty$$

where

$$\ddot{q}=\frac{\ddot{q}_0}{\pi}\exp\{-(r_p/r_0)^2\}$$
$$r_p^2=x^2+y^2$$

Let

$$\mathbf{r}=r_0\mathbf{x}(\tilde{x},\tilde{y},\tilde{z}), \quad t=\frac{r_0}{u_\infty}\tilde{t}$$
$$\mathrm{Pe}_i=\frac{k}{\rho C_p r_0 u_\infty}$$
$$T-T_\infty=\frac{q_0 r_0}{k}\theta(\tilde{x},\tilde{y},\tilde{z},\tilde{t})$$

Then, Eq. (A1) becomes

$$\frac{\partial\theta}{\partial\tilde{t}}+\frac{\partial\theta}{\partial\tilde{x}}=\mathrm{Pe}_i\Delta\theta \tag{A2}$$

We take the Laplace transformation of Eq. (A2) in time and then apply to the Fourier transformation in x and y. Then, Eq. (A2) becomes

$$\frac{d^2\bar{\theta}(p,\xi,\eta,\tilde{z})}{d\tilde{z}^2}-\left\{\xi^2+\eta^2+\frac{1}{\mathrm{Pe}_i}(p+i\xi)\right\}\bar{\theta}=0 \tag{A3}$$

and boundary conditions are

$$\text{At } \tilde{z}=\infty, \qquad \bar{\theta}=0$$
$$\text{At } \tilde{z}=0, \qquad \bar{q}(\xi,\eta)=\exp\{-(\xi^2+\eta^2)/4\}$$

The solution of Eq. (A3) with the above boundary conditions becomes

$$\bar{\theta}=\frac{\exp\left\{-\sqrt{(\xi^2+\eta^2)+\frac{1}{\mathrm{Pe}_i}(p+i\xi)}\,\tilde{z}\right\}}{p\sqrt{(\xi^2+\eta^2)+\frac{1}{\mathrm{Pe}_i}(p+i\xi)}}\,e^{\frac{-(\xi^2+\eta^2)}{4}} \tag{A4}$$

We invert the Laplace transformation of the above solution using the convolution theorem and obtain the inverted solution

$$\theta^*=\exp\left[\frac{-(\xi^2+\eta^2)}{4}\right]\int_0^{\tilde{t}}d\tau\sqrt{\frac{\mathrm{Pe}_i}{\pi\tau}}\exp\times\left[\frac{-\tilde{z}^2}{4\mathrm{Pe}_i\tau}\right]\exp[-\{\mathrm{Pe}_i(\xi^2+\eta^2)+i\xi\}\tau] \tag{A5}$$

Next we proceed with Fourier inversion of Eq. (A5) to obtain the solution of Eq. (A1).

$$\theta=\int_0^{\tilde{t}}\frac{\sqrt{\mathrm{Pe}_i}\exp\{-[(\tilde{x}-\tau)^2+\tilde{y}^2]/(1+4\mathrm{Pe}_i\tau)-\tilde{z}^2/4\mathrm{Pe}_i\tau\}}{\pi^{3/2}\sqrt{\tau}(1+4\mathrm{Pe}_i\tau)}\,d\tau \tag{A6}$$

Y. Sudo
Head, Division of HTTR Project Management,
Oarai Research Establishment,
Japan Atomic Energy
Research Institute (JAERI),
Oarai-machi, Higashiibaraki-gun,
Ibaraki-ken, 311-13 Japan

M. Kaminaga
Research Engineer,
Research Reactor Technology
Development Division,
Department of Research Reactor,
Tokai Research Establishment,
Japan Atomic Energy
Research Institute (JAERI),
2-4 Shirakata-Shirane, Tokai-mura,
Naka-gun, Ibaraki-ken, 319-11 Japan

A New CHF Correlation Scheme Proposed for Vertical Rectangular Channels Heated From Both Sides in Nuclear Research Reactors

In this study, an investigation was carried out to identify the important parameters affecting critical heat flux (CHF) in rectangular channels, focusing on the effects of flow direction, channel inlet subcooling from 1 to 213 K, the channel outlet condition extending from subcooling of 0–74 K to quality of 0–1.0, pressure of 0.1 to 4 MPa, water mass flux of −25,800 to +6250 kg/m²s, and channel configuration. In particular, the effect of the outlet subcooling in upflow and downflow on the CHF was quantitatively investigated. As a result of this study, a new CHF scheme covering downflow, countercurrent flow, and upflow was established in the rectangular channels within the ranges of parameters investigated in this study.

Introduction

The quantitative understanding of critical heat flux (CHF) for vertical rectangular channels is essential and required for core thermohydraulic design and safety analysis of nuclear research reactors in which flat-plate-type fuel is employed. In the safety design, some abnormal operational occurrences and accidents have been assumed. In the case of a pool-type nuclear research reactor in which steady-state core flow is downward, a transient core flow is considered in which the flow rate decreases from a steady-state downward flow to a zero flow, and then an upward flow is established as a cooling mode of natural convection to remove the decay heat after a reactor scram in case of abnormal operational occurrences and accidents. A detailed understanding of CHF is, accordingly, essential not only for a downward flow but also for an upward flow, including a flow subject to flooding conditions, that is, a countercurrent flow, in order to assure the intactness of fuel under normal operations, abnormal operational occurrences, and accidents. It should be noted that when the coolant flow rate decreases to zero and the flow becomes stagnant, the flow would become a countercurrent flow with downward water flow and upward flow of bubbles or steam generated in the channel. This is a flooding condition, because the flow channels are submerged in a water pool in the nuclear research reactor.

Many existing nuclear research reactors are approaching the end of their lifetime. Nuclear research reactors that are to be reconstructed or planned in the near future will be designed to have a higher neutron flux and a higher power density than ever. Therefore, to remove heat generated in the core, coolant mass flux will be very high and the coolant will be pressurized. Under such conditions, the channel outlet coolant would be subcooled not only for normal operation but also in abnormal occurrences.

The existing correlations and schemes for predicting CHF in the rectangular channels were investigated by the authors from the point of view of their applicability to the core thermohydraulic design and safety analysis. It was found that differences in CHF between an upward flow and a downward flow under the subcooled condition at the channel outlet, i.e., at a rather high mass flux region, have not been fully clarified systematically for vertical rectangular channels heated from both sides or from one side.

Therefore, in this study, the effect of dominant factors on CHF was investigated based on the existing CHF experimental data to establish a CHF scheme that is applicable for nuclear research reactors using flat-plate-type fuel. A new correlation scheme was proposed as the results of this investigation.

Previous CHF Correlation Scheme for Rectangular Channels

A CHF correlation scheme for rectangular channels previously proposed by the authors consists of three CHF correlations (Sudo et al., 1985a), which were used for the core thermohydraulic design and safety analysis of the upgraded JRR-3 (Sudo et al., 1985b; Hirano and Sudo, 1986).

The authors' CHF correlation scheme is illustrated in Fig. 1. The correlations used in the scheme are shown as follows:

$$q^*_{\mathrm{CHF},1} = 0.005 \cdot |G^*|^{0.611} \tag{1}$$

for both upflow ($G^* > G^*_2$) and downflow ($G^* > G^*_1$),

$$q^*_{\mathrm{CHF},2} = \frac{A}{A_H} \cdot \Delta T^*_{\mathrm{SUB},in} \cdot |G^*| \tag{2}$$

for downflow in the region where $q^*_{\mathrm{CHF},2} \le q^*_{\mathrm{CHF},1}$, that is, $G^* \le G^*_1$, and

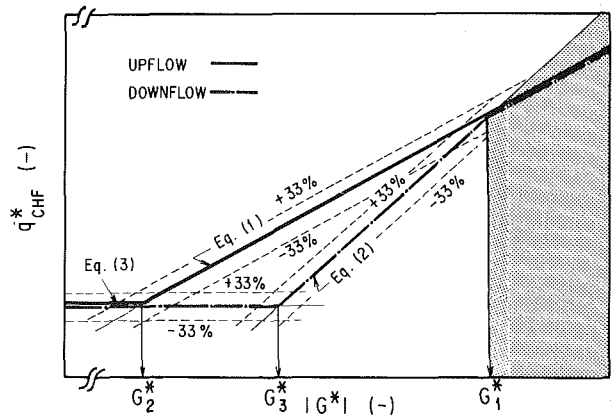

Fig. 1 Previous CHF correlation scheme proposed by authors for rectangular channels for $\Delta T^*_{\mathrm{SUB},0} = 0$

Contributed by the Heat Transfer Division and presented at the 1st JSME-ASME Joint International Conference on Nuclear Engineering, Tokyo, Japan, November 5-7, 1991. Manuscript received by the Heat Transfer Division January 1992; revision received December 1992. Keywords: Boiling, Forced Convection, Multiphase Flows. Associate Technical Editor: L. C. Witte.

$$q^*_{CHF,3} = 0.7 \frac{A}{A_H} \cdot \frac{\sqrt{W/\lambda}}{\{1+(\rho_g/\rho_l)^{1/4}\}^2} \quad (3)$$

as the minimum CHF for both upflow ($G^* \le G^*_2$) and downflow ($G^* \le G^*_3$), where G^*_1 is given by $q^*_{CHF,1} = q^*_{CHF,2}$, G^*_2 by $q^*_{CHF,1} = q^*_{CHF,3}$, and G^*_3 by $q^*_{CHF,2} = q^*_{CHF,3}$, respectively; and

$$G^* = \frac{G}{\sqrt{\lambda g \rho_g (\rho_l - \rho_g)}},$$

$$q^*_{CHF} = \frac{q_{CHF}}{h_{fg}\sqrt{\lambda g \rho_g (\rho_l - \rho_g)}}.$$

It should be pointed out here that Eq. (2) gives the condition that the outlet subcooling equals zero, that is, $\Delta T^*_{SUB,0} = 0$.

Equation (1) is a correlation proposed by Sudo et al. (1985a). Equations (2) and (3) are correlations proposed originally by Mishima (1984; Mishima et al., 1983). Mishima could not make clear the applicability of these correlations fully enough because of small number of available experimental data. The authors accumulated the available experimental data, carrying out the experiments with rectangular channels. They have shown that the correlation error of the CHF scheme is within 33 percent of rms error against the experimental data. It was found that the scheme is applicable for the region of $0 \le |G^*| < 3000$.

According to the results previously investigated by the authors (Sudo et al., 1985a), it was concluded that the CHF for upflow in the region of $q^*_{CHF,1} \ge q^*_{CHF,2}$ was expressed by Eq. (1) and the CHF for downflow in the region of $q^*_{CHF,1} \ge q^*_{CHF,2}$ was expressed by Eq. (2). For both upflow and downflow, there is a minimum CHF, which is defined by Eq. (3). On the other hand, the CHF for both upflow and downflow in the region of $q^*_{CHF,1} \le q^*_{CHF,2}$, which is shown as a shaded region in Fig. 1, was expressed by Eq. (1). In the shaded region, a channel outlet coolant condition is a subcooled one with a very high coolant mass flux $|G^*|$. An effect of channel outlet subcooling $\Delta T_{SUB,0}$ on the CHF was not considered in Eq. (1) in the CHF scheme described above because such a highly subcooled condition at the outlet was not expected in the core thermohydraulic design and safety analysis of the upgraded JRR-3 where the outlet subcooling is in the range of 0 to 20 K.

Other typical existing correlations considered to be applicable to the rectangular channels would be those proposed by Katto (1981), Mirshak et al. (1959), Zenkevich (1959), and Gambill and Bundy (1961).

Katto proposed the following correlations for the CHF in the rectangular channels through comparison between the previous experimental data of Yücel and Kakac (1978), Gambill and Bundy (1961), and others and the correlations he originally proposed for round and annular tubes.

Katto's correlations are expressed as follows for low mass flux, medium mass flux, and high mass flux, respectively:

$$q^*_{CHF,41} = 0.25\left(\frac{Dh}{L}\right)(1+\Delta T^*_{SUB,in})G^* \quad (4)$$

for low mass flux,

$$q^*_{CHF,42} = \left\{0.25+0.0009\left(\frac{L}{Dh}-50\right)\right\}\left(\frac{Dh}{L}\right)\left\{\frac{1}{L}\left(\frac{\sigma}{\rho_l g}\right)^{1/2}\left(\frac{\rho_l}{\rho_g}\right)\frac{1}{G^{*2}}\right\}^{0.043} \cdot \left[1+\frac{1.043\Delta T^*_{SUB,in}}{4\left\{0.25+0.0009\left(\frac{L}{Dh}-50\right)\right\}\left\{\frac{1}{L}\left(\frac{\sigma}{\rho_l g}\right)^{1/2}\left(\frac{\rho_l}{\rho_g}\right)\frac{1}{G^{*2}}\right\}^{0.043}}\right]G^* \quad (5)$$

for medium mass flux, and

$$q^*_{CHF,43} = 0.15\left(\frac{\rho_l}{\rho_g}\right)^{0.133}\frac{\left\{\frac{1}{L}\left(\frac{\sigma}{\rho_g g}\right)^{1/2}\left(\frac{\rho_l}{\rho_g}\right)^{1/2}\frac{1}{G^{*2}}\right\}^{1/3}}{1+0.0077\frac{L}{Dh}} \cdot \left[1+\frac{5}{9}\frac{\left(0.0308+\frac{Dh}{L}\right)\cdot\Delta T^*_{SUB,in}}{\left\{\frac{1}{L}\left(\frac{\sigma}{\rho_g g}\right)^{1/2}\left(\frac{\rho_l}{\rho_g}\right)^{1/2}\frac{1}{G^{*2}}\right\}^{1/3}\left(\frac{\rho_g}{\rho_l}\right)^{0.133}}\right]G^* \quad (6)$$

for high mass flux.

Here, the low mass flux region is defined for G^* of $q^*_{CHF,41} \le q^*_{CHF,42}$, the medium mass flux region for G^* of $q^*_{CHF,42} \le$

Nomenclature

A = flow area of channel, m^2
A_H = heated area of channel, m^2
Cp = specific heat of liquid, J/(kg•K)
De = equivalent hydraulic diameter, m
Dh = equivalent heated diameter, m
g = acceleration of gravity, m/s^2
G = mass flux, $kg/m^2 \cdot s$
G^* = dimensionless mass flux
G^*_1 = boundary value of G^* given by $q^*_{CHF,1} = q^*_{CHF,2}$
G^*_2 = boundary value of G^* given by $q^*_{CHF,1} = q^*_{CHF,3}$
G^*_3 = boundary value of G^* given by $q^*_{CHF,2} = q^*_{CHF,3}$
h = heat transfer coefficient, kW/m^2K
h^* = dimensionless heat transfer coefficient $= h/Cp\sqrt{\lambda \rho_g g(\rho_l - \rho_g)}$
h_{fg} = latent heat of evaporation, J/kg
L = length of channel, m
P = pressure, MPa
q = heat flux, kW/m^2
q^* = dimensionless heat flux
$q^*_{CHF,1}$ = defined by Eq. (1)
$q^*_{CHF,2}$ = defined by Eq. (2)
$q^*_{CHF,3}$ = defined by Eq. (3)
T = temperature, K
T^* = dimensionless temperature $= Cp \cdot T/h_{fg}$
W = width of channel, m
ΔT_s = superheat $= T_w - T_s$, K
ΔT^*_s = dimensionless superheat $= Cp(T_w - T_s)/h_{fg}$, K
ΔT_{SUB} = subcooling, K
ΔT^*_{SUB} = dimensionless subcooling $= Cp \cdot \Delta T_{SUB}/h_{fg}$
λ = characteristic length $= [\sigma/(\rho_l - \rho_g) \cdot g]^{1/2}$, m
ν = kinematic viscosity, m^2/s
ρ = density, kg/m^3
σ = surface tension, N/m

Subscripts

b = bulk
CHF = critical heat flux
g = vapor
in = inlet
l = liquid
o = outlet
s = saturation
w = heated surface

$q^*_{CHF,43}$, and the high mass flux region for G^* of $q^*_{CHF,42} > q^*_{CHF,43}$, respectively.

The effects of pressure, mass flux, subcooling, and the ratio of channel length to heated equivalent diameter were taken into account as key parameters in the above correlations. As the number of available experimental data was small, as stated in his article, only the availability of Eq. (5) could be investigated for high mass flux. He noticed that the magnitude of CHF in downflow obtained by Gambill and Bundy (1961) were clearly smaller than that in upflow obtained previously but the number of available existing data was so small that he could not investigate the difference in CHF characteristics between upflow and downflow. A feature of Katto's correlations is that the CHF approaches zero as the G^* approaches zero.

Mirshak et al. (1959) proposed for downflow the following correlation in which the effects of water velocity, subcooling, and pressure were taken into account as key parameters, based on the experiments for downflow with a medium mass flux of 500 to 1300 kg/m^{2}s and outlet subcooling of 6 to 74 K:

$$q^*_{CHF} = 360 \cdot \frac{1 + 0.129G^* \left\{ \lambda \left(\frac{\rho_g}{\rho_l} \right) \left(1 - \frac{\rho_g}{\rho_l} \right) g \right\}^{1/2}}{h_{fg} \cdot \{ \lambda \rho_g (\rho_l - \rho_g) g \}^{1/2}} \cdot \left\{ 1 + 0.009 \left(\frac{h_{fg}}{Cp} \right) \Delta T^*_{SUB,0} \right\} (1 + 1.86P) \quad (7)$$

A feature of the correlation proposed by Mirshak et al. is that CHF approaches a constant, which is not zero and is determined by pressure and subcooling, as shown below, when G^* approaches zero:

$$q^*_{CHF} = \frac{360 \left\{ 1 + 0.009 \left(\frac{h_{fg}}{Cp} \right) \Delta T^*_{SUB,0} \right\} (1 + 1.86P)}{h_{fg} \{ \lambda \cdot \rho_g (\rho_l - \rho_g) g \}^{1/2}} \quad (8)$$

Zenkevich (1959) proposed for upflow the following correlation, in which the effect of pressure, subcooling, and mass flux were taken into account:

$$q^*_{CHF} = \frac{2.5 \times 10^{-5} \left(\frac{\sigma}{\nu_l} \right)^{1/2}}{\{ \lambda \rho_g (\rho_l - \rho_g) g \}^{1/4}} (1 + 73.6 \cdot \Delta T^*_{SUB,0}) \cdot G^{*1/2} \quad (9)$$

A feature of Eq. (9) is that CHF is proportional to $G^{*1/2}$, and then approaches zero as G^* approaches zero.

Gambill and Bundy (1961) proposed a correlation with a form shown below for a subcooled forced-convection flow in a vertical rectangular channel.

$$q^*_{CHF} = 0.18 \cdot \left\{ 1 + \frac{1}{9.8} \left(\frac{\rho_l}{\rho_g} \right)^{3/4} \Delta T^*_{SUB} \right\} + h^* (\Delta T^*_s + \Delta T^*_{SUB}) \quad (10)$$

Here, ΔT^*_s is given by a correlation that is determined with the saturation temperature T_s and the critical heat flux, and h^* is given by a heat transfer correlation for a single-phase turbulent forced convection flow. A feature of Eq. (10) is that q^*_{CHF} does not approach zero with decreasing G^*, but approaches a constant given by $q^*_{CHF} = 0.18$ with G^* approaching zero under saturated conditions.

In Fig. 2, for comparison, Eqs. (1), (3), (4), (5), (6), (9), and (10) are illustrated for upflow with the conditions of $P = 0.11$ MPa, $\Delta T^*_{SUB,in} = 0$ and $\Delta T^*_{SUB,0} = 0$ along with the typical experimental data whose $\Delta T^*_{SUB,0}$ is less than 4 K. Here, Eqs. (3), (4), (5), (6), and (10) are illustrated for a rectangular channel heated from both sides ($L = 0.75$ m, $W = 0.05$ m, and gap = 2.25 mm), which were investigated by Sudo et al. (1985a). These equations include the effects of channel configuration. Zenkevich's correlation gives overly conservative predictions for the experimental data for high mass flux. On the other hand, Katto's correlation for low mass flux gives overly conservative predictions to the experimental data. The correlation given by Eq. (1) shows a good prediction for the experimental data whose $\Delta T^*_{SUB,0}$ is almost zero.

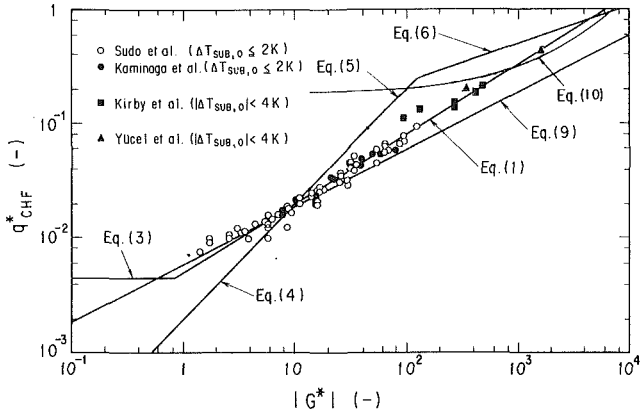

Fig. 2 Comparison of typical previous CHF correlations ($\Delta T^*_{SUB,0} = 0$) with experimental data for upflow (Kaminaga et al., 1991; Kirby et al., 1967; Sudo et al., 1985a; Yücel and Kakac, 1978)

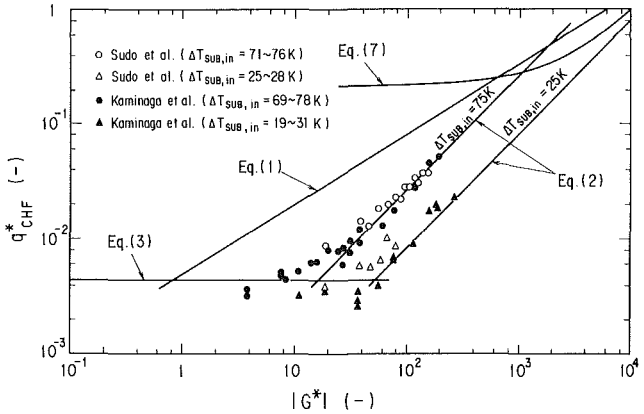

Fig. 3 Comparison of typical previous CHF correlations with experimental data for downflow (Kaminaga et al., 1991; Sudo et al., 1985a)

In Fig. 3, on the other hand, Eqs. (2), (3), and (7) are illustrated with the condition of $P = 0.11$ MPa and are compared with the typical experimental results for downflow with G^* less than G^*_1. Here, Eq. (7) is illustrated for $\Delta T^*_{SUB,0} = 0$, Eq. (3) for a rectangular channel heated from both sides ($L = 0.75$ m, $W = 0.05$ m, and gap = 2.25 mm) and Eq. (2), which gives the condition of $\Delta T^*_{SUB,0} = 0$ as already described, for the rectangular channel with two cases of $\Delta T_{SUB,in} = 25$ and 75 K.

Equation (1) is also illustrated in Fig. 3 so as to make clear the differences in CHF characteristics between upflow and downflow. Equations (2) and (3) show a good prediction for the experimental data of downflow for the low and medium mass fluxes of $G^* \le G^*_1$.

From the discussion described above, it is very clear for $G^* \le G^*_1$ that Eq. (1) would be a proper correlation for predicting the experimental data of $\Delta T^*_{SUB,0} = 0$ for upflow, and Eqs. (2) and (3) for downflow. However, the effect of subcooling, $\Delta T^*_{SUB,0}$, is not clear on the CHF for $G^* \ge G^*_1$, although the effect should be properly taken into account in Eq. (1) for both upflow and downflow so that the thermohydraulic design and safety analysis may be reasonably done without giving overly conservative results for $G^* \ge G^*_1$.

Effects of Channel Outlet Subcooling ($\Delta T_{SUB,0}$)

In this study, Eq. (1) was selected as a base correlation to

Table 1 Test conditions of existing tests investigated in this study

Author(s)	Pressure (MPa)	Mass flux (kg/m^{2}s)	Inlet water subcooling (K)	Outlet condition subcooling (K)	Outlet condition quality (-)	CHF (kW/m^2)	L/De (-)	A/A$_H$ (-)	Number of data(-)
Sudo et al. (1985a)*	0.1~0.12 (Inlet)	-600~+480	20~81	0.0~27	0.0~1.0	32~320	170	1.88×10^{-3}	40[U,D]*1)
						66~830	71	4.67×10^{-3}	37[U,D]
Kaminaga, et al. (1991)*	0.1~0.12 (Inlet)	-2,200~+450	2.3~78	0.0~33	0.0~1.0	22~1,190	170	1.88×10^{-3}	203[U,D]
	0.1 (Inlet)	-340~+330	1.3~75	0.0~24	0.0~1.0	54~540	83	4.17×10^{-3}	63[U,D]
Yücel and Kakac (1978)**	0.1 (Inlet)	-6,250~+6,250	3.2~44	0.0~37	0.0~0.01	1,580~5,820	40	3.35×10^{-2}	16[U,D]
Kirby et al. (1967)***	0.18 (Inlet)	-2,720~+2,720	2.9~46	0.6~43	-	1,170~5,810	8	1.65×10^{-1}	49[U,D]
Mirshak et al. (1959)**	0.17~0.6 (Outlet)	-12,500~-5,030	27~104	6.0~74	-	3,980~10,000	41	8.51×10^{-3}	51[D]
							~77	1.65×10^{-2}	
Gambill and Bundy (1961)**	1.1~4.0 (Outlet)	-25,800~-9,210	151~213	14~55	-	8,270~19,400	128	1.18×10^{-3}	10[D]
							~240	$\sim2.20\times10^{-3}$	
Mishima (1984)*,**	0.1 (Inlet)	-610~+360	13~71	0.0~21	0.0~1.0	56~1,170	77	4.57×10^{-3}	51[U,D]
								$\sim9.14\times10^{-3}$	58[U,D]
Komori et al. (1990)*	0.1~0.72 (Inlet)	-2,440~-610	51~117	0.0~12	0.0~0.03	322~1,630	150	2.93×10^{-3}	18[D]

* Rectangular channel, Heated from both sides. ** Rectangular channel, Heated from one side.
*** Rectangular channel, Heated by round tube. *1) U : Upflow, D : Downflow

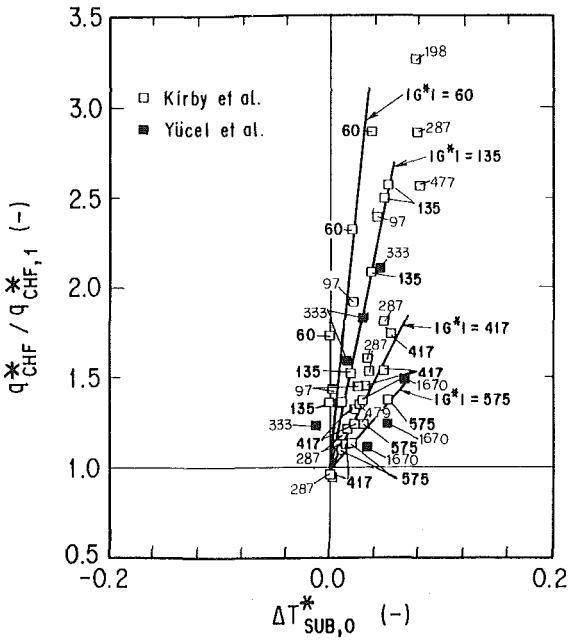

Fig. 4 Effects of $\Delta T^*_{SUB,0}$ on CHF in upflow

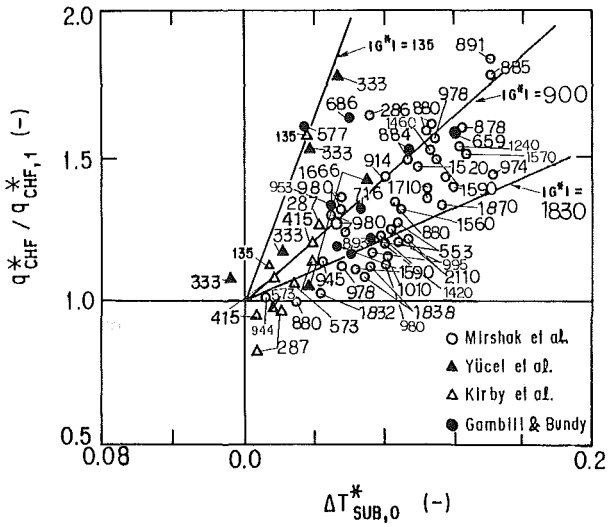

Fig. 5 Effects of $\Delta T^*_{SUB,0}$ on CHF in downflow

estimate effects of $\Delta T_{SUB,0}$, based on previously investigated results. In the region of $q^*_{CHF,1} \geq q^*_{CHF,2}$, CHF is well correlated by Eq. (1) for the saturated single phase and two-phase flow conditions, i.e., under the condition with no subcooling at the outlet of channel. Experimental conditions of the available existing CHF tests investigated in this study are listed in Table 1. The experimental data were investigated within the ranges of pressure of 0.1 to 4 MPa, mass flux of $-25{,}800$ to $+6250$ kg/m^{2}s including stagnant flow conditions, inlet subcooling of 1 to 213 K, outlet condition extending from subcooling of 0–74 K to quality of 0–1.0, and ratio of heated length to equivalent hydraulic diameter L/De of 8 to 240.

It should be mentioned here that the experimental data of Sudo et al. and Kaminaga et al. constitute 58 percent of total experimental data listed in Table 1. The estimated uncertainty of these CHF data was 3 percent based on the estimations of heat loss from the test channel and so on. Besides, the CHF data in Table 1 would be mixed with the flow excursion data because no criteria were applied for distinguishing one from the other.

The CHF experimental data for upflow and downflow are shown in Figs. 4 and 5, respectively, to make clear the effects of the outlet subcooling $\Delta T_{SUB,0}$ on the CHF, taking the ratio of $q^*_{CHF}/q^*_{CHF,1}$ as the ordinate and $Cp \cdot \Delta T_{SUB,0}/h_{fg}$ ($= \Delta T^*_{SUB,0}$), which is a dimensionless parameter for $\Delta T_{SUB,0}$, as the abscissa. These CHF experimental data were obtained in rectangular channels, except for those of Kirby et al. In the figures straight lines are illustrated to show a rough tendency on $|G^*|$. The fluid conditions of experimental data shown in Figs. 4 and 5 are subcooled at the channel outlet. It is pointed out on the

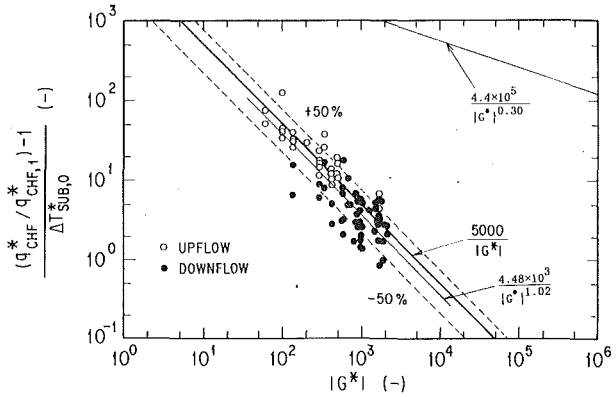

Fig. 6 Effects of $\Delta T^*_{SUB,0}$ on CHF as a function of G^* for both upflow and downflow (Gambill and Bundy, 1961; Kirby et al., 1967; Mirshak et al., 1959; Yücel and Kakac, 1978)

whole from Figs. 4 and 5 that the value of q^*_{CHF} for both upflow and downflow is greater than the values predicted by Eq. (1), and it increases with increases of $\Delta T^*_{SUB,0}$, under the same $|G^*|$ in the region of $\Delta T^*_{SUB,0}$ greater than zero, though the data scatter over a rather wide range. It is recognized in the figures that $|G^*|$ in the data for upflow is rather smaller than that for downflow at the same condition of $\Delta T^*_{SUB,0}$, but a significant and systematic tendency seems to be recognized commonly to upflow and downflow in Figs. 4 and 5: that $q^*_{CHF}/q^*_{CHF,1}$ increases with decreasing $|G^*|$ under the same $\Delta T^*_{SUB,0}$.

Figure 6 shows the data for both upflow and downflow to make clear a relationship between the effects of $\Delta T^*_{SUB,0}$ and $|G^*|$, taking $(q^*_{CHF}/q^*_{CHF,1} - 1)/\Delta T^*_{SUB,0}$ as the ordinate and $|G^*|$ as the abscissa. A bold solid line shown in Fig. 6 is a best-fit line for the data and is expressed as follows:

$$\frac{q^*_{CHF}}{q^*_{CHF,1}} = 1 + \frac{5000}{|G^*|}\Delta T^*_{SUB,0} \tag{11}$$

It should be mentioned here in Fig. 6 and in Eq. (11) that the CHF increases with an increase of $\Delta T^*_{SUB,0}$ and the effect of $\Delta T^*_{SUB,0}$ increases with a decrease of $|G^*|$. From Figs. 4 and 5, the effect of $\Delta T^*_{SUB,0}$ on q^*_{CHF} for upflow seemed to be different from that for downflow. It is now understood that it was due to the difference in the magnitude of $|G^*|$ and was not to the difference in flow direction. The CHF for both upflow and downflow can be expressed by Eq. (11) in the same way, considering the effects of both $\Delta T^*_{SUB,0}$ and $|G^*|$.

Theoretical and physical reasoning do not yet explain why the effects of $\Delta T^*_{SUB,0}$ and $|G^*|$ can be expressed in the form of Eq. (11), but the following discussion should help in understanding the reason or give us some clue for it.

Under the condition of subcooled forced-convection flow, the dimensionless heat flux q^* is expressed as below by using dimensionless heat transfer coefficient h^* and dimensionless temperatures, T^*_w and T^*_b.

$$q^* = h^*(T^*_w - T^*_b) = h^*(\Delta T^*_s + \Delta T^*_b)$$

The q^*_{CHF} under the subcooled condition can, therefore, be expressed as

$$q^*_{CHF} = h^*\Delta T^*_s\left(1 + \frac{\Delta T^*_{SUB,0}}{\Delta T^*_s}\right)$$

at the channel exit.

Here, $h^*\Delta T^*_s$ is assumed to be approximately equal to $q^*_{CHF,1}$, which is the CHF under the saturated condition, and thus,

$$\frac{(q^*_{CHF}/q^*_{CHF,1}) - 1}{\Delta T^*_{SUB,0}} \simeq \frac{1}{\Delta T^*_s}.$$

It is well known that a form of $\Delta T^*_s = A \cdot q^{*n}$ can be applied not only in the fully developed nucleate boiling region but also in the region from the departure of nucleate boiling to the critical heat flux point.

Thom et al. (1966) reported that n is 1/2 for forced-convection nucleate boiling. On the other hand, Gaertner (1965) reported from a photographic study of nucleate pool boiling that n is 1/0.6 in the second transition region where the burnout will follow after the departure of fully developed nucleate boiling.

By using the correlation $q^*_{CHF,1} = 0.005|G^*|^{0.611}$ under the saturated conditions obtained so far, the following are introduced from the correlations proposed by Thom et al. and Gaertner, respectively:

$$\frac{(q^*_{CHF}/q^*_{CHF,1}) - 1}{\Delta T^*_{SUB,0}}\left(=\frac{1}{\Delta T^*_s}\right) = \frac{4.4\times 10^5}{|G^*|^{0.30}}$$

and

$$\frac{(q^*_{CHF}/q^*_{CHF,1}) - 1}{\Delta T^*_{SUB,0}}\left(=\frac{1}{\Delta T^*_s}\right) = \frac{4.48\times 10^3}{|G^*|^{1.02}}$$

These correlations are illustrated in Fig. 6 for comparison. It is very suggestive that the latter gives almost the same prediction as Eq. (11). More accumulation of experimental data on q^* versus ΔT^*_s in the region from the departure of fully developed nucleate boiling to the CHF point should, therefore, help in understanding the mechanism of critical heat flux.

It is also pointed out as one of the major features in Fig. 6 that no significant differences in the tendency of $(q^*_{CHF}/q^*_{CHF,1} - 1)/\Delta T^*_{SUB,0}$ versus $|G^*|$ are observed between upflow and downflow for $|G^*|$ larger than about 500. On the other hand, there seems to be a tendency that the values of $(q^*_{CHF}/q^*_{CHF,1} - 1)/\Delta T^*_{SUB,0}$ for downflow are smaller than those for upflow for $|G^*|$ less than 200.

It would be pointed out as a major reason for this that heat transfer will deteriorate near the heated surface because of accumulation of bubbles generated near the heated surface, due to the intensified effect of buoyancy when mass flux becomes relatively low in the subcooled downflow. The speed of bubbles rising in a stagnant water column will be 0.01 to 0.3 m/s. Bubbles will be stagnant in downflow with $|G^*|$ of 2 to 80 when bubbles are assumed to be 0.1 to 1 mm in diameter at a system pressure of 0.1 to 4 MPa, according to the experimental results of Peebles and Garber (1953). It would be, therefore, understood that there is no difference in characteristics of the CHF between upflow and downflow for $|G^*|$ larger than 500, which is significantly larger than 2–80. On the other hand, the CHF for downflow would become smaller than that for upflow when $|G^*|$ approaches 80–2.

A Modified CHF Correlation Scheme

From the discussion above, a new CHF correlation, in which the effect of subcooling at the channel outlet is considered, is proposed by using Eqs. (1) and (11), and is expressed as follows:

$$q^*_{CHF,4} = 0.005 \cdot |G^*|^{0.611}\left(1 + \frac{5000}{|G^*|}\cdot\Delta T^*_{SUB,0}\right) \tag{12}$$

Equation (12) shows that the CHF increases with an increase of $\Delta T^*_{SUB,0}$ and the effect of $\Delta T^*_{SUB,0}$ on the CHF increases with a decrease of $|G^*|$ compared with Eq. (1). Now, Eq. (12) can be applicable to both upflow and downflow in the range of $q^*_{CHF,1} \le q^*_{CHF,2}$.

Equation (12) is rewritten as follows with the subcooling at the inlet of the channel, $\Delta T^*_{SUB,in}$ $(= Cp \cdot \Delta T_{SUB,in}/h_{fg})$ because of $\Delta T^*_{SUB,0} = \Delta T^*_{SUB,in} - (q^*/G^*) \cdot (A_H/A)$:

$$q^*_{CHF,4} = 0.005 \cdot |G^*|^{0.611} \cdot \frac{1 + \dfrac{5000}{|G^*|}\cdot\Delta T^*_{SUB,in}}{1 + 25 \cdot |G^*|^{-1.389} \cdot \dfrac{A_H}{A}} \tag{13}$$

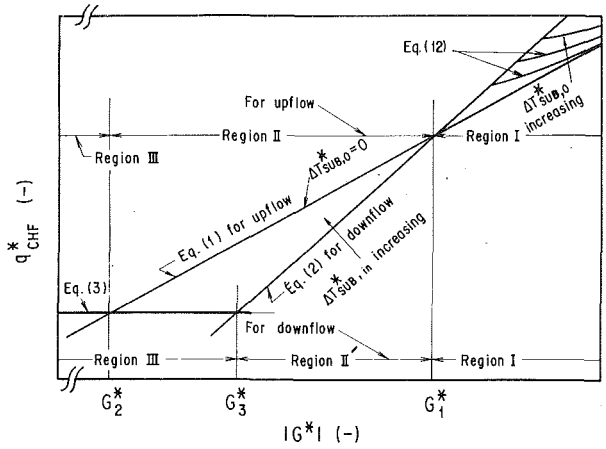

Fig. 7 Modified CHF scheme proposed in this study

It should be noted here that in the case of nonuniform heat flux channels, such as those of Kaminaga et al., Eq. (13) cannot be applied directly to the prediction of CHF. Some additional consideration, such as adoption of the maximum heat flux as the CHF, should be paid to Eq. (13), though this gives a conservative prediction of the CHF for nonuniform heat flux channels.

Thus, Fig. 7 presents the scheme of CHF correlations proposed newly in this study for upflow and downflow, taking q^*_{CHF} as the ordinate and $|G^*|$ as the abscissa. Equation (12) is a new correlation for predicting the CHF under high mass flux for both upflow and downflow. In Fig. 7, three regions for a high, medium, and low mass flux are defined as Region I. Region II, and Region III for upflow, and Region I, Region II′, and Region III for downflow.

It should be mentioned here that Eq. (2) gives the upper limits for Eq. (12) in Region I of $G^* > G^*_1$ as shown in Fig. 7 because Eq. (2) gives the condition of $\Delta T^*_{SUB,0} = 0$ for both upflow and downflow in Region I of $G^* > G^*_1$.

In Region I where the mass flux is high, a difference in CHF is not observed between upflow and downflow in this study and the CHF for both upflow and downflow is well predicted by Eq. (12). In this region, $\Delta T^*_{SUB,0}$ and G^* have significant effects on the CHF. A larger $\Delta T^*_{SUB,0}$ gives a larger CHF with the same $|G^*|$ and a larger $|G^*|$ gives a larger CHF with the same $\Delta T^*_{SUB,0}$.

In the medium mass flux region, the CHF for downflow is expressed by Eq. (2) and is much lower than that for upflow with the same $|G^*|$. Therefore, a flow direction has a significant effect on the CHF in the medium mass flux region. In Region II for upflow where $\Delta T^*_{SUB,0} = 0$, the CHF is predicted solely by Eq. (1) and only G^* has a significant effect on the CHF. On the other hand, in Region II′ for downflow, the CHF is predicted by Eq. (2). In this region, $\Delta T^*_{SUB,in}$, $|G^*|$ and a ratio of the flow area to the heated area, A/A_H, have significant effects on CHF.

In Region III for both upflow and downflow where mass flux is very low or the flow condition is a countercurrent flow with $G^* = 0$, CHF is predicted by Eq. (3). In this region, the ratio of the flow area to the heated area, A/A_H, and a channel width W have significant effects on the CHF. Under the CCFL condition with a large L/De the temperature of water supplied into the channel would at last become a saturated temperature because water is well mixed with upflowing steam generated in the channel at the top of the channel, even if water is subcooled at first. Therefore, $\Delta T^*_{SUB,in}$ and $|G^*|$ would have no significant effects on the CHF. Equation (3) is a common correlation for predicting the minimum CHF for both upflow and downflow.

Figures 8(*a*) and 8(*b*) illustrate the regions described above for upflow and downflow, respectively, taking $|G^*|$ as the ordinate and $\Delta T^*_{SUB,in}$ as the abscissa. These regions are functions of not only $|G^*|$ but also $\Delta T^*_{SUB,in}$.

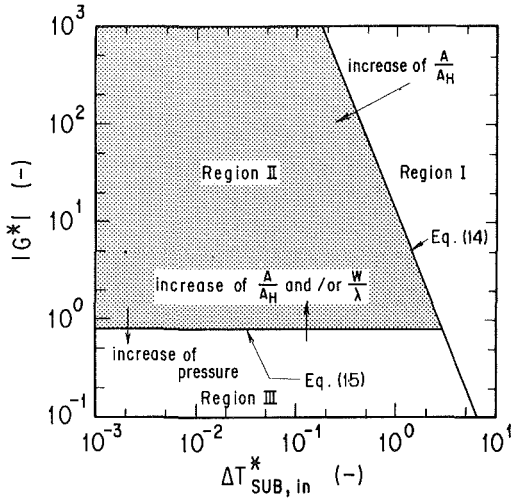

Fig. 8(*a*) Identification of Regions I, II, and III for upflow

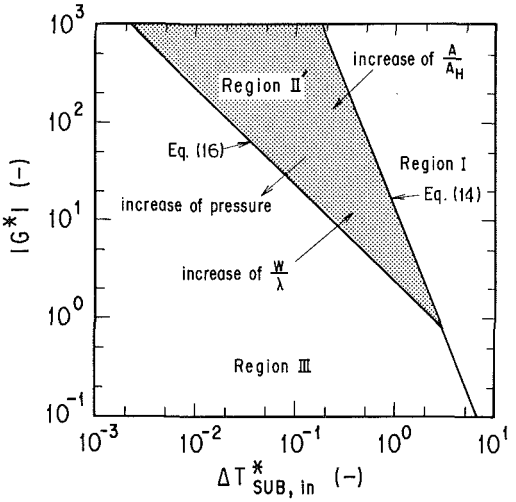

Fig. 8(*b*) Identification of Regions I, II′, and III for downflow

A boundary between Region I and Region II or II′ is calculated and identified as follows by using Eqs. (1) and (2):

$$G^*_1 = \left(\frac{0.005}{\frac{A}{A_H} \Delta T^*_{SUB,in}} \right)^{\frac{1}{0.389}} \tag{14}$$

Equation (14) shows that G^*_1 decreases with an increase of $\Delta T^*_{SUB,in}$ and a larger A/A_H gives a smaller G^*_1 with the same $\Delta T^*_{SUB,in}$.

A boundary between Region II and Region III is calculated and identified as follows by using Eqs. (1) and (3):

$$G^*_2 = \left[140 \cdot \frac{A}{A_H} \cdot \frac{\sqrt{W/\lambda}}{\left\{ 1 + \left(\frac{\rho_g}{\rho_l} \right)^{1/4} \right\}^2} \right]^{\frac{1}{0.611}} \tag{15}$$

Equation (15) shows that G^*_2 increases with an increase of A/A_H and W/λ. With increasing pressure, ρ_g/ρ_l would increase; therefore, G^*_2 would decrease. Equation (15) is not a function of $\Delta T^*_{SUB,in}$.

A boundary between Region II′ and Region III is calculated and identified as follows by using Eqs. (2) and (3):

$$G_3^* = 0.7 \cdot \frac{\sqrt{W/\lambda}}{\left\{1 + \left(\frac{\rho_g}{\rho_l}\right)^{1/4}\right\}^2 \cdot \Delta T^*_{SUB,in}} \quad (16)$$

Equation (16) shows that G_3^* increases with an increase of W/λ and decreases with an increase of $\Delta T^*_{SUB,in}$. With increasing pressure, ρ_g/ρ_l would increase, and therefore, G_3^* would decrease.

Comparison of Modified CHF Correlation Scheme and Experimental Data

Figures 9(*a–d*) show the comparisons of all the available experimental data shown in Table 1 with the modified CHF scheme, taking the measured q^*_{CHF} as the ordinate and q^*_{CHF} predicted by the CHF scheme as the abscissa, in order to estimate the error of the CHF scheme. The figures on the right-hand side show the region where the data belong, taking $|G^*|$ as the ordinate and $\Delta T^*_{SUB,in}$ as the abscissa.

Figure 9(*a*) shows the comparison of all the experimental data that belong to Region I for both upflow and downflow with Eq. (12), $q^*_{CHF,4}$. Region I is identified by using Eq. (14). The comparison shows that Eq. (12) gives a good prediction, allowing the rms error of ±33 percent to the lower and upper limits of the experimental data.

Figure 9(*b*) shows the comparison of all the experimental data that belong to Region II for upflow with Eq. (1), $q^*_{CHF,1}$. Region II is identified by using the combination of Eqs. (14) and (15). The comparison shows that Eq. (1) gives a good prediction, allowing the rms error of −33 percent as the lower limit of the experimental data. In this region some of the data are greater than +33 percent of the values predicted by Eq. (1).

Figure 9(*c*) shows the comparison of all the experimental data that belong to Region II′ for downflow with Eq. (2), $q^*_{CHF,2}$. Region II′ is identified by using the combination of Eqs. (14) and (16). The comparison shows that Eq. (2) gives a good prediction, allowing the rms error of −33 percent as the lower limit of the experimental data. In this region some of the data show the errors greater than +33 percent to the values predicted by Eq. (2).

Figure 9(*d*) shows the comparison of all the experimental data that belong to Region III for both upflow and downflow with Eq. (3), $q^*_{CHF,3}$. Region III is identified by using Eq. (15) for upflow and Eq. (16) for downflow. The comparison shows that Eq. (3) gives a good prediction, allowing the rms error of −33 percent as the lower limit of the experimental data. In this region some of the data also show rms errors greater than +33 percent for the values predicted by Eq. (3).

Figures 10(*a, b, c*) show comparisons of the Zenkevich, Katto, and Gambill correlations, which can evaluate the effects of mass flux and subcooling with experimental data for Region I in both upflow and downflow, respectively. The predictions from the correlations are not as good as that from Eq. (12).

Comparison of the results of all the experimental data with

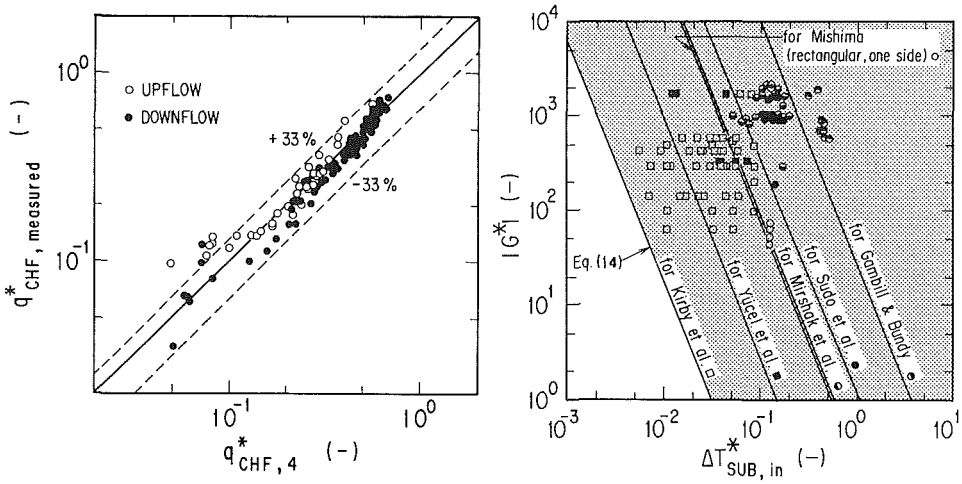

Fig. 9(*a*) Comparison of CHF between prediction (Eq. (12)) and the experimental results (Gambill and Bundy, 1961; Kirby et al., 1967; Mirshak et al., 1959; Mishima, 1984; Sudo et al., 1985a; Yücel and Kakac, 1978) for Region I in both upflow and downflow

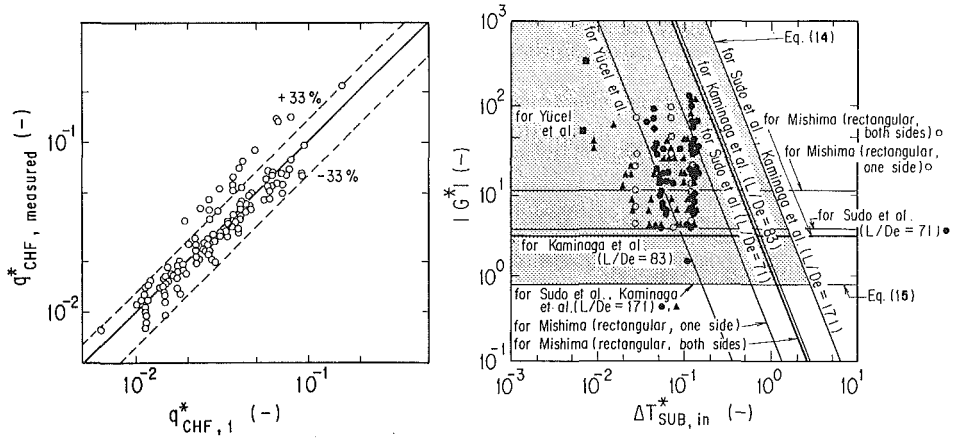

Fig. 9(*b*) Comparison of CHF between prediction (Eq. (1)) and experimental results (Kaminaga et al., 1991; Mishima, 1984; Sudo et al., 1985a; Yücel and Kakac, 1978) for Region II in upflow

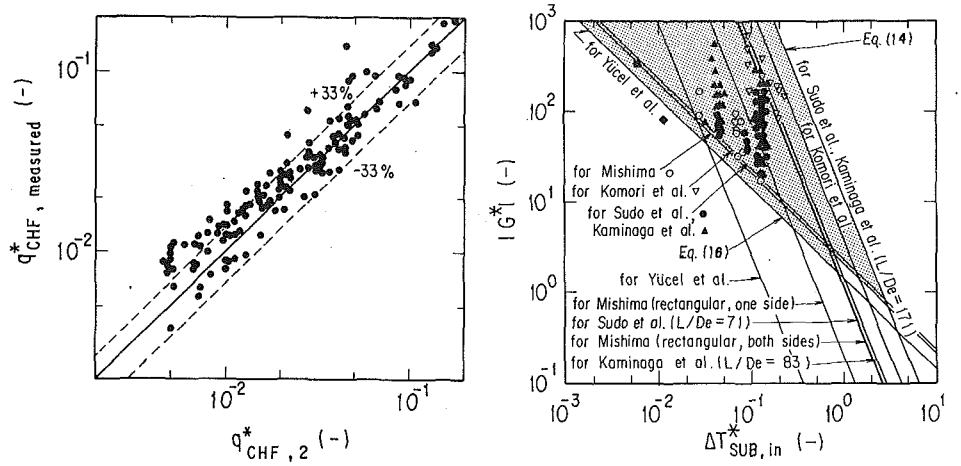

Fig. 9(*c*) Comparison of CHF between prediction (Eq. (2)) and the experimental results (Kaminaga et al., 1991; Komori et al., 1990; Mishima, 1984; Sudo et al., 1985a; Yücel and Kakac, 1978) for Region II′ in downflow

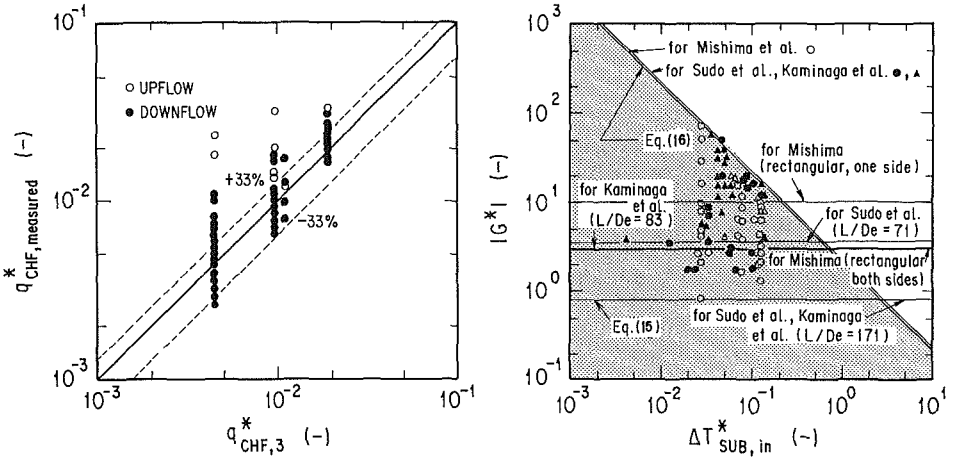

Fig. 9(*d*) Comparison of CHF between prediction (Eq. (3)) and the experimental results (Kaminaga et al., 1991; Mishima, 1984; Sudo et al., 1985a) for Region III in both upflow and downflow

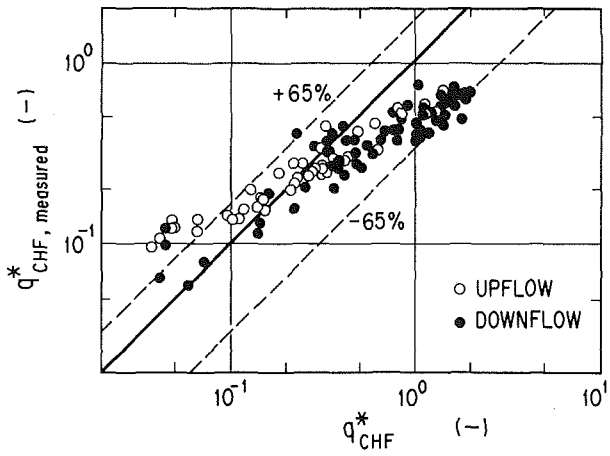

Fig. 10(*a*) Comparison of Zenkevich correlation (Eq. (9)) with experimental data for Region I in both upflow and downflow (Gambill and Bundy, 1961; Kirby et al., 1967; Mirshak et al., 1959; Mishima, 1984; Sudo et al., 1985a; Yücel and Kakac, 1978)

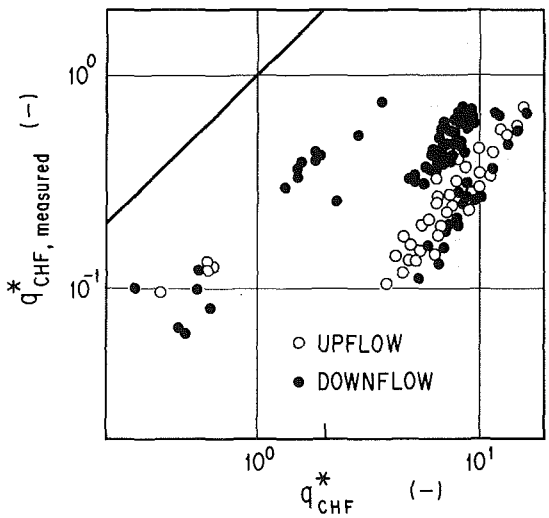

Fig. 10(*b*) Comparison of Katto correlations (Eqs. (4)-(6)) with experimental data for Region I in both upflow and downflow (Gambill and Bundy, 1961; Kirby et al., 1967; Mirshak et al., 1959; Mishima, 1984; Sudo et al., 1985a; Yücel and Kakac, 1978)

the modified CHF scheme described above show that Eqs. (1), (2), (3), and (12) give good predictions against almost all the experimental data. But Eqs. (1), (2), and (3) somewhat underpredict the CHF against some of the experimental data even though the rms errors of 33 percent are allowed. It is considered that these errors are due to the following reasons: (1) The experimental data were obtained under various experimental conditions (pressure, configuration of channels, etc.) as shown in Table 1, but the predicted CHF for each of Regions I, II, II′, and III was calculated by only one correlation, which was

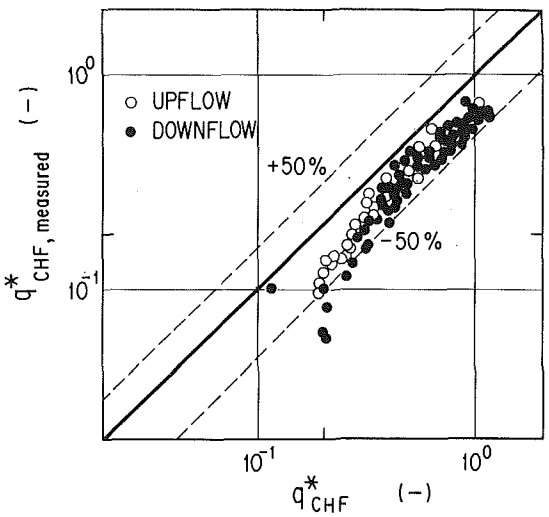

Fig. 10(c) Comparison of the correlation of Gambill et al. (Eq. (10)) with experimental data for Region I in both upflow and downflow (Gambill and Bundy, 1961; Kirby et al., 1967; Mirshak et al., 1959; Mishima, 1984; Sudo et al., 1985a; Yücel and Kakac, 1978)

proposed by the authors. (2) For Region III, the experimental data themselves scattered widely because the flow in this region was not stable due to low flow rates. (3) For Region II′, the experimental data themselves also scattered widely, even though flow rate in this region was greater than that in Region III, because the flow was not stable under the condition of co-current downflow or countercurrent flow.

From the viewpoint of thermohydraulic design and safety evaluation of the nuclear research reactors, however, it is considered that these underpredictions are the margin for using these correlations. As the rms error of −33 percent is estimated for the CHF scheme, it is recommended that the Minimum DNB (Departure from Nucleate Boiling) Ratio should be larger than 1.5, which is equivalent to an rms error of −33 percent in this study, in the case that the proposed CHF scheme is adopted in the core thermohydraulic design.

Conclusions

This study investigated the kind of factors that affect CHF, and it was found that mass flux, inlet subcooling, outlet subcooling, flow direction, pressure, and configuration of channels have significant effects on CHF. The effects of these factors on CHF were also estimated. A CHF scheme for both upward and downward flows was, thus, established within the ranges of pressure of 0.1 to 4 MPa, mass flux of −25,800 to +6250 kg/m^{2}s including stagnant flow conditions, inlet subcooling of 1 to 213 K, outlet condition extending from subcooling of 0–74 K to quality of 0–1.0, and the ratio of heated length to equivalent hydraulic diameter L/De of 8 to 240. It was also made clear that rms errors of CHF correlations used in the proposed CHF scheme were within −33 percent. It is proposed that when this CHF scheme is applied, the Minimum DNB Ratio should be larger than 1.5, which is equivalent to the correlation error of −33 percent, in the core thermohydraulic design of nuclear research reactors.

References

Gaertner, R. F., 1965, "Photographic Study of Nucleate Pool Boiling on a Horizontal Surface," ASME JOURNAL OF HEAT TRANSFER, Vol. 87, pp. 17–29.

Gambill, W. R., and Bundy, R. D., 1961, "HFIR Heat Transfer Studies of Turbulent Water Flow in Thin Rectangular Channels," ORNL-3079.

Hirano, M., and Sudo, Y., 1986, "Analytical Study on Thermal-Hydraulic Behavior of Transient From Forced Circulation to Natural Circulation in JRR-3," *J. Nucl. Sci. Technol.*, Vol. 23(4), pp. 352–368.

Kaminaga, M., Sudo, Y., Usui, T., and Murayama, Y., 1991, "Experimental Study of Critical Heat Flux in a Narrow Vertical Rectangular Channel," *Heat Transfer—Japanese Research*, Vol. 20(1), pp. 72–85.

Katto, Y., 1981, "Dimensionless Critical Heat Flux of Forced Convection Boiling in Uniformly Heated Rectangular Channel," *JSME, B*, Vol. 47[424], pp. 2351–2357 [in Japanese].

Kirby, G. J., Stanforth, R., and Kinneir, J. H., 1967, "A Visual Study of Forced Convection Boiling, Part 2, Flow Patterns and Burnout for a Round Tube Test Section," AEEW-R506.

Komori, Y., Kaminaga, M., Sakurai, F., Ando, H., Nakata, H., Sudo, Y., and Futamura, Y., 1990, "Experimental Study on DNB Heat Flux Correlations for JMTR Safety Analysis," presented at the Int. Mtg. on Reduced Enrichment for Research and Test Reactors, Newport, RI, Sept. 23–27.

Mirshak, S., Durant, W. S., and Towell, R. H., 1959, "Heat Flux at Burnout," DP-355, U.S.AEC.

Mishima, K., et al., 1983, "CHF Correlation Related to the Core Cooling of a Research Reactor," *Proc. Int. Mtg. on Reduced Enrichment for Research and Test Reactors*, Tokai, Japan, Oct. 24–27, pp. 311–320.

Mishima, K., 1984, "Boiling Burnout at Low Flow Rate and Low Pressure Conditions," Dissertation Thesis, Kyoto University, Japan.

Peebles, F. N., and Garber, H. J., 1953, "Studies on the Motion of Gas Bubbles in Liquids," *Chem. Eng. Prog.*, Vol. 49-2, pp. 88–97.

Siman-Tov, M., Gambill, W. R., Nelson, W. R., Ruggles, A. E., and Yoder, G. L., 1991, "Thermal-Hydraulic Correlations for the Advanced Neutron Source Reactor Fuel Element Design and Analysis," presented at the ASME Winter Annual Meeting, Atlanta, GA, Dec. 1–6.

Sudo, Y., Miyata, K., Ikawa, H., Kaminaga, M., and Ohkawara, M., 1985a, "Experimental Study of Differences in DNB Heat Flux Between Upflow and Downflow in Vertical Rectangular Channel," *J. Nucl. Sci. Technol.*, Vol. 22(8), pp. 604–618.

Sudo, Y., Ando, H., Ikawa, H., and Ohnishi, N., 1985b, "Core Thermodynamic Design With 20% LEU Fuel for Upgraded Research Reactor JRR-3," *J. Nucl. Sci. Technol.*, Vol. 22(7), pp. 551–563.

Thom, J. R. S., Walker, W. M., Fallon, T. A., and Reising, G. F. S., 1966, "Boiling in Sub-cooled Water During Flow up Heated Tubes or Annuli," *Proc. Inst. Mech. Engrs.*, Vol. 180, Pt. 3C, pp. 226–246.

Yücel, B., and Kakac, S., 1978, "Forced Flow Boiling and Burnout in Rectangular Channels," *Proc. 6th Int. Heat Transfer Conf.*, Vol. 1, pp. 387–392.

Zenkevich, B. A., 1959, "The Generalization of Experimental Data on Critical Heat Fluxes in Forced Convection of Sub-cooled Water," *J. Nucl. Energy, Part B: Reactor Technology*, Vol. 1, pp. 130–133.

The Numerical and Experimental Study of a Power Plant Condenser

C. Zhang
Department of Mechanical Engineering,
University of Windsor,
Windsor, Ontario, Canada N9B 3P4

A. C. M. Sousa

J. E. S. Venart

Department of Mechanical Engineering,
University of New Brunswick,
Fredericton, N.B., Canada E3B 5A3

A numerical and experimental study to evaluate the performance of a power plant condenser has been carried out. Numerically, physically relevant effects are taken into consideration through a quasi-three-dimensional approach. The equations governing the conservation of mass, momentum, and air mass fraction are solved in primitive variable form using a semi-implicit consistent control-volume formulation in which a segregated pressure correction linked algorithm is employed. The modeling of the condenser geometry, including tube bundle and baffle plates, is carried out based on a porous medium concept using applicable flow, heat, and mass transfer resistances. The measurement program included determinations of the steam pressures on the tube bundle perimeter (96 points), steam temperatures (96 locations), inlet tube sheet water pressure distributions (26 measurements), outlet tube sheet flows and temperatures (26 points), hot well flow, and enthalpy in addition to all makeup and extraction flow rates as a function of load. The measurement program and its implementation are briefly described. One data set is compared with the numerical predictions.

I Introduction

Steam surface condenser failure can be a major cause in loss of unit availability and performance in the power industry (Diaz-Tous, 1983). This may be associated with current trends of increasing power output, which have imposed additional demands upon condenser efficiency and size. Improved condenser designs are therefore required, which, in turn, require both a better understanding of the physical phenomena involved and enhanced design tools. Numerical modeling can provide a viable and reasonably inexpensive route to study the latter. Ultimately, fully benchmarked and tested design tools based on numerical models and techniques may provide means of studying new configurations at minimum cost, and thus the need for time-consuming and expensive full-scale prototype testing can be reduced.

Early studies of fluid flow and heat transfer in power plant condensers used the network method, e.g., Barsness (1963) and Chisholm et al. (1966). Although this technique has proved to be very useful, it has the shortcoming of relying heavily on experimental data for performance prediction. In this method, an a priori knowledge of flow patterns is required and the shape of the tube nest cannot be taken into account. In recent years, with the development of large computers, it has been possible to use more sophisticated numerical techniques, which allow detailed analysis of steam flow, heat transfer, and tube nest shape in condensers. The advantage of using these techniques in the prediction of condenser performance is that the details of the tube nest shape can be accounted for. This permits the designer to investigate the influence of alternatives to the shape of the tube nest and placement of baffles or other flow obstacles. It also provides detailed information on pressure, temperature, velocity, and noncondensable gas concentration distributions.

A considerable amount of research has been conducted in modeling condensers; however, in most cases the modeling is conducted under the assumption of two dimensionality for the flow. Relevant works are those of Davidson and Rowe (1981), Caremoli (1983), Al-Sanea et al. (1983), and Shida et al. (1982). The choice of a two-dimensional representation can be reasoned in terms of computational speed and memory, and, in addition, the thermal hydraulic phenomena are not sufficiently understood to permit their description in a well-defined set of three-dimensional constitutive equations. The two-dimensionality condition, however, may impose undue restrictions upon the analysis as explained by Brickell (1981). The shell-side flow within large power plant condensers is, in general, highly three dimensional. A practical approach is thus needed to establish an algorithm, particularly for power plant condensers, to include three-dimensional effects realistically and practically in both the untubed and tubed regions of the condenser. The open literature has given little attention to predicting and measuring the three-dimensional fluid flow and heat transfer in power plant condensers. The present study is a first step to fullfill this need.

In this work, a numerical procedure has been developed to evaluate the thermal performance of a power plant condenser using coupled heat transfer and fluid flow calculation procedures. The three-dimensional effects due to the difference of cooling water temperature have been included in the calculation. The predicted results are compared with measurements obtained on a 350 MW_e unit to benchmark the procedure and validate the computer program. The condenser considered is a dual bundle underslung, axial "one path" tube bundles in a single shell condenser. Only one bundle is considered with a plane between and equidistant to the two tube bundles in the shell assumed to be a plane of symmetry. This exercise also provides an additional indication on the applicability and predictive capability of the algorithm for this type of configuration. The present work is a further extension of recent work by Zhang and Sousa (1989a, 1990). In the previous work (Zhang and Sousa, 1989a), the proposed two-dimensional numerical procedure was used to predict the steam flow and heat transfer for an experimental condenser described by Fujii et al. (1972); those predicted results agreed well with the experimental data.

The governing equations describe conservation of mass and momentum of the mixture, and noncondensable gas mass fraction, which include the diffusive terms. Tube bundles and baffle plates are modeled using hydraulic resistances. The conversion of the differential equations into equivalent finite-difference equations is carried out by a control-volume formulation. A staggered grid is used to perform the discretization, and the resulting discretized equations are solved in

Contributed by the Heat Transfer Division and presented at the ASME Winter Annual Meeting, Dallas, Texas, November 25-30, 1990. Manuscript received by the Heat Transfer Division March 11, 1991; revision received July 27, 1992. Keywords: Heat Exchangers, Numerical Methods, Porous Media. Associate Technical Editor: W. A. Fiveland.

primitive variables using the algorithm suggested by Van Doormaal and Raithby (1984).

II Numerical Method

The shell-side and water-side flows are treated as steady state, and the steam-side flow is assumed to behave as an ideal mixture made up of noncondensable gases and steam only. The steam is taken as saturated. The mixture of noncondensable gases (primarily air) and steam is, for simplicity, assumed to be a perfect gas, although other equations of state could be considered. The density is computed locally according to the perfect gas state equation. The air is assumed to be of sufficiently small volume; consequently the air momentum differences can be neglected and the flow can be treated solely by diffusion theory.

2.1 Conservation Equations. The two-dimensional steady-state porous medium volume-averaged conservation equations of mass, momentum, and air mass fraction, with flow, heat, and mass transfer resistances, are written in the Cartesian coordinate system. An isotropic porosity, β, which is employed to describe the flow volume reduction due to the tube bundle and baffles for each control volume, is defined as:

$$\beta = \frac{\text{Volume occupied by the fluid}}{\text{Total volume}} \tag{1}$$

β is thus a function of the local tube placement and grid selection. This results in the following set of equations:

Mass Conservation Equation for the Mixture:

$$\frac{\partial}{\partial x}(\beta\rho u) + \frac{\partial}{\partial y}(\beta\rho v) = -\beta\dot{m} \tag{2}$$

Momentum Conservation Equations for the Mixture:

$$\frac{\partial}{\partial x}(\beta\rho uu) + \frac{\partial}{\partial y}(\beta\rho vu) = \frac{\partial}{\partial x}\left(\beta\mu_e \frac{\partial u}{\partial x}\right) + \frac{\partial}{\partial y}\left(\beta\mu_e \frac{\partial u}{\partial y}\right) - \beta\frac{\partial p}{\partial x} - \beta\dot{m}u - \beta F_u \tag{3}$$

$$\frac{\partial}{\partial x}(\beta\rho uv) + \frac{\partial}{\partial y}(\beta\rho vv) = \frac{\partial}{\partial x}\left(\beta\mu_e \frac{\partial v}{\partial x}\right) + \frac{\partial}{\partial y}\left(\beta\mu_e \frac{\partial v}{\partial y}\right) - \beta\frac{\partial p}{\partial y} - \beta\dot{m}v - \beta F_v \tag{4}$$

Conservation of Air Mass Fraction:

$$\frac{\partial}{\partial x}(\beta\rho\phi u) + \frac{\partial}{\partial y}(\beta\rho\phi v) = \frac{\partial}{\partial x}\left(\beta\rho D \frac{\partial \phi}{\partial x}\right) + \frac{\partial}{\partial y}\left(\beta\rho D \frac{\partial \phi}{\partial y}\right) \tag{5}$$

where the dependent variables are: velocity components, u and v; pressure, p; air mass fraction, ϕ.

2.2 Auxiliary Relationships

(*i*) *Momentum Source Term.* The local hydraulic flow resistances , F_u and F_v, in the momentum equations caused by the tube bundle and/or baffles, are related to the pressure loss coefficients, ξ_u and ξ_v, by

$$F_u = \xi_u \rho u U_p, \tag{6}$$

$$F_v = \xi_v \rho v U_p. \tag{7}$$

There is no general expression for the pressure loss in condensing tube banks, as most of the existing correlations for the pressure loss were developed based on the experimental data for specific configurations of single phase flow. Since

Nomenclature

A = heat transfer area, m^2
C = gas constant, J/kg K
c_p = specific heat at constant pressure J/kg K
D = diffusivity of air in vapor, m^2/s
D_i = inner diameter of tube, m
D_o = outer diameter of tube, m
ERRX = error norm for x-momentum equation
ERRY = error norm for y-momentum equation
ERRM = ratio of maximum absolute continuity error to inflow rate
Fr = Froude number = $M^2/\rho_s^2 g D_o$
F_u, F_v = flow resistance forces in momentum equations, N/m^3
f_u, f_v = friction factors
g = gravitational acceleration, m/s^2
L = latent heat of condensation, J/kg
M = mass velocity of steam through maximum flow area, kg/m^2s
$\dot{M}$ = total steam condensation rate, kg/s
$\dot{M}_n$ = steam condensation rate on the nth tube row, kg/s
$\Sigma\dot{M}_n$ = total water flow rate over the nth tube row, kg/s
$\dot{m}$ = steam condensation rate per unit volume, kg/m^3s
N = number of tubes in each control volume
P = tube pitch, m
Pr = Prandtl number = $c_p\mu/k$
p = pressure, Pa
R = thermal resistance, m^2K/W
Re_m = Reynolds number for maximum flow area = $\rho_c M D_o/\rho_s\mu_c$
Re_u = x-direction Reynolds number = $\rho u D_o/\mu$
Re_v = y-direction Reynolds number = $\rho v D_o/\mu$
T = temperature, K
U_p = velocity vector magnitude = $(u^2+v^2)^{1/2}$ m/s
u = velocity component in the x direction, m/s
V = volume, m^3
v = velocity component in the y direction, m/s
x = main flow direction coordinate, m
y = cross-stream coordinate, m
α = heat transfer coefficient of shell side = $1(R_c+R_a)$ W/m^2K
β = local volume porosity
β_t = porosity in tube bundle region
λ = thermal conductivity, W/m K
μ = dynamic viscosity, kg/m s
μ_e = effective dynamic viscosity, kg/m s
μ_t = turbulent dynamic viscosity, kg/m s
ρ = density, kg/m^3
ϕ = air mass fraction = ρ_a/ρ
ξ_u, ξ_v = pressure loss coefficients, 1/m

Subscripts

a = air
c = condensate
cs = steam/condensate interface
s = steam
t = tube wall or tube bundle
u = parameter in x-momentum equation
v = parameter in y-momentum equation
w = cooling water

Unsubscripted properties are properties for the mixture.

both x and y components of the velocity are normal to the tube bundle, the equations for ξ_u and ξ_v have a similar form, so as a first approximation, these coefficients are calculated by using a modified form of the expressions proposed by Rhodes and Carlucci (1983), namely:

$$\xi_u = 2\left(\frac{f_u}{P}\right)\left(\frac{P\beta}{P-D_o}\right)^2\left(\frac{1-\beta}{1-\beta_t}\right), \tag{8}$$

$$\xi_v = 2\left(\frac{f_v}{P}\right)\left(\frac{P\beta}{P-D_o}\right)^2\left(\frac{1-\beta}{1-\beta_t}\right). \tag{9}$$

The friction factors, f_u and f_v, are given as:

$$f_u = \begin{cases} 0.619\ \mathrm{Re}_u^{-0.198}; & \mathrm{Re}_u < 8000 \\ 1.156\ \mathrm{Re}_u^{-0.2647}; & 8000 \le \mathrm{Re}_u < 2\times 10^5, \end{cases}$$

$$f_v = \begin{cases} 0.619\ \mathrm{Re}_v^{-0.198}; & \mathrm{Re}_v < 8000 \\ 1.156\ \mathrm{Re}_v^{-0.2647}; & 8000 \le \mathrm{Re}_v < 2\times 10^5. \end{cases}$$

This type of expression, when applied to single-phase flow, is accurate to ± 12 to ± 18 percent, as stated by Zukauskas et al. (1988).

In the present work, the tube bundle is laid out in an equilateral triangular pattern, and the porosity within the entirely tube-filled region, β_t, is defined as

$$\beta_t = 1 - \frac{\pi}{2\sqrt{3}}\left(\frac{D_o}{P}\right)^2.$$

The local porosity, β, is determined by

$$\beta = 1 - \frac{N}{N_t}(1-\beta_t),$$

where N is actual tube number in the given control volume and N_t is the tube number under the assumption that the control volume is within the entirely tube-filled region.

(*ii*) *Mass Source Term.* The steam condensation rate per unit volume, $\dot{m}$, can be obtained by a simple energy balance equating the phase change enthalpy with the heat transfer rate, namely:

$$\dot{m}LV = \frac{T-T_w}{R}A, \tag{10}$$

where V is the volume of the given control volume and A is the surface area of the tubes within the control volume.

The cooling water temperature for each control volume, T_w, is obtained by a heat balance between the steam and cooling water. The overall thermal resistance for each control volume, R, is calculated from various empirical heat transfer correlations.

For the water side thermal resistance, the McAdams relation (ASHRAE, 1989) is employed:

$$\frac{1}{R_w} = 0.023\,\frac{\lambda_w}{D_i}\,\mathrm{Re}_w^{0.8}\,\mathrm{Pr}_w^{0.4}. \tag{11}$$

The fouling resistance, R_f, is taken as 3.5×10^{-5} m^{2}K/W, as suggested by Naviglio et al. (1988). The wall resistance for each tube is obtained with the assumption of one-dimensional, steady-state conduction, and it is given by:

$$R_t = \frac{D_o \ln\left(\frac{D_o}{D_i}\right)}{2\lambda_t}. \tag{12}$$

The existing data for heat transfer coefficients when condensation occurs do not lead to easy generalization, and, in general, information from different sources is required in order that a wide range of flow conditions can be studied. In this paper, since its purpose is to demonstrate the numerical calculation method rather than to conduct a detailed analysis of the process, filmwise condensation is assumed and its resistance is calculated based on the work of Fujii et al. (1972):

$$\frac{1}{R_{Fu}} = K\chi\left(1+\frac{0.276}{\chi^4\mathrm{Fr}H}\right)^{1/4}\mathrm{Re}_m^{1/2}\,\frac{\lambda}{D_o}, \tag{13}$$

where

$K = 0.8$ for in-line arrangement;

$K = 1.0$ for staggered arrangement;

$\chi = 0.9\,[1 + 1/(rH)]^{1/3}$;

$\mathrm{Fr} = M^2/\rho_s^2 g D_o$;

$H = c_{pc}(T - T_t)/\mathrm{Pr}_c L$;

$\mathrm{Re}_m = \rho_c M D_o/\rho_s \mu_c$;

$r = (\rho_c\mu_c/\rho_s\mu_s)^{1/2}$.

Equation (13) does not consider the condensate from the tubes above the nth tube where the condensate can reduce the effective heat transfer between the steam and the cooling water. The effect of inundation on condensation heat transfer is accounted for by using the correction term proposed by Grant and Osment (1968). The condensate resistance, R_c, is evaluated by

$$\frac{1}{R_c} = \frac{1}{R_{Fu}}\left[\frac{\Sigma\dot{M}_n}{\dot{M}_n}\right]^{-0.223}. \tag{14}$$

The resistance, to account for condensing steam having to diffuse through an air film close to tube surface, is evaluated by the Berman and Fuks (1958) relation:

$$\frac{1}{R_a} = \frac{aD}{D_o}\,\mathrm{Re}_s^{1/2}\left(\frac{p}{p-p_s}\right)^b p^{1/3}\left(\frac{\rho_s L}{T}\right)^{2/3}\frac{1}{(T-T_{cs})^{1/3}}, \tag{15}$$

where

$a = 0.52$ and $b = 0.7$ for $\mathrm{Re}_s < 350$;

$a = 0.82$ and $b = 0.6$ for $\mathrm{Re}_s > 350$.

The overall resistance to heat transfer for each control volume, R, is the sum of all individual resistances; thus, R, when related to the outer surface of the tube, can be written as

$$R = R_w\left(\frac{D_o}{D_i}\right) + R_f + R_t + R_c + R_a. \tag{16}$$

(*iii*) *Equation of State.* The air and steam mixture is assumed to behave as a perfect gas. The perfect gas state equation is used to calculate the local mixture density,

$$\rho = \frac{p}{CT}, \tag{17}$$

where p is the local mixture pressure obtained from momentum and continuity equations, C is the gas constant for the mixture, and T is the saturation temperature determined by the partial steam pressure, p_s. C and p_s are calculated by

$$C = \phi C_a + (1-\phi)C_s, \tag{18}$$

$$p_s = \frac{C_s}{C}(1-\phi)p \tag{19}$$

where C_a and C_s are the gas constants for air and steam, respectively, and their values are 287.0 J/kg K and 461.4 J/kg K.

(*iv*) *Effective Viscosity.* The concept of an effective vis-

cosity is used, which is defined as the sum of the laminar and turbulent viscosities, namely:

$$\mu_e = \mu + \mu_t. \tag{20}$$

For all simulations the turbulent viscosity, μ_t, is assumed to be constant based on previous work by Zhang and Sousa (1990, 1989b), mainly to save computer time. Typical values of the turbulent viscosity, μ_t, are about twenty times the value of the dynamic viscosity, μ; however, studies indicate that severalfold variations in μ_t have no significant effect on the results (Zhang et al., 1991). This to some extent is not surprising, since the effect of turbulent wall shear stresses is introduced via the local hydraulic flow resistances.

2.3 Boundary Conditions. The boundary conditions for the inlet, vent, solid walls, and plane of symmetry are:

Inlet: The velocity and air mass fraction are specified at the inlet boundary.

Vent: A mass imbalance correction scheme as described by Theodossiou et al. (1988) is used to update the velocity at the vent. The air mass fraction at the vent is determined by equating the inlet air mass flow rate to the air mass flow rate at the vent, $\phi_{\text{inlet}} \times$ inlet mixture mass flow rate $= \phi_{\text{vent}} \times$ outlet mixture mass flow rate, where the mixture mass flow rate at the vent is calculated based on the inlet mixture mass flow rate and the condensation rate.

Walls: The shell walls of the condenser are assumed to be nonslip, impervious to flow, and adiabatic. Thus, the normal velocity components are equal to zero and air mass fraction gradients normal to the walls are set to zero

Plane of symmetry: Along the center line the derivatives with respect to the cross-stream direction of all field variables are set to zero.

The inlet steam pressure is specified as an input.

2.4 Solution Procedure. The discretization of the differential equations, Eqs. (2), (3), (4), and (5), is carried out by integrating over small control volumes in a staggered grid. Since these equations are coupled together and are highly nonlinear, an iterative approach is used for their solution. An outer iteration is employed comprising the following sequence of operations:

(*i*) The momentum equations, Eqs. (3) and (4) after discretization, are solved based on a pressure field taken from the previous iteration.

(*ii*) A Poisson equation for the pressure correction, derived from the continuity equation, Eq. (2), is solved, and at the end of each outer iteration loop, pressures and velocities are corrected.

(*iii*) The air mass fraction ϕ is obtained from the discretized form of its transport equation, Eq. (5).

(*iv*) The density, momentum source, and mass source terms are then updated from Eqs. (17), (6), (7) and (10).

(*v*) The new cycle is repeated from (*i*) unless the convergence criteria described below are satisfied.

2.5 Convergence Criteria. Based on numerical tests, the convergence criteria for the overall computational procedure have been specified as:

(*i*) The error norms for the momentum equations are reduced to less than 10^{-5}.

(*ii*) The maximum absolute continuity error is reduced to less than 0.001 percent of the inflow.

The error norms for the x- and y-momentum equations are defined as:

$$\text{ERRX} = \left[\Sigma \left(\frac{u^{(n+1)} - u^{(n)}}{u^{(n)}} \right)^2 \right]^{1/2} / (\text{Total No. of grids})$$

$$\text{ERRY} = \left[\Sigma \left(\frac{v^{(n+1)} - v^{(n)}}{v^{(n)}} \right)^2 \right]^{1/2} / (\text{Total No. of grids})$$

where $u^{(n+1)}$ and $v^{(n+1)}$ are current values, and $u^{(n)}$ and $v^{(n)}$ are values from the previous cycle.

2.6 Three-Dimensional Effects. Three-dimensional effects occur in large power plant condensers primarily due to cooling water temperature gradients, which lead to a space-variable sink potential. For power plant condensers with partition plates and large entrance area, however, a valid assumption is to consider that the shell-side flow has negligible velocity components parallel to the tube bundle since the partition plates restrict flow in the third direction. Thus, the condenser shell-side may be subdivided into a number of two-dimensional domains normal to the cooling water flow direction. In each subdomain, the flow is therefore assumed to be two dimensional, with the domains interacting with each other through the "thermal memory" of the cooling water on the tubeside. Calculations for each plane are made sequentially starting from the cooling water inlet end. The outlet cooling water temperature of the preceding subdomain is used as the inlet cooling water temperature for the successive subdomain. A similar marching procedure is used for the successive sections of the condensers. Thus, the two-dimensional approach described above is extended to a three-dimensional one by a series of step-by-step two-dimensional calculations, each being for one sector. The validity of this approach is enhanced by the fact that maximum temperature difference over the total length of the test condenser is only approximately 2°C.

III Flow Configuration

The geometric and operating parameters for the Unit #1 steam condenser at Coleson Cove Generating Station (New Brunswick Electric Power Commission) are given in Table 1. Figure 1 depicts a side view of this dual bundle in-line underslung condenser. The dimension of the condenser is $5.2 \times 3.5 \times 17$ m^3 and consists of 6720 tubes in two bundles. There are 15 full partition plates (tube bundle supports), which divide the condenser into 16 sectors in the direction of the cooling water flow. The system shown in Fig. 1 is considered to be symmetric with respect to a vertical center plane. The tube layout of the tube bundle for one half of the condenser placed in the shell is shown in Fig. 2. The right-hand side and the bottom are solid walls and the left-hand side is a presumed symmetric center line. The air extraction vent is located in the middle of the tube bundle. Steam enters the condenser from top as shown in Fig. 2.

IV Measurement Program

The experimental data employed in this study are referred to operating conditions of Oct. 19, 1989. The instrumentation layout is shown in Fig. 1. Figure 3 indicates the steam pressure, steam temperature, and cooling water temperature measurement locations. The measurements of steam pressure and steam

Table 1 Geometric and operating parameters for a 350-MW$_e$ condenser

Geometrical Parameters	
Condenser Length (m)	17
Tube Outer Diameter (mm)	25.4
Tube Inner Diameter (mm)	22.9
Tube Pitch (mm)	33.3
Operating Parameters at 350 MW$_e$	
Inlet Temperature of Cooling Water (°C)	11.1
Inlet Velocity of Cooling Water (m/s)	2.2

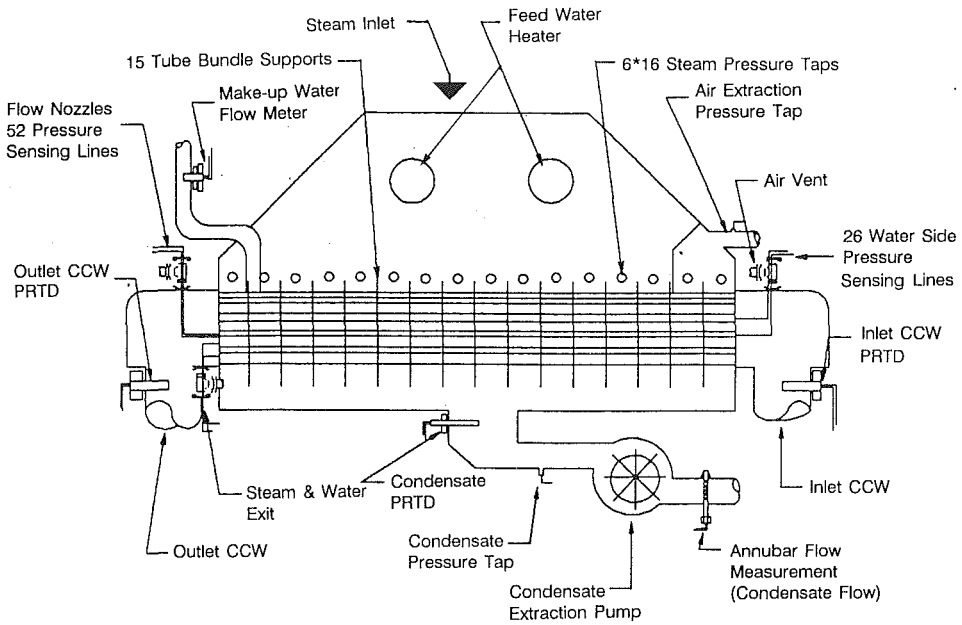

Fig. 1 Longitudinal section of unit #1 condenser at NBEPC Coleson Cove

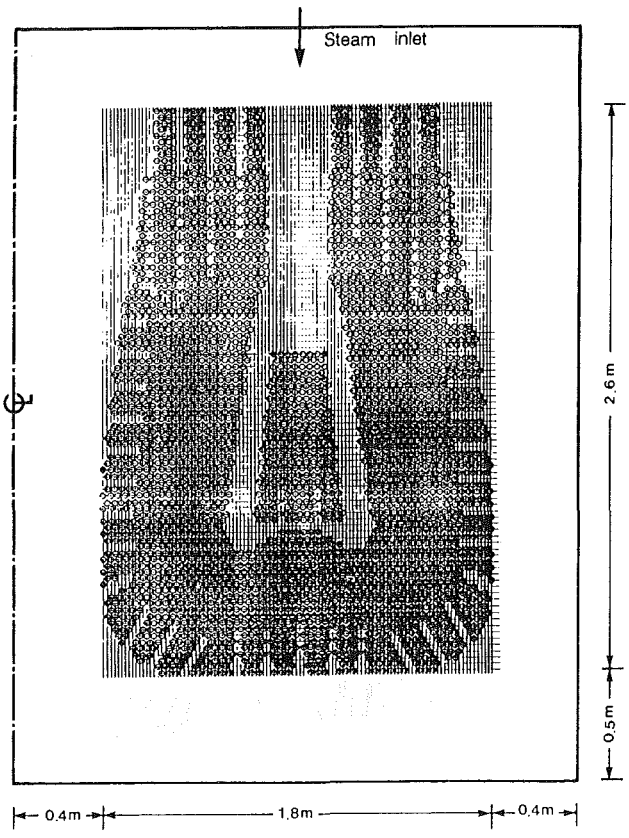

Fig. 2 Tubing arrangement of condenser

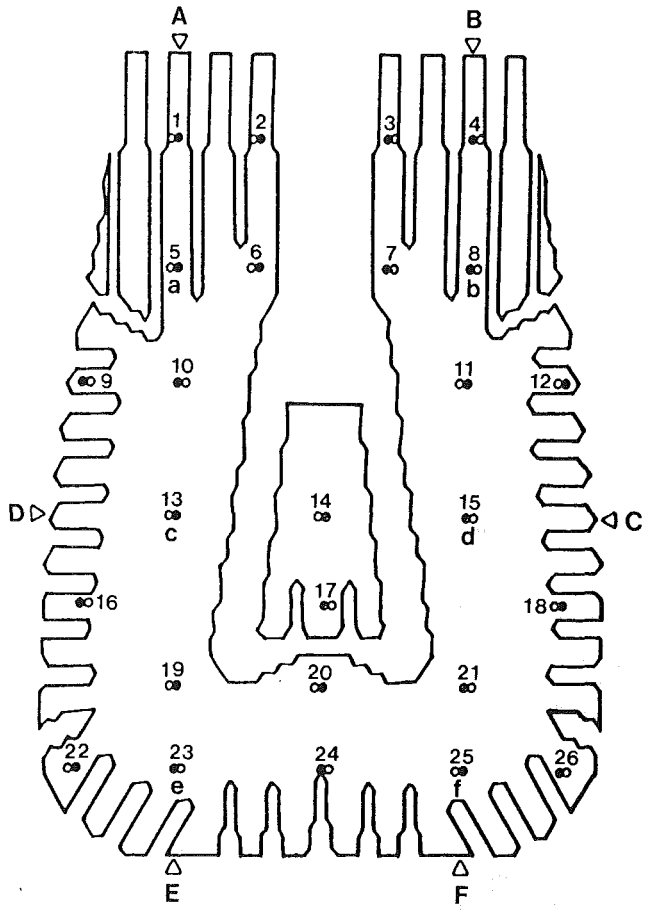

Fig. 3 Locations of steam pressure, steam temperature, and cooling water temperature measurement: A–F = steam pressures; a–f = steam temperatures; 1–26 = outlet cooling water temperatures

temperature are made on 16 planes transverse to the tube bundle axis at points of midspan between support plates. The steam total pressure and temperature measurements were obtained at six fixed locations in each plane. Cooling water flow rates, temperatures, and pressures at the outlet were obtained in 26 fully instrumented tubes located strategically in the bundle.

4.1 Steam Pressure Measurement. The steam total pressure measurements were obtained at six fixed locations external to the tube bundle as shown in Fig. 3. Each fixed pressure port on a given plane is connected to an absolute pressure transducer, externally located to the condenser shell through a manifold arrangement using a stepping motor controlled "0"

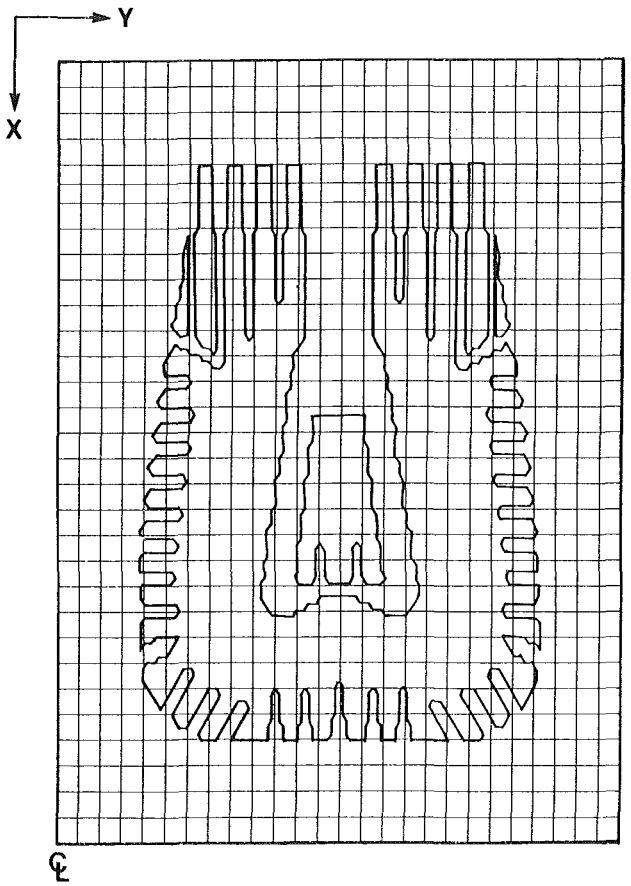

Fig. 4 Grid used for the simulation

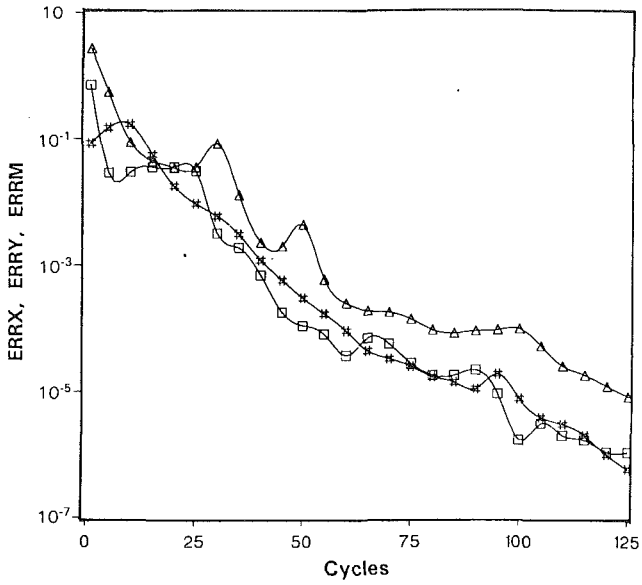

Fig. 5 Rate of convergence (plane No. 1): □-ERRX; △-ERRY; #-ERRM

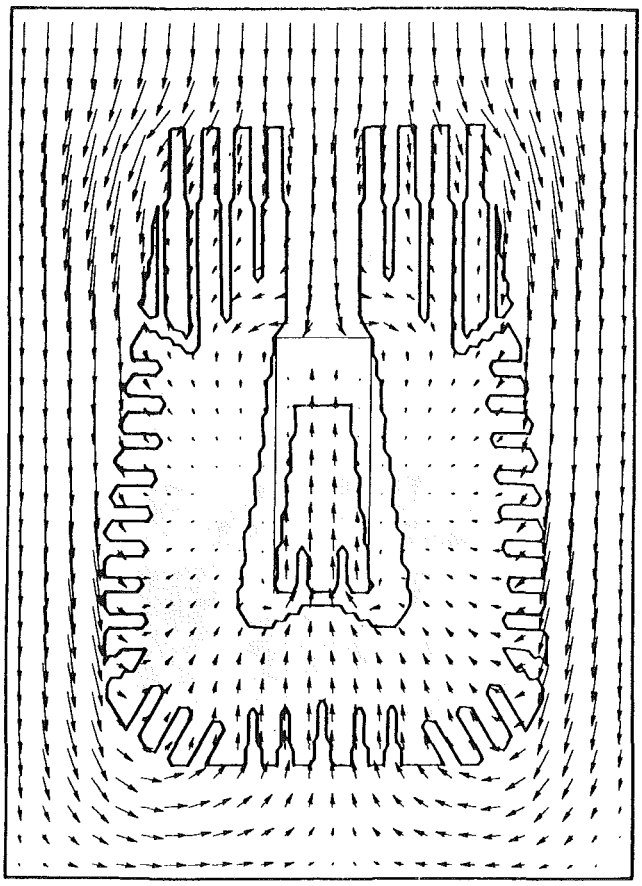

Fig. 6 Velocity vector plot (plane No. 1)

ring sealed valve. To obtain pressure measurements sequentially for each port, these valve are automatically operated by a data acquisition system.

4.2 Steam Temperature Measurement. The steam temperature measurements were obtained using thermocouple probes through plugged tubes on the waterside. Since there is no water flow through the plugged tubes, these tubes are assumed to be in thermal equilibrium with the surrounding steam. The thermocouples located along the inner wall of the tubes give a good measurement of the local total steam or adiabatic tube wall temperatures. The condensate falling on the plugged tubes containing the thermocouples will certainly interfere with the measurements of steam temperatures, particularly in the region of lower tube rows. The authors, however, have considerable confidence in these measurements. They check well with operating values, energy balance, and hot well temperatures. Furthermore, the eventual errors in these measurements tend to be minimal since no condensation occurs on the plugged tubes, and the splashing and turbulence are present in most of the shell-side flow.

The results utilized here are only a preliminary set of experimental data. Complete details of the measurement program, reliability, accuracy, and instrumentation are to be made available by Cooper et al. (1990).

V Predicted Results

The predictions are carried out in all 16 sections of the condenser. The flow is assumed to be two dimensional in each sector, since the partition plates restrict the fluid flow in the third direction. The calculations are thus made for 16 planes, which are located halfway between two successive partition plates. It may be expected that fluid flow and heat transfer conditions should differ in each sector due to the increase of cooling water temperature. The calculation domain is limited to only one half of the condenser due to symmetry as shown in Fig. 2. The calculations are performed in a mesh of 31 × 26 in the main and crossflow directions, respectively, as shown in Fig. 4. Previous studies conducted by Zhang et al. (1991) indicate that a grid of this size adequately reflects the geometry, flow, and heat transfer. Figure 5 shows the rate of convergence

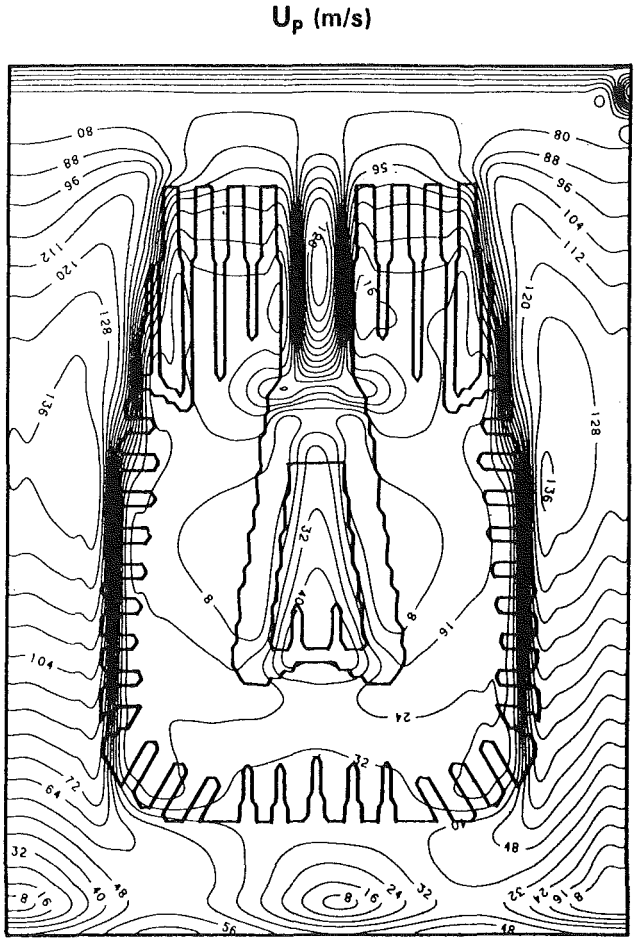

Fig. 7 Velocity distribution (plane No. 1)

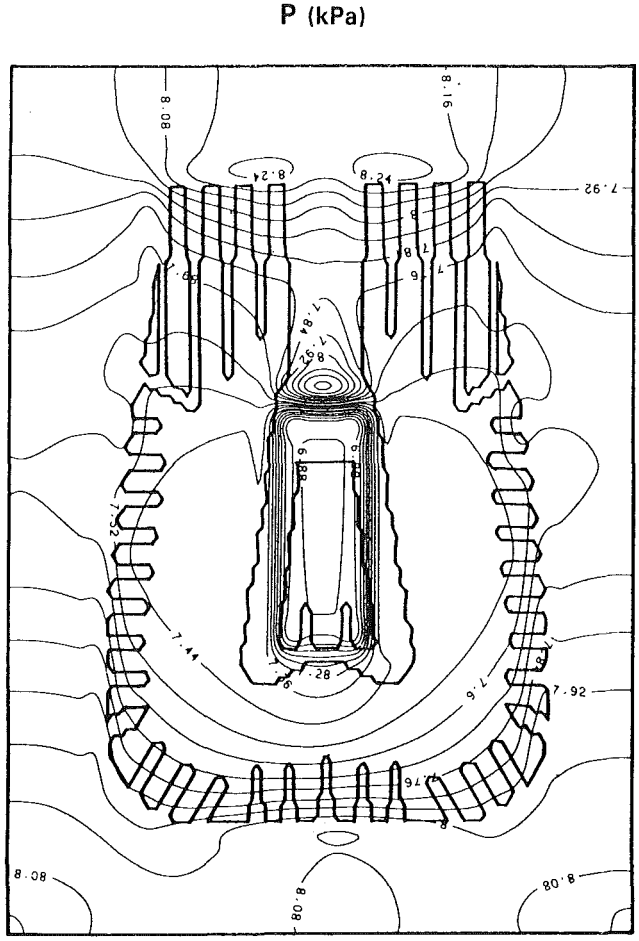

Fig. 8 Pressure distribution (plane No. 1)

for the first plane. 125 outer cycles are required to satisfy the prescribed criteria for the first plane. An average of 90 outer cycles for 16 planes is required.

In order to solve the governing equations, the inlet boundary conditions for the steam flow must be known. The steam inlet conditions are complicated due to the rotational effects of the turbine exhaust flow, the hood configuration, and internal structures. It is assumed, as a first approximation in this paper, that the inlet velocity profile is uniform for each sector. The mass flow rate for each sector is assumed to be equal to its maximum condensation rate at this sector, and the magnitude of inlet velocity in each sector is determined by the mass flow rate at this sector. The pressure at B is chosen as a reference pressure. Since the inlet air mass fraction is not available at this stage, a tentative value of 0.15 percent of inlet air mass fraction was made based upon air extraction capacity. The sensitivity studies on the effects of inlet air mass fraction indicate that an increase of 0.1 percent in the inlet air mass fraction yields to a decrease of 0.48 percent of the steam condensation rate.

The velocity vector plot for the first plane is shown in Fig. 6. It can be seen from this figure that the velocity distribution in the vicinity of the bundle is nearly "parallel" to the tube bundle edge except for the "hot well" region. This particular flow pattern can be inferred from the experimental observations, and since a large proportion of the steam flow goes through the steam lanes, the result is not unexpected. Figures 7 and 8 provide contour maps of velocity and steam pressure distribution in the first plane of the condenser. The pressure distribution around the tube bundle, in agreement with the measurement, is not uniform. The air mass fraction contour map is given in Fig. 9, which shows a sharp increase of air mass fraction in the vent region. There are two large air bubbles in regions 13 and 15 (Fig. 3) since steam velocities are lower in these regions. It is expected that regions 13 and 15 are poor condensation regions. The air mass fraction is as much as 25 percent at region 13 in the first plane. The air mass fraction at the vent is relatively low. This may be attributed to the vent treatment. In the present approach, the air mass fraction at the vent is not specified as a boundary condition; instead, it is calculated based on the inlet air mass flow rate, which is equal to the outlet air mass flow rate, and the outlet mixture mass flow rate. The mixture mass flow rate at the vent is equal to the difference of the inlet mixture mass flow rate and steam condensation rate, and is of the order of 2 percent of inlet mixture mass flow rate. The air mass fraction at the vent is very sensitive to the condensation rate. A 1 percent error in the prediction of the steam condensation rate could result in as much as 100 percent difference to the air mass fraction at the vent. Figures 10 and 11 show the distribution of the condensation rates and mean outlet cooling water temperatures in each plane. It is interesting to note that the condensation rates in the first and last sectors are nearly twice and less than one half, respectively, the average value. To evaluate the effect of inundation upon condensation heat transfer further, the computations were also carried out without this effect. The shell-side heat transfer coefficient distributions with and without inundation are depicted in Figs. 12(a) and 12(b). The differences are dramatic. Inundation causes the shell-side heat transfer coefficient to drop by as much as 70 percent on the lower tube rows as compared to a noninundation condition. This drop leads to a condensation rate decrease of approxi-

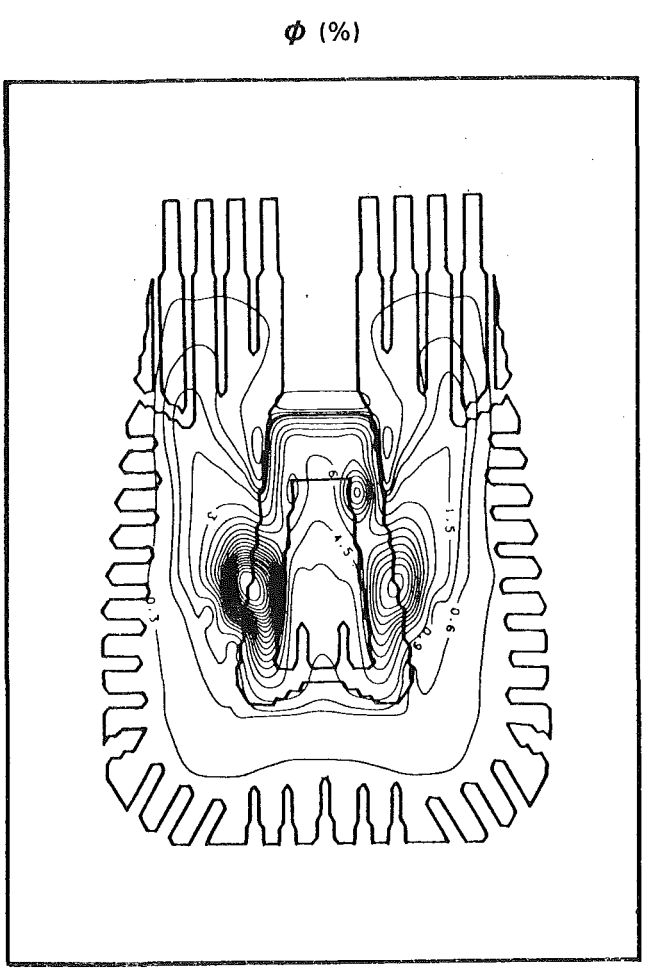

Fig. 9 Air concentration distribution (plane No. 1)

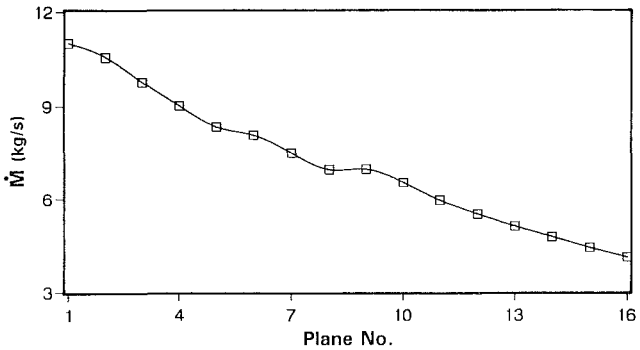

Fig. 10 Distribution of condensation rate

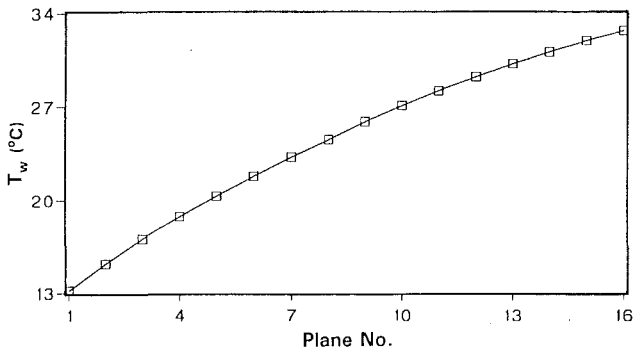

Fig. 11 Distribution of cooling water temperature

Table 2 Comparison of predicted and experimental steam pressures

Steam pressure (Pa)

Location		A	B	C	D	E	F
Plane #1	Pred.	8193.6	8211.9	7819.6	7744.0	7919.8	7967.6
	Exp.	7731.5	8211.9	7991.0	7681.5	8001.8	7973.9
Plane #2	Pred.	8479.5	8496.6	8138.7	8069.5	8230.3	8272.3
	Exp.	8042.1	8496.6	8169.6	7795.9	8111.7	8117.8
Plane #3	Pred.	8390.7	8406.4	8101.3	8039.2	8175.6	8212.9
	Exp.	8143.7	8406.4	8203.0	7826.1	8069.8	8187.8
Plane #4	Pred.	8290.8	8305.2	8045.4	7989.7	8105.4	8138.5
	Exp.	8273.7	8305.2	8278.3	7462.5	8117.8	8269.9
Plane #5	Pred.	8189.3	8202.6	7976.4	7925.6	8026.7	8055.8
	Exp.	8168.8	8202.6	8270.0	8136.2	8266.1	8278.8
Plane #6	Pred.	8486.4	8498.9	8291.1	8244.0	8337.1	8363.4
	Exp.	8526.1	8498.9	8295.1	7959.2	8236.5	8328.7
Plane #7	Pred.	8455.9	8467.5	8286.5	8243.5	8324.8	8348.2
	Exp.	8287.0	8467.5	8319.2	8059.6	8315.9	8383.5
Plane #8	Pred.	8441.3	8451.9	8297.3	8258.6	8327.9	8348.8
	Exp.	8326.7	8451.9	8314.1	8287.0	8388.0	8402.4
Plane #9	Pred.	9072.5	9082.2	8942.7	8907.4	8968.9	8988.8
	Exp.	8916.3	9082.2	8894.9	8768.6	8924.4	9013.0
Plane #10	Pred.	9127.9	9136.8	9015.0	8982.9	9036.7	9054.4
	Exp.	9051.4	9136.8	8858.1	8509.9	8855.8	8975.7
Plane #11	Pred.	8939.1	8947.3	8841.9	8812.5	8859.7	8875.0
	Exp.	8923.2	8947.3	8834.3	8737.5	8889.3	8917.0
Plane #12	Pred.	8874.4	8882.1	8789.0	8762.0	8804.0	8817.5
	Exp.	9002.9	8882.1	8881.6	8908.2	8868.3	8881.6
Plane #13	Pred.	8867.6	8874.7	8793.3	8768.6	8805.6	8817.6
	Exp.	8959.9	8874.7	8856.3	8618.2	8772.3	8870.8
Plane #14	Pred.	8892.2	8898.7	8827.9	8805.4	8837.7	8848.4
	Exp.	8819.2	8898.7	8792.6	8670.2	8788.9	8813.4
Plane #15	Pred.	8862.9	8868.9	8807.0	8786.5	8814.9	8824.3
	Exp.	8821.4	8868.9	8778.1	8782.0	8771.7	8775.5
Plane #16	Pred.	8851.5	8857.0	8803.2	8784.5	8809.3	8817.7
	Exp.	8865.8	8857.0	8716.8	8735.8	8778.0	8771.8

Table 3 Comparison of predicted and experimental steam temperatures

Steam temperature (°C)

Location		a	b	c	d	e	f
Plane #1	Pred.	40.44	40.53	38.81	39.57	40.57	40.70
	Exp.	39.77	43.71	37.40	39.88	43.63	40.69
Plane #2	Pred.	41.27	41.35	39.98	40.52	41.38	41.49
	Exp.	40.02	44.06	37.77	40.50	43.54	41.21
Plane #3	Pred.	41.24	41.31	40.01	40.56	41.33	41.43
	Exp.	*	44.36	38.18	40.42	43.50	41.26
Plane #4	Pred.	41.15	41.22	39.97	40.53	41.23	41.32
	Exp.	40.68	44.64	38.50	40.45	43.41	*
Plane #5	Pred.	41.03	41.09	40.01	40.48	41.09	41.17
	Exp.	41.15	45.11	*	41.35	43.26	41.72
Plane #6	Pred.	41.80	41.86	40.93	41.31	41.86	41.93
	Exp.	41.43	45.38	39.45	41.33	43.06	41.70
Plane #7	Pred.	41.82	41.87	41.04	41.39	41.87	41.94
	Exp.	41.83	45.81	*	41.70	42.92	42.18
Plane #8	Pred.	41.88	41.92	41.10	41.47	41.92	41.98
	Exp.	42.08	45.52	40.46	42.47	42.73	42.53
Plane #9	Pred.	43.34	43.37	42.38	42.92	43.38	43.43
	Exp.	42.46	45.12	40.91	42.47	42.57	42.58
Plane #10	Pred.	43.51	43.55	42.59	43.13	43.55	43.60
	Exp.	42.94	*	41.20	42.70	42.33	42.62
Plane #11	Pred.	43.16	43.19	42.43	42.83	43.20	43.24
	Exp.	42.73	44.60	41.69	43.19	41.93	42.77
Plane #12	Pred.	43.06	43.09	42.46	42.77	43.09	43.13
	Exp.	43.23	44.55	42.16	43.84	41.72	43.33
Plane #13	Pred.	43.09	43.11	42.53	42.82	43.11	43.15
	Exp.	43.32	44.24	42.59	43.82	41.23	42.67
Plane #14	Pred.	43.18	43.20	42.64	42.93	43.20	43.23
	Exp.	43.33	43.81	44.63	43.96	41.01	43.39
Plane #15	Pred.	43.15	43.16	42.66	42.92	43.17	43.19
	Exp.	43.55	43.53	44.57	44.16	40.96	43.80
Plane #16	Pred.	43.15	43.16	42.69	42.94	43.17	43.19
	Exp.	43.60	43.52	44.59	44.60	40.46	43.99

* - Experimental data are not available.

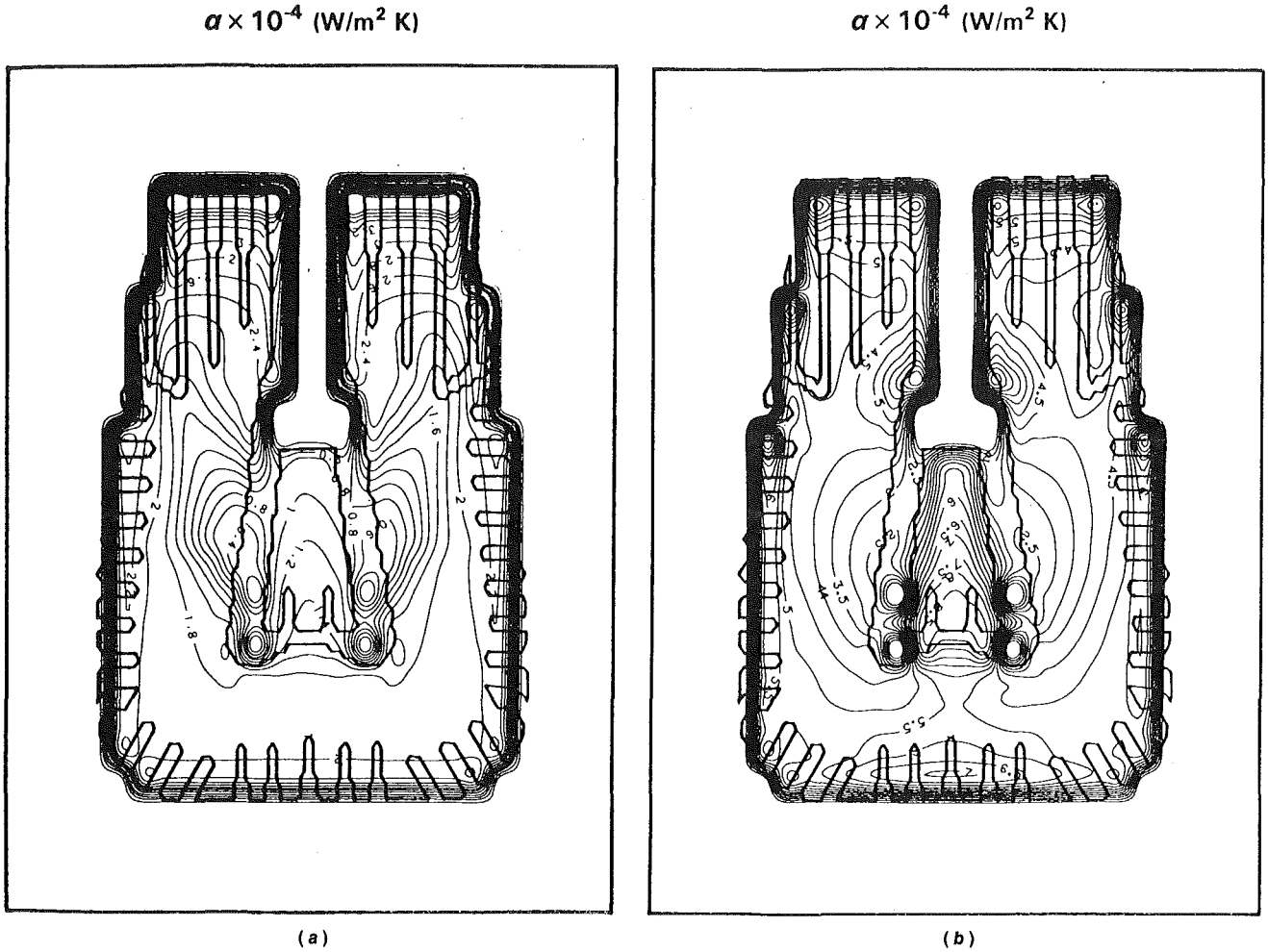

Fig. 12 Shell-side heat transfer coefficient distribution (plane No. 1): (*a*) with inundation; (*b*) without inundation

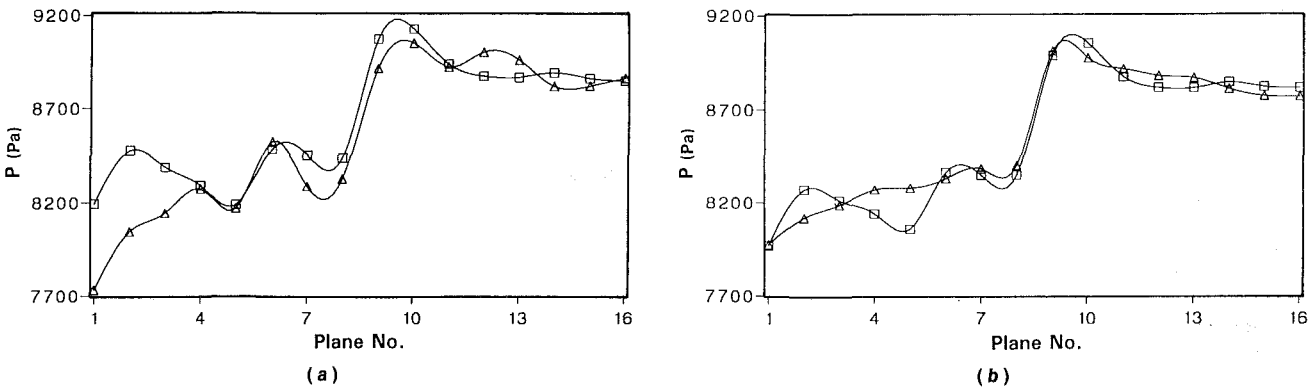

Fig. 13 Comparison of predicted and experimental steam pressures: (*a*) at location *A*; (*b*) at location *F*; □ -predicted values; △ -experimental values

mately 13 percent for the first plane and 5 percent for total condensation rate.

VI Comparisons and Discussion

Comparisons for the steam pressures and steam temperatures at the locations shown in Fig. 2 are listed in Tables 2 and 3, respectively, for all 16 planes. Comparisons for the steam pressures at *A* and *F* for 16 planes are also shown in Fig. 13. The overall agreement is good considering the complex inlet conditions and the simplifying assumptions made. The maximum difference between the predicted and experimental pressures is 5.9 percent, which occurs at location *A* of Plane #1. The errors of predicted pressure are less than or equal to 3 percent for 89 out of 96 locations. The errors of predicted temperatures are less than or equal to 5 percent for 83 out of 96 points. For the first three planes, the difference of experimental pressures at *A* and *B* is large and pressure at *A* is much lower than pressure at *B*, while the difference of the predicted

Table 4 Comparison of predicted and experimental outlet cooling water temperatures

	Outlet cooling water temperature (°C)						
Location	1	2	3	4	5	6	7
Pred.	34.23	34.30	34.33	34.26	33.34	33.65	33.74
Exp.	33.78	34.73	34.55	33.73	33.60	34.70	32.78
Location	8	9	10	11	12	13	14
Pred.	33.30	33.32	32.45	32.36	33.39	29.78	31.05
Exp.	35.51	*	34.06	33.27	34.22	32.86	*
Location	15	16	17	18	19	20	21
Pred.	31.33	32.99	31.59	33.05	32.68	32.59	32.73
Exp.	34.94	33.93	29.43	34.49	32.37	29.23	34.05
Location	22	23	24	25	26		
Pred.	33.01	32.86	32.85	32.89	33.06		
Exp.	34.05	37.32	30.45	34.18	36.36		

* - Experimental data are not available.

pressures at A and B is small. After the third plane, the experimental pressure difference between A and B is small, and the predicted pressures at A agree well with the experimental data, which can be seen from Fig. 13. A possible explanation for the large pressure difference between A and B may be attributed to the inlet flow distribution for which, unfortunately, at this stage of the experimental program, there is no available information. This is a prime source of uncertainty between the predictions and the experimental data. The assumption of flow symmetry between bundles for this type of condenser may also be questionable. The experimental data show that the temperatures at a and b nearly correspond to the saturated temperatures for the pressures at A and B, respectively. In the simulation, however, significant pressure drop occurs between A and a, and B and b. Since pressure B is made equal to the experimental value, it results in the predicted temperature at b being lower than the corresponding experimental values.

The comparison of the predicted and experimental cooling water temperatures at the outlet is given in Table 4. The comparison indicates that the predicted outlet cooling water temperatures agree well with the experimental data in the upper bundle. The comparison also indicates that the outlet cooling water temperatures in the lower bundle are underestimated, which means that the steam condensation rate is underestimated in this region. This may be attributed to the value of the exponent used in the inundation correction term. The values of the exponent have been ascribed between 0.07 (Fuks, 1957) and 0.223 (Grant and Osment, 1968). In this study, a value of 0.223 is used, which generally provides a more conservative correction factor for inundation and may cause the underprediction of steam condensation rate in the lower bundle. It can be seen that the outlet cooling water temperatures in the vent region are overpredicted. This means that the steam condensation rate is overpredicted in the vent region, which can be explained by considering the lower air mass fraction in the vent region. The predicted mean outlet cooling water and mean condensate temperatures (32.89°C and 42.14°C) compare well with the experimental values of 33.69°C and 42.20°C, respectively. The difference between the predicted and experimental mean cooling water temperature increases is approximately 3.5 percent. The experimental value of the total condensation rate is not available for this set of data.

VII Concluding Remarks

A simulation of shell-side flow and heat transfer for a industrial steam surface condenser has been carried out. The flow was assumed to be quasi-three-dimensional and incompressible; however, density was allowed to vary with temperature and air concentration. The numerical method proposed in the present study has shown the capability of predicting the performance of condensers including the three-dimensional effects due to the increase of cooling water temperature. The predictions have produced physically meaningful results, and when consideration is given to the uncertainties of the experimental data, the assumptions undertaken, and the limitations of the computational procedure, the predictive capability of the model is very encouraging.

This preliminary attempt to validate the proposed numerical model has led to credible predictions for shell-side fluid flow and heat transfer over the full condenser, despite considerable uncertainties in the input data used. If particular concern is the inlet velocity and noncondensable distribution, the adequacy of the constitutive relation for fluid flow and heat transfer not withstanding, the algorithm developed holds good potential as an analytical and design tool.

Full benchmarking of the procedure for the condenser simulation is still required and for this purpose extensive experimental data, including fluid and temperature fields, and flow visualization data will be needed.

Acknowledgments

The assistance of the New Brunswick Electric Power Commission staff of the Coleson Cove Generating Station, Mr. W. Cooper and Mr. K. Diab, is gratefully acknowledged. The work has been supported through a joint University Industry NSERC Cooperative Research grant (NSERC Grant No. CRD-0039112), and the NSERC operating grant to one of the authors (ACMS)(NSERC grant No. A1398). The authors also acknowledge the referees for their helpful comments and suggestions.

References

Al-Sanea, S., Rhodes, N., Tatchell, D. G., and Wilkinson, T. S., 1983, "A Computer Model for Detailed Calculation of the Flow in Power Station Condensers," in: *Condensers: Theory and Practice*, Int. Chem. E. Symposium Series, No. 75, Pergamon Press, New York, pp. 70–88.

ASHRAE Handbook, 1989, *Fundamentals*, SI Edition, American Society of Heating, Refrigerating and Air Conditioning Engineers Inc., Atlanta, GA, p. 3.14.

Barsness, E. J., 1963, "Calculation of the Performance of Surface Condenser by Digital Computer," ASME Paper No. 63-PWR-2.

Berman, L. D., and Fuks, S. N., 1958, "Mass Transfer in Condensers With Horizontal Tubes When the Steam Contains Air," *Teploenergetica*, Vol. 5, No. 8, pp. 66–74.

Brickell, G. M., 1981, "Potential Problem Areas in Simulating Condenser Performance," in: *Power Condenser Heat Transfer Technology*, P. J. Marto and R. H. Nunn, eds., Hemisphere, Washington, DC. pp. 51–61.

Caremoli, C., 1983, "Numerical Computation of Steam Flows in Power Plant Condensers," *Condensers: Theory and Practice*, Int. Chem. E. Symposium Series, No. 75, Pergamon Press, New York, pp. 89–96.

Chisholm, D., Osment, B. D. J., McFarlane, M. W., and Choudhury, M. H., 1966, "The Performance of an Experimental Condenser," *Proc. of 3rd Int. Heat Transfer Conf.*, Chicago, IL, Vol. 1, pp. 179–185.

Cooper, W., Diab, K., Sollows, K., Venart, J. E. S., and Sousa, A. C. M., 1990, "Experimental Study of a 350MW$_e$ Surface Condenser," in press.

Davidson, B. J., and Rowe, M., 1981, "Simulation of Power Plant Condenser Performance by Computational Method: An Overview," in: *Power Condenser Heat Transfer Technology*, P. Marto and R. Nunn, eds., Hemisphere, Washington, pp. 17–49.

Diaz-Tous, I. A., 1983, "Keynote Address," *Proc. Symposium on State-of-the-Art Condenser Technology*, I. A. Diaz-Tous and R. J. Bell, eds., Orlando, FL, pp. 1:1–1:22.

Fujii, T., Uehara, H., Hirata, K., and Oda, K., 1972, "Heat Transfer and Flow Resistance in Condensation on Low Pressure Steam Flowing Through Tube Banks," *Int. J. Heat Mass Transfer*, Vol. 15, pp. 247–260.

Fuks, S. N., 1957, "Heat Transfer With Condensation of Steam Flowing in a Horizontal Tube Bundle," *Teploenergetica*, Vol. 4, No. 1, pp. 35–39.

Grant, I. D. R., and Osment, B. D. J., 1968, "The Effect of Condensate Drainage on Condenser Performance," NEL Report No. 350.

Naviglio, A., Sala, M., Socrate, S., Stefani, A., and Vigevano, L., 1988, "Distribution of Non-condensable Gases Within the Tube Bundle of Surface Condensers," TEC 88-Conference, *Recent Advances in Heat Exchangers*, Grenoble, France.

Rhodes, D. B., and Carlucci, L. N., 1983, "Predicted and Measured Velocity Distributions in a Model Heat Exchanger," presented at the International Conference on Numerical Methods in Nuclear Engineering, Canadian Nuclear Society/American Nuclear Society, Montreal.

Shida, H., Kuragasaki, M., and Adachi, T., 1982, "On the Numerical Analysis Method of Flow and Heat Transfer in Condensers," *Proc. 7th Int. Heat Transfer Conference*, Munchen, Fed. Rep. of Germany, Vol. 6, pp. 347-352.

Theodossiou, V. M., Sousa, A. C. M., and Carlucci, L. N., 1988, "Flow Field Predictions in a Model Heat Exchanger," *Int. J. Computational Mechanics*, Vol. 3, pp. 419-428.

Van Doormaal, J. P., and Raithby, G. D., 1984, "Enhancements of the SIMPLE Method for Predicting Incompressible Fluid Flow," *Numer. Heat Transfer*, Vol. 7, pp. 147-163.

Zhang, C., and Sousa, A. C. M., 1989a, "Numerical Predictions of Steam Flow and Heat Transfer in a Condenser," in: *Numerical Methods in Thermal Problems*, R. W. Lewis and K. Morgan, eds., Pineridge Press, Swansea, United Kingdom, Vol. VI, Part 2, pp. 1368-1378.

Zhang, C., and Sousa, A. C. M., 1989b, "Comparison of Different Turbulence Models for Shell-Side Flow in a Model Heat Exchanger," *International Journal of Heat and Technology*, Vol. 7, No. 1, pp. 99-110.

Zhang, C., and Sousa, A. C. M., 1990, "Numerical Simulation of Turbulent Shear Flow in an Isothermal Heat Exchanger Model," ASME *Journal of Fluids Engineering*, Vol. 112, No. 1, pp. 48-55.

Zhang, C., Sousa, A. C. M., and Venart, J. E. S., 1991, "Numerical Simulation of Different Types of Steam Surface Condensers," ASME *Journal of Energy Resources Technology*, Vol. 113, pp. 63-70.

Zukauskas, A., Ulinskas, R., and Katinas, V., 1988, *Fluid Dynamics and Flow-Induced Vibrations of Tube Banks*, Hemisphere, New York, pp. 109-116.

Modeling of Temperature Distributions in the Workpiece During Abrasive Waterjet Machining

M. M. Ohadi

K. L. Cheng[1]

Center for Environmental Energy Engineering,
Department of Mechanical Engineering,
University of Maryland,
College Park, MD 20742

Modeling of temperature distributions in a block-type workpiece during cutting with an abrasive waterjet (AWJ) was the subject of an analytical/experimental investigation in the present study. The experiments included measurement of detailed time-temperature distributions in the workpiece for selected AWJ/workpiece operational parameters. Mathematical modeling of the problem made use of a two-part process. In the first part, the measured experimental data were fed into an inverse heat conduction algorithm, which determined the corresponding heat flux in the workpiece. In the second part, this heat flux was fed into a two-dimensional transient heat conduction model that calculated the corresponding temperature distributions in the workpiece. It is demonstrated that the proposed model can serve as a useful thermal analysis tool for AWJ cutting processes so long as a quasi-steady-state condition can be established in the workpiece.

1 Introduction

Material cutting using abrasive waterjets (AWJs) is a new technology that has found many industrial applications. Materials that can be cut include metals, hard rock, steel-reinforced concrete, glass, ceramics, super alloys, and many other hard-to-machine materials. Details of the technique, its applications and limitations can be found elsewhere (Hashish, 1984a, 1984b).

The technical and economical advantages of AWJs over traditional cutting techniques have initiated many analytical and experimental studies of the subject in the past decade. However, a comprehensive search of the literature failed to identify any previous study that had addressed the thermal aspects of AWJs. The mechanism is frequently referred to as a cold cutting technique, implying that no thermal effects are associated with the cutting process. This implication has been mainly on the basis that for most materials the workpiece temperature at the end of the cut is only a few degrees warmer than that of the human body. On the other hand, observation of sparks and steam generation at the cutting interface suggests the possibility of highly localized thermal effects for some materials. Such effects are particularly important for thermally sensitive materials (such as certain polycarbonates and plastic derivatives) in which temperatures as low as a few degrees above room value may alter their structural properties (Durelli and Riley, 1965).

The objective of the present combined experimental/analytical study was to develop a model that can predict temperature distributions in the workpiece as a function of various jet/workpiece operational parameters in an AWJ cutting process. Such a model will be particularly useful in identifying the appropriate AWJ operational parameters that prevent thermal damage to the workpiece during the cutting process.

The experimental work included measurement of detailed time-temperature distributions in the workpiece as a function of controlling parameters such as jet pressure, jet traverse speed, workpiece material, and the abrasive parameters. The experimental data were essential in the initial approach and final refinement of the mathematical modeling of the process. In designing the experiments the main objective was to collect data that were truly representative of the actual process. This required data collection in a workpiece that was exposed to a high-speed (Mach number up to 3), three-phase jet (water, abrasives, and air). Due to random distribution of water droplets and abrasives on the workpiece upon jet impingement, exact boundary conditions on the workpiece were not known. Moreover, material removal from the workpiece results in extraction of an unknown amount of energy from the workpiece, which adds to the complexity of a direct energy balance on the workpiece. Measurement of jet temperature before and after impingement is not practical either, as the excessively high jet velocities and the presence of randomly distributed abrasive particles in the jet preclude use of conventional measurement techniques. These factors limited the options that were available in mathematical modeling of the problem.

As will be shown, final modeling of the problem made use of a two-part process. In the first part, the measured experimental data were fed into an inverse heat conduction algorithm, which determined the corresponding heat flux in the workpiece. Next, this heat flux was used as an input to a two-dimensional transient heat conduction model that calculated the corresponding temperature distributions in the workpiece. Comparison of model predicted results with experimental data demonstrates that the model can be used as an effective thermal design analysis tool for AWJ processes so long as a two-dimensional quasi-steady condition can be established in the workpiece.

2 Experiments

Waterjet System. The main component of the experimental setup was an abrasive waterjet system, the essential components of which are shown in Fig. 1(*a*). The high-pressure water intensifier employed a 125 hp motor to drive a variable displacement hydraulic pump, which in turn drove two dual intensifier pumps, each capable of delivering water at pressures up to 380 MPa (≈55,000 psi). The high-pressure water from the intensifier was delivered to the orifice/nozzle assembly through high-pressure flexible hoses and swivel joints. The abrasive waterjet was formed by mixing abrasive particles with

[1]Present Address: Department of Mechanical Engineering, Massachusetts Institute of Technology, Cambridge, MA 02139.

Contributed by the Heat Transfer Division for publication in the JOURNAL OF HEAT TRANSFER. Manuscript received by the Heat Transfer Division June 1991; revision received September 1992. Keywords: Conduction, Materials Processing and Manufacturing Processes, Modeling and Scaling. Associate Technical Editor: H. R. Jacobs.

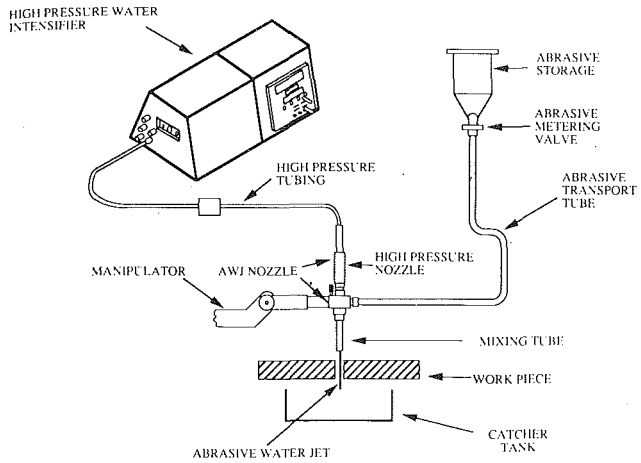

Fig. 1(*a*) Essential components of the abrasive waterjet system

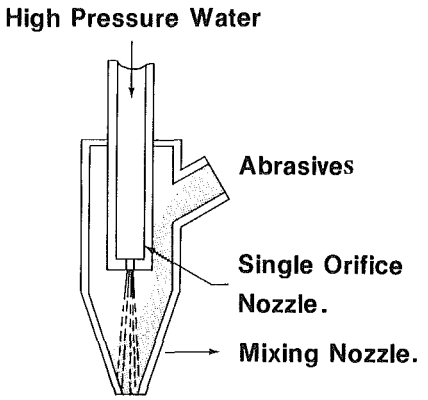

Fig. 1(*b*) Schematic of the orifice/nozzle assembly

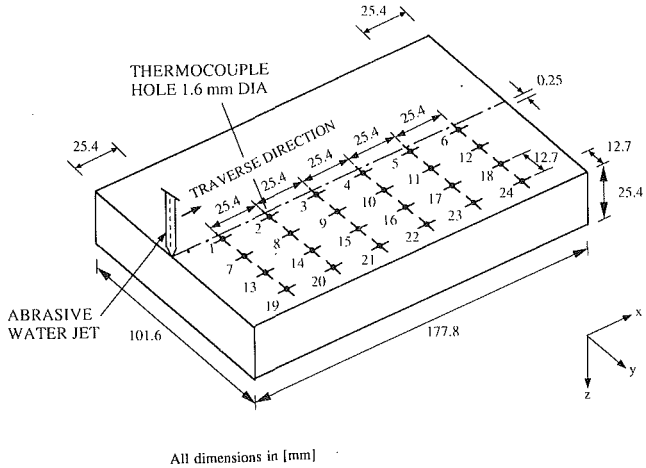

Fig. 2 Thermocouple positions in workpiece configuration No. 1

the high-pressure water jet in an orifice/nozzle assembly (Fig. 1(*b*)). Drawing of the abrasives into the mixing chamber was through the combined venturi and gravitational effects. Garnet (mesh size #80) was used as the abrasive material with a mass flow rate of 0.681 kg/min (1.50 lb/min).

In the mixing chamber, momentum transfer from water to the abrasive particles causes their rapid acceleration before being ejected into the mixing tube. In the present experiments the mixing tube (also referred to as the collimating tube) was a 76.2 mm (3.00 in.) long and 1.194 mm (0.047 in.) diameter tube. The purpose of this tube was to provide further mixing of the abrasives with the waterjet to form a highly coherent jet at the exit of the tube. The stand-off distance (distance between the exit of the collimating tube and the workpiece) was kept at 3.175 mm (0.125 in.) in all experiments At a pressure of 306 MPa (≈45,000 psi), the velocity of the jet at the exit of the mixing tube was approximately 700 m/s (≈2300 ft/s). Cutting or material removal takes place as a result of the erosive action of large number of impacts (up to 10^5/s) by the abrasives and the resulting excessive local stress deformation at the cutting interface.

Workpieces. Two different workpiece configurations were used in the present experiments. In the first configuration (Fig. 2) general temperature distributions in the workpiece were measured by instrumenting the workpiece with 24 thermocouples (type E, gage 30) embedded in four rows, each consisting of six thermocouples. The second workpiece configuration (Fig. 3) was designed to address the entry and exit zone effects on temperature distributions. As seen there, more closely spaced thermocouples were placed in the first row at the entry and exit zones of the workpiece. Due to highly transient nature of the process, it was imperative to install the first row of thermocouples as closely as possible to the cutting interface and with minimum contact resistance between the junction beads and the workpiece. To satisfy the first requirement, thermocouples were initially placed directly on the cutting interface so that the jet could cut through them. The aim was to capture the highest temperature experienced by a given thermocouple before it was cut by the jet. However, despite modifications made in the thermocouple electrical circuitry and the data acquisition system, the procedure resulted in erratic response

Nomenclature

AFR = abrasive flow rate
AWJ = abrasive water jet
C, C_1, C_2 = arbitrary constants
E = Euler number
$g(x, y)$ = an arbitrary function
h = workpiece thickness
i = position index
j = time index
$I_o(w)$ = modified Bessel function of the first kind of order zero
k = thermal conductivity
$K_o(w)$ = modified Bessel function of the second kind of order zero
$K_1(w)$ = first derivative of $K_o(w)$
$K(i, j, q)$ = gain coefficient
m = number of measurement points
n = number of future time steps
q = line heat source intensity, J/s
$\hat{q}$ = estimated heat flux, J/s
q^* = arbitrary heat flux, J/s
r = radial distance to the heat source
S = least-square function
t = time
T = temperature
T_o = surrounding temperature
$T(i, j, q)$ = calculated temperature
T.C. = thermocouple
u = jet traverse speed
w = dummy variable
$xyzt$ = moving coordinate system
$x'y'z't'$ = fixed coordinate system
$Y(i, j)$ = measured temperature
$Z(i, j, q)$ = sensitivity coefficient
α = diffusivity
ρ = density

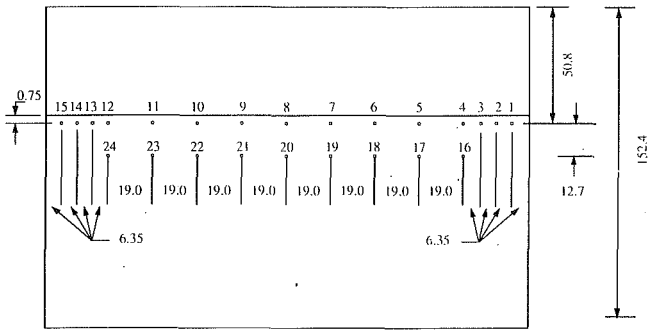

All dimensions in [mm]

Fig. 3 Thermocouple positions in workpiece configuration No. 2

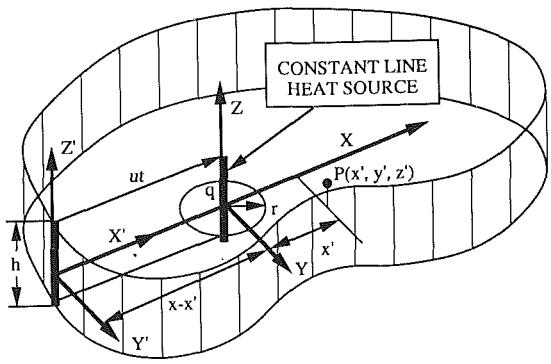

Fig. 4 Workpiece/jet coordinate system

and unstable readings of thermocouples. To avoid this problem, the first row of thermocouples was positioned slightly away from the cutting interface. However, the distance was kept short enough to minimize the difference between the actual and measured temperatures.

Mounting of thermocouples in the workpiece was through precisely drilled holes of 1.6 mm (0.0625 in.) diameter. The location, depth, and diameter of the thermocouple locating holes were kept within tight tolerances. For example, the center-to-center distance between the holes was kept within ± 0.051 mm (±0.002 in.). The remaining dimensions were kept within a tolerance of ±0.025 mm (±0.001 in.). To reduce the contact resistance between thermocouple junctions and the workpiece, holes were filled with a high-conductivity thermal paste (thermal conductivity of 2.31 W/(m·°C)). Thermocouples were held in place by a silicon-based adhesive, which also protected the junctions against seepage of water droplets or stream during the cutting process. A detailed description of the experimental apparatus and procedure is given by Ohadi et al. (1988).

Data Acquisition System. Collection and storage of the data took place with the aid of a microcomputer-based, high-speed data acquisition system (DAS). The DAS, under software control, sampled the thermocouple outputs at a rate of 10 KHz, resulting in a time period of only 2.4 ms to complete sampling of all the 24 thermocouples for a given scan. For the problem at hand, this time period was short enough to be thought of as a "thermal picture" of the workpiece at the instant of the scan. One thousand such scans were performed during each experimental run with a 72 ms pause time between successive scans. During a given experimental run, the collected data were stored in the computer RAM and saved permanently at the conclusion of the run. A combination of pre-amplification, analog, and digital filtering was used to eliminate electrical noise in the data acquisition process. Further details of the DAS and its accessories can be found from Ohadi and Whipple (1991).

3 Analysis

3.1 The Direct Heat Conduction Problem. In the developmental stages of the modeling process the AWJ was found best to correlate with a moving line heat source. On that basis, earlier studies in welding applications (Tsai, 1982) have shown that the convective and radiative components of heat transfer in such a problem for temperatures less than approximately 40°C are negligible. This assumption is found reasonable for the range of temperatures encountered in a typical AWJ machining process. The general energy equation for an isotropic and homogeneous material with constant properties and negligible heat losses then reduces to

$$\frac{\partial^2 T}{\partial x'^2}+\frac{\partial^2 T}{\partial y'^2}+\frac{\partial^2 T}{\partial z'^2}=\frac{1}{\alpha}\frac{\partial T}{\partial t'} \tag{1}$$

where α is the thermal diffusivity and $x'y'z'$ is the fixed coordinate system. Next, consider the jet as a moving line heat source q that travels with a constant velocity u in the fixed coordinate system $x'y'z't'$ from infinity perpendicularly toward the edge of a semi-infinite workpiece with thickness h (Fig. 4). If the source is assigned to the origin of the moving coordinate system $xyzt$, then transformation of a point $P(x', y', z', t')$ by $x=x'-ut'$ in the fixed system $x'y'z't'$ becomes $P(x, y, z, t)$ in the moving system $xyzt$. The transformed form of Eq. (1) then becomes

$$\frac{\partial^2 T}{\partial x^2}+\frac{\partial^2 T}{\partial y^2}+\frac{\partial^2 T}{\partial z^2}=\left(\frac{1}{\alpha}\frac{\partial T}{\partial t}\right)-\left(\frac{u}{\alpha}\frac{\partial T}{\partial x}\right) \tag{2}$$

Assuming the workpiece is long enough so that "quasi-steady-state" conditions can be established, and that the workpiece thickness is much smaller than its width and length so that temperature gradients in the z direction can be neglected, Eq. (2) reduces to

$$\frac{\partial^2 T}{\partial x^2}+\frac{\partial^2 T}{\partial y^2}=-\frac{u}{\alpha}\frac{\partial T}{\partial x} \tag{3}$$

Equation (3) can be solved using the separation of variables method assuming a solution of the form

$$T=T_o+\exp(-Cx)g(x, y) \tag{4}$$

in which T_o is the initial workpiece temperature and C is an arbitrary constant. The solution is available in the literature (Schneider, 1955) and is given as

$$T=T_o+\frac{q}{2\pi kh}\exp\left(-\frac{ux}{2\alpha}\right)K_o\left(\frac{ur}{2\alpha}\right) \tag{5}$$

In rectangular coordinates with $x=x'-ut$, this equation can be re-expressed as

$$T=T_o+\frac{q}{2\pi\, kh}\exp\left[\frac{u(x'-ut)}{2\alpha}\right]K_o\left[\frac{u\sqrt{(x'-ut)^2+y^2}}{2\alpha}\right] \tag{6}$$

The maximum temperature along the y axis can be found by setting $x=0$ in Eq. (5), resulting in

$$T_{\max,y}=T_o+\frac{q}{2\pi\, kh}K_o\left(\frac{u|y|}{2\alpha}\right) \tag{7}$$

Similarly, along the x axis ($y=0$, $x=r$) the maximum temperature reduces to

$$T_{\max,x}=T_o+\frac{q}{2\pi\, kh}\exp\left(-\frac{ux}{2\alpha}\right)K_o\left(\frac{u|x|}{2\alpha}\right) \tag{8}$$

The heat flux q in the above equations is an unknown quantity, which is determined using the inverse heat conduction tech-

nique described in the following section. The assumptions involved with Eqs. (5)–(8) include: a two-dimensional coordinate system with no radial effects, negligible heat loss from the plate due to convection or radiation, the source being a line heat source, and a quasi-steady condition in the workpiece.

3.2 The Inverse Heat Conduction Problem. Calculation of heat flux to the workpiece was through the use of a special Inverse Heat Conduction (IHC) method. The technique uses experimentally determined temperature histories in the workpiece to calculate the corresponding input heat flux for a given set of jet/system parameters. In handling the IHC problems several basic techniques have been suggested (Beck et al., 1985). For the present case, since temperature has a linear relationship with the heat flux q (Eqs. (5)–(8)), a parameter estimation approach (Beck and Arnold, 1977) with multiple temperature sensors and multiple time steps is selected. In order to reduce the sensitivity of the IHC technique to measurement errors while minimizing the computational requirements, a sequential time domain choice was selected over the whole time domain.

For m temperature sensors and n future time steps the typical thermocouple installation arrangements in Fig. 2 or 3 was found appropriate for the problem at hand. The relatively large number of thermocouples selected here combined with selection of small time steps serves to minimize the least-square errors S between the computed temperature $T(i, j, q)$ and the measured temperature $Y(i, j)$, defined as

$$S=\sum_{i=1}^{m}\sum_{j=1}^{n}[Y(i,j)-T(i,j,q)]^2 \tag{9}$$

The value of q minimizing S is then

$$\frac{\partial S}{\partial q}=\sum_{i=1}^{m}\sum_{j=1}^{n}[Y(i,j)-T(i,j,q)]\left[-2\frac{\partial T(i,j,q)}{\partial q}\right]=0 \tag{10}$$

where $\partial T(i, j, q)/\partial q$ represents the sensitivity coefficient $Z(i, j, q)$, which is defined as the first derivative of the dependent variable $T(i, j, q)$ with respect to the unknown parameter q,

$$Z(i,j,q)=\frac{\partial T(i,j,q)}{\partial q} \tag{11}$$

Equation (10) can then be rewritten as

$$\sum_{i=1}^{m}\sum_{j=1}^{n}[Y(i,j)-T(i,j,q)]\,Z(i,j,q)=0 \tag{12}$$

The Taylor series expansion about an arbitrary heat flux q^* is

$$T(i,j,q)=T(i,j,q^*)+(q-q^*)\frac{\partial T(i,j,q^*)}{\partial q}+\frac{(q-q^*)}{2!}\frac{\partial^2 T(i,j,q^*)}{\partial q^2}+\cdots. \tag{13}$$

The first derivative of Eq. (5) with respect to q evaluated at the arbitrary heat flux q^* is the sensitivity coefficient, given as

$$Z(i,j,q)=\frac{\partial T(i,j,q^*)}{\partial q}=\frac{1}{2\pi\, kh}\exp\left(-\frac{xu}{2\alpha}\right)K_o\left(\frac{ur}{2\alpha}\right) \tag{14}$$

Note that Eq. (14) is independent of q. That is, $Z(i, j, q)=Z(i, j, q^*)=Z(i, j)$. Hence, the problem is linear and will not require an iteration procedure. Moreover, the second and higher order derivatives in Eq. (13) are zero, reducing this equation to

$$T(i,j,q)=T(i,j,q^*)+(q-q^*)\frac{\partial T(i,j,q^*)}{\partial q} \tag{15}$$

Substitution of Eq. (15) into Eq. (12) yields

$$\sum_{i=1}^{m}\sum_{j=1}^{n}[Y(i,j)-T(i,j,q^*)]\,Z(i,j,q)-(q-q^*)\sum_{i=1}^{m}\sum_{j=1}^{n}Z(i,j,q)^2=0 \tag{16}$$

Rearranging and solving for q gives:

$$\hat{q}=q^*+\sum_{i=1}^{m}\sum_{j=1}^{n}[Y(i,j)-T(i,j,q^*)]\,K(i,j,q) \tag{17}$$

where

$$K(i,j,q)=\frac{Z(i,j,q)}{\sum_{i=1}^{m}\sum_{j=1}^{n}Z(i,j,q)^2} \tag{18}$$

is defined as the gain coefficient. In Eq. (17), $\hat{q}$ is the estimated heat flux and q is the calculated (or actual) heat flux. The quantity $T(i, j, q^*)$ is the temperature evaluated at the arbitrary heat flux q^*,

$$T(i,j,q^*)=\frac{q^*}{2\pi\, kh}\exp\left(-\frac{xu}{2\alpha}\right)K_o\left(\frac{ur}{2\alpha}\right) \tag{19}$$

Substituting Eq. (19) into Eq. (17) and making use of Eq. (14) yields the final form of estimated heat flux $\hat{q}$ as

$$\hat{q}=q^*+\sum_{i=1}^{m}\sum_{j=1}^{n}[Y(i,j,q)-(q^*Z(i,j,q))]\,K(i,j,q) \tag{20}$$

in which the sensitivity coefficient $Z(i, j, q)$ and the gain coefficient $K(i, j, q)$ are calculated from Eqs. (14) and (18), respectively.

4 Results and Discussion

The mathematical model was exercised for the base case workpiece configuration (Fig. 2) and parameters listed in Table 1. The first step in the analysis was to calculate the heat input to workpiece using the aforementioned inverse heat conduction technique. Table 2 presents the corresponding heat flux quantities at each of the four rows of the workpiece in Fig. 2. It is seen that the sensitivity of calculated heat flux to the time increment is minute.However, as the distance from the cutting interface increases, a gradual rise in heat flux values sets in. This is consistent with the suggestion that the accuracy of heat

Table 1 Workpiece/AWJ base case configuration parameters

Workpiece		
Material	steel 4041	
Density	7860 kg/m^3	[491 lbm/ft^3]
Thermal Conductivity	48.2 W/(m·K)	[27.85 Btu/(hr·ft·°F)]
Thermal Diffusivity	1.296 x 10^{-5} m^2/s	[13.95 x 10^{-5} ft^2/s]
Dimensions (length, width, thickness)	see Fig. 2	
Abrasive Waterjet		
Jet Pressure	310.3 MPa	[45,000 Psia]
Orifice diameter	0.457 mm	[0.018 in.]
Mixing tube length	7.62 mm	[3.0 in.]
Mixing tube I.D.	1.19 mm	[0.047 in.]
Abrasive material	Garnet	
Abrasive grain size	#80	
Abrasive flow rate	0.681 kg/min	[1.5 lb/min]

Table 2 Calculated heat flux for different rows and time increments

	Time Increment	Heat Flux [W]			
	[sec]	Row 1	Row 2	Row 3	Row 4
	0.14	92.32	98.13	100.30	109.91
	0.72	98.23	97.99	100.08	109.96
	1.44	98.11	98.01	100.12	109.93
	2.16	97.43	97.94	100.21	109.95
	2.88	96.08	98.36	100.68	109.96
	3.60	95.06	98.34	100.20	109.93
Average	1.82	96.20	98.12	100.26	109.93

flux estimation procedure in most IHC techniques decreases with increasing distance from the moving heat source (Beck, 1961).

The average heat flux of the first row (96.2 W) was then fed into the direct heat conduction model to calculate temperature distributions in the workpiece. Results for rows 1 and 2 of the workpiece in Fig. 2 are shown in Figs. 5(*a*) and 5(*b*), respectively. Using the Kline–McClintock (1953) method the compounded uncertainty in the measured temperatures was calculated to be ±6.8 percent. However, in addition to the uncertainty in the average estimated heat flux, another primary factor in the deviation between experiments and model predicted results in Figs. 5(*a*) and 5(*b*) can be attributed to the procedure by which the experimental data reduction was performed. During a given experimental run 1000 data points were collected for each thermocouple. However, to preserve the clarity of figures, the experimental data reported here represent one out of every ten data points. On the average, this was found to introduce approximately an additional 5 percent uncertainty. Therefore, the compound uncertainty reported in Figs. 5(*a*) and 5(*b*) is ±8.5 percent.

From Figs. 5(*a*) and 5(*b*), it is seen that the agreement between experimental and model predicted results degrades as the distance from the cutting interface increases. This is consistent with the heat flux results in Table 1 discussed earlier. However, the main objective of a thermal analysis on the workpiece in an AWJ cutting process is prediction of maximum temperatures so that material failure can be avoided. Moreover, because temperatures closest to the cutting interface are used to estimate the heat flux, temperature distributions in rows 2–4 should be of minimum interest from a practical point of view.

To quantify the entry and exit zone effects, temperature measurements similar to those presented in Fig. 5 were performed for the workpiece in Fig. 3. From these experiments it was found (Cheng, 1990) that the entry and exit zone lengths represented approximately the first 20 seconds into the run which, at a traverse speed of 7.62 cm/min (3 in./min), translated into the first 2.54 cm (1 in.) in the workpiece. With the workpiece thickness of 2.54 cm (1 in.) in the present experiments, this in turn represents an entry or exit length equivalent to one workpiece thickness. As expected, because a Taylor series expansion around a quasi-steady solution was employed for the entry and the exit zones (thermocouples No. 1–4 and 12–15 in Fig. 3) the agreement between the measured and model predicted results was poor. For all other locations, the agreement was satisfactory and the general trends observed in Fig. 5 were confirmed.

Comparison of experimental and model predicted temperatures for column 3 (positions No. 3, 9, 15, and 21) of the workpiece in Fig. 2 is presented in Fig. 6. The results confirm the general trends observed in Figs. 5(*a*) and 5(*b*). As expected, maximum temperatures take place in the first row and decay sharply thereafter with increasing distance from the cutting interface. It is interesting to note that only the first and second

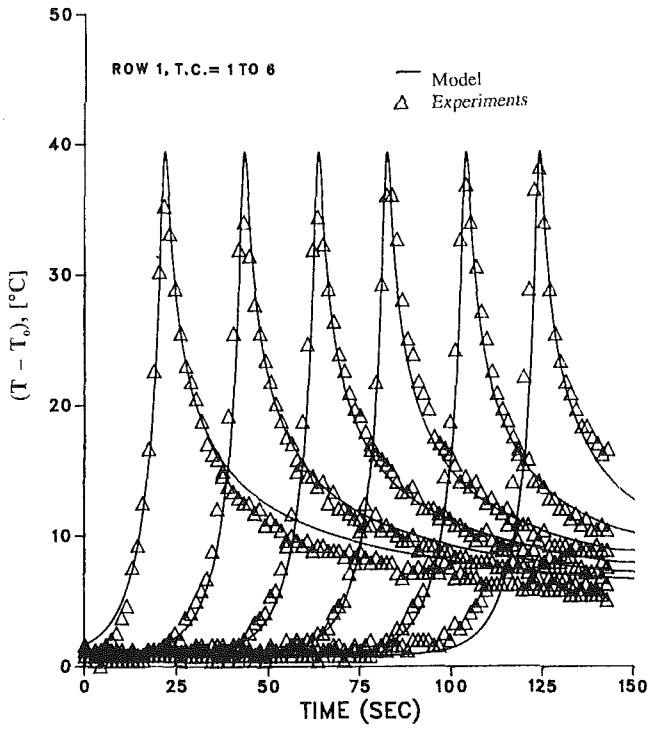

Fig. 5(*a*)

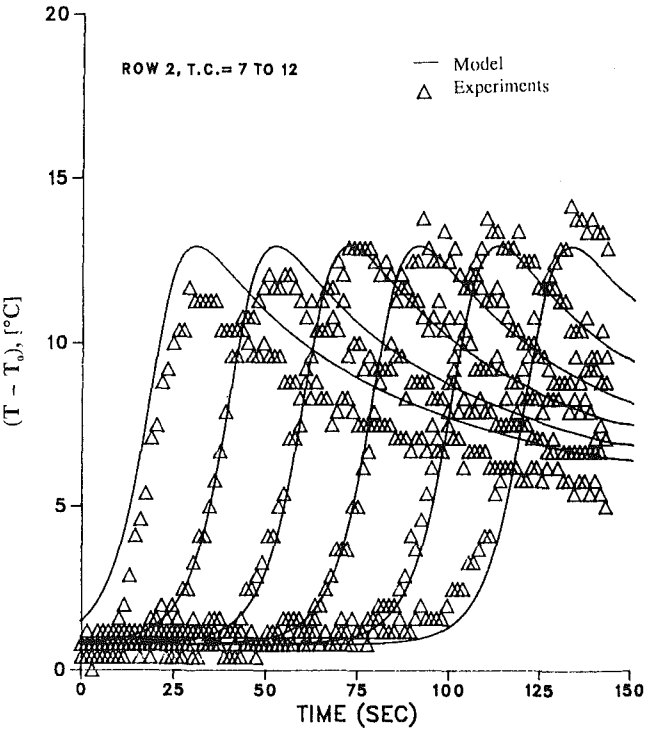

Fig. 5(*b*)

Fig. 5 Comparison of calculated and experimental temperature distributions

rows experience a sharp peak point and a subsequent drop-off portion. Those farther away from the cutting interface experience a much more moderate rise and a corresponding gradual decay to the quasi-steady state level as the cutting process proceeds to its completion.

Attention is next drawn to Fig. 7, which conveys a three-dimensional presentation of temperature distribution in the

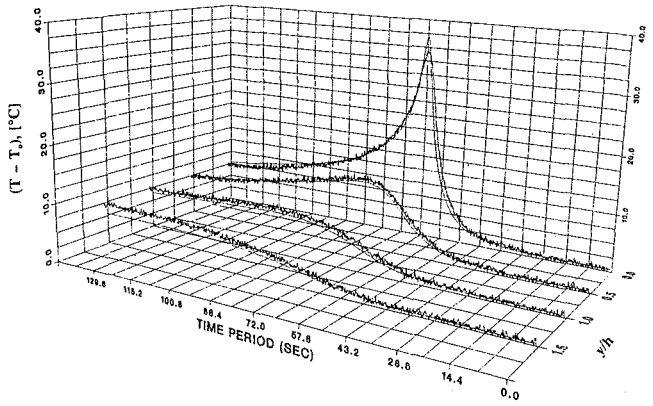

Fig. 6 Temperature distributions for column 3 of the workpiece in Fig. 2

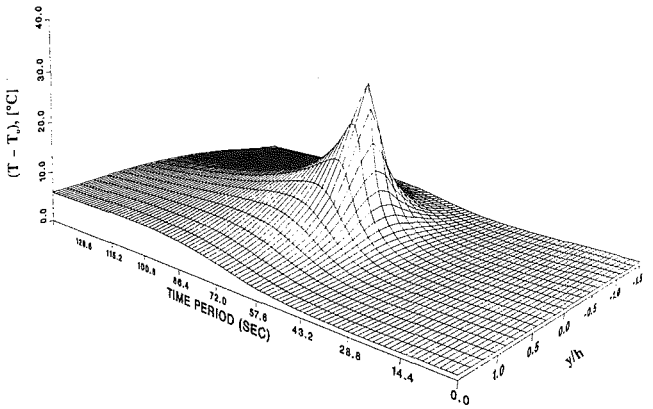

Fig. 7 Three-dimensional presentation of temperature distribution in the workpiece

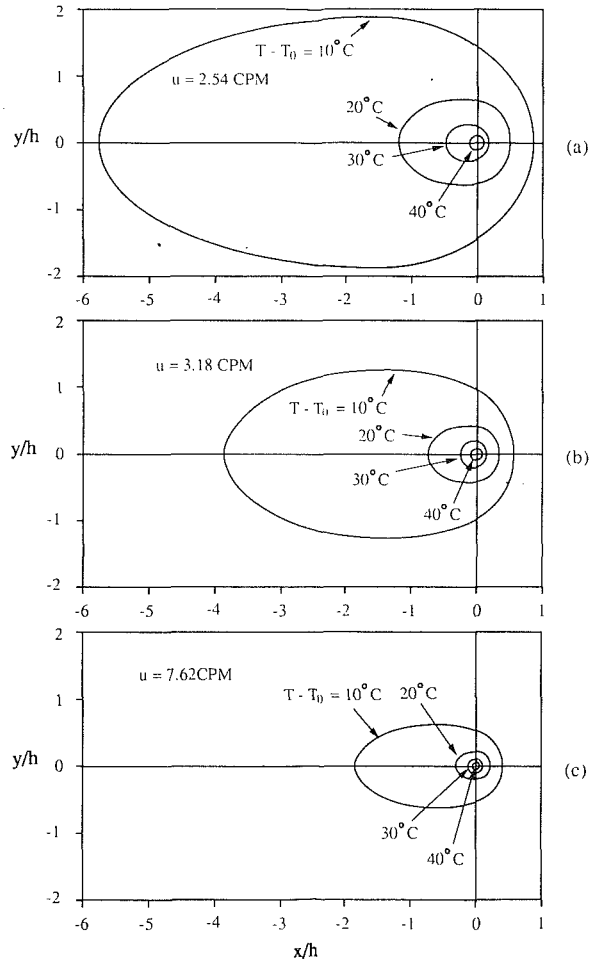

Fig. 8 Effect of traverse speed on temperature distributions in the workpiece

workpiece for position number 4 of the workpiece in Fig. 2. The thermocouple position can be thought of as the site of an observer who monitors the jet from the time it enters the workpiece until completion of the cut. At distances far away from the moving heat source, the observer does not feel any significant temperature rise in his surroundings, as represented by a modest temperature rise in the first 30 seconds in Fig. 7. Thereafter, the jet enters the "sensing zone" where a corresponding temperature rise is experienced. The temperature reaches its peak at the point where the jet passes by the observer. As the jet moves away from the observer, a sharp decay in temperatures and an approach toward quasi-steady-state conditions is observed.

5 Parametric Studies

Once the heat flux to the workpiece is determined, parametric studies similar to those demonstrated in Fig. 8 can be performed. Effect of jet traverse speed on temperature distributions in the workpiece at three different traverse rates is presented in this figure. Here $y/h>0$ and $y/h<0$ correspond, respectively, to the distance ahead of and behind the jet in the moving coordinate system x, y, z. From an overview of Fig. 8 two general observations can be made. First, at the immediate vicinity of the jet temperature contours approach the contour of the heat wave from a stationary jet, which is a family of concentric circles. With increasing distance from the jet, temperature contours approach a family of ellipses with steeper temperature gradients corresponding to the areas ahead of the jet ($y/h>0$).

The second observation in Fig. 8 is that a lower traverse speed results in a higher heat input to the workpiece. This can be attributed to the larger number of abrasive particle impacts per unit traverse length of the workpiece at a lower jet traverse rate. A larger number of abrasive impacts in turn is associated with higher viscous dissipation of the jet at the cutting interface, thus higher jet-induced heat transfer rates.

6 Conclusions

The combined experimental/analytical work presented here appears to be the first systematic study of thermal energy distributions in the workpiece during cutting with an abrasive waterjet. It was shown that due to the complexity of the process, the thermal energy input to the workpiece was an unknown quantity and had to be determined experimentally using an inverse heat conduction technique. Next, using this heat flux, temperature distributions in the workpiece were determined by modeling the AWJ as a moving heat source. Comparison with experimental results indicated a satisfactory agreement between the two sets. The exception to this was in the entry and exit zones where a poor agreement between model-predicted results and those of the experiments is observed. It was demonstrated that maximum temperatures are found at the immediate vicinity of the cutting interface and decay rapidly thereafter with increasing distance from the interface. Although the average workpiece temperature at the end of the cut was close to the room value, much higher local temperatures were experienced at the cutting interface. The insufficiency of the model in its present stage is its inability to predict temperatures accurately at the entry and exit zones. Tests for different materials and for a wide range of workpiece/jet operating conditions are needed to identify additional limitations/applicability of the model. From a practical point of

view, the model can serve as a useful thermal analysis tool so long as a two-dimensional quasi-steady-state condition can be established in the workpiece.

Acknowledgments

Financial support of this work in part by the National Science Foundation and Quest Integrated Inc. (formerly Flow Research, Inc. is gratefully acknowledged. Special thanks are due Dr. M. Hashish (Quest Integrated, Inc.) and Dr. A. I. Ansari (University of Maryland) for their helpful suggestions in the experimental part of this study.

References

Beck, J. V., 1961, "Correction of Transient Thermocouple Temperature Measurements in Heat Conduction Solids, Part II, The Calculation of Transient Heat Fluxes Using the Inverse Convolution," AVCO Corp. Technical Report RAD-TR-7-60-38, Part II.

Beck, J. V., and Arnold, K. J., 1977, *Parameter Estimation in Engineering and Sciences*, Wiley, New York.

Beck, J. V., Blackwell, B., and St. Clair, C. R., 1985, *Inverse Heat Conduction Ill-Posed Problems*, Wiley, New York.

Cheng, K. L., 1990, "Analytical and Experimental Study of Thermal Energy Transfer in a Workpiece During Cutting With an Abrasive Waterjet," M. S. Thesis, Michigan Technological University, Houghton, MI.

Durelli, A. J., and Riley, W. F., 1965, *Introduction to Photomechanics*, Prentice-Hall, New York, pp. 116–160.

Hashish, M., 1984a, "Cutting With Abrasive-Waterjets," *Mechanical Engineering*, Jan., pp. 69–69.

Hashish, M., 1984b, "A Modeling Study of Metal Cutting With Abrasive Waterjets," ASME *Journal of Engineering Materials and Technology*, Vol. 106, No. 1, pp. 88–100.

Kline, S. J., and McClintock, F. A., 1953, "Describing Uncertainties in Single-Sample Experiments," *Mechanical Engineering*, Vol. 75, Jan., pp. 3–8.

Ohadi, M. M., Ansari, A. I., and Hashish, M., 1988, "An Experimental Study on the Role of Thermal Energy Transfer in Material Removal Processes," in: *3rd International Symposium on Liquid–Solid Flows*, M. C. Roco, ed., ASME FED-Vol. 75, pp. 153–160.

Ohadi, M. M., and Whipple, R. L., 1991, "Measurement of Transient Temperatures in a Tubular Workpiece During Cutting With an Abrasive Waterjet," *SEM Transaction, J. Experimental Techniques*, Vol. 15, No. 4, pp. 38–42.

Rosenthal, D., 1946, "The Theory of Moving Heat Sources of Heat and Its Applications to Metal Treatments," *Trans. ASME*, Vol. 68, pp. 849–866.

Schneider, P. J., 1955, *Conduction Heat Transfer*, Addison Wesley, Reading, MA.

Tsai, C. L., 1982, "Modeling of Thermal Behaviors of Metals During Welding," *Trends in Welding Research*, ASME, New York, p. 91.

Thermal Analysis of the Hot Dip-Coating Process

Hui Zhang

M. Karim Moallemi

Sunil Kumar

Department of Mechanical and Industrial Engineering, Polytechnic University, Brooklyn, NY 11201

In this study a thermal analysis is performed on the hot dip-coating process where solidification of metal occurs on a bar moving through a finite molten bath. A continuum model is considered that accounts for important transport mechanisms such as axial heat diffusion, buoyancy, and shear-induced melt motion in the bath. A numerical solution procedure is developed, and its predictions are compared with those of an analytical approximate solution, as well as available experimental data. The predictions of the numerical scheme are in good agreement with the experimental data. The results of the approximate solution, however, exhibit significant disagreement with the data, which is attributed to the simplifying assumptions used in its development. Parametric effects of the bath geometry, and initial and boundary temperatures and solid velocity, as characterized by the Reynolds number, Grashof number, and Stefan numbers, are presented.

Introduction

The hot-dip coating process has been utilized extensively during the last few decades in the manufacturing and cladding of wire, and galvanizing and coating of metal strips, sheets, and wires (for example, see Prior and Tonini, 1984; Cook et al., 1986). Applications of closed-loop computer controls have made this process more attractive by improving product consistency and reducing excessive use of coating material (Townsend and Bilski, 1988). Recently, fabrication of tapers, lenslike waveguides, and mono- and multilayer antireflection coatings has renewed interest in the dip-coating technology, where micro-controlled processes are envisioned that would permit precise control of the complex spatial variations of coating thickness (Herrmann and Wildmann, 1983; Tiefenthaler et al., 1983). In spite of the broad range of applications, a fundamental understanding of the process heat and mass transfer mechanisms involved during the solidification over a moving surface in a finite bath is not available.

The dip-coating process has its roots in dip-forming, which is a continuous casting process (Carreker, 1963). The objective of the parent process (dip-forming) is to produce moldless castings, which is achieved by pulling a cold wire, rod, or strip through a molten bath of similar metal. Optimal process utilization is achieved when the overall solidification is maximized, and sophisticated modeling of the heat transfer mechanisms has therefore not been necessary. Horvay (1965) modeled this process by using simple thermal resistance network analysis in a laterally unbounded bath and obtained comparisons with experimental results to within 10 percent.

In the dip-coating process the objective is to coat wires, rods, or plates with layers of different materials of controlled thickness. Thus it is essential to have an in-depth understanding of the heat transfer mechanisms involved in the process to predict and control the coating thickness. However, there are no published works in the area of hot dip-coating that address these issues, and a few relevant studies are based on oversimplified models. Seeniraj and Bose (1981) performed an analysis of freeze-coating of polymeric materials over a moving metallic substrate by assuming the temperature of the metallic object to remain constant and uniform, and the molten bath to be at its melting temperature. The first assumption is physically incorrect while the second limits the analysis to the one considered. Cheung (1985) analyzed freeze coating on a flat plate where constant plate temperature and saturated liquid temperature conditions were relaxed. Whereas Seeniraj and Bose (1981) predicted a monotonic increase of coating thickness over the plate, Cheung (1985) was able to predict initial deposition followed by remelting. However, both of these studies cannot be rigorously used for analyzing dip-coating since they assume the existence of leading edges for the solidification front as well as for the melt flow. In doing so the effects of bath geometry are ignored.

The modern applications of dip-coating require sophisticated modeling of heat and mass transfer in a finite molten bath where important effects such as axial diffusion, buoyancy, and shear-induced melt flow must be included. The present paper describes a model developed to predict the transient solidification process over a circular rod being pulled through a melt pool at a constant speed. The temperature distributions in the solid and melt, as well as the flow field in the melt, are calculated for different initial temperatures of the rod and its Reynolds number. The influence of the natural convection in the melt pool, subcooling of the solid entering the bath, and the superheating of the melt entering the bath on the rod radius profile are also investigated and reported. The role of the geometric parameters, namely, the radius and depth of the melt pool scaled by the rod radius, are also investigated. An approximate solution is also developed based on the energy integral method and presented in the appendix. The predictions of the numerical scheme are found to be in good agreement with the experimental data. The results of the approximate solution, however, exhibit significant disagreement with the data, particularly at greater axial positions in the bath, which is attributed to the simplifying assumptions used in its development.

Analysis

The dip-coating system is schematically depicted in Fig. 1. A metal rod of inlet temperature T_{si} and radius r_{si} is pulled at speed U_s through the bath of a molten metal. As the cold rod enters the bath, a rapid solidification of metal on the rod occurs, which may be followed by melt-out if the bath is of a great height or if the velocity of the rod is small. A semi-analytical seminumerical approximate solution for the problem is included in the appendix, and here; after a short review of possible numerical approaches, the mathematical model used and solution procedure adopted are explained.

The dip-coating process, like other solidification processes, can be modeled via two different approaches. The first and

Contributed by the Heat Transfer Division and presented at the National Heat Transfer Conference, Minneapolis, Minnesota, July 28-31 1991. Manuscript received by the Heat Transfer Division, June 1992; revision received September 1992. Keywords: Materials Processing and Manufacturing Processes, Moving Boundaries, Phase-Change Phenomena. Associate Technical Editor: Y. Bayazitoglu.

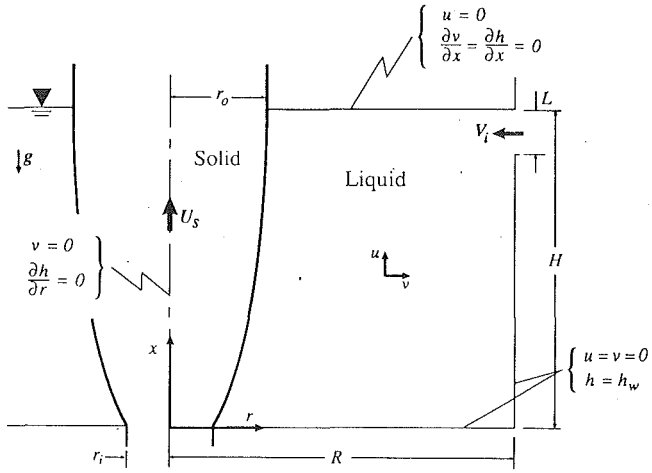

Fig. 1 Schematic diagram of the hot dip-coating system

more traditional approach uses conservation equations for each phase that are coupled through the energy balance at the interface. The location of the solid–liquid interface, however, is not known *a priori* and has to be obtained as a part of the solution. The numerical implementation of this approach requires a quasi-steady approximation for the interface motion, along with either coordinate remapping schemes or adaptive grid transformations (Moallemi and Viskanta, 1986). In the second approach, the continuum formulation, one set of conservation equations are developed for the entire region. This is achieved by introducing volume averaging of the conservation equations for the two phases and by writing the energy equation in terms of enthalpy, which eliminates temperature as a dependent variable of the problem (Shamsundar and Sparrow, 1975; Prandtl and Dawson, 1983; Bennon and Incropera, 1987). The single region formulation eliminates the need for tracking the interface via an auxiliary equation, i.e., energy balance at the interface, there by facilitating numerical implementation.

For solidifications of mixtures, where no distinct interface between the two phases is present, the value of h is related to the mass fraction f_s of material solidified in the two-phase (mushy) zone. The solid mass fraction varies continuously between 0 and 1 in this zone. In solidification of a pure substance, however, the presence of a multiphase (mushy) zone is precluded. The mass fraction of the solidified matter is thus a discontinuous function in space and takes the discrete values of zero and unity. When the governing equations are converted to finite difference equations, the mass fraction indicates the fraction of material solidified in the individual control volumes or elements. The mass fraction is either zero or unity except in the control volume containing the interface. This approach has been successfully employed in the modeling of different solidification processes such as solidification of binary mixture over vertical surfaces (Christenson et al., 1989) and solidification of pure substance in absence of convective effects (Prandtl and Dawson, 1983). The continuum formulation can introduce "smearing" of the interface due to the presence of control volumes with nondiscrete mass fractions. This is avoided in the continuum approach adopted in the present study by introducing fine mesh sizes in the interface region and by other numerical steps discussed in the following sections.

To formulate the problem, it is assumed that the melt behaves like a Newtonian fluid; and its flow is two dimensional, axisymmetric (r, z), and laminar. Local thermodynamic equilibrium is assumed, and the thermophysical properties are taken to be invariant to temperature with the exception of density in the buoyancy term (Boussinesq approximation). Changes in thermal conductivity and heat capacity with change of phase are accounted for, but mass densities of the melt and its solid are assumed to be the same (i.e., no volumetric change upon phase change). The phase change of a pure substance with a precise fusion and freezing temperature is modeled. In simulations that include the melting of the moving substrate, the bath and substrate materials are assumed to be the same, so that no species transport equation has to be solved. These assumptions do not exclude situations that the solid substrate and bath (coating) materials are not the same, and only the solidified coat goes through remelting.

With these assumptions, the problem is governed by continuum conservation equations for mass, momentum, and energy, which are written as follows (Bennon and Incropera, 1987):

$$\nabla \cdot (\rho \mathbf{V}) = 0, \tag{1}$$

$$\frac{\partial(\rho u)}{\partial t} + \nabla \cdot (\rho \mathbf{V} u) = \nabla \cdot (\mu \nabla u) - \frac{\partial P}{\partial x} + f_l \rho g \, \beta (T - T_f), \tag{2}$$

$$\frac{\partial(\rho v)}{\partial t} + \nabla \cdot (\rho \mathbf{V} v) = \nabla \cdot (\mu \nabla v) - \frac{\partial P}{\partial r}, \tag{3}$$

$$\frac{\partial(\rho h)}{\partial t} + \nabla \cdot (\rho \mathbf{V} h) = \nabla \cdot \left(\frac{k}{c_s} \nabla h\right) + \nabla \cdot \left(\frac{k}{c_s} \nabla (h_s - h)\right) - \nabla \cdot [f_s \rho (h_l - h_s)(\mathbf{V} - \mathbf{V}_s)]. \tag{4}$$

Here u and v are the components of the mass averaged velocity vector $\mathbf{V}$ defined as

$$\mathbf{V} = f_l \mathbf{V}_l + f_s \mathbf{V}_s, \tag{5}$$

Nomenclature

c = heat capacity
f = mass fraction
g = gravitational acceleration
Gr = Grashof number = $g\beta H^3 (T_w - T_f)/\nu_l^2$
h = enthalpy
h_f = latent heat of fusion
H = melt height in the bath
L = height of the melt inlet port
p = pressure (isotropic stress component)
Pr = Prandtl number = ν_l/α_l
r, x = radial and axial coordinates, Fig. 1
r_s = rod radius
R = bath radius
Re = Reynolds number = $U_s H/\nu_l$
Ste_l = liquid Stefan number = $c_l (T_w - T_f)/h_f$
Ste_s = solid Stefan number = $c_s (T_f - T_{si})/h_f$
t = time
T = temperature
u, v = velocity components in axial and radial directions
U_s = velocity of the solid rod
$\mathbf{V}$ = velocity vector
V_i = melt inlet velocity
α_l = thermal diffusivity of melt = $k_l/\rho c_l$
α_s = thermal diffusivity of solid = $k_s/\rho c_s$
Θ = dimensionless temperature = $(T - T_f)/(T_w - T_f)$
κ = thermal conductivity ratio = $(f_s k_s + f_l k_l)/k_l$
ν = kinematic viscosity
ρ = mass density

Subscripts

f = fusion
i = inlet
l = liquid
o = outlet
s = solid
w = wall

with f_l and f_s being the mass fractions of liquid and solid, respectively. It should be noted that as the densities of the two phases are assumed to be equal, mass fractions of the phases are identical to their corresponding volume fractions. The continuum viscosity μ is expressed as the harmonic mean of the phase viscosities as follows:

$$\mu = \left(\frac{f_l}{\mu_l} + \frac{f_s}{\mu_s}\right)^{-1} = \frac{\mu_l}{f_l}. \tag{6}$$

The last equality is obtained by substituting $\mu_s = \infty$. This equation yields appropriate limits in the pure liquid ($\mu = \mu_l$) and pure solid ($\mu = \mu_s = \infty$) regions. The equation for conservation of energy, Eq. (4), is expressed in terms of the continuum enthalpy h, defined as

$$h = h_s + f_l\,(h_l - h_s), \tag{7}$$

where, in general, the phase enthalpies are related to temperature by

$$h_s = c_s T,\ h_l = c_l T + T_f\,(c_s - c_l) + h_f. \tag{8}$$

The mass averaging defines the continuum thermal conductivity as

$$k = f_s k_s + f_l k_l. \tag{9}$$

The liquid mass fraction is defined as

$$f_l = \begin{cases} 0 & h \le c_s T_f \\ (h - c_s T_f)/h_f & c_s T_f < h < c_s T_f + h_f \\ 1 & h \ge c_s T_f + h_f \end{cases}. \tag{10}$$

It should be noted that even though the phase mass fractions should either be zero or unity for solidification of a pure substance, a nondiscrete distribution of phase mass fraction has to be defined for the control volumes containing the interface in the finite difference formulation. In the same context, the last term in the energy equation, Eq. (4), which represents the energy flux associated with the relative phase motion, has been retained in the numerical formulation of the problem. This term, which is identically zero in the solid or liquid regions, provides an accurate account of energy exchanges in the control volumes that contain the interface.

A two-dimensional axisymmetric dip-coating process under continuous operation is considered. The problem is a steady-state (with respect to a coordinate system fixed to the bath), but is cast in time-dependent form for convenience in the numerical implementation. The initial conditions are arbitrary and are taken to be such that the melt bath and the rod are at rest and at the fusion temperature of the phase-change material. At the initiation of the numerical simulation the temperature of the bath walls is changed to a prescribed value T_w, and a fresh rod is introduced into the bath with a constant vertical velocity U_s and a uniform temperature T_{si}. The height of the melt bath H is kept constant during a simulation by compensating for the melt removed from the bath via solidification on the rod. Liquid phase-change material, at T_w, is introduced into the bath from a port on its wall with a velocity

$$V_i = U_s(r_{so}^2 - r_{si}^2)/(2RL), \tag{11}$$

where r_{so} is the radius of the solid rod as it exits from the bath. The height of the port L is adjusted in different simulations such that the velocity of melt entering the bath is not greater than 10 percent of the solid velocity. Other boundary conditions of the problem, as shown in Fig. 1, are no-slip impermeable solid surfaces, and constant temperature on the bath walls. An adiabatic boundary condition at the bottom of the bath is also examined for comparison. The free surface of the bath is planar and adiabatic.

The governing equations are nondimensionalized using the following dimensionless variables:

$$(x^*, r^*) = (x, r)/H,\quad t^* = tU_s/H,\quad P^* = P/(\rho U_s^2),$$
$$\mathbf{V}^* = \mathbf{V}/U_s,\quad (u^*, v^*) = (u, v)/U_s,\quad \nabla^* = H\nabla,$$
$$\Theta = (T - T_f)/(T_w - T_f),\quad h^* = (h - c_s T_f)/h_f.$$

The transformed dimensionless equations are:

$$\nabla^* \cdot \mathbf{V}^* = 0, \tag{12}$$

$$\frac{\partial u^*}{\partial t^*} + \nabla^* \cdot (\mathbf{V}^* u^*) = \nabla^* \cdot \left(\frac{1}{f_l\,\mathrm{Re}} \nabla^* u^*\right) - \frac{\partial P^*}{\partial x^*} + f_l \frac{\mathrm{Gr}}{\mathrm{Re}^2}\,\Theta, \tag{13}$$

$$\frac{\partial v^*}{\partial t^*} + \nabla^* \cdot (\mathbf{V}^* v^*) = \nabla^* \cdot \left(\frac{1}{f_l \mathrm{Re}}\,\nabla^* v^*\right) - \frac{\partial P^*}{\partial r^*}, \tag{14}$$

$$\frac{\partial h^*}{\partial t^*} + \nabla^* \cdot (\mathbf{V}^* h^*) = \nabla^* \cdot \left(\frac{\kappa}{\mathrm{RePr}}\,\frac{c_l}{c_s}\,[\nabla^* h^* + \nabla^*\,(h_s^* - h^*)]\right) - \nabla^* \cdot (f_s (h_l^* - h_s^*)\,(\mathbf{V}^* - \mathbf{V}_s^*)). \tag{15}$$

These equations reveal that the problem is characterized by dimensionless numbers Re, Gr, and Pr, which are all based on liquid properties, the ratio of specific heats of the two phases c_l/c_s, and the ratio of the thermal conductivity of the continuum to that of the liquid κ. The dimensionless boundary conditions introduce the dependence on the solid and liquid Stefan numbers, i.e., the solid rod enters the bath at

$$h^* = -\mathrm{Ste}_s, \tag{16}$$

and the bath walls are at

$$h^* = 1 + \mathrm{Ste}_l. \tag{17}$$

The dimensionless boundary conditions also add two geometric parameters, namely, $r_{si}^* \equiv r_{si}/H$ and $R^* \equiv R/H$, to the list of governing parameters of the problem.

Method of Solution

The continuum formulation, Eqs. (12)–(15), is valid throughout the entire solution domain; therefore, explicit consideration need not be given to internal boundaries between the solid and liquid phases. An elliptic control volume based finite difference scheme (Patankar, 1980) has been used to solve the continuum equations. The sequence of numerical operations is identical to that used to solve conventional single phase problems (Patankar, 1980). Coupling that exists between the energy and momentum equations is accommodated through iteration and underrelaxation.

A series of grid sensitivity runs were peformed on nonuniform grid ranging from 22 × 22 to 52 × 52, which suggested that grid independent results could be obtained using 42 × 42 grid. Very fine grid mesh was used near the top and bottom surfaces of the bath to resolve the large velocity and temperature gradients. The grid lines were also clustered near the solidification interface to reduce the smearing effect caused by the continuous variation of the solid mass fraction.

The numerical experiments indicated that improper choice of the grid aspect ratio could increase the smearing effect at the interface, particularly if the Δx's were very large or the Δr's were very small to make the interface straddle more than one control volume at each vertical location x. Therefore, the grid was chosen such that the interface was always contained in only one control volume at vertical location. In other words, the mass fraction f_s in only one horizontal control volume, adjacent to the one with $f_s = 1$, is allowed numerically to be nondiscrete at each vertical location. The mass fraction was examined throughout any numerical simulation, and if this condition was violated, the simulation would be terminated, and then restarted with a new grid system with smaller Δx.

Table 1 Experimental data

Thermophysical Properties			Operating Conditions		
$\rho_l = \rho_s$	kg/m^3	8.0×10^3	H	m	0.0508
$c_l = c_s$	$J/kg\cdot K$	420.0	r_{si}	m	0.0039
k_s	$W/m\cdot K$	390.0	U_s	m/s	0.15
k_l	$W/m\cdot K$	120.0	T_{si}	°C	25.0
ν_l	m^2/s	6.27×10^{-7}	T_w	°C	1140.0
T_f	°C	1085.0			
h_f	J/kg	2.1×10^5			
β	K^{-1}	1.8×10^{-4}			
Pr		0.015			

As mentioned earlier, although a steady-state solution was sought, the problem was cast in time-dependent form for numerical convenience. The initial conditions are arbitrary and were typically taken to be fully developed flow with the melt and the moving solid at the fusion temperature, and the simulation of the process started by imposing the thermal boundary conditions. The fully implicit form of discretized equations were solved iteratively. The time marching calculations were conducted over time steps which were initially small ($\Delta t^* = 0.1$) and were increased gradually ($\Delta t^*_{\max} = 5.0$) as the solution developed. At any time step the solution is considered converged if

$$\frac{|\psi^{n+1}(i,j) - \psi^n(i,j)|}{\text{Max}|\psi^{n+1}(i,j)|} < 10^{-3}, \tag{18}$$

where n is the iteration loop counter and ψ is u^*, v^*, or h^*. The number of iterations required during the early stages of any simulation was about 80, which decreased as the solution developed. When the criteria of Eq. (18) were satisfied, the residual source of mass, momentum, and energy was less than 10^{-7} for all the cases examined. The solution was considered the steady-state one when the change at any point on the solid–melt interface was less than 0.1 percent over a time step.

Results and Discussion

Before proceeding with a parametric study, the validity of the numerical model is verified by comparing its predictions with the experimental data of Carreker (1963) who examined coating of pure copper on a copper rod. The limitation of an approximate solution, which is presented as an appendix for the sake of continuity in the text, is also examined by comparing its results with the experimental data. The representative thermophysical properties of the material used in the experiments and the operating conditions are presented in Table 1.

The variation of the rod radius in the bath calculated by the numerical simulation of the experiments is shown in Fig. 2 and is compared with those of the original experiment. The prediction of the approximate solution procedure is also presented in the figure for comparison. It should be noted that the experiments by Carreker were conducted on baths of different melt depth for different solid (pull) speeds. The results were presented in terms of casting ratio (cast weight after emerging over input weight) versus immersion time (calculated from the bath depth and the pull speed). The experimental data presented in Fig. 2 are all for the same solid velocity, but different bath depths, and are plotted against the dimensionless position in the bath, as presentation versus the immersion time would have confused the steady-state feature of the data and calculations. For the numerical results, at each of the 42 axial positions corresponding to the center of the computational

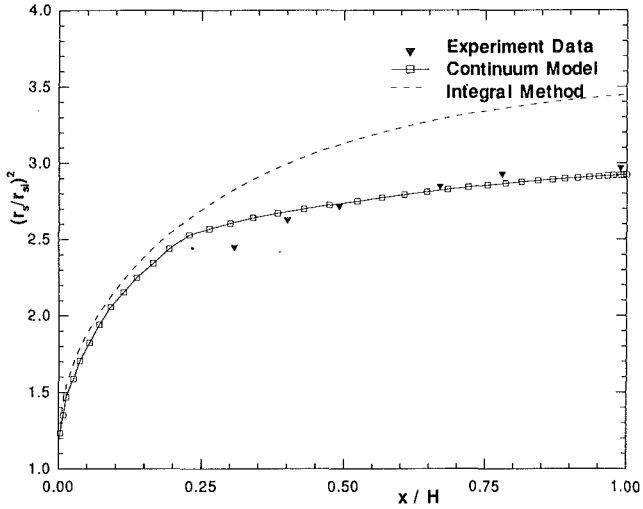

Fig. 2 Comparison of experimental data with the predictions of the numerical scheme (solid line) and the approximate solution (dashed line)

grid, the radial position of interface is evaluated by interpolation on the radial side of the grid using the calculated value of the solid volume fraction, f_s.

Figure 2 indicates that the numerical predictions compare well with the experimental data, thus establishing confidence in the model. The approximate solution results are in agreement with the numerical predictions and the experimental data at the early stages of the solid's travel in the bath (i.e., for small x^*'s). The deviation of the approximate results from the numerical and experimental results increases with x^*, which may be explained in terms of the simplifying assumptions employed in the development of the approximate solution. As stated in the appendix, the major assumptions of the approximate model are: (*a*) The axial heat conduction in the solid is negligible, and (*b*) the melt flow is induced solely by the moving solid (i.e., the effects of bath geometry, free surface, and thermal buoyancy on the melt flow over the solid are neglected). From these two, the first assumption appears to be the source of the discrepancy observed in Fig. 2, since the extent of the disagreement increases with x^*. It must be noted, however, that the degree of agreement or disagreement between the numerical results and the approximate solution was found to depend on the governing parameters of the problem, particularly, Re, Ste_s, and Ste_l. For example, for the conditions that resulted in extensive remelting of the solidified layer (e.g., large Ste_l), the approximate model predicted smaller solid diameters when compared to the numerical predictions. Also, the approximate solution is generally in better agreement with the numerical solutions for smaller Re's, indicating that the boundary layer approximation and the assumption regarding the existence of a leading edge in the melt flow are valid for smaller Re's.

For the parametric study, one set of baseline calculations is first performed and then compared with parametric variations of the operating conditions, and bath geometry. The baseline case considered corresponds to the following parameters: $\text{Re} = 4\times10^4$, $\text{Gr} = 10^8$, $\text{Ste}_s = 2.11$, $\text{Ste}_l = 0.40$, $\kappa = 1$, $c_l/c_s = 1$, $r_{si}/H = 1/20$, and $R/H = 1$. These are in the range of operating conditions as indicated by the experiments of Carreker (1963), Table 1, with the exception of Ste_s that the experimental conditions suggested 21.1. The high value of Ste_s used in the experiments is representative of the dip-forming process, whereas in the parametric study, smaller values of Ste_s typical of the dip-coating process are used. The baseline case serves as a reference for comparison with the results of variations of the various dimensionless parameters.

Figures 3(*a*) and 3(*b*) present the flow fields in the bath for $\text{Re} = 4\times10^4$ (baseline case) and $\text{Re} = 2\times10^4$, respectively, where

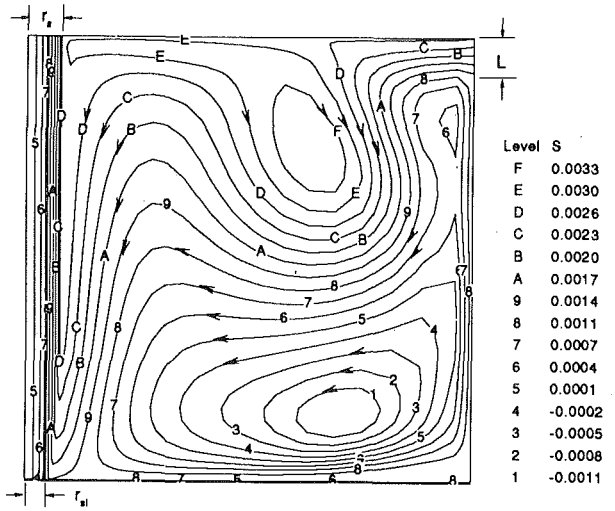

(a)

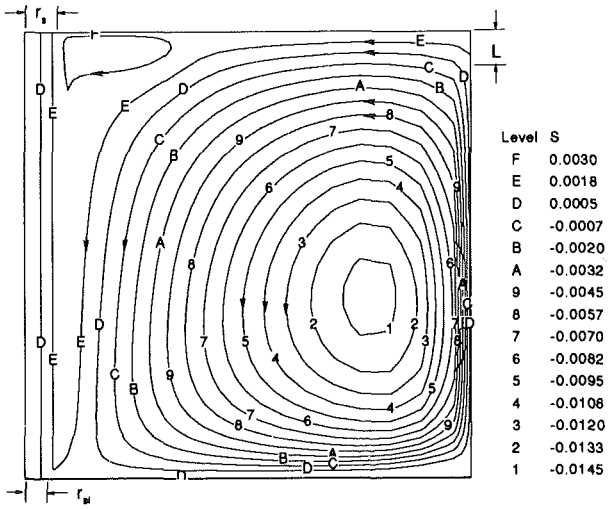

(b)

Fig. 3 Stream function distribution in the bath: (*a*) $Re = 4 \times 10^4$, (*b*) $Re = 2 \times 10^4$

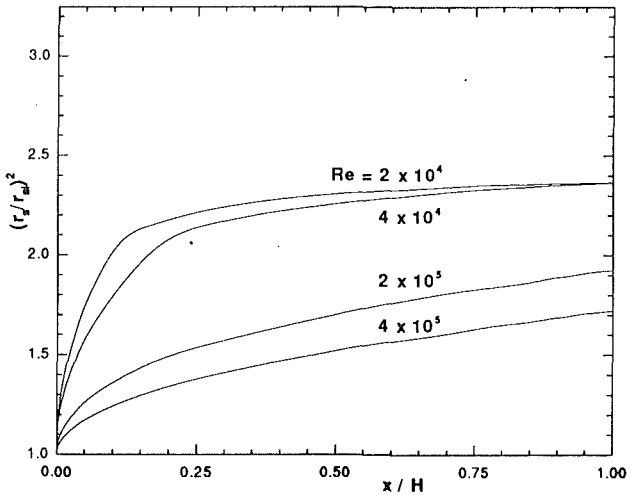

Fig. 4 Effect of Reynolds number on solidification thickness

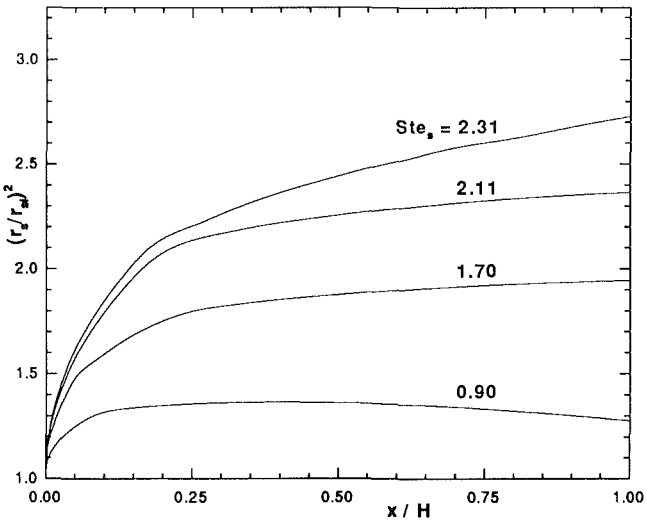

Fig. 5 Effect of solid Stefan number on solidification thickness

all other parameters remain at their baseline values. The left boundary of the graphs is the centerline of the moving solid rod and the fresh melt is introduced from the upper right corner. It is seen that the flow field established is due to an interaction between the buoyancy in the melt and the shear induced by the solid motion. By reducing the contribution of shear, i.e., decreasing the Reynolds number, a larger natural convection cell is generated, Fig. 3(*b*). The temperature distributions in the bath represented typical characteristics (almost parallel temperature contours) of liquid metal flow, and thus are not presented here. The shear-induced boundary layer over the rod is always present and isolates the rod from the buoyancy-induced motion in the bath. The corresponding variation of the solidification thickness is presented in Fig. 4. The Reynolds number is assigned the values 2×10^4, 4×10^4, 2×10^5, and 4×10^5 while the other parameters are held to their baseline values. Reducing the Reynolds number leads to increased residence time of the rod in the bath, which results in more solidification and larger exit thickness. The variation of the coating growth with Re is quite nonlinear, and indicates the significance of the convection effects. This may be observed by examining Fig. 4 and comparing the rod thicknesses for two values of Re at any given residence time. However, since the sensible heat of the solid rod is limited by its inlet temperature, an increase of residence time will not lead to appreciable increase in solidification after a certain limit. This limit is a function of the solid and liquid Stefan numbers. Additionally, if the residence time were to increase indefinitely, the rod would start to remelt even at small levels of Ste_l.

The effects of the two Stefan numbers Ste_s and Ste_l are presented in Figs. 5 and 6. Different values of Ste_s chosen are 0.90, 1.70, 2.11, and 2.31 for Fig. 5, and those of Ste_l are 0.0, 0.10, 0.40, 1.00, and 1.60 for Fig. 6. The other parameters are at their baseline values. The Stefan number of the solid is a measure of its level of subcooling, and its influence on the solidification thickness is shown in Fig. 5. The thickness decreases with decreasing Ste_s as expected. The growth is defined by the energy balance at the interface, and remelting of the solidified layer occurs if the subcooling is not sufficient to compensate for the heat transferred to the solid from the molten liquid. The liquid Stefan number indicates the level of superheating of the molten metal, and its increase reduces the solidification rate. For large enough values of Ste_l the rod radius may be reduced, even to values smaller than that at the inlet.

A change of Ste_l is accompanied by a change of Gr if the geometric parameters and phase-change material are kept the same. The variations observed in Fig. 6 are essentially due to change in Ste_l. This point is illustrated in Fig. 7, which shows the results for different values of Grashof number, $Gr = 10^8$ and 1.6×10^9, the other parameters remaining at their baseline values. The effect of Grashof number is seen to be minimal

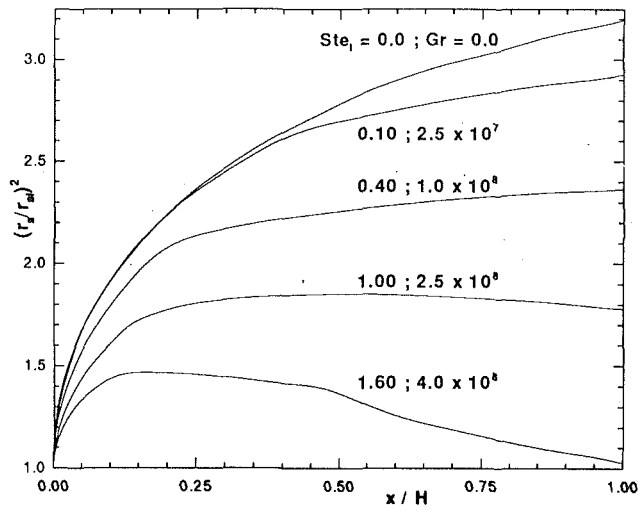

Fig. 6 Effect of liquid Stefan number on solidification thickness

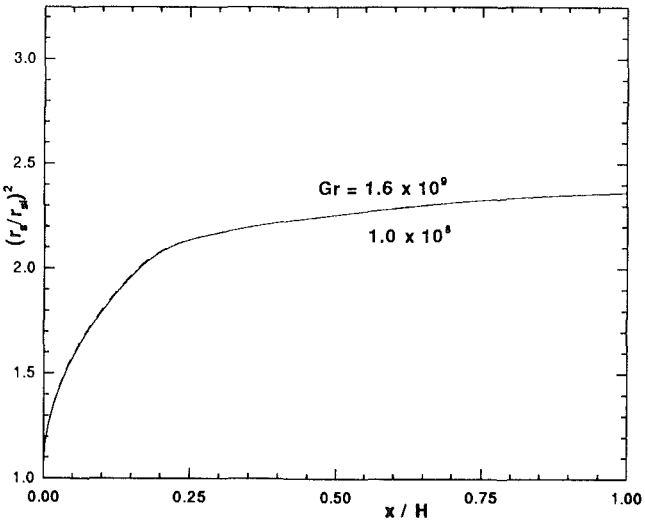

Fig. 7 Effect of Grashof number on solidification thickness

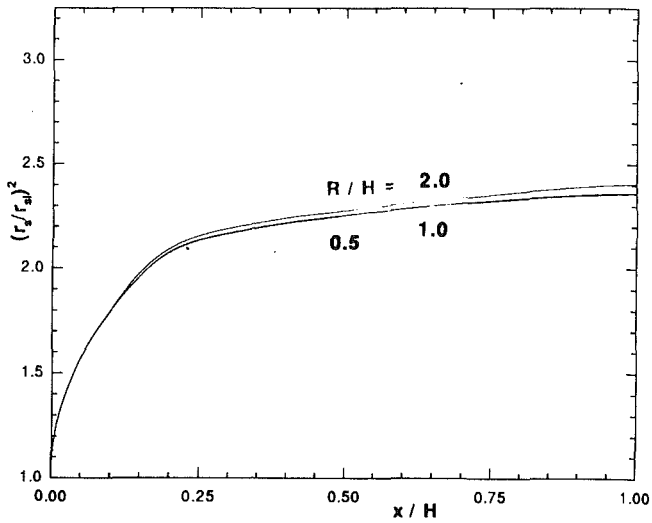

Fig. 8 Effect of bath radius on solidification thickness

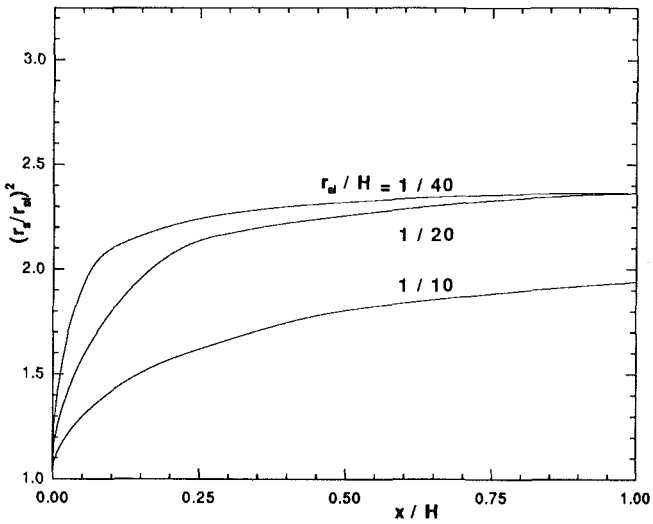

Fig. 9 Effect of solid inlet radius on solidification thickness

and the solidification profiles are nearly the same. This is due to the fact that the solidification is primarily influenced by the shear-driven boundary layer on the solid rod, which tends to isolate it from the buoyancy effects in the bath. The insignificant effect of the thermal buoyancy on the solidification rate justifies the use of forced convection correlation in the development of the approximate solution.

Figures 8 and 9 explore the effect of geometric parameters on the solidification process. The results indicate that the lateral dimension R of the bath, as represented by R/H, is not an important variable for the set of parameters considered. Increasing R results in more solidification because the hot walls are at a greater distance from the interface. The effect of the inlet solid radius r_{si} is indicated in Fig. 9. The smaller radius rod reaches thermal saturation faster due to its smaller thermal mass, and the ratio of local to inlet areas thus reaches an asymptotic value.

Figure 10 presents the effect of two different types of boundary condition at the bottom boundary of the bath. The bottom wall is assumed either to be adiabatic, or to be at the same temperature as the side walls. The constant parameters for these two cases are those corresponding to the baseline case. The solidification thickness for the adiabatic condition is larger because the overall liquid temperatures are smaller in magnitude than those for the constant wall temperature case. For the adiabatic case, the entering solid rod encounters liquid at lower temperatures and thus rapid solidification occurs. All the previous results (Figs. 3–9) are for the case where the bottom wall is held constant at the same temperature T_w as that specified for the side walls of the molten bath.

Conclusions

Although laminar, mixed convection flow in a finite cavity has been extensively studied in the literature, the related problem of flow with solidification of a pure medium over a moving surface in a finite bath has received comparatively little attention. Such an analysis, required for the modeling of the dip-coating process, is presented in the present study. A continuum model, which includes axial diffusion, thermal buoyancy, and shear-induced flow, has been used to investigate the solidification of metal during dip-coating. In general, in the range of normal operating parameters, the solidification thickness was found to depend strongly on the Reynolds and Stefan numbers and the ratio of inlet radius to height, and weakly on the Grashof number and the ratio of bath radius to height unless the bath radius is much smaller than the height.

An approximate solution for the problem was developed using the energy integral method, which is presented in the appendix. Its predictions of the variation of the solid radius in the bath did not compare well with the numerical predictions or the experimental data. This was attributed to the simplifying

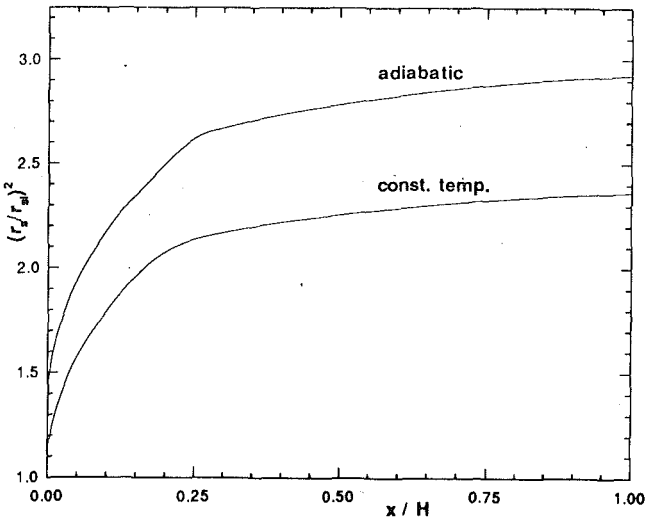

Fig. 10 Effect of boundary conditions on solidification thickness

assumptions employed in the development of the approximate solution.

Future studies of the dip-coating process are required to evaluate the non-steady-state operation of the process where the solid velocity is continually varied in a controlled manner to obtain thicknesses of complex, albeit prescribed, variations. The dip-coating technology is moving toward such applications, which would be computer controlled with appropriate feedback mechanisms. In order to prescribe velocity changes to induce exit thickness variations of the solidified metal, the time lag between the cause and effect has to be modeled and accurately predicted via thermal analysis of the type presented in this study. In addition to the effects included in the present analysis, secondary effects such as surface tension will also have to be included.

References

Bennon, W. D., and Incropera, F. P., 1987, "A Continuum Model for Momentum, Heat, and Species Transport in Binary Solid-Liquid Phase Change Systems. I. Model Formulation," *International Journal of Heat and Mass Transfer*, Vol. 30, pp. 2161–2170.

Carreker, R. P., 1963, "Dip-Forming—A Continuous Casting Process," *Journal of Metals*, Vol. 15, pp. 774–780.

Cheung, F. B., 1985, "Analysis of Freeze Coating on a Nonisothermal Moving Plate by a Perturbation Method," ASME JOURNAL OF HEAT TRANSFER, Vol. 107, pp. 549–556.

Christenson, M. S., Bennon, W. D., and Incropera, F. P., 1989, "Solidification of an Aqueous Ammonium Chloride Solution in a Rectangular Cavity—II. Comparison of Predicted and Measured Results," *International Journal of Heat and Mass Transfer*, Vol. 32, pp. 69–79.

Cook, T. H., Mergen, D. E., and Clark, D. L., 1986, "Increasing Profits in Hot Dip Galvanizing," *Metal Finishing*, Vol. 84, No. 5, pp. 23–27.

Eckert, E. R. G., and Drake, R. M., Jr., 1972, *Analysis of Heat and Mass Transfer*, McGraw-Hill, New York, pp. 439–445.

Epstein, M., 1976, "The Growth and Decay of a Frozen Layer in Forced Flow," *Int. J. Heat Transfer*, Vol. 19, pp. 1281–1288.

Herrmann, P. P., and Wildmann, D., 1983, "Fabrication of Planar Dielectric Waveguide With High Optical Damage Threshold," *IEEE Journal of Quantum Electronics*, Vol. QE-19, No. 12, pp. 1735–1738.

Horvay, G., 1965, "The Dip-Forming Process," ASME JOURNAL OF HEAT TRANSFER, Vol. 87, pp. 1–16.

Moallemi, M. K., and Viskanta, R., 1986, "Analysis of Melting Around a Moving Heat Source," *International Journal of Heat and Mass Transfer*, Vol. 29, pp. 1271–1282.

Patankar, S. V., 1980, *Numerical Heat Transfer and Fluid Flow*, McGraw-Hill, New York.

Prandtl, V. C., and Dawson, P. R., 1983, "Application of Mixture Theory to Continuous Casting," in: *Transport Phenomenon in Materials Processing*, M. M. Chen, J. Mazumder, and C. L. Tucker, eds., ASME HTD-Vol. 29, pp. 47–54.

Press, W. H., Flannery, B. P., Teukolsky, S. A., and Vetterling, W. T., 1989, *Numerical Recipes*, Cambridge University Press, Cambridge, United Kingdom, p. 554.

Prior, D. C., and Tonini, D. E., 1984, "Hot Dip Galvanizing of High Strength Low Alloy Steel," *Metal Finishing*, Vol. 82, No. 5, pp. 15–19.

Seeniraj, R. V., and Bose, T. K., 1981, "Freeze-Coating on a Continuous Moving Sheet and on an Axially Moving Cylinder," *Wärme- und Stoffübertragung*, Vol. 15, pp. 239–243.

Shamsundar, N., and Sparrow, E. M., 1975, "Analysis of Multidimensional Conduction Phase Change via the Enthalpy Model," ASME JOURNAL OF HEAT TRANSFER, Vol. 97, pp. 333–340.

Tiefenthaler, K., Briguet, V., Buser, E., Horisberger, M., and Lukosz, M., 1983, "Preparation of Planar Optical SiO_2-TiO_2 and $LiNbO_3$ Waveguides With a Dip Coating Method and a Embossing Technique for Fabricating Grating Couplers and Channel Waveguides," *Proceedings of the Society of Photo-optical Instrumentation Engineers*, Vol. 401, pp. 165–173.

Townsend, C. S., and Bilski, W. C., 1988, "Closed Loop Control of Coating Weight on a Hot Dip Galvanizing Line," *Iron and Steel Engineer*, Vol. 65, No. 7, pp. 44–47.

APPENDIX

The purpose of this section is to develop an approximate analysis of solidification on a moving substrate. As mentioned in the introduction, the available analyses of the problem are based on oversimplified models (Seeniraj and Bose, 1981; Cheung, 1985). In this study, the isothermal conditions for the solidified layer (Seeniraj and Bose, 1981) and the moving substrate (Cheung, 1985) are relaxed. The saturated-melt temperature condition (Seeniraj and Bose, 1981) is also removed. In other words, the freeze coating of a superheated liquid on a nonisothermal moving substrate with a limited cooling capacity is investigated.

In addition to the basic assumption made in the general model, Eqs. (1)–(4), the following simplifications are made in developing the approximate solution:

1 A steady-state freeze-coating process is considered. This implies that the solid velocity, the bath height, and the far-field (inlet) liquid temperature remain constant in time. The transient growth of the solidified layer is then expressed as

$$\frac{\partial r_s}{\partial t} = U_s \frac{\partial r_s}{\partial x} \tag{A.1}$$

2 The axial heat conduction in the solid is neglected. This may be justified because the solid radius (including the solidified layer) is small compared to the height of the bath.

3 The melt flow is assumed to be solely induced by the moving solid. The effects of bath walls and free surface, as well as the effect of thermal buoyancy on the melt flow, are neglected to enable the development of the approximate solution.

In view of the last assumption, only the equation for the conservation of energy in the solid is solved, and the local convective heat flux from the warm liquid to the moving solid is treated as an input parameter, which may be directly obtained from the conventional solution of forced convection over a moving surface without phase change such as those given by Eckert and Drake (1972). In this practice, negligible interaction between the melt flow and the shape of the solid-liquid interface is implied, which is understood to be only valid for the growth of thin crusts. Similar arguments have been successfully employed by previous investigators, e.g., Epstein (1976) and Cheung (1985).

With the above assumptions, the equations governing the conservation of energy in the solid in terms of its temperature $T_s(r, x)$, and the solid profile $r_s(x)$ can be written as follows:

$$U_s \frac{\partial T_s}{\partial x} = \frac{\alpha_s}{r} \frac{\partial}{\partial r}\left(r \frac{\partial T_s}{\partial r}\right) \text{ for } x \geq 0,\ 0 \leq r \leq r_s, \tag{A.2a}$$

$$\rho U_s h_f \frac{dr_s}{dx} = k_s \frac{\partial T_s}{\partial r}\Big|_{r=r_s} - h_x\,(T_\infty - T_f) \tag{A.2b}$$

where T_∞ is the melt temperature far from the interface, equal to T_w of the general model. The local coefficient h_x of con-

vective heat transfer from the liquid to the interface is an input parameter that for laminar boundary layer flow of a fluid with Pr $\ll$ 1 over a flat plate is given as (Eckert and Drake, 1972).

$$\mathrm{Nu}_x = \frac{h_x x}{k_l} = C_1\,\mathrm{Re}_x^{1/2}\,\mathrm{Pr}^{1/2}, \tag{A.3}$$

where $\mathrm{Re}_x = U_s x/\nu$ is the local Reynolds number, and C_1 is a constant order of 0.5. The boundary conditions of the problem are as follows:

$$r = r_s: \quad T_s = T_f, \tag{A.4a}$$

$$r = 0: \quad \frac{\partial T_s}{\partial r} = 0, \tag{A.4b}$$

$$x = 0: \quad T_s = T_{si}, \text{ and } r_s = r_{si}. \tag{A.4c}$$

To find the spatial variation of the crust thickness, the energy equation, Eq. (A.2*a*), is integrated over the cross section of the solid, after first nondimensionalizing it using the dimensionless variables defined in the text, to yield

$$\frac{d}{dx^*}\int_0^{r_s^*} \Theta_s r^*\, dr^* = \frac{r_s^*}{\mathrm{RePr}}\frac{\alpha_s}{\alpha_l}\frac{\partial \Theta_s}{\partial r^*}\bigg|_{r_s^*} \tag{A.5}$$

The dimensionless solid temperature Θ_s is defined as $(T_s - T_f)/(T_w - T_f)$ and the Reynolds number is based on the bath height H. In reducing Eq. (A.5), boundary conditions Eqs. (A.4*a*) and (A4.*b*) have been invoked. The interface energy balance equation, Eq. (A.2), is nondimensionalized after substituting h_x from Eq. (A.3) to yield

$$\frac{dr_s^*}{dx^*} = \frac{\kappa \mathrm{Ste}_l}{\mathrm{RePr}}\frac{\partial \Theta_s}{\partial r^*}\bigg|_{r_s^*} - \frac{C_1 \mathrm{Ste}_l}{\sqrt{\mathrm{RePr}x^*}} \tag{A.6}$$

To simplify the solution of Eq. (A.6), different solid temperature profiles are assumed to characterize the thermal development of the solid as it travels through the bath. The temperature profiles are required to satisfy the integral energy equation Eq. (A.5) and the boundary conditions Eqs. (A.4*a*) and (A.4*b*). As shown in Fig. A.1, the first profile is consistent with the notion of a thermal penetration thickness $\Delta(x^*)$, beyond which the effects of the interface conditions are negligible, i.e.,

$$\Theta_s = \begin{cases} \Theta_{si} & \text{for } 0 \le r^* \le r_s^* - \Delta \\ \Theta_{si}\,[1 - (r^* - r_s^* + \Delta)^2/\Delta^2] & \text{for } r_s^* - \Delta \le r^* \le r_s^*. \end{cases} \tag{A.7}$$

where $0 \le \Delta(x^*) \le r_s^*(x^*)$. Substituting this temperature profile into Eqs. (A.5) and (A.6) results in

$$\frac{d}{dx^*}\left[6r_s^{*2} - 4\Delta r_s^* + \Delta^2\right] = \frac{-24 r_s^*}{\mathrm{RePr}\Delta} \tag{A.8}$$

$$\frac{dr_s^*}{dx^*} = \frac{\kappa \mathrm{Ste}_l}{\mathrm{RePr}}\left(\frac{-2\Theta_{si}}{\Delta}\right) - \frac{C_1 \mathrm{Ste}_l}{\sqrt{\mathrm{RePr}x^*}} \tag{A.9}$$

Equations (A.8) and (A.9) form a system of first-order nonlinear differential equations, which is solved for the unknown functions $r_s^*(x^*)$ and $\Delta(x^*)$ with Eq. (A.4*c*) and $\Delta(0) = 0$ as boundary conditions. The system is integrated using fourth-order Runge–Kutta scheme with adaptive step-size control (Press et al., 1989). The first step of the marching integration required special consideration to ensure the correct starting behavior since both r_s^* and Δ have infinitely large gradient at $x^* = 0$. The system of Eqs. (A.8) and (A.9), however, may be simplified using the following facts:

$$\Delta \ll r_s^* \text{ and } \frac{dr_s^*}{dx^*} \ll \frac{d\Delta}{dx^*} \tag{A.10}$$

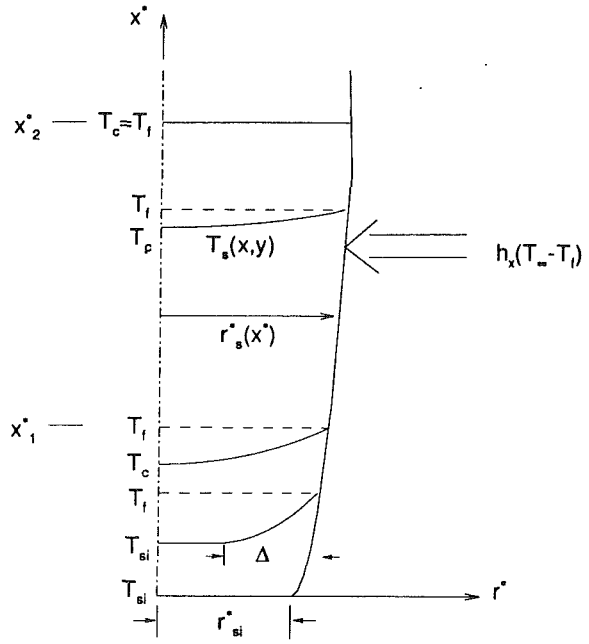

Fig. A1 Idealized dip-coating system

near the starting point, $x^* = 0$. Applying the conditions of Eq. (A.10) to Eqs. (A.8) and (A.9), the thermal penetration thickness and solid radius for small x^*'s are calculated as

$$\Delta = \left(\frac{12x^*}{\mathrm{RePr}}\right)^{1/2} \text{ and}$$

$$r_s^* = r_{si}^* - 2\mathrm{Ste}_l(\kappa\Theta_{si} + C_1\sqrt{3}\left(\frac{x^*}{3\mathrm{RePr}}\right)^{1/2}. \tag{A.11}$$

(Note that $\Theta_{si} < 0$ due to the choice of nondimensionalization.)

The thermal penetration thickness and solid radius are calculated from Eqs. (A.8) and (A.9) up to $x^* = x_1^*$ where $\Delta(x_1^*) = r_s^*(x_1^*)$, and beyond that a quadratic temperature profile is assumed,

$$\Theta_s = \Theta_c\left[1 - \frac{r^{*2}}{r_s^{*2}}\right] \quad \text{for } 0 \le r^* \le r_s^*, \tag{A.12}$$

where $\Theta_c(x^*)$ is the centerline temperature of the solid, which is calculated along with the solid radius by substituting the above profile into Eqs. (A.5) and (A.6),

$$\frac{d}{dx^*}\left[r_s^{*2}\Theta_c\right] = \frac{-8\Theta_c}{\mathrm{RePr}} \tag{A.13}$$

$$\frac{dr_s^*}{dx^*} = \frac{\kappa \mathrm{Ste}_l}{\mathrm{RePr}}\left(\frac{-2\Theta_c}{r_s^*}\right) - \frac{C_1 \mathrm{Ste}_l}{\sqrt{\mathrm{RePr}x^*}} \tag{A.14}$$

The system of Eqs. (A.13) and (A.14) is solved using a fourth-order Runge–Kutta scheme with the starting condition provided from the endpoint solution of system of Eqs. (A.8) and (A.9). This marching integration is carried on up to a point x_2^* where Θ_c and thus the entire solid reached the uniform fusion temperature. Beyond x_2^*, therefore, the first term on the right-hand side of Eq. (A.7) vanishes, and the rest is integrated to yield

$$r_s^*(x^*) = r_s^*(x_2^*) - \frac{2C_1 \mathrm{Ste}_l}{\mathrm{RePr}}\left(\sqrt{x^*} - \sqrt{x_2^*}\right). \tag{A.15}$$

The marching integration routines and Eq. (A.15) are used with the bounding conditions

$$r_s^* \ge 0 \text{ and } x^* \le 1.0$$

Journal of Heat Transfer

Technical Notes

This section contains shorter technical papers. These shorter papers will be subjected to the same review process as that for full papers

Analysis and Optimization of Convective Trapezoidal Profile Longitudinal Fins

P. Razelos[1] and B. R. Satyaprakash[1]

Nomenclature

A = area perpendicular to heat flow, m^2/m
Bi = Biot number = hw/k
d = width of the fin = 1 m
h = heat transfer coefficient, W/m^2-K
k = thermal conductivity of fin material, W/m-K
L = fin height, m
L^* = optimum fin height, Eq. (19)
N_r = removal number = $q_f/2hw\Theta_o$
N_r^* = optimum N_r, Eq. (21)
P = fin perimeter, m/m
p = dimensionless parameter = $u/(1-\lambda)$
Q = dimensionless heat dissipation = $q_f/2k\Theta_o$
q_f = heat dissipated by the fin, W/m
r = coordinate, m
T = dimensionless temperature = Θ/Θ_o
u = aspect number = $L(hP_o/kA_o)^{1/2}$ = $(L/w)\ \mathrm{Bi}^{1/2}$
V = volume of the fin, m^3/m
V^* = optimum volume, Eq. (20)
w = base fin semi-thickness, m
w^* = optimum base semi-thickness, Eq. (18)
x = dimensionless coordinate = r/L
y = thickness of the fin at r, m
z = dimensionless fin profile, Eq. (5)
α = slope of the fin's lateral surface
Θ = fin temperature in excess of ambient, °C
ζ = dimensionless parameter = $B_i^{1/2}$
λ = ratio of tip to base thickness = w_e/w
ξ = dimensionless parameter = $2p$

Superscripts and Subscripts

e = conditions at the tip of the fin
o = conditions at the base of the fin
* = optimum dimensionless quantities

[1]Department of Applied Sciences, The College of Staten Island CUNY, Staten Island, NY 10301.

Contributed by the Heat Transfer Division of the THE AMERICAN SOCIETY OF MECHANICAL ENGINEERS. Manuscript received by the Heat Transfer Division June 1992; revision received December 1992. Keywords: Finned Surfaces, Numerical Methods. Associate Technical Editor: Y. Bayazitoglu.

Introduction

One of the most commonly used types of extended surface is the longitudinal or straight fin. Gardener (1945) derived the efficiency of five different profile straight fins, which, except for the one of constant thickness, all had profiles with zero tip surface. However, real fins do not have zero thickness surfaces, nor is it desired to have one. Therefore, Gardner's analysis, except for one case, is only of academic interest. In technical applications the most widely used fins are those with trapezoidal profile, and this is the subject of this investigation.

These fins were first treated by Harper and Brown (1922) who derived an approximate formula for their effectiveness. Recently Chung (1989) solved the optimization problem for trapezoidal profile fins: fins that produce the maximum heat dissipation when the volume is specified. Their results are presented in three graphs that can be used to determine the dimensionless base and tip thickness, and heat dissipation, respectively. The optimum quantities are expressed as functions of the nondimensional volume $hV^{1/2}/k$ and the ratio of the heat transfer coefficients h_e/h. However, their results are unnecessarily complicated by the inclusion of the heat transfer from the tip of the fin. As was shown recently by Razelos and Georgiou (1992) in properly designed fins (fins with Bi of O(0.01)), the heat transfer from the tip can be neglected without any appreciable error.

In this paper we present an analysis of trapezoidal profile longitudinal fins that delineates their thermal performance. We also give an improved solution of the optimal problem using the method introduced by Razelos (1979, and 1983).

Analysis

The fin considered here is depicted schematically in Fig. 1. We define a dimensionless fin profile z as

$$z=\frac{y}{w}=\lambda+(1-\lambda)\frac{r}{L}=\lambda+(1-\lambda)x \tag{1}$$

The mathematical treatment is based on the well-known Murray (1938) and Gardner (1945) simplifying assumptions. Under these assumptions the fin temperature is governed by the following differential equation and boundary conditions:

$$\frac{d}{dz}\left(z\frac{dT}{dz}\right)=p^2T \tag{2}$$

$$T=1 \qquad \text{at } z=1 \tag{3}$$

$$\frac{dT}{dz}=0 \qquad \text{at } z=\lambda \quad W_e>0 \tag{4}$$

where $\lambda = w_e/w$, $p=u/(1-\lambda)$, and $u = (L/w)\ \mathrm{Bi}^{1/2}$ the aspect number. The solution of Eq. (2) is the zero-order Modified Bessel function (Abramowitz and Stegan, 1972).

Thus the dimensionless temperature T is equal to

$$T=C_1I_o(2pz^{1/2})+C_2K_o(2pz^{1/2}) \tag{5}$$

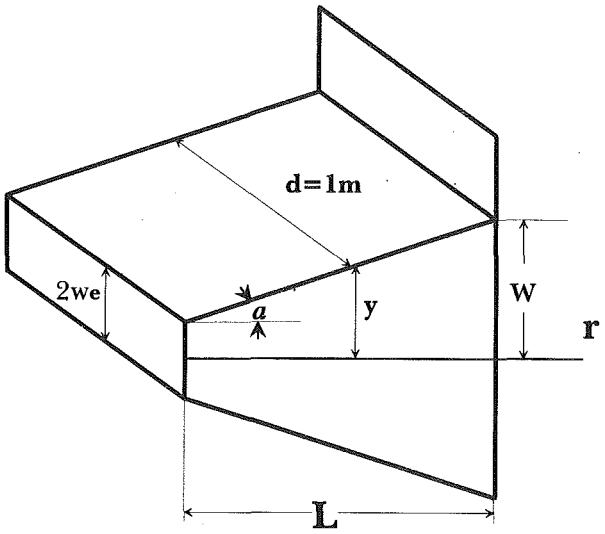

Fig. 1 Schematic diagram of a trapezoidal profile fin

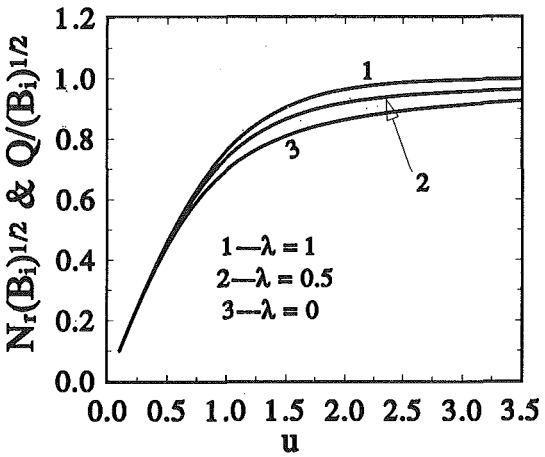

Fig. 2 Variation of the nondimensional quantities $Q/\mathrm{Bi}^{1/2}$ and $N_r\mathrm{Bi}^{1/2}$ with the aspect number u

The constants C_1 and C_2 are determined from the boundary conditions Eqs. (3) and (4).

The temperature for the two limiting cases of the slope $\lambda = 0$ (triangular profile fin), and $\lambda = 1$ (constant thickness fin) can be readily derived from this general solution. In the first case the finite fin temperature dictates that $C_2 = 0$. In the second case the solution is obtained from the asymptotic values for large argument ($p \to \infty$) of the modified Bessel functions.

The heat transfer from the fin is equal to

$$Q=\frac{q_f}{2k\Theta_o}=\frac{w}{L}\left(\frac{dT}{dx}\right)_{x=1}=\mathrm{Bi}^{1/2}D \tag{6}$$

where $D = (dT/d(2pz^{1/2}))_{z=1}$ and is equal to

$$D=C_1I_1(2p)-C_2K_1(2p) \tag{7}$$

Note that D is a function of u and the slope λ. The variation of $Q/\mathrm{Bi}^{1/2}$ with u is plotted in Fig. 2 for $\lambda = 0$, 0.5 and 1. One measure of the fin's thermal performance is the removal number N_r (Gardner named it effectiveness) and is defined as "the ratio of the heat dissipated by the fin q_f to the heat that would be dissipated by the fin's base area if the fin was absent with the same h and Θ_o. Therefore N_r is equal to

$$N_r=\frac{q_f}{2hw\Theta_o}=\frac{D}{\mathrm{Bi}^{1/2}} \tag{8}$$

Thus, Fig. 2 is also a plot of the product $N_r\mathrm{Bi}^{1/2}$. We propose that this figure should be used to evaluate the fin's thermal performance, instead of the commonly used efficiency graph.

The Optimum Fin

Following Razelos's (1979, 1983) approach, we define a nondimensional volume U as

$$U=\frac{h^2V}{2k^2}=\frac{h^2(1+\lambda)wL}{2k^2}=\frac{(1+\lambda)u\mathrm{Bi}^{3/2}}{2} \tag{9}$$

For a given slope λ the dimensionless heat dissipation Q, Eq. (6), and the dimensionless volume U are functions of $\mathrm{Bi}^{1/2}$ and u. Thus the stationary values of Q for given U must satisfy the relation

$$\frac{\partial U}{\partial \zeta}\frac{\partial Q}{\partial u}-\frac{\partial U}{\partial u}\frac{\partial Q}{\partial \zeta}=0 \tag{10}$$

where for brevity in Eq. (10) we denote $\mathrm{Bi}^{1/2}$ with ζ. Note that the problem of maximizing Q for a given U is equivalent to the problem of minimizing U for a given Q, since both problems are characterized by the root of the Eq. (10). Performing the differentiation in Eq. (10), we obtain the following transcendental equation:

$$3p\frac{dD}{dp}-D=0 \tag{11}$$

The derivative D can be conveniently written as a ratio of two determinants D_1/D_2

$$D=D_1/D_2=\frac{\begin{vmatrix} I_1(2p) & K_1(2p) \\ I_1(2pv) & K_1(2pv) \end{vmatrix}}{\begin{vmatrix} I_o(2p) & -K_o(2p) \\ I_1(2pv) & K_1(2pv)) \end{vmatrix}} \tag{12}$$

where $v = \lambda^{1/2}$. Introducing Eq. (12) into Eq. (11) we get

$$\frac{dD_1}{d\xi}-D\frac{dD_2}{d\xi}-\frac{D_1}{3\xi}=0 \tag{13}$$

The derivatives of the determinants D_1 and D_2 are equal to

$$\frac{dD_1}{d\xi}=\begin{vmatrix} I_1'(\xi) & K_1(\xi) \\ vI_1'(\xi v) & K_1(\xi v) \end{vmatrix}+\begin{vmatrix} I_1(\xi) & K_1'(\xi) \\ I_1(\xi v) & vK_1'(\xi v) \end{vmatrix} \tag{14}$$

$$\frac{dD_2}{d\xi}=\begin{vmatrix} I_o'(\xi) & -K_o \\ vI_1'(\xi v) & K_1(\xi v) \end{vmatrix}+\begin{vmatrix} I_o(\xi) & -K_o'(\xi) \\ I_1(\xi v) & vK_1'(\xi v) \end{vmatrix} \tag{15}$$

where the prime means derivative with respect to the argument $\xi = 2p$ or $\xi v = 2pv$. For a given λ the root of the above equation uniquely determines a u_{opt} and consequently a D_{opt}. We have used the subroutine "fzero" of the software package MATLAB (1991) to obtain the roots of Eq. (13) for several values of λ. Subsequently, we used the subroutine "polyfit" of the same software that performs a least-square fit, to express the quantities u_{opt} and D_{opt} as polynomial of λ as follows:

$$u_{\mathrm{opt}}=(12.18947*\lambda+129.7844)/100 \tag{16}$$

$$D_{\mathrm{opt}}=(-2.34264*\lambda^2+13.8986*\lambda+130.6659)/100 \tag{17}$$

Equations (16) and (17) represent the dimensionless parameters u_{opt} and D_{opt} in the region $0.2 \le \lambda \le 1$ with an error of less than 0.03 percent.

In order to acquire a good understanding of the influence of the material properties upon the optimal results, we introduce the following optimum nondimensional parameters that for a given λ are functions of u_{opt} and D_{opt}:

$$w^*=\frac{hkw_{\mathrm{opt}}}{(q_f/\Theta_o)^2}=\frac{0.25}{D_{\mathrm{opt}}^2} \tag{18}$$

$$L^*=\frac{hL_{\mathrm{opt}}}{(q_f/\Theta_o)}=\frac{0.5u_{\mathrm{opt}}}{D_{\mathrm{opt}}} \tag{19}$$

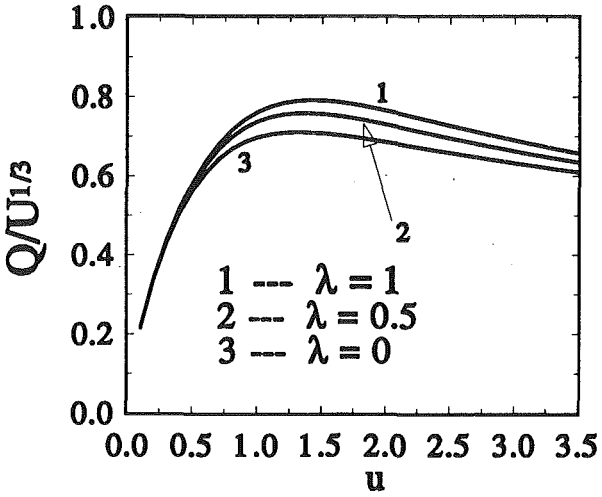

Fig. 3 Variation of the ratio of $Q/U^{1/3}$ with the aspect number u

$$V^* = \frac{h^2 k V_{\text{opt}}}{(q_f/\Theta_o)^3} = \frac{0.25(1+\lambda)u_{\text{opt}}}{2D_{\text{opt}}^2} \tag{20}$$

$$N_r^* = N_r Q = D_{\text{opt}}^2 \tag{21}$$

From the above parameters we can conclude that the optimum base thickness and volume are inversely proportional to the thermal conductivity k or to k/ρ (ρ is the density) for a specified heat dissipation. However, if the volume is specified, the above optimum quantities are only proportional to the 1/3 power of k or k/ρ.

To illustrate our method we take, for comparison purposes, the example given by Chung et al. (1989). The following are given: volume $V = 0.00488$ ft^3/ft, film coefficient $h = 25.29$ Btu/hr-ft^2-R, thermal conductivity $k = 79.79$ Btu/hr-ft-R, and $\Theta_o = 140$ R. Since the authors optimize the slope, we must take their value of λ, which is determined from the following equation:

$$\frac{w(1-\lambda)}{L} = \frac{V(1-\lambda)}{L^2(1+\lambda)} = \tan(\alpha) \tag{22}$$

Their values of $\alpha = 1.59$ deg and $L = 3.58$ in are substituted into Eq. (22) to get $\lambda = 0.32804$. Employing Eqs. (20), (21), and (18) we obtain $u_{\text{opt}} = 1.3378$, $D_{\text{opt}} = 0.8155$, and $V^* = 0.40956$. Then from Eq. (18) we determine $q_f = 1186.1$ Btu/hr-ft and from Eq. (21) we determine $N_r = 12.5$. Our value of heat dissipation is in excellent agreement with the authors' $q_f = 1189.3$. However, if one employs the results presented graphically to obtain the fin's optimum dimensions, some errors may be introduced. In addition, they cannot be used directly for computer calculations and in this respect our method offers an improvement.

For this example it is interesting to compare the above results with those obtained by using a rectangular profile fin ($\lambda = 1$) having the same volume. In this case we have $V^* = 0.5043$ and $D_{\text{opt}} = 0.8894$, which yields $q = 635.3$ Btu/hr-ft and $N_r = 18.9$. We can observe that while the constant thickness fin dissipates 46.5 percent less heat than the trapezoidal profile fin, it dissipates 51.2 percent more heat per unit length. Therefore, in designing fins, the choice of the profile does not depend on the heat transfer but on structural considerations.

Finally, we should point out that in many situations it is desirable to know the fin's performance at off-optimum conditions. This can be accomplished by examining the ratio

$$\frac{Q}{U_{1/3}} = \frac{D(u,\lambda)}{u_{1/3}} \tag{23}$$

In Fig. 3 the values of $Q/U^{1/3}$ are plotted versus u for the three values of the slope $\lambda = 0$, 0.5, and 1. We may conclude by inspection of Fig. 2 that for a good fin design the value of the aspect number u must be between 1 and 1.5. This result is in contrast with the customary practice of using small values of u that result in large (close to 1) values of efficiency.

Concluding Remarks

Although the analytical solution of the trapezoidal profile longitudinal fins was known, the results presented here, such as those depicted in Figs. 2 and 3, are more useful than the graphs presented in textbooks and handbooks that depict fin efficiencies. We have also presented here an improved solution of the optimum problem. One can employ our method to determine the optimum heat dissipation and dimensions of the fin, without having to consult any graphs. In addition, the results presented in Fig. 3 can be used to estimate the fin's thermal performance, when it is designed off the optimum conditions ($u <$ or $> u_{\text{opt}}$).

References

Abramowitz, M., and Stegun, I., 1972, *Handbook of Mathematical Functions*, 9th ed., Dover Publications Inc., New York, p. 374.

Chung, B. T. F., 1989, "Optimization of Convective Longitudinal Fins of Trapezoidal Profile," *Chem. Eng. Comun.*, Vol. 80, p. 211.

Gardner, K. A., 1945, "Efficiency of Extended Surface," *Trans. ASME*, Vol. 67, p. 621.

Harper, D. R., and Brown, W. B., 1922, "Mathematical Equations of Heat Conduction in the Fins of Air-Cooled Engines," NACA Technical Report 158.

Murray, W. M., 1938, "Heat Transfer Through an Annular Disk or Fin of Uniform Thickness," ASME *Journal of Applied Mechanics*, Vol. 5, p. A78.

Razelos, P., 1979, "The Optimization of Longitudinal Convective Fins With Internal Heat Generation," *Nuclear Eng. and Design*, Vol. 84, p. 289.

Razelos, P., 1983, "The Optimal Dimensions of Convective Pin Fins," ASME JOURNAL OF HEAT TRANSFER, Vol. 105, p. 411.

Razelos, P., and Georgiou, E., 1992, "Two Dimensional Effects and Design Criteria for Convective Extended Surfaces," *Heat Transfer Engineering*, Vol. 13, p. 38.

An Analytical Solution to Melting in a Finite Slab With a Boundary Condition of the Second Kind

Y. W. Zhang,[1] Y. Y. Jin,[1] Z. Q. Chen,[1] Z. F. Dong,[2] and M. A. Ebadian[2,3]

Introduction

The solid-liquid phase change phenomenon appears in nature and many industrial processes and has received much attention recently. Because of the strong nonlinearity of the solid-liquid interface (cf. Özişik, 1980), an exact solution to the melting of solids is nearly impossible, except for a few cases of the Stefan problem. Even for the simple case of the melting of a finite slab, a closed form of an exact solution cannot be obtained. A literature search indicates that melting

[1]Department of Power Machinery Engineering, Xi'an Jiaotong University, Xi'an 710049, People's Republic of China.

[2]Department of Mechanical Engineering, Florida International University, Miami, FL 33199.

[3]Mem. ASME.

Contributed by the Heat Transfer Division of THE AMERICAN SOCIETY OF MECHANICAL ENGINEERS. Manuscript received by the Heat Transfer Division April 1992; revision received December 1992. Keywords: Conduction, Moving Boundaries, Phase Change Phenomena. Associate Technical Editor: Y. Bayazitoglu.

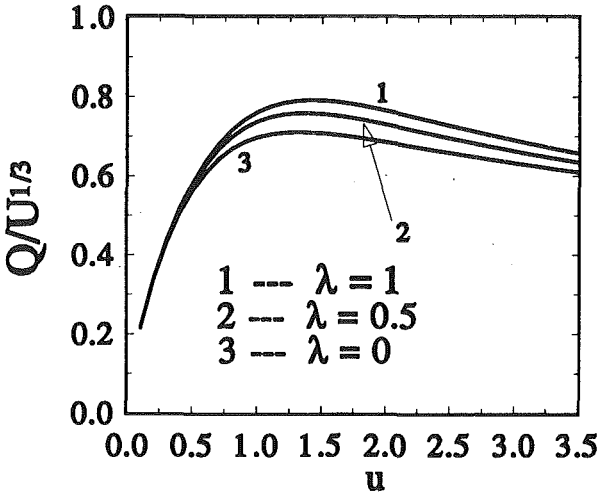

Fig. 3 Variation of the ratio of $Q/U^{1/3}$ with the aspect number u

$$V^* = \frac{h^2 k V_{\text{opt}}}{(q_f/\Theta_o)^3} = \frac{0.25(1+\lambda)u_{\text{opt}}}{2D_{\text{opt}}^2} \tag{20}$$

$$N_r^* = N_r Q = D_{\text{opt}}^2 \tag{21}$$

From the above parameters we can conclude that the optimum base thickness and volume are inversely proportional to the thermal conductivity k or to k/ρ (ρ is the density) for a specified heat dissipation. However, if the volume is specified, the above optimum quantities are only proportional to the 1/3 power of k or k/ρ.

To illustrate our method we take, for comparison purposes, the example given by Chung et al. (1989). The following are given: volume $V = 0.00488$ ft^3/ft, film coefficient $h = 25.29$ Btu/hr-ft^2-R, thermal conductivity $k = 79.79$ Btu/hr-ft-R, and $\Theta_o = 140$ R. Since the authors optimize the slope, we must take their value of λ, which is determined from the following equation:

$$\frac{w(1-\lambda)}{L} = \frac{V(1-\lambda)}{L^2(1+\lambda)} = \tan(\alpha) \tag{22}$$

Their values of $\alpha = 1.59$ deg and $L = 3.58$ in are substituted into Eq. (22) to get $\lambda = 0.32804$. Employing Eqs. (20), (21), and (18) we obtain $u_{\text{opt}} = 1.3378$, $D_{\text{opt}} = 0.8155$, and $V^* = 0.40956$. Then from Eq. (18) we determine $q_f = 1186.1$ Btu/hr-ft and from Eq. (21) we determine $N_r = 12.5$. Our value of heat dissipation is in excellent agreement with the authors' $q_f = 1189.3$. However, if one employs the results presented graphically to obtain the fin's optimum dimensions, some errors may be introduced. In addition, they cannot be used directly for computer calculations and in this respect our method offers an improvement.

For this example it is interesting to compare the above results with those obtained by using a rectangular profile fin ($\lambda = 1$) having the same volume. In this case we have $V^* = 0.5043$ and $D_{\text{opt}} = 0.8894$, which yields $q = 635.3$ Btu/hr-ft and $N_r = 18.9$. We can observe that while the constant thickness fin dissipates 46.5 percent less heat than the trapezoidal profile fin, it dissipates 51.2 percent more heat per unit length. Therefore, in designing fins, the choice of the profile does not depend on the heat transfer but on structural considerations.

Finally, we should point out that in many situations it is desirable to know the fin's performance at off-optimum conditions. This can be accomplished by examining the ratio

$$\frac{Q}{U_{1/3}} = \frac{D(u,\lambda)}{u_{1/3}} \tag{23}$$

In Fig. 3 the values of $Q/U^{1/3}$ are plotted versus u for the three values of the slope $\lambda = 0$, 0.5, and 1. We may conclude by inspection of Fig. 2 that for a good fin design the value of the aspect number u must be between 1 and 1.5. This result is in contrast with the customary practice of using small values of u that result in large (close to 1) values of efficiency.

Concluding Remarks

Although the analytical solution of the trapezoidal profile longitudinal fins was known, the results presented here, such as those depicted in Figs. 2 and 3, are more useful than the graphs presented in textbooks and handbooks that depict fin efficiencies. We have also presented here an improved solution of the optimum problem. One can employ our method to determine the optimum heat dissipation and dimensions of the fin, without having to consult any graphs. In addition, the results presented in Fig. 3 can be used to estimate the fin's thermal performance, when it is designed off the optimum conditions ($u <$ or $> u_{\text{opt}}$).

References

Abramowitz, M., and Stegun, I., 1972, *Handbook of Mathematical Functions*, 9th ed., Dover Publications Inc., New York, p. 374.

Chung, B. T. F., 1989, "Optimization of Convective Longitudinal Fins of Trapezoidal Profile," *Chem. Eng. Comun.*, Vol. 80, p. 211.

Gardner, K. A., 1945, "Efficiency of Extended Surface," *Trans. ASME*, Vol. 67, p. 621.

Harper, D. R., and Brown, W. B., 1922, "Mathematical Equations of Heat Conduction in the Fins of Air-Cooled Engines," NACA Technical Report 158.

Murray, W. M., 1938, "Heat Transfer Through an Annular Disk or Fin of Uniform Thickness," ASME *Journal of Applied Mechanics*, Vol. 5, p. A78.

Razelos, P., 1979, "The Optimization of Longitudinal Convective Fins With Internal Heat Generation," *Nuclear Eng. and Design*, Vol. 84, p. 289.

Razelos, P., 1983, "The Optimal Dimensions of Convective Pin Fins," ASME JOURNAL OF HEAT TRANSFER, Vol. 105, p. 411.

Razelos, P., and Georgiou, E., 1992, "Two Dimensional Effects and Design Criteria for Convective Extended Surfaces," *Heat Transfer Engineering*, Vol. 13, p. 38.

An Analytical Solution to Melting in a Finite Slab With a Boundary Condition of the Second Kind

Y. W. Zhang,[1] Y. Y. Jin,[1] Z. Q. Chen,[1] Z. F. Dong,[2] and M. A. Ebadian[2,3]

Introduction

The solid-liquid phase change phenomenon appears in nature and many industrial processes and has received much attention recently. Because of the strong nonlinearity of the solid-liquid interface (cf. Özişik, 1980), an exact solution to the melting of solids is nearly impossible, except for a few cases of the Stefan problem. Even for the simple case of the melting of a finite slab, a closed form of an exact solution cannot be obtained. A literature search indicates that melting

[1]Department of Power Machinery Engineering, Xi'an Jiaotong University, Xi'an 710049, People's Republic of China.

[2]Department of Mechanical Engineering, Florida International University, Miami, FL 33199.

[3]Mem. ASME.

Contributed by the Heat Transfer Division of THE AMERICAN SOCIETY OF MECHANICAL ENGINEERS. Manuscript received by the Heat Transfer Division April 1992; revision received December 1992. Keywords: Conduction, Moving Boundaries, Phase Change Phenomena. Associate Technical Editor: Y. Bayazitoglu.

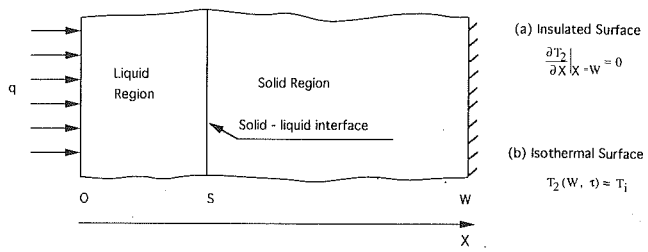

Fig. 1 Schematic of the melting problems

of a finite slab subject to a constant temperature on one surface, while the other surface is insulated, is analyzed by Cho and Sunderland (1969). The same problem with boundary conditions of the second kind has been solved by Goodman and Shea (1960) applying the perturbation method to the integral equations. They addressed the melting of a finite slab with one surface at a constant heat flux with the other surface insulated or kept at its initial uniform temperature. The perturbation method is also applied by Pedroso and Domoto (1973) to obtain the solution of planar solidification of a saturated liquid with convection on one surface. It is well known that melting of a finite slab depends on the boundary conditions imposed when the initial temperature is uniform and lower than the melting temperature. The melting process starts immediately when a constant temperature, which is higher than the melting point, is subjected to one surface of the slab. However, for the second kind of boundary condition, melting begins only after a definite period of preheating when the temperature at the heated surface reaches the melting point. Goodman and Shea (1960) introduced the parameter $\alpha = [aW/2k_2(T_m - T_i)]$ to distinguish between two cases of slabs melting with the second kind of boundary condition, where q is the heat flux on the surface; and W, k_2, T_m, and T_i are the thickness, thermal conductivity, melting temperature, and initial temperature of the slab, respectively. When $\alpha > 1$, the left wall temperature (the left surface is suppose to be heated) will achieve the melting point faster than the thermal penetration layer approaches the right end, indicating that a shorter preheating time is needed. However, for $\alpha < 1$, the left wall temperature will still be below the melting point. Even though the thermal layer penetrates the right surface, further heating is still needed for the left wall to reach the melting point. The solution to the case of $\alpha > 1$ is still not available in the open literature in spite of the solution to the case of $\alpha \le 1$ reported by Goodman and Shea (1960). Therefore, it is the aim of this technique note to analyze the constant heat flux melting of the finite slab, and the case of $\alpha > 1$ will be considered.

Problem Formulation

The problem considered in this investigation is shown in Fig. 1. The one-dimensional finite slab having width W is composed of phase-change material with an initial uniform temperature, T_i, which is below the melting temperature, T_m. It is assumed that a constant heat flux is considered to be on the left surface, and the right surface is either insulated or maintained at the initial temperature. Considering the following dimensionless variables:

$$X = x/W, \quad \tau = a_1/W^2, \quad \Theta = C_{p1}(T - T_m)/L, \quad S = s/W$$
$$\mathrm{Ste} = C_{p1}qW/k_1L, \quad Sc = C_{p2}(T_m - T_i)/L, \quad K_a = a_1/a_2,$$

where a is the thermal diffusivity; C_p is specific heat; k is thermal conductivity; and L is the latent heat of the melting; s is the solid–liquid interface location; Ste is the Stefan number; and Sc is the subcooling parameter. The subscripts 1, 2, m, and i refer to liquid, solid, melting, and initial state, respectively. The governing equations and boundary conditions are given in the following dimensionless form:

$$\frac{\partial^2\Theta_1}{\partial X^2} = \frac{\partial\Theta_1}{\partial\tau}, \qquad 0 < X < S(\tau), \quad \tau > \tau_m \tag{1}$$

$$\frac{\partial\Theta_1}{\partial X} = -\mathrm{Ste}, \qquad X = 0, \qquad \tau > \tau_m \tag{2}$$

$$\frac{\partial^2\Theta_2}{\partial X^2} = K_a\frac{\partial\Theta_2}{\partial\tau}, \qquad S(\tau) < X < 1, \quad \tau < \tau_m \tag{3}$$

$$\Theta_1(X, \tau) = \Theta_2(X, \tau) = 0, \qquad X = S(\tau), \qquad \tau > \tau_m \tag{4}$$

$$\frac{\partial\Theta_2}{\partial X} - K_a\frac{\partial\Theta}{\partial X} = K_a\frac{dS}{d\tau}, \qquad X = S(\tau), \qquad \tau > \tau_m \tag{5}$$

The right surface of the slab will be:

(*a*) *The insulated case*:

$$\frac{\partial\Theta_2}{\partial X} = 0, \qquad X = 1, \qquad \tau > \tau_m \tag{6a}$$

(*b*) *The isothermal case*:

$$\Theta_2(X, \tau) = -Sc, \qquad X = 1. \tag{6b}$$

where τ_m is the preheating duration.

Solution Method

As mentioned earlier, this technical note considers the case of $\alpha > 1$. That is, after a short time of preheating duration, the melting process will begin before the thermal penetration layer approaches the right surface of the slab, and then continue after the thermal penetration layer reaches the right surface. When the right surface is insulated, the entire slab will have melted; otherwise, the melting process will reach a steady state. Therefore, the solutions to the melting of a finite slab are obtained based on different stages, the first being the preheating duration and temperature distribution; the second, the solution before the thermal penetration layer reaches the right surface; and finally, the solution after the thermal penetration layer reaches the right surface, which is insulated or kept at a uniform temperature.

The preheating duration, thermal penetration depth, and temperature in the slab are obtained by the integral approximation method (Zhang et al., 1990). The results are given here for convenience in a subsequent discussion.

$$\tau_m = \frac{2Sc^2}{3K_a\mathrm{Ste}^2} \tag{7}$$

$$\Delta_m = \frac{2Sc}{K_a\mathrm{Ste}} \tag{8}$$

$$\Theta_2(X, \tau_m) = \begin{cases} Sc\left[\left(1 - \dfrac{X}{\Delta_m}\right)^2 - 1\right], & 0 \le X \le \Delta_m \\ -Sc, & \Delta_m < X \le 1, \end{cases} \tag{9}$$

where Δ_m is the dimensionless thermal penetration layer depth.

Solution Before the Thermal Penetration Layer Reaches the Right Surface. In this case, the melting in the slab can be considered as melting in a semi-infinite region because the boundary condition of the right surface slab has no effect on the temperature distribution in the slab. Thus, the solution to melting in a subcooled, semi-infinite solid given by Zhang et al. (1990) can be applied here. The temperature distribution in the solid phase is presented as:

$$\Theta_2(X, \tau) = Sc\left[\left(\frac{\Delta - X}{\Delta - S}\right)^2 - 1\right]. \tag{10}$$

The differential equation to relate the thermal penetration with the solid-liquid interface location is:

$$\frac{6}{K_a(\Delta - S)} = 2\frac{dS}{d\tau} + \frac{d\Delta}{d\tau}. \tag{11}$$

The temperature distribution of the liquid phase has been obtained by El-Genk and Cronenberg (1979) as follows:

$$\Theta_1(X, \tau) = \mathrm{Ste}\sqrt{4(\tau - \tau_m)} \times \left[\mathrm{ierfc}\left(\frac{X}{\sqrt{4(\tau-\tau_m)}}\right) - \mathrm{ierfc}\left(\frac{S}{\sqrt{4(\tau-\tau_m)}}\right)\right], \tag{12}$$

where ierfc is the integral of the complementary error function. The differential equation of the solid-liquid interface location is expressed as:

$$\frac{ds}{d\tau} = \mathrm{Ste}\ \mathrm{erfc}\left(\frac{S}{\sqrt{4(\tau-\tau_m)}}\right) - \frac{2Sc}{K_a(\Delta - S)}, \tag{13}$$

and the initial conditions of Eqs. (11) and (13) are:

$$S(\tau_m) = 0 \tag{14}$$

$$\Delta(\tau_m) = \Delta_m. \tag{15}$$

Now, solving Eqs. (13) and (15) by applying the Runge-Kutta technique, the interface location and the thermal penetration depth can be determined for the time period $\tau_m \sim \tau_1$. τ_1 is the time at which the thermal penetration layer reaches the right surface. Obviously, $\Delta(\tau_1) = 1$.

Solution After the Thermal Penetration Layer Reaches the Insulated Right Wall. After the thermal penetration layer reaches the insulated right wall, the temperature of the liquid phase can still be calculated by applying Eq. (12), while simultaneously, the temperature distribution in the solid phase can be determined by the following integral method.

Integrating Eq. (3) with respect to X between (S, 1), and considering the boundary conditions, Eqs. (4) and (6*a*), the integral equation of the solid phase is:

$$-\left.\frac{\partial \Theta_2}{\partial X}\right|_{x=s} = K_a \frac{dH_2}{d\tau}, \tag{16}$$

where

$$H_2 = \int_s^1 \Theta_2 dX.$$

Assume that $\Theta_2(X, \tau)$ is of the form:

$$\Theta_2(X, \tau) = B_1(X - S) + B_2(X - S)^2, \tag{17}$$

where B_1 and B_2 are functions of τ. Substitution of Eq. (6*a*) into Eq. (17) gives:

$$\Theta_2 = B_2[(X - S)^2 - 2(1 - S)(X - S)]. \tag{18}$$

Substituting Eq. (18) into integral Eq. (16), and defining $\eta(\tau) = B_2(1 - S)^3$, one then obtains:

$$\frac{d\eta}{d\tau} + \frac{3\eta}{K_a(1-S)^2} = 0. \tag{19}$$

The initial value of η is obtained from Eq. (10):

$$\eta(\tau_1) = Sc[1 - S(\tau_1)]. \tag{20}$$

By means of separation of the variables, $\eta(\tau)$ is obtained as:

$$\eta(\tau) = Sc[1 - S(\tau_1)]\exp\left[-\int_{\tau_1}^{\tau} \frac{3}{K_a(1-S)^2}\, d\tau\right]. \tag{21}$$

The temperature distribution of the solid phase is then given by:

$$\Theta_2(X, \tau) = \frac{\eta(\tau)}{(1-S)^3}[(X - S)^2 - 2(1 - S)(X - S)]. \tag{22}$$

Substituting Eqs. (22) and (12) into Eq. (5), one obtains:

$$\frac{dS}{d\tau} = \mathrm{Ste}\ \mathrm{erfc}\left(\frac{S}{\sqrt{4(\tau-\tau_m)}}\right) - \frac{2\eta(\tau)}{K_a(1-S)^2}, \tag{23}$$

where erfc is the complementary error function. Therefore, the solid-liquid interface location and temperature distribution in the solid phase are calculated by solving coupled Eqs. (21)-(23) with the help of the Runge-Kutta method.

Solution After the Thermal Penetration Layer Reaches the Isothermal Right Wall. The solution after the thermal penetration layer reaches the right isothermal wall is found by the integral approximation method. With a similar derivation of Eq. (16), the integral equation in the solid phase with a constant wall temperature at the right end is given as:

$$\left.\frac{\partial \Theta_2}{\partial X}\right|_{x=1} - \left.\frac{\partial \Theta_2}{\partial X}\right|_{x=s} = K_a \frac{dH_2}{d\tau}. \tag{24}$$

Assuming the temperature distribution in the solid phase to be a second-order polynomial and considering the boundary condition of Eq. (6*b*), the temperature distribution in the solid phase will be expressed as:

$$\Theta_2(X, \tau) = -\frac{Sc}{1-S}(X - S) + \frac{\eta(\tau)}{(1-S)^3}[(X - S)^2 - (1 - S)(X - S)]. \tag{25}$$

With the substitution of Eq. (25) into Eq. (24), an ordinary differential equation with $\eta(\tau)$ as a dependent variable is obtained:

$$\frac{d\eta}{d\tau} + \frac{12}{K_a(1-S)^2}\eta - 3Sc\frac{dS}{d\tau} = 0. \tag{26}$$

The initial value of $\eta(\tau)$ is determined from Eq. (20).

Assuming that the temperature distribution is of a quadratic form in the liquid phase, and taking into account the boundary conditions of Eqs. (2), (4), and (5), the temperature distribution expression in the liquid phase can be derived in a similar manner (cf. Zhang et al., 1990).

$$\Theta_1(X, \tau) = \frac{\mathrm{Ste}}{2S}(X - S)^2 - \frac{p}{2S^2}(X^2 - S^2), \tag{27}$$

where

$$p = \frac{1}{2}\sqrt{\left[\frac{ScS}{K_a(1-S)} + \frac{S\eta(\tau)}{K_a(1-S)^2} - 1\right]^2 + 4S\ \mathrm{Ste}} + \frac{1}{2}\left[\frac{ScS}{K_a(1-S)} + \frac{S\eta(\tau)}{K_a(1-S)^2} - 1\right].$$

Integrating Eq. (1) with respect to X from 0 to S, we have:

$$\left.\frac{\partial \Theta_1}{\partial X}\right|_{x=s} + \mathrm{Ste} = \frac{dH_1}{d\tau}, \tag{28}$$

where

$$H_1 = \int_0^s \Theta_1 dX.$$

Substituting integral Eqs. (24) and (28) into the solid-liquid interface Eq. (5), one obtains:

$$\left(1 - \frac{1}{4}Sc\right)\frac{dS}{d\tau} + \frac{1}{12}\frac{d\eta}{d\tau} + \frac{dH_1}{d\tau} + \frac{dH_2}{d\tau} + \frac{Sc}{K_a(1-S)} = \mathrm{Ste}. \tag{29}$$

Integrating both sides of Eq. (29) with respect to (τ_1, τ), one obtains:

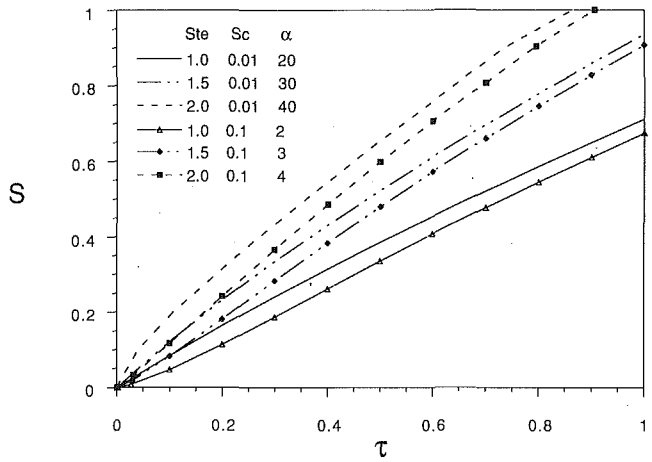

Fig. 2 Solid-liquid interface variation with time for the insulated right surface

$$[12+3Sc+2(\mathrm{Ste}S+2p)]S=\eta(\tau)-Sc\{5+4[S(\tau_1)-\Delta_m]\}$$
$$+12\mathrm{Ste}(\tau-\tau_m)-\int_{\tau_1}^{\tau}\frac{12Sc}{K_a(1-S)}\,d\tau. \quad (30)$$

Equations (20), (25), (26), (27), and (30) are used to obtain the temperature distributions in the solid and liquid phases and the solid-liquid interface location. This is accomplished by using the Runge-Kutta method.

Results and Discussion

In this section, the discussion will emphasize variation of the solid-liquid interface location with time. The two cases of the insulated right surface and the isothermal right surface of the slab are considered. All the solutions are obtained for the value of $\alpha > 1$.

The first case is the melting of a slab subjected to an insulated right surface. Figure 2 shows the variation of the solid-liquid interface location with dimensionless time and with Stefan numbers Ste = 1.0, 1.5, and 2.0, and the subcooling parameters of $Sc = 0.01$ and 0.1. The corresponding values of α are given in the figure. It is seen from this figure that the solid-liquid interface varies almost linearly with time. The effect of the Stefan number on melting is positive. That is, the greater the Stefan number, the greater the value of S (or the more liquid fraction). This is because all the heat added is used for melting without any loss at the right surface. The subcooling parameter, Sc, has an opposite effect on melting. More heat is needed to increase the solid phase temperature to the melting temperature.

In the case of the slab having a right isothermal surface, the variation of the solid-liquid interface location with time is depicted in Figs. 3(*a*) and 3(*b*). The corresponding parameters used to draw these figures are displayed on each figure. It is obvious that the melting process will reach a steady state, and the interface location does not change with time. It is seen that under the same subcooling conditions, the time it takes to reach a steady state decreases as the Stefan number increases. Also, the liquid fraction increases as the Stefan number increases. From Eq. (29), when the process reaches the steady state, the solid-liquid interface location can be expressed as:

$$S(\infty)=1-\frac{Sc}{K_a\mathrm{Ste}}=1-\frac{1}{2\alpha},$$

which means that the solid-liquid interface location in the steady state approaches 1 as parameter, α, increases. A greater

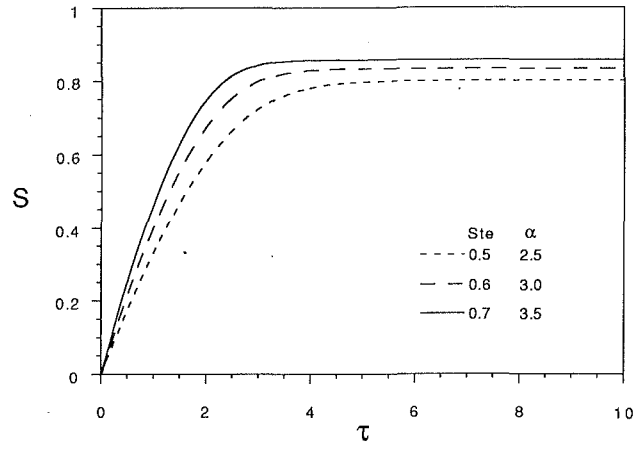

(a) Sc = 0.04

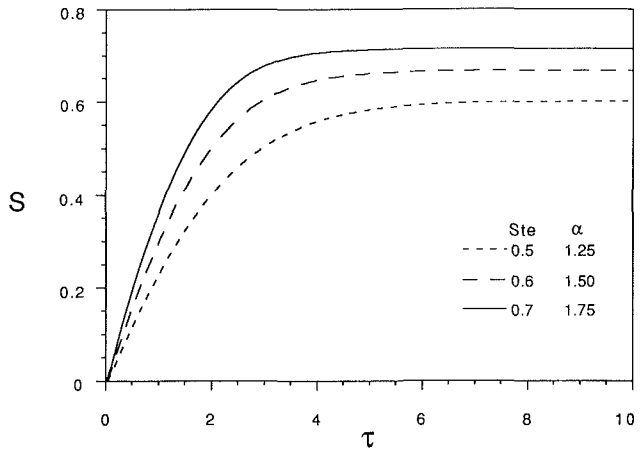

(b) Sc = 0.08

Fig. 3 Solid-liquid interface variation with time for the isothermal right surface

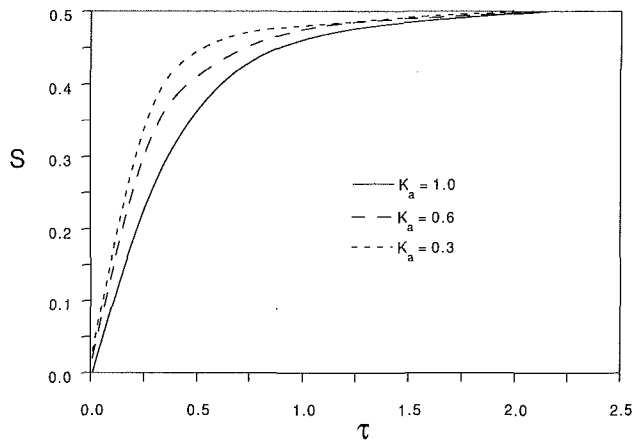

Fig. 4 Solid-liquid interface variation with time for the isothermal right surface ($\alpha = 1$, $Sc = 5.0$)

quantity of liquid can be obtained before a steady state is achieved when more heat is added.

On the other hand, the present method can be applied to analyze the case of $\alpha \geq 1$ (cf. Zhang, 1991) and the comparison of the predicted results show excellent agreement with Goodman and Shea (1960). Furthermore, using the present method of analysis, one can obtain the solution in the event the Goodman and Shea method fails. For example, for the case of $\alpha = 1$

and $Sc = 5.0$, the solid–liquid interface location variation with time with the parameter $K_a = 0.3$, 0.6, and 1.0 is demonstrated in Fig. 4. It is seen that as K_a decreases, the liquid fraction increases. Finally, the melting process reaches the steady state, $S = 0.5$.

Concluding Remarks

In this paper, the melting of a finite slab has been analyzed. The slab is subjected to the conditions of a constant heat flux on one surface, and either an insulated or a constant temperature maintained on the other surface. The solutions were obtained using the Runge–Kutta and integral approximation methods for the case of $\alpha > 1$. Some of the results are shown in the figures to discuss the influences of associated parameters, such as K_a, Sc, Ste, or α.

Acknowledgments

The results presented in this technical note were obtained partially in the course of research sponsored by the Chinese National Science Foundation.

References

Cho, S. H., and Sunderland, J. E., 1969, "Heat Conduction Problem With Melting or Freezing," ASME JOURNAL OF HEAT TRANSFER, Vol. 91, pp. 421–426.

El-Genk, M. A., and Cronenberg, A. W., 1979, "Solidification in a Semi-infinite Region With Boundary Conditions of the Second Kind: An Exact Solution," *Letters in Heat Mass Transfer*, Vol. 6, pp. 321–327.

Goodman, T. R., and Shea, J. J., 1960, "The Melting of Finite Slabs," ASME *Journal of Applied Mechanics*, Vol. 27, pp. 16–24.

Özişik, M. N., 1980, *Heat Conduction*, Wiley-Interscience, New York.

Pedroso, R. I., and Domoto, G. A., 1973, "Exact Solution by Perturbation Method for Planar Solidification of a Saturated Liquid With Convection at the Wall," *Int. J. Heat Mass Transfer*, Vol. 6, pp. 1816–1819.

Zhang, Y. W., Chen, Z. Q., and Wang, Q. J., 1990, "Analytical Solution of Melting in a Subcooled Semi-infinite Solid With a Boundary Condition of the Second Kind," *Int. Symp. on Manufacturing and Materials Processing*, Dubrovnik, Yugoslavia.

Zhang, Y. W., 1991, "Melting Heat Transfer in an Enclosure With Discrete Heat Sources," Ph.D. Thesis, Xi'an Jiatong University, People's Republic of China.

Stability and Recovery Behavior of Tape/Film-Type Superconductors

A. Ünal,[1] M.-C. Chyu,[1] and T. M. Kuzay[2]

Introduction

Thermal stability is one of the major issues in the design of superconducting devices. Stability of superconductors has been investigated from different viewpoints such as cryogenic stability, normal zone propagation, and adiabatic stability. For a thin-film superconductor, found in technologies for energy conservation, nuclear fusion, MHD-power generation, linear motor cars, nuclear magnetic resonance, superconducting switches, and superconducting quantum interferometric devices, it was pointed out by Flik and Tien (1990) that the stability criterion should be based on the consideration of intrinsic stability. They considered the criterion of intrinsic stability for a thin-film superconductor subjected to a heat release from a centrally located line heat source, as depicted in Fig. 1. The criterion is expressed as

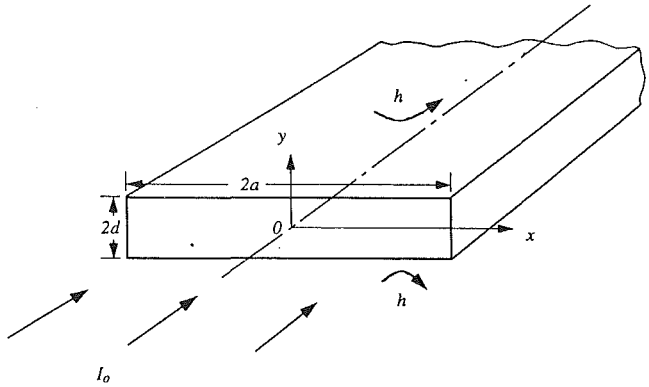

Fig. 1 Definition of geometry of a tape/film superconductor

$$J_r \le 1 - \phi_{\max} \tag{1}$$

where $J_r = J_o/J_{co}$, with J_o being the operating current density, and J_{co} the critical current density at the operating temperature T_o. $\phi_{\max}$ is the maximum value of the instability parameter ϕ during the process, with ϕ defined as

$$\phi(t) = \frac{1}{ad}\int_0^d \int_0^a g(\theta)\,dxdy \tag{2}$$

where

$$g(\theta) = \begin{cases} \theta, & 0 \le \theta \le 1; \\ 1, & \theta > 1 \end{cases} \tag{3}$$

and $\theta = (T - T_o)/(T_c - T_o)$ with T_c being the critical temperature.

Flik and Tien (1990) calculated ϕ for the thin-film superconductor of Fig. 1 by solving the heat diffusion equation using a finite-difference method. In the present work, the heat diffusion equation is solved analytically through separation of variables. Based on the result of the intrinsic stability analysis, the present work further addresses the issue of recoverability of a quenched superconductor, and studies the recovery mechanism based on the instability parameter, cryogenic cooling rate, and Joule heating rate. Recovery of superconductivity based on a different stability criterion for a one-dimensional infinite superconducting winding structure has been studied by Bejan and Tien (1978).

Analysis

In accordance with Eq. (1), intrinsic stability fails at the instant t_1 that $\phi(t_1) = 1 - J_r$. Before intrinsic stability fails, i.e., $0 < t < t_1$, for the thin-film superconductor subjected to an instantaneous heat release at the axis, and convective heat transfer on the surfaces, as depicted in Fig. 1, the temperature distribution is obtained by solving the following heat conduction problem:

$$\frac{\partial^2\theta}{\partial\xi^2} + \frac{\partial^2\theta}{\partial\eta^2} = \frac{\partial\theta}{\partial\tau},\ \theta(\xi, \eta, \tau), \quad 0 < \xi < r, \quad 0 < \eta < 1, \quad 0 < \tau \le \tau_1 \tag{4}$$

with insulated boundary conditions at $\xi = 0$ and $\eta = 0$, and convective boundary condition at $\xi = r$ and $\eta = 1$ (Ünal et al., 1991). The initial condition is based on the assumption that energy is initially deposited in an area of $4\Delta x \times \Delta y$, of which the normalized form is:

[1]Department of Mechanical Engineering, Texas Tech University, Lubbock, TX 79409-1021.

[2]Materials and Components Technology Division, Argonne National Laboratory, Argonne, IL 60439-4838.

Contributed by the Heat Transfer Division and based on a paper presented at the Intersociety Energy Conversion Engineering Conference, Boston, Massachusetts, August 4–9, 1991. Manuscript received by the Heat Transfer Division July 1991; revision received April 1992. Keywords: Conduction, Transient and Unsteady Heat Transfer. Associate Technical Editor: L.S. Fletcher.

and $Sc = 5.0$, the solid–liquid interface location variation with time with the parameter $K_a = 0.3$, 0.6, and 1.0 is demonstrated in Fig. 4. It is seen that as K_a decreases, the liquid fraction increases. Finally, the melting process reaches the steady state, $S = 0.5$.

Concluding Remarks

In this paper, the melting of a finite slab has been analyzed. The slab is subjected to the conditions of a constant heat flux on one surface, and either an insulated or a constant temperature maintained on the other surface. The solutions were obtained using the Runge–Kutta and integral approximation methods for the case of $\alpha > 1$. Some of the results are shown in the figures to discuss the influences of associated parameters, such as K_a, Sc, Ste, or α.

Acknowledgments

The results presented in this technical note were obtained partially in the course of research sponsored by the Chinese National Science Foundation.

References

Cho, S. H., and Sunderland, J. E., 1969, "Heat Conduction Problem With Melting or Freezing," ASME JOURNAL OF HEAT TRANSFER, Vol. 91, pp. 421–426.

El-Genk, M. A., and Cronenberg, A. W., 1979, "Solidification in a Semi-infinite Region With Boundary Conditions of the Second Kind: An Exact Solution," *Letters in Heat Mass Transfer*, Vol. 6, pp. 321–327.

Goodman, T. R., and Shea, J. J., 1960, "The Melting of Finite Slabs," ASME *Journal of Applied Mechanics*, Vol. 27, pp. 16–24.

Özişik, M. N., 1980, *Heat Conduction*, Wiley-Interscience, New York.

Pedroso, R. I., and Domoto, G. A., 1973, "Exact Solution by Perturbation Method for Planar Solidification of a Saturated Liquid With Convection at the Wall," *Int. J. Heat Mass Transfer*, Vol. 6, pp. 1816–1819.

Zhang, Y. W., Chen, Z. Q., and Wang, Q. J., 1990, "Analytical Solution of Melting in a Subcooled Semi-infinite Solid With a Boundary Condition of the Second Kind," *Int. Symp. on Manufacturing and Materials Processing*, Dubrovnik, Yugoslavia.

Zhang, Y. W., 1991, "Melting Heat Transfer in an Enclosure With Discrete Heat Sources," Ph.D. Thesis, Xi'an Jiatong University, People's Republic of China.

Stability and Recovery Behavior of Tape/Film-Type Superconductors

A. Ünal,[1] M.-C. Chyu,[1] and T. M. Kuzay[2]

Introduction

Thermal stability is one of the major issues in the design of superconducting devices. Stability of superconductors has been investigated from different viewpoints such as cryogenic stability, normal zone propagation, and adiabatic stability. For a thin-film superconductor, found in technologies for energy conservation, nuclear fusion, MHD-power generation, linear motor cars, nuclear magnetic resonance, superconducting switches, and superconducting quantum interferometric devices, it was pointed out by Flik and Tien (1990) that the stability criterion should be based on the consideration of intrinsic stability. They considered the criterion of intrinsic stability for a thin-film superconductor subjected to a heat release from a centrally located line heat source, as depicted in Fig. 1. The criterion is expressed as

$$J_r \le 1 - \phi_{\max} \tag{1}$$

where $J_r = J_o/J_{co}$, with J_o being the operating current density, and J_{co} the critical current density at the operating temperature T_o. $\phi_{\max}$ is the maximum value of the instability parameter ϕ during the process, with ϕ defined as

$$\phi(t) = \frac{1}{ad}\int_0^d \int_0^a g(\theta)\,dxdy \tag{2}$$

where

$$g(\theta) = \begin{cases} \theta, & 0 \le \theta \le 1; \\ 1, & \theta > 1 \end{cases} \tag{3}$$

and $\theta = (T - T_o)/(T_c - T_o)$ with T_c being the critical temperature.

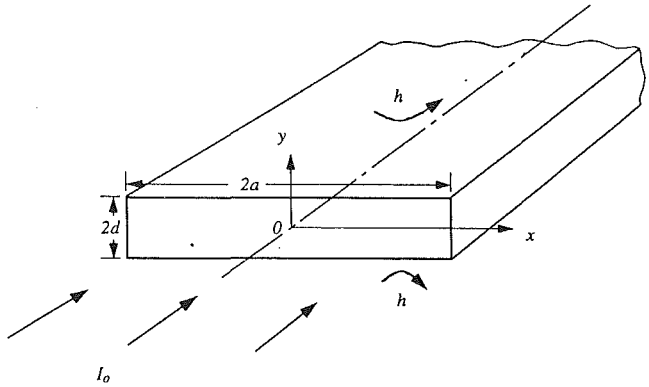

Fig. 1 Definition of geometry of a tape/film superconductor

Flik and Tien (1990) calculated ϕ for the thin-film superconductor of Fig. 1 by solving the heat diffusion equation using a finite-difference method. In the present work, the heat diffusion equation is solved analytically through separation of variables. Based on the result of the intrinsic stability analysis, the present work further addresses the issue of recoverability of a quenched superconductor, and studies the recovery mechanism based on the instability parameter, cryogenic cooling rate, and Joule heating rate. Recovery of superconductivity based on a different stability criterion for a one-dimensional infinite superconducting winding structure has been studied by Bejan and Tien (1978).

Analysis

In accordance with Eq. (1), intrinsic stability fails at the instant t_1 that $\phi(t_1) = 1 - J_r$. Before intrinsic stability fails, i.e., $0 < t < t_1$, for the thin-film superconductor subjected to an instantaneous heat release at the axis, and convective heat transfer on the surfaces, as depicted in Fig. 1, the temperature distribution is obtained by solving the following heat conduction problem:

$$\frac{\partial^2\theta}{\partial\xi^2} + \frac{\partial^2\theta}{\partial\eta^2} = \frac{\partial\theta}{\partial\tau},\ \theta(\xi, \eta, \tau), \quad 0 < \xi < r, \quad 0 < \eta < 1, \quad 0 < \tau \le \tau_1 \tag{4}$$

with insulated boundary conditions at $\xi = 0$ and $\eta = 0$, and convective boundary condition at $\xi = r$ and $\eta = 1$ (Ünal et al., 1991). The initial condition is based on the assumption that energy is initially deposited in an area of $4\Delta x \times \Delta y$, of which the normalized form is:

[1]Department of Mechanical Engineering, Texas Tech University, Lubbock, TX 79409-1021.

[2]Materials and Components Technology Division, Argonne National Laboratory, Argonne, IL 60439-4838.

Contributed by the Heat Transfer Division and based on a paper presented at the Intersociety Energy Conversion Engineering Conference, Boston, Massachusetts, August 4–9, 1991. Manuscript received by the Heat Transfer Division July 1991; revision received April 1992. Keywords: Conduction, Transient and Unsteady Heat Transfer. Associate Technical Editor: L.S. Fletcher.

$$\theta(\xi, \eta, 0) = \begin{cases} \theta_d, & 0 \le \xi \le \Delta\xi, \quad 0 \le \eta \le \Delta\eta \\ 0, & \Delta\xi < \xi < r, \quad \Delta\eta < \eta < 1 \end{cases} \tag{5}$$

The nondimensional parameters involved in the above formulation are defined as

$$\xi = \frac{x}{d\sqrt{k_r}} \quad k_r = \frac{k_x}{k_y} \quad \eta = \frac{y}{d} \quad \tau = \frac{k_y t}{d^2 \rho C} \quad r = \frac{a}{d\sqrt{k_r}}$$

$$\mathrm{Bi} = \frac{hd}{k} \quad k = (k_x k_y)^{1/2} \quad \theta_d = \frac{\epsilon_d \tau}{\Delta\xi \Delta\eta} \quad \epsilon_d = \frac{e_d}{\rho C (T_c - T_o) 4ad} \tag{6}$$

where k is thermal conductivity, ρ is density, C is specific heat, h is heat transfer coefficient, e_d is the disturbance thermal energy per unit length.

The above problem can be readily solved following the standard method of separation of variables described, for example, by Özişik (1980), and the result is

$$\theta(\xi, \eta, \tau) = \theta_d \sum_{m=1}^{\infty} \sum_{n=1}^{\infty} \frac{\sin(\beta_m \Delta\xi)}{\beta_m N(\beta_m)} \frac{\sin(\gamma_n \Delta\eta)}{\gamma_n N(\gamma_n)} \times \cos(\beta_m \xi) \cos(\gamma_n \eta) e^{-(\beta_m^2 + \gamma_n^2)\tau} \tag{7}$$

where

$$\beta_m \tan(\beta_m r) = \mathrm{Bi}, \quad \frac{1}{N(\beta_m)} = \frac{2(\beta_m^2 + \mathrm{Gi}^2)}{r(\beta_m^2 + \mathrm{Bi}^2) + \mathrm{Bi}},$$

$$\gamma_n \tan \gamma_n = k_r^{1/2} \mathrm{Bi}, \quad \frac{1}{N(\gamma_n)} = \frac{2(\gamma_n^2 + k_r \mathrm{Bi}^2)}{\gamma_n^2 + k_r \mathrm{Bi}_2 + k_r^{1/2} \mathrm{Bi}} \tag{8}$$

It was found that the temperature solution is independent of the dimensions of the heat source, $\Delta\xi$ and $\Delta\eta$, when very small dimensional values simulating a line heat source are used. All the data presented in this work are independent of the heat source dimensions. Based on the temperature solution, the instability parameter ϕ, as defined in Eq. (2), is calculated through numerical integration.

After intrinsic stability fails, the entire superconductor starts generating heat. Assuming temperature-independent properties, the heat conduction equation becomes

$$\frac{\partial^2 \theta}{\partial \xi^2} + \frac{\partial^2 \theta}{\partial \eta^2} + \frac{J_o^2 \sigma d^2}{k_y (T_e - T_o)} = \frac{\partial \theta}{\partial \tau}, \quad \tau_1 < \tau < \tau_2 \tag{9}$$

where τ_2 corresponds to the time t_2 when superconductivity is restored, or when intrinsic stability is again satisfied; i.e., $\phi(t_2) = 1 - J_r$. Beyond t_2, there is no heat generation, and heat diffusion is again described by Eq. (4). Equation (9) was solved using a simple explicit finite difference scheme found from, for example, Anderson et al. (1984).

Results and Discussion

The quenching and recovery behavior of an NbTi superconductor was studied based on the variation of instability parameter with time as exhibited in Fig. 2, as well as the q_r versus time data in Fig. 3, where $q_r = q_g/q_{cv}$, with the Joule heating rate $q_g = J_o^2 \sigma a d$ after stability fails, and q_{cv} being the convective cooling heat transfer rate. The data in Figs. 2 and 3 are based on an aspect ratio $a_r = a/d = 10$, Bi = 0.18, $h = 1 \times 10^4$ W/m^2-K, $d = 2 \times 10^{-6}$ m, and $k = 0.11$ W/m-K for an NbTi superconductor operating at $T_o = 4.2$ K. Other properties include $\sigma = 6 \times 10^{-7}$ Ω-m, $J_{co} = 1 \times 10^9$ A/m^2, $T_c = 9.6$ K, $\rho = 6200$ kg/m^3, $C = 0.87$ J/kg-K (Tien et al., 1989).

The ϕ data in Fig. 2 demonstrate that superconductor is intrinsically stable if $0 < J_r < 0.1039$. The upper limit of J_r is equal to $1 - \phi_{\max}$, and J_r's within this range satisfy Eq. (1). Since Joule heating never takes place in this range, the parameter ϕ is simply governed by the passive diffusion of heat from the initial thermal disturbance, and it is independent of J_r. This ϕ versus τ curve is designated as the curve of intrinsic stability. The curve of intrinsic stability in fact covers J_r up to 0.10385796677425O1. When J_r is increased to 0.10385796677425O2, the data shift to the curve marked with $J_r = 0.1039$.

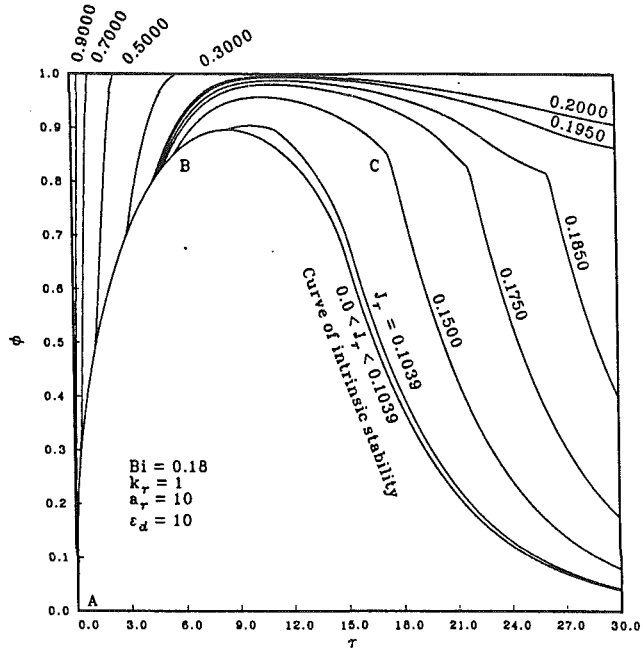

Fig. 2 Variation of ϕ with time for a low-T_c superconductor with a small aspect ratio

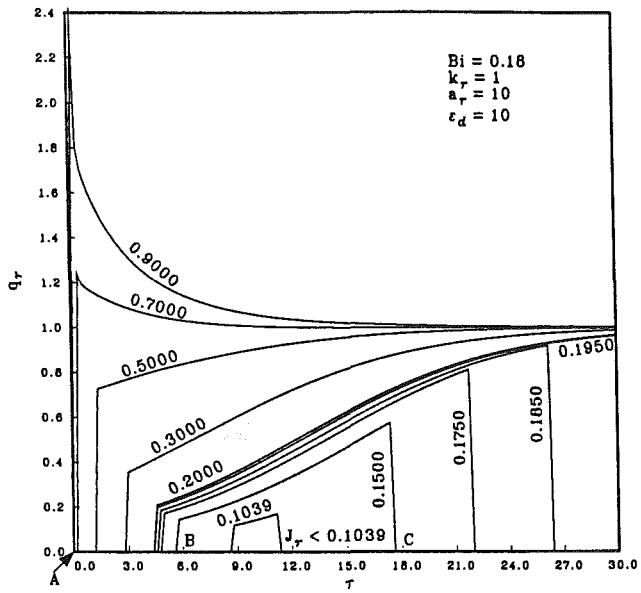

Fig. 3 Variation of q_r with time for a low-T_c superconductor with a small aspect ratio

After intrinsic stability fails, there is a chance that the superconductor reverts to its original operation state if J_r is small. This phenomenon is only observed with a small a_r. A typical recovery process of a superconductor is illustrated by the data of $J_r = 0.15$ in Fig. 2. This relatively low current density ratio was selected in order to illustrate better the characteristics of superconductivity recovery. After the thermal energy release at point A, the normal zone grows as the result of heat diffusion, leading to the failure of intrinsic stability at point B where $\phi = 1 - J_r$. Right after stability fails, heat starts to be generated throughout the conductor, which causes a discontinuity of slope at point B (Fig. 2), and a step jump in q_r at the same time in Fig. 3. After heat generation begins, the

convective heat transfer rate remains several times greater than the heat generation rate (Fig. 3), which eventually lowers the temperature as well as the parameter ϕ. The superconducting state is restored at point C when the intrinsic stability criterion ($\phi = 1 - J_r$) is again satisfied (Fig. 2). Point C marks a slope discontinuity in the ϕ versus τ curve, due to the abrupt cease of heat generation when superconductivity is restored, as shown by the step drop of q_r to zero at the same time in Fig. 3. Beyond point C, ϕ gradually decreases to zero, and the superconductor fully recovers from quenching.

It is noted that the time span between the failure of stability (point B) and recovery of superconductivity (point C) increases with J_r (Fig. 2), denoting that at a smaller current density, superconductivity is recovered within a shorter time after stability fails. The time span decreases to a minimum for $J_r = 0.1039$, which, according to the stability criterion, corresponds to the maximum ϕ value of the curve of intrinsic stability, 0.8961. It is noted that the point of stability failure (point B) moves toward the apex of the intrinsic stability curve as J_r decreases. The point never exceeds the apex, because no instability will occur if the conductor remains superconducting at the maximum ϕ [Eq. (1)].

Recovery of superconductivity can occur only if the current density ratio J_r is small. In Fig. 3, it is demonstrated that if J_r is higher than a critical value (approximately 0.195 in the present case), an equilibrium will be reached between the convective cooling rate and the Joule heating rate, as the q_r data asymptotically approaching unity, and superconductivity will never be recovered. The irrecoverability at high J_r's is confirmed by carrying the calculation to $\tau = 150$.

The q_r value generally increases with J_r for a particular instant of time. At high J_r levels ($J_r = 0.7, 0.9$), the heating rate is always higher than the cooling rate after stability fails (Fig. 3). The cooling rate then increases as a result of surface temperature hike until a steady-state equilibrium is reached, and superconductivity is never restored. The ϕ data at high J_r's also demonstrate trends never reaching zero in Fig. 2.

The condition of superconductivity recovery was studied by comparing the present data with those of conventional cryogenic stability. Stekly and Zar (1965) considered that, if the Joule heating rate is smaller than convective cooling rate, the superconductor should cool down continuously until stability resumes. The recovery condition can thus be written as $q_r < 1$. The data in Fig. 3 show that such a condition is satisfied for $J_r < 0.5$ at least. (The actual value should be between 0.5 and 0.7). However, the data also show that superconductivity can not be recovered for $J_r > 0.1900$. Apparently, the conventional concept of cryogenic stability leads to a criterion too liberal for the recovery of superconductivity for the present case.

Analysis was also conducted for a NbTi superconductor with a large aspect ratio, $a_r = 100$ (Ünal et al., 1991). It was found that stability is maintained in $0 < J_r < 0.8574$, a range wider than $a_r = 10$. Such increase of the stability range is due to the fact that the normal zone occupies a smaller portion of a superconductor with a larger a_r before the heat is transferred to the surface and is dissipated through convective cooling. Unlike the aforementioned behavior of the superconductor with a small a_r, with $a_r = 100$, superconductivity can never be recovered once the intrinsic stability fails. Data were also generated for a similar high-T_c $YBa_2Cu_3O_7$ superconductor operating at 77 K (Ünal et al., 1991). It was found that at $a_r = 100$, the YBCO superconductor generally demonstrates a similar trend but slightly lower values of ϕ compared with NbTi, due to the slightly higher Bi. The q_r data also display similar trends as those of NbTi, except that the values are higher due to a high normal-state resistivity. This high normal state resistivity inhibits recovery of superconductivity after failure of intrinsic stability even at a small aspect ratio. Both the ϕ data and the q_r data indicate that the operation of superconductor can be either intrinsically stable (at low J_r's) or irrecoverably unstable (at high J_r's). However, recovery was observed in cases involving very small aspect ratios and current densities (e.g., at $a_r = 5$ and $J_r < 0.1$). The process of recovery is qualitatively similar to that of the NbTi superconductor (Figs. 2 and 3).

Conclusions

Thermal stability of tape/film type superconductors is studied by considering the influence of the thermal disturbance from a centrally located line heat source. A model was developed that includes an analytical solution for the temperature distribution prior to the failure of intrinsic stability, and a numerical solution thereafter. It is found that for a typical NbTi superconductor, recovery can occur with a small aspect ratio (thick and narrow), and three characteristic regions can be identified. In the low current density region, the operation is always stable. In the medium current density region, the superconductor experiences a failure of intrinsic stability first; then recovers as the result of cryogenic cooling. In the high current density region, intrinsic stability fails and superconductivity is never recovered. For an NbTi superconductor of a large aspect ratio and a high-T_c YBCO superconductor with either large or small aspect ratio, superconductivity cannot be restored after intrinsic stability fails.

References

Anderson, D. A., Tannehill, J. C., and Pletcher, R. A., 1984, *Computational Fluid Mechanics and Heat Transfer*, Hemisphere Publishing Corp., New York.

Bejan, A., and Tien, C. L., 1978, "Effect of Axial Conduction and Metal-Helium Heat Transfer on the Local Stability of Superconducting Composite Media," *Cryogenics*, Vol. 18, pp. 433–441.

Flik, M. I., and Tien, C. L., 1990, "Intrinsic Thermal Stability of Anisotropic Thin-Film Superconductors," ASME JOURNAL OF HEAT TRANSFER, Vol. 112, pp. 10–15.

Özişik, M. N., 1980, *Heat Conduction*, Wiley, New York.

Stekly, Z. J. J., and Zar, J. L., 1965, "Stable Superconducting Coils," *IEEE Transactions on Nuclear Science*, Vol. 12, No. 3, pp. 367–372.

Tien, C. L., Flik, M. I., and Phelan, P. E., 1989, "Mechanisms of Local Thermal Stability in High-Temperature Superconductors," *Cryogenics*, Vol.29, p. 602.

Ünal, A., Chyu, M.-C., and Kuzay, T. M., 1991, "Intrinsic Stability and Recovery Analysis for Tape/Film Type Superconductors," *Proc. of 26th Intersociety Energy Conversion Engineering Conference*, Vol. 4, pp. 497–502.

Conjugate Laminar Forced Convection From a Flat Plate With Imposed Pressure Gradient

B. V. S. S. Prasad[1] and S. Dey Sarkar[2]

Nomenclature

b = thickness of plate
c_p = specific heat
k = thermal conductivity
k_r = thermal conductivity ratio = k_s/k_f

[1]Assistant Professor, Department of Mechanical Engineering, Indian Institute of Technology, Kharagur-721 302, India.

[2]M. Tech. Student, Department of Mechanical Engineering, Indian Institute of Technology, Kharagpur-721 302, India.

Contributed by the Heat Transfer Division of THE AMERICAN SOCIETY OF MECHANICAL ENGINEERS. Manuscript received by the Heat Transfer Division December 1991; revision received June 1992. Keywords: Conjugate Heat Transfer, Forced Convection. Associate Technical Editor: R. J. Simoneau.

convective heat transfer rate remains several times greater than the heat generation rate (Fig. 3), which eventually lowers the temperature as well as the parameter ϕ. The superconducting state is restored at point C when the intrinsic stability criterion ($\phi = 1 - J_r$) is again satisfied (Fig. 2). Point C marks a slope discontinuity in the ϕ versus τ curve, due to the abrupt cease of heat generation when superconductivity is restored, as shown by the step drop of q_r to zero at the same time in Fig. 3. Beyond point C, ϕ gradually decreases to zero, and the superconductor fully recovers from quenching.

It is noted that the time span between the failure of stability (point B) and recovery of superconductivity (point C) increases with J_r (Fig. 2), denoting that at a smaller current density, superconductivity is recovered within a shorter time after stability fails. The time span decreases to a minimum for $J_r = 0.1039$, which, according to the stability criterion, corresponds to the maximum ϕ value of the curve of intrinsic stability, 0.8961. It is noted that the point of stability failure (point B) moves toward the apex of the intrinsic stability curve as J_r decreases. The point never exceeds the apex, because no instability will occur if the conductor remains superconducting at the maximum ϕ [Eq. (1)].

Recovery of superconductivity can occur only if the current density ratio J_r is small. In Fig. 3, it is demonstrated that if J_r is higher than a critical value (approximately 0.195 in the present case), an equilibrium will be reached between the convective cooling rate and the Joule heating rate, as the q_r data asymptotically approaching unity, and superconductivity will never be recovered. The irrecoverability at high J_r's is confirmed by carrying the calculation to $\tau = 150$.

The q_r value generally increases with J_r for a particular instant of time. At high J_r levels ($J_r = 0.7, 0.9$), the heating rate is always higher than the cooling rate after stability fails (Fig. 3). The cooling rate then increases as a result of surface temperature hike until a steady-state equilibrium is reached, and superconductivity is never restored. The ϕ data at high J_r's also demonstrate trends never reaching zero in Fig. 2.

The condition of superconductivity recovery was studied by comparing the present data with those of conventional cryogenic stability. Stekly and Zar (1965) considered that, if the Joule heating rate is smaller than convective cooling rate, the superconductor should cool down continuously until stability resumes. The recovery condition can thus be written as $q_r < 1$. The data in Fig. 3 show that such a condition is satisfied for $J_r < 0.5$ at least. (The actual value should be between 0.5 and 0.7). However, the data also show that superconductivity can not be recovered for $J_r > 0.1900$. Apparently, the conventional concept of cryogenic stability leads to a criterion too liberal for the recovery of superconductivity for the present case.

Analysis was also conducted for a NbTi superconductor with a large aspect ratio, $a_r = 100$ (Ünal et al., 1991). It was found that stability is maintained in $0 < J_r < 0.8574$, a range wider than $a_r = 10$. Such increase of the stability range is due to the fact that the normal zone occupies a smaller portion of a superconductor with a larger a_r before the heat is transferred to the surface and is dissipated through convective cooling. Unlike the aforementioned behavior of the superconductor with a small a_r, with $a_r = 100$, superconductivity can never be recovered once the intrinsic stability fails. Data were also generated for a similar high-T_c $YBa_2Cu_3O_7$ superconductor operating at 77 K (Ünal et al., 1991). It was found that at $a_r = 100$, the YBCO superconductor generally demonstrates a similar trend but slightly lower values of ϕ compared with NbTi, due to the slightly higher Bi. The q_r data also display similar trends as those of NbTi, except that the values are higher due to a high normal-state resistivity. This high normal state resistivity inhibits recovery of superconductivity after failure of intrinsic stability even at a small aspect ratio. Both the ϕ data and the q_r data indicate that the operation of superconductor can be either intrinsically stable (at low J_r's) or irrecoverably unstable (at high J_r's). However, recovery was observed in cases involving very small aspect ratios and current densities (e.g., at $a_r = 5$ and $J_r < 0.1$). The process of recovery is qualitatively similar to that of the NbTi superconductor (Figs. 2 and 3).

Conclusions

Thermal stability of tape/film type superconductors is studied by considering the influence of the thermal disturbance from a centrally located line heat source. A model was developed that includes an analytical solution for the temperature distribution prior to the failure of intrinsic stability, and a numerical solution thereafter. It is found that for a typical NbTi superconductor, recovery can occur with a small aspect ratio (thick and narrow), and three characteristic regions can be identified. In the low current density region, the operation is always stable. In the medium current density region, the superconductor experiences a failure of intrinsic stability first; then recovers as the result of cryogenic cooling. In the high current density region, intrinsic stability fails and superconductivity is never recovered. For an NbTi superconductor of a large aspect ratio and a high-T_c YBCO superconductor with either large or small aspect ratio, superconductivity cannot be restored after intrinsic stability fails.

References

Anderson, D. A., Tannehill, J. C., and Pletcher, R. A., 1984, *Computational Fluid Mechanics and Heat Transfer*, Hemisphere Publishing Corp., New York.

Bejan, A., and Tien, C. L., 1978, "Effect of Axial Conduction and Metal-Helium Heat Transfer on the Local Stability of Superconducting Composite Media," *Cryogenics*, Vol. 18, pp. 433–441.

Flik, M. I., and Tien, C. L., 1990, "Intrinsic Thermal Stability of Anisotropic Thin-Film Superconductors," ASME JOURNAL OF HEAT TRANSFER, Vol. 112, pp. 10–15.

Özişik, M. N., 1980, *Heat Conduction*, Wiley, New York.

Stekly, Z. J. J., and Zar, J. L., 1965, "Stable Superconducting Coils," *IEEE Transactions on Nuclear Science*, Vol. 12, No. 3, pp. 367–372.

Tien, C. L., Flik, M. I., and Phelan, P. E., 1989, "Mechanisms of Local Thermal Stability in High-Temperature Superconductors," *Cryogenics*, Vol.29, p. 602.

Ünal, A., Chyu, M.-C., and Kuzay, T. M., 1991, "Intrinsic Stability and Recovery Analysis for Tape/Film Type Superconductors," *Proc. of 26th Intersociety Energy Conversion Engineering Conference*, Vol. 4, pp. 497–502.

Conjugate Laminar Forced Convection From a Flat Plate With Imposed Pressure Gradient

B. V. S. S. Prasad[1] and S. Dey Sarkar[2]

Nomenclature

b = thickness of plate
c_p = specific heat
k = thermal conductivity
k_r = thermal conductivity ratio = k_s/k_f

[1]Assistant Professor, Department of Mechanical Engineering, Indian Institute of Technology, Kharagur-721 302, India.

[2]M. Tech. Student, Department of Mechanical Engineering, Indian Institute of Technology, Kharagpur-721 302, India.

Contributed by the Heat Transfer Division of THE AMERICAN SOCIETY OF MECHANICAL ENGINEERS. Manuscript received by the Heat Transfer Division December 1991; revision received June 1992. Keywords: Conjugate Heat Transfer, Forced Convection. Associate Technical Editor: R. J. Simoneau.

L = length of the plate
Nu = Nusselt number
Pr = Prandtl number = $\mu c_p/k_f$
Ps = pressure gradient parameter = $(x/u_e)(du_e/dx)$
Re_x or Re_s = local Reynold number based on u_e
t = thickness parameter of plate = $\sqrt{(b^* u_\infty/L\nu)}$
T = temperature
u = fluid velocity in the boundary layer = u^*/u_∞^*
u_e = fluid velocity external to the boundary layer
x = coordinate measured along the plate from the leading edge = x^*/L^*
y = transverse coordinate = $y^*\sqrt{(u_\infty/L^*\nu)}$
β = wedge parameter
δ = hydrodynamic boundary layer thickness parameter = $\delta^*\sqrt{(u_\infty^*/L\nu)}$
δ_t = thermal boundary layer thickness parameter = $\delta_t^*\sqrt{(u_\infty^*/L^*\nu)}$
η = transverse coordinate = y/δ
η_t = transverse coordinate = y/δ_t
θ = temperature of the fluid, Eq. (11)
μ = dynamic viscosity
ν = kinetic viscosity
ξ = ratio of thermal to hydrodynamic boundary layer thickness = δ_t/δ

Superscript

* = dimensional quantity

Subscripts

b = lower surface of the plate
c = conjugate
f = fluid
r = ratio
ref = arbitrary reference
s = solid
t = thermal
Ⓣ = constant temperature boundary condition
w = upper surface of plate
∞ = free-stream condition

Introduction

Heat transfer from an isothermal flat plate in an external laminar forced convection is a classical information, represented by the extensively used correlation:

$$\mathrm{Nu}_s = 0.331 \mathrm{Re}_s^{0.5} \mathrm{Pr}^{0.33} \tag{1}$$

However, when a pressure gradient is impressed upon the flat plate, by means of, say, a flexible tunnel wall (see for example, Kearney et al., 1975, and Blair et al., 1981), Eq. (1) might be modified in line with similar solutions for wedge type flows with included angle $\pi\beta$. While summarizing the heat transfer values from simulated pressure gradient flows on flat plate and on different body shapes, Mohanty and Prasad (1991) suggested a correlation: $\mathrm{Nu}_s = 0.343\ \mathrm{Re}_s^{0.5}\ (1 + Ps)^{0.7}\ \mathrm{Pr}^{0.33}$ for $\mathrm{Pr} \cong 0.7$. Here, $Ps = \beta/(2-\beta)$ and the potential flow velocity for the wedge problem is given by

$$u_e = \{s\}^{Ps} \tag{2}$$

The foregoing expressions for Nusselt number are essentially valid for the isothermal surface Ⓣ condition. Several procedures also exist (e.g., Eckert and Drake, 1972) when the surface temperature or heat flux is known a priori. In practice, however, the surface thermal condition is one of conjugate nature, determined by the continuity of temperature and heat flux at the solid–fluid interface. This condition obviously does not allow a similarity solution. Luikov (1974) adopted the integral method to solve the flat plate problem and reported significant changes in Nusselt number with conjugate condition vis-à-vis the Ⓣ condition. Although Luikov's analysis makes certain drastic assumptions and simplifications, no further work seems to have been done on the flat plate, with or without superimposed pressure gradient. However, more recently the influence of wall thermal resistance has been studied for the supersonic wedge flows by Luchini et al. (1990) and for natural convection from a vertical circular pin by Gorla (1990).

The present note addresses the problem of conjugate forced convection in laminar imcompressible flow past a flat plate of finite thickness with and without externally imposed pressure gradient.

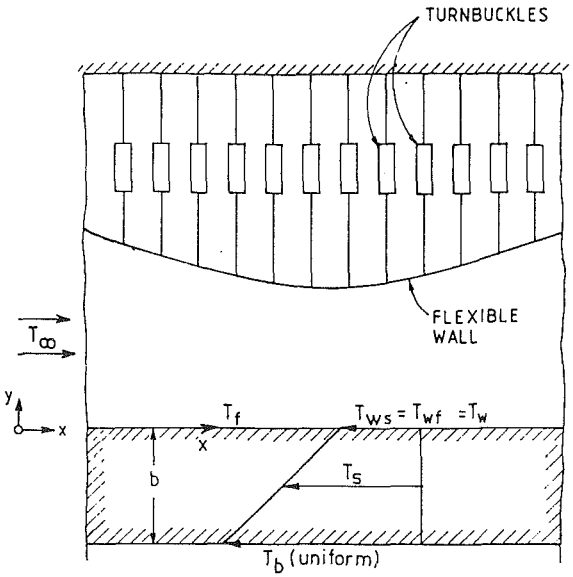

Fig. 1 Flat plate in a wind tunnel with flexible top

Analysis

Figure 1 represents the physical model consisting of a flat plate whose bottom surface is maintained at a (dimensionless) uniform surface temperature T_b. While the flat plate could form the bottom surface of a wind tunnel, the top surface is a flexible wall, which can simulate a desired pressure gradient on the plate. Such an arrangement is also used for simulation of incompressible boundary layer flows on turbine blades (Blair et al., 1981). The dimensionless values of velocity and temperature are u_e and T_∞ in the free stream, and u and T_f in the boundary layer, respectively.

In the conventional problem, the temperature at the solid–fluid interface (T_w) will be specified. On the other hand, in the conjugate problem T_w is determined by the conditions

$$T_{ws} = T_{wf} = T_w \text{ and } k_r \frac{\delta T_s}{\delta y} = \frac{\delta T_f}{\delta y} \text{ at } y = 0 \tag{3}$$

where

$$k_r = \frac{k_s}{k_f}.$$

In other words, the wall temperature is now linked to conduction in the solid as well as convection in the fluid. For the sake of simplicity, we consider a linear variation in the y direction of temperature in the solid; refer to Fig. 1.

Continuity of heat flux at the solid–fluid interface (Eq. (3)) yields

$$\frac{k_r}{t}(T_b - T_w) = \frac{3}{2\delta_t}(T_w - T_\infty) \tag{4}$$

which results in

$$T_w = \frac{k_r \frac{T_b}{t} + 3\frac{T_\infty}{2\delta_t}}{\frac{k_r}{t} + \frac{3}{2\delta_t}} \tag{5}$$

It is evident from Eq. (5) that the interface temperature is a function of thermal conductivity ratio k_r and the thermal boundary layer thickness δ_t. The value of δ_t may bo obtained by solving the boundary layer integral energy equation:

$$\frac{d}{dx}\left[(T_\infty - T_w) \int_o^{\delta_t} u(1-\theta)dy \right] = \frac{1}{\mathrm{Pr}}(T_\infty - T_w)\frac{\partial \theta}{\partial y}\bigg]_{y=0} \tag{6}$$

Following Schlichting (1987), the velocity profile in the boundary layer can be chosen as

$$\frac{u}{u_e} = a\eta + b\eta^2 + c\eta^3 + d\eta^4 \tag{7}$$

where

$$\eta = \frac{y}{\delta}; \tag{8}$$

$$a = 2 + \frac{1}{6}\delta^2\frac{du_e}{dx},\ b = -\frac{1}{2}\delta^2\frac{du_e}{dx}$$

$$c = \frac{1}{2}\delta^2\frac{du_e}{dx} - 2 \text{ and } d = 1 - \frac{1}{6}\delta^2\frac{du_e}{dx} \tag{9}$$

such that it satisfies all the essential hydrodynamic boundary conditions. After substitution of Eq. (9) into the integral momentum equation and certain simplifications, we have

$$\frac{d\delta}{dx} = f\left(\delta,\ u_e,\ \frac{du_e}{dx},\ \frac{d^2u}{dx^2}\right) \tag{10}$$

Here the expression for the function f is not given, as it is also available from Schlichting (1987), albeit in a different form.

Similarly a temperature profile can be chosen in the form

$$\theta = \frac{T_f - T_w}{T_\infty - T_w} = \frac{3}{2}\eta_t - \frac{1}{2}\eta_t^3 \tag{11}$$

where

$$\eta_t = \frac{y}{\delta_t} \tag{12}$$

Substitution of velocity and temperature profiles (Eqs. (7) and (11)) and T_w (Eq. 5)) into Eq. (6) results in the integrodifferential equation for δ_t. Depending on the relative values of Prandtl number, two cases arise for integration of Eq. (6) and appropriate velocity and temperature profiles are chosen within and external to the boundary layers.

Case 1 ($\delta > \delta_t$)

$$\frac{d\xi}{dx} = \frac{A_1 + A_2 + A_3 + A_4}{R\left[1 - \frac{Y - E}{R(T_\infty - T_w)}\right]} \tag{13a}$$

Case 2 ($\delta < \delta_t$)

$$\frac{d\xi}{dx} = \frac{B_1\frac{du_e}{dx} + B_2 + B_3 + B_4}{B_5} \tag{13b}$$

Here $\xi = \delta_t/\delta$, and $A_1,\ldots, B_1,\ldots, Y, R, E$ appearing in Eqs (13) are functions of various independent variables, which in turn appear in Eqs. (3)–(12). The expressions for these functions are again omitted for the sake of brevity.

Equations (10) and (13), being first-order ordinary differential equations, are solved by the fourth-order Runge–Kutta method. Typically, a boundary layer thickness of 10^{-5} and $\xi = 1$ and $x = 10^{-4}$ have been used as the initial guess. Final values of initial conditions are arrived by the criteria that for a given perturbation of 10 percent in the initial values, the boundary layer thickness at $x/b = 10$ should not change by more than 0.1 percent. The step length during these calculation is chosen to be 10^{-5}. Once the initial conditions are so chosen, the step range is increased to 0.01. The computational domain has been $0 < x/b \le 10$. For further details, see Dey Sarkar (1991).

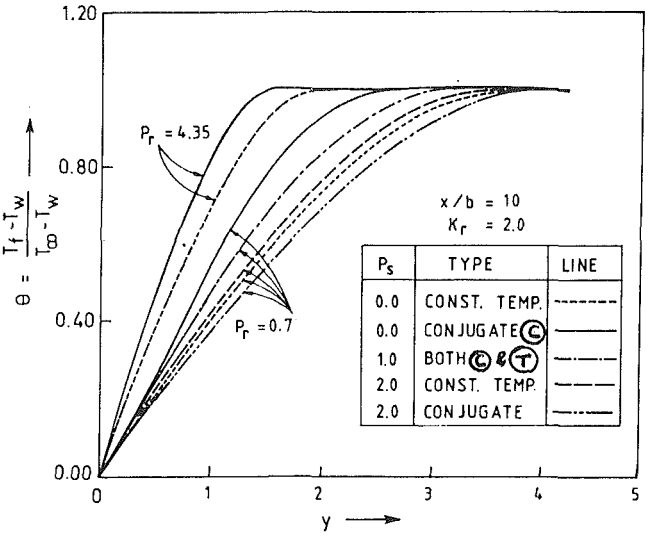

Fig. 2 Dimensionless temperature distribution

Results

Temperature distributions are obtained by solving the Eqs. (10) and (13) for a wide range of variables: $0.5 \le k_r \le 10{,}000$; $0 < x/b$ 10; $0 \le Ps \le 4$; $100 \le \mathrm{Re}_L \le 50{,}000$, and Pr = 0.7 and 4.35. The accuracy of the numerical results has been verified by corroborating the present values computed for the special case of k_r = 10,000 with the exact solutions given by Eckert and Drake (1972) and with Luikov's (1974) approximate solutions wherever applicable. The agreement with those has been found to be very good, the maximum deviation being 2 percent.

Typical temperature distributions are plotted in Fig. 2 for Pr = 0.7 and 4.35 at one longitudinal position (x/b = 10). The natures of the temperature profiles for conjugate condition resemble those with (T) condition (see Eckert and Drake, 1972) for all values of Prandtl number (Pr) and pressure gradient (Ps). However, at any transverse location (y), the values of θ for the conjugate condition are (*a*) larger for $Ps < 1$, (*b*) identical for $Ps = 1$ and (*c*) lesser for $Ps > 1$, in comparison with the (T) condition.

The values of δ and ξ are computed from Eqs. (10) and (13) and are used to evaluate the Nusselt number from

$$\mathrm{Nu}_x = \frac{3(x)\frac{1-Ps}{2}}{2\delta_t}\mathrm{Re}_x^{0.5} \tag{14}$$

Typical Nusselt number variations, calculated from Eq. (14) for different values of k_r, x/b, and Ps at Pr = 0.7 are plotted as $\mathrm{Nu}_x/\mathrm{Re}_x^{0.5}$ versus Ps in Fig. 3. It is evident from this figure, as well as the temperature distributions in Fig. 2, that the thermal boundary condition will have no influence on Nu at Ps = 1 (i.e., stagnation condition). As k_r takes relatively smaller values, say between 1 and 10, and values of $\mathrm{Nu}_x/\mathrm{Re}_x^{0.5}$ differ significantly from the uniform temperature condition. The effect of x/b, on the other hand, is comparatively less; refer to Fig. 3.

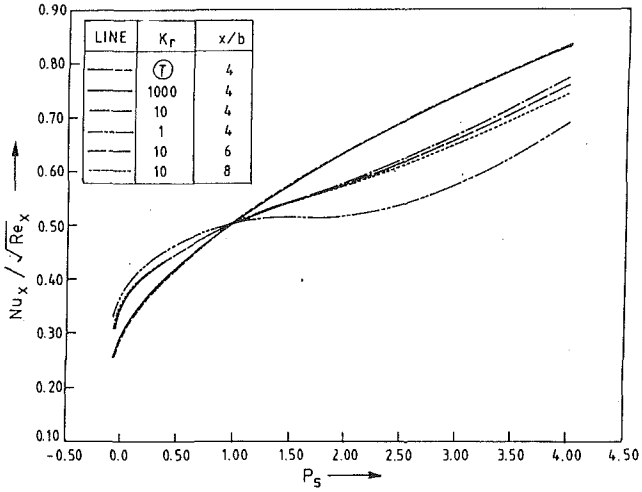

Fig. 3 Variation of local Nusselt number with the pressure gradient parameter

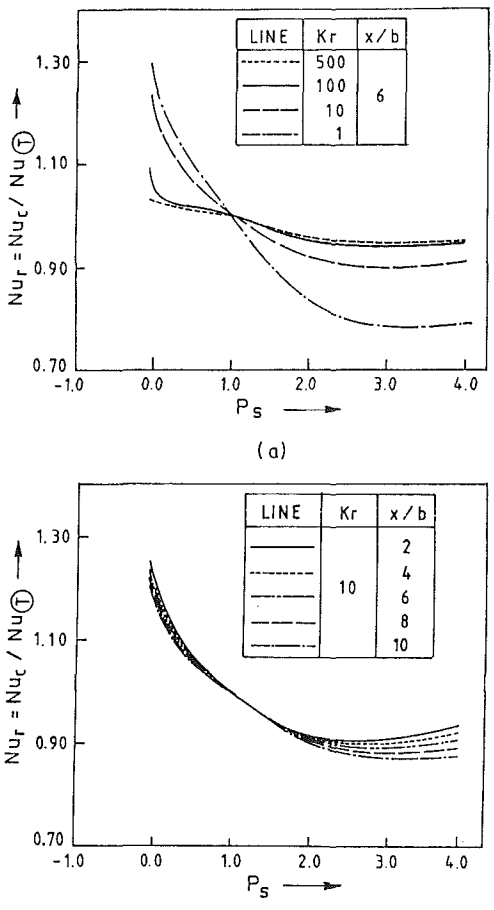

Fig. 4 Conjugate to isothermal Nusselt number ratio with: (*a*) varying k_r and (*b*) varying x/b

The significance of conjugate thermal condition vis-à-vis the Ⓣ boundary condition is obvious from Fig. 4. The ratio of the conjugate Nusselt number Nu_c to $Nu_Ⓣ$ as a function of Ps is presented (*i*) for varying k_r and at $x/b = 6$ in Fig. 4(*a*) and (*ii*) for varying x/b and $k_r = 10$ in Fig. 4(*b*). At $k_r = 1$, Nu_r varies between 1.3 and 0.8 for Ps varying from 0 to 3. The influence of the conjugate conditions is to decrease Nu_r for $Ps < 1$ but to increase for $Ps > 1$; refer to Fig. 4(*b*). The influence thus seems to be increasingly important as the value departs further from unity. However, beyond $Ps > 3$, the change in Nu_r is found to be diminishing. Also, for large values for k_r (500 or larger), Nu_r is nearly equal to 1.0, and therefore the uniform temperature condition is sufficiently accurate. Figure 4(*b*) further indicates that the conjugate condition is relatively more significant nearer to the leading edge, i.e., for smaller values of x/b.

Table 1 Constants appearing in the correlation, Eq. (15)

Ps	A	B	C	r.m.s error %
-0.0654	0.347	-0.02749	-0.05126	4.40
0	0.390	-0.02577	-0.04770	3.89
1/9	0.401	-0.02411	-0.04408	4.21
1/3	0.451	-0.01610	-0.02850	3.21
1	0.488	-0.00030	-0.00023	0.08
2	0.591	0.00404	0.00286	5.68
4	0.794	0.00078	0.00042	0.24

The foregoing results could be summarized in the form of a correlation in the following.

$$Nu_c = A[k_r]^B[x/b]^C Re_x^{0.5} \quad (15)$$

Typically the constants A, B, and C, determined for the range of parameters $k_r = 0.5$ to 10,000, $x/b = 1$ to 10, and $Pr = 0.7$ (air) are listed in Table 1.

References

Blair, M. F., Bailey, D. A., and Schlinker R. H., 1981, "Development of Large-Scale Wind Tunnel for the Simulation of Turbomachinery Airfoil Boundary Layers," ASME *Journal of Engineering for Power*, Vol. 103, pp. 678-687.

Dey Sarkar, S., 1991, "Conjugate Heat Transfer in Some External Forced Convection Problems," M. Tech. Thesis, Ind. Inst. Technology, Kharagpur, India.

Eckert, E. R. G., and Drake, S. M., 1972, *Analysis of Heat and Mass Transfer*, McGraw-Hill, New York.

Gorla, R. S. R., 1990, "Conjugate Combined Convective and Conductive Heat Transfer Along a Vertical Pin in a Non-Newtonian Ambient Medium," *Applied Scientific Research*, Vol. 47, pp. 341-356.

Kearney, D. W., Kays, W. M., and Moffat, R. J., 1973, "Heat Transfer to a Strongly Turbulent Boundary Layer: Some Experimental Results, Including Transpiration," *Int. J. Heat Transfer*, Vol. 16, pp. 1268-1305.

Luchini, P., Lupo, M., and Pozzi, A., 1990, "The Effect of Wall Thermal Resistance on Forced Convection Around Two-Dimensional Bodies," ASME Journal of Heat Transfer, Vol. 112, pp. 572-578.

Luikov, A. V., 1974, "Conjugate Convective Heat Transfer Problems," *Int. J. Heat Mass Transfer*, Vol. 17, pp. 257-265.

Mohanty, A. K., and Prasad, B. V. S. S. S., 1991, "Experimental Study of Heat Transfer From Pressure Gradient Surfaces," *Experimental Thermal and Fluid Science*, Vol. 4, pp. 44-55.

Schlichting, H., 1987, *Boundary Layer Theory*, McGraw-Hill, New York.

Extremely High Heat Fluxes Beneath Impinging Liquid Jets

X. Liu[1] and J. H. Lienhard V[1]

1 Introduction

This note reports measurements of jet-impingement heat fluxes exceeding 100 MW/m^2, including the highest steady-

[1]W. M. Rohsenow Heat and Mass Transfer Laboratory, Department of Mechanical Engineering, Massachusetts Institute of Technology, Cambridge, MA 02139.

Contributed by the Heat Transfer Division and presented at the ASME Winter Annual Meeting, Anaheim, California, November 8-13, 1992. Manuscript received by the Heat Transfer Division July 1992; revision received December 1992. Keywords: Boiling, Forced Convection, Jets.

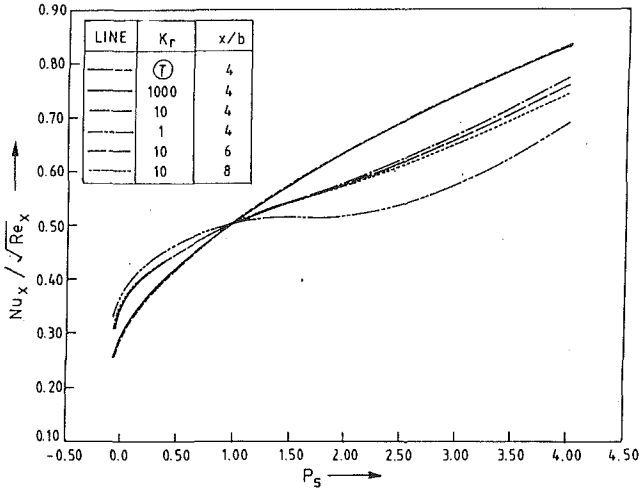

Fig. 3 Variation of local Nusselt number with the pressure gradient parameter

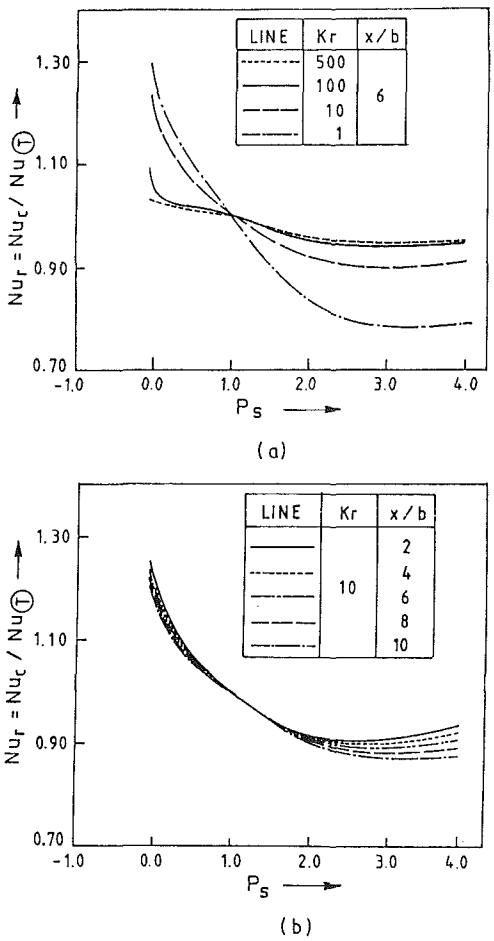

Fig. 4 Conjugate to isothermal Nusselt number ratio with: (*a*) varying k_r and (*b*) varying *x/b*

The significance of conjugate thermal condition vis-à-vis the Ⓣ boundary condition is obvious from Fig. 4. The ratio of the conjugate Nusselt number Nu_c to $Nu_Ⓣ$ as a function of *Ps* is presented (*i*) for varying k_r and at $x/b = 6$ in Fig. 4(*a*) and (*ii*) for varying x/b and $k_r = 10$ in Fig. 4(*b*). At $k_r = 1$, Nu_r varies between 1.3 and 0.8 for *Ps* varying from 0 to 3. The influence of the conjugate conditions is to decrease Nu_r for $Ps < 1$ but to increase for $Ps > 1$; refer to Fig. 4(*b*). The influence thus seems to be increasingly important as the value departs further from unity. However, beyond $Ps > 3$, the change in Nu_r is found to be diminishing. Also, for large values for k_r (500 or larger), Nu_r is nearly equal to 1.0, and therefore the uniform temperature condition is sufficiently accurate. Figure 4(*b*) further indicates that the conjugate condition is relatively more significant nearer to the leading edge, i.e., for smaller values of x/b.

Table 1 Constants appearing in the correlation, Eq. (15)

Ps	A	B	C	r.m.s error %
-0.0654	0.347	-0.02749	-0.05126	4.40
0	0.390	-0.02577	-0.04770	3.89
1/9	0.401	-0.02411	-0.04408	4.21
1/3	0.451	-0.01610	-0.02850	3.21
1	0.488	-0.00030	-0.00023	0.08
2	0.591	0.00404	0.00286	5.68
4	0.794	0.00078	0.00042	0.24

The foregoing results could be summarized in the form of a correlation in the following.

$$Nu_c = A[k_r]^B[x/b]^C Re_x^{0.5} \quad (15)$$

Typically the constants A, B, and C, determined for the range of parameters $k_r = 0.5$ to 10,000, $x/b = 1$ to 10, and $Pr = 0.7$ (air) are listed in Table 1.

References

Blair, M. F., Bailey, D. A., and Schlinker R. H., 1981, "Development of Large-Scale Wind Tunnel for the Simulation of Turbomachinery Airfoil Boundary Layers," ASME *Journal of Engineering for Power*, Vol. 103, pp. 678-687.

Dey Sarkar, S., 1991, "Conjugate Heat Transfer in Some External Forced Convection Problems," M. Tech. Thesis, Ind. Inst. Technology, Kharagpur, India.

Eckert, E. R. G., and Drake, S. M., 1972, *Analysis of Heat and Mass Transfer*, McGraw-Hill, New York.

Gorla, R. S. R., 1990, "Conjugate Combined Convective and Conductive Heat Transfer Along a Vertical Pin in a Non-Newtonian Ambient Medium," *Applied Scientific Research*, Vol. 47, pp. 341-356.

Kearney, D. W., Kays, W. M., and Moffat, R. J., 1973, "Heat Transfer to a Strongly Turbulent Boundary Layer: Some Experimental Results, Including Transpiration," *Int. J. Heat Transfer*, Vol. 16, pp. 1268-1305.

Luchini, P., Lupo, M., and Pozzi, A., 1990, "The Effect of Wall Thermal Resistance on Forced Convection Around Two-Dimensional Bodies," ASME Journal of Heat Transfer, Vol. 112, pp. 572-578.

Luikov, A. V., 1974, "Conjugate Convective Heat Transfer Problems," *Int. J. Heat Mass Transfer*, Vol. 17, pp. 257-265.

Mohanty, A. K., and Prasad, B. V. S. S. S., 1991, "Experimental Study of Heat Transfer From Pressure Gradient Surfaces," *Experimental Thermal and Fluid Science*, Vol. 4, pp. 44-55.

Schlichting, H., 1987, *Boundary Layer Theory*, McGraw-Hill, New York.

Extremely High Heat Fluxes Beneath Impinging Liquid Jets

X. Liu[1] and J. H. Lienhard V[1]

1 Introduction

This note reports measurements of jet-impingement heat fluxes exceeding 100 MW/m^2, including the highest steady-

[1]W. M. Rohsenow Heat and Mass Transfer Laboratory, Department of Mechanical Engineering, Massachusetts Institute of Technology, Cambridge, MA 02139.

Contributed by the Heat Transfer Division and presented at the ASME Winter Annual Meeting, Anaheim, California, November 8-13, 1992. Manuscript received by the Heat Transfer Division July 1992; revision received December 1992. Keywords: Boiling, Forced Convection, Jets.

state heat fluxes achieved in any configuration to date. Our results show that the strongest limitations on heat flux are associated with the conduction resistance and mechanical integrity of the solid heat transfer surface, rather than the liquid heat transfer mechanism.

Steady heat transfer at very high heat flux usually refers to heat removal from a solid wall, normally by a moving liquid. Tungsten is an example of a wall material having high thermal conductivity, high melting point, and good mechanical strength; an easy calculation shows that the maximum steady heat flux through a wall of 1 mm thickness is about 500 MW/m^2. Such a wall is very thin and unlikely to carry much load, a difficulty if a boundary between high and low-pressure regions coincides with the flux-carrying wall; furthermore, the temperature drop through this wall is roughly 3000°C. We conclude that conduction resistance through the boundary is always important, if not dominant, at extremely high flux and that mechanical strength is traded against thermal resistance.

The opposite side of this wall may be cooled by convection or convective boiling.[2] Convection heat fluxes, in particular, do not face the critical-flux limitations of phase change and are determined by the thickness of the thermal boundary layer. The boundary layer, unlike the load-bearing solid wall, can be made as thin as we like by varying the flow conditions (to a value approaching wall roughness height). Since the boundary layer usually grows in the flow direction (without a very strong favorable pressure gradient), the best that we can do is probably to work at the entrance to a channel or at the stagnation point of a blunt body.

This fact drives our interest in the liquid jet stagnation zone. By increasing the jet Reynolds number, we can thin the thermal boundary layer and thus increase heat flux while limiting the liquid-side temperature difference. If the liquid should also undergo a phase change, additional cooling may occur, particularly away from the high-pressure region at the jet's stagnation point.

2 Experiments

Two significant experimental problems arise at extremely high heat fluxes. One is to provide the required power in sufficiently localized form: Since cooling technology has not been developed at heat fluxes above 100 MW/m^2, relatively little controlled heating technology is available either. The second difficulty is that of local calorimetry under conditions typical of large heat fluxes. These problems were central to the design of our experiments.

A heat flux of 1 GW/m^2 over a 1 mm^2 area requires 1 kW of total power. Electrical resistance heating in this situation suffers the difficulty of localizing the Joule heating in the stagnation zone. Further, the heating film itself must remain very thin at these fluxes, so as to avoid thermal conduction-resistance temperature-rise; and corrosion or damage of the heater by the jet may introduce large errors. Even very attractive thin-film designs (e.g., Samant and Simon, 1984) are configured for fluxes orders of magnitude smaller than the present ones. Alternative techniques include optical heating, laser heating, and plasma-arc heating, each involving an energy beam projected directly onto a surface. Bhunia and Lienhard (1991) explored the design of a 1 GW/m^2 optical heater using a nonimaging optical-concentrator. While such optical heating is possible, the cost proves astronomical; similarly, cost prohibits the use of a 1 kW laser source. A plasma-arc heat source, on the other hand, is easily and inexpensively constructed from commercial welding equipment; thus, it was the heating method adopted for the present experiments.

[2]Thermal radiation from a wall at 3300°C, near the melting point of tungsten, will not exceed $\sigma T^4 \approx 10$ MW/m^2; thermal radiation has little importance at extremely high heat fluxes.

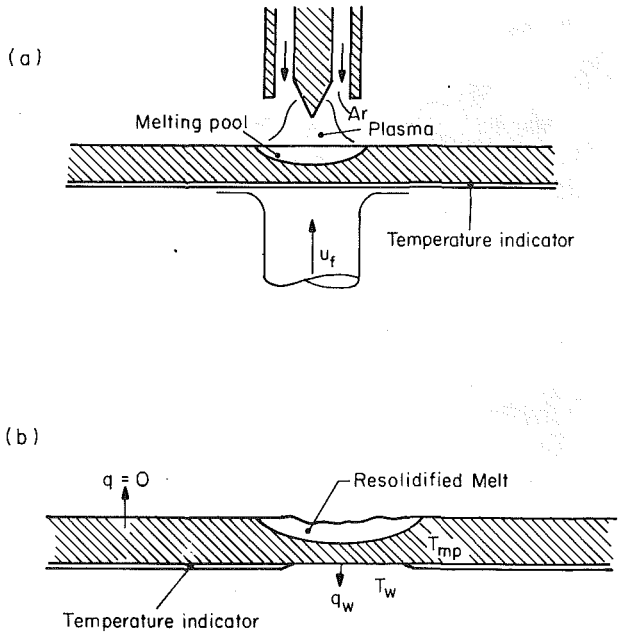

Fig. 1 Experimental arrangement showing the melting pool and fusible temperature indicator on a target plate: (*a*) during heating; (*b*) after heating (not to scale)

The experimental arrangement is shown in Fig. 1. A thin metal plate is heated from one side with a plasma arc and cooled from the other side with an unsubmerged, impinging water jet. The plasma arc was produced by AIRCO-3A/DDR245 TIG welder of 21.8 kW total power.

Calorimetry for this experiment is also challenging. On the liquid side, a (smooth) sensor attached to the wall may introduce conduction and contact resistances that are intolerable, owing to the large temperature difference implied at large flux. Noncontact measurements, such as infrared sensors, are precluded on the jet side owing to the rough-surfaced liquid on the plate and the presence of many airborne, splattered droplets.

Instead, fusible temperature indicators (metals and alloys that have known melting temperatures) were used for the wall temperature measurements on the liquid side. A layer of indicator several microns thick was coated on the jet side of the plate. If a region of this side of the wall exceeded the melting temperature, the coating was melted and entirely washed away by the high speed jet. Otherwise the coating stayed on the plate. By repeating the experiment with different coatings, while holding other variables fixed, we obtained upper and lower bounds on the liquid-side wall temperature under fixed operating conditions. The accuracy of these measurements is obviously somewhat lower than might be expected for other sensors; however, the temperature differences through the plate are so large (1000–2200°C) that uncertainties of even 100°C in wall temperature are of minor significance in the determination of the heat flux.

Because high heat fluxes cause very high temperature gradients in the target, only a thin section of the target can remain below the melting point. Consequently, on the arc side a portion of the plate is melted before a steady state is reached. The border of the melted pool is an isotherm at the melting temperature of the plate material, which can be used to complete the calorimetry. Once a steady state is reached, we stop the arc and then the jet, and take the quenched plate as a sample. Low-carbon steel plates of 1.53 mm thickness were used for most of these experiments. The minimum thickness of the unmelted region ranged from 0.15 mm to 1.04 mm. A few experiments were completed with 1.2 mm molybdenum targets. Other wall materials are discussed below.

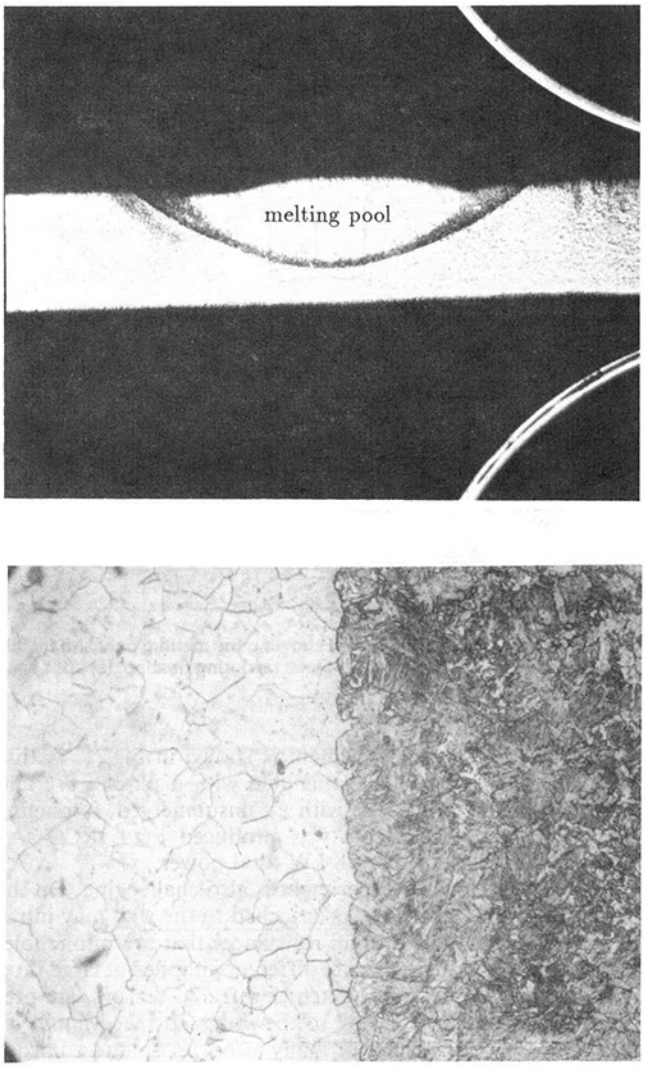

Fig. 2 (*a*) The melting pool in a steel sample plate (× 15 magnification); (*b*) the crystal structure of the resolidified melting-pool (right) and the unmelted region (left) for a steel sample (× 300 magnification)

Steady state can be held indefinitely—we ran most of our experiments for several minutes. In contrast, the targets that failed did so almost immediately after the arc started. Note that if ongoing melting had consumed even 10 percent of the specified heat flux, a melting rate of several mm/s would have resulted; since we could hold the rated flux for minutes at a time, we can be sure that latent heat effects had no significant influence on our heat balance.

To locate the melting temperature isotherm, we cut the plate along a line passing through the *center* of the resolidified melt-pool. The cross section is polished to a mirror finish and chemically etched to bring out the crystal structure of the metal, making the border of the melt-pool clearly visible. Figures 2(*a*, *b*) show microscope photos of a typical steel sample. Two different crystal structures can be easily identified. The crystal structures are closely related to the cooling history of the material. In the melting pool, the molten metal was rapidly quenched by the jet cooling once the arc was stopped. Since the jet cooling rate is so large and the temperature change is so fast, the resulting crystal structure is martensitic. The material that did not melt retains its original ferritic crystal structure. The melting temperature isotherm is easily located between the two structures. Similar procedures were used for the molybdenum targets.

After determining the melting-temperature-isotherm profile and the upper and lower bound temperatures on the liquid side of the plate, we used these temperatures as boundary conditions in a numerical conduction calculation of the heat flux through the plate. Since the plasma arc was concentrated at the center of the plate, the heat flux quickly decreases with radius. The extreme flux region is confined to about one jet diameter from the stagnation point; beyond a radius of four plate thicknesses from the stagnation point, the temperature change in the plate is almost negligible. Based on the upper and lower bound temperatures, we made lower bound and upper bound calculations of the heat flux for each sample plate. The results are shown in Tables 1 and 2 and in Fig. 3. (For some cases in

Table 1 Present stagnation-point heat flux data (q_w) for high-speed water jets as a function of jet speed (u_f) for fixed bounds on liquid-side wall temperature (steel targets, excluding 129 m/s data)

u_f, m/s	q_w, MW/m^2		
	upper bound back > 190°C	spinodal lower bound back < $T_{spinodal}$	lower bound back < 419.5 °C
134.	231.	201.	186.
130.	187.	163.	151.
128.	170.	150.	138.
123.	78.3	68.5	63.1
120.	130.	115.	106.
117.	129.	113.	104.
117.	80.0	70.1	64.5
114.	120.	105.	97.0
111.	119.	104.	95.7
111.	116.	102.	93.9
111.	112.	98.3	90.4
108.	108.	95.2	87.5
105.	129.	113.	104.
105.	107.	93.8	86.1
105.	98.6	86.7	79.6
102.	94.8	83.4	76.5
102.	90.6	79.7	73.1
102.	83.4	73.4	67.3
91.0	76.6	67.5	61.8
81.4	69.6	61.5	56.2
78.8	68.5	60.5	55.3
64.3	49.6	44.0	40.1

Table 2 Stagnation-point heat transfer data for a high speed water jet as power is decreased. Corresponding bounds on liquid-side temperature difference are shown, with $\Delta T_l = T_w - T_f$ for T_w the wall temperature bound and T_f the incoming jet temperature. The lower bound for the first nine points is based on $T_w = T_{spinodal}$. (Note that the uncertainty in the liquid-side ΔT_l is much greater than that in the solid-side $\Delta T = T_{melt} - T_w$; thus q_w is much less uncertain than ΔT_l.)

$u_f \approx 129$ m/s				
upper bound q_w		lower bound q_w		
q_w, MW/m^2	ΔT_l, °C	q_w, MW/m^2	ΔT_l, °C	material
423	0	370	326	molybdenum
364	0	319	326	molybdenum
331	0	290	326	molybdenum
327	285	320	326	steel
186	263	182	326	steel
177	285	173	326	steel
153	224	142	326	steel
132	176	117	326	steel
128	176	97.4	326	steel
108	0	93	176.0	steel
99.6	0	69.9	176.0	steel
93.6	0	81.5	176.0	steel
89.5	0	63.7	176.0	steel
84.9	0	59.6	176.0	steel
83.8	0	58.8	176.0	steel
70.6	0	49.6	176.0	steel
46.0	0	32.3	176.0	steel

Table 2, the lower bound on wall temperature is simply the incoming jet temperature.)

In addition to the fusible indicator results, Tables 1 and 2 also show lower bound fluxes based on the assumption that the liquid side of the targets cannot exceed the spinodal limit of the liquid state, i.e., based on the maximum possible temperature for superheated liquid at the stagnation pressure (Lienhard et al., 1986). The justifications for this bound are that (*i*) a vapor layer that could conduct the measured lower bound heat flux (film boiling) would have a thickness on the order of 0.1 μm, generally less than the surface roughness of the targets, and (*ii*) a vapor layer would probably be unstable in the pressure-gradients of the stagnation-point flow field and with the pressure fluctuations of the partially atomized jet (viz., the wall would always be wetted). The molybdenum heat fluxes, in particular, rely on the spinodal temperature for the lower bound on flux; for all steel targets, the back temperature was measured to be less than 420°C, but the spinodal temperature has been used to provide a finer bound.

The free water jet was produced by a 34 MPa (5000 psi) piston pump supplying a large cylindrical plenum (0.19 m diameter, 1.4 m length). Pressure fluctuations within the plenum were negligible. The plenum flow was stabilized by (*i*) dissipating the supply momentum by directing the inlet pipe toward the wall, and (*ii*) by placing honeycomb beyond the inlet region, about 1 meter from the outlet end. A 1.9 mm sharp-edged nozzle was counterbored into a 3.18 cm diameter plug screwed into the head plate of the pressure vessel at the end opposite the inlet. The pressure, ranging from 2.06 to 8.97 MPa, was measured by a gage near the outlet of the plenum.

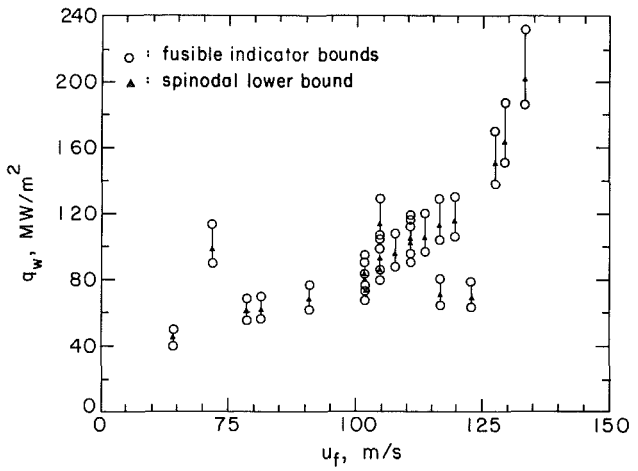

Fig. 3 Heat flux versus jet velocity for fixed bounds on liquid-side wall temperature (steel wall, data of Table 1). The circles represent the lower and upper bound fluxes for each measurement; the triangles represent the spinodal-temperature lower bound flux.

The jet velocity was calculated from the pressure using the Bernoulli equation; because the nozzle was a sharp-edged type, the viscous loss was negligible ($C_v \approx 1$). Owing to the very high velocities of the jets and their length of about 50 jet diameters, all were partially atomized by air drag prior to reaching the target.

The estimated uncertainty for the jet velocity is 5 percent, for the thickness of the plate less than 2 percent, and for the melting point temperature of the fusible temperature indicators it is a few degrees Celsius. The effect of fusible indicator thickness on lower bound heat flux is less than 9 percent. Because the temperature on the jet side was bounded by two temperatures, the uncertainty of the heat fluxes were determined mainly by the difference of the upper and lower bound temperatures. Since the melting temperatures of the plates, 1370°C for steel, were relatively high (and thus the ΔT across the plate was high), the uncertainty for heat flux was ± 19 percent for the steel samples with largest temperature difference between the upper and lower bounds and only ± 11 percent for those with the smallest temperature difference. For molybdenum, which has a melting point of 2620°C, the uncertainties in flux are lower, at ± 7 percent.

3 Heat Flux Measurements and Wall Material Limitations on Heat Flux

The present data are compared to other extremely high heat flux data in Table 3. For jet impingement, the present data are the only ones in the range above 100 MW/m^2. The present data include the highest steady heat fluxes ever reported.

It is important to note that most of the data in Table 3 are critical heat fluxes, representing a limiting flux for given conditions beyond which a change in boiling mechanism leads to an abrupt wall-temperature rise. The present data are not critical heat fluxes; instead, they are limited only by the power available in our plasma arc or by the mechanical failure of the target plates. With additional arc power and stronger wall-materials, jet impingement heat fluxes can undoubtedly become much higher.

Figure 3 shows the increase of heat flux with jet velocity for fixed bounds on liquid-side wall temperature (data of Table 1). In comparison, the heat flux at the surface of the sun is about 63 MW/m^2. Owing to the severe splattering of the impinging jet, it is difficult to verify the presence or absence of phase change. Bounds on the liquid-side temperature difference are too uncertain to resolve this question (Table 2).

The jet impingement configuration was used specifically because of its thin thermal boundary layer (on the order of micrometers thick) and high stagnation point pressures (more than 100 atm at our highest speed). These conditions were selected to push single-phase convective heat flux toward the limits set by wall roughness (a lower bound on boundary layer thickness) and liquid properties (an upper bound on $T_w - T_f$ for subcritical liquid). A comparison of the measured Nusselt

Table 3 The parameters of previous and present extremely high heat flux experiments for water: * jet diameter or tube internal diameter; ** jet stagnation pressure or tube inlet pressure; + bulk velocity of jet or tube flow (some data from Nariai, 1990)

q_{max} (MW/m^2)	method	d (mm)*	P (MPa)**	v (m/s)+	ΔT_{sub} (K)	material	reference
40.1 – 327	jet (not CHF)	1.9	2.07 – 8.97	64.3 – 134.	166 – 285	steel	Present
291 – 423	jet (not CHF)	1.9	8.31	129.	280	molybdenum	Present
208.8 – 337.0	straight tube (nonuniform q_w)	0.5	3.13	90	60 – 180	Cu Alloy	Ornatskii and Vinyarskii
29.1 – 224.5	straight tube	0.4 – 2.0	1.12 – 7.2	10 – 90	36 – 195	Cu Alloy	(same)
51.4 – 173	tube (slot vortex)	4.85 – 6.35	2.4 – 6.5	8.05 – 29.9	16 – 70	Inc. *etc.*	Gambill *et al.*
8.7 – 117.8	tube (Inconel tape)	3.45 – 10.2	0.1 – 3.8	4.5 – 47.5	0 – 144.4	Nickel	(same)
23 – 80	tube (spiral vortex)	6.4 – 7.6	0.75 – 3.0	3.4 – 8.4	0 – 83	Cu *etc.*	(same)
5.58 – 81.3	tube (constantan tape)	1.6	0.4 – 1.4	4 – 25	22.3 – 71.4	Cu	Drizius *et al.*
90.9 – 130.0	straight tube	3.05	1.31 – 1.61	46.9 – 61.9	161.9 – 170.2	SUS	Schaefer *et al.*
14 – 66	straight tube	1 – 3	0.1	20			Nariai
42.9	straight tube	11.68	3.0	45.2	167.7	SUS	Mayersak *et al.*
1.5 – 18.26	jet (CHF)	2.0	0.1	3.9 – 26.0	10 – 30	copper	Monde & Katto

numbers to Nusselt numbers for pure convection under these conditions (following Lienhard et al., 1992) shows that convective heat fluxes are of the same order as the total heat fluxes, and it suggests that convective heat transfer remains an important contributor (if not the primary contributor) to the total liquid-side heat flux. However, further assessment of the convective flux in this situation must await better characterization of the liquid side temperature drop, the target's surface roughness, and the influence of liquid property variations for a 300°C temperature change in a thin boundary layer.

Extremely high heat flux cooling situations are, generically, high Biot number situations, in which the reduction of wall thickness (and thus wall thermal resistance) is limited by structural requirements. In the present extremal flux experiments, the major thermal resistance is not the liquid-side thermal resistance (be it convection or boiling) but the wall resistance, which amounts to more than 80 percent of the total at the highest fluxes. Structural and mechanical limits to heat flux, set by the wall material, represent a more significant barrier to raising the flux than do issues related to liquid-side transport mechanism. For generic studies of extremal fluxes, the development of better wall materials is the logical focus.

On a purely thermal basis, a material's ability to carry large heat fluxes depends on its melting-point temperature and its thermal conductivity. For comparison, it is convenient to consider a specific heat flux, $(q_w t) = k_{\text{solid}}(T_{\text{melt}} - 0°\text{C})$. The materials used for the target plates in the present experiments included the highest specific-flux metals, tungsten (441 kW/m) and copper (426 kW/m), as well as molybdenum (387 kW/m), tantalum (167 kW/m), and low-carbon steel (45 kW/m). Most of the heat transfer results described above were for steel targets. Those targets have low specific flux, but very high mechanical strength, and thus they reached very high fluxes by melting to a very thin solid layer.

Tungsten has the highest conductivity and highest melting point of materials we tried; however, brittle failure was observed for 0.5-mm-thick plates in the range of 100 MW/m^2 shortly after the arc was powered. Fracture appeared to be caused by the thermal stress in the target. Copper targets proved unsuitable for these experiments owing to the large fin effects in 1.5 mm targets (they did not melt) and the low mechanical strength of thinner targets (they ruptured under the jet).

Molybdenum is the most promising material among those we tried, having high specific flux and high yield strength. We found it necessary to switch from argon to helium as the arc gas in order to achieve sufficient flux to melt these targets. If further arc power were available, a higher flux could easily be achieved, as no tendency toward mechanical failure was observed in molybdenum. Recent developments in diamond technology also promise a route to reduced Biot number with high mechanical strength (Lienhard and Khounsary, 1993).

In general, we observed structural failure caused by rupture, buckling, and fracture in our experiments. The wall experiences a thermal stress due to the large temperature gradient, and also a large mechanical stress from the force of the jet. Estimates for both stresses are discussed by Liu and Lienhard (1992). Our results suggest that the mechanical properties of the wall are entirely as important as its thermal properties when high fluxes are desired.

4 Summary

High-speed liquid jets have been used to produce heat fluxes of up to 400 MW/m^2. These data include the highest heat fluxes ever achieved in any configuration.

The present studies, in which heating is confined to the stagnation region, show no evidence of a critical heat flux, even up to our maximum power. The large fluxes reported here are limited only by wall failure and the power of our heating source, and not by liquid-side thermal resistance. By selecting or developing wall materials having lower conduction resistance and higher mechanical strength, higher heat fluxes can be achieved. Of available metallic materials, molybdenum is particularly promising for the construction of high-flux walls. For these high-speed jets, convection appears to account for a large portion of the total heat flux, and the stagnation-zone heat transfer depends on the velocity throughout the range of our velocities.

This work was supported by the National Science Foundation (CBTE-8858288) and the A. P. Sloan Foundation.

References

Bhunia, S. K., and Lienhard, J. H., V, 1991, "Design of a High Power Density Radiant Heater Using a Non-imaging Optical Concentrator," Heat Transfer Laboratory Internal Report, MIT, Cambridge, MA.

Gambill, W. R., Bundy, R. D., and Wansbrough, R. W., 1961, "Heat Transfer, Burnout, and Pressure Drop for Water in Swirl Flow Through Tubes With Twisted Internal Tapes," *Chem. Engr. Prog. Symp. Series*, Vol. 57, No. 32, pp. 127–137.

Lienhard, J. H., Shamsundar, N., and Biney, P. O., 1986, "Spinodal Lines and Equations of States: A Review," *Nuclear Engr. Design*, Vol. 95, pp. 297–314.

Lienhard V, J. H., and Khounsary, A. M., 1993, "Liquid Jet Impingement Cooling in Conjunction With Diamond Substrates for Extremely High Heat Flux Applications," presented at the SPIE Conference on High Heat Flux Engineering, San Diego, CA.

Lienhard V, J. H., Liu, X., and Gabour, L. A., 1992, "Splattering and Heat Transfer During Impingement of a Turbulent Liquid Jet," ASME JOURNAL OF HEAT TRANSFER, Vol. 114, pp. 362–372.

Liu, X., and Lienhard V, J. H., 1992, "Extremely High Heat Flux Removal by Sub-cooled Liquid Jet Impingement," *Fund. Subcooled Flow Boiling*, ASME HTD-Vol. 217, pp. 11–20.

Monde, M., and Katto, Y., 1978, "Burnout in a High Heat-Flux Boiling System With an Impinging Jet," *Intl. J. Heat Mass Transfer*, Vol. 21, pp. 295–305.

Nariai, H., 1990, "High Heat Flux Boiling Heat Transfer," presented at the Topical Workshop: Research of Boiling Heat Transfer, Heat Transfer Society of Japan, University of Tokyo, July 20.

Ornatskii, A. P., and Vinyarskii, L. S., 1969, "Heat Transfer Crisis in a Forced Flow of Underheated (Subcooled) Water in Small-Bore Tubes," *High Temperature*, Vol. 3, No. 3, pp. 400–406.

Samant, K. R., and Simon, T. W., 1984, "Using Thin-Film Technology to Fabricate a Small-Patch Boiling Heat Transfer Test Section," ASME HTD-Vol. 31, pp. 33–38.

Natural Convection Heat Transfer in Slender Window Cavities

M. H. Novak[1] and E. S. Nowak[2]

Nomenclature

Gr = Grashof number based on the cavity height $= g\beta(t_1 - t_2)H^3/\nu^2$
g = gravitational acceleration, m/s^2
H = cavity height, m
h = mean convection heat transfer coefficient, W/m^2·K
k = thermal conductivity of air, W/m·K
- = cold side wall temperature, K
β = volumetric thermal expansion coefficient, K^{-1}
θ = dimensionless temperature
ν = kinematic viscosity, m^2/s

[1]Research Associate, Faculty of Engineering Science, University of Western Ontario, Canada, N6A5B9.

[2]Professor, Mechanical Engineering, Faculty of Engineering Science, University of Western Ontario, Canada, N6A5B9.

Contributed by the Heat Transfer Division of THE AMERICAN SOCIETY OF MECHANICAL ENGINEERS. Manuscript received by the Heat Transfer Division April 1992; revision received September 1992. Keywords: Enclosure Flows, Natural Convection, Numerical Methods. Associate Technical Editor: J. R. Lloyd.

numbers to Nusselt numbers for pure convection under these conditions (following Lienhard et al., 1992) shows that convective heat fluxes are of the same order as the total heat fluxes, and it suggests that convective heat transfer remains an important contributor (if not the primary contributor) to the total liquid-side heat flux. However, further assessment of the convective flux in this situation must await better characterization of the liquid side temperature drop, the target's surface roughness, and the influence of liquid property variations for a 300°C temperature change in a thin boundary layer.

Extremely high heat flux cooling situations are, generically, high Biot number situations, in which the reduction of wall thickness (and thus wall thermal resistance) is limited by structural requirements. In the present extremal flux experiments, the major thermal resistance is not the liquid-side thermal resistance (be it convection or boiling) but the wall resistance, which amounts to more than 80 percent of the total at the highest fluxes. Structural and mechanical limits to heat flux, set by the wall material, represent a more significant barrier to raising the flux than do issues related to liquid-side transport mechanism. For generic studies of extremal fluxes, the development of better wall materials is the logical focus.

On a purely thermal basis, a material's ability to carry large heat fluxes depends on its melting-point temperature and its thermal conductivity. For comparison, it is convenient to consider a specific heat flux, $(q_w t) = k_{\text{solid}}(T_{\text{melt}} - 0°\text{C})$. The materials used for the target plates in the present experiments included the highest specific-flux metals, tungsten (441 kW/m) and copper (426 kW/m), as well as molybdenum (387 kW/m), tantalum (167 kW/m), and low-carbon steel (45 kW/m). Most of the heat transfer results described above were for steel targets. Those targets have low specific flux, but very high mechanical strength, and thus they reached very high fluxes by melting to a very thin solid layer.

Tungsten has the highest conductivity and highest melting point of materials we tried; however, brittle failure was observed for 0.5-mm-thick plates in the range of 100 MW/m^2 shortly after the arc was powered. Fracture appeared to be caused by the thermal stress in the target. Copper targets proved unsuitable for these experiments owing to the large fin effects in 1.5 mm targets (they did not melt) and the low mechanical strength of thinner targets (they ruptured under the jet).

Molybdenum is the most promising material among those we tried, having high specific flux and high yield strength. We found it necessary to switch from argon to helium as the arc gas in order to achieve sufficient flux to melt these targets. If further arc power were available, a higher flux could easily be achieved, as no tendency toward mechanical failure was observed in molybdenum. Recent developments in diamond technology also promise a route to reduced Biot number with high mechanical strength (Lienhard and Khounsary, 1993).

In general, we observed structural failure caused by rupture, buckling, and fracture in our experiments. The wall experiences a thermal stress due to the large temperature gradient, and also a large mechanical stress from the force of the jet. Estimates for both stresses are discussed by Liu and Lienhard (1992). Our results suggest that the mechanical properties of the wall are entirely as important as its thermal properties when high fluxes are desired.

4 Summary

High-speed liquid jets have been used to produce heat fluxes of up to 400 MW/m^2. These data include the highest heat fluxes ever achieved in any configuration.

The present studies, in which heating is confined to the stagnation region, show no evidence of a critical heat flux, even up to our maximum power. The large fluxes reported here are limited only by wall failure and the power of our heating source, and not by liquid-side thermal resistance. By selecting or developing wall materials having lower conduction resistance and higher mechanical strength, higher heat fluxes can be achieved. Of available metallic materials, molybdenum is particularly promising for the construction of high-flux walls. For these high-speed jets, convection appears to account for a large portion of the total heat flux, and the stagnation-zone heat transfer depends on the velocity throughout the range of our velocities.

This work was supported by the National Science Foundation (CBTE-8858288) and the A. P. Sloan Foundation.

References

Bhunia, S. K., and Lienhard, J. H., V, 1991, "Design of a High Power Density Radiant Heater Using a Non-imaging Optical Concentrator," Heat Transfer Laboratory Internal Report, MIT, Cambridge, MA.

Gambill, W. R., Bundy, R. D., and Wansbrough, R. W., 1961, "Heat Transfer, Burnout, and Pressure Drop for Water in Swirl Flow Through Tubes With Twisted Internal Tapes," *Chem. Engr. Prog. Symp. Series*, Vol. 57, No. 32, pp. 127–137.

Lienhard, J. H., Shamsundar, N., and Biney, P. O., 1986, "Spinodal Lines and Equations of States: A Review," *Nuclear Engr. Design*, Vol. 95, pp. 297–314.

Lienhard V, J. H., and Khounsary, A. M., 1993, "Liquid Jet Impingement Cooling in Conjunction With Diamond Substrates for Extremely High Heat Flux Applications," presented at the SPIE Conference on High Heat Flux Engineering, San Diego, CA.

Lienhard V, J. H., Liu, X., and Gabour, L. A., 1992, "Splattering and Heat Transfer During Impingement of a Turbulent Liquid Jet," ASME JOURNAL OF HEAT TRANSFER, Vol. 114, pp. 362–372.

Liu, X., and Lienhard V, J. H., 1992, "Extremely High Heat Flux Removal by Sub-cooled Liquid Jet Impingement," *Fund. Subcooled Flow Boiling*, ASME HTD-Vol. 217, pp. 11–20.

Monde, M., and Katto, Y., 1978, "Burnout in a High Heat-Flux Boiling System With an Impinging Jet," *Intl. J. Heat Mass Transfer*, Vol. 21, pp. 295–305.

Nariai, H., 1990, "High Heat Flux Boiling Heat Transfer," presented at the Topical Workshop: Research of Boiling Heat Transfer, Heat Transfer Society of Japan, University of Tokyo, July 20.

Ornatskii, A. P., and Vinyarskii, L. S., 1969, "Heat Transfer Crisis in a Forced Flow of Underheated (Subcooled) Water in Small-Bore Tubes," *High Temperature*, Vol. 3, No. 3, pp. 400–406.

Samant, K. R., and Simon, T. W., 1984, "Using Thin-Film Technology to Fabricate a Small-Patch Boiling Heat Transfer Test Section," ASME HTD-Vol. 31, pp. 33–38.

Natural Convection Heat Transfer in Slender Window Cavities

M. H. Novak[1] and E. S. Nowak[2]

Nomenclature

Gr = Grashof number based on the cavity height $= g\beta(t_1 - t_2)H^3/\nu^2$
g = gravitational acceleration, m/s^2
H = cavity height, m
h = mean convection heat transfer coefficient, W/m^2·K
k = thermal conductivity of air, W/m·K
- = cold side wall temperature, K
β = volumetric thermal expansion coefficient, K^{-1}
θ = dimensionless temperature
ν = kinematic viscosity, m^2/s

[1]Research Associate, Faculty of Engineering Science, University of Western Ontario, Canada, N6A5B9.

[2]Professor, Mechanical Engineering, Faculty of Engineering Science, University of Western Ontario, Canada, N6A5B9.

Contributed by the Heat Transfer Division of THE AMERICAN SOCIETY OF MECHANICAL ENGINEERS. Manuscript received by the Heat Transfer Division April 1992; revision received September 1992. Keywords: Enclosure Flows, Natural Convection, Numerical Methods. Associate Technical Editor: J. R. Lloyd.

1 Introduction

During the last 25 years, many numerical studies of natural convection heat transfer in rectangular closed cavities have been conducted. Most of the early studies were related to square or moderately high cavities with Grashof numbers, based on the cavity height H, of $\mathrm{Gr} \leq 10^6$. Wilkes and Churchill (1966) published their numerical study dealing with natural convection in a rectangular cavity for aspect ratios $R = \text{height}/\text{width} = H/L$ ranging from 1 to 3. To solve the two-dimensional incompressible Navier–Stokes equations, they chose the vorticity-stream function approach and applied the ADI (alternating direction) finite difference method to the vorticity and energy equations and SOR (successive overrelaxation) method to the stream function equation. Newell and Schmidt (1970) solved this problem numerically using the Crank–Nicholson implicit method for cavities with aspect ratios $R \leq 20$ and $\mathrm{Gr} \leq 5.6 \times 10^8$. Based on the results reached, they presented numerous correlations in terms of the Nusselt number $\mathrm{Nu} = f(\mathrm{Gr})$. Spradley and Churchill (1975) solved the heat transfer by natural convection in the closed cavity by using an explicit, time-dependent, finite-difference technique. They did not accept the Boussinesq simplification, retained the effects of variable density, and showed that the nonlinear, variable density profile has little effect on the steady-state isotherms. Chu and Churchill (1977) used again the ADI method to solve the simplified N-S equations by adopting the Boussinesq approximation for the gravitational term. They described the solution of heat transfer in a cavity with aspect ratios $0.4 \leq R \leq 5$ and Rayleigh number $\mathrm{Ra} = \mathrm{GrPr} \leq 50000$ provided that one side wall is cold while the other wall is heated by a heater whose size varies from 0 to H.

Probably the most interesting numerical studies dealing with topics closely related to this work were presented by Korpela et al. (1982) and by Lee and Korpela (1983). They described multicellular convection flow, a common phenomenon occurring with rather high cavity aspect ratios and Rayleigh numbers. Using the Arakava explicit finite difference scheme for the convective terms and the explicit DuFort–Frankel method for the diffusive terms, they determined numerically (Korpela et al., 1982) the boundaries between conduction, multicellular, and transition fluid flow regimes in the window cavity for aspect ratios $R \leq 20$. Compared with Korpela et al. (1982), the newer study by Lee and Korpela (1983) brings more general numerical results valid for cavity aspect ratio $R \leq 40$ and for various Prandtl numbers.

The purpose of this paper is to evaluate the boundaries between multicellular and conduction fluid flow regimes numerically for high window cavities. To accomplish this, the ADI finite difference scheme and the SOR by lines technique are used for solving the Navier–Stokes equations. The method was efficiently programmed and extensively employed to evaluate various fluid flow regime boundaries for cavity aspect ratios $10 \leq R \leq 90$ and Grashof numbers ranges $1 \times 10^8 \leq \mathrm{Gr} \leq 3 \times 10^9$. This parameter extent, particularly for $40 < R < 80$, is not sufficiently covered in the literature despite its practical importance for window design.

2 Analysis

To transform the Navier–Stokes equations to the simplified form, a Boussinesq approximation to the gravitational term is accepted. The pressure elimination from the equations of motion leads to the well-known system of dimensionless equations for vorticity, energy, and the stream function. This system is solved numerically by the finite difference technique for the boundary conditions shown in Fig. 1. The spatial derivatives in each equation solved are approximated by second-order central differences. In order to assure computational stability,

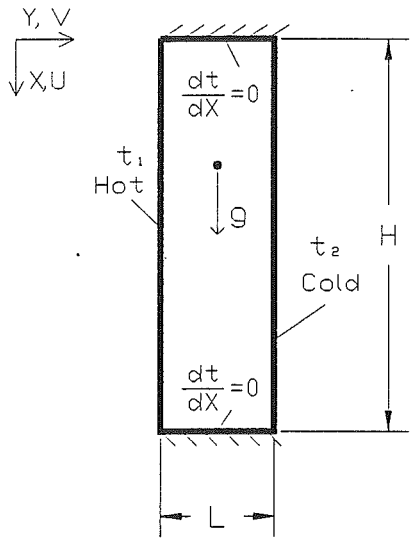

Fig. 1 Rectangular cavity scheme

the alternating direction implicit finite difference method (ADI) is used for the vorticity equation, while the successive overrelaxation (SOR) by lines technique, described by Anderson et al. (1984), is applied for both the energy equation and the stream function equation. Compared with the common technique, in which both the vorticity and energy equations involve dimensionless time, the transformation of the vorticity equation alone to the parabolic form accelerates the whole iteration process. Once the temperature field in the cavity is known, then each local Nusselt number value is determined as the dimensionless temperature drop at the boundary from $\mathrm{Nu}_{\mathrm{loc}} = h_{\mathrm{loc}} H/k = \partial\theta/\partial Y|_{\mathrm{wall}}$. Finally, to obtain the cavity mean Nusselt number, the Simpson rule is applied for the integration of the local Nusselt number values along the vertical cavity walls.

The vorticities at the walls (boundaries), Ω_W, are computed using the relationship originally derived by Thom. The advantages of this first-order term are discussed in detail by Roache (1972) and Anderson et al. (1984).

For most of the calculations reported here, a 152×32 grid was chosen to optimize the relation between the accuracy required and the computing time. To reach the steady state in the transition or conduction regime takes up to 1 hour (PC 386 33 MHz) of computational time for a 152×32 grid. This time corresponds to several hundreds of iteration steps. For the multicellular flow, the computational time increases progressively (up to hours), especially in the case where the Grashof number $\mathrm{Gr} \geq 2 \times 10^9$. For these high Grashof numbers also some solution instabilities were encountered for aspect ratios falling near the middle of the multicellular regime. For such situations the evaluation process diverged and no results were accepted.

To ensure the reliability of results, various error estimates were made. For the chosen points it turned out that a change in the number of grid points in the horizontal direction from 16 to 26 does not affect the mean Nusselt number by more than 2.3 percent either in the conduction or in the multicellular regime. However, in this range of number of grid points the multicellular fluid flow structure (number of cells) depends on the number of grid points. This effect diminishes entirely for smoother grid consisting of 26 or more points. A further increase in the number of grid points from 26 to 32 affects the mean Nusselt number by less than 0.9 percent and leaves the fluid flow patterns unchanged and similar to those depicted in the research papers by Lee and Korpela (1983) and by Korpela et al. (1982). Finally, the horizontal grid consisting of 40 points was tested; however, compared with 32 points, no no-

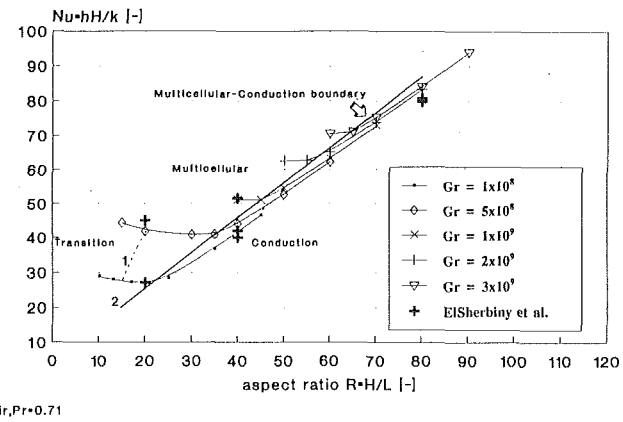

Fig. 2 Numerically evaluated various fluid flow regime boundaries in a slender cavity filled with air

ticeable differences were observed. In the vertical direction, the various grid densities were also compared using 82, 152, and 202 points. As evaluated, the change from 82 to 152 and from 152 to 202 points causes the differences in the cavity mean Nusselt number maximally by 2 and 0.7 percent, respectively. Consequently, a 152×32 grid seems to be sufficiently smooth for proper representation of the flow patterns in the cavity.

Residual errors in steady state were evaluated at each grid point for all equations solved. For the temperature equation, the value of the maximum residue divided by the smallest equation term at the same grid point did not exceed 11/1360. Under these conditions, the maximum changes of the local Nusselt number do not exceed 0.007 percent for two subsequent iteration steps and the corresponding mean Nusselt numbers evaluated independently for the hot and cold vertical walls do not differ by more than 0.3 percent one from another. For the Rayleigh number $\mathrm{Ra} = 10^5$ and the square cavity, the present numerical achievements on a 33×33 grid were also compared with those obtained by Phillips (1984) on the same grid and with those by Chu and Churchill (1977) performed on a 20×20 grid. It was found that the mean Nusselt number value obtained using the present technique, $\mathrm{Nu} = 4.65$, falls exactly between their results, which differ by 4.8 percent. Another comparison showed that Phillips' (1984) achievements, obtained by using the dynamic ADI methods on a 65×65 grid, do not differ from present calculations performed on a 33×33 grid by more than 1.9 percent.

3 Results and Discussion

Typical results of the analysis are presented in Fig. 2. In this figure the mean Nusselt number is shown as a function of the cavity aspect ratio R. The Grashof number, based on the cavity height, $\mathrm{Gr} = g\beta(t_1 - t_2)H^3/\nu^2$, is chosen as a parameter for each curve. The nondimensional numbers are based on the cavity height, H, because each curve depicted gives the real image of how the various aspect ratios affect the heat transfer through the cavity of a constant height. Shown in Fig. 2 are two curves (1 and 2) indicating the approximate boundaries between transition-multicellular and multicellular-conduction fluid flow regimes. As the multicellular-conduction boundary 2 shows, the influence of the aspect ratio on the heat transfer in the multicellular regime near this boundary is nearly negligible. Thus, to minimize the heat loss, the windows should be designed

Table 1 Cavity mean Nusselt number based on the height; comparison of results from various sources

Aspect ratio R	12.5	15	20	40		80	
Grashof number Gr	1×10^8			5×10^8	1×10^9	2×10^9	3×10^9
Present study	28.2	27.7	27.1	41.9	44.0	51.2	83.4	84.1
+ElSherbiny et al			27.0	45.2	42.0	51.5	80.0	80.4
*Korpela et al.	28.4	28.0	26.9					
* Lee & Korpela			26.8		43.0	51.8		

* numerical values read from a graph, + experimental values given by a correlation

for this specific range of aspect ratios. Expressed in terms of Grashof number based on the cavity width, L, for aspect ratios $R > 30$, this gives approximately the value of $\mathrm{Gr}_L = g\beta(t_1 - t_2)L^3/\nu^2 = 11{,}300 \pm 400$, which is in a good agreement with the conclusions obtained numerically by Lee and Korpela (1983). Consequently, for side walls, the temperature drop $dt = 20°\mathrm{C}$ (this roughly corresponds to ASHRAE winter conditions) and the mean air temperature $t_{\mathrm{mean}} = 0°\mathrm{C}$, the designed double-paned window width should be at least $L = 14$ mm.

The results of the present calculations are depicted in Fig. 2, together with the experimental data of ElSherbiny et al. (1982). In order to keep this figure easy to look at, a detailed comparison of the present results with the available numerical investigations of Korpela et al. (1982), Lee and Korpela (1983), and the ElSherbiny experimental data is depicted in Table 1. As the cavity mean Nusselt number values shown in this table suggest, the difference between previously published numerical data, obtained using the Arakawa scheme, and the present calculations is nearly negligible. This indicates that the use of the simple ADI method together with successive overrelaxation, SOR, by the lines technique gives reliable results for the range of aspect ratios investigated. Compared with the experimental achievements of ElSherbiny et al. (1982), on the cavity with a highly conducting top and bottom for aspect ratios 5, 10, 20, 40, 80, and 110, the present results do not differ either in the multicellular or in the conduction regime from their experimental data by more than 5 percent.

However, unlike the ElSherbiny experimental results, all numerical calculations reported here were performed on the cavity with the adiabatic top and bottom. To express the difference between these two methods, two types of task either for linear (conductor) or adiabatic (insulator) top and bottom boundary conditions were solved numerically. Based on numerous calculations, it turned out that for aspect ratios higher than $R > 25$ the linear top and bottom boundary conditions do not cause an increase in the cavity mean Nusselt number by more than 2 percent compared with adiabatic boundary conditions.

In order to demonstrate the temperature, stream function, and local Nusselt number distribution in the multicellular fluid flow regime, Fig. 3 is presented. In this regime, which occurs as a consequence of the hydrodynamic instability, described by Lee and Korpela (1983) in detail, the heat is transferred mainly by convection along the finite number of convection cells. Consequently, the local Nusselt number in the middle area, which is not affected by the cavity ends, has local peaks. In Fig. 3, the local Nusselt number values, evaluated from the Nusselt number definition in the form $\mathrm{Nu}_{\mathrm{loc}} = \partial\theta/\partial Y|_{\mathrm{wall}}$, are depicted along each cavity vertical wall. The zoomed view of the local values of Nusselt number distribution along the hot wall is also shown in the right part of Fig. 3. In the steady state, for the boundary conditions according to Fig. 1, the

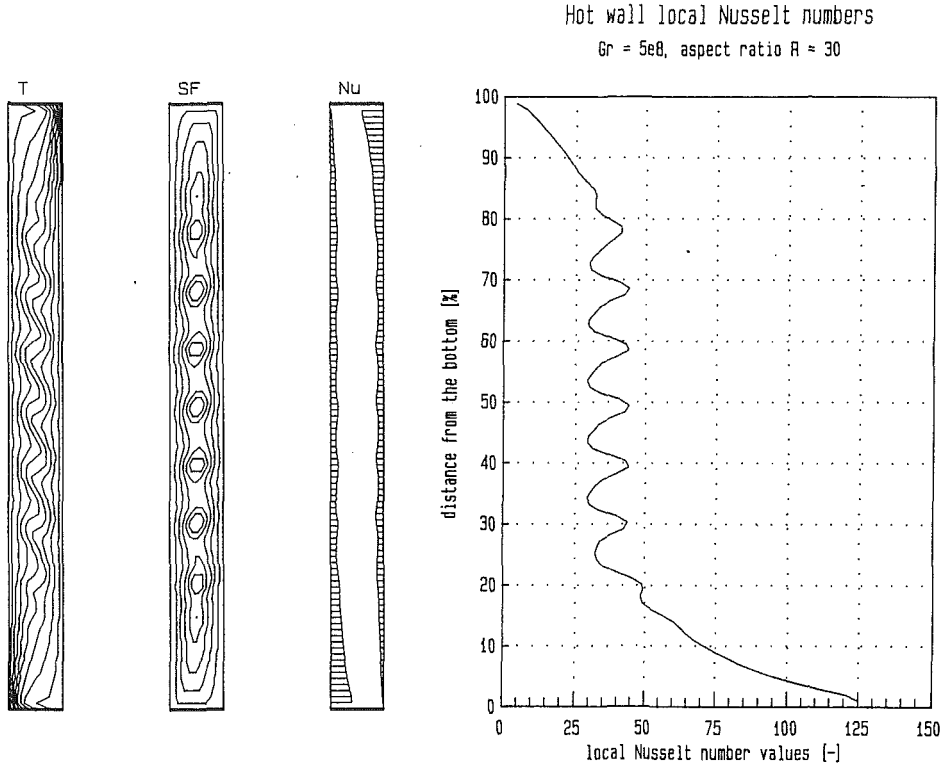

Fig. 3 Temperature, stream lines, and local Nusselt number distribution in a cavity filled with air for $Gr = 5 \times 10^8$ and aspect ratio $R = 30$

cavity mean Nusselt number will be the same evaluated either from the hot or cold wall local Nusselt number values. Finally, provided that the Grashof number is constant, the local Nusselt number peaks diminish if the value of aspect ratio is higher than that defined by the multicellular-conduction boundary in Fig. 2.

4 Conclusions

Natural convection heat transfer in a double-paned window cavity with high aspect ratios was investigated theoretically using the finite difference technique. The following conclusions emerge:

1 The boundaries between the conduction-multicellular fluid flow regimes were determined for high cavity aspect ratios $R \leq 90$ and Grashof numbers $Gr \leq 3 \times 10^9$.

2 Compared with the adiabatic boundary conditions, for aspect ratios of 25 the linear boundary conditions imposed on the cavity top and bottom cause the decrease of the cavity mean Nusselt number by approximately 2 percent. For aspect ratios higher than 30 this difference is nearly negligible.

3 As the comparison with other works indicates, to analyze the conduction-multicellular fluid flow boundaries for natural convection heat transfer regimes in very slender cavities, the finite difference alternating direction implicit method (ADI), combined with the successive overrelaxation by lines technique (SOR), is well suited as it is for lower aspect ratios.

4 For the temperature difference between the vertical walls of 20°C and mean cavity air temperature $t_{mean} = 0$°C, to operate a window in the low heat loss regime, the double-paned window width should be greater than 14 mm. In the range of aspect ratios investigated, this thickness corresponds to the transition from the conduction to the multicellular fluid flow regime. As proved by evaluation, for a window height of 0.9 m and side wall temperature difference $dt = 20$°C the use of a 14 mm cavity instead of a 10 mm cavity decreases the heat loss by natural convection through the window gap by about 30 percent.

Acknowledgments

The authors gratefully acknowledge the financial support from The Renewable Energy Branch of The Department of Energy, Mines and Resources, Canada.

References

Anderson, D. A., Tannehill, J. C., and Pletcher, R. H., 1984, *Computational Fluid Mechanics and Heat Transfer*, Hemisphere Publishing Corp., Washington, DC.

Chu, H. N. S., and Churchill, S. W., 1977, "The Development and Testing of a Numerical Method for Computation of Laminar Natural Convection in Enclosures," *Computers and Chemical Engineering*, Vol. 1, pp. 103–108.

ElSherbiny, S. M., Raithby, G. D., and Hollands, K. G. T., 1982, "Heat Transfer by Natural Convection Across Vertical and Inclined Air Layers," ASME JOURNAL OF HEAT TRANSFER, Vol. 104, pp. 159–167.

Korpela, S. A., Lee, Y., and Drummond, J. E., 1982, "Heat Transfer Through a Double Pane Window," ASME JOURNAL OF HEAT TRANSFER, Vol. 104, pp. 539–544.

Lee, Y., and Korpela, S. A., 1983, "Multicellular Natural Convection in a Vertical Slot," *Journal of Fluid Mechanics*, Vol. 126, pp. 91–121.

Newell, M. E., and Schmidt, F. W., 1970, "Heat Transfer by Natural Convection Within Rectangular Enclosures," ASME JOURNAL OF HEAT TRANSFER, Vol. 92, pp. 159–167.

Phillips, T. N., 1984, "Natural Convection in an Enclosed Cavity," *Journal of Computational Physics*, Vol. 54, pp. 365–381.

Roache, P. J., 1972, *Computational Fluid Dynamics*, Hermosa Publisher, Albuquerque, NM.

Spradley, L. W., and Churchill, S. W., 1975, "Pressure- and Buoyancy-Driven Thermal Convection in a Rectangular Enclosure," *Journal of Fluid Mechanics*, Vol. 70, pp. 705–720.

Wilkes, J. O., and Churchill, S. W., 1966, "The Finite-Difference Computation of Natural Convection in a Rectangular Enclosure," *AIChE Journal*, Vol. 12, pp. 161–168.

Effects of Heat Losses (or Gains) From Insulated Portions of Closed-Loop Thermosyphons With Vertical Heat Transfer Sections

M. A. Bernier[1] and B. R. Baliga[2]

Nomenclature

A = cross-sectional area of pipe
C_p = specific heat at constant pressure
D = internal diameter of the pipe $= 2r_i$
f = Fanning friction factor $= \tau_w/(\rho V^2)/2$
Gr_m = modified Grashof number $= D^3 g\beta q/\nu V_{\mathrm{ref}} k_f$
g = acceleration due to gravity
i = axial grid location
k_f = thermal conductivity of the fluid
L = total length of the closed loop
$L_1 \ldots L_9$ = various lengths of the closed loop (Fig. 1)
$L1$ = number of grid points in the axial direction
P_w = power input
Pr = Prandtl number $= \mu C_p/k_f$
q = heat flux
Q_L = rate of heat loss around the loop
Re = Reynolds number
$\mathrm{Re}_{\mathrm{ref}}$ = reference Reynolds number $= V_{\mathrm{ref}} D/\nu$
R = radius of 180 deg bends
r_i = internal radius of the pipe
s = axial coordinate around the closed-loop
St_m = modified Stanton number $= UD/\rho V_{\mathrm{ref}} AC_p$
$s_1 \ldots s_{10}$ = given values of the axial coordinate (Fig. 1)
T = area-weighted mean cross-sectional temperature
T_a = ambient temperature
T_w = mean wall temperature in the cooled section
$T_1 \ldots T_9$ = temperatures evaluated at $s_1 \ldots s_9$
U = overall heat loss coefficient, W/m-°C
V = average velocity
V^* = nondimensional average velocity $= V/V_{\mathrm{ref}}$
V_{ref} = reference velocity $= [P_w \beta g \Delta Z/8\pi\mu C_p L]^{1/2}$
β = thermal volumetric expansion coefficient
Δs = length of control volume
ΔZ = height difference between the middles of the heated and cooled sections (Fig. 1)
μ = dynamic viscosity
ν = kinematic viscosity
ξ = parameter used in Eq. (1)
ρ = density
ϕ_∞ = dimensionless ambient temperature $= (T_a - T_w)/(qD/k_f)$
Ω = modified heat loss coefficient $= U/\rho VAC_p$

Subscripts

cs = refers to the cooled section
hs = refers to the heated section

[1]Département de génie mécanique, Ecole Polytechnique de Montréal, Montréal, Québec, Canada, H3C 3A7.
[2]Department of Mechanical Engineering, McGill University, Montréal, Québec, Canada, H3A 2K6.

Contributed by the Heat Transfer Division of THE AMERICAN SOCIETY OF MECHANICAL ENGINEERS. Manuscript received by the Heat Transfer Division June 1991; revision received May 1992. Keywords: Heat Pipes and Thermosyphons, Natural Convection. Associate Technical Editor: J. H. Kim.

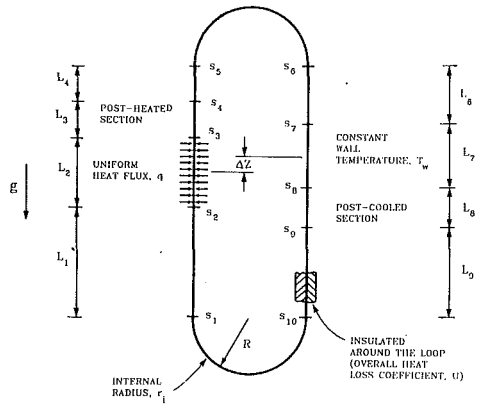

Fig. 1 Schematic representation of the closed-loop thermosyphon considered in this study

1.0 Introduction

Closed-loop thermosyphons are used in numerous engineering applications where there is a need to transport heat from a source to a sink without the use of a mechanical pump. Models of closed-loop thermosyphons with vertical heat transfer sections have been presented by Greif (1988), Hallinan and Viskanta (1985), Huang and Zelaya (1988), and Lewis et al. (1990). Recently, Bernier and Baliga (1992) proposed a one-dimensional/two-dimensional model that accounts for heat losses (or gains) from such loops. The objective of this note is to use this model to demonstrate the importance of accounting for heat losses (or gains) in the modeling of thermosyphons.

The geometry of interest is presented schematically in Fig. 1. The circulating liquid is heated by a constant and uniform heat flux, q, in the heated section of the loop, and it is cooled in a cooling section maintained at a constant wall temperature, T_w. Elsewhere, around the loop, the pipes are insulated from the ambient fluid; in these insulated sections, the overall heat loss coefficient, U, is expressed on a unit length basis (W/m-°C). The middles of the heated and cooled sections are separated by a vertical distance ΔZ, as shown in Fig. 1.

2.0 Governing Equations

The one-dimensional/two-dimensional model of Bernier and Baliga (1992) involves an iterative coupling procedure between the local results of two-dimensional numerical simulations of laminar mixed-convection flows, performed in the "extended" heated and cooled sections, and a traditional one-dimensional analysis. The extended heated (or cooled) section includes the heated (or cooled) and the post-heated (or post-cooled) sections. The "post" sections are included in the two-dimensional simulations because both the velocity and the temperature profiles remain distorted, from their fully developed shapes, for some distance after the heated or cooled sections.

The governing equations and the underlying assumptions as well as the iterative solution procedure of this one-dimensional/two-dimensional model have been presented by Bernier and Baliga (1992). The model was also validated by Bernier and Baliga (1992) by comparing its results to corresponding experiments, and the agreement was shown to be very good.

The closed-loop thermosyphon illustrated in Fig. 1 is governed by five independent dimensionless parameters (Bernier, 1991): Gr_m $(= D^3 g\beta q/\nu V_{\mathrm{ref}} k_f)$, a modified Grashof number; St_m $(= UD/\rho V_{\mathrm{ref}} AC_p)$, a modified Stanton number; $\mathrm{Re}_{\mathrm{ref}}$ $(= V_{\mathrm{ref}} D/\nu)$, a reference Reynolds number; Pr $(= \mu C_p/k_f)$, the Prandtl number; ϕ_∞ $(= [T_a - T_w]/[qD/k_f])$, a dimensionless ambient temperature. In these relationships, V_{ref} is defined as: $V_{\mathrm{ref}} = [P_w \beta g \Delta Z/8\pi C_p \mu L]^{1/2}$, where P_w is the power input to

the loop, and L is the total length of the loop. The reference velocity, V_{ref}, corresponds to the average velocity given by traditional one-dimensional models for a perfectly insulated loop (Bernier and Baliga, 1992).

In their proposed one-dimensional/two-dimensional model, Bernier and Baliga (1992) have shown that, if the form losses associated with the 180 deg bends are neglected, the general one-dimensional momentum equation around the thermosyphon shown in Fig. 1 can be expressed by:

$$V=\frac{2r_i^2g\beta\left[\sum_n\left[\xi\frac{(T_n-T_a)}{\Omega}(1-e^{-\Omega L_n})+\xi T_aL_n\right]+\sum_{i=1}^{i=L1}T_{hs,i}\Delta s_i-\sum_{i=1}^{i=L1}T_{cs,i}\Delta s_i+\frac{\Omega R^2(e^{-\pi R\Omega}+1)}{(\Omega^2R^2+1)}(T_5-T_{10})\right]}{\nu\left[16(L_1+L_4+L_6+L_9+2\pi R)+\sum_{i=1}^{i=L1}f_{hs,i}\mathrm{Re}\Delta s_i+\sum_{i=1}^{i=L1}f_{cs,i}\mathrm{Re}\Delta s_i\right]} \quad (1)$$

where: $n = 1, 4, 6, 9$ (cf. Fig. 1); $\xi = +1$ for $n = 1, 4$ and $\xi = -1$ for $n = 6, 9$; V is the average velocity inside the loop; Ω ($= U/\rho VAC_p$) is a modified heat loss coefficient; $L_1 \ldots L_9$ represent the lengths of various segments of the loop identified in Fig. 1; and the temperatures $T_1 \ldots T_{10}$ represent the fluid temperatures prevailing at axial locations, $s_1 \ldots s_{10}$, respectively. The values $f_{cs,i}$ and $f_{hs,i}$ are the local friction factors at the axial grid point "i" in the extended heated and cooled sections, respectively; and $T_{hs,i}$ and $T_{cs,i}$ are the area-weighted mean cross-sectional temperatures at axial grid point "i" in the extended heated and cooled sections, respectively. These discrete values of f and T, which prevail over certain finite distances, Δs, are obtained from two-dimensional numerical simulations of mixed-convection flows in the extended heat transfer sections using the finite volume method of Patankar (1980).

It is convenient to consider the right-hand side of Eq. (1) as the ratio of "total buoyancy" and "total friction" (Lavine, 1984). By adding the appropriate temperature-related terms in the numerator and then dividing them by the sum of the corresponding lengths, average "hot" and "cold" side temperatures, T_{hot} and T_{cold}, respectively, can be determined:

$$T_{hot}=\frac{\frac{(T_1-T_a)}{\Omega}(1-e^{-\Omega L_1})+T_aL_1+\sum_{i=1}^{i=L1}T_{hs,i}\Delta s_i+\frac{(T_4-T_a)}{\Omega}(1-e^{-\Omega L_4})+T_aL_4}{L_1+L_2+L_3+L_4} \quad (2)$$

$$T_{cold}=\frac{\frac{(T_6-T_a)}{\Omega}(1-e^{-\Omega L_6})+T_aL_6+\sum_{i=1}^{i=L1}T_{cs,i}\Delta s_i+\frac{(T_9-T_a)}{\Omega}(1-e^{-\Omega L_9})+T_aL_9}{L_6+L_7+L_8+L_9} \quad (3)$$

The difference between T_{hot} and T_{cold} drives the flow in the thermosyphon. As $T_{hot} - T_{cold}$ increases, total buoyancy increases. The last term in the numerator of Eq. (1), which involves $(T_5 - T_{10})$ and accounts for heat losses (or gains) in the 180 deg bends, has been omitted in the definition of T_{hot} and T_{cold}; for the range of results presented here, the impact of this term on total buoyancy is insignificant and can be neglected (Bernier, 1991).

Opposing the total buoyancy is the total friction, the denominator of Eq. (1). This total friction can be divided by the total length of the loop to give an average value that is representative of the frictional resistance, $\overline{f\mathrm{Re}}$:

$$\overline{f\mathrm{Re}}=\frac{16(L_1+L_4+L_6+L_9+2\pi R)+\sum_{i=1}^{i=L1}f_{hs,i}\mathrm{Re}\Delta s_i+\sum_{i=1}^{i=L1}f_{cs,i}\mathrm{Re}\Delta s_i}{L_1+L_2+L_3+L_4+L_6+L_7+L_8+L_9+2\pi R} \quad (4)$$

3.0 Results

The results presented in this section are for one particular set of dimensions of the geometry of interest. These dimensions are presented in Table 1. Furthermore, the results were obtained using water as the circulating fluid. All results presented in Fig. 2 were obtained using $T_w = 20.3°C$. The fluid properties were evaluated at that temperature giving a Pr = 7.0. The results generated by the one-dimensional/two-dimensional model are presented in terms of a nondimensional average velocity, V^* ($= V/V_{ref}$).

In Fig. 2, values of V^* are plotted against ϕ_∞ for $\mathrm{Gr}_m = 500$ and for three different values of St_m. When $\mathrm{St}_m = 0$, the thermosyphon is perfectly insulated. As is seen in Fig. 2, the impact of heat losses (or gains) on V^* can be significant. For example, for $\mathrm{St}_m = 1 \times 10^{-4}$ and $\phi_\infty = -10$, V^* is equal to 0.571. This corresponds to a 45 percent decrease in the value of V^* compared to that obtained for $\mathrm{St}_m = 0$. At the other extreme, a 28 percent increase in the value of V^* is noted for $\mathrm{St}_m = 1 \times 10^{-4}$ and $\phi_\infty = 10$.

It is important to note that the amount of heat loss (or gain) is not the same in the various sections of the loop. In each section, the amount of heat loss (or gain) is proportional to the overall heat loss coefficient, U, to the length of the section, and to the difference between the average temperature of the fluid in that section and the ambient fluid temperature. For example, consider the post-heated and post-cooled sections, which, as shown in Fig. 1 and in Table 1, have the same U and are of equal length. If the temperature at the outlet of the cooled section, T_8, is lower than T_a, heat gains in the post-cooled section will be higher than in the post-heated section. Such imbalances between heat losses (or gains) in various sections of the loop imply that the average hot and cold side temperatures do not increase (or decrease) at the same rate. In turn, these influence total buoyancy and the average velocity. This imbalance phenomenon is amplified when the insulation level is decreased or, alternatively, when St_m is increased. Therefore, for a given ϕ_∞, the magnitude of the difference between the values of V^* obtained with a specified St_m and for $\mathrm{St}_m = 0$ increases as St_m is increased, as shown in Fig. 2.

The amount of heat removed in the cooled section is greatly influenced by the cumulative amount of heat losses (or gains) from the insulated portions of the loop. This is illustrated in Table 2 where two extreme cases ($\mathrm{St}_m = 1 \times 10^{-4}$; $\phi_\infty = -10$ and 10) are examined, along with the case of the perfectly

Table 1 Dimensions of the specific thermosyphon studied

D = 0.02 m	
L_1 = 1.00 m	L_1/D = 50.0
L_2 = 1.00 m	L_2/D = 50.0
L_3 = 1.50 m	L_3/D = 75.0
L_4 = 1.50 m	L_4/D = 75.0
L_6 = 1.00 m	L_6/D = 50.0
L_7 = 1.00 m	L_7/D = 50.0
L_8 = 1.50 m	L_8/D = 75.0
L_9 = 1.50 m	L_9/D = 75.0
R = 0.2 m	R/D = 10.0
L = 11.26 m	L/D = 563.0
ΔZ = 2.00 m	

Table 2 Effects of heat losses (or gains) on total buoyancy and total friction

Gr_m = 500	Q_L/P_w	T_{hot} (°C)	T_{cold} (°C)	$T_{hot} - T_{cold}$ (°C)	$\overline{fRe}$	V^*
St_m = 0	0	21.019	20.650	0.369	17.86	1.030
ϕ_∞ = 10, St_m = 1x10^{-4}	1.23	21.547	21.064	0.482	18.24	1.317
ϕ_∞ = -10, St_m = 1x10^{-4}	-1.27	20.196	20.004	0.193	16.81	0.571

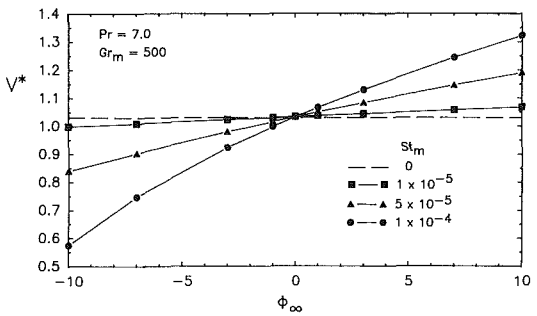

Fig. 2 Variation of V^* as a function of St_m and ϕ_∞: Gr_m = 500 and Pr = 7.0

insulated loop ($St_m = 0$). In this table, Q_L/P_w represents the ratio of heat losses from the insulated portions of the loop over the power input in the heated section. The first thing to note is that $\overline{fRe}$ is close to the fully developed value of 16 in all three cases. This indicates that the velocity profiles are only mildly affected by mixed-convection effects, and the total friction does not change significantly from one case to the other. However, the variation in total buoyancy (or $T_{hot} - T_{cold}$) is much greater.

For the case where $\phi_\infty = +10$, $Q_L/P_w = 1.23$. Therefore, the amount of heat removed in the cooled section has to be 2.23 times the power input supplied in the heated section. Thus, the overall temperature drop across the cooled section has to be higher than the overall temperature rise in the heated section. Consequently, the difference ($T_{hot} - T_{cold}$), the total buoyancy, and the average velocity all increase when compared to the case where $St_m = 0$, as indicated in Table 2.

As for the case where $\phi_\infty = -10$, the ratio of $Q_L/P_w = -1.27$. This implies that heat losses from the insulated portions of the loop exceed the power input in the heated section, and heat is supplied (and not removed) in the cooled section. As shown in Table 2, this profoundly affects the resulting average velocity.

The analysis presented in this note is specific to the geometry shown in Fig. 1 and to the corresponding dimensions presented in Table 1. Nonetheless, the results obtained in this study indicate that the performance of a closed-loop thermosyphon can be markedly affected by heat gains (or losses) in the insulated sections of the loop.

Acknowledgments

This research was financially supported by the Natural Sciences and Engineering Research Council of Canada in the form of a Post-Graduate Scholarship granted to M. A. Bernier and through individual operating grants awarded to Prof. B. R. Baliga.

References

Bernier, M. A., 1991, "Investigation of a Closed-Loop Thermosyphon," Ph.D. thesis, McGill University, Montréal, Canada.

Bernier, M. A., and Baliga, B. R., 1992, "A 1-D/2-D Model and Experimental Results for a Closed-Loop Thermosyphon With Vertical Heat Transfer Sections," *Int. J. Heat Mass Transfer*, Vol. 35, No. 11, pp. 2969–2982.

Greif, R., 1988, "Natural Circulation Loops," ASME JOURNAL OF HEAT TRANSFER, 50th Anniversary Issue, Vol. 110, pp. 1243–1258.

Hallinan, K. P., and Viskanta, R., 1985, "Heat Transfer From a Vertical Tube Bundle Under Natural Circulation Conditions," *Int. J. Heat Fluid Flow*, Vol. 6, No. 4, pp. 256–264.

Huang, B. J., and Zelaya, R., 1988, "Heat Transfer Behavior of a Rectangular Thermosyphon Loop," ASME JOURNAL OF HEAT TRANSFER, Vol. 110, pp. 487–493.

Lavine, A. G., 1984, "A Three-Dimensional Analysis of Natural Convection in a Toroidal Loop," Ph.D. thesis, U.C. Berkeley, California.

Lewis, J. S., Collins, M. W., and Allen, P. H. G., 1990, "Flow Rate Predictions for a Thermosyphon Loop," *Proc. of the 9th Int. Heat Transfer Conference*, Vol. 2, pp. 549–554.

Patankar, S. V., 1980, *Numerical Heat Transfer and Fluid Flow*, Hemisphere, Washington, DC.

The Importance of Prandtl Number in Mixed-Convection Instability

B. B. Rogers[1] and L. S. Yao[1]

Nomenclature

- g = gravitational acceleration
- K = annulus curvature parameter = $r_i/(r_o - r_i)$
- n = azimuthal wavenumber
- Pr = Prandtl number = ν/γ
- Ra = Rayleigh number = $\mu\beta\, g(r_o - r_i)^4/\nu\gamma$
- Re = Reynolds number = $W_{ave}\,(r_o - r_i)/\nu$
- r_i = inner cylinder radius
- r_o = outer cylinder radius
- $\hat{u}$ = radial disturbance velocity
- $\hat{v}$ = azimuthal disturbance velocity
- $\hat{w}$ = axial disturbance velocity
- W = axial velocity
- β = thermal expansion coefficient
- γ = thermal diffusivity
- $\hat{\theta}$ = temperature disturbance
- Θ = dimensionless temperature
- μ = vertical temperature gradient
- ν = kinematic viscosity
- ρ = density

[1]Department of Mechanical and Aerospace Engineering, Arizona State University, Tempe, AZ 85287.

Contributed by the Heat Transfer Division of THE AMERICAN SOCIETY OF MECHANICAL ENGINEERS. Manuscript received by the Heat Transfer Division May 1992; revision received September 1992. Keywords: Flow Instability, Mixed Convection. Associate Technical Editor: F. P. Incropera.

Table 1 Dimensions of the specific thermosyphon studied

D = 0.02 m	
L_1 = 1.00 m	L_1/D = 50.0
L_2 = 1.00 m	L_2/D = 50.0
L_3 = 1.50 m	L_3/D = 75.0
L_4 = 1.50 m	L_4/D = 75.0
L_6 = 1.00 m	L_6/D = 50.0
L_7 = 1.00 m	L_7/D = 50.0
L_8 = 1.50 m	L_8/D = 75.0
L_9 = 1.50 m	L_9/D = 75.0
R = 0.2 m	R/D = 10.0
L = 11.26 m	L/D = 563.0
ΔZ = 2.00 m	

Table 2 Effects of heat losses (or gains) on total buoyancy and total friction

Gr_m = 500	Q_L/P_w	T_{hot} (°C)	T_{cold} (°C)	$T_{hot} - T_{cold}$ (°C)	$\overline{fRe}$	V^*
St_m = 0	0	21.019	20.650	0.369	17.86	1.030
ϕ_∞ = 10, St_m = 1x10^{-4}	1.23	21.547	21.064	0.482	18.24	1.317
ϕ_∞ = -10, St_m = 1x10^{-4}	-1.27	20.196	20.004	0.193	16.81	0.571

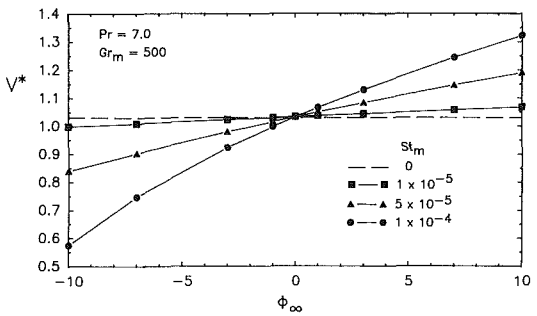

Fig. 2 Variation of V^* as a function of St_m and ϕ_∞: Gr_m = 500 and Pr = 7.0

insulated loop ($St_m = 0$). In this table, Q_L/P_w represents the ratio of heat losses from the insulated portions of the loop over the power input in the heated section. The first thing to note is that $\overline{fRe}$ is close to the fully developed value of 16 in all three cases. This indicates that the velocity profiles are only mildly affected by mixed-convection effects, and the total friction does not change significantly from one case to the other. However, the variation in total buoyancy (or $T_{hot} - T_{cold}$) is much greater.

For the case where $\phi_\infty = +10$, $Q_L/P_w = 1.23$. Therefore, the amount of heat removed in the cooled section has to be 2.23 times the power input supplied in the heated section. Thus, the overall temperature drop across the cooled section has to be higher than the overall temperature rise in the heated section. Consequently, the difference ($T_{hot} - T_{cold}$), the total buoyancy, and the average velocity all increase when compared to the case where $St_m = 0$, as indicated in Table 2.

As for the case where $\phi_\infty = -10$, the ratio of $Q_L/P_w = -1.27$. This implies that heat losses from the insulated portions of the loop exceed the power input in the heated section, and heat is supplied (and not removed) in the cooled section. As shown in Table 2, this profoundly affects the resulting average velocity.

The analysis presented in this note is specific to the geometry shown in Fig. 1 and to the corresponding dimensions presented in Table 1. Nonetheless, the results obtained in this study indicate that the performance of a closed-loop thermosyphon can be markedly affected by heat gains (or losses) in the insulated sections of the loop.

Acknowledgments

This research was financially supported by the Natural Sciences and Engineering Research Council of Canada in the form of a Post-Graduate Scholarship granted to M. A. Bernier and through individual operating grants awarded to Prof. B. R. Baliga.

References

Bernier, M. A., 1991, "Investigation of a Closed-Loop Thermosyphon," Ph.D. thesis, McGill University, Montréal, Canada.

Bernier, M. A., and Baliga, B. R., 1992, "A 1-D/2-D Model and Experimental Results for a Closed-Loop Thermosyphon With Vertical Heat Transfer Sections," *Int. J. Heat Mass Transfer*, Vol. 35, No. 11, pp. 2969–2982.

Greif, R., 1988, "Natural Circulation Loops," ASME JOURNAL OF HEAT TRANSFER, 50th Anniversary Issue, Vol. 110, pp. 1243–1258.

Hallinan, K. P., and Viskanta, R., 1985, "Heat Transfer From a Vertical Tube Bundle Under Natural Circulation Conditions," *Int. J. Heat Fluid Flow*, Vol. 6, No. 4, pp. 256–264.

Huang, B. J., and Zelaya, R., 1988, "Heat Transfer Behavior of a Rectangular Thermosyphon Loop," ASME JOURNAL OF HEAT TRANSFER, Vol. 110, pp. 487–493.

Lavine, A. G., 1984, "A Three-Dimensional Analysis of Natural Convection in a Toroidal Loop," Ph.D. thesis, U.C. Berkeley, California.

Lewis, J. S., Collins, M. W., and Allen, P. H. G., 1990, "Flow Rate Predictions for a Thermosyphon Loop," *Proc. of the 9th Int. Heat Transfer Conference*, Vol. 2, pp. 549–554.

Patankar, S. V., 1980, *Numerical Heat Transfer and Fluid Flow*, Hemisphere, Washington, DC.

The Importance of Prandtl Number in Mixed-Convection Instability

B. B. Rogers[1] and L. S. Yao[1]

Nomenclature

g = gravitational acceleration
K = annulus curvature parameter = $r_i/(r_o - r_i)$
n = azimuthal wavenumber
Pr = Prandtl number = ν/γ
Ra = Rayleigh number = $\mu\beta\, g(r_o - r_i)^4/\nu\gamma$
Re = Reynolds number = $W_{ave}\,(r_o - r_i)/\nu$
r_i = inner cylinder radius
r_o = outer cylinder radius
$\hat{u}$ = radial disturbance velocity
$\hat{v}$ = azimuthal disturbance velocity
$\hat{w}$ = axial disturbance velocity
W = axial velocity
β = thermal expansion coefficient
γ = thermal diffusivity
$\hat{\theta}$ = temperature disturbance
Θ = dimensionless temperature
μ = vertical temperature gradient
ν = kinematic viscosity
ρ = density

[1]Department of Mechanical and Aerospace Engineering, Arizona State University, Tempe, AZ 85287.

Contributed by the Heat Transfer Division of THE AMERICAN SOCIETY OF MECHANICAL ENGINEERS. Manuscript received by the Heat Transfer Division May 1992; revision received September 1992. Keywords: Flow Instability, Mixed Convection. Associate Technical Editor: F. P. Incropera.

1 Introduction

It is a common misconception that thermally induced instabilities in mixed convection can occur only under extreme heating conditions, and may be ignored under normal circumstances. These instabilities have, however, been observed in the laboratory with small temperature gradients. For example, Kemeny and Somers (1962) describe thermally induced instabilities in mixed convection in a 0.75-in. radius circular pipe when the vertical temperature gradient was 2.5°F/ft, which resulted in a 30 percent increase in the Nusselt number. As will be demonstrated in this paper, as the radius of the tube increases, the temperature gradient necessary to induce instability will decrease even further. This implies that thermal instability exists as long as the flow is *not* isothermal. These instabilities are an inherent property of nonisothermal flows. Any design method that ignores these effects is unrealistic and unreliable.

The results in this note will demonstrate that the onset of thermally induced instability in mixed convection depends strongly on the Prandtl number. The role of the Prandtl number in determining the relative thicknesses of the momentum and thermal boundary layers is well known. However, in more complicated nonisothermal flows, such as mixed convection inside ducts, the effect of the Prandtl number is not as obvious. In this study, we will demonstrate that the Prandtl number plays a fundamental role in the hydrodynamic instability of nonisothermal flows as well as the flow transition process. This is because the structures of the complex unsteady flows resulting from mixed-convection instability are completely different and depend on the value of Pr. Consequently, the associated heat transfer rate varies and the Prandtl number is a key parameter to determine its value. Its importance cannot be explained by the traditional understanding of Prandtl number effects.

A study of the energetics of nonisothermal flow reveals that there are two sources of energy to sustain instability (Rogers and Yao, 1992a). The first of these is the shear production, which is the product of the Reynolds stress and the mean-flow strain rate, similar to isothermal flow. In the case of nonisothermal flow, however, energy is also obtained from the buoyant potential, and the flow transition is modified by the buoyant energy production. The Prandtl number plays a key role in this energy transfer that has not been previously investigated in any depth. In this study, we investigate these phenomena by considering the linear instability of nonisothermal flow in a vertical annulus with a constant heat flux maintained on the inner cylinder and the outer cylinder insulated.

There are several previous studies that are relevant to the current work. Linear-instability analyses by Yao (1987a, 1987b) showed close agreement with experimental observations of buoyancy induced instabilities in pipe flow (Scheele and Hanratty, 1962; Kemeny and Somers, 1962). Linear-instability analyses of the flow of air (Pr = 0.71) in a vertical concentric annulus with the cylinders maintained at different temperatures has demonstrated that the stability boundary in the Grashof number–Reynolds number (Gr–Re) plane consists of three distinct instabilities (Yao and Rogers, 1989a, 1989b). These modes were identified as a shear instability, which is induced by viscous effects as Re increases, the thermal-shear instability, caused by an unstable velocity distribution induced by the buoyant force as Gr increases, and the interactive instability, which bridged the gap between the shear and thermal-shear modes. However, all of these instabilities obtain most of their kinetic energy through the shear production mechanism. In the natural-convection limit of this problem, Choi and Korpela (1980) predicted and observed experimentally a thermal-shear instability. They also predicted the presence of a thermal-buoyant instability at large Pr, but their experimental apparatus was incapable of producing the conditions necessary to observe this mode in the laboratory. The natural convection limit of the current problem, with a heated inner cylinder and an insulated outer cylinder, is that of a fluid trapped in a tall vertical annulus with a uniformly increasing temperature. The mathematical formulation of the problem in this limit is identical to that of natural convection in an annulus with a uniform internal heat source in the fluid. The associated boundary conditions are constant temperature on the inner cylinder with an insulated outer cylinder. This problem has been studied by Rogers and Yao (1993a), and the results have shown that both thermal-shear and thermal-buoyant instabilities are present, depending on the annular geometry and the value of the Prandtl number.

Experimental results for mixed convection of water in a heated vertical annulus indicate that, as the rate of heat addition to the fluid is increased, the flow becomes unstable, and the measured heat transfer rates increase by as much as 45 percent above those predicted by laminar flow models (Maitra and Subba Raju, 1975). Nonlinear instability analyses using the shape assumption (Rogers and Yao, 1990) and a formal weakly nonlinear theory (Yao and Rogers, 1992) have predicted Nusselt numbers that are in agreement with the experimental results both in the case of the heated annulus and a heated circular pipe (Rogers and Yao, 1993b). These specific cases illustrate the importance of accounting for hydrodynamic instability in heat transfer calculations. In addition, the earlier linear-instability studies have illuminated the roles of the Reynolds number and Rayleigh number (or Grashof number) in nonisothermal instability. However, the effects of the Prandtl number on these phenomena have not been studied previously.

An important difference between the problem studied here, that of flow in an annulus with a heated inner cylinder and an insulated outer cylinder, and that of the constant wall temperature problems is that in this case the vertical temperature gradient leads to a vertical density stratification. This stratification is stable when the temperature increases in the vertical direction (Ra > 0), but is potentially unstable when the density decreases in the vertical direction (Ra < 0). Our results will show that the stability characteristics are substantially different for each case. We find that four different instabilities are present in this flow. With no heating, the flow becomes unstable to the shear instability of isothermal flow as Re increases. The shear instability is found to be strongly stabilized by heating (Ra > 0) and strongly destabilized by cooling (Ra < 0). In stably stratified flow, one of two thermally induced instabilities will appear, depending on the value of the Prandtl number. The first of these occurs when the Prandtl number is small, and is caused by an unstable velocity profile induced by thermal effects. This is the *thermal-shear* instability, since it obtains kinetic energy primarily by shear production. The second instability occurs at larger Prandtl number, and is the *thermal-buoyant* instability because it is driven primarily by buoyant effects. The thermal-buoyant instability is found to be potentially much more sensitive to thermal effects than the thermal-shear mode. In the case of unstably stratified flow, a thermally induced instability caused by the unstable density stratification appears as the magnitude of Ra increases. This is the *Rayleigh–Taylor* instability. In unstably stratified flow, the Rayleigh–Taylor mode is always more unstable than the thermal-shear mode, and will be the dominant thermal instability except at very large Prandtl numbers (Pr > 100), when the thermal buoyant mode will become pre-eminent.

Our analysis shows that in stably stratified flow, linear instability is initiated in low Prandtl number fluids due to the thermal-shear instability, which occurs when increasing Ra distorts the basic-state velocity profiles sufficiently so that the velocity profile becomes unstable. In larger Prandtl number fluids, however, the flow becomes unstable to the thermal-buoyant instability when a local disruption of the buoyant

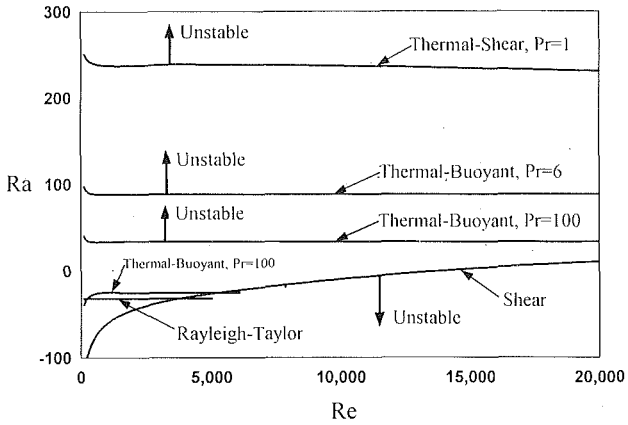

Fig. 1 Neutral stability curves in the Re-Ra plane

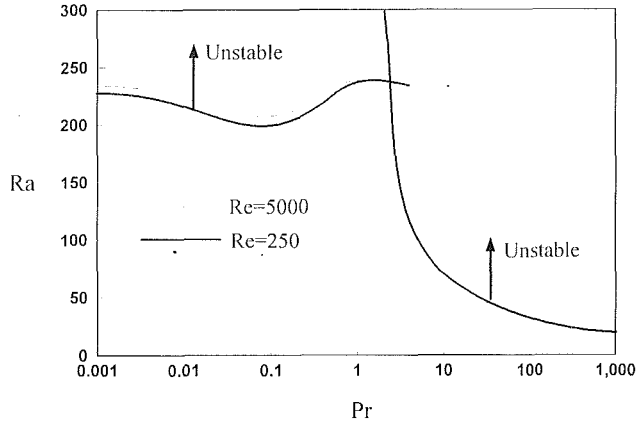

Fig. 2 Neutral stability curves in the Pr-Ra plane

force, induced by a temperature fluctuation, causes a disruption of the velocity field, with the kinetic energy being obtained from the fluctuating buoyant potential. The reason low Prandtl number fluids do not exhibit this behavior is because the "penetration depth" of temperature disturbances increases as the Prandtl number decreases. Therefore, in low Prandtl number fluids, temperature fluctuations are rapidly smoothed by conduction. On the other hand, as the Prandtl number increases, the fluids do not conduct heat as well, the temperature disturbances remain more localized, and the concentrated disruption of the buoyant force initiates instability. This also explains why the critical Ra for the thermal-buoyant mode decreases substantially in poorly conducting high Prandtl number fluids, as our results will demonstrate.

2 Analysis

The problem under consideration is that of fluid flow driven by an external pressure gradient in a heated vertical annulus. A constant vertical temperature gradient is maintained on the inner cylinder and the outer cylinder is insulated. The governing equations are the Boussinesq equations in cylindrical coordinates. The basic state of the fluid is steady, laminar, parallel, fully developed flow. The basic-state velocity and temperature profiles are independent of Re and Pr, and depend on Ra only. The linear instability of the basic state is studied by subtracting the basic state from the governing equations and neglecting the nonlinear terms. The governing equations, those of the basic state and linear instability, and details of the analysis procedure are discussed by Yao and Rogers (1992).

3 Results

The instability boundary for the shear, thermal-shear, thermal-buoyant, and Rayleigh-Taylor instabilities in the Ra-Re plane for an annulus with a curvature parameter of $K = 0.6$, is shown in Fig. 1. Referring to this figure, it is seen that the shear instability becomes unstable in isothermal flow ($Ra = 0$) at $Re = 14017$ to a disturbance with an azimuthal wavenumber of $n = 1$, in agreement with the results of Mahadevan and Lilley (1977). This instability is strongly stabilized by heating and strongly destabilized by cooling. As Re increases above Re_c, the unstable region due to this disturbance will consist of the area between the $Ra = 0$ axis and a critical Rayleigh number, which becomes nearly constant for large Re at about $Ra_c = 10$. At Re less than Re_c, the stable region consists of the area between the $Ra = 0$ axis and a critical Ra whose magnitude increases slowly as Re decreases. The curve given on Fig. 1 for the shear instability is valid for all Pr because this instability does not exhibit any Pr dependence. The results have shown that the least stable azimuthal wavenumber for the shear instability is always the first azimuthal mode in this geometry.

At $Ra < 0$, as Re decreases from Re_c of isothermal flow, the flow still becomes unstable to the shear disturbance as the magnitude of Ra increases. However, as Re decreases further, thermally driven instabilities appear, which become more unstable than the shear mode, as Fig. 1 illustrates. For all Re, at $Re = -32$, an instability appears due to the unstable stratification of the flow, and is therefore the *Rayleigh–Taylor* instability. For $Re < 4000$, this instability is less stable than the shear mode. The least stable Rayleigh–Taylor mode has an azimuthal wavenumber of $n = 1$, and the minimum critical Ra in this case occurs as the axial wavenumber, α, approaches zero. Therefore, the instability will consist of long waves in the axial direction. Similar to the shear instability, Ra_c for the Rayleigh–Taylor mode does not depend on Pr, and the curve shown on Fig. 1 is valid for all Pr. For the unstably stratified case, this is the dominant thermally induced instability except at values of Pr greater than 100, as illustrated.

At $Ra > 0$, the flow is stably stratified and the Rayleigh–Taylor mode doesn't appear. However, as Ra increases, other thermally induced instabilities, called the thermal-shear and thermal-buoyant modes, appear. In this region, the dominant thermal instability will depend on the value of Pr. The thermal-shear instability for $Pr = 1$ and the thermal-buoyant instabilities for $Pr = 6$ and $Pr = 100$ are illustrated in Fig. 1. As the results shown, the critical Rayleigh numbers for these instabilities are almost independent of Re for the range of data presented. Therefore, at small Re, the flow will become unstable to these modes as the rate of heating increases. In contrast to the results for the constant wall temperature thermal boundary conditions (Yao and Rogers, 1989), in this case no interactive instability has been found to bridge the gap between the thermal and shear instabilities. Therefore, as Ra increases at $Re > 14000$, the flow will be linearly unstable from $Ra = 0$ until the maximum Ra_c for the shear instability, followed by a linearly stable region until the minimum Ra_c for the dominant thermal instability is reached, as Fig. 1 illustrates.

As was implied in the discussion of Fig. 1, Ra_c for the thermal-shear and thermal-buoyant instabilities depends on Pr. This is illustrated more clearly in Fig. 2, which is a plot of the instability boundaries in the Ra–Pr plane for positive Ra at $Re = 250$ and $Re = 5000$. These results demonstrate more clearly that there are two distinct thermal instabilities present, neither of which is affected significantly by Re. At smaller values of Pr, the dominant instability occurs at a Rayleigh number of about 200, with Ra_c being a relatively weak function of Pr. This instability is hydrodynamic in origin, resulting from

an unstable velocity profile, and is therefore called the thermal-shear instability. At larger values of Pr, an instability appears in which Ra_c is more strongly influenced by Pr. This instability is driven by buoyant effects, and is therefore a thermal-buoyant instability. In this case, the thermal-shear instability is the most unstable mode for Pr less than 2.5, while at Pr greater than 2.5, the thermal-buoyant mode becomes more unstable. With the thermal-buoyant instability, Ra_c initially decreases rapidly with increasing Pr, but as Pr increases further, the rate of decrease diminishes, and Ra_c approaches a constant value of about $Ra_c = 20$ at large Pr. Consequently, the thermal-buoyant instability is potentially much more sensitive to thermal effects than the thermal-shear instability.

4 Energetics

In this section we will study the energy transfer in the unstable flow in more detail so that the physical mechanisms responsible for the occurrence of the thermal-shear and thermal-buoyant instabilities may be clarified. With this in mind, the kinetic energy balance for the disturbance may be written as:

$$\frac{\partial}{\partial t}\langle \hat{u}^2+\hat{v}^2+\hat{w}^2\rangle = -\left\langle \hat{u}\hat{w}\frac{dW}{d\eta}\right\rangle - \frac{\mathrm{Ra}}{\mathrm{Re}}\langle \hat{w}\hat{\theta}\rangle$$

$$-\frac{1}{\mathrm{Re}}\langle(\nabla\hat{u})^2+(\nabla\hat{v})^2+(\nabla\hat{w})^2\rangle = E_s+E_b+E_d. \quad (1)$$

The balance of thermal variance yields:

$$\frac{\partial}{\partial t}\langle\hat{\theta}^2\rangle = -\left\langle \hat{u}\hat{\theta}\frac{dW}{d\eta}\right\rangle + \frac{1}{\mathrm{RePr}}\langle\hat{w}\hat{\theta}\rangle - \frac{1}{\mathrm{RePr}}\langle(\nabla\hat{\theta})^2\rangle$$

$$= E_t - \frac{1}{\mathrm{RaPr}}E_b + E_c. \quad (2)$$

W and Θ are the basic-state velocity and temperature, respectively, the $\hat{}$ denotes the disturbance velocities and temperature, and the symbols $\langle\ \rangle$ imply integration over the volume of the disturbance wave. On the curve of neutral stability, the disturbances are neither growing nor decaying, and the left-hand sides of Eqs. (1) and (2) are zero. In Eq. (1), the first term, given the symbol E_s, represents the shear production of disturbance kinetic energy. The second term, given the symbol E_b, represents the production of kinetic energy through work done by the fluctuating body force, and is the buoyant production term. The last term, given the symbol E_d in Eq. (1), represents the dissipation of energy due to viscous effects. Therefore, Eq. (1) represents a balance of the production of disturbance kinetic energy by both the shear and buoyant mechanisms with the dissipation of disturbance kinetic energy by viscous action. In Eq. (2), the first term, given the symbol E_t, is the product of the disturbance heat flux and the mean temperature gradient, and is therefore the gradient production of thermal variance. The next term in Eq. (2) represents the exchange of thermal and kinetic energy due to the buoyant force, and is the negative of the buoyant production term in Eq. (1) divided by RaPr. Therefore, this term represents the transfer of energy from the thermal field to the velocity field by the buoyant force. The last term in Eq. (2), given the symbol E_c, represents the dissipation of thermal variance by conduction. Therefore, Eq. (2) represents a balance of the gradient production of thermal variance with the sum of the transfer of thermal energy to kinetic energy through the buoyant exchange term and the dissipation of thermal variance by conduction.

These results demonstrate that the disturbance waves may gain kinetic energy from both shear and buoyant production. The transfer of thermal energy to the momentum wave occurs because components of the disturbance heat flux appear both in the balance of disturbance kinetic energy and in the balance of thermal variance. In this problem, the vertical component of the disturbance heat flux appears in both the kinetic energy balance and in the balance of thermal variance. Therefore, in this case, an exchange of energy occurs directly at the same wavelength along the direction of the body force. However, there is also an indirect exchange of energies between the radial disturbance heat flux, which appears in the gradient production term of the thermal variance, and the axial disturbance heat flux, which appears in the buoyant production term. This is because the axial and radial disturbance velocities are coupled through pressure scrambling (Rogers and Yao, 1993a). In non-isothermal flows that do not have an axial temperature gradient, the direct transfer term will not appear in the balance of thermal variance. However, the indirect transfer mechanism will always be present.

Table 1 Energetics for shear, thermal shear, thermal buoyant, and Rayleigh-Taylor instabilities (S stands for the shear instability, TS stands for the thermal-shear instability, TB stands for the thermal-buoyant instability, and RT stands for the Rayleigh-Taylor instability)

Re	Pr	Type	Ra_c	E_s	E_b	E_d
4000	1	S	-32.4	0.97	0.03	-1.0
8000	1	S	-16.1	0.99	0.01	-1.0
12000	1	S	-4.4	0.99	0.01	-1.0
14017	1	S	0.0	1.0	0.0	-1.0
16000	1	S	3.4	1.0	0.0	-1.0
250	2	TB	322	0.12	0.88	-1.0
250	2	TS	238	0.90	0.10	-1.0
250	3	TB	152	0.11	0.89	-1.0
250	3	TS	236	0.89	0.11	-1.0
1000	1	RT	-32.0	0.0	1.0	-1.0
1000	100	TB	-27.6	-0.02	1.02	-1.0

The integrals in Eqs. (1) and (2) may be evaluated using the eigenvectors from the linear-instability analysis. The results of the analysis of Eq. (1) for each of the instabilities at representative points on the neutral curve are given in Table 1. The results for the shear and thermal-shear instabilities demonstrate that they are driven primarily by shear production, and the thermal-buoyant and Rayleigh-Taylor modes are driven primarily by buoyant production. These results clearly illustrate the fundamental difference between the instabilities.

An important difference between the shape of the disturbance temperature distributions in the thermal-shear and thermal buoyant instabilities is the fact that the temperature disturbance is more concentrated in the case of the thermal-buoyant mode. This explains why the thermal-buoyant mode becomes dominant as Pr increases. The thermal-shear instability is caused by an unstable velocity distribution. Since the velocity profile depends only on Ra, the critical Ra for this instability will not be strongly dependent on Pr. On the other hand, the thermal-buoyant instability is driven by a local disturbance in the buoyant force caused by a temperature (density) wave. The temperature disturbance is primarily dissipated by conduction, except for a small fraction, which may be converted from thermal to kinetic energy through the buoyant force. Therefore, low Pr fluids, which are good conductors of heat, will smooth out the thermal-buoyant temperature disturbance before the disruption of the buoyant force is large enough to cause instability. On the other hand, as Pr increases, the penetration depth of the temperature disturbance also decreases, the disruption of the buoyant force becomes more concentrated, and instability is initiated. When Pr becomes large enough, the threshold of instability for this mode becomes smaller than that of the thermal-shear mode. This also explains why the critical Ra continues to decrease with increasing Pr for the thermal-buoyant mode, since the temperature disturb-

ances will become more and more concentrated as the rate of heat conduction decreases.

References

Choi, I. G., and Korpela, S. A., 1980, "Stability of the Conduction Regime of Natural Convection in a Tall Vertical Annulus," *J. Fluid Mech.*, Vol. 99, pp. 725–738.

Kemeny, G. A., and Somers, E. V., 1962, "Combined Free and Forced Convection Flow in Vertical Circular Tubes—Experiments With Water and Oil," ASME JOURNAL OF HEAT TRANSFER, Vol. 84, pp. 339–346.

Maitra, D., and Subba Raju, K., 1975, "Combined Free and Forced Convection Laminar Heat Transfer in a Vertical Annulus," ASME JOURNAL OF HEAT TRANSFER, Vol. 97, pp. 135–137.

Mahadevan, R., and Lilley, G.M., 1977, "The Stability of Axial Flow Between Concentric Cylinders Due to Asymmetric Disturbances," *AGARD Conf. Proc.*, No. 224, Paper No. 9.

Rogers, B. B., and Yao, L. S., 1990, "The Effect of Mixed-Convection Instability on Heat Transfer in a Vertical Annulus," *Intl. J. Heat Mass Transfer*, Vol. 33, pp. 79–90.

Rogers, B. B., and Yao, L. S., 1993a, "Natural Convection in a Heated Annulus," *Int. J. Heat Mass Transfer*, Vol. 36, No. 1, pp. 35–47.

Rogers, B. B., and Yao, L. S., 1993b, "Finite-Amplitude Instability of Mixed-Convection in a Heated Vertical Pipe," to appear in *Int. J. Heat Mass Transfer*.

Scheele, G. F., and Hanratty, T. J., 1962, "Effect of Natural-Convection on Stability of Flow in a Vertical Pipe," *J. Fluid Mech.*, Vol. 14, pp. 244–256.

Yao, L. S., 1987a, "Is Fully-Developed and Non-Isothermal Flow Possible in a Vertical Pipe?" *Int. J. Heat Mass Transfer*, Vol. 30, pp. 707–716.

Yao, L. S., 1987b, "Linear Stability Analysis for Opposing Mixed-Convection in a Vertical Pipe," *Int. J. Heat Mass Transfer*, Vol. 30, pp. 810–811.

Yao, L. S., and Rogers, B. B., 1989, "The Linear Stability of Mixed-Convection in a Vertical Annulus," *J. Fluid Mech.*, Vol. 201, pp. 279–298.

Yao, L. S., and Rogers, B. B., 1992, "Finite-Amplitude Instability of Non-isothermal Flow in a Vertical Annulus," *Proc. R. Soc. Lond.*, Vol. A437, pp. 267–290.

Multidimensional Modeling of Radiative Heat Transfer in Scattering Media

M. da Graça Carvalho,[1] T. Farias,[1] and P. Fontes[1]

Introduction

There exist various numerical techniques for computing radiative transfer in combustion systems. Among others are included the Hottel zone, Monte Carlo, and flux (or differential approximation) methods. Lockwood and Shah (1981) developed another method, called the discrete transfer method, as an alternative to the well-established techniques. This method not only keeps features of the previous zone, Monte Carlo, and flux methods, but also offers other peculiar advantages such as economy of computation, ease of application to complex geometries, and simplicity of concepts. It is due to these advantages and the easy treatment by numerical techniques used to solve the conservation equations for turbulent flows that this discrete transfer method has been employed, together with solutions of the flow equations, to address such a variety of problems as computing the performance of an industrial glass furnace (Carvalho et al., 1987, 1988), calculating the working conditions of a gas turbine combustor (Carvalho and Coelho, 1989), and predicting the performance of a pulverized fuel fired furnace (Fiveland and Wessel, 1986). The above applications, among others, to full-scale industrial furnaces were very successful. However, the results for a one-dimensional scattering medium did not show the same level of agreement with the benchmark results as did the nonscattering medium predictions (Shah, 1979). Although it is claimed that the method is capable of accounting for scattering in the medium with accuracy, no results have been reported or compared against other benchmark results in multidimensional enclosures (Viskanta and Menguç, 1987).

In the present paper, the discrete transfer model is applied to solve the radiative heat transfer problem in two- and three-dimensional rectangular enclosures containing absorbing-emitting and scattering medium. Results obtained with this technique are compared with other well-established methods, namely the Hottel zone method, the S_n discrete ordinates method, and the P-N differential approximation method. Geometries and surface and gas properties were used in a wide variety of situations to understand the performances of the method better. Required computer times and number of iterations are also reported as a function of number of rays, size of the grid, wall emissivity, and gas scattering coefficient.

Description of the Model

General Features. The fundamental equation for the transfer of thermal radiation may be expressed as:

$$\frac{dI}{ds} = -(k_a + k_s)I + k_a \frac{E_g}{\pi} + \frac{k_s}{4\pi} \int_{4\pi} P(\bar{\Omega}, \bar{\Omega}')I(\bar{\Omega}')d\Omega' \quad (1)$$

where I is the radiant intensity in the direction of $\bar{\Omega}$, s is distance in the $\bar{\Omega}$ direction, E_g is the black body emission power of the gas at temperature T_g, k_a and k_s are the gas absorption and scattering coefficients, and $P(\bar{\Omega}, \bar{\Omega}')$ is the probability that incident radiation in the direction $\bar{\Omega}'$ will be scattered into the increment of solid angle $d\Omega$ about $\bar{\Omega}$. If, for conciseness, we define an extinction coefficient $k_c \equiv k_a + k_s$, an elemental optical depth $ds^* = k_c ds$, and a modified emissive power

$$E^* \equiv 1/k_c \left(k_a E_g + (k_s/4) \int_{4\pi} P(\bar{\Omega}, \bar{\Omega}')I(\bar{\Omega}')d\bar{\Omega}' \right), \quad (2)$$

the radiation transfer Eq. (1) may be re-expressed as:

$$\frac{dI}{ds^*} = -I + \frac{E^*}{\pi} \quad (3)$$

For a ray traveling through the domain in study, this equation describes the change of the ray's intensity when passing through an absorbing-emitting and scattering medium.

The discrete transfer method is based on solving Eq. (3) for representative rays that will travel through the considered domain. The directions of the rays are specified in advance (the values of the polar and azimuthal angles, θ and ϕ, are established) and they are traced along paths between the two boundary walls. The enclosure is subdivided into control volumes or cells. The intensities along each of the chosen directions are solved for, and the values of the intensities entering and leaving each cell are calculated.

Consideration of In-Scattering. The in-scattering term, like the emissive power (see Lockwood and Shah, 1981), is presumed constant over each small control volume. The in-scattering energy contributed by each ray that crosses the control volume, through which the ray being traced is "traveling," is discretized as (see Lockwood and Shah, 1981):

$$I_s \approx \frac{k_s}{\pi} P(\bar{\Omega}_{P_I Q_I}, \bar{\Omega}'_{P_I Q_m}) \, I(\bar{\Omega}'_{P_I Q_m})_{\text{avg}} \, \delta\Omega'_{P_I Q_m} \quad (4)$$

[1]Mechanical Engineering Department, Instituto Superior Técnico, Technical University of Lisbon, Lisbon Codex, Portugal.

Contributed by the Heat Transfer Division of THE AMERICAN SOCIETY OF MECHANICAL ENGINEERS. Manuscript received by the Heat Transfer Division July 1991; revision received June 1992. Keywords: Radiation. Associate Technical Editor: R. O. Buckius.

ances will become more and more concentrated as the rate of heat conduction decreases.

References

Choi, I. G., and Korpela, S. A., 1980, "Stability of the Conduction Regime of Natural Convection in a Tall Vertical Annulus," *J. Fluid Mech.*, Vol. 99, pp. 725–738.

Kemeny, G. A., and Somers, E. V., 1962, "Combined Free and Forced Convection Flow in Vertical Circular Tubes—Experiments With Water and Oil," ASME JOURNAL OF HEAT TRANSFER, Vol. 84, pp. 339–346.

Maitra, D., and Subba Raju, K., 1975, "Combined Free and Forced Convection Laminar Heat Transfer in a Vertical Annulus," ASME JOURNAL OF HEAT TRANSFER, Vol. 97, pp. 135–137.

Mahadevan, R., and Lilley, G.M., 1977, "The Stability of Axial Flow Between Concentric Cylinders Due to Asymmetric Disturbances," *AGARD Conf. Proc.*, No. 224, Paper No. 9.

Rogers, B. B., and Yao, L. S., 1990, "The Effect of Mixed-Convection Instability on Heat Transfer in a Vertical Annulus," *Intl. J. Heat Mass Transfer*, Vol. 33, pp. 79–90.

Rogers, B. B., and Yao, L. S., 1993a, "Natural Convection in a Heated Annulus," *Int. J. Heat Mass Transfer*, Vol. 36, No. 1, pp. 35–47.

Rogers, B. B., and Yao, L. S., 1993b, "Finite-Amplitude Instability of Mixed-Convection in a Heated Vertical Pipe," to appear in *Int. J. Heat Mass Transfer*.

Scheele, G. F., and Hanratty, T. J., 1962, "Effect of Natural-Convection on Stability of Flow in a Vertical Pipe," *J. Fluid Mech.*, Vol. 14, pp. 244–256.

Yao, L. S., 1987a, "Is Fully-Developed and Non-Isothermal Flow Possible in a Vertical Pipe?" *Int. J. Heat Mass Transfer*, Vol. 30, pp. 707–716.

Yao, L. S., 1987b, "Linear Stability Analysis for Opposing Mixed-Convection in a Vertical Pipe," *Int. J. Heat Mass Transfer*, Vol. 30, pp. 810–811.

Yao, L. S., and Rogers, B. B., 1989, "The Linear Stability of Mixed-Convection in a Vertical Annulus," *J. Fluid Mech.*, Vol. 201, pp. 279–298.

Yao, L. S., and Rogers, B. B., 1992, "Finite-Amplitude Instability of Non-isothermal Flow in a Vertical Annulus," *Proc. R. Soc. Lond.*, Vol. A437, pp. 267–290.

Multidimensional Modeling of Radiative Heat Transfer in Scattering Media

M. da Graça Carvalho,[1] T. Farias,[1] and P. Fontes[1]

Introduction

There exist various numerical techniques for computing radiative transfer in combustion systems. Among others are included the Hottel zone, Monte Carlo, and flux (or differential approximation) methods. Lockwood and Shah (1981) developed another method, called the discrete transfer method, as an alternative to the well-established techniques. This method not only keeps features of the previous zone, Monte Carlo, and flux methods, but also offers other peculiar advantages such as economy of computation, ease of application to complex geometries, and simplicity of concepts. It is due to these advantages and the easy treatment by numerical techniques used to solve the conservation equations for turbulent flows that this discrete transfer method has been employed, together with solutions of the flow equations, to address such a variety of problems as computing the performance of an industrial glass furnace (Carvalho et al., 1987, 1988), calculating the working conditions of a gas turbine combustor (Carvalho and Coelho, 1989), and predicting the performance of a pulverized fuel fired furnace (Fiveland and Wessel, 1986). The above applications, among others, to full-scale industrial furnaces were very successful. However, the results for a one-dimensional scattering medium did not show the same level of agreement with the benchmark results as did the nonscattering medium predictions (Shah, 1979). Although it is claimed that the method is capable of accounting for scattering in the medium with accuracy, no results have been reported or compared against other benchmark results in multidimensional enclosures (Viskanta and Menguç, 1987).

In the present paper, the discrete transfer model is applied to solve the radiative heat transfer problem in two- and three-dimensional rectangular enclosures containing absorbing-emitting and scattering medium. Results obtained with this technique are compared with other well-established methods, namely the Hottel zone method, the S_n discrete ordinates method, and the P-N differential approximation method. Geometries and surface and gas properties were used in a wide variety of situations to understand the performances of the method better. Required computer times and number of iterations are also reported as a function of number of rays, size of the grid, wall emissivity, and gas scattering coefficient.

Description of the Model

General Features. The fundamental equation for the transfer of thermal radiation may be expressed as:

$$\frac{dI}{ds} = -(k_a + k_s)I + k_a \frac{E_g}{\pi} + \frac{k_s}{4\pi}\int_{4\pi} P(\bar{\Omega}, \bar{\Omega}')I(\bar{\Omega}')d\Omega' \quad (1)$$

where I is the radiant intensity in the direction of $\bar{\Omega}$, s is distance in the $\bar{\Omega}$ direction, E_g is the black body emission power of the gas at temperature T_g, k_a and k_s are the gas absorption and scattering coefficients, and $P(\bar{\Omega}, \bar{\Omega}')$ is the probability that incident radiation in the direction $\bar{\Omega}'$ will be scattered into the increment of solid angle $d\Omega$ about $\bar{\Omega}$. If, for conciseness, we define an extinction coefficient $k_c \equiv k_a + k_s$, an elemental optical depth $ds^* = k_c ds$, and a modified emissive power

$$E^* \equiv 1/k_c\left(k_a E_g + (k_s/4)\int_{4\pi} P(\bar{\Omega},\bar{\Omega}')I(\bar{\Omega}')d\bar{\Omega}'\right), \quad (2)$$

the radiation transfer Eq. (1) may be re-expressed as:

$$\frac{dI}{ds^*} = -I + \frac{E^*}{\pi} \quad (3)$$

For a ray traveling through the domain in study, this equation describes the change of the ray's intensity when passing through an absorbing-emitting and scattering medium.

The discrete transfer method is based on solving Eq. (3) for representative rays that will travel through the considered domain. The directions of the rays are specified in advance (the values of the polar and azimuthal angles, θ and ϕ, are established) and they are traced along paths between the two boundary walls. The enclosure is subdivided into control volumes or cells. The intensities along each of the chosen directions are solved for, and the values of the intensities entering and leaving each cell are calculated.

Consideration of In-Scattering. The in-scattering term, like the emissive power (see Lockwood and Shah, 1981), is presumed constant over each small control volume. The in-scattering energy contributed by each ray that crosses the control volume, through which the ray being traced is "traveling," is discretized as (see Lockwood and Shah, 1981):

$$I_s \approx \frac{k_s}{\pi} P(\bar{\Omega}_{P_I Q_I}, \bar{\Omega}'_{P_I Q_m}) I(\bar{\Omega}'_{P_I Q_m})_{\text{avg}} \delta\Omega'_{P_I Q_m} \quad (4)$$

[1]Mechanical Engineering Department, Instituto Superior Técnico, Technical University of Lisbon, Lisbon Codex, Portugal.

Contributed by the Heat Transfer Division of THE AMERICAN SOCIETY OF MECHANICAL ENGINEERS. Manuscript received by the Heat Transfer Division July 1991; revision received June 1992. Keywords: Radiation. Associate Technical Editor: R. O. Buckius.

where $I(\bar{\Omega}'_{P_l Q_m})$avg is a value averaged over the control volume; the arithmetic mean of its values at k and $k+1$ (entering and leaving the control volume in the Ω' direction) would be convenient. The in-scattering term will then be given by the summation of the contributions of all the rays that crossed the control volume. This means that the memorized averaged energies of all rays that crossed each cell in the previous iteration will now be used to evaluate the in-scattering term. It is then to be expected that the CPU time necessary for each iteration will increase and the number of iterations may also increase (convergence of the in-scattering terms will additionally be required).

Results

In this section we consider various illustrative examples for two- and three-dimensional rectangular enclosures.

Two-Dimensional Rectangular Enclosures. For this type of geometry, two cases are examined: (*i*) scattering in a black enclosure, (*ii*) scattering in a gray enclosure. These examples were chosen to benchmark the discrete transfer method against the S_n discrete-ordinate method, the P-N differential approximation, and the Hottel zone method. The results obtained with the discrete transfer method were compared with the S_2, S_4, and S_6 approximation results obtained by Fiveland (1984), with the results obtained by Ratzel and Howell (1983) using a P_3 approximation and with the results obtained by Larsen (1981) using the Hottel zone method.

Results are presented using nondimensional values; radiant intensities are normalized using a characteristic emissive power, while coordinate directions are normalized with a characteristic length.

(*i*) *Pure Scattering in Black Enclosures.* The studies focused on radiative transfer with isotropic scattering in a square enclosure with black walls and a scattering cross section of unity. The emissive power of surface 1 is unity, while the emissive powers of surfaces 2, 3, and 4 are zero. This geometry was analyzed by Larsen (1981), Ratzel and Howell (1983), and Fiveland (1984).

For these cases, the discrete transfer method using typical values of size mesh and number of rays for two-dimensional problems without scattering led to unsatisfactory results. As suggested by Viskanta and Menguç (1987), this behavior of the discrete transfer method may result from the so-called "ray effect" (Lathrop, 1968, 1971). In scattering media each ray is not only responsible for carrying information from one wall to another, but also for contribution to the in-scattering term in Eq. (3). With this in mind it is understandable that in scattering media the ray effect tends to be more notorious. To overcome this problem, an increase in the size of the mesh and especially in the number of rays used was necessary to obtain the results presented in Fig. 1. The number of rays and the size of the mesh are intimately linked and optimization has to be achieved in order to get an acceptable number of rays crossing each cell. The number of rays crossing each cell should be maximized without loosing accuracy due to lowering the number of grid cells. Independent studies of the grid and number of rays should be performed in conjunction.

Figure 1 shows the comparison of centerline distributions of radiant intensities for different rectangular enclosures. Discrete transfer predictions, using a 10×10 mesh and 64 rays per node, are compared with the P_3 solution method results and the S_4 discrete ordinates solutions. The results presented by Modest (1975) using the zone method are also shown. For high aspect ratios (hot wall much larger than side walls) an increase in the number of ϕ's was used leaving the number of θ's similar to the values used in typical two-dimensional non-scattering problems so that rays (coming from the hot wall)

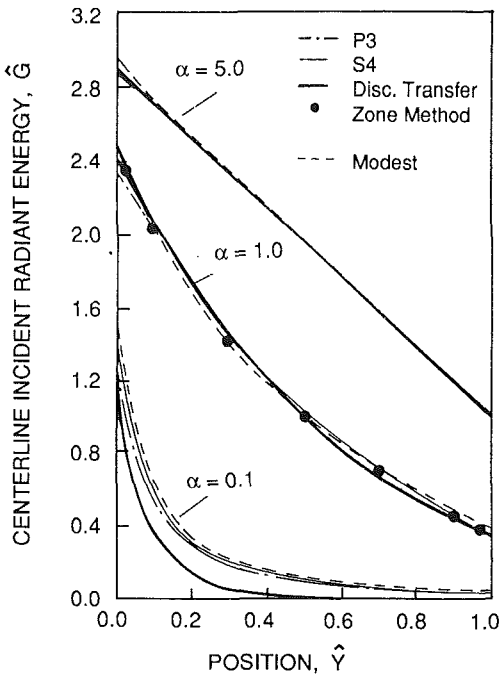

Fig. 1 Centerline incident radiant energy for different aspect ratios in an square enclosure with a scattering medium; surface 1; $\epsilon=1$, $E_w=1$; surfaces 2-4: $\epsilon=1$, $E_w=0$; $k_s=1$; $k_a=0$

could reach the side zones of the domain. For $\alpha=0.1$ the opposite was done.

The discrete transfer method presents very good results both for high and intermediate aspect ratios. For very low aspects ratios ($\alpha=0.1$: emitting wall is ten times smaller than side walls), as we move away from the hot wall, fewer rays (carrying information about the emitting wall) will reach the cells. For this reason, the incident radiation energy values are underpredicted by the discrete transfer method when compared with the other ones.

(*ii*) *Pure Scattering in a Gray Enclosure.* Predictions of mean radiant intensity were obtained using the discrete transfer method for a radiative gray square enclosure with isotropic scattering. A scattering cross section of unity was assumed. The predictions were compared with the discrete-ordinate S_n solutions (Fiveland, 1984), Hottel's zone method (Larsen, 1981), and the P_3 differential results (Ratzel and Howell, 1983).

As in the previous case, a 10×10 mesh and a large number of rays had to be used (64 rays power wall node). From Fig. 2(*a*) it can be noticed that the results obtained with the discrete transfer method are satisfactory, being very similar to the ones obtained by the S_6 discrete ordinates predictions.

In Fig. 2(*b*) heat transfer rates to the hot surface are shown for different wall emissivities. The discrete transfer predictions clearly follow the S_4 and S_6 solutions (which, according to Fiveland, 1984, are the solutions that adequately predict the surface heat transfer rates) for both gray and black enclosures.

Three-Dimensional Rectangular Enclosures. The three-dimensional absorbing-emitting and isotropic scattering case studied is based on the idealized furnace presented by Menguç and Viskanta (1985).

The results obtained with the discrete transfer method, using a $10\times5\times5$ mesh and 64 rays per wall node, were compared with the S_2, S_4, S_6, and S_8 discrete ordinates predictions (Jamaluddin and Smith, 1988) and the zone model results (Truelove, 1987). Increasing the number of rays or the size of the mesh did not change the results more than 1 percent.

Figure 3 shows the heat fluxes to the firing end and exit end

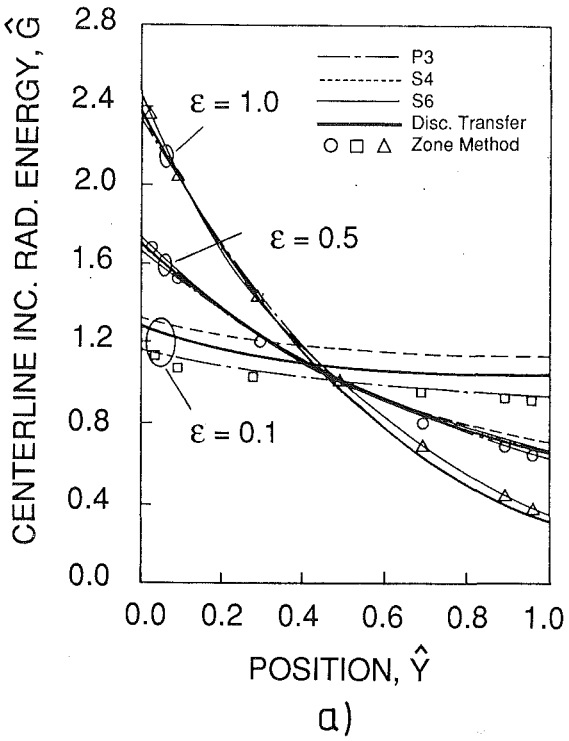

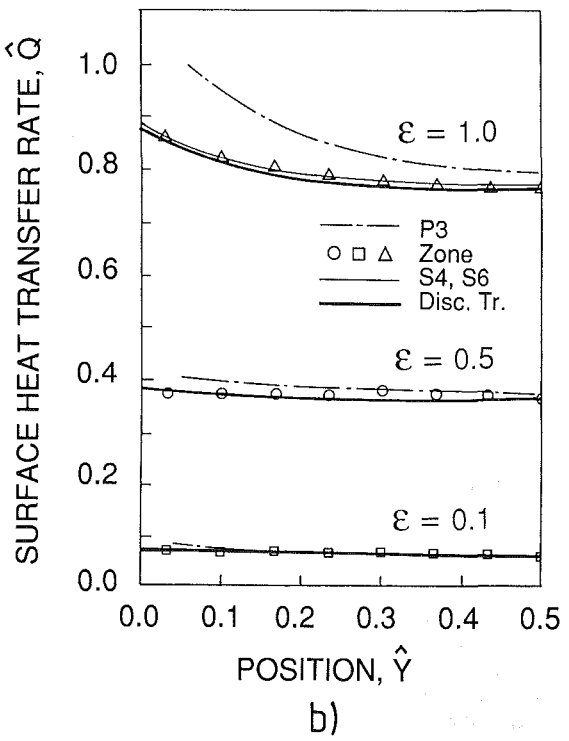

Fig. 2 Square gray enclosure with isotropic scattering medium: (*a*) centerline incident radiant energy; (*b*) hot surface heat transfer rate; surface 1: $E_w = 1$; sufaces 2-4: $E_w = 0$; $k_s = 1$; $k_a = 0$

walls of the furnace. The results clearly show the good performance of the discrete transfer method for the calculation of heat transfer in a three-dimensional enclosure containing as absorbing emitting and isotropic scattering medium.

The results obtained with the S_4, S_6, and S_8 discrete-ordinate method are very similar to the discrete transfer predictions, and due to the increase in computational effort, as reported

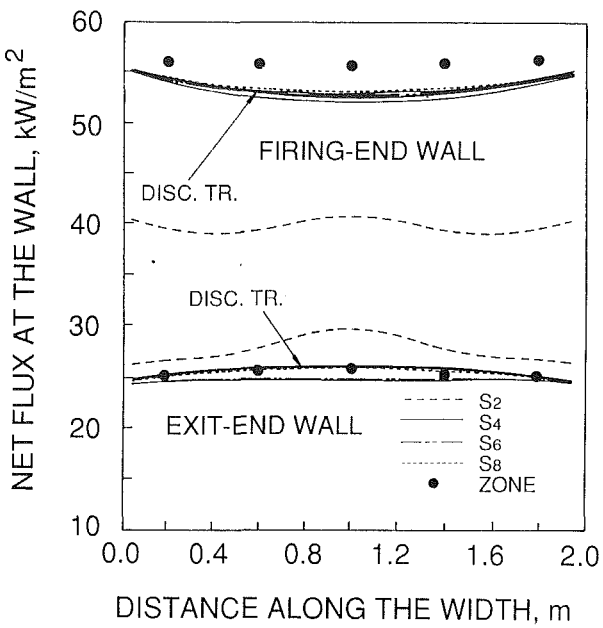

Fig. 3 Predicted radiative heat fluxes at the firing end and exit end walls of the rectangular enclosure idealized by Menguç and Viskanta (1985)

by Jamaluddin and Smith (1988), no advantages are obtained by using S_6 or S_8 when compared with the S_4 method.

Required Computer Times

To evaluate the required computer times and number of iterations for different situations, the test case considered was the same as previously presented for two-dimensional enclosures containing an isotropic scattering medium.

In Fig. 4(*a*) the CPU time required in a VAX 6000 machine to obtain a preset error (heat balance error at the wall surface not exceed 0.1 percent) are shown for different computational grids (64 rays per wall node were used) and different number of rays (a 10×10 grid was used). Whenever better accuracy is desired, it is preferable to increase the number of rays used, rather than the size of the grid. This is due to the fact that an increase in the size of grid implies an increase in the number of walls cells and therefore also in the number of rays emitted.

In Fig. 4(*b*), the iterations needed to obtain the same present error mentioned above are shown for different wall emissivities (pure isotropic scattering was considered: $k_s = 1.0\ m^{-1}$) and different scattering coefficients (black walls were assumed). A 10×10 uniform grid and 64 rays per wall node were considered. As expected, the number of iterations required to obtain the solution increases with the value of the scattering coefficient. Wall emissivities also influence the number of iteractions required for convergence. For high values of the wall emissivity, the number of iteractions required is low; nevertheless, as the emissivity approaches zero the number of iteractions increases considerably.

For comparisons with other radiative methods, namely the discrete ordinates method, Fiveland (1984) presents, for the same test case, the CPU times required to obtain the S_2, S_4, and S_6 solutions for different wall emissivities. The CPU times for the discrete transfer and S_4 methods are of the same order of magnitude.

Conclusions

The discrete transfer solutions were compared to other solution methods for two- and three-dimensional rectangular

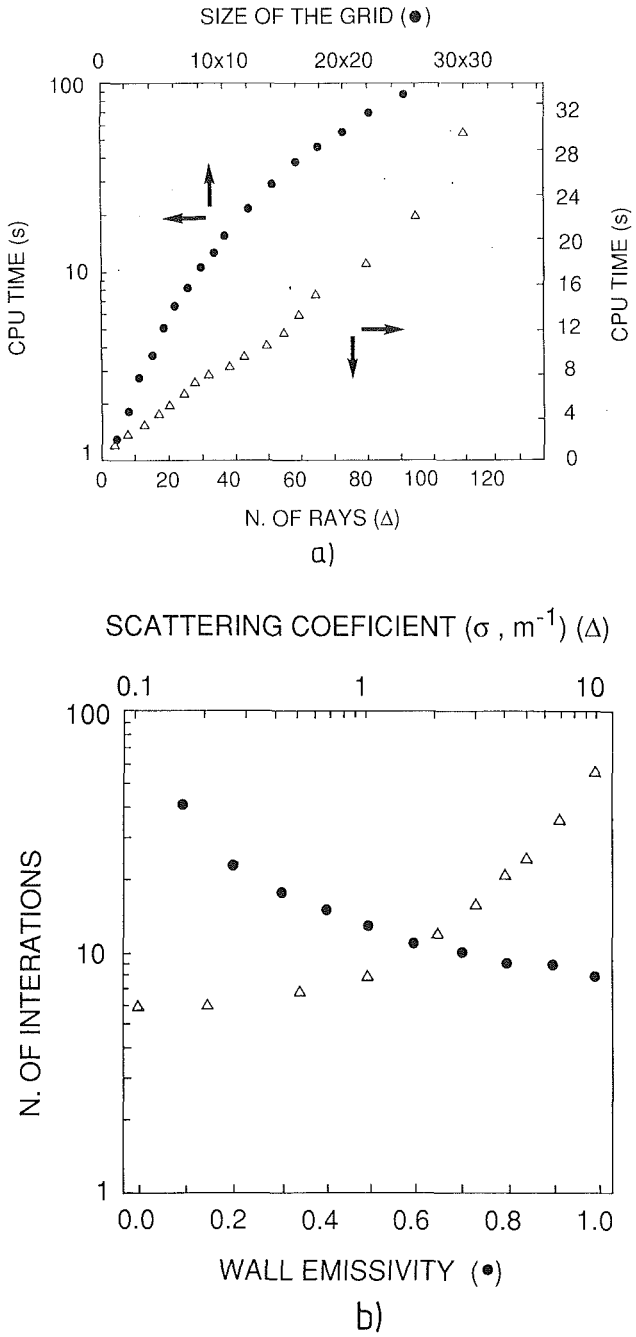

Fig. 4 Computational load: (*a*) CPU time required to achieve convergence for different computational grids and number of rays; (*b*) iterations required to achieve convergence for different wall emissivities and scattering coefficients

enclosures containing an absorbing-emitting and isotropic scattering medium.

The discrete transfer method has shown very good results when scattering was considered. However, the number of representative directions used had to be increased, when compared to normal situations where scattering is not considered. Only for very small aspect ratio (where the emitting wall is much smaller than the side walls) did the discrete transfer method present significant deviations. This behavior of the discrete transfer method results from the "ray effect." It was found that, for the studied cases, the best remedy to reduce the ray effect is to increase the number of rays that cross each cell. In order to avoid a prohibitive CPU time, an optimization of the number of the grid cells and rays should be sought.

Acknowledgments

The authors are thankful to Prof Raymond Viskanta from Purdue University and to Dr. Woodrow Fiveland from Babcock & Wilcox, Ohio, for their helpful suggestions and discussions. A scholarship from CIENCIA (JNICT—Junta Nacional de Investigação Científica e Tecnológica of Portugal) is acknowledged.

References

Carvalho, M. G., Durão, D. F. G., and Pereira, J. C. F., 1987, "Prediction of the Flow, Reaction and Heat Transfer in an Oxy-Fuel Glass Furnace," *International Journal of Engineering Computations*, Vol. 4, No. 1, pp. 23–34.

Carvalho, M. G., Oliveira, P., and Semião, V., 1988, "A Three-Dimensional Modelling of an Industrial Glass Furnace," *Journal of the Institute of Energy*, Vol. LXI, No. 448, pp. 143–156.

Carvalho, M. G., and Coelho, P. J., 1989, "Heat Transfer in Gas Turbine Combustors," *AIAA J. Thermophysics and Heat Transfer*, Vol. 3, No. 2, p. 123.

Fiveland, W. A., 1984, "Discrete-Ordinates Solutions of the Radiative Transport Equation for Rectangular Enclosures," ASME JOURNAL OF HEAT TRANSFER, Vol. 106, pp. 699–706.

Fiveland, W. A., and Wessel, R., 1986, "FURMO: A Numerical Model for Predicting Performance of Three-Dimensional Pulverized-Fuel Fired Furnaces," ASME Paper No. 86-HT-35.

Jamaluddin, A. S., and Smith, P. J., 1988, "Predicting Radiative Transfer in Rectangular Enclosures Using the Discrete Ordinates Method," *Combustion Science and Technology*, Vol. 59, pp. 321–340.

Larsen, M., 1981, "Hottel Zone Code," PhD Thesis, University of Texas Austin.

Lathrop, K. D., 1968, "Ray Effects in Discrete Ordinate Equations," *Nuclear Science and Engineering*, Vol. 32, pp. 357–369.

Lathrop, K. D., 1971, "Remedies for Ray Effects," *Nuclear Science and Engineering*, Vol. 45, pp. 235–268.

Lockwood, F. C., and Shah, N. G., 1981, "A New Radiation Solution Method for Incorporation in General Combustion Prediction Procedures," *18th Symposium (Int.) on Combustion*, pp. 1405–1414.

Mengüç, M. P., and Viskanta, R., 1985, "Radiative Transfer in Three-Dimensional Rectangular Enclosures Containing Inhomogeneous Anisotropically Scattering Media," *J. Quant. Spect. Radiat. Transfer*, Vol. 33, p. 533.

Modest, M., 1975, "Radiative Equilibrium in a Rectangular Enclosure Bounded by Gray Walls," *J. Quant. Spectrosc. Radiat. Transfer*, Vol. 15, No. 6, pp. 445–461.

Ratzel, A. C., III, and Howell, J. R., 1983, "Two-Dimensional Radiation in Absorbing-Emitting Media Using the P-N Approximation," ASME JOURNAL OF HEAT TRANSFER, Vol. 105, pp. 333–340.

Shah, N. G., 1979, "A New Method of Computation of Radiant Heat Transfer in Combustion Chambers," PhD Thesis, Imperial College, London.

Truelove, J. S., 1987, "Discrete-Ordinate Solutions of the Radiation Transport Equation," ASME JOURNAL OF HEAT TRANSFER, Vol. 109, pp. 1048–1051.

Viskanta, R., and Mengüç, M. P., 1987, "Radiation Heat Transfer in Combustion Systems," *Progress in Energy Combustion Science*, Vol. 13, pp. 97–160.

Suitable Configuration Factors for Radiation Calculation Concerning Tilted Flames

A. Guelzim,[1,4] J. M. Souil,[2,4] and J. P. Vantelon[3,4]

Nomenclature

$a = H/R$

$b = X/R$

$A = (b^2-1)(b^2-\sin^2\theta)+b^4\sin^2\theta\tan^2\alpha$

[1]Graduate Student.

[2]Research Assistant.

[3]Directeur de Recherche au CNRS.

[4]Laboratoire de Chimie Physique de la Combustion, UA 872 CNRS, University of Poitiers, Domaine du Deffend, 86550 Mignaloux-Beauvoir, France.

Contributed by the Heat Transfer Division of THE AMERICAN SOCIETY OF MECHANICAL ENGINEERS. Manuscript received by the Heat Transfer Division January 1992; revision received December 1992. Keywords: Environmental Heat Transfer, Fire/Flames, Radiation Interactions. Associate Technical Editor: R. O. Buckius.

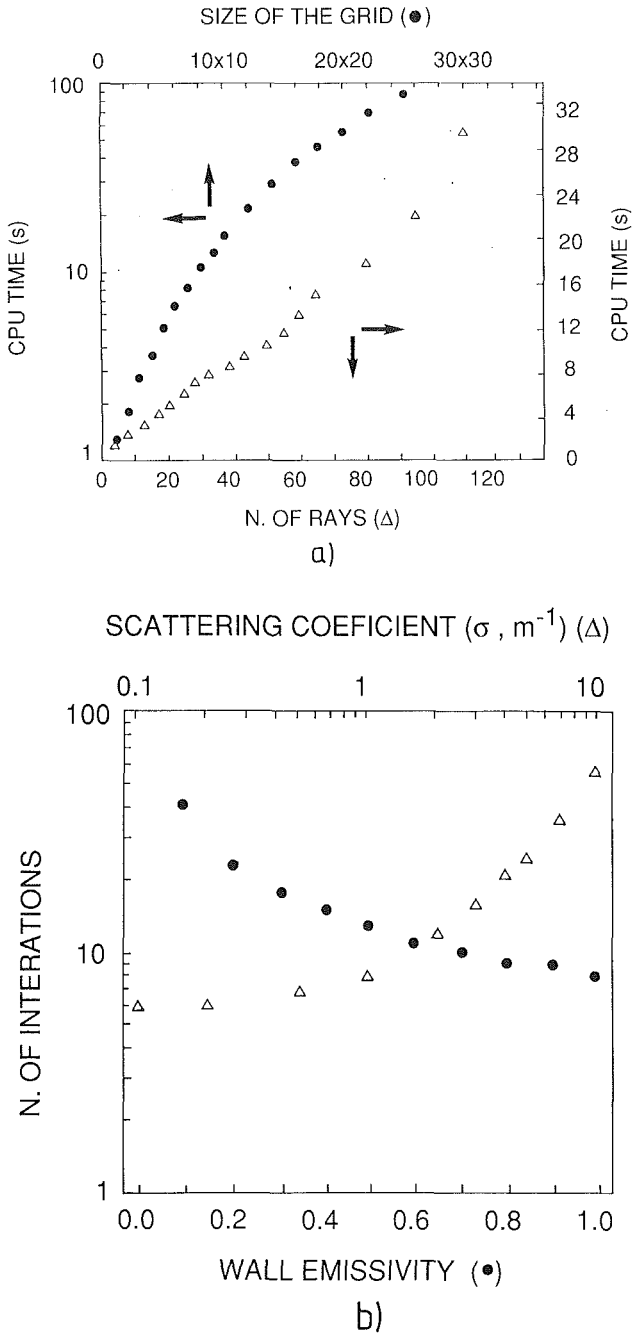

Fig. 4 Computational load: (*a*) CPU time required to achieve convergence for different computational grids and number of rays; (*b*) iterations required to achieve convergence for different wall emissivities and scattering coefficients

enclosures containing an absorbing-emitting and isotropic scattering medium.

The discrete transfer method has shown very good results when scattering was considered. However, the number of representative directions used had to be increased, when compared to normal situations where scattering is not considered. Only for very small aspect ratio (where the emitting wall is much smaller than the side walls) did the discrete transfer method present significant deviations. This behavior of the discrete transfer method results from the "ray effect." It was found that, for the studied cases, the best remedy to reduce the ray effect is to increase the number of rays that cross each cell. In order to avoid a prohibitive CPU time, an optimization of the number of the grid cells and rays should be sought.

Acknowledgments

The authors are thankful to Prof Raymond Viskanta from Purdue University and to Dr. Woodrow Fiveland from Babcock & Wilcox, Ohio, for their helpful suggestions and discussions. A scholarship from CIENCIA (JNICT—Junta Nacional de Investigação Científica e Tecnológica of Portugal) is acknowledged.

References

Carvalho, M. G., Durão, D. F. G., and Pereira, J. C. F., 1987, "Prediction of the Flow, Reaction and Heat Transfer in an Oxy-Fuel Glass Furnace," *International Journal of Engineering Computations*, Vol. 4, No. 1, pp. 23–34.

Carvalho, M. G., Oliveira, P., and Semião, V., 1988, "A Three-Dimensional Modelling of an Industrial Glass Furnace," *Journal of the Institute of Energy*, Vol. LXI, No. 448, pp. 143–156.

Carvalho, M. G., and Coelho, P. J., 1989, "Heat Transfer in Gas Turbine Combustors," *AIAA J. Thermophysics and Heat Transfer*, Vol. 3, No. 2, p. 123.

Fiveland, W. A., 1984, "Discrete-Ordinates Solutions of the Radiative Transport Equation for Rectangular Enclosures," ASME JOURNAL OF HEAT TRANSFER, Vol. 106, pp. 699–706.

Fiveland, W. A., and Wessel, R., 1986, "FURMO: A Numerical Model for Predicting Performance of Three-Dimensional Pulverized-Fuel Fired Furnaces," ASME Paper No. 86-HT-35.

Jamaluddin, A. S., and Smith, P. J., 1988, "Predicting Radiative Transfer in Rectangular Enclosures Using the Discrete Ordinates Method," *Combustion Science and Technology*, Vol. 59, pp. 321–340.

Larsen, M., 1981, "Hottel Zone Code," PhD Thesis, University of Texas Austin.

Lathrop, K. D., 1968, "Ray Effects in Discrete Ordinate Equations," *Nuclear Science and Engineering*, Vol. 32, pp. 357–369.

Lathrop, K. D., 1971, "Remedies for Ray Effects," *Nuclear Science and Engineering*, Vol. 45, pp. 235–268.

Lockwood, F. C., and Shah, N. G., 1981, "A New Radiation Solution Method for Incorporation in General Combustion Prediction Procedures," *18th Symposium (Int.) on Combustion*, pp. 1405–1414.

Mengüç, M. P., and Viskanta, R., 1985, "Radiative Transfer in Three-Dimensional Rectangular Enclosures Containing Inhomogeneous Anisotropically Scattering Media," *J. Quant. Spect. Radiat. Transfer*, Vol. 33, p. 533.

Modest, M., 1975, "Radiative Equilibrium in a Rectangular Enclosure Bounded by Gray Walls," *J. Quant. Spectrosc. Radiat. Transfer*, Vol. 15, No. 6, pp. 445–461.

Ratzel, A. C., III, and Howell, J. R., 1983, "Two-Dimensional Radiation in Absorbing-Emitting Media Using the P-N Approximation," ASME JOURNAL OF HEAT TRANSFER, Vol. 105, pp. 333–340.

Shah, N. G., 1979, "A New Method of Computation of Radiant Heat Transfer in Combustion Chambers," PhD Thesis, Imperial College, London.

Truelove, J. S., 1987, "Discrete-Ordinate Solutions of the Radiation Transport Equation," ASME JOURNAL OF HEAT TRANSFER, Vol. 109, pp. 1048–1051.

Viskanta, R., and Mengüç, M. P., 1987, "Radiation Heat Transfer in Combustion Systems," *Progress in Energy Combustion Science*, Vol. 13, pp. 97–160.

Suitable Configuration Factors for Radiation Calculation Concerning Tilted Flames

A. Guelzim,[1,4] J. M. Souil,[2,4] and J. P. Vantelon[3,4]

Nomenclature

$a = H/R$

$b = X/R$

$A = (b^2-1)(b^2-\sin^2\theta)+b^4\sin^2\theta\tan^2\alpha$

[1]Graduate Student.

[2]Research Assistant.

[3]Directeur de Recherche au CNRS.

[4]Laboratoire de Chimie Physique de la Combustion, UA 872 CNRS, University of Poitiers, Domaine du Deffend, 86550 Mignaloux-Beauvoir, France.

Contributed by the Heat Transfer Division of THE AMERICAN SOCIETY OF MECHANICAL ENGINEERS. Manuscript received by the Heat Transfer Division January 1992; revision received December 1992. Keywords: Environmental Heat Transfer, Fire/Flames, Radiation Interactions. Associate Technical Editor: R. O. Buckius.

$$B = 2b^2(b^2-1)^{1/2}\sin\theta\cos\theta\tan\alpha$$
$$C = (b+1)^2 + b^2\tan^2\alpha$$
$$D = (b-1)^2 + b^2\tan^2\alpha$$
$$E = a^2 - 2a(b+1)\sin\theta - 2ab\cos\theta\tan\alpha$$
$$F = \left[1 + (b^2-1)\cos^2\theta + \frac{b^4\sin^2\theta\tan^2\alpha}{b^2-1} - 2b^2\sin\theta\cos\theta\tan\alpha\right]^{1/2}$$
$$G = a^2 + b^2 + b^2\tan^2\alpha - 2ab\cos\theta\tan\alpha$$
$$I = \frac{a\cos\theta - b\tan\alpha}{b - a\sin\theta}$$
$$J = a^2 + b^2 + b^2\tan^2\alpha - 2ab\tan\alpha$$
$$K = \frac{2a(b^2-1)^{1/2}}{b}\sin\theta$$
$$L = \sin\theta(b^2-1)^{1/2}$$
$$M = \cos\theta(b^2-1)^{1/2}$$
$$N = \frac{b^2\tan\alpha - ab\cos\theta}{b^2 + a^2\sin\theta}$$
$$P = b^2 + a^2\sin^2\theta$$
$$Q = b^2\cos\theta\tan\alpha$$
$$W = \left(\frac{b-1}{b+1}\right)^{1/2}$$

Introduction

Among the buoyant diffusion flames arising from circular burning pools, the ones deflected by wind are of considerable practical interest. A simple approach widely used to evaluate the thermal radiation field is the solid flame model, which assumes that the flame radiates uniformly from its visible envelope. Hence, computation of view factors related to inclined cylinder or disk geometries is implied.

In this paper, closed-form expressions of view factors, evaluated using an integration technique, are presented for exchanges between plane differential element and tilted cylindrical source, the element being positioned downwind, upwind, or crosswind and its normal being parallel or perpendicular to the base of the cylinder.

1 Calculation Procedure. The derivation of view factors between a differential element and a finite area requires integration of the classical expression:

$$F_{dS_1-S_2} = \frac{1}{\pi}\int\int_{S_2}\frac{\cos\beta_1\cos\beta_2}{r^2}\,dS_2$$

where r is the distance between differential element dS_1 and the finite area S_2 and β_1 and β_1 are the angles formed by normals to these surfaces with the line connecting them.

The integration over those parts of S_2 that are visible to dS_2 is more often complex, and mathematical techniques of evaluation are useful when straightforward analytical integration methods appear to be a tedious algebraic exercise. Different valuable techniques are described in most heat transfer textbooks. One practical tool is the application of Stokes' theorem for reduction of multiple integration over a surface to a single integration around the boundary of the area. The so-called contour integration approach, detailed by De Bastos (1961) and Sparrow (1963), is employed here. Note that this already old technique is used to obtain the view factors under consideration in a closed-form expression, but that the integration can be also done using different existing softwares.

2 View-Factors Under Consideration. The geometry of the tilted cylinder with the definition of the receiving elements is shown in Fig. 1. Insofar as most of the expressions obtained are very long, they are reduced by setting a long repeated term equal to defined constants repacked in the Nomenclature.

• *Case 1.* Plane vertical element arbitrarily placed with respect to the base of a cylinder tilted toward or upward of the element.

The view-factor is given by:

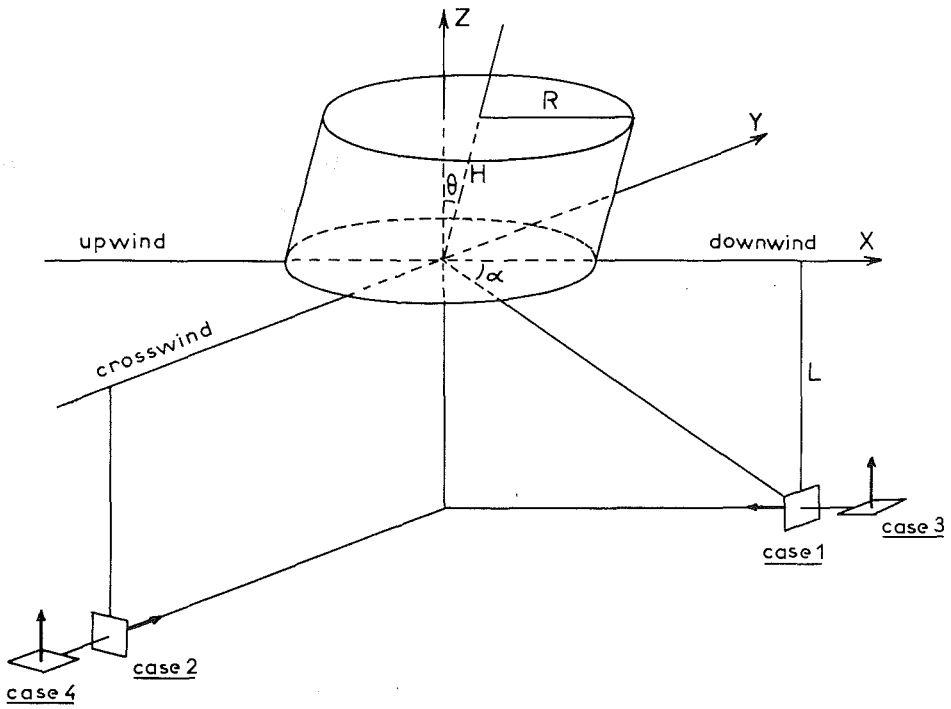

Fig. 1 Coordinate system for an inclined cylinder geometry

$$\pi F_v = -I\tan^{-1}W + I\frac{(E+C)+2(a\sin\theta-b)}{(E+C)^{1/2}(E+D)^{1/2}}\tan^{-1}\left[W\frac{(E+C)^{1/2}}{(E+D)^{1/2}}\right] + \frac{\cos\theta}{F}\left[\tan^{-1}\left(\frac{ab-((b^2-1)\sin\theta+Q)}{F(b^2-1)^{1/2}}\right) + \tan^{-1}\left(\frac{(b^2-1)\sin\theta+Q}{F(b^2-1)^{1/2}}\right)\right] - \tan\alpha\tan^{-1}W + \tan\alpha\frac{C-2b}{(CD)^{1/2}}\tan^{-1}\left[W\left(\frac{C}{D}\right)^{1/2}\right] \quad (1)$$

Note that in this expression $\theta>0$ corresponds to a downwind observer's location and $\theta<0$ to an upwind observer's location. When the observer is above the base level, $\alpha>0$ and the downwind location implies $L\sin\theta<(X-R)\cos\theta$ as a limit of applicability; when the observer is under the base level, $\alpha<0$ and the upwind location implies the same limit.

To give some sources of comparison it is also noteworthy that:

- if $\alpha = 0$ and $\theta \neq 0$ (normal to element passes through center of the base of the cylinder) the expression reduces and agrees with the expression given by Rein et al. (1970) (downwind observer location) and Mudan (1987) (downwind and upwind locations).
- if $\alpha = 0$ and $\theta = 0$ (normal to element passes through center of the base of a right cylinder and is perpendicular to cylinder axis) the expression reduces and agrees with the expression reported in all catalogs of references for view-factors (e.g., Siegel and Howell, 1981).

- *Case 2.* Plane vertical element arbitrarily placed with respect to the base of a cylinder tilted parallely to element; normal to element is in a plane that intersects the plane of tilt through the center of the base.

The view factor is given by:

$$2\pi F_v = \frac{a}{2b}N\sin\theta\ln\left(\frac{G-K-1}{G+K-1}\right) + \frac{M-Q\tan\theta}{(A-B)^{1/2}}\left[\tan^{-1}\left(\frac{L+Q}{(A-B)^{1/2}}\right)+\tan^{1}\left(\frac{ab-(L+Q)}{(A-B)^{1/2}}\right)\right] + \frac{M+Q\tan\theta}{(A+B)^{1/2}}\left[\tan^{-1}\left(\frac{ab+(L-Q)}{(A+B)^{1/2}}\right)+\tan^{-1}\left(\frac{Q-L}{(A+B)^{1/2}}\right)\right] + 2N\tan W - N\frac{G+1}{((G+1)^2-4P)^{1/2}}\left[\tan^{-1}\frac{(G+1+2b)^2W-2a\sin\theta}{((G+1)^2-4P)^{1/2}} + \tan^{-1}\frac{(G+1+2b)^2W+2a\sin\theta}{((G+1)^2-4P)^{1/2}}\right] + 2\tan\alpha\tan^{-1}W + 2\tan\alpha\frac{C-2b}{(CD)^{1/2}}\tan^{-1}\left[W\left(\frac{C}{D}\right)^{1/2}\right] \quad (2)$$

with the previously used sign convection for angle α.

Setting $\alpha = 0$ and $\theta \neq 0$ (normal to the element passes through the center of the base) gives an expression consistent with the one proposed by Mudan (1987) and, as above, the particular cases corresponding to a right cylinder, $\theta = 0$, $\alpha \neq 0$, and $\theta = 0$, $\alpha = 0$, are easily deduced.

- *Case 3.* Plane horizontal element arbitrarily placed with respect to the base of a cylinder tilted toward or upward of the element.

Two configurations must be distinguished depending on how the observer views the cylinder: bottom view or upper view.

Consider the observer as a function of its location with respect to the base of the cylinder.

- If $\alpha > 0$ and $L \geq H\cos\theta$, the upper view factor is of course zero, while the bottom view factor is given by:

$$-\pi F_H = \frac{C-2(b+1)}{(CD)^{1/2}}\tan^{-1}\left[W\left(\frac{C}{D}\right)^{1/2}\right] + \frac{\sin\theta}{F}\left[\tan^{-1}\left(\frac{ab-(L+Q)}{F(b^2-1)^{1/2}}\right)+\tan^{-1}\left(\frac{L+Q}{F(b^2-1)^{1/2}}\right)\right] - \frac{G-1-2ab\sin\theta}{(E+C)^{1/2}(E+D+4a\sin\theta)^{1/2}}\tan^{-1}\times\left[\frac{W(E+C)^{1/2}}{(E+C)^{1/2}(E+D+4a\sin\theta)^{1/2}}\right] \quad (3)$$

A positive angle of tilt corresponds to the "downwind" observer location, implying the limit of validity $L\sin\theta<(X-R)\cos\theta$; a negative angle of tilt corresponds to the "upwind" observer location, without upper limit for L.

The particular case $\theta = 0$ corresponds to $L \geq H$ and is easily deduced:

$$\pi F_H = \frac{2(b+1)-C}{(CD)^{1/2}}\tan^{-1}\left(W\left(\frac{C}{D}\right)^{1/2}\right) + \frac{(J-1)}{(J+2b+1)^{1/2}(J-2b+1)^{1/2}}\tan^{-1}\left[W\frac{(J+2b+1)^{1/2}}{(J+2b-1)^{1/2}}\right] \quad (4)$$

- If $\alpha > 0$ and $0 < L < H\cos\theta$, the bottom view factor is given by the general expression (3) where it is necessary only to replace $a = H/R$ by $a = L/R\cos\theta$. There is no readily available expression for the upper view factor. However, expression (3) multiplied by -1 may be used, modifying the coordinate system or utilizing a shortcut method of configuration-factor algebra. In these two cases a positive angle of tilt always corresponds to the "downwind" observer location and a negative to the "upwind" observer location. If the angle of tilt is zero, the bottom and upper view factors are given by expression (4) in which a is respectively equal to L/R and $(H-L)/R$.

- At last, if $\alpha < 0$, namely $L < 0$, the bottom view factor is of course zero, while the upper view factor is given by the general expression (3) multiplied by -1. As in the preceding, the angle of tilt is positive for "downwind" observer location and negative for "upwind" observer location with the limit of validity $|L|\sin\theta < (X-R)\cos\theta$.

If the angle of tilt is zero, the upper view factor is given by expression (4) multiplied by -1. Moreover, for proof of correctness of the more general expression presented, it should be observed that the expression proposed by Mudan (1987) for horizontal upper view factors, the receiving element being in the same plane as the base of an inclined cylinder or of a right cylinder, is easily inferred from expression (3), making respectively $L=0$ (namely $\alpha=0$) or $L=0$ and $\theta=0$.

- *Case 4.* Plane horizontal element arbitrarily placed with respect to the base of a cylinder tilted in plane parallel to normal to element; normal to element is in a plane that intersects the plane of tilt through the center of the base.

Consider again the observer as a function of its location with respect to the base of the cylinder.

- If $\alpha > 0$ and $L \geq H\cos\theta$, the upper view factor is zero and the bottom view factor is given by:

$$2\pi F_H=\frac{L(b^2-1)^{1/2}}{(A-B)^{1/2}}\left[\tan^{-1}\frac{L+Q}{(A-B)^{1/2}}+\tan^{-1}\left(\frac{ab-(L+Q)}{(A-B)^{1/2}}\right)\right]-\frac{L(b^2-1)^{1/2}}{(A+B)^{1/2}}\left[\tan^{-1}\left(\frac{ab+(L-Q)}{(A+B)^{1/2}}\right)+\tan^{-1}\left(\frac{Q-L}{(A+B)^{1/2}}\right)\right]+\frac{4(b+1)-2C}{(CD)^{1/2}}\tan^{-1}\left(W\left(\frac{C}{D}\right)^{1/2}\right)+\frac{(G-1)}{((G+1)^2-4P)^{1/2}}\left[\tan^{-1}\left(\frac{(G+1+2b)W-2a\sin\theta}{((G+1)^2-4P)^{1/2}}\right)+\tan^{-1}\left(\frac{(G+1+2b)W+2a\sin\theta}{((G+1)^2-4P)^{1/2}}\right)\right] \quad (5)$$

In the particular case where $\theta = 0$ and $L \geq H$, this expression reduces to expression (4) given above.

- If $\alpha > 0$ and $0 < L < H\cos\theta$, the bottom view-factor is given by the general expression (5) with $a = L/R\cos\theta$ while the upper view-factor, not readily available, may be obtained by modifying the coordinate system or by utilizing a shortcut method of configuration factor algebra. If the angle of tilt is zero, the corresponding simplified bottom and upper view-factors are easily deduced, making respectively $a = L/R$ and $a = H - L/R$.
- At last, if $\alpha < 0$, the bottom view-factor is of course zero and the upper view factor is given by the general expression (5) multiplied by -1. By comparison, it should be observed, that $\alpha = 0$ in this general expression multiplied by -1 gives the horizontal upper view-factor for a receiving observer located in the same plane as the base of an inclined cylinder, an expression in agreement with the one proposed by Mudan (1987), and moreover $\theta = 0$ gives the horizontal upper view-factor for an observer located in the same plane as the base of a right cylinder.

Conclusion

Closed-form expressions of geometric view factors between a vertical or horizontal receiving element and an inclined cylinder are determined. They are obtained by means of the very convenient contour integration method. The complexity of the resulting expression illustrates well the difficulty encountered in accounting the geometric relations involved in how the implicated surfaces view each other. Some simplified cases (right configurations) for which similar expressions are published in the literature are accounted for to prove the correctness of the more general expressions presented. Moreover, it is advisable to point out that for all intermediate tilting of the receiving element between horizontal and vertical positions, and providing that the plane of the tilted element does not intersect the finite surface, the view-factor can be obtained by:

$$F_I=\frac{m}{2\pi}F_v+\frac{n}{2\pi}F_H$$

with an appropriate choice of the direction cosines m and n.

All these view-factors are very useful, particularly in the computation of radiative heat transfer from fires developed in the open.

References

De Bastos, R., 1961, "Computation of Radiation Configuration Factors by Contour Integration," M.S. thesis, Oklahoma State University, Stillwater, OK.

Mudan, K. S., 1987, "Geometric View Factors for Thermal Radiation Hazard Assessment," *Fire Safety Journal*, Vol. 12, pp. 89–96.

Rein, R. G., Sliepcevich, C. M., and Welker, J. R., 1970, "Radiation View-Factors for Tilted Cylinders," *J. Fire Flammability*, Vol. 1, pp. 140–153.

Siegel, R., and Howell, J. R., 1981, *Thermal Radiative Heat Transfer*, 2nd ed., Hemisphere Publishing Corp., Washington, DC.

Sparrow, E. M., 1963, "A New and Simpler Formulation for Radiative Angle Factors," ASME JOURNAL OF HEAT TRANSFER, Vol. 85, pp. 81–88.

Uniform Isotropic Emission From an Involute Reflector

S. Maruyama[1]

1 Introduction

Recently, radiation heat transfer control has received increasing attention as a factor in industrial processes. It is critical for precision temperature control during thermal annealing of silicon wafers for LSI with halogen flash lamps and materials processing in image furnaces (Aihara et al., 1989). For these purposes, a parabolic or ellipsoidal mirror is utilized for irradiating the energy from a xenon or halogen lamp. Those mirrors are effective for a small radiation source. However, when one of these reflectors is actually applied with an emitter of finite size, some rays are reflected back to the emitter, and the distribution of the emissive power at the aperture is not uniform.

Directional emittance from various surfaces depends not only on the surface material, but also on the shape of the surface. Perlmutter and Howell (1963) and Masuda (1980) showed that a specular V-groove with a flat black base becomes a highly directional emitter. The above-mentioned research works were concerned with collimation of isotropic thermal radiation emitted from an isotropic flat surface.

In the present work, the objective is to obtain the opposite radiation characteristics from a reflector. Namely, an involute reflector with a cylindrical emitter of finite radius is considered in order to provide a uniform and isotropic emission of radiation from the aperture of the involute reflector. Two-dimensional numerical analysis, taking into account the directional reflectivity of a mirror surface, is carried out for analyzing the radiation characteristics of the involute and circular arc reflectors. The directional emission characteristics of the involute reflector are demonstrated in comparison with those of the circular arc reflector.

2 Involute Reflector

The surface of an emitter such as a cylindrical radiator or a fluorescent lamp emits thermal radiation or light in all directions of a hemispherical solid angle. Reflectors that use a specular mirror of a circular arc or parabola reflect some of the radiation back to the emitter surface. Accordingly, the emission efficiency of the reflector decreases, and the distribution of the emissive power is not uniform at the aperture.

A reflector whose specular surface is composed of a involute of a cylinder is shown in Fig. 1. A circular arc reflector used for the calculation example is also shown in the figure. The coordinates of the involute are expressed by the following equation:

$$\left.\begin{aligned} x &= r(\phi\cos\phi-\sin\phi)\\ y &= -r(\phi\sin\phi+\cos\phi+1)\end{aligned}\right\}\ -\pi\leq\phi\leq\pi \quad (1)$$

Considering a point P on the cylindrical emitter and the intersection C of the tangent at P and the involute, the line PC is the normal of the involute at C. Considering one pencil

[1]Associate Professor, Institute of Fluid Science, Tohoku University, Aoba-ku, Katahira 2-1-1, Sendai 980, Japan; Mem. ASME.

Contributed by the Heat Transfer Division and presented in part at the ASME/JSME Thermal Engineering Joint Conference, Reno, Nevada, March 17–22, 1991. Manuscript received by the Heat Transfer Division July 1991; revision received March 1992. Keywords: Materials Processing and Manufacturing Processes, Radiation, Radiation Interactions. Associate Technical Editor: R. O. Buckius.

$$2\pi F_H=\frac{L(b^2-1)^{1/2}}{(A-B)^{1/2}}\left[\tan^{-1}\frac{L+Q}{(A-B)^{1/2}}+\tan^{-1}\left(\frac{ab-(L+Q)}{(A-B)^{1/2}}\right)\right]-\frac{L(b^2-1)^{1/2}}{(A+B)^{1/2}}\left[\tan^{-1}\left(\frac{ab+(L-Q)}{(A+B)^{1/2}}\right)+\tan^{-1}\left(\frac{Q-L}{(A+B)^{1/2}}\right)\right]+\frac{4(b+1)-2C}{(CD)^{1/2}}\tan^{-1}\left(W\left(\frac{C}{D}\right)^{1/2}\right)+\frac{(G-1)}{((G+1)^2-4P)^{1/2}}\left[\tan^{-1}\left(\frac{(G+1+2b)W-2a\sin\theta}{((G+1)^2-4P)^{1/2}}\right)+\tan^{-1}\left(\frac{(G+1+2b)W+2a\sin\theta}{((G+1)^2-4P)^{1/2}}\right)\right] \quad (5)$$

In the particular case where $\theta = 0$ and $L \geq H$, this expression reduces to expression (4) given above.

- If $\alpha > 0$ and $0 < L < H\cos\theta$, the bottom view-factor is given by the general expression (5) with $a = L/R\cos\theta$ while the upper view-factor, not readily available, may be obtained by modifying the coordinate system or by utilizing a shortcut method of configuration factor algebra. If the angle of tilt is zero, the corresponding simplified bottom and upper view-factors are easily deduced, making respectively $a = L/R$ and $a = H - L/R$.
- At last, if $\alpha < 0$, the bottom view-factor is of course zero and the upper view factor is given by the general expression (5) multiplied by -1. By comparison, it should be observed, that $\alpha = 0$ in this general expression multiplied by -1 gives the horizontal upper view-factor for a receiving observer located in the same plane as the base of an inclined cylinder, an expression in agreement with the one proposed by Mudan (1987), and moreover $\theta = 0$ gives the horizontal upper view-factor for an observer located in the same plane as the base of a right cylinder.

Conclusion

Closed-form expressions of geometric view factors between a vertical or horizontal receiving element and an inclined cylinder are determined. They are obtained by means of the very convenient contour integration method. The complexity of the resulting expression illustrates well the difficulty encountered in accounting the geometric relations involved in how the implicated surfaces view each other. Some simplified cases (right configurations) for which similar expressions are published in the literature are accounted for to prove the correctness of the more general expressions presented. Moreover, it is advisable to point out that for all intermediate tilting of the receiving element between horizontal and vertical positions, and providing that the plane of the tilted element does not intersect the finite surface, the view-factor can be obtained by:

$$F_I = \frac{m}{2\pi} F_v + \frac{n}{2\pi} F_H$$

with an appropriate choice of the direction cosines m and n.

All these view-factors are very useful, particularly in the computation of radiative heat transfer from fires developed in the open.

References

De Bastos, R., 1961, "Computation of Radiation Configuration Factors by Contour Integration," M.S. thesis, Oklahoma State University, Stillwater, OK.

Mudan, K. S., 1987, "Geometric View Factors for Thermal Radiation Hazard Assessment," *Fire Safety Journal*, Vol. 12, pp. 89–96.

Rein, R. G., Sliepcevich, C. M., and Welker, J. R., 1970, "Radiation View-Factors for Tilted Cylinders," *J. Fire Flammability*, Vol. 1, pp. 140–153.

Siegel, R., and Howell, J. R., 1981, *Thermal Radiative Heat Transfer*, 2nd ed., Hemisphere Publishing Corp., Washington, DC.

Sparrow, E. M., 1963, "A New and Simpler Formulation for Radiative Angle Factors," ASME JOURNAL OF HEAT TRANSFER, Vol. 85, pp. 81–88.

Uniform Isotropic Emission From an Involute Reflector

S. Maruyama[1]

1 Introduction

Recently, radiation heat transfer control has received increasing attention as a factor in industrial processes. It is critical for precision temperature control during thermal annealing of silicon wafers for LSI with halogen flash lamps and materials processing in image furnaces (Aihara et al., 1989). For these purposes, a parabolic or ellipsoidal mirror is utilized for irradiating the energy from a xenon or halogen lamp. Those mirrors are effective for a small radiation source. However, when one of these reflectors is actually applied with an emitter of finite size, some rays are reflected back to the emitter, and the distribution of the emissive power at the aperture is not uniform.

Directional emittance from various surfaces depends not only on the surface material, but also on the shape of the surface. Perlmutter and Howell (1963) and Masuda (1980) showed that a specular V-groove with a flat black base becomes a highly directional emitter. The above-mentioned research works were concerned with collimation of isotropic thermal radiation emitted from an isotropic flat surface.

In the present work, the objective is to obtain the opposite radiation characteristics from a reflector. Namely, an involute reflector with a cylindrical emitter of finite radius is considered in order to provide a uniform and isotropic emission of radiation from the aperture of the involute reflector. Two-dimensional numerical analysis, taking into account the directional reflectivity of a mirror surface, is carried out for analyzing the radiation characteristics of the involute and circular arc reflectors. The directional emission characteristics of the involute reflector are demonstrated in comparison with those of the circular arc reflector.

2 Involute Reflector

The surface of an emitter such as a cylindrical radiator or a fluorescent lamp emits thermal radiation or light in all directions of a hemispherical solid angle. Reflectors that use a specular mirror of a circular arc or parabola reflect some of the radiation back to the emitter surface. Accordingly, the emission efficiency of the reflector decreases, and the distribution of the emissive power is not uniform at the aperture.

A reflector whose specular surface is composed of a involute of a cylinder is shown in Fig. 1. A circular arc reflector used for the calculation example is also shown in the figure. The coordinates of the involute are expressed by the following equation:

$$\left.\begin{aligned} x &= r(\phi\cos\phi - \sin\phi) \\ y &= -r(\phi\sin\phi + \cos\phi + 1) \end{aligned}\right\} -\pi \leq \phi \leq \pi \quad (1)$$

Considering a point P on the cylindrical emitter and the intersection C of the tangent at P and the involute, the line PC is the normal of the involute at C. Considering one pencil

[1]Associate Professor, Institute of Fluid Science, Tohoku University, Aoba-ku, Katahira 2-1-1, Sendai 980, Japan; Mem. ASME.

Contributed by the Heat Transfer Division and presented in part at the ASME/JSME Thermal Engineering Joint Conference, Reno, Nevada, March 17–22, 1991. Manuscript received by the Heat Transfer Division July 1991; revision received March 1992. Keywords: Materials Processing and Manufacturing Processes, Radiation, Radiation Interactions. Associate Technical Editor: R. O. Buckius.

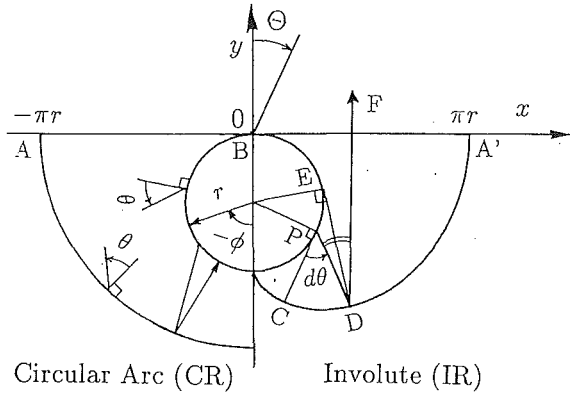

Fig. 1 Cross section of an involute reflector (IR) and a circular arc reflector (CR)

of radiation rays emitted from P to D, the reflected ray DF is not absorbed by the emitting cylinder because DE is the normal of the involute at D. The above argument is valid for all rays emitted in a hemispherical direction from the cylindrical emitter. That is, every ray emitted from the cylinder is emitted from the aperture AB without being absorbed by the cylinder.

The above discussion has not yet proved that uniform and isotropic emission is obtained at the aperture of the involute reflector. In the following section, a ray tracing scheme for analyzing the directional emission characteristics of various reflectors taking into account the directional reflectivity of the mirror surface is presented.

3 Numerical Analysis

Extensive research work has been done on radiative exchange between solid surfaces. Among these proposed methods, a few numerical methods, such as the authors' (Maruyama and Aihara, 1987) and the Monte Carlo method (for example, Siegel and Howell, 1981) can be applied to arbitrary configurations.

Recent progress in computer graphics has brought rapid improvement in the ray tracing method for visualizing calculated data. In the ray tracing method, each ray carries information about the intensity, which changes in accordance with the characteristics of the hit points. On the other hand, the Monte Carlo method assumes that a number of rays are emitted in the same direction because each bundle of rays has a discrete intensity of one or zero, and absorption or reflection is decided statistically. Hayasaka et al. (1986) demonstrated that use of the ray tracing method can result in a substantial saving in calculation time compared with the Monte Carlo method.

In the present numerical analysis, the ray tracing method is adopted for analyzing directional emission characteristics of various reflectors. The details of the numerical method were discussed in the author's previous study (Maruyama, 1991).

No real surface is perfectly diffuse or specular. For simplicity, light of wavelength λ whose incident angle is θ' is assumed to be subjected to specular reflection according to Fresnel's law. The directional spectral reflectivity $\rho(\theta', \lambda)$ of the material is obtained from the complex refractive index $\hat{n} = n - ik$, and n and k are expressed by functions of the wavelength λ (for example, Siegel and Howell, 1981).

Two kinds of specular surfaces are considered for numerical calculation. One is an aluminum surface (Al), for visible light of wavelength $\lambda = 0.5$ μm. The other is a nickel surface (Ni) for radiation from a gray emitter at temperature $T = 1000$ K. The values of the complex refractive indices of Al were quoted from values recommended by Smith et al. (1985), and the values of the Ni surface were quoted from the data by Lynch and Hunter (1985) for the range of $0.2 \leq \lambda \leq 12$ μm. The directional reflectivities of these surfaces are available elsewhere (Maruyama, 1991).

4 Experimental Instrumentation

Experiments were performed to verify the theoretically obtained directional emission characteristics. Two kinds of reflector were made. One was an involute reflector and the other was a circular arc reflector as shown in Fig. 1. Each reflector was made of acrylic resin for a cylindrical emitter 23.8 mm in diameter. The aperture of the reflectors was 74.8 mm, and the length was 300 mm. Aluminum was plated on the surfaces of the mirrors by vacuum deposition.

A fluorescent lamp was used for a cylindrical emitter. The reflectivity of the lamp surface for visible light was measured by a chromatic analyzer (Minolta CR300), and the reflectivity ρ_0 was 0.62 with an accuracy of 3 percent.

The directional radiant intensity at the aperture of a reflector emitted by a fluorescent lamp was measured by a luminance meter (Minolta nt-1°P) with a closeup lens. The measuring circle was 3.5 mm in diameter. The accuracy of the luminance meter was 4 percent for uniform emission, and the accuracy became worse if there was abrupt change in local luminance in the measuring circle.

The luminance meter was pointed at the center (z direction) of the reflector, in the direction normal to the aperture of the reflector. The error due to the finite aspect ratio of the reflector and emitter was negligible when the measurement was taken at the center of the reflector. Then the reflector was moved in the x direction by an automatic traverse stage whose position accuracy was 0.02 mm. During the experiment, the local luminance at the emitter surface in the normal direction was 11,000 cd/m^2.

5 Results and Discussion

5.1 Reflectors With Perfect Reflection. Before proceeding with the case of metallic surfaces whose directional reflectivities are taken into account, a perfect reflector surface of $\rho(\theta) = 1$ independent of incident angle and an emitter with unit absorptivity and emissivity ($\rho_0 = 0$) is considered for the purpose of simplifying the problem.

In order to estimate directional emission characteristics, the dimensionless directional radiant intensity $i^*(\Theta)$ normalized to the intensity on the emitter surface, i_0, is introduced. For the case of a blackbody emitter as shown in the present section, the value coincides with the local directional emissivity. For the case of visible light or in optics, the value of $i(\Theta)$ corresponds to the distribution of local luminance at the aperture seen from angle Θ.

The distribution of local directional radiant intensity of IR is expressed by the three-dimensional plots of location $x/\pi r$ and direction angle Θ in Fig. 2. The local directional radiant intensity for the negative Θ is expressed by the distribution for negative $x/\pi r$. The involute has a uniform isotropic radiant intensity at the aperture.

For the case of a perfect mirror, the present involute reflector has uniform emissive power, and shows isotropic emission at the aperture. It should be noted that the characteristic is independent of the emissivity at the emitter surface because the ray emitted from the surface does not hit the surface again.

5.2 Reflectors With Metallic Surfaces. The distributions of local hemispherical emissive power e_a at the apertures of

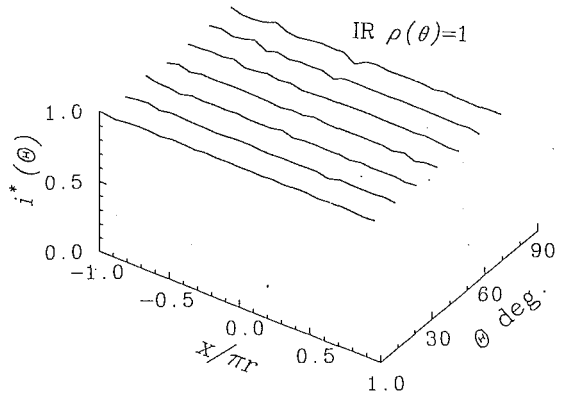

Fig. 2 Directional radiant intensity of an involute reflector with perfect mirror and black-body emitter

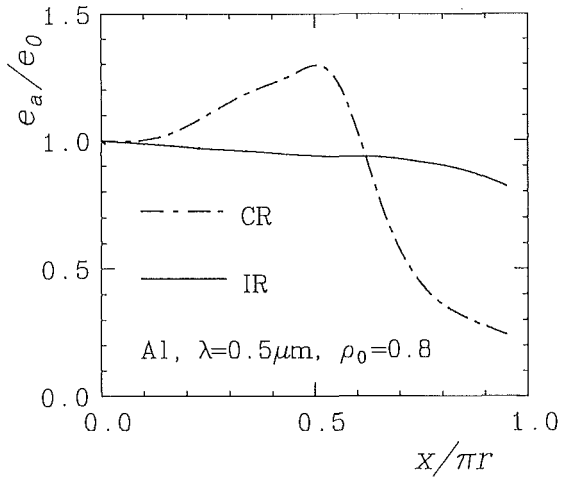

Fig. 3 Distributions of hemispherical emissive power of involute and circular arc reflectors with an aluminum surface and emitter reflectivity 0.8

IR and CR reflectors are plotted in Fig. 3. In the figure, e_a was normalized to the emissive power e_0 at the surface of the emitter. The reflector surface is aluminum for visible light (λ = 0.5 μm), and the emitter reflectivity ρ_0 = 0.8.

A large variation in the emissive power is observed for CR; in particular, e_a/e_0 shows a maximum value of 1.3. However, the distribution for the IR is very uniform compared with those for CR. The emissive power of IR for the Al surface is lower than that for a perfect mirror, particularly in the region near the aperture edge. However, the values are much closer to the ideal one for a perfect mirror than the values found for CR as shown in Fig. 3.

Calculation was conducted for the Ni surface for thermal radiation T = 1000 K. The Ni surface for thermal radiation shows a slightly smaller value of emissive power in the vicinity of the edge; however, this difference is very small.

When silicon wafers are placed near the aperture of the involute reflector, a uniform heating condition can be obtained for the entire area of the aperture. However, the circular arc reflector has a significant variation in the distribution of emissive power, and this variation may cause serious defect on the silicon wafers when the reflector is used for the annealing process.

The distributions of directional radiant intensity for a circular arc reflector with an Al surface are plotted in Fig. 4. The emitter reflectivity ρ_0 = 0.62 was chosen considering the measured value of the fluorescent lamp used in the experiment. There are peaks of i^* near $x = \pm \pi r/2$ and for small Θ, and

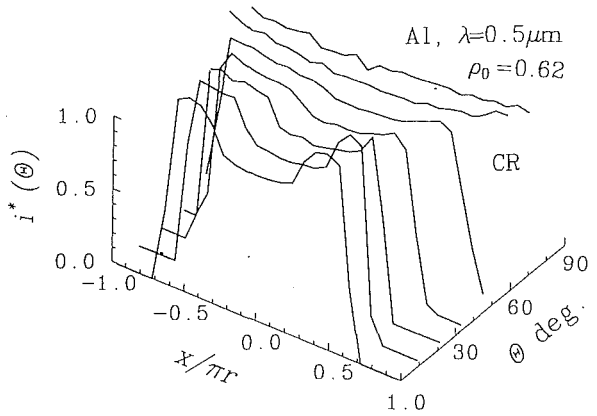

Fig. 4 Directional radiant intensity of an involute reflector with an aluminum surface

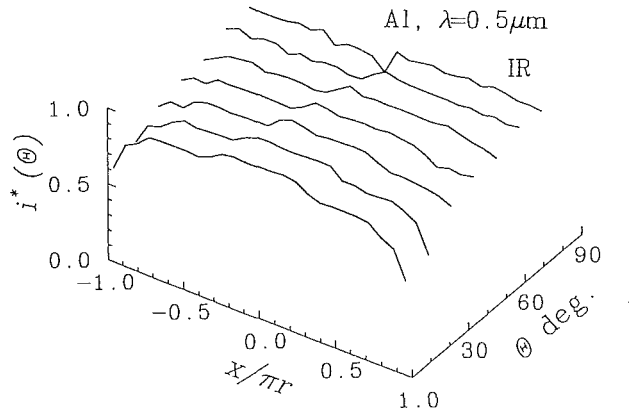

Fig. 5 Directional radiant intensity of a circular arc reflector with an aluminum surface and emitter reflectivity 0.62

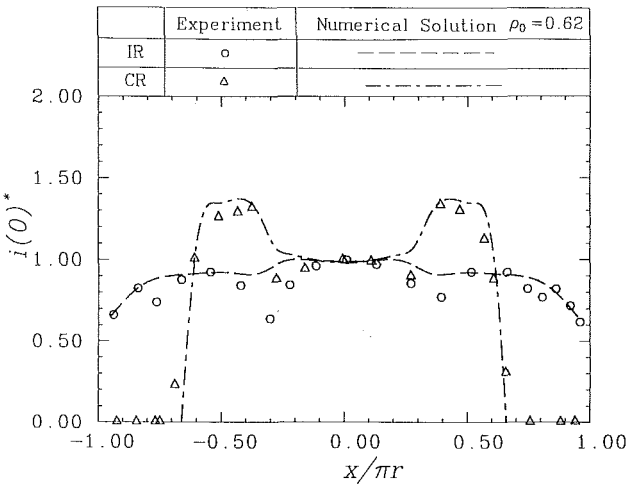

Fig. 6 Comparison between experimental data and theoretical results of directional radiant intensity normal to the aperture (Θ = 0)

the values are larger than 1. These peaks are due to the fact that some reflected rays strike the emitter surface, and the diffusely reflected rays increase the emissive power at the points, and the radiant intensity at the aperture is larger than that on the emitter surface. Consequently, the variation in the directional radiant intensity for $\rho_0 \rightarrow 1$ becomes larger than that

for the case of $\rho_0 = 0$. The rays striking the emitter surface may cause the temperature increase, and may damage the heater surface. The heater is not damaged for the involute reflector because the emitted rays are not absorbed by the emitter.

Figure 5 is the three-dimensional plot of dimensionless directional radiant intensity $i^*(\Theta)$ of the involute reflector with an Al surface for visible light. The decrease in i^* near the edges is larger for small Θ rather than for large Θ; however, the decrease in i^* is remarkably small compared with the decreases seen in CR, as shown in Fig. 5.

5.3 Comparison With Experimental Data. Figure 6 shows the comparison of theoretical and experimental results of directional radiant intensity $i(\Theta)$ normal to the aperture surfaces ($\Theta = 0$) normalized by the value of emitter surface i_0.

The experimental data for involute and circular arc reflectors show relatively good accordance. Especially the values in the vicinity of the aperture edges of IR agreed; nevertheless, the directional reflectivity of the aluminum was derived from the theoretical value for $\lambda = 0.5$ μm.

In the experimental data, there are several parts that are smaller than the theoretical prediction. This is due to the fact that the directional radiant intensity on the surface of the fluorescent lamp is not ideally uniform, but is of a smaller value at large emission angle θ; hence, the effect results in a lower value of experimental data than the prediction. For practical application of the involute reflector, some deformation of the involute may be needed for improving the effect of unisotropic emission characteristics of the emitter surface.

Acknowledgments

The author wishes to express his gratitude to Mr. S. Hayasaka of Institute of Fluid Science, Tohoku University, and KEIKO Corp. for their assistance in the experiments.

References

Aihara, T., Maruyama, S., Oishi, N., and Kohguchi, H., 1989, "Design and Performance of a Compact, Xenon Arc-Image Furnace Producing a High Heat-Flux of 2–10 MW/m^2," *The Memoirs of the Institute of High Speed Mechanics*, Tohoku University, Vol. 61, No. 191, pp. 81–101.

Hayasaka, H., Kudo, K., Taniguchi, H., Nakamachi, I., Omori, T., and Katayama, T., 1986, "Radiative Heat Transfer Analysis by the Radiation Heat Ray Method (Analysis in a Two-Dimensional Model)," *Transactions of the Japan Society of Mechanical Engineers*, Vol. 52, No. 476B, pp. 1734–1740.

Lynch, D. W., and Hunter, W. R., 1985, "Comments on the Optical Constants of Metals and an Introduction to the Data for Several Metals," in: *Handbook of Optical Constants of Solids*, E. D. Palik, ed., Academic Press, Orlando, FL, pp. 313–323.

Maruyama, S., and Aihara, T., 1987, "Numerical Analysis of Radiative Heat Transfer From Three Dimensional Bodies of Arbitrary Configurations," *JSME International Journal*, Vol. 30, No. 270, pp. 1982–1987.

Maruyama, S., 1991, "Uniform Isotropic Emission From an Aperture of a Reflector," *Proc. ASME/JSME Thermal Engineering Joint Conference*, Vol. 4, pp. 47–53.

Masuda, H., 1980, "Directional Control of Radiation Heat Transfer by V-Groove Cavities—Collimation of Energy in Direction Normal to Cavity Opening," ASME JOURNAL OF HEAT TRANSFER, Vol. 102, pp. 563–567.

Perlmutter, M., and Howell, J. R., 1963, "A Strongly Directional Emitting and Absorbing Surface," ASME JOURNAL OF HEAT TRANSFER, Vol. 85, pp. 282–283.

Siegel, R., and Howell, J. R., 1981, *Thermal Radiation Heat Transfer*, 2nd ed., Hemisphere, New York.

Smith, D. Y., Shiles, E., and Inokuti, M., 1985, "The Optical Properties of Metallic Aluminum," in: *Handbook of Optical Constants of Solids*, E. D. Palik, ed., Academic Press, Orlando, FL, pp. 369–408.

Dielectrophoresis-Driven Nucleate Boiling in a Simulated Microgravity Environment

D. M. Pachosa[1] and J. N. Chung[2]

Introduction

One of the main problems associated with the microgravity boiling process is finding an effective method of removing the vapor bubbles from the heater surface in order to initiate and sustain nucleate boiling. When vapor is allowed to accumulate on the surface, film boiling results, and this is a much less efficient mode of heat transfer. On earth, the problem is simply solved by the action of a buoyancy force due to a pressure gradient and density difference between the vapor and liquid phases. Since gravity is nonexistent in space, however, other forces must be provided to remove the vapor from the heater surface.

This paper examines the effect of a nonuniform electric field on the heat transfer characteristics of boiling induced from a small nichrome wire immersed in a dielectric fluid. This nonuniform field, which creates a dielectric force on the generated vapor bubbles, was studied to determine its feasibility for use as the bubble removal mechanism in a microgravity environment. Bubble size, heating rates, and boiling classifications were also studied with the aid of high-speed photography using Freon-113 and FC-72 as the working fluids.

Experiment

Using the information provided from a feasibility study (Pachosa, 1990), the apparatus for the microgravity boiling simulator was designed and built as shown also by Pachosa (1990). Since the electric field required is relatively high, Freon-113 and FC-72 were chosen as the working fluids because of their strong insulating capability and appropriate heat transfer properties.

In the preliminary experiment, the DEP force showed great promise as a mechanism for bubble detachment and downward acceleration; however, a slight problem was encountered. After the bubble reached its equilibrium position, it would remain stationary. This would allow newly generated bubbles to combine with the first bubble, creating a vapor film between the electrodes—definitely an unwanted occurrence for a nucleate boiling study. Therefore, it was necessary to find a way of removing the bubbles generated before a film could develop. The solution was found by allowing the plates to diverge not only in the vertical direction, but also in the lateral direction. This electrode arrangement creates a DEP force in both the vertical and lateral directions. Once a bubble enters the electric field, the DEP force acts to move the bubble downward and also horizontally. The path of the bubbles was now a parabolic trajectory due to the fact that the vertical DEP force weakens as the bubble travels laterally.

Using this new electrode arrangement, the heater wire was

[1]Graduate student, Department of Mechanical and Materials Engineering, Washington State University, Pullman, WA 99164-2920.

[2]Professor, Department of Mechanical and Materials Engineering, Washington State University, Pullman, WA 96164-2920; Mem. ASME.

Contributed by the Heat Transfer Division of THE AMERICAN SOCIETY OF MECHANICAL ENGINEERS. Manuscript received by the Heat Transfer Division April 1991; revision received August 1992. Keywords: Boiling, Microgravity Heat Transfer, Phase-Change Phenomena. Associate Technical Editor: L. C. Witte.

for the case of $\rho_0 = 0$. The rays striking the emitter surface may cause the temperature increase, and may damage the heater surface. The heater is not damaged for the involute reflector because the emitted rays are not absorbed by the emitter.

Figure 5 is the three-dimensional plot of dimensionless directional radiant intensity $i^*(\Theta)$ of the involute reflector with an Al surface for visible light. The decrease in i^* near the edges is larger for small Θ rather than for large Θ; however, the decrease in i^* is remarkably small compared with the decreases seen in CR, as shown in Fig. 5.

5.3 Comparison With Experimental Data. Figure 6 shows the comparison of theoretical and experimental results of directional radiant intensity $i(\Theta)$ normal to the aperture surfaces ($\Theta = 0$) normalized by the value of emitter surface i_0.

The experimental data for involute and circular arc reflectors show relatively good accordance. Especially the values in the vicinity of the aperture edges of IR agreed; nevertheless, the directional reflectivity of the aluminum was derived from the theoretical value for $\lambda = 0.5$ μm.

In the experimental data, there are several parts that are smaller than the theoretical prediction. This is due to the fact that the directional radiant intensity on the surface of the fluorescent lamp is not ideally uniform, but is of a smaller value at large emission angle θ; hence, the effect results in a lower value of experimental data than the prediction. For practical application of the involute reflector, some deformation of the involute may be needed for improving the effect of unisotropic emission characteristics of the emitter surface.

Acknowledgments

The author wishes to express his gratitude to Mr. S. Hayasaka of Institute of Fluid Science, Tohoku University, and KEIKO Corp. for their assistance in the experiments.

References

Aihara, T., Maruyama, S., Oishi, N., and Kohguchi, H., 1989, "Design and Performance of a Compact, Xenon Arc-Image Furnace Producing a High Heat-Flux of 2–10 MW/m^2," *The Memoirs of the Institute of High Speed Mechanics*, Tohoku University, Vol. 61, No. 191, pp. 81–101.

Hayasaka, H., Kudo, K., Taniguchi, H., Nakamachi, I., Omori, T., and Katayama, T., 1986, "Radiative Heat Transfer Analysis by the Radiation Heat Ray Method (Analysis in a Two-Dimensional Model)," *Transactions of the Japan Society of Mechanical Engineers*, Vol. 52, No. 476B, pp. 1734–1740.

Lynch, D. W., and Hunter, W. R., 1985, "Comments on the Optical Constants of Metals and an Introduction to the Data for Several Metals," in: *Handbook of Optical Constants of Solids*, E. D. Palik, ed., Academic Press, Orlando, FL, pp. 313–323.

Maruyama, S., and Aihara, T., 1987, "Numerical Analysis of Radiative Heat Transfer From Three Dimensional Bodies of Arbitrary Configurations," *JSME International Journal*, Vol. 30, No. 270, pp. 1982–1987.

Maruyama, S., 1991, "Uniform Isotropic Emission From an Aperture of a Reflector," *Proc. ASME/JSME Thermal Engineering Joint Conference*, Vol. 4, pp. 47–53.

Masuda, H., 1980, "Directional Control of Radiation Heat Transfer by V-Groove Cavities—Collimation of Energy in Direction Normal to Cavity Opening," ASME JOURNAL OF HEAT TRANSFER, Vol. 102, pp. 563–567.

Perlmutter, M., and Howell, J. R., 1963, "A Strongly Directional Emitting and Absorbing Surface," ASME JOURNAL OF HEAT TRANSFER, Vol. 85, pp. 282–283.

Siegel, R., and Howell, J. R., 1981, *Thermal Radiation Heat Transfer*, 2nd ed., Hemisphere, New York.

Smith, D. Y., Shiles, E., and Inokuti, M., 1985, "The Optical Properties of Metallic Aluminum," in: *Handbook of Optical Constants of Solids*, E. D. Palik, ed., Academic Press, Orlando, FL, pp. 369–408.

Dielectrophoresis-Driven Nucleate Boiling in a Simulated Microgravity Environment

D. M. Pachosa[1] and J. N. Chung[2]

Introduction

One of the main problems associated with the microgravity boiling process is finding an effective method of removing the vapor bubbles from the heater surface in order to initiate and sustain nucleate boiling. When vapor is allowed to accumulate on the surface, film boiling results, and this is a much less efficient mode of heat transfer. On earth, the problem is simply solved by the action of a buoyancy force due to a pressure gradient and density difference between the vapor and liquid phases. Since gravity is nonexistent in space, however, other forces must be provided to remove the vapor from the heater surface.

This paper examines the effect of a nonuniform electric field on the heat transfer characteristics of boiling induced from a small nichrome wire immersed in a dielectric fluid. This nonuniform field, which creates a dielectric force on the generated vapor bubbles, was studied to determine its feasibility for use as the bubble removal mechanism in a microgravity environment. Bubble size, heating rates, and boiling classifications were also studied with the aid of high-speed photography using Freon-113 and FC-72 as the working fluids.

Experiment

Using the information provided from a feasibility study (Pachosa, 1990), the apparatus for the microgravity boiling simulator was designed and built as shown also by Pachosa (1990). Since the electric field required is relatively high, Freon-113 and FC-72 were chosen as the working fluids because of their strong insulating capability and appropriate heat transfer properties.

In the preliminary experiment, the DEP force showed great promise as a mechanism for bubble detachment and downward acceleration; however, a slight problem was encountered. After the bubble reached its equilibrium position, it would remain stationary. This would allow newly generated bubbles to combine with the first bubble, creating a vapor film between the electrodes—definitely an unwanted occurrence for a nucleate boiling study. Therefore, it was necessary to find a way of removing the bubbles generated before a film could develop. The solution was found by allowing the plates to diverge not only in the vertical direction, but also in the lateral direction. This electrode arrangement creates a DEP force in both the vertical and lateral directions. Once a bubble enters the electric field, the DEP force acts to move the bubble downward and also horizontally. The path of the bubbles was now a parabolic trajectory due to the fact that the vertical DEP force weakens as the bubble travels laterally.

Using this new electrode arrangement, the heater wire was

[1]Graduate student, Department of Mechanical and Materials Engineering, Washington State University, Pullman, WA 99164-2920.

[2]Professor, Department of Mechanical and Materials Engineering, Washington State University, Pullman, WA 96164-2920; Mem. ASME.

Contributed by the Heat Transfer Division of THE AMERICAN SOCIETY OF MECHANICAL ENGINEERS. Manuscript received by the Heat Transfer Division April 1991; revision received August 1992. Keywords: Boiling, Microgravity Heat Transfer, Phase-Change Phenomena. Associate Technical Editor: L. C. Witte.

inserted between the electrodes and the electrode mounting rods clamped into position. Pictures were taken of the system in order to determine the system dimensions. Pachosa (1990) shows a top view of the electrods along with a second view at the location of the heater wire, including the important dimensions. These dimensions were later used to determine the magnitude of the DEP force at various locations along the bubbles trajectory.

In order to develop relations among bubble size, electric field strength, power input, and bubble frequency, two experiments were run. In the first experiment, the bubble volume was measured as a function of electric field strength. For Freon-113 the voltage level was set at 10 kV and increased by 2 kV until 19 kV was reached. This range was chosen because at voltages lower than 10 kV, the DEP force was not strong enough to detach the vapor bubbles and accelerate them downward. At voltages higher than 19 kV, the electrode spacing was not large enough to resist the voltage and electrode arcing would occur. With each voltage setting, five pictures were taken of the vapor bubbles from both the top and front views in order to obtain at least three sets of acceptable photographs for volume measurement. From these pictures, an optical measurescope was used to determine the exact bubble dimensions. These measurements were then used along with an ellipsoid model to calculate bubble volumes accurately. The ellipsoid model was needed in order to account for distortion of the bubbles caused from the electric field, as mentioned previously by Cheng and Chaddock (1985). This exact process was repeated using FC-72 as the working fluid in the allowable voltage range of 15–21 kV.

For the second experiment, the bubble detachment frequency was determined as a function of the power input to the heater wire. In order to be consistent, the bubble frequency measurements were taken at the same voltage levels as applied during the first experiment. For each voltage level, the rheostat was set to a high resistance and the number of vapor bubble detachments counted for a twenty second time interval. At the same time, a multimeter was used to record the voltages dropped across the alternator and resistor. To ensure accurate measurements, the process was repeated three times and then the rheostat resistance decreased. Data were taken at three different rheostat settings for each voltage level in both Freon-113 and FC-72. To determine the heat flux produced by the heater wire, the voltage measurements recorded earlier from the alternator and resistor were needed. These measurements were used along with elementary circuit analysis to determine the power dissipated through the heater wire. Once the power is known, the wire surface area can be used to calculate surface heat flux. The uncertainties associated with the experimental data were estimated and are given here. For voltage measurement, they are less than ±3 percent, for bubble volume, they are between ±3 and ±21 percent, for bubble frequency, they are below ±11 percent, and for power, they are lower than ±6 percent.

Results and Discussion

In order to represent the data in a cleaner fashion, the magnitude of the DEP force exerted at the tip of the heater wire was used instead of electrode voltage as the independent variable. This parameter not only encompassed the electrode voltage, but also took into consideration the properties of the fluid and geometric concerns. In order to be consistent across the range of bubble sizes, the DEP force per volume was calculated for each voltage level according to the following equation:

$$F = 3\epsilon_1 \frac{(\epsilon_2 - \epsilon_1)}{(\epsilon_2 - 2\epsilon_1)} \frac{v^2}{r^3 \alpha^2} \quad (1)$$

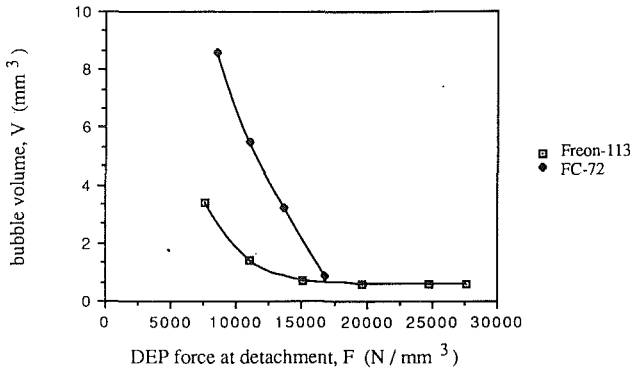

Fig. 1 Vapor bubble volume versus DEP forces

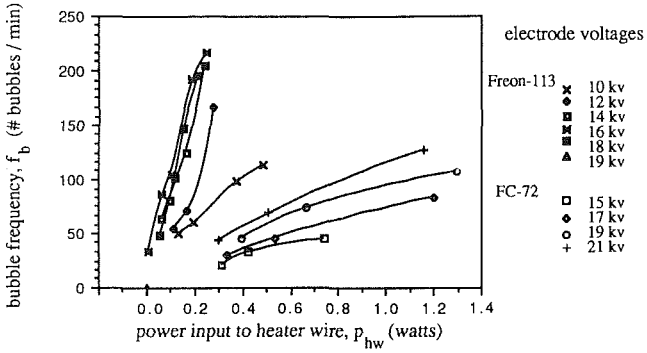

Fig. 2 Bubble detachment frequency versus heater wire power input

where ϵ_1 and ϵ_2 are the dielectric strength of the liquid and the vapor phase, respectively, v is the voltage of the electric field and α is the angle between the electrodes. The values for geometric dimensions are taken from Pachosa (1990). In the above, r, the distance from fictitious intersection to tip of heater wire = 15.9 mm, and α = 13 deg. A graphic representation of the bubble volume versus DEP force per volume is given in Fig. 1 for both Freon-113 and FC-72.

From the second experiment, the bubble frequencies from the three readings were averaged and converted into bubbles per minute. Then the input power was determined by circuit analysis for each position of the rheostat. The data for both Freon-113 and FC-72 are combined in Fig. 2, which shows the relation between bubble frequency and power input.

In Fig. 1 it is noted that increasing voltages dramatically decrease the volumes of the detaching bubbles for both Freon-113 and FC-72. This can be explained by using static force balance arguments. Higher electric field strengths create higher DEP forces, which overpower surface tension and buoyancy forces at an earlier stage of bubble development. Once this critical bubble radius is reached, detachment occurs, creating smaller bubbles for higher field strengths. Also in Fig. 1, the curve for Freon-113 seems to approach a minimum bubble size asymptotically. This minimum bubble size does make sense, however, if the processes behind vapor bubble generation from the heater probe are analyzed. The bubble size generated by the heater wire will depend on the superheat of the surrounding liquid and also the active nucleation cavity size associated with the wire. Once heat is applied, a vapor bubble embryo will form on the surface of the wire. This bubble will experience two growth stages: an initial stage where a bubble embryo will form instantaneously, with a minimum starting volume governed by the degree of superheat and critical radius; and a final stage where the bubble will continue to grow at a slow pace until surface tension is overcome and detachment occurs.

If bubble detachment occurs immediately after the initial stage, the minimum bubble volume that can be formed is equal to the initial forming embryo.

An explanation for why larger bubbles occur at the minimum voltage for FC-72 compared with Freon-113 may be explained by using previous information. Because FC-72 is a weaker dielectric, the critical detachment radius is larger than the radius for Freon-113 at the same applied voltage. As the bubble grows, the DEP force will eventually surpass the surface tension force and cause detachment. This is due to the fact that the DEP force is proportional to the cube of the bubble radius, as compared to the surface tension force being proportional to the radius alone. However, as the bubble grows to overcome the original component of surface tension, it becomes large enough to attach to the electrodes and the other side of the U-shaped wire, picking up additional components of surface tension. This forces the critical bubble size to be pushed ahead still further until the DEP force is large enough to overcome surface tension. Therefore, larger bubbles should be produced by FC-72 than Freon-113 due to its weaker dielectric strength and added components of surface tension with increasing bubble size.

As shown in Fig. 2, the bubble frequency increases with higher power input. The explanation for this is obvious due to the fact that higher heating rates occur with increased power. These higher rates of heating generate faster bubble growth, which decreases the waiting time between consecutive bubbles. Therefore, more bubbles form and detach over a given time period for higher power inputs than lower power inputs.

Another observation is that higher bubble frequencies occur for a given power input as the electrode voltage is raised. This phenomenon occurs because at higher electrode voltages, the critical bubble radius is smaller than for lower voltages. For a constant power, more bubbles will detach at higher voltages because their critical size will be reached more quickly than for larger bubbles. By assuming the amount of vapor bubble generation is constant for a given power input, the data should collapse on one curve by considering the bubble size and frequency together. If this assumption is true then the total volume of vapor should approach a constant for a given power input in a particular fluid.

One other observation from Fig. 2 is that the bubble frequency versus power input curves for FC-72 are located to the right of those for Freon-113. Because FC-72 has a higher boiling point temperature, more power is required to initiate boiling than for Freon-113.

Comparison With Published Results

In order to determine the accuracy of the measurement techniques used in the experiments, an attempt was made to compare the heat flux produced in this study to analytical models of heat flux produced in the nucleate boiling range. The best method was to plot the boiling curve (heat flux versus degree of superheat, ΔT_{sup}) for both Freon-113 and FC-72, and compare with our results. Because of the use of electric fields, surface temperature measurements of the heater wire could not be taken in the experiments. This prohibited us from expressing the data in boiling curve format; however, the surface heat flux could be determined and plotted as a range of values instead. This would give some insight as to which part of the nucleate boiling curve the experiment was operating in.

To plot the analytical expressions of the nucleate boiling curve for Freon-113 and FC-72, use was made of the heat flux correlation developed by Forster and Zuber (1955). These curves were plotted in the nucleate boiling range taking thermodynamic data from the ASHRAE *Handbook* (1985) for Freon-113 and data from the 3M Company Manual (1990) for FC-72.

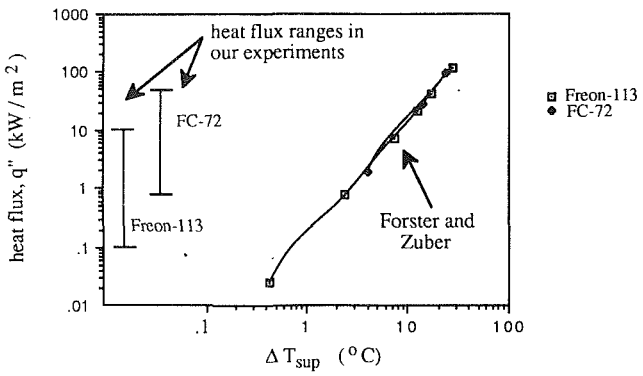

Fig. 3 Comparison of heat flux ranges in the nucleate boiling regime for both Freon-113 and FC-72

To determine the heat flux produced in our experiments, the active nucleation area of the heater wire was needed. This task was difficult to accomplish due to the high degree of nonuniformity over the entire heater wire surface. Therefore it was decided to pick a minimum and maximum active nucleation area and represent the data over this range of heat fluxes. From observations of the boiling experiments and high-speed photography, it was noticed that the majority of the bubble nucleation was occurring on the part of the heater wire where the copper wire was wrapped around the nichrome wire. Examining the heater wire under magnification shows that much larger nucleation cavities appear on and between the copper wire surfaces than on the very smooth nichrome surface. Because this boiling experiment is operating on the low end of the superheat range, larger nucleation cavities become the most probable site for nucleate boiling to occur. Using the above information, the maximum area of nucleation was measured as the entire surface area covering the wrapped copper wire (2.02 mm^2). The minimum nucleation area was taken as the area between each consecutive coil of the copper wire (0.39 mm^2):

$$q'' = \frac{f_b V \rho_v \lambda'}{A_s} \tag{2}$$

where f_b is the bubble detachment frequency, V is the bubble volume, ρ_v is the vapor density, λ' is a combination of latent heat and sensible heat, and A_s is the surface area of bubble nucleation. Equation (2) was used along with the information presented in Figs. 1 and 2 to calculate the heat flux ranges for both Freon-113 and FC-72. These results are shown in Fig. 3 along with the boiling curves plotted for Freon-113 and FC-72 using the Forster and Zuber correlation.

As shown in Fig.3, our results agree very well with those produced by the analytical expression for Forster and Zuber (1955). By examing both heat flux ranges, the wire superheat in our experiments settles between 1 and 20° C. This range of superheat seems very appropriate for nucleate boiling, considering the source of input power used, and provides additional proof that the measurements of bubble size, frequency, and power input were very accurate.

Microgravity Numerical Simulation

The experimental results clearly demonstrate that the magnitude of the DEP force can overcome surface tension and buoyancy forces to detach and accelerate a vapor bubble in the downward direction. Therefore, use of the DEP force in a microgravity environment should be able to initiate and maintain the nucleate boiling process. For microgravity applications, the required DEP forces are much less than that needed in the ground-based experiment. It is informative to estimate what would be required in a space environment. To do this,

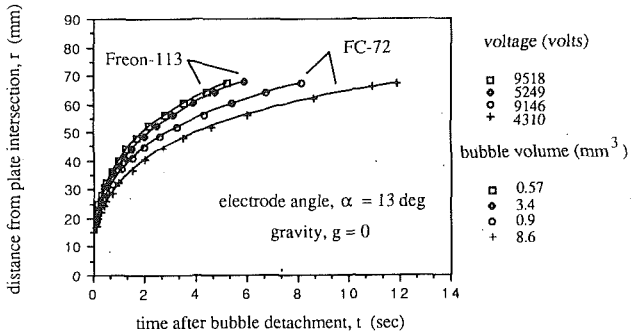

Fig. 4 Results from microgravity numerical simulation of vapor bubble position versus time after detachment

a computer program was written using two-phase flow relations to predict the motion of a vapor bubble in microgravity under the presence of the DEP force. This simulation was produced under the same conditions and electrode dimensions as the experiment. By being consistent, good comparisons and conclusions can be drawn about the similarities and differences between the two. The details of the numerical simulation are given by Pachosa (1990).

The results of the simulation for each of the four bubble volumes are depicted in Fig. 4. The plot represents the bubbles position versus time after detachment. For each of the bubble volumes, the required detachment voltage is also represented in the legend of the graph. Examination of Fig. 4 shows proof that the DEP force is strong enough to carry the vapor bubbles completely away from the heater wire surface. For this particular simulation, the bubble driving force is terminated at the end of the electrodes at approximately 67 mm. Also, it can be seen that the bubble position approaches a final destination of approximately 70 mm in an exponential manner. This exponential dependence in bubble position is explained by examining the nature of the DEP force. Because its strength is proportional to r^3, the DEP force is very strong near the heater wire and decreases as the bubble approaches the end of the electrodes. As the bubble moves outward, the weakened DEP force is overcome by the viscous drag forces causing the bubble to slow down with time and eventually stop outside the electrodes where a driven force no longer exists.

For all four test runs, the DEP force was strong enough to push the bubbles entirely out of the electrodes. However, the smaller bubbles took much less time than the larger bubbles to accomplish this task. This is due to the reduced drag force on smaller bubbles, and a higher initial acceleration once the bubble detaches from the wire surface. This acceleration is created by the relatively higher voltages required to overcome surface tension during detachment of the smaller bubbles.

Due to the weaker dielectric nature of FC-72, it is also apparent in the figures that a considerably longer period of time is required in order for these bubbles to reach the end of the electrodes as compared with Freon-113. However, the two fluids exhibit the same trends and are able to accelerate the bubbles away from the heater wire. This should provide an efficient vapor removal mechanism to initiate and sustain nucleate boiling in a microgravity environment.

Comparison of Simulation and Experiment

The largest difference between the two sets of results is in the amount of voltage required to initiate detachment from the heater wire. Comparing the voltages in Fig. 4 with those in Fig. 2 for the same bubble volumes, shows that the voltage requirement in microgravity is nearly half as much as in the ground-based experiment. Because the DEP force is only competing against surface tension in microgravity, the requirement for detachment is less than if it also had to compete against a buoyancy force. This would allow for reduced voltage ranges in microgravity conditions, making bubble detachment much easier to attain, and also would be safer by eliminating the risks of electrode arcing. Also from the simulation, the vapor bubbles are able to travel several centimeters before coming to rest as compared to only a few millimeters in the experiments. This increased distance should create a perfect environment for nucleate boiling, by allowing the heater wire to remain virtually vapor free.

Acknowledgments

The first author was supported by a NASA Graduate Researcher's Fellowship. 3M Company donated the FC-72 fluids.

References

ASHRAE, 1985, *Fundamental SI Handbook*, American Society of Heating, Refrigeration, and Air Conditioning Engineers, Inc., Atlanta, GA, pp. 16.1–16.8.

Cheng, J. K., and Chaddock, J. B., 1985, "Effect of an Electric Field on Bubble Growth Rate," *Int. Comm. Heat Mass Transfer*, Vol. 12, pp. 259–268.

Forster, H. K., and Zuber, N., 1955, "Dynamics of Vapor Bubbles and Boiling Heat Transfer," *AIChE Journal*, Vol. 1, No. 4, pp. 531–535.

The 3M Company, 1990, "Product Information, Fluoroinert Liquids," pp. 9–57.

Pachosa, D. M., 1990, "Dielectrophoresis Driven Nucleate Boiling in a Microgravity Environment," M.S. Thesis, Department of Mechanical and Materials Engineering, Washington State University, Pullman, WA.

On the Dominant Unstable Wavelength During Film Boiling on a Horizontal Cylinder of Small Diameter

Rui-Qing Li[1] and R. Harris[2]

Introduction

There exist three types of boiling, namely, nucleate, transition, and film boiling. The film boiling regime is characterized by the steady formation and release of bubbles at the liquid-over-vapor interface on top of a heating element. Chang (1957, 1959), Zuber (1958), and Zuber and Tribus (1958) presented mathematical models for film boiling on horizontal flat plates. These models are based on the Rayleigh (1900)–Taylor (1950) instability of the liquid–vapor interface. Capillary waves are propagated along this interface, which becomes unstable if the wavelength exceeds a certain critical value. Berenson (1961) refined these models by emphasizing the importance of the "most dangerous" wavelength, instead of the critical wavelength.

Based on the asymmetric assumption of the cylindrical vapor–liquid interface as shown in Fig. 1, Lienhard and Wong (1964) extended the validity of the hydrodynamic instability

[1]Graduate Student, Mining and Metallurgical Engineering, McGill University, Montreal, Quebec, Canada, H3A 2A7.

[2]Associate Professor, Mining and Metallurgical Engineering, McGill University, Montreal, Quebec, Canada, H3A 2A7.

Contributed by the Heat Transfer Division of THE AMERICAN SOCIETY OF MECHANICAL ENGINEERS. Manuscript received by the Heat Transfer Division August 1991; revision received June 1992. Keywords: Boiling, Flow Instability, Multiphase Flows. Associate Technical Editor: L. C. Witte.

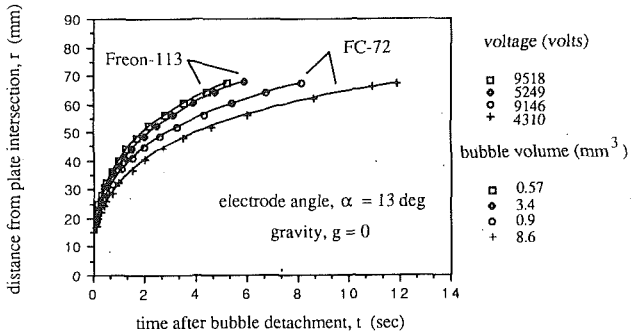

Fig. 4 Results from microgravity numerical simulation of vapor bubble position versus time after detachment

a computer program was written using two-phase flow relations to predict the motion of a vapor bubble in microgravity under the presence of the DEP force. This simulation was produced under the same conditions and electrode dimensions as the experiment. By being consistent, good comparisons and conclusions can be drawn about the similarities and differences between the two. The details of the numerical simulation are given by Pachosa (1990).

The results of the simulation for each of the four bubble volumes are depicted in Fig. 4. The plot represents the bubbles position versus time after detachment. For each of the bubble volumes, the required detachment voltage is also represented in the legend of the graph. Examination of Fig. 4 shows proof that the DEP force is strong enough to carry the vapor bubbles completely away from the heater wire surface. For this particular simulation, the bubble driving force is terminated at the end of the electrodes at approximately 67 mm. Also, it can be seen that the bubble position approaches a final destination of approximately 70 mm in an exponential manner. This exponential dependence in bubble position is explained by examining the nature of the DEP force. Because its strength is proportional to r^3, the DEP force is very strong near the heater wire and decreases as the bubble approaches the end of the electrodes. As the bubble moves outward, the weakened DEP force is overcome by the viscous drag forces causing the bubble to slow down with time and eventually stop outside the electrodes where a driven force no longer exists.

For all four test runs, the DEP force was strong enough to push the bubbles entirely out of the electrodes. However, the smaller bubbles took much less time than the larger bubbles to accomplish this task. This is due to the reduced drag force on smaller bubbles, and a higher initial acceleration once the bubble detaches from the wire surface. This acceleration is created by the relatively higher voltages required to overcome surface tension during detachment of the smaller bubbles.

Due to the weaker dielectric nature of FC-72, it is also apparent in the figures that a considerably longer period of time is required in order for these bubbles to reach the end of the electrodes as compared with Freon-113. However, the two fluids exhibit the same trends and are able to accelerate the bubbles away from the heater wire. This should provide an efficient vapor removal mechanism to initiate and sustain nucleate boiling in a microgravity environment.

Comparison of Simulation and Experiment

The largest difference between the two sets of results is in the amount of voltage required to initiate detachment from the heater wire. Comparing the voltages in Fig. 4 with those in Fig. 2 for the same bubble volumes, shows that the voltage requirement in microgravity is nearly half as much as in the ground-based experiment. Because the DEP force is only competing against surface tension in microgravity, the requirement for detachment is less than if it also had to compete against a buoyancy force. This would allow for reduced voltage ranges in microgravity conditions, making bubble detachment much easier to attain, and also would be safer by eliminating the risks of electrode arcing. Also from the simulation, the vapor bubbles are able to travel several centimeters before coming to rest as compared to only a few millimeters in the experiments. This increased distance should create a perfect environment for nucleate boiling, by allowing the heater wire to remain virtually vapor free.

Acknowledgments

The first author was supported by a NASA Graduate Researcher's Fellowship. 3M Company donated the FC-72 fluids.

References

ASHRAE, 1985, *Fundamental SI Handbook*, American Society of Heating, Refrigeration, and Air Conditioning Engineers, Inc., Atlanta, GA, pp. 16.1–16.8.

Cheng, J. K., and Chaddock, J. B., 1985, "Effect of an Electric Field on Bubble Growth Rate," *Int. Comm. Heat Mass Transfer*, Vol. 12, pp. 259–268.

Forster, H. K., and Zuber, N., 1955, "Dynamics of Vapor Bubbles and Boiling Heat Transfer," *AIChE Journal*, Vol. 1, No. 4, pp. 531–535.

The 3M Company, 1990, "Product Information, Fluoroinert Liquids," pp. 9–57.

Pachosa, D. M., 1990, "Dielectrophoresis Driven Nucleate Boiling in a Microgravity Environment," M.S. Thesis, Department of Mechanical and Materials Engineering, Washington State University, Pullman, WA.

On the Dominant Unstable Wavelength During Film Boiling on a Horizontal Cylinder of Small Diameter

Rui-Qing Li[1] and R. Harris[2]

Introduction

There exist three types of boiling, namely, nucleate, transition, and film boiling. The film boiling regime is characterized by the steady formation and release of bubbles at the liquid-over-vapor interface on top of a heating element. Chang (1957, 1959), Zuber (1958), and Zuber and Tribus (1958) presented mathematical models for film boiling on horizontal flat plates. These models are based on the Rayleigh (1900)–Taylor (1950) instability of the liquid–vapor interface. Capillary waves are propagated along this interface, which becomes unstable if the wavelength exceeds a certain critical value. Berenson (1961) refined these models by emphasizing the importance of the "most dangerous" wavelength, instead of the critical wavelength.

Based on the asymmetric assumption of the cylindrical vapor–liquid interface as shown in Fig. 1, Lienhard and Wong (1964) extended the validity of the hydrodynamic instability

[1]Graduate Student, Mining and Metallurgical Engineering, McGill University, Montreal, Quebec, Canada, H3A 2A7.

[2]Associate Professor, Mining and Metallurgical Engineering, McGill University, Montreal, Quebec, Canada, H3A 2A7.

Contributed by the Heat Transfer Division of THE AMERICAN SOCIETY OF MECHANICAL ENGINEERS. Manuscript received by the Heat Transfer Division August 1991; revision received June 1992. Keywords: Boiling, Flow Instability, Multiphase Flows. Associate Technical Editor: L. C. Witte.

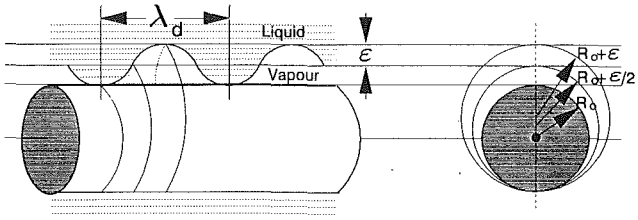

Fig. 1 Assumed geometry of film boiling on a horizontal cylindrical heater

theory to the case of thin horizontal heating wires by accounting for the effect of surface tension along the curved periphery of the liquid-vapor interface in a vertical cross section and derived the following expression for the most dangerous wavelength (dimensionless):

$$\Lambda_d \equiv \lambda_d \sqrt{\frac{\rho_1 g}{\sigma}} = \frac{2\pi\sqrt{3}}{\sqrt{1+\frac{1}{2\Pi^2}}} \tag{1}$$

where λ_d is the most dangerous wavelength; ρ_1 is the density of fluid 1 (liquid); σ is the gas-liquid surface tension; g is the acceleration due to gravity; Π is the dimensionless radius and is defined as:

$$\Pi = R_0 \sqrt{\frac{\rho_1 g}{\sigma}} \tag{2}$$

where R_0 is the radius of the cylindrical heater. By assuming that the spacing between bubbles is dominated by the dangerous wavelength, they predicted and measured the distance between bubbles in the isopropanol and benzene systems as a function of heater diameters. The experimental bubble spacing exceeds the theoretical value by 25 percent in both isopropanol and benzene. In order to overcome the underestimation of the dangerous wavelength by Lienhard and Wong's model, two subsequent attempts were accordingly made. The first was by Siegel and Keshock (1965) who assumed that the interface was axisymmetric and who retained a minimum blanket thickness, b, in their equation for the most dangerous wavelength:

$$\Lambda_d = \frac{2\pi\sqrt{3}}{\sqrt{1+\frac{1}{\left(1+\frac{b}{R_0}\right)^2 \Pi^2}}} \tag{3}$$

The second was by Lienhard and Sun (1970) who modified Lienhard and Wong's formula by accounting for the minimum blanket thickness of vapor, b. Their result was:

$$\Lambda_d = \frac{2\pi\sqrt{3}}{\sqrt{1+\frac{1}{2\left(1+\frac{b}{R_0}\right)^2 \Pi^2}}} \tag{4}$$

Equations (3) and (4) still underpredict the wavelength (Lienhard and Sun, 1970).

In fact, all previous investigators oversimplified the instability problem due to the use of the Cartesian coordinates since the velocity potentials of the two fluids should be expressed as a solution of Laplace's equation in cylindrical coordinates.

Theory

In the present analysis, the geometry of the vapor-liquid interface is assumed to be the same as that of Lienhard and Wong (1964), Fig. 1. A cylindrical heater with radius R_0 is immersed in a liquid, and the geometry of the liquid-vapor interface surrounding a wire during film boiling is assumed to take a sinusoidally undulating, asymmetric form. The vapor blanket surrounding the heater is assumed to be sufficiently thin that the smallest radius of the interface is negligibly larger than the radius of heater. The maximum perturbing amplitude, ϵ, of the dominant wave occurs at the top of the interface.

If the flow is assumed to be irrotational and the interface between the vapor and the liquid remains circular as shown in Fig. 1, we then have the following expressions for the velocity potentials of liquid and vapor in cylindrical coordinates:

$$\Phi_1 = AK_0(kr)\exp[i(Gt+kz)] \quad \text{for liquid}$$

$$\Phi_2 = BI_0(kr)\exp[i(Gt+kz)] \quad \text{for vapor} \tag{5}$$

where $I_0(kr)$ and $K_0(kr)$ are modified Bessel functions of the first and second kind, respectively; k is the wave number; G is the growth rate; A and B are constants; r is the radial coordinate; t is the time; z is the horizontal coordinate. The disturbance, ξ, of the interface through a vertical cross section is expressed as:

$$\xi = \int U_r dt = \int \frac{\partial \Phi_1}{\partial r} dt = \int \frac{\partial \Phi_2}{\partial r} dt$$

$$= \frac{A}{iG}\left(\frac{\partial K_0(kr)}{\partial r}\right)_{r=R_0} \exp[i(Gt+kz)]$$

$$= \frac{B}{iG}\left(\frac{\partial I_0(kr)}{\partial r}\right)_{r=R_0} \exp[i(Gt+kz)] = \epsilon \exp[i(Gt+kz)] \tag{6}$$

where U_r is the radial velocity.

By considering the continuity of the radial velocity component and the dynamic boundary condition at the interface (the pressure difference between the two fluids equals the capillary effect) as well as the assumption that the cylindrical interface is asymmetric as shown in Fig. 1, we get the following expression for the growth rate as a function of wave number:

$$G^2 = \frac{\sigma k\left(k^2 - \frac{1}{2R_0^2} - \frac{(\rho_1-\rho_2)g}{\sigma}\right)}{\rho_1\epsilon_1 + \rho_2\epsilon_2} \tag{7}$$

where ρ_2 is the density of fluid 2 (vapor) and

$$\epsilon_1 = -\frac{K_0(kR_0)}{\left[\frac{dK_0(kr)}{d(kr)}\right]_{r=R_0}} = \frac{K_0(kR_0)}{K_1(kR_0)},$$

$$\epsilon_2 = \frac{I_0(kR_0)}{\left[\frac{dI_0(kr)}{d(kr)}\right]_{r=R_0}} = \frac{I_0(kR_0)}{I_1(kR_0)} \tag{8}$$

The term $1/2R_0^2$ of Eq. (7) comes from the disturbance pressure in the transverse direction. The pressure due to the surface tension in the transverse direction ranges between σ/R_0 in the valleys and $\sigma/(R_0+\epsilon)$ at the peaks of the wave, it has an average value of $\sigma/(R_0+\epsilon/2)$ and an amplitude of $\sigma\epsilon/(2R_0^2)$.

Equation (7) gives the relationship between the exponential growth rate, G, and the wave number, k. The nature of G governs the stability of the disturbance. If G is real, the stabilizing effect of surface tension in the axial direction will smooth out the disturbance. If G is imaginary, the force of

gravity will dominate and the disturbance will increase exponentially in accordance with Eq. (7). G passes from real to imaginary as the right-hand side of Eq. (7) passes through zero. The critical wave number, k_c, and wavelength, λ_c, are then obtained by equating the right-hand side of Eq. (7) to zero. The most dangerous wave number, k_d, and wavelength, λ_d, were numerically obtained by maximizing $-G^2$.

In order to express Eq. (7) in convenient dimensionless form, we define:

Dimensionless wavenumber:

$$K = k\sqrt{\frac{\sigma}{\rho_1 g}} \tag{9}$$

Dimensionless growth rate:

$$\Omega = iG\left[\frac{\sigma}{\rho_1 g^3}\right]^{1/4} \tag{10}$$

From Eq. (9), we have dimensionless wavelength:

$$\Lambda = \frac{2\pi}{K} = \frac{2\pi}{k}\sqrt{\frac{\rho_1 g}{\sigma}} = \lambda\sqrt{\frac{\rho_1 g}{\sigma}} = 2\pi\sqrt{3}\,\frac{\lambda}{\lambda_d^\infty} \tag{11}$$

where λ_d^∞ is the most dangerous wavelength when R_0 is infinite (planar interface).

Finally, combining Eqs. (2), (7), (9), and (10), and assuming the density of vapor to be zero, Eq. (7) becomes:

$$\Omega^2 = -\frac{1}{\epsilon_1}\left[K^2 - \frac{1}{2\Pi^2} - 1\right]K \tag{12}$$

where

$$\epsilon_1 = \frac{K_0(kR_0)}{K_1(kR_0)} = \frac{K_0(K\Pi)}{K_1(K\Pi)} \tag{13}$$

Equation (12) is independent of the properties of fluids. Since Eq. (12) contains a "correcting factor," ϵ_1, in comparison with Lienhard and Wong's expression for dimensionless growth rate, it is expected that present theory should give more accurate results. By equating Ω to zero, we get the dimensionless critical wavelength:

$$\Lambda_c = \frac{2\pi}{\sqrt{1+\dfrac{1}{2\Pi^2}}} \tag{14}$$

From Eq. (14), it is obvious that when the dimensionless radius, Π, becomes large (e.g., $\Pi > 3$), the critical wavelength is independent of the radius, and so is the most dangerous wavelength.

Application of Theory

Lienhard et al. (Lienhard and Wong, 1964; Lienhard and Sun, 1970) experimentally determined the dominant unstable wavelength during film boiling of isopropanol, benzene, acetone, and methanol liquids.

Figure 2 shows the dimensionless most dangerous wavelengths predicted by Eqs. (1) and (12). Evidently, the present model gives the best representation of measured average wavelength. In reality, there is not a precise value of the wavelength; the most dangerous wavelength that occurs at the maximum growth rate corresponds to the measured average data. It is assumed that the wavelengths arise from the growth rate greater than some fraction of the maximum growth rate. By setting the cutoff for the wavelength at 90 percent of the maximum growth rate, the variation in the measured data is encompassed, Fig. 2.

Figure 3 shows the ratios of the calculated values of the most dimensionless dangerous wavelengths to the critical wavelengths; the ratios are greater than the $\sqrt{3}$ reported by Lienhard and Wong (1964); this is why the present model gives a better correlation to the observed values than the previous model. The data shown in Fig. 3 are fitted by Eq. (15):

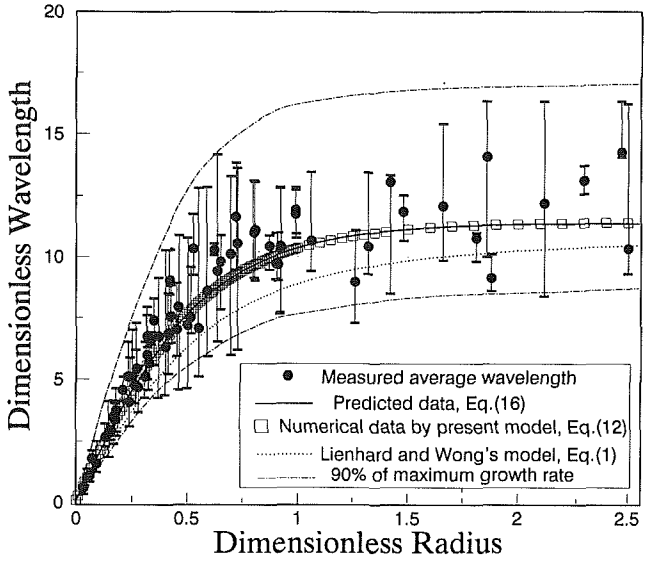

Fig. 2 Relationship between the dimensionless wavelength and the dimensionless radius

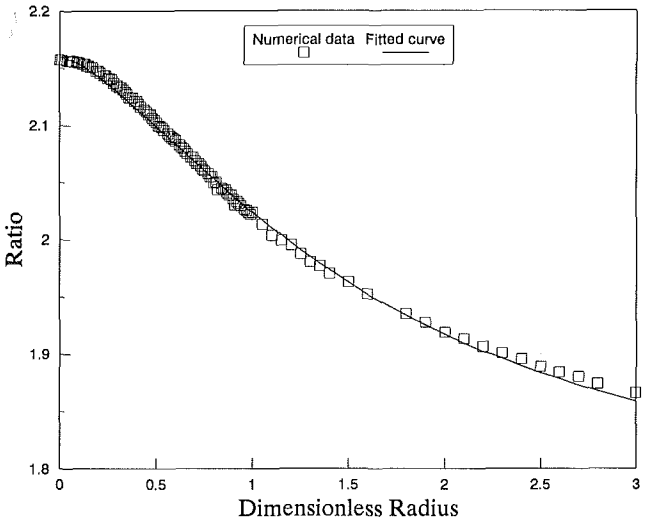

Fig. 3 Calculated ratio between the dangerous wavelength and the critical wavelength as a function of dimensionless radius

$$\frac{\Lambda_d}{\Lambda_c} = \frac{2.16 + \sqrt{3}\ 0.4672\ \Pi^{1.491}}{1 + 0.4672\ \Pi^{1.491}} \tag{15}$$

Equation (15) gives $\Lambda_d/\Lambda_c = \sqrt{3}$ when the dimensionless radius is infinitely large and $\Lambda_d/\Lambda_c = 2.16$ when the dimensionless radius is zero. From Eqs. (14) and (15), we have an expression for the dimensionless dangerous wavelength in a closed form:

$$\Lambda_d = \frac{2.16 + \sqrt{3}\ 0.4672\ \Pi^{1.491}}{1 + 0.4672\ \Pi^{1.491}} \cdot \frac{2\pi}{\sqrt{1+\dfrac{1}{2\Pi^2}}} \tag{16}$$

The predicted dimensionless most dangerous wavelength based on Eq. (16) is also shown in Fig. 2 by a solid line. Equation (16) can be used to predict the dimensionless wavelength with great success.

Conclusions

1 The dominant unstable dimensionless wavelength during

film boiling on a horizontal cylinder is predicted by Eq. (16).

2 The geometric assumption made by Lienhard and Wong (1963) is reasonable.

3 Lienhard and Sun's (1970) conclusion about the invalidity of theory below $\Pi \approx 0.1$ is also suitable for the present theory.

References

Berenson, P. J., 1961, "Film-Boiling Heat Transfer From a Horizontal Surface," ASME JOURNAL OF HEAT TRANSFER, Vol. 83, pp. 351-358.

Chang, Y. P., 1957, "A Theoretical Analysis of Heat Transfer in Natural Convection and in Boiling," *Trans. ASME*, Vol. 79, pp. 1501-1513.

Chang, Y. P., 1959, "Wave Theory of Heat Transfer in Film Boiling," ASME JOURNAL OF HEAT TRANSFER, Vol. 81, pp. 1-12.

Lienhard, J. H., and Wong, P. T. Y., 1964, "The Dominant Unstable Wavelength and Minimum Heat Flux During Film Boiling on a Horizontal Cylinder," ASME JOURNAL OF HEAT TRANSFER, Vol. 86, pp. 220-226.

Lienhard, J. H., and Sun, K. H., 1970, "Effect of Gravity and Size Upon Film Boiling From Horizontal Cylinders," ASME JOURNAL OF HEAT TRANSFER, Vol. 92, pp. 292-298.

Rayleigh, Lord, 1900, "Investigation of the Character of the Equilibrium of an Incompressible Heavy Fluid of Variable Density," *Scientific Papers*, Cambridge University Press, Cambridge, England, Vol. II, pp. 200-207.

Siegel, R., and Keshock, E. G., 1965, "Nucleate and Film Boiling in Reduced Gravity From Horizontal and Vertical Wires," NASA TR R-216, Feb.

Taylor, G., 1950, "The Instability of Liquid Surface When Accelerated in a Direction Perpendicular to Their Planes. I," *Proc. Roy. Soc.*, Vol. (A)201, pp. 192-196.

Zuber, N., 1958, "On the Stability of Boiling Heat Transfer," *Trans. ASME*, Vol. 80, pp. 711-720.

Zuber, N., and Tribus, M., 1958, "Further Remarks on the Stability of Boiling Heat Transfer," UCLA Report No. 58-5, University of California, Los Angeles, CA.

Observations on an Evaporative, Elbow Thermosyphon

G. S. H. Lock[1] and Jialin Fu[1]

Nomenclature

D = tube diameter
h = heat transfer coefficient
P = pressure
$\dot{q}$ = heat flux density
$\dot{Q}$ = heat flux
T = temperature
v = filling fraction
θ = temperature difference

Subscripts

C = condenser
H = evaporator
I = saturated
R = reference, ratio

1 Introduction

Under evaporative conditions, only the linear thermosyphon has been studied extensively (Lock, 1992). For the present purpose, the nearest work is that conducted on inclined tubes (Negishi and Sawada, 1983; Terdtoon et al., 1990). In right-angled form, some empirical observations have appeared (Zarling and Haynes, 1987; Haynes et al., 1991), but there appear to have been few, if any, fundamental investigations. The purpose of this note is therefore to remedy this defect and provide an exploration of the heat transfer characteristics of the right-angled thermosyphon under evaporative conditions. This will be done using laboratory experiments on a small-scale apparatus with two configurations: vertical condenser (with horizontal evaporator) and horizontal condenser (with vertical evaporator).

Before describing the experiments, it is important to state the basis of the analysis on which they are founded. This stems from the fundamental assumption that the heat flux $\dot{Q}$ is a function of the two *independent* wall temperatures T_H, T_C of the heated and cooled sections, respectively. Thus

$$\dot{Q} = f(T_H, T_C) \tag{1}$$

or equivalently,

$$\dot{q} = g(\theta, T_R) \tag{2}$$

where $\dot{q}$ is the heat flux density, here based on the heated surface area, and $\theta = T_H - T_C$. The variable T_R is a convenient, but otherwise arbitrary, reference temperature such that

$$T_R = t(T_H, T_C) \tag{3}$$

is a single-valued function providing a second relation, which, together with θ, determines both T_H and T_C, and hence prescribes the heat transfer rate. The choice of $t(T_H, T_C)$ will be discussed later.

2 The Experiments

The apparatus has been described by Lock and Ladoon (1991), who previously studied the system under single-phase conditions. The experimental procedure was as follows. Before the apparatus was completely assembled, the inner surfaces of the tubes were cleaned using first benzene, then alcohol, and finally distilled water, the filling fluid. Assembly was then completed and a vacuum pump connected. The internal pressure was lowered toward the triple point value (near 1 kPa) and the apparatus then left for several hours with the pump switched off to ascertain that no leaks were present. At this point, a charge of water v_R (fraction of evaporator volume) was measured and introduced using a hypodermic syringe, following which the vacuum pump was again switched on along with the electric heater. In the presence of boiling, the remaining air was withdrawn and the tube finally sealed. Subsequently, periodic checks were made of the vapor pressure and temperature to confirm that they lay on the saturation curve. The test data reported here are limited to water but are representative of any fluid well below its critical pressure.

With the apparatus thus prepared, the test runs began. Each was conducted by selecting an evaporator wall temperature T_H and then plotting the (net) heat flux density against θ for a series of condenser wall temperatures T_C, noting the vapor pressure P_I at each point. The wall temperatures were spatially averaged from at least ten individual readings. Figure 1 illustrates the form of the data obtained. Altering the evaporator wall temperature, the process was then repeated until the limits of the apparatus had been spanned. Depending on the tube configuration, measured temperatures lay in the following ranges: $23°C < T_C < 42°C$; $45°C < T_I < 65°C$; $46°C < T_H < 107°C$; $20\ K < \theta < 75\ K$. As the saturation temperature range indicates, the system pressure was subatmospheric.

A formal error analysis of each of the variables was undertaken. Uncertainty bars are shown on the figures discussed below.

3 Discussion of Results

3.1 Upright Condenser. With the condenser upright and

[1]Department of Mechanical Engineering, University of Alberta, Edmonton, Alberta, Canada, T6G 2G8.

Contributed by the Heat Transfer Division of THE AMERICAN SOCIETY OF MECHANICAL ENGINEERS. Manuscript received by the Heat Transfer Division January 1992; revision received October 1992. Keywords: Heat Exchangers, Heat Pipes and Thermosyphons, Heat Recovery. Associate Technical Editor: J. H. Kim.

film boiling on a horizontal cylinder is predicted by Eq. (16).

2 The geometric assumption made by Lienhard and Wong (1963) is reasonable.

3 Lienhard and Sun's (1970) conclusion about the invalidity of theory below $\Pi \approx 0.1$ is also suitable for the present theory.

References

Berenson, P. J., 1961, "Film-Boiling Heat Transfer From a Horizontal Surface," ASME JOURNAL OF HEAT TRANSFER, Vol. 83, pp. 351-358.

Chang, Y. P., 1957, "A Theoretical Analysis of Heat Transfer in Natural Convection and in Boiling," *Trans. ASME*, Vol. 79, pp. 1501-1513.

Chang, Y. P., 1959, "Wave Theory of Heat Transfer in Film Boiling," ASME JOURNAL OF HEAT TRANSFER, Vol. 81, pp. 1-12.

Lienhard, J. H., and Wong, P. T. Y., 1964, "The Dominant Unstable Wavelength and Minimum Heat Flux During Film Boiling on a Horizontal Cylinder," ASME JOURNAL OF HEAT TRANSFER, Vol. 86, pp. 220-226.

Lienhard, J. H., and Sun, K. H., 1970, "Effect of Gravity and Size Upon Film Boiling From Horizontal Cylinders," ASME JOURNAL OF HEAT TRANSFER, Vol. 92, pp. 292-298.

Rayleigh, Lord, 1900, "Investigation of the Character of the Equilibrium of an Incompressible Heavy Fluid of Variable Density," *Scientific Papers*, Cambridge University Press, Cambridge, England, Vol. II, pp. 200-207.

Siegel, R., and Keshock, E. G., 1965, "Nucleate and Film Boiling in Reduced Gravity From Horizontal and Vertical Wires," NASA TR R-216, Feb.

Taylor, G., 1950, "The Instability of Liquid Surface When Accelerated in a Direction Perpendicular to Their Planes. I," *Proc. Roy. Soc.*, Vol. (A)201, pp. 192-196.

Zuber, N., 1958, "On the Stability of Boiling Heat Transfer," *Trans. ASME*, Vol. 80, pp. 711-720.

Zuber, N., and Tribus, M., 1958, "Further Remarks on the Stability of Boiling Heat Transfer," UCLA Report No. 58-5, University of California, Los Angeles, CA.

Observations on an Evaporative, Elbow Thermosyphon

G. S. H. Lock[1] and Jialin Fu[1]

Nomenclature

D = tube diameter
h = heat transfer coefficient
P = pressure
$\dot{q}$ = heat flux density
$\dot{Q}$ = heat flux
T = temperature
v = filling fraction
θ = temperature difference

Subscripts

C = condenser
H = evaporator
I = saturated
R = reference, ratio

1 Introduction

Under evaporative conditions, only the linear thermosyphon has been studied extensively (Lock, 1992). For the present purpose, the nearest work is that conducted on inclined tubes (Negishi and Sawada, 1983; Terdtoon et al., 1990). In right-angled form, some empirical observations have appeared (Zarling and Haynes, 1987; Haynes et al., 1991), but there appear to have been few, if any, fundamental investigations. The purpose of this note is therefore to remedy this defect and provide an exploration of the heat transfer characteristics of the right-angled thermosyphon under evaporative conditions. This will be done using laboratory experiments on a small-scale apparatus with two configurations: vertical condenser (with horizontal evaporator) and horizontal condenser (with vertical evaporator).

Before describing the experiments, it is important to state the basis of the analysis on which they are founded. This stems from the fundamental assumption that the heat flux $\dot{Q}$ is a function of the two *independent* wall temperatures T_H, T_C of the heated and cooled sections, respectively. Thus

$$\dot{Q} = f(T_H, T_C) \tag{1}$$

or equivalently,

$$\dot{q} = g(\theta, T_R) \tag{2}$$

where $\dot{q}$ is the heat flux density, here based on the heated surface area, and $\theta = T_H - T_C$. The variable T_R is a convenient, but otherwise arbitrary, reference temperature such that

$$T_R = t(T_H, T_C) \tag{3}$$

is a single-valued function providing a second relation, which, together with θ, determines both T_H and T_C, and hence prescribes the heat transfer rate. The choice of $t(T_H, T_C)$ will be discussed later.

2 The Experiments

The apparatus has been described by Lock and Ladoon (1991), who previously studied the system under single-phase conditions. The experimental procedure was as follows. Before the apparatus was completely assembled, the inner surfaces of the tubes were cleaned using first benzene, then alcohol, and finally distilled water, the filling fluid. Assembly was then completed and a vacuum pump connected. The internal pressure was lowered toward the triple point value (near 1 kPa) and the apparatus then left for several hours with the pump switched off to ascertain that no leaks were present. At this point, a charge of water v_R (fraction of evaporator volume) was measured and introduced using a hypodermic syringe, following which the vacuum pump was again switched on along with the electric heater. In the presence of boiling, the remaining air was withdrawn and the tube finally sealed. Subsequently, periodic checks were made of the vapor pressure and temperature to confirm that they lay on the saturation curve. The test data reported here are limited to water but are representative of any fluid well below its critical pressure.

With the apparatus thus prepared, the test runs began. Each was conducted by selecting an evaporator wall temperature T_H and then plotting the (net) heat flux density against θ for a series of condenser wall temperatures T_C, noting the vapor pressure P_I at each point. The wall temperatures were spatially averaged from at least ten individual readings. Figure 1 illustrates the form of the data obtained. Altering the evaporator wall temperature, the process was then repeated until the limits of the apparatus had been spanned. Depending on the tube configuration, measured temperatures lay in the following ranges: $23°C < T_C < 42°C$; $45°C < T_I < 65°C$; $46°C < T_H < 107°C$; $20\ K < \theta < 75\ K$. As the saturation temperature range indicates, the system pressure was subatmospheric.

A formal error analysis of each of the variables was undertaken. Uncertainty bars are shown on the figures discussed below.

3 Discussion of Results

3.1 Upright Condenser. With the condenser upright and

[1]Department of Mechanical Engineering, University of Alberta, Edmonton, Alberta, Canada, T6G 2G8.

Contributed by the Heat Transfer Division of THE AMERICAN SOCIETY OF MECHANICAL ENGINEERS. Manuscript received by the Heat Transfer Division January 1992; revision received October 1992. Keywords: Heat Exchangers, Heat Pipes and Thermosyphons, Heat Recovery. Associate Technical Editor: J. H. Kim.

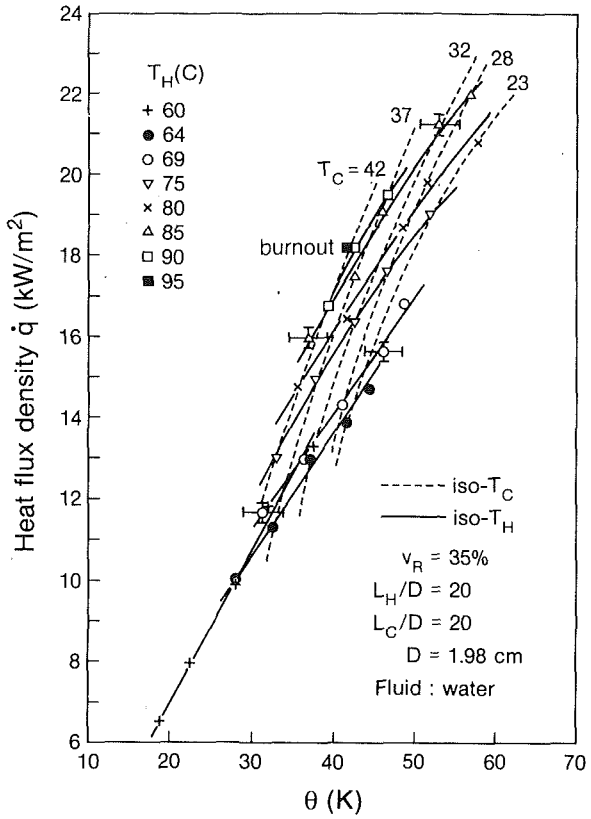

Fig. 1 Heat flux density versus temperature difference for an upright condenser

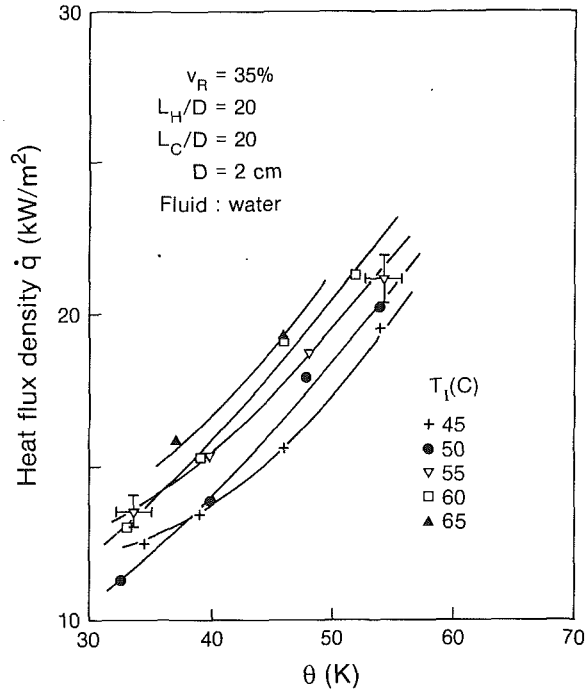

Fig. 2 The effect of vapor temperature on heat transfer with an upright condenser

the evaporator lying horizontally below, the heat transfer data obtained are shown in Fig. 1. Following the form of Eq. (2), this displays the heat flux density $\dot{q}$, based on the evaporator surface area, plotted against θ for each of a series of average evaporator wall temperatures T_H. Curves of constant average condenser wall temperature T_C are cross-plotted on the same figure. The reference temperature T_R in Eq. (3) thus takes one of two readily available values.

The figure illustrates the general situation in which the heat flux density is a function of both T_H and T_C, not just their difference. The curves for constant evaporator temperature would be useful in the design of an isothermal heat source; the constant condenser temperature curves would be more appropriate to an isothermal sink. The alternative choice is T_I, which reflects the system pressure. Interpolated data using the saturation temperature are shown in Fig. 2. These are not markedly different from the data of Fig. 1. A designer is thus free to choose according to the application (Lock, 1992).

Figure 3 shows the iso-T_H data of Fig. 1 replotted in the form of the overall heat transfer coefficient h versus the overall temperature difference θ. The values of h obtained were noticeably higher than those obtained in single-phase conditions (Lock and Ladoon, 1991) but lower than those measured by Imura et al. (1979) using a vertical, linear thermosyphon. However, they were not much less than values obtained in our own apparatus when it was arranged linearly. Within experimental error, the data fit the form

$$h = a(T_H) - b\theta \tag{4}$$

in which a and b reflect the peculiarities of the filling fluid and chosen geometry. In view of the similarity in the individual effects of T_C, T_H, and T_I, it is to be expected that a similar form applies to the iso-T_C and iso-T_I data.

3.2 Upright Evaporator. Corresponding data were also obtained with the evaporator positioned upright beneath a horizontal condenser. Figure 4 shows the results plotted with the evaporator wall temperature as a parameter. These data differ from those in Fig. 1 in two ways. First, they exhibit greater downward curvature, thus making cross plots of constant T_C curves more difficult to construct; of course, it is always possible to present the data in the alternative iso-T_C or iso-T_I forms if desired. Secondly, the data set, as a whole, lies above the upright condenser data.

Although the two configurations yield data that are similar in form, their detailed behavior can be quite different, not least in indicating that the upright evaporator configuration is superior to the upright condenser configuration. This finding is consistent with the expectation that refluent film condensation in a horizontal tube would be more efficient than in a vertical tube where the film is thicker and longer. Likewise, it is to be expected that refluent boiling in a horizontal tube would be less efficient than in a vertical tube where replacement liquid more easily covers the tube wall. However, it was surprising to find that the vertical evaporator combined with the horizontal condenser did not outperform the other configuration by much, at least for the range of conditions studied.

3.3 Limits. The limiting performance of the upright condenser configuration is typified in Fig. 1 by the data for T_H = 90°C and 95°C. Under these conditions, the local evaporator wall temperature nearer the closed end was found to rise suddenly. This indicates a simple dryout failure caused by the inability of the returning liquid to reach the closed end of the horizontal evaporator. Such a failure has been observed by several authors, most recently by Negishi and Sawada (1983).

The limiting performance with the evaporator upright did not correspond to a simple dryout limit. It was accompanied by a periodic rise and fall in the local evaporator wall temperature near the adiabatic junction piece, thus indicating a local dryout associated with flooding and holdup in the condenser while a pool continued to exist in the evaporator below. With a charge of 35 percent of the evaporator volume, this flooding limit normally lies well above the simple dryout limit in a vertical, linear thermosyphon; the presence of a horizontal condenser with poor draining characteristics evidently offsets the advantage of a fully wetted evaporator.

The limiting performance of the upright-evaporator, elbow

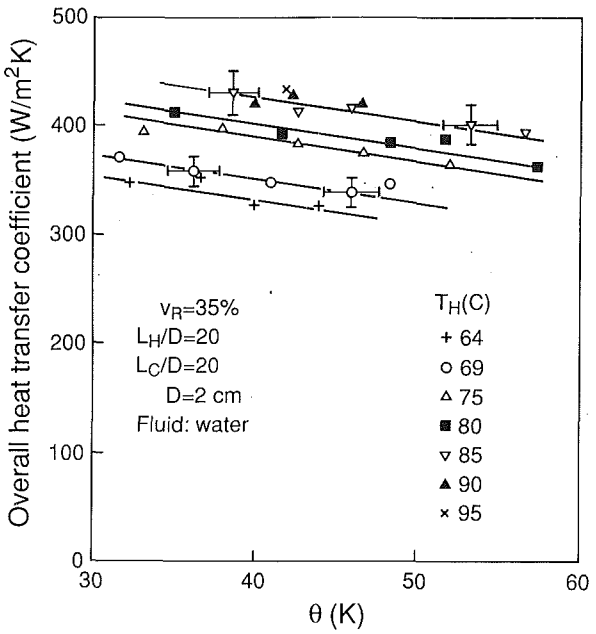

Fig. 3 Overall heat transfer coefficient versus temperature difference for an upright condenser

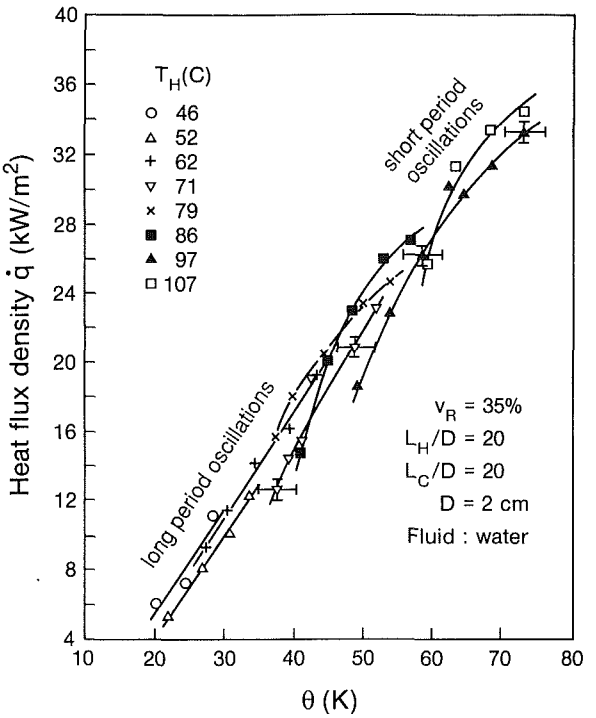

Fig. 4 Heat flux density versus temperature difference for an upright evaporator

thermosyphon thus appears to correspond to the well-established flooding limit observed in linear thermosyphons. This is particularly true for the data at higher values of θ and T_I. However, oscillatory behavior was also noticed at lower values of T_I (and P_I) when the geyser phenomenon may be expected to operate. The difference between these two limiting behavioral forms was not found to be distinct in the experiments reported here with v_R = 35 percent. With lower pressures and temperatures, e.g., below θ = 50 K in Fig. 4, the period of oscillation was found to be longer, typically about 5 min. Above θ = 60 K, the period was noticeably shorter, typically about 1 min. In any event, it was found that the limit could be extended by simply tilting the condenser up slightly.

4 Conclusions

The performance of the evaporative elbow system was found to be superior to that of the nonevaporative system, but comparable to the performance of the linear system. The parametric role of the evaporator wall temperature, the condenser wall temperature, and the vapor saturation temperature was demonstrated, each revealing a similar monotonic effect.

With the evaporator upright, the data were found to be similar to, but displaced from, the upright condenser data. The upright evaporator gave the better performance, but not overwhelmingly so. The limit of performance with the condenser upright was found to be dictated by evaporator dryout. In the upright evaporator configuration, the limit may be attributed to flooding in the poorly draining condenser; this limit was indistinguishable from geyser behavior at low vapor pressures.

Acknowledgments

This work was undertaken under the auspices of the Natural Sciences and Engineering Research Council of Canada, to whom we are grateful. We would also like to thank the technicians and machinists of the Department of Mechanical Engineering, Mr. B. Ceilin and Mr. A. Muir in particular.

References

Haynes, F. D., Zarling, J. P., Quinn, W. F., and Gooch, G. W., 1991, "Laboratory Tests With a Hybrid Thermosyphon," *Proc. 10th Int. Conf. on Offshore Mech. and Arctic Eng.*, ASME Vol. IV, pp. 93-100.

Imura, H., Kusuda, H., Ogata, J., Miyazaki, T., and Sakamoto, N., 1979, "Heat Transfer in Two-Phase Closed-Type Thermosyphons," *Heat Transfer—Japanese Research*, Vol. 8(2), pp. 41-53.

Lock, G. S. H., and Ladoon, D., 1991, "Heat Transfer in a Right-Angled Thermosyphon," *Proc. 10th Int. Conf. on Offshore Mech. and Arctic Eng.*, ASME Vol. IV, pp. 261-266.

Lock, G. S. H., 1992, *The Tubular Thermosyphon*, Oxford University Press, United Kingdom.

Negishi, K., and Sawada, T., 1983, "Heat Transfer Performance of an Inclined, Two-Phase, Closed Thermosyphon," *Int. J. Heat Mass Transf.*, Vol. 26(2), pp. 1207-1313.

Terdtoon, P., Shiraishi, M., and Murakami, M., 1990, "Investigation of Effect of Inclination Angle on Heat Transfer Characteristics of Closed Two-Phase Thermosyphon," *Proc. 6th Int. Heat Pipe Conf.*, Minsk B9P.

Zarling, J. P., and Haynes, F. D., 1987, "Heat Transfer Characteristics of a Commercial Thermosyphon With an Inclined Evaporator Section," *Proc. 6th Int. Offshore Mechanics and Arctic Engineering Symposium*, Vol. IV, pp. 79-84.

Convective Heat Transfer From a Sphere Embedded in Unheated Porous Media

V. X. Tung[1] and V. K. Dhir[2]

Nomenclature

D = diameter, m
q = surface heat flux, W/m²
Ra = Rayleigh number = $q\Delta\rho D^3/\mu_f a_f$

[1]Idaho National Engineering Laboratory, EG&G Idaho, Inc., Idaho Falls, ID 83415-2508.

[2]Mechanical, Aerospace, and Nuclear Engineering Department, School of Engineering and Applied Science, University of California, Los Angeles, Los Angeles, CA 90024-1597.

Contributed by the Heat Transfer Division of the THE AMERICAN SOCIETY OF MECHANICAL ENGINEERS. Manuscript received by the Heat Transfer Division July 1990; revision received May 1992. Keywords: Forced Convection, Geophysical Heat Transfer, Porous Media. Associate Technical Editor: J. H. Kim.

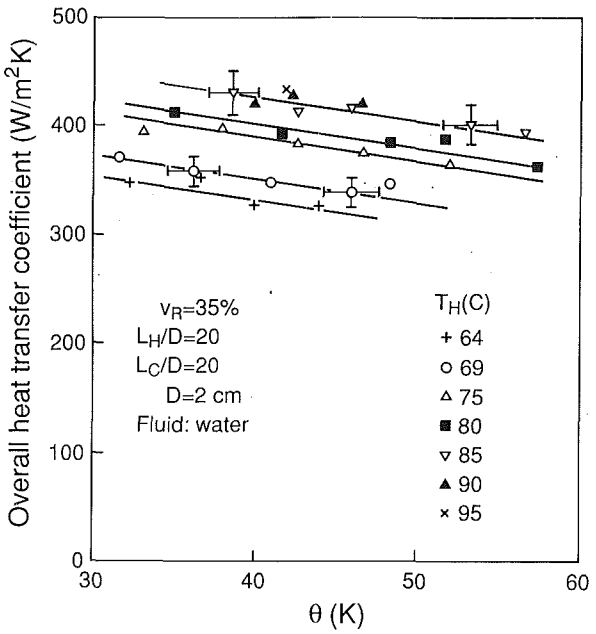

Fig. 3 Overall heat transfer coefficient versus temperature difference for an upright condenser

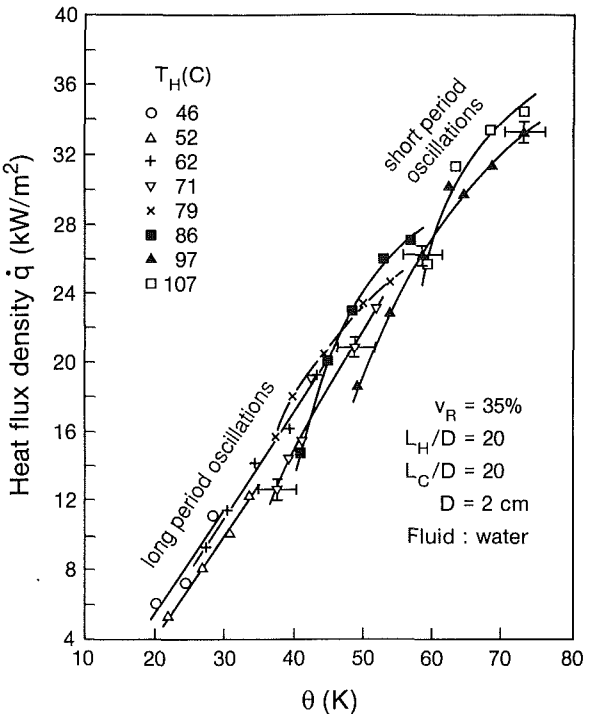

Fig. 4 Heat flux density versus temperature difference for an upright evaporator

thermosyphon thus appears to correspond to the well-established flooding limit observed in linear thermosyphons. This is particularly true for the data at higher values of θ and T_I. However, oscillatory behavior was also noticed at lower values of T_I (and P_I) when the geyser phenomenon may be expected to operate. The difference between these two limiting behavioral forms was not found to be distinct in the experiments reported here with v_R = 35 percent. With lower pressures and temperatures, e.g., below θ = 50 K in Fig. 4, the period of oscillation was found to be longer, typically about 5 min. Above θ = 60 K, the period was noticeably shorter, typically about 1 min. In any event, it was found that the limit could be extended by simply tilting the condenser up slightly.

4 Conclusions

The performance of the evaporative elbow system was found to be superior to that of the nonevaporative system, but comparable to the performance of the linear system. The parametric role of the evaporator wall temperature, the condenser wall temperature, and the vapor saturation temperature was demonstrated, each revealing a similar monotonic effect.

With the evaporator upright, the data were found to be similar to, but displaced from, the upright condenser data. The upright evaporator gave the better performance, but not overwhelmingly so. The limit of performance with the condenser upright was found to be dictated by evaporator dryout. In the upright evaporator configuration, the limit may be attributed to flooding in the poorly draining condenser; this limit was indistinguishable from geyser behavior at low vapor pressures.

Acknowledgments

This work was undertaken under the auspices of the Natural Sciences and Engineering Research Council of Canada, to whom we are grateful. We would also like to thank the technicians and machinists of the Department of Mechanical Engineering, Mr. B. Ceilin and Mr. A. Muir in particular.

References

Haynes, F. D., Zarling, J. P., Quinn, W. F., and Gooch, G. W., 1991, "Laboratory Tests With a Hybrid Thermosyphon," *Proc. 10th Int. Conf. on Offshore Mech. and Arctic Eng.*, ASME Vol. IV, pp. 93-100.

Imura, H., Kusuda, H., Ogata, J., Miyazaki, T., and Sakamoto, N., 1979, "Heat Transfer in Two-Phase Closed-Type Thermosyphons," *Heat Transfer—Japanese Research*, Vol. 8(2), pp. 41-53.

Lock, G. S. H., and Ladoon, D., 1991, "Heat Transfer in a Right-Angled Thermosyphon," *Proc. 10th Int. Conf. on Offshore Mech. and Arctic Eng.*, ASME Vol. IV, pp. 261-266.

Lock, G. S. H., 1992, *The Tubular Thermosyphon*, Oxford University Press, United Kingdom.

Negishi, K., and Sawada, T., 1983, "Heat Transfer Performance of an Inclined, Two-Phase, Closed Thermosyphon," *Int. J. Heat Mass Transf.*, Vol. 26(2), pp. 1207-1313.

Terdtoon, P., Shiraishi, M., and Murakami, M., 1990, "Investigation of Effect of Inclination Angle on Heat Transfer Characteristics of Closed Two-Phase Thermosyphon," *Proc. 6th Int. Heat Pipe Conf.*, Minsk B9P.

Zarling, J. P., and Haynes, F. D., 1987, "Heat Transfer Characteristics of a Commercial Thermosyphon With an Inclined Evaporator Section," *Proc. 6th Int. Offshore Mechanics and Arctic Engineering Symposium*, Vol. IV, pp. 79-84.

Convective Heat Transfer From a Sphere Embedded in Unheated Porous Media

V. X. Tung[1] and V. K. Dhir[2]

Nomenclature

D = diameter, m
q = surface heat flux, W/m²
Ra = Rayleigh number = $q\Delta\rho D^3/\mu_f a_f$

[1]Idaho National Engineering Laboratory, EG&G Idaho, Inc., Idaho Falls, ID 83415-2508.

[2]Mechanical, Aerospace, and Nuclear Engineering Department, School of Engineering and Applied Science, University of California, Los Angeles, Los Angeles, CA 90024-1597.

Contributed by the Heat Transfer Division of the THE AMERICAN SOCIETY OF MECHANICAL ENGINEERS. Manuscript received by the Heat Transfer Division July 1990; revision received May 1992. Keywords: Forced Convection, Geophysical Heat Transfer, Porous Media. Associate Technical Editor: J. H. Kim.

ϵ = porosity of the porous layer
ϵ_s = emissivity of the sphere surface

Subscripts

cond = conduction
eff = effective
f = fluid
forced = forced convection
nat = natural convection
p = particles forming the porous layer
rad = radiation
s = test sphere

Introduction

A knowledge of heat transfer from a spherical heat source embedded in unheated porous media is of interest in many geological, nuclear, geophysical, and chemical applications. The purpose of this work was to establish the effect of the surrounding particles' size on forced convective heat transfer from a sphere.

Several studies of convective heat transfer in uniformly heated porous layers have been reported in the literature. Gnielinski (1978) proposed a semi-empirical correlation for pebble beds by extending the theory applicable to a single sphere. The correlation was supported with a large data base covering a range of porosity from 0.28 to 0.935, Pr from 0.7 to 10^4, and Re/ϵ from 2 to 10^4. Another correlation was recommended by Achenbach (1982a) for $10 < \mathrm{Re} < 10^5$ and $0.36 < \epsilon < 0.42$ in KTA (1982). It was found that Gnielinski's correlation agreed well with the data at high Reynolds numbers; however, it has a tendency to overpredict data at lower Reynolds numbers. KTA's equation matched Gnielinski's predictions at higher Reynolds numbers to within a few percent. Moreover, it also agreed with data obtained at lower Reynolds numbers.

Using mass transfer results of sublimation of naphthalene spheres in air and assuming that the rate of mass transfer depends on a 1/3 power of Schmidt number, Achenbach (1982b) arrived at yet another correlation for $1 < \mathrm{Re} < 10^5$ and Pr = 0.71. This correlation, however, was limited by the restriction on the Prandtl number.

All of the above reported studies were for pebble beds of uniform particles. In many nuclear and geological applications, the heated or cooled particles and the surrounding particles may be of different sizes. At present, no study addressing this concern exists in the literature. The objective of the present work was to provide such information.

Experiments

The experimental apparatus was the same one used by Tung (1988). The main test section consisted of a 101.5 mm i.d. Pyrex tube mounted on an aluminum base. Coolant entered at the bottom and was collected at the top. Flow rates were measured with float-type flowmeters. Two 304 SS test spheres, one at the centerline and one at 30 mm off-center, were located at 1 m above the inlet. Results obtained with both were compared to detect any flow maldistribution. The surrounding porous layer was formed with spherical glass particles. Two sets of experiments were performed with test spheres 6.35 mm and 19 mm in diameter heat by an induction coil outside the tube. The surrounding glass particles were transparent to induction and were not heated. Due to the high frequency (450 kHz), heating was confined to a thin layer on the test spheres. As such, there was no temperature gradient inside the test spheres at steady state.

Experimental Procedures. Prior to each experiment a calibration was made to determine the heat input to the test spheres. It involved applying power to the induction coil and noting the rate of temperature rise of the test spheres. Heat lost to the surrounding glass particles was accounted for by cutting off power and recording the rate of temperature drop of the test spheres. The power input can then be found as the sum of the stored and lost heat. When water was used as coolant, heat transfer coefficients were high and higher power had to be applied to the test spheres. Then, the heat lost was typically on the order of 5–10 percent of the total heat flux. However, when air was used as the test fluid, heat transfer coefficients were quite low and power input had to be reduced to avoid excessive temperatures. Then, the heat lost could be as high as 50 percent of the total heat flux. The heat flux obtained on the 6.35-mm-dia test sphere was also correlated against the rms current through the induction coil. The maximum deviation from a quadratic dependence of heat flux on current was found to be only ± 3 percent. Hence, the calibration procedure outlined above is expected to be repeatable to within ± 3 percent.

Once power calibration had been made, coolant flow through the test section was initiated. The fluid temperature and the temperature of the test spheres was monitored with different thermocouples. At each flow rate, the temperatures were allowed to settle to steady state before being recorded. Fluid properties were evaluated at the mean film temperature. The procedure was repeated for different flow rates while power input to the test spheres was kept at a constant value.

Measurement Uncertainty. As mentioned earlier, the power input to the test sphere was accurate to ± 3 percent. Temperature measurements, however, had an uncertainty of ± 5 percent or $\pm 0.25°C$, whichever was higher. As such, the uncertainty in measured Nusselt number was ± 6 percent. The flow velocity and Reynolds numbers were accurate to ± 5 percent as long as the reading was confined to the midrange of the flowmeter.

Results and Discussion

The observed Nusselt number based on the total heat flux on a 6.35-mm-dia sphere in air are plotted as a function of Reynolds number in Fig. 1. These Nusselt and Reynolds numbers are based on the diameter of the heated sphere and the superficial velocity of the fluid. It is very surprising that data obtained with 1.3, 2.9, and 5.8 mm glass particles nearly overlap each other. This result, however, can be explained by considering the effect of D_p on the local velocity near the heated surface. With increasing D_p, the porosity near the heated surface increases (similar to what is observed near a flat wall in contact with a porous matrix). This results in a lower local velocity due to the larger flow area. Such an increase in local porosity, however, must be accompanied by a diversion of flow from the surrounding porous medium toward the heated surface. As such, the local increase in area will be canceled out by the increase in mass flow resulting in a fairly constant velocity near the heated surface. When the surrounding particles are much larger than the heated sphere ($D_p/D_s \gg 1$) and the particles are packed randomly (as was the case here), it is possible that some glass particles in the first layer did not contact the heated sphere. This, in turn, leads to the formation of large pockets of fluid near the heated sphere. The diversion of flow toward the sphere discussed earlier, however, is not present in this case since the heated sphere is now perceived by the porous medium as a local obstruction. Consequently, the heat transfer coefficient for this case is lowered. From the data shown in Fig. 1 it can be concluded that D_p has little or no effect on the heat transfer coefficient of the heated sphere as long as $D_p/D_s \leq 1$.

A comparison of results obtained with both air and water as the test fluids and $D_p/D_s \leq 1$ with predictions made by using Gnielinski's and KTA's correlations was also carried out in this work. At higher Reynolds numbers, both correlations were found to agree well with the air data. Gnielinski's cor-

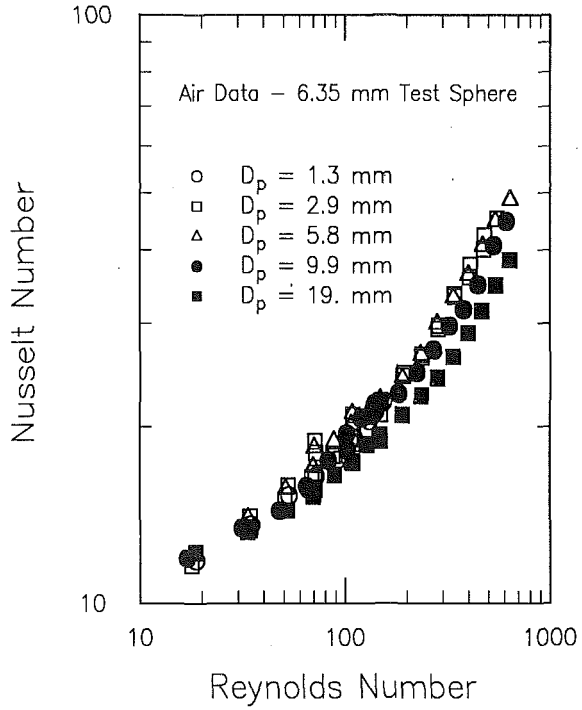

Fig. 1 Measured Nusselt number; 6.35 mm test sphere; air data

relation, however, tends to underpredict the water data at higher Reynolds numbers. Moreover, both correlations appear to overpredict the data obtained at lower Reynolds numbers. This overprediction may have resulted from the lumping of other modes of heat transfer in the development of these correlations. To eliminate this discrepancy, one must isolate the contributions from each component of heat transfer and combine them properly. This is particularly important at lower Reynolds numbers where forced convection is weaker than conduction and natural convection.

Several heat transfer mechanisms such as conduction, radiation, natural convection, and forced convection contribute to the total heat transfer from a sphere embedded in unheated porous media. Since the objective of the present work was to determine the contribution of forced convection only, contributions from other modes of heat transfer has to be eliminated from the total heat flux.

Conduction. In the absence of any other modes of heat transfer, the conductive heat transfer from a sphere is given by $\mathrm{Nu}_{\mathrm{cond}} = 2\, k_{\mathrm{eff}}/k_f$. Theoretical evaluation of the effective thermal conductivity, k_{eff}, is very difficult due to uncertainty in the contact area between the particles, the pressure at such points of contact, and the average thickness of the intervening layer. Generally, upper and lower limits are obtained by arranging solid and fluid volumes in parallel and in series, respectively. In most cases, k_{eff} may be different from that given by either limit. When the ratio k_f/k_p is small, it appears that k_{eff} is approximately equal to that given by the series solution. In the work of Rayleigh, as discussed by Gorring and Churchill (1961), a solution for k_{eff} was obtained for uniform size cylindrical elements. For $k_f/k_p \ll 1$ it yields a k_{eff} closer to the lower limit. Recently, Prasad et al. (1989) reviewed and compared correlations proposed by Kunii and Smith (1960), Zehner and Schlunder (1970), and Krupiczka (1958). They found that, for $k_f/k_p < 1$, all three correlations yielded similar results. Within that limitation, these correlations agreed fairly well with experimental data obtained by Prasad et al. (1989), Kladias (1988), and Combarnous (1970). In this work, Krupiczka's correlation was chosen for its overall accuracy and simplicity. The conductive Nusselt number then can be calculated to be 10 and 2.3 for air and water, respectively. These results are also in close agreement with those obtained by Nozad et al. (1985).

Radiation. Assuming that all the radiative energy emitted by the heated sphere is absorbed by the surrounding fluid and porous medium, the radiative heat flux can be evaluated as $q_{\mathrm{rad}} = \epsilon_s \sigma (T_s^4 - T_f^4)$. At a maximum surface temperature of 500 K, the emissivity ϵ_s is expected to be less than 0.5. For a fluid temperature of 300 K, the maximum q_{rad} is calculated to be 0.3 W/cm^2. This heat flux is about 14 percent of the lowest total heat flux measured in the experiments. In most experiments, especially with water, the contribution of the radiative heat flux is less than 1 percent of the total heat flux.

Natural Convection. Natural convection in packed beds of spheres has been studied experimentally by Karabelas et al. (1971) and Achenbach (1982a). From these studies, it is found that natural convection in packed beds can be described by the same expression as that obtained for a single sphere submerged in a large pool of fluid. Also, these investigators reported that there is little effect of porosity on heat transfer. The correlations proposed by both investigators are very similar to the correlation developed for single spheres: $\mathrm{Nu}_{\mathrm{nat}} = K\mathrm{Ra}^{1/4}$. Karabelas et al. found K to be 0.46 whereas Achenbach recommended a value of 0.4. If K is taken to be 0.46, the worst case in air tests results in a $\mathrm{Nu}_{\mathrm{nat}} = 7$ while the total heat flux for this case corresponds to Nu = 32. As such, the low Reynolds number data in this work are perhaps within the mixed free-forced convection regime. In the worst case (for water) $\mathrm{Nu}_{\mathrm{nat}} = 39$ compared to Nu = 79. Therefore, the effect of natural convection is even more pronounced in water tests.

Forced Convection. Based on previous studies (Churchill, 1977, 1986), the contributions from all modes of heat transfer are assumed to be combined as:

$$\mathrm{Nu} = \mathrm{Nu}_{\mathrm{cond}} + \mathrm{Nu}_{\mathrm{rad}} + (\mathrm{Nu}_{\mathrm{nat}}^3 + \mathrm{Nu}_{\mathrm{forced}}^3)^{1/3} \quad (1)$$

Once the contributions from conduction, radiation, and natural convection are known, the Nusselt number for forced convection can be isolated from the above equation. Figure 2 shows the data for Nusselt numbers based on the total heat flux along with the Nusselt numbers when contributions of conduction, radiation, and natural convection are excluded from the total heat flux. Only the data for $D_p/D_s < 1$ are plotted. The data indicate that, with air as the test fluid, the combined contribution of conduction, radiation, and natural convection at low Reynolds numbers can be much higher than that of forced convection. Thus an appreciable error in the evaluation of forced convective heat transfer is possible if contributions from other mechanisms are not properly accounted for. The Nusselt number dependence on Reynolds number is remarkably similar between the air and water data shown in Fig. 2. The Prandtl number dependence, however, is not quite as clear since only two fluids were used in the experiments. Since KTA's correlation appears to be in good agreement with both air and water data at higher Reynolds number, it is expected that a similar dependence on Prandtl number ($\mathrm{Pr}^{1/2}$) will collapse both air and water data into a single curve. All of the data for forced convection in water and air are plotted in Fig. 3 for $D_p/D_s < 1$. The convective Nusselt numbers have been normalized by $\mathrm{Pr}^{1/2}$. Again, no discernible effect of glass particle size on forced convective heat transfer is found. Moreover, both water and air data have collapsed together and can be correlated to within ±10 percent by:

$$\mathrm{Nu}_{\mathrm{forced}} = 0.29\,\mathrm{Re}^{0.8}\mathrm{Pr}^{1/2};\ 0.7 \le \mathrm{Pr} \le 5;\ \mathrm{Re} \le 2400 \quad (2)$$

Finally, a word of caution must be mentioned regarding the use of a forced convection correlation in conjunction with other

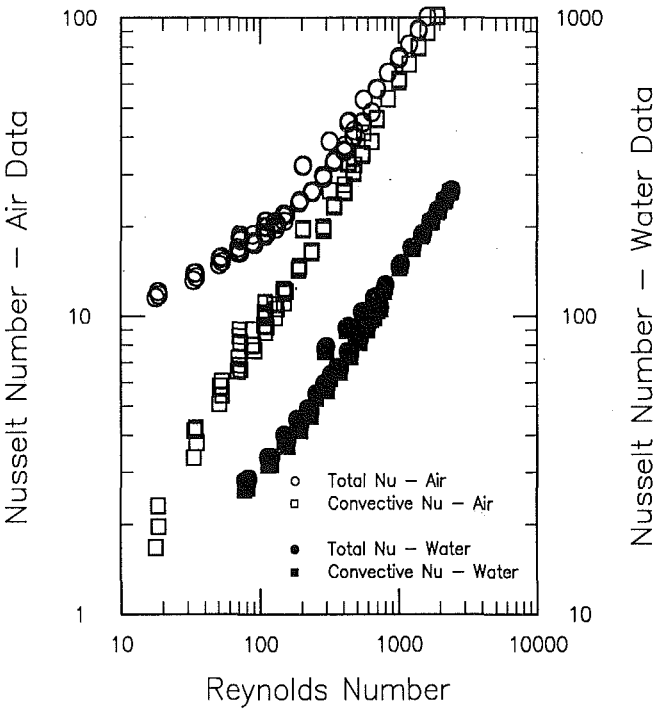

Fig. 2 Comparison of total and convective Nusselt numbers

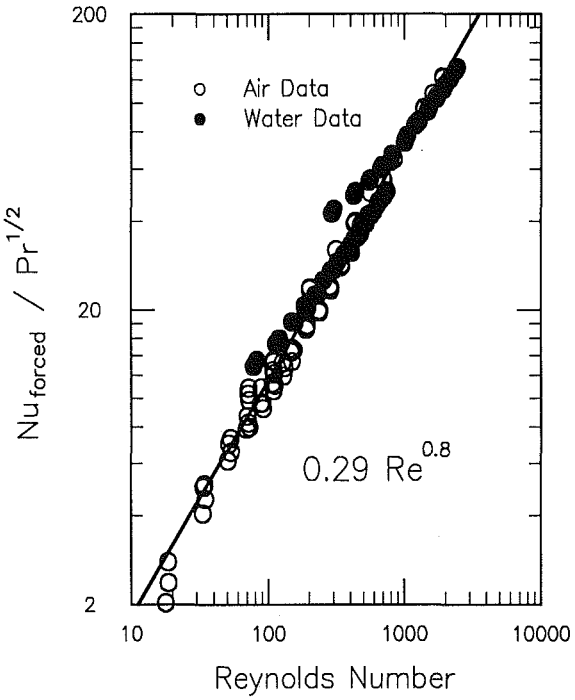

Fig. 3 Forced convection correlation; air and water data

components as shown in Eq. (1). In real applications, not all terms shown in Eq. (1) exist and one must be prudent in deciding which terms to include. For example, in mass transfer applications the radiative component clearly is not involved. On the other hand, when both the porous medium and the body are heated, the conduction term may not exist at all.

Conclusions

Convective heat transfer coefficient from a large heated sphere embedded in unheated porous media is independent of the size of the particles forming the porous media as long as $D_p/D_s < 1$.

The contributions from other modes of heat transfer such as conduction, radiation, and natural convection are significant at lower Reynolds numbers. The total rate of heat transfer, however, can be predicted by an equation such as Eq. (1).

In the range of low to moderate Reynolds numbers, $Re < 2400$, the present correlation Eqs. (1) and (2) may be used for their simplicity. At higher Reynolds numbers, the correlation of KTA is recommended.

References

Achenbach, E., 1982a, "Pressure Drop, Forced Convective, Free Convective and Radiant Heat Transfer of Pebble Beds," *Proceedings of the Fifth Post Accident Heat Removal Information Exchange Meeting*, Karlsruhe, Germany, pp. 204–213.

Achenbach, E., 1982b, "Heat Transfer and Pressure Drop of Pebble Beds up to High Reynolds Number," *Proceedings of the Seventh Int. Heat Transfer Conference*, Vol. 6, pp. 3–8.

Churchill, S. W., 1977, "A Comprehensive Correlating Equation for Laminar Assisting Forced and Free Convection," *AIChE Journal*, Vol. 23, pp. 10–16.

Churchill, S. W., 1986, "Combined Free and Forced Convection Around Immersed Bodies," *Heat Exchanger Design Handbook*, Hemisphere Publishing, New York, Section 2.5.9.

Combarnous, M., 1970, "Convection Naturelle et Convection Mixte en Milieu Poreux," Doctoral Dissertation, University of Paris, France.

Gnielinski, V., 1978, "Gleichungen zur Berechnung des Wärme- und Stoffaustausches in durch Strömten ruhenden Kugelschüttungen bei Mittleren und großen Pecletzahlen," *Verfahrenstechnik 12*, No. 6, pp. 63–66.

Gorring, R. L., and Churchill, S. W., 1961, "Thermal Conductivity of Heterogeneous Materials," *Chemical Engineering Progress*, Vol. 57, No. 7, pp. 53–59.

Karabelas, A. J., Wegner, T. H., and Hanratty, T. J., 1971, "Use of Asymptotic Relations to Correlate Mass Transfer Data in Packed Beds," *Chemical Engineering Science*, Vol. 26, pp. 1581–1589.

Kladias, N., 1988, "Non-Darcy Free Convection in Horizontal Porous Layers," Doctoral Dissertation, Columbia University, New York.

Krupiczka, R., 1958, "Analysis of Thermal Conductivity in Granular Materials," *Int. Chem. Eng.*, Vol. 7, p. 122.

Kunii, D., and Smith, J. M., 1960, "Heat Transfer Characteristics of Porous Rocks," *AIChE Journal*, Vol. 49, p. 71.

Nozad, I., Carbonell, R. G., and Whitaker, S., 1985, "Heat Conduction In Multiphase System—I. Theory and Experiment for Two-Phase Systems," *Chemical Engineering Science*, Vol. 40, pp. 857–863.

Prasad, V., Kladias, N., Bandyopadhaya, A., and Tian, Q., 1989, "Evaluation of Correlations for Stagnant Thermal Conductivity of Liquid-Saturated Porous Beds of Spheres," *Int. J. Heat Mass Transfer*, Vol. 32, No. 9, pp. 1793–1796.

Sicherheitstechnische Regeln des KTA, 1982, KTA 3102-2, Wärmeübergang Kugelhaufen, KTA-DOK-No. 3102/82/1.

Tung, V. X., 1988, "Hydrodynamic and Thermal Aspects of Two-Phase Flow Through Porous Media," PhD Dissertation, University of California, Los Angeles.

Zehner, P., and Schlunder, E. U., 1970, "Thermal Conductivity of Granular Materials at Moderate Temperatures" [in German], *Chemie-Ingr-Tech.*, Vol. 42, p. 933.

Non-Darcian Effects on Mixed Convection in a Vertical Packed-Sphere Annulus

C. Y. Choi[1] and F. A. Kulacki[2]

Nomenclature

d = average particle diameter, m
D = gap width = $r_o - r_i$, m

[1]Department of Aerospace and Mechanical Engineering, The University of Arizona, Tucson, AZ 85721.

[2]Department of Mechanical Engineering, Colorado State University, Fort Collins, CO 80523.

Contributed by the Heat Transfer Division of THE AMERICAN SOCIETY OF MECHANICAL ENGINEERS. Manuscript received by the Heat Transfer Division September 1991; revision received May 1992. Keywords: Geophysical Heat Transfer, Mixed Convection, Porous Media. Technical Editor: R. Viskanta.

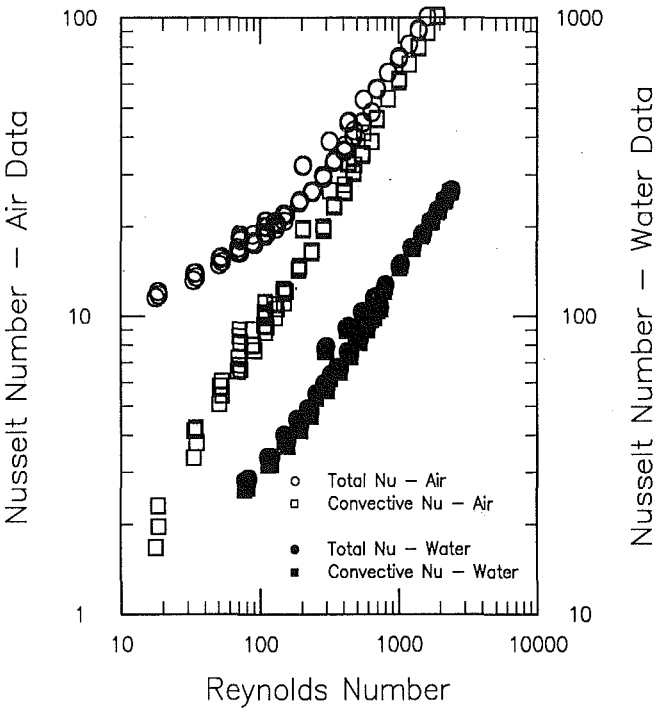

Fig. 2 Comparison of total and convective Nusselt numbers

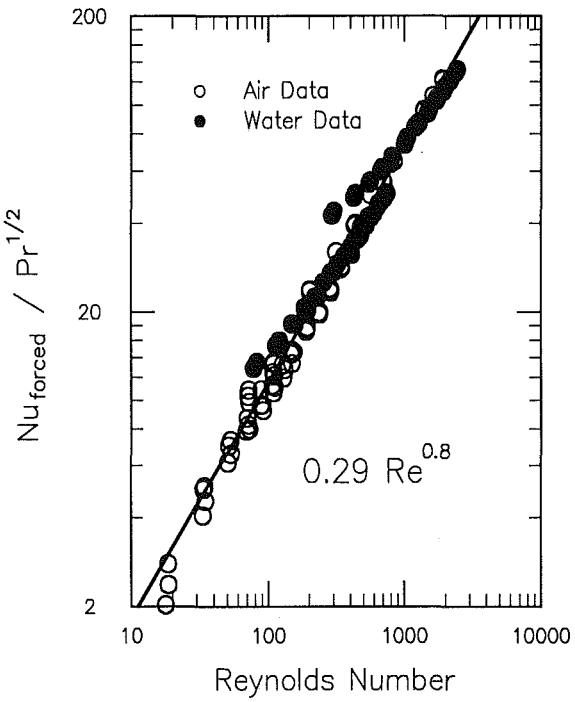

Fig. 3 Forced convection correlation; air and water data

components as shown in Eq. (1). In real applications, not all terms shown in Eq. (1) exist and one must be prudent in deciding which terms to include. For example, in mass transfer applications the radiative component clearly is not involved. On the other hand, when both the porous medium and the body are heated, the conduction term may not exist at all.

Conclusions

Convective heat transfer coefficient from a large heated sphere embedded in unheated porous media is independent of the size of the particles forming the porous media as long as $D_p/D_s < 1$.

The contributions from other modes of heat transfer such as conduction, radiation, and natural convection are significant at lower Reynolds numbers. The total rate of heat transfer, however, can be predicted by an equation such as Eq. (1).

In the range of low to moderate Reynolds numbers, $Re < 2400$, the present correlation Eqs. (1) and (2) may be used for their simplicity. At higher Reynolds numbers, the correlation of KTA is recommended.

References

Achenbach, E., 1982a, "Pressure Drop, Forced Convective, Free Convective and Radiant Heat Transfer of Pebble Beds," *Proceedings of the Fifth Post Accident Heat Removal Information Exchange Meeting*, Karlsruhe, Germany, pp. 204–213.

Achenbach, E., 1982b, "Heat Transfer and Pressure Drop of Pebble Beds up to High Reynolds Number," *Proceedings of the Seventh Int. Heat Transfer Conference*, Vol. 6, pp. 3–8.

Churchill, S. W., 1977, "A Comprehensive Correlating Equation for Laminar Assisting Forced and Free Convection," *AIChE Journal*, Vol. 23, pp. 10–16.

Churchill, S. W., 1986, "Combined Free and Forced Convection Around Immersed Bodies," *Heat Exchanger Design Handbook*, Hemisphere Publishing, New York, Section 2.5.9.

Combarnous, M., 1970, "Convection Naturelle et Convection Mixte en Milieu Poreux," Doctoral Dissertation, University of Paris, France.

Gnielinski, V., 1978, "Gleichungen zur Berechnung des Wärme- und Stoffaustausches in durch Strömten ruhenden Kugelschüttungen bei Mittleren und großen Pecletzahlen," *Verfahrenstechnik 12*, No. 6, pp. 63–66.

Gorring, R. L., and Churchill, S. W., 1961, "Thermal Conductivity of Heterogeneous Materials," *Chemical Engineering Progress*, Vol. 57, No. 7, pp. 53–59.

Karabelas, A. J., Wegner, T. H., and Hanratty, T. J., 1971, "Use of Asymptotic Relations to Correlate Mass Transfer Data in Packed Beds," *Chemical Engineering Science*, Vol. 26, pp. 1581–1589.

Kladias, N., 1988, "Non-Darcy Free Convection in Horizontal Porous Layers," Doctoral Dissertation, Columbia University, New York.

Krupiczka, R., 1958, "Analysis of Thermal Conductivity in Granular Materials," *Int. Chem. Eng.*, Vol. 7, p. 122.

Kunii, D., and Smith, J. M., 1960, "Heat Transfer Characteristics of Porous Rocks," *AIChE Journal*, Vol. 49, p. 71.

Nozad, I., Carbonell, R. G., and Whitaker, S., 1985, "Heat Conduction In Multiphase System—I. Theory and Experiment for Two-Phase Systems," *Chemical Engineering Science*, Vol. 40, pp. 857–863.

Prasad, V., Kladias, N., Bandyopadhaya, A., and Tian, Q., 1989, "Evaluation of Correlations for Stagnant Thermal Conductivity of Liquid-Saturated Porous Beds of Spheres," *Int. J. Heat Mass Transfer*, Vol. 32, No. 9, pp. 1793–1796.

Sicherheitstechnische Regeln des KTA, 1982, KTA 3102-2, Wärmeübergang Kugelhaufen, KTA-DOK-No. 3102/82/1.

Tung, V. X., 1988, "Hydrodynamic and Thermal Aspects of Two-Phase Flow Through Porous Media," PhD Dissertation, University of California, Los Angeles.

Zehner, P., and Schlunder, E. U., 1970, "Thermal Conductivity of Granular Materials at Moderate Temperatures" [in German], *Chemie-Ingr-Tech.*, Vol. 42, p. 933.

Non-Darcian Effects on Mixed Convection in a Vertical Packed-Sphere Annulus

C. Y. Choi[1] and F. A. Kulacki[2]

Nomenclature

d = average particle diameter, m
D = gap width = $r_o - r_i$, m

[1]Department of Aerospace and Mechanical Engineering, The University of Arizona, Tucson, AZ 85721.

[2]Department of Mechanical Engineering, Colorado State University, Fort Collins, CO 80523.

Contributed by the Heat Transfer Division of THE AMERICAN SOCIETY OF MECHANICAL ENGINEERS. Manuscript received by the Heat Transfer Division September 1991; revision received May 1992. Keywords: Geophysical Heat Transfer, Mixed Convection, Porous Media. Technical Editor: R. Viskanta.

Da = Darcy number = $K/D^2 = \epsilon^3\eta^2/\{150(1-\epsilon)^2\}$
F = Forchheimer number = $1.75\,\eta/\{150(1-\epsilon)\}$
K = permeability of porous medium, m^2
Nu = overall Nusselt number
Pe = Peclet number = VD/α
R, Z = dimensionless coordinates
Ra = Rayleigh number = $g\beta kD^2q/\alpha\nu k_m$
U, V = R- and Z-direction dimensionless velocity
γ = radius ratio parameter = D/r_i
ϵ = porosity
η = dimensionless particle diameter = d/D
θ = dimensionless temperature = $(T - T_c)/(qD/k)$
ψ = stream function
ω = dimensionless vorticity = $\partial V/\partial R - \partial U/\partial Z$

Introduction

The study of non-Darcy effects in a porous medium attracted a great deal of interest from many investigators in the previous decade. Both inertia and boundary effects were examined analytically by Vafai and Tien (1981) and Plumb and Huenefeld (1981). The results they obtained indicate that these effects decrease the heat transfer rate significantly. Raganathan and Viskanta (1984) also investigated these effects on natural convection boundary layer flow along a vertical surface with low-blowing velocity perpendicular to the boundary. A series of interesting non-Darcy natural convection studies was also reported by Tong and Subramanian (1985), Beckermann et al. (1986), Prasad and Tuntomo (1987), Lauriat and Prasad (1987, 1989), and Parang and Keyhani (1987). More recently, a numerical study of variable porosity effects on natural convection in a cavity has been performed by David et al. (1989, 1991). They reported that a high value of the dimensionless sphere diameter leads to wall channeling, which results in an increase in heat transfer rate. All the abovementioned studies show that care should be exercised near the boundary and in high-porosity media since the non-Darcy effects are expected to become significant for convective transport.

A literature survey, however, indicates that very few results have been reported for the case of combined natural and forced convection based on either the Darcy or non-Darcy model. Without consideration of the non-Darcy effects, Reda studied opposing mixed convection in an annulus (1988). Recently, the present authors (1992) investigated the effects of external flows on the buoyancy-induced convection in vertical porous annuli as a first step toward the complete understanding of this transport phenomenon. Based on Darcy's law, the numerical data are correlated by the parameter groups $Nu/Pe^{1/2}$ and $Ra/Pe^{3/2}$. The comparison of their numerical and experimental results shows good agreement. Particularly important for opposing flow, the decrease of the Nusselt number in a limited range of the Peclet number has been experimentally identified.

In this study, we consider both aiding and opposing external flows on the buoyancy-induced convection in a vertical porous annulus, taking both viscous and inertial effects into account. Numerical calculations cover a wide range of Rayleigh and Peclet numbers ($10 \le Ra \le 200$ and $0 \le Pe \le 200$) for a fixed radius ratio parameter ($\gamma = 1$). The radius ratio parameter is chosen for the present study because the Darcy results for this particular case have been experimentally verified by the present authors (1992). The primary purpose of the study is to investigate the effects of Brinkman and Forchheimer terms in the mixed convection regime.

Mathematical Formulation and Numerical Method

The geometry of the problem under consideration is a vertical annulus filled with a saturated, homogeneous, and isotropic porous medium. As shown in Fig. 1, a pressure-driven

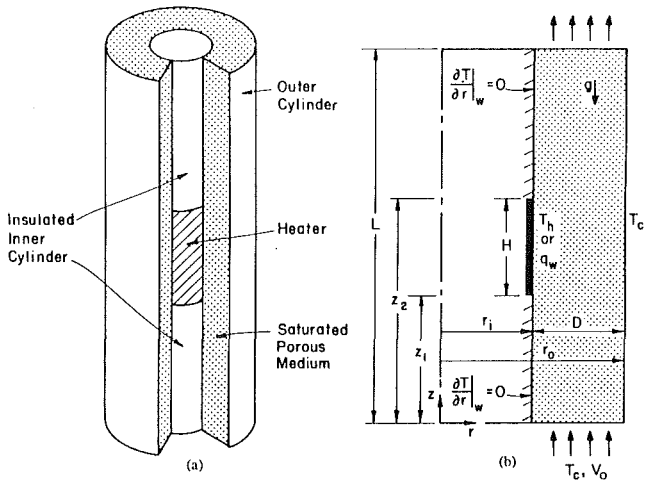

Fig. 1 A vertical packed-sphere annulus with a finite heat source of a length $H = D$: (*a*) schematic figure, (*b*) two-dimensional model with aiding external flow

external flow, either aiding or opposing the buoyancy-induced flow, is maintained through the vertical channel, and the inlet fluid temperature is constant across the cross section. Throughout the present study, the heater length, H, is the same as the gap width, D, and the radius ratio parameter, $\gamma = D/r_i$, is fixed at unity. The steady-state, two-dimensional governing equations for isotropic, homogeneous, fluid-saturated porous media based on Darcy's law with the Brinkman–Forchheimer modification can be written in the following dimensionless form:

$$\frac{\partial}{\partial R}\left(\frac{1}{\gamma R+1}\frac{\partial\psi}{\partial R}\right)+\frac{1}{\gamma R+1}\frac{\partial^2\psi}{\partial^2 R}=-\omega, \tag{1}$$

$$\frac{\epsilon}{\mathrm{Da}}\omega-\left(\frac{\partial^2\omega}{\partial R^2}+\frac{\gamma}{\gamma R+1}\frac{\partial\omega}{\partial R}+\frac{\partial^2\omega}{\partial Z^2}\right)+\frac{\gamma^2}{(\gamma R+1)^2}\omega-\frac{\mathrm{Ra}\cdot\epsilon}{\mathrm{Pe}\cdot\mathrm{Da}}\frac{\partial\theta}{\partial R}$$
$$+\frac{\mathrm{F}\cdot\epsilon}{\mathrm{Pr}\cdot\mathrm{Da}}\left[\frac{1}{\sqrt{V^2+U^2}}\left\{UV\left(\frac{\partial U}{\partial R}-\frac{\partial V}{\partial Z}\right)+V^2\frac{\partial V}{\partial R}-U^2\frac{\partial U}{\partial R}\right\}+\omega\cdot\sqrt{V^2+U^2}\right]=0, \tag{2}$$

$$\frac{\partial}{\partial R}\left(\theta\frac{\partial\psi}{\partial Z}\right)-\frac{\partial}{\partial Z}\left(\theta\frac{\partial\psi}{\partial R}\right)=\frac{1}{\mathrm{Pe}}\left[\frac{\partial}{\partial R}\left\{(1+\gamma R)\frac{\partial\theta}{\partial R}\right\}+\frac{\partial}{\partial Z}\left\{(1+\gamma R)\frac{\partial\theta}{\partial Z}\right\}\right]. \tag{3}$$

The governing Eqs. (2) and (3) can be reduced to those based on Darcy's law (Choi et al., 1992) as $Da \to 0$ and $F \to 0$. The Darcy (Da) and the Forchheimer (F) numbers are respectively presented by the well-known forms given by Ergun (1952). Since Da and F are interrelated as a function of η and ϵ, they should not be estimated individually. For the present study, computations are carried out for $0.01 \le \eta \le 0.5$ and $0.1 \le \epsilon \le 0.9$. In these ranges, some cases require specially structured porous media. Therefore, it is hoped that the present study covers all physically possible cases including some extreme cases.

Since the viscous terms are accounted for in the Brinkman term, the no-slip conditions should hold formally. For the vorticity boundary condition along the walls, three different forms (Thom's, Jensen's, and Wood's) are examined (Roache, 1982). Through a series of computational experiments, it is found that Thom's as well as Wood's forms produce stable

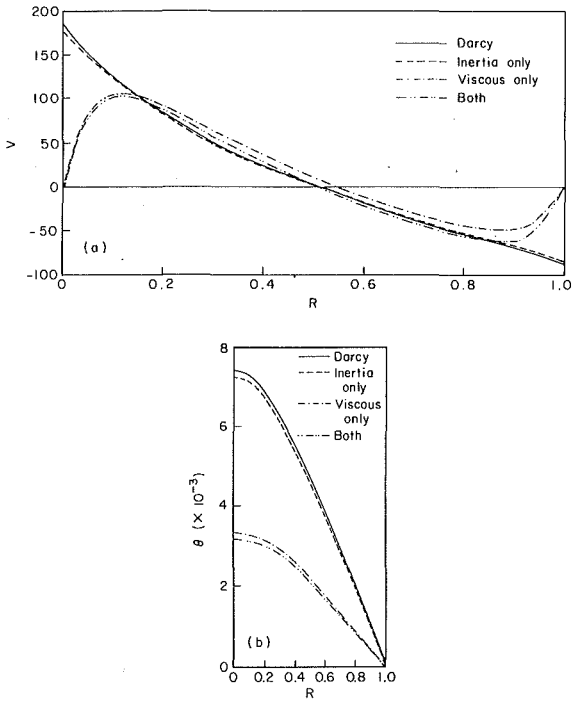

Fig. 2 Effects of the inertial and viscous terms at the top of the heater (Ra = 100, Pe = 0.1, aiding flow); (*a*) dimensionless vertical velocity, (*b*) dimensionless temperature when $\eta = 0.2$ and $\epsilon = 0.7$

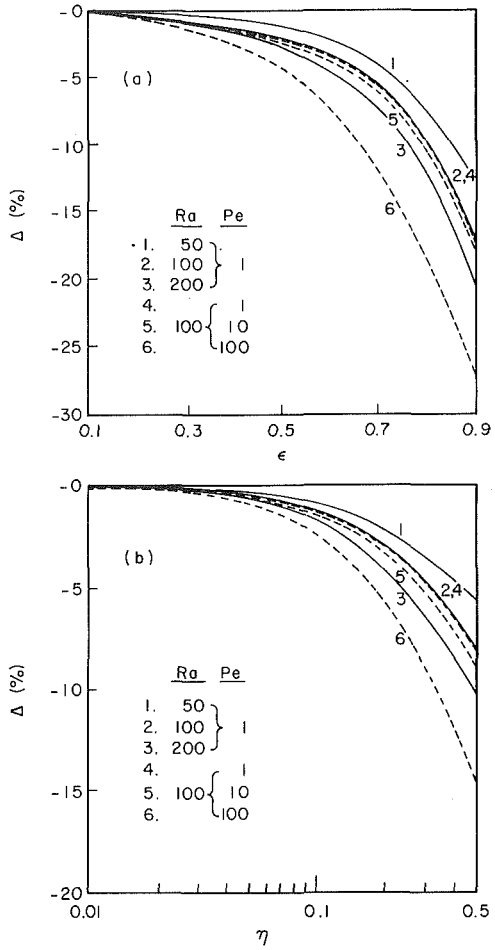

Fig. 3 Effects of the Rayleigh and Peclet numbers on Δ; (*a*) $0.01 \leq \eta \leq 0.5$ at $\epsilon = 0.4$, (*b*) $0.1 \leq \epsilon \leq 0.9$, $\eta = 0.1$.

solutions, while Jensen's formula gives unstable solutions for all cases. It is also observed that the results using the first-order Thom's formula and the second-order Wood's formula are essentially the same. For the present study, therefore, Thom's formula has been used. The inlet and exit boundary conditions for the vorticity can be written in the following mathematical forms: (*i*) $\omega = 0$ at the inlet, (*ii*) $\partial\omega/\partial Z = 0$ at the exit.

The coupled and nonlinear governing partial equations were solved using the upwind finite difference scheme. Based on numerical experiments, the calculation procedure was repeated until the variations of ψ and θ were less than 10^{-4} for Pe $\leq$ 10 and 10^{-5} for Pe $>$ 10 between two successive iterations. To improve the convergence of iteration, both ψ and θ were over-relaxed when Pe $<$ 20. Unlike the previous study (Choi and Kulacki, 1992), steep velocity gradients are expected near the wall due to the no-slip boundary conditions. Therefore, a nonuniform grid was employed with 26 grid points normal to the wall and 401 grid points in vertical direction. The improvement in the prediction of temperature and flow fields by further refinement is negligible; e.g., a 31 $\times$ 626 nonuniform mesh changes the Nusselt numbers and the maximum stream functions less than 1 percent. A fine mesh was used near the walls and the heat source in particular, and a relatively coarse mesh was used away from the heater in the Z direction. The Forchheimer term has been split into two parts, and the first part was treated as a source while the remaining part was combined with the Darcy and the viscous terms. Computations were performed on a CYBER 205 supercomputer after a vectorization of algorithm.

Results

Figures 2(*a*, *b*) demonstrate the influence of the individual and combined inertial and viscous terms on the velocity and temperature profiles. It is clear that the viscous term contributes most to the deviation from the result obtained when Darcy's model is used, while the effect of the inertial term is negligible. Further numerical calculations for the various values of η, ϵ, Ra, and Pe indicate that the viscous term is a dominant factor for the significant change of the velocity and temperature profiles. Consequently, the overall Nusselt number on the heat source changes noticeably as η or ϵ increases due to the viscous term. The reduction of the overall Nusselt number as $\eta \rightarrow 0.5$ or $\epsilon \rightarrow 0.9$ is always observed in the natural and forced convection regimes. The percentage deviation, Δ,

$$\Delta = \frac{(\mathrm{Nu})_{\text{non-Darcy}} - (\mathrm{Nu})_{\text{Darcy}}}{(\mathrm{Nu})_{\text{Darcy}}} \times 100 \text{ (percent)}, \qquad (4)$$

which estimates the change of the Nusselt number by including the inertial and the viscous terms, is proposed as a measure of the "correctness" of the solution obtained when the Darcy model is used. As shown in Figs. 3(*a*, *b*), it is found that the value of Δ decreases as $\eta \rightarrow 0.5$ or $\epsilon \rightarrow 0.9$. The figures also indicate that the change of Δ is more pronounced for higher Ra and Pe. These graphs and further numerical calculations indicate that the Darcy model can be safely used without producing unacceptable error (3 percent or less) when $\eta \leq 0.05$ and $\epsilon \leq 0.4$; the corresponding Darcy and Forchheimer numbers are approximately 10^{-6} and 10^{-4}, respectively. Additional results, such as the streamlines, velocity, and temperature profiles at different Ra and Pe, are omitted for brevity and available from the reference by Choi (1990).

Beckermann et al. (1986) and Lauriat and Prasad (1989) systematically studied the effects of Brinkman's and Forchheimer's extensions on the Nusselt number in a square cavity as shown in Table 1. The table indicates that the reduction in

Table 1 The negative values of the percentage of deviation, $-\Delta$, due to the inertial and viscous terms in a square cavity (reported by Beckermann et al., 1986, and Lauriat et al., 1989*) when Ra = 10^4

Da	F/Pr	Inertial term only	Viscous term only	Both
10^{-1}	0.174	81.7	90.3 (90.4*)	91.0 (91.1*)
10^{-1}	17.4	95.5	90.3 (90.4*)	96.6 (96.0*)
10^{-4}	5.5×10^{-3}	56.6	48.9 (47.4*)	57.9 (62.4*)
10^{-4}	0.55	81.0	48.9 (47.4*)	81.3 (87.3*)
10^{-8}	5.5×10^{-5}	3.0	0.0 (2.3*)	3.0 (9.4*)
10^{-8}	5.5×10^{-3}	25.7	0.0 (2.3*)	25.7 (-)

Table 2 The negative values of the percentage of deviation, $-\Delta$, due to the inertial and viscous effects

	Pe	Da	F/Pr	Ra 100	200	500	1000	5000
Lauriat *et al.*	-	10^{-6}	-	1.0	1.2	1.4	1.5	2.0
(1987): viscous	-	10^{-4}	-	8.1	10.6	16.9	22.9	35.1
term only	-	10^{-2}	-	44.0	53.7	62.7	69.2	77.9
Prasad *et al.*	-	-	10^{-4}	-	-	1.1	6.2	-
(1987): inertial	-	-	10^{-3}	-	-	8.1	27.0	-
term only	-	-	10^{-2}	-	-	31.4	55.0	-
	-	-	10^{-1}	-	-	58.3	75.6	-
Present: both	0.01	10^{-3}	7.8×10^{-3}	10.5	13.4	-	-	-
terms (aiding	20.0	10^{-3}	7.8×10^{-3}	13.0	14.8	-	-	-
flow)	200.0	10^{-3}	7.8×10^{-3}	22.2	22.3	-	-	-

the Nusselt number is most pronounced when Da and/or F/Pr is 10^{-1} or greater, while there are no significant effects of the non-Darcy terms when Da $< 10^{-8}$ and F/Pr $< 5.5 \times 10^{-5}$. It should be further noted that Lauriat and Prasad (1989) demonstrated the importance of the conductivity and aspect ratios.

For the different geometries and boundary conditions, several studies reported (Lauriat and Prasad, 1987; Tong and Subramanian, 1985) that the Brinkman term can be neglected without an appreciable loss of accuracy when the Darcy term is less than approximately 10^{-5}. It should be further noted that the reported criteria may vary depending on the nature of each problem, the characteristic length, and the upper limit of the Rayleigh number. Prasad and Tuntomo (1987) also investigated the inertial effects on natural convection in a vertical porous cavity. The values of the percentage of deviation are tabulated in Table 2 from the results by Lauriat and Prasad (1987), Prasad and Tuntomo (1987), and the present study. The table indicates that the overall Nusselt number decreases as either Ra or Pe increases. Hence, based on the previous reports, the Brinkman and the Forchheimer terms should be carefully examined at the high Rayleigh or Peclet number although Da and F are relatively small.

In the previous study by the present authors (1992), a deviation of experimental data from the numerical results based on Darcy's model was found. The non-Darcy effects had a negligible impact on the discrepancy, which was briefly explained in conjunction with the Reynolds number based on the permeability. The porosity and dimensionless particle diameter of the experiment are respectively 0.3811 and 0.0394 (i.e., Da = 1.4932×10^{-6} and F/Pr = 8.0581×10^{-5}), and Figs. 3(*a*, *b*) indirectly show little influence of non-Darcy terms for the reported case. To verify this precisely, a set of numerical calculations including non-Darcy terms has been performed and listed in the publication by Choi (1990); as an example, Nu_{Darcy} and $Nu_{non\text{-}Darcy}$ are 12.89 and 12.86 when Ra = 197.66 and Pe = 100.88 for opposing flow. This confirms that the viscous and inertial effects are not the primary factor for the deviation of the experimental data.

To investigate the effect of the non-Darcy terms in the mixed convection regime, a series of calculations has been carried out for a selected case of $\eta = 0.2$ and $\epsilon = 0.7$ (Da = 1.0663×10^{-3} and F = 7.7778×10^{-3}). For aiding flow, as we observed in Figs. 3(*a*), 3(*b*), and 4, a reduction of the Nusselt number is more pronounced as either Ra or Re increases. Such a trend is consistent with the results for the aiding case by Parang and Keyhani (1987); i.e., their report shows a considerable reduction in the Nusselt number as GrDa/Re increases from 1 to 10 when $Da/\epsilon > 10^{-4}$.

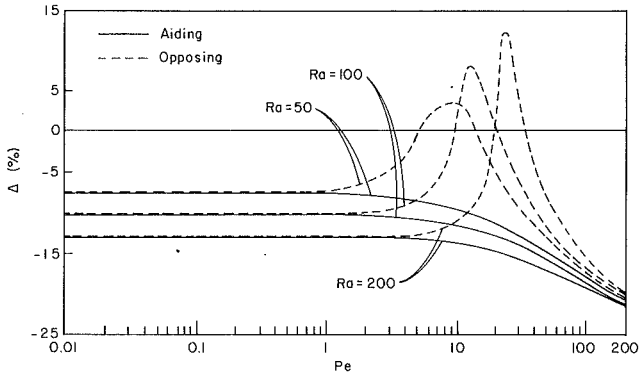

Fig. 4 The percentage of deviation, Δ, as a function of Rayleigh number and Peclet numbers when $\eta = 0.2$ and $\epsilon = 0.7$

For opposing flow, however, Fig. 4 shows that the Nusselt number increases substantially due to the non-Darcy terms in the region of mixed convection. As discussed in the previous paper (Choi and Kulacki, 1992), the Nusselt number at a given Rayleigh number reaches a minimum point in the mixed convection regime for the opposing flow, and the minimum point occurs at the lower Rayleigh number due to the non-Darcy terms. Figure 4 indicates that the Nusselt numbers for the non-Darcy model are larger than those for the Darcy model as the Peclet number increases; then, they fall below Darcy values as Pe becomes large.

Conclusion

A numerical study of combined free and forced convection in a vertical porous annulus has been performed by using the Darcy-Brinkman-Forchheimer equation of motion. It is found that the viscous term changes the flow and temperature fields significantly near the boundaries of the highly porous media, while the inertia term has a negligible effect on the fields. For both aiding and opposing flows, the reduction of the Nusselt number is pronounced as the Rayleigh number increases in the natural convection regime, and as the Peclet number increases in the forced convection regime. For opposing flows in the mixed convection region, however, the influence of the non-Darcy terms is not simple because of the interaction between buoyancy-induced upflow and the external downflow. Contrary to the previously obtained results of other investigators, the increases of the Nusselt number are observed due to the viscous and inertia terms in a certain range of the Peclet number.

References

Beckermann, C., Viskanta, R., and Ramadhyani, S., 1986, "Numerical Study of Non-Darcian Natural Convection in a Vertical Enclosure Filled With a Porous Medium," *Numerical Heat Transfer*, Vol. 10, pp. 557-570.

Choi, C. Y., 1990, "Mixed Convection in Vertical Porous Annuli," Ph.D Dissertation, Colorado State University, Fort Collins, CO.

Choi, C. Y., and Kulacki, F. A., 1992, "Mixed Convection Through Vertical Porous Annuli Locally Heated From Inner Cylinder," ASME JOURNAL OF HEAT TRANSFER, Vol. 114, pp. 143-151.

David, E., Lauriat, G., and Prasad, V., 1989, "Non-Darcy Natural Convection in Packed-Sphere Beds Between Concentric Vertical Cylinders," *AIChE Symposium Series*, Vol. 85, pp. 90-95.

David, E., Lauriat, G., and Cheng, P., 1991, "A Numerical Solution of Variable Porosity Effects on Natural Convection in a Packed-Sphere Cavity," ASME JOURNAL OF HEAT TRANSFER, Vol. 113, pp. 391-399.

Ergun, S., 1952, "Fluid Flow Through Packed Bed Columns," *Chemical Engineering Progress*, Vol. 48, pp. 89-94.

Gosman, A. D., Pun, W. M., Runchal, A. K., Spalding, D. B., and Wolfstein, M., 1969, *Heat and Mass Transfer in Recirculating Flows*, Academic Press, New York.

Lauriat, G., and Prasad, V., 1987, "Numerical Convection in a Vertical Porous Cavity—A Numerical Study of Brinkman-Extended Darcy Formulation," ASME JOURNAL OF HEAT TRANSFER, Vol. 109, pp. 688-696.

Lauriat, G., and Prasad, V., 1989, "Non-Darcian Effects on Natural Convection in a Vertical Porous Enclosure," *International Journal of Heat and Mass Transfer*, Vol. 32, No. 11, pp. 2135-2148.

Parang, M., and Keyhani, M., 1987, "Boundary Effects in Laminar Mixed Convection Flow Through Annular Porous Medium," ASME JOURNAL OF HEAT TRANSFER, Vol. 109, pp. 1039-1041.

Plumb, O. A., and Huenefeld, J. C., 1981, "Non-Darcy Natural Convection From Heated Surfaces in Saturated Porous Media," *International Journal of Heat and Mass Transfer*, Vol. 24, pp. 765-758.

Prasad, V., and Tuntomo, A., 1987, "Inertia Effects on Natural Convection in a Vertical Porous Cavity," *Numerical Heat Transfer*, Vol. 11, pp. 295-320.

Raganathan, P., and Viskanta, R., 1984, "Mixed Convection Boundary-Layer Flow Along a Vertical Surface in a Porous Medium," *Numerical Heat Transfer*, Vol. 109, pp. 305-317.

Reda, D. C., 1988, "Mixed Convection in a Liquid-Saturated Porous Medium," ASME JOURNAL OF HEAT TRANSFER, Vol. 110, pp. 147-154.

Roache, P. J., 1982, *Computational Fluid Dynamics*, Hermosa Publishers, Albuquerque, NM.

Tong, T. W., and Subramanian, E., 1985, "A Boundary Model for Natural Convection in Vertical Porous Enclosure—Use of the Brinkman-Extended Darcy Model," *International Journal of Heat and Mass Transfer*, Vol. 28, pp. 563-571.

Vafai, K., and Tien, C. L., 1981, "Boundary and Inertia Effects on Flow and Heat Transfer in Porous Media," *International Journal of Heat and Mass Transfer*, Vol. 24, pp. 195-203.

A Similarity Solution for Free Convection From a Point Heat Source Embedded in a Non-Newtonian Fluid-Saturated Porous Medium

A. Nakayama[1]

Nomenclature

C_p = specific heat of fluid at constant pressure
f = dimensionless stream function
g = acceleration due to gravity
k = equivalent thermal conductivity of the fluid-saturated porous medium
K^* = intrinsic permeability of the porous media for flow of power-law fluids
n = power-law index of the inelastic non-Newtonian fluid
q^* = strength of point heat source
Ra_x = local Rayleigh number based on q^* defined in Eq. (11)
T = temperature
T_e = ambient constant temperature
u, v = Darcian or superficial velocity components
x, r = cylindrical coordinates
α = equivalent thermal diffusivity of the fluid-saturated porous medium
β = expansion coefficient of the fluid
δ = diameter of plume
ϵ = porosity of porous medium
η = similarity variable defined in Eq. (14)
θ = dimensionless temperature difference
μ^* = fluid consistency of the inelastic non-Newtonian power-law fluid
ρ = density of the fluid
ψ = stream function

[1]Dept. of Energy and Mechanical Engineering, Shizuoka University, 3-5-1 Johoku, Hamamatsu, 432 Japan.

Contributed by the Heat Transfer Division of THE AMERICAN SOCIETY OF MECHANICAL ENGINEERS. Manuscript received by the Heat Transfer Division December 3, 1991; revision received June 18, 1992. Keywords: Natural Convection, Non-Newtonian Flows and Systems, Porous Media. Technical Editor: R. Viskanta.

Introduction

Convection problems associated with concentrated heat sources within fluid-saturated porous media are of great practical significance, for there are a number of practical applications in geophysics and energy-related problems, such as recovery of petroleum resources, geophysical flows, cooling of underground electric cables, and environmental impact of buried heat generating waste. The phenomena can be classified into two distinct regimes, namely, the low Rayleigh number regime where the temperature distribution is primarily due to thermal diffusion, and the high Rayleigh number regime where the flow driven by the heat source is a slender vertical plume such that the boundary layer approximation holds. The problems in the low Rayleigh number regime were tackled by Bejan (1978), Hickox (1981), and Nield and White (1982), while Yih (1965), Cheng (1978), Masuoka et al. (1986), Ingham (1988), and Lai (1990) followed Wooding (1963) who exploited the boundary layer approximation for obtaining similarity solutions for buoyant plumes in the high Rayleigh number regime. Hickox and Watts (1980) numerically obtained the results for arbitrary values of Rayleigh number, for both the infinite and semi-infinite regions.

However, all these previous studies assume that the fluid is Newtonian. Needless to say, a number of industrially important fluids, including fossile fuels, which may saturate underground beds, exhibit non-Newtonian behavior. Despite its importance in practical engineering applications, only a limited number of studies have been reported on free convection in non-Newtonian fluid-saturated porous medium. Chen and Chen (1988a, 1988b) solved the boundary layer equations for free convection of non-Newtonian fluids over a vertical flat plate, a horizontal circular cylinder and a sphere in porous media, using the power-law model, proposed by Christopher and Middleman (1965), while a general similarity transformation procedure has been proposed by Nakayama and Koyama (1991) to find a class of possible similarity solutions for free convective flow of non-Newtonian fluids over a non-isothermal body of arbitrary shape in porous media. However, the simplest and perhaps most important free convection configuration, namely, a buoyant plume above a point heat source in a non-Newtonian fluid-saturated porous medium, has not been treated yet in the literature.

In this note, a boundary layer analysis is presented for free convection from a point heat source embedded in a porous medium saturated with a non-Newtonian power-law fluid. The governing equations are found to possess a similarity solution for an arbitrary value of the power-law index. Closed-form solutions are presented for both flow and temperature fields, and the effects of pseudoplasticity on the plumes are examined.

Analysis

Consider the problem of a plume rising from a point source of strength q^* in a non-Newtonian fluid-saturated porous medium, as illustrated in Fig. 1. When the heat source is sufficiently strong, the streamwise thermal diffusion above the heat source may well be neglected so that the boundary layer approximation holds.

The equation of continuity in terms of the apparent (Dar-

Lauriat, G., and Prasad, V., 1987, "Numerical Convection in a Vertical Porous Cavity—A Numerical Study of Brinkman-Extended Darcy Formulation," ASME JOURNAL OF HEAT TRANSFER, Vol. 109, pp. 688–696.

Lauriat, G., and Prasad, V., 1989, "Non-Darcian Effects on Natural Convection in a Vertical Porous Enclosure," *International Journal of Heat and Mass Transfer*, Vol. 32, No. 11, pp. 2135–2148.

Parang, M., and Keyhani, M., 1987, "Boundary Effects in Laminar Mixed Convection Flow Through Annular Porous Medium," ASME JOURNAL OF HEAT TRANSFER, Vol. 109, pp. 1039–1041.

Plumb, O. A., and Huenefeld, J. C., 1981, "Non-Darcy Natural Convection From Heated Surfaces in Saturated Porous Media," *International Journal of Heat and Mass Transfer*, Vol. 24, pp. 765–758.

Prasad, V., and Tuntomo, A., 1987, "Inertia Effects on Natural Convection in a Vertical Porous Cavity," *Numerical Heat Transfer*, Vol. 11, pp. 295–320.

Raganathan, P., and Viskanta, R., 1984, "Mixed Convection Boundary-Layer Flow Along a Vertical Surface in a Porous Medium," *Numerical Heat Transfer*, Vol. 109, pp. 305–317.

Reda, D. C., 1988, "Mixed Convection in a Liquid-Saturated Porous Medium," ASME JOURNAL OF HEAT TRANSFER, Vol. 110, pp. 147–154.

Roache, P. J., 1982, *Computational Fluid Dynamics*, Hermosa Publishers, Albuquerque, NM.

Tong, T. W., and Subramanian, E., 1985, "A Boundary Model for Natural Convection in Vertical Porous Enclosure—Use of the Brinkman-Extended Darcy Model," *International Journal of Heat and Mass Transfer*, Vol. 28, pp. 563–571.

Vafai, K., and Tien, C. L., 1981, "Boundary and Inertia Effects on Flow and Heat Transfer in Porous Media," *International Journal of Heat and Mass Transfer*, Vol. 24, pp. 195–203.

A Similarity Solution for Free Convection From a Point Heat Source Embedded in a Non-Newtonian Fluid-Saturated Porous Medium

A. Nakayama[1]

Nomenclature

C_p = specific heat of fluid at constant pressure
f = dimensionless stream function
g = acceleration due to gravity
k = equivalent thermal conductivity of the fluid-saturated porous medium
K^* = intrinsic permeability of the porous media for flow of power-law fluids
n = power-law index of the inelastic non-Newtonian fluid
q^* = strength of point heat source
Ra_x = local Rayleigh number based on q^* defined in Eq. (11)
T = temperature
T_e = ambient constant temperature
u, v = Darcian or superficial velocity components
x, r = cylindrical coordinates
α = equivalent thermal diffusivity of the fluid-saturated porous medium
β = expansion coefficient of the fluid
δ = diameter of plume
ϵ = porosity of porous medium
η = similarity variable defined in Eq. (14)
θ = dimensionless temperature difference
μ^* = fluid consistency of the inelastic non-Newtonian power-law fluid
ρ = density of the fluid
ψ = stream function

[1]Dept. of Energy and Mechanical Engineering, Shizuoka University, 3-5-1 Johoku, Hamamatsu, 432 Japan.

Contributed by the Heat Transfer Division of THE AMERICAN SOCIETY OF MECHANICAL ENGINEERS. Manuscript received by the Heat Transfer Division December 3, 1991; revision received June 18, 1992. Keywords: Natural Convection, Non-Newtonian Flows and Systems, Porous Media. Technical Editor: R. Viskanta.

Introduction

Convection problems associated with concentrated heat sources within fluid-saturated porous media are of great practical significance, for there are a number of practical applications in geophysics and energy-related problems, such as recovery of petroleum resources, geophysical flows, cooling of underground electric cables, and environmental impact of buried heat generating waste. The phenomena can be classified into two distinct regimes, namely, the low Rayleigh number regime where the temperature distribution is primarily due to thermal diffusion, and the high Rayleigh number regime where the flow driven by the heat source is a slender vertical plume such that the boundary layer approximation holds. The problems in the low Rayleigh number regime were tackled by Bejan (1978), Hickox (1981), and Nield and White (1982), while Yih (1965), Cheng (1978), Masuoka et al. (1986), Ingham (1988), and Lai (1990) followed Wooding (1963) who exploited the boundary layer approximation for obtaining similarity solutions for buoyant plumes in the high Rayleigh number regime. Hickox and Watts (1980) numerically obtained the results for arbitrary values of Rayleigh number, for both the infinite and semi-infinite regions.

However, all these previous studies assume that the fluid is Newtonian. Needless to say, a number of industrially important fluids, including fossile fuels, which may saturate underground beds, exhibit non-Newtonian behavior. Despite its importance in practical engineering applications, only a limited number of studies have been reported on free convection in non-Newtonian fluid-saturated porous medium. Chen and Chen (1988a, 1988b) solved the boundary layer equations for free convection of non-Newtonian fluids over a vertical flat plate, a horizontal circular cylinder and a sphere in porous media, using the power-law model, proposed by Christopher and Middleman (1965), while a general similarity transformation procedure has been proposed by Nakayama and Koyama (1991) to find a class of possible similarity solutions for free convective flow of non-Newtonian fluids over a non-isothermal body of arbitrary shape in porous media. However, the simplest and perhaps most important free convection configuration, namely, a buoyant plume above a point heat source in a non-Newtonian fluid-saturated porous medium, has not been treated yet in the literature.

In this note, a boundary layer analysis is presented for free convection from a point heat source embedded in a porous medium saturated with a non-Newtonian power-law fluid. The governing equations are found to possess a similarity solution for an arbitrary value of the power-law index. Closed-form solutions are presented for both flow and temperature fields, and the effects of pseudoplasticity on the plumes are examined.

Analysis

Consider the problem of a plume rising from a point source of strength q^* in a non-Newtonian fluid-saturated porous medium, as illustrated in Fig. 1. When the heat source is sufficiently strong, the streamwise thermal diffusion above the heat source may well be neglected so that the boundary layer approximation holds.

The equation of continuity in terms of the apparent (Dar-

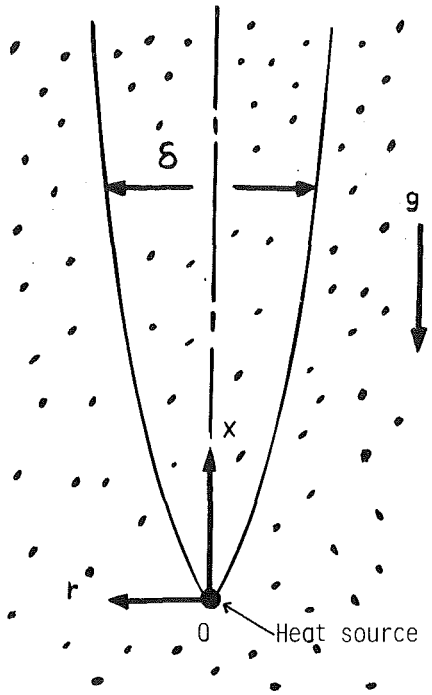

Fig. 1 Physical model and its coordinates

cian) velocities can be written using the cylindrical coordinates (x, r) as

$$\frac{\partial u}{\partial x}+\frac{1}{r}\frac{\partial}{\partial r}(rv)=0 \tag{1}$$

Darcy's law for the non-Newtonian power-law isotropic fluids has the general form:

$$-\nabla p=\frac{\mu^*}{K(|u|)}u-\rho g$$

where u and g are the Darcian velocity vector and the gravitational acceleration vector, respectively. Along the x axis, the equation can be written as

$$-\frac{\partial p}{\partial x}=\frac{\mu^*}{K^*}u^n-\rho g$$

where the boundary layer approximation is exploited as

$$K(|u|)=K^*/|u|^{n-1}\doteq K^*/u^{n-1}$$

since $u^2 \gg v^2$. Thus, the non-Newtonian power-laws proposed by Christopher and Middleman (1965) and Dharmadhikari and Kale (1985) have a common form, which, when combined with the Boussinesq approximation, can be written as

$$\frac{\mu^*}{K^*}u^n=\rho g\beta(T-T_e) \tag{2}$$

where n is the power-law index, while μ^* is the consistency index for the power-law fluid, and K^* is the modified permeability for power-law fluids as defined below:

$$K^*=\begin{cases}\dfrac{6}{25}\left(\dfrac{n\epsilon}{3n+1}\right)^n\left(\dfrac{d\epsilon}{3(1-\epsilon)}\right)^{n+1} & \text{[Christopher and Middleman]} \quad (3a)\\[2ex] C\left(\dfrac{n\epsilon}{3n+1}\right)^n\left(\dfrac{d\epsilon}{3(1-\epsilon)}\right)^{n+1} & \text{[Dharmadhikari and Kale]} \quad (3b)\end{cases}$$

where

$$C=\frac{3}{4}\left(\frac{9n+3}{8n}\right)^n\left(\frac{6n+1}{10n-3}\right)\left(\frac{16}{75}\right)^{\frac{3(10n-3)}{\cdot 10n+11}} \tag{4}$$

Note that for Newtonian fluids $n = 1$, $C = 6/25$ and the two expressions for K^* are then identical. In the above equations d is the particle diameter and ϵ is the porosity. The energy equation is given as follows:

$$r\left(u\frac{\partial T}{\partial x}+v\frac{\partial T}{\partial r}\right)=\alpha\frac{\partial}{\partial r}\left(r\frac{\partial T}{\partial r}\right) \tag{5}$$

where α is the effective thermal diffusivity of the fluid–solid system. The energy equation must satisfy the boundary condition:

$$y=\infty:\ T=T_e \tag{6}$$

and the enthalpy conservation constraint:

$$2\pi\rho C_p\int_0^\infty u(T-T_e)rdr=q^* \tag{7}$$

where ρ and C_p are the density and specific heat at constant pressure of the fluid, respectively.

A scale analysis on Eqs. (1), (2), (5), and (7), such as proposed by Bejan (1984), reveals that the centerline temperature and velocity decay as

$$(T_c-T_e)\sim q^*/kx \tag{8}$$

$$u_c\sim\left(\frac{K^*\rho g\beta q^*}{\mu^* kx}\right)^{1/n}=\frac{\alpha}{x}\mathrm{Ra}_x \tag{9}$$

and the plume diameter δ is of the order

$$\delta\sim\left\{\frac{\mu^* C_p(\alpha x)^{1+n}}{K^* g\beta q^*}\right\}^{1/2n}=\frac{x}{\mathrm{Ra}_x^{1/2}} \tag{10}$$

where

$$\mathrm{Ra}_x=\left(\frac{K^*\rho g\beta q^* x^{n-1}}{\alpha^n\mu^* k}\right)^{1/n} \tag{11}$$

is the local Rayleigh number based on point heat source strength, which is constant for the case of Newtonian fluids ($n = 1$), and k ($=\rho C_p\alpha$) is the effective thermal conductivity of the fluid-saturated porous medium. The foregoing scale argument suggests that δ grows in proportion to $x^{(1+n)/2n}$ as illustrated in Fig. 2, where distinct difference can be seen among the shapes of the plume envelopes. The boundary layer type of slender plumes can be obtained if the source is strong and therefore Ra_x is made sufficiently large. Since $\mathrm{Ra}_x \to 0$ for $x \to \infty$ when $n < 1$, the boundary layer analysis for the case of pseudoplastic fluids ($n < 1$) is valid in some limited intermediate region above the heat source where Ra_x is sufficiently greater than unity. (Note that u_c for the pseudoplastic fluid plume decreases so drastically away from the heat source that $\mathrm{Ra}_x \sim u_c x/\alpha$ diminishes downstream.) To gain some feeling of the extent of this intermediate region for the case of pseudoplastic fluids, consider a point heat source embedded in a bed of packed spheres of diameter 1 mm, saturated with an aqueous carboxymethyl cellulose solution in which $n = 0.94$, $\mu^* = 1.2 \times 10^{-2}$ Pa $s^{0.94}$, $\rho = 10^3$ kg/m^3, $g = 9.8$ m/s^2, $\beta = 1.8 \times 10^{-4}$/K, $k = 0.88$ W/m, $\alpha = 2.1 \times 10^{-7}$ m^2/s, and $K^* = 2 \times 10^{-9}$ m$^{1.94}$ (Asano, 1992). The condition $\mathrm{Ra}_x \gg 1$ may be translated for the case as, $x \ll 50$ m for $q^* = 2$ W and $x \ll 40$ km for $q^* = 3$ W. Thus, the boundary layer approximation holds even far downstream.

Having established appropriate scales, the following transformations are proposed:

$$\psi=\alpha x f(\eta) \tag{12}$$

$$T-T_e=(q^*/kx)\theta(\eta) \tag{13}$$

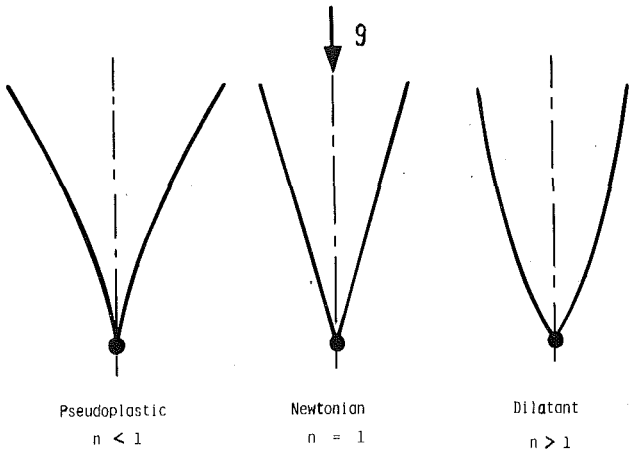

Fig. 2 Plume shapes

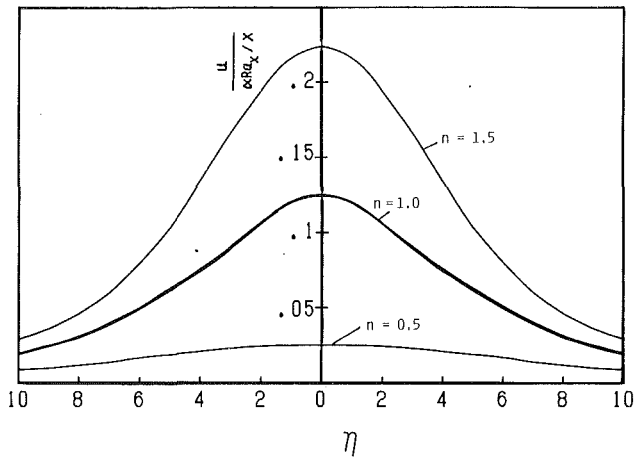

Fig. 3 Velocity profiles

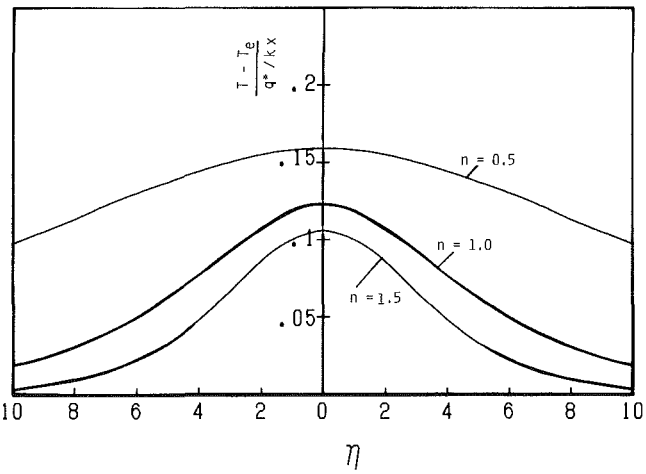

Fig. 4 Temperature profiles

and

$$\eta = \frac{r}{x}\,\mathrm{Ra}_x^{1/2} \tag{14}$$

The stream function ψ is introduced to satisfy the continuity equation. Thus, the velocity components u and v are given in terms of the proposed transformed variables as

$$u = \frac{1}{r}\frac{\partial \psi}{\partial r} = \frac{\alpha}{x}\,\mathrm{Ra}_x \frac{f'}{\eta} \tag{15}$$

and

$$v = -\frac{1}{r}\frac{\partial \psi}{\partial x} = \frac{\alpha \mathrm{Ra}_x^{1/2}}{x}\left(\frac{1+n}{2n} f' - \frac{f}{\eta}\right) \tag{16}$$

After some manipulations on Eqs. (2) and (5) using Eqs. (13)–(16), the following set of the ordinary differential equations can be obtained:

$$(f'/\eta)^n = \theta \tag{17}$$

and

$$(\eta\theta' + f\theta)' = 0 \tag{18}$$

Integrating Eq. (18) once and noting $\theta = \theta' = 0$ as $\eta \to \infty$

$$\eta\theta' + f\theta = 0 \tag{19}$$

Then, combining the above equation with Eq. (17) in favor of f,

$$n(\eta f'' - f') + ff' = 0 \tag{20}$$

It can be shown that the solution satisfying Eq. (20) and the appropriate boundary condition, namely, $f = 0$ at $\eta = 0$, must have the form:

$$f = \frac{(A\eta)^2}{1 + \dfrac{(A\eta)^2}{4n}} \tag{21}$$

where the constant A is determined from the enthalpy conservation constraint transformed as

$$2\pi \int_0^\infty \eta \left(\frac{f'}{\eta}\right)^{1+n} d\eta = 1 \tag{22}$$

Hence, the final expressions for the streamwise velocity and temperature distributions are given by

$$\frac{u}{(\alpha \mathrm{Ra}_x/x)} = \frac{2A^2}{\left(1 + \dfrac{(A\eta)^2}{4n}\right)^2} \tag{23}$$

and

$$\frac{T - T_e}{(q^*/kx)} = \frac{(2A^2)^n}{\left(1 + \dfrac{(A\eta)^2}{4n}\right)^{2n}} \tag{24}$$

where

$$A = \left(\frac{1+2n}{2^{3+n} n\pi}\right)^{1/2n} \tag{25}$$

When $n = 1$, the results naturally reduce to those of Newtonian fluids, reported by Masuoka et al. (1986) and Lai (1990).

Results and Discussion

The resulting velocity and temperature profiles for $n = 0.5$, 1.0, and 1.5 are presented in Figs. 3 and 4, respectively. It can be seen from Fig. 3 that the dilatant fluids ($n > 1$) make the velocity profile somewhat more peaked, while the pseudoplastic fluids ($n < 1$) tend to produce more uniform velocity profiles, as in the case of power-law fluid flow in the absence of porous media. The effects of pseudoplasticity on the temperature field can be examined from Fig. 4, which clearly shows that the temperature profiles become flatter and the temperature level is maintained higher as the pseudoplastic index n decreases. To visualize the effect of buoyancy on the temperature field the isotherms for $(T - T_e)/\Delta T_{\mathrm{ref}} = 0.1$ generated for $n = 0.5$, 1.0, and 1.5 at Ra = 500 and 5000 from Eq. (24) are plotted in Figs. 5(*a*) and 5(*b*). The ordinate and abscissa variables are set to

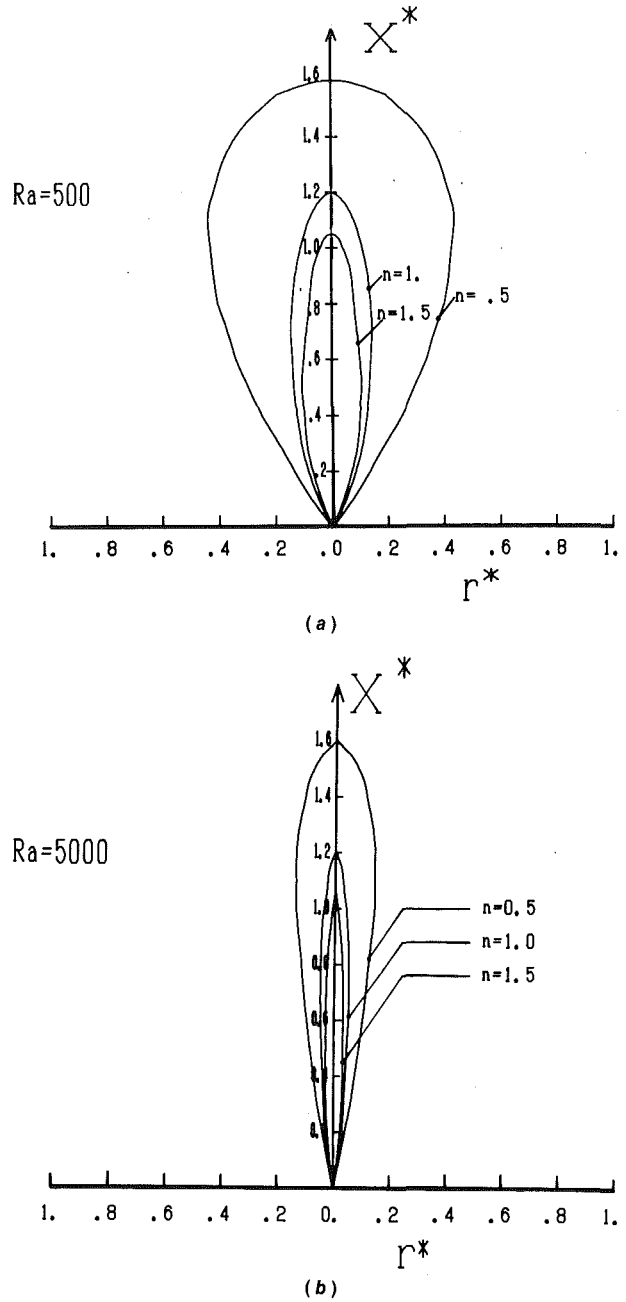

Fig. 5 Isotherms for $(T - T_e)/\Delta T_{ref} = 0.1$: (*a*) Ra = 500, (*b*) Ra = 5000

$$x^* = x/(q^*/k\Delta T_{ref})$$
$$r^* = r(q^*/k\Delta T_{ref})$$

and

$$\mathrm{Ra} = \left\{\frac{K^* \rho g \beta (q^*/k)^n}{\alpha^n \mu^* \Delta T_{ref}^{n-1}}\right\}^{1/n}$$

where ΔT_{ref} is an arbitrary temperature scale. The figures show that a high temperature zone expands farther for smaller n, as may be expected from the velocity and temperature profiles shown in Figs. 3 and 4. Comparison of Figs. 5(*a*) and 5(*b*) leads to the obvious conclusion that the effect of Ra is to make the plume slender.

Acknowledgments

The author would like to express his sincere thanks to Professors A. V. Shenoy and F. Kuwahara for helpful discussions.

References

Asano, N., 1992, "Transient Non-Darcy Forced Convection From a Flat Plate," M.S. Thesis, Dept. of Energy and Mechanical Engineering, Shizuoka University, Japan.

Bejan, A., 1978, "Natural Convection in an Infinite Porous Medium With a Concentrated Heat Source," *J. Fluid Mech.*, Vol. 89, pp. 97–107.

Bejan, A., 1984, *Convection Heat Transfer*, Wiley, New York.

Chen, H. T., and Chen, C. K., 1988a, "Free Convection of Non-Newtonian Fluids Along a Vertical Plate Embedded in a Porous Medium," ASME JOURNAL OF HEAT TRANSFER, Vol. 110, pp. 257–260.

Chen, H. T., and Chen, C. K., 1988b, "Natural Convection of a Non-Newtonian Fluid About a Horizontal Cylinder and a Sphere in a Porous Medium," *Int. Comm. Heat Mass Transfer*, Vol. 15, pp. 605–614.

Cheng, P., 1978, "Heat Transfer in Geothermal Systems," *Adv. Heat Transfer*, Vol. 14, pp. 59–60.

Christopher, R. V., and Middleman, S., 1965, "Power-Law Flow Through a Packed Tube," *Ind. Engng. Chem. Fundls.*, Vol. 4(4), pp. 422–426.

Dharmadhikari, R. V., and Kale, D. D., 1985, "Flow of Non-Newtonian Fluids Through Porous Media," *Chem. Engng. Sci.*, Vol. 40(3), pp. 527–529.

Hickox, C. E., and Watts, H. A., 1980, "Steady Thermal Convection From a Concentrated Source in a Porous Medium," ASME JOURNAL OF HEAT TRANSFER, Vol. 102, pp. 248–253.

Hickox, C. E., 1981, "Thermal Convection at Low Rayleigh Number From Concentrated Sources in Porous Media," ASME JOURNAL OF HEAT TRANSFER, Vol. 103, pp. 232–236.

Ingham, D. B., 1988, "An Exact Solution for Non-Darcy Free Convection From a Horizontal Line Source of Heat," *Wärme- und Stoffübertragung*, Vol. 22, pp. 125–127.

Lai, F. C., 1990, "Natural Convection From a Concentrated Heat Source in a Saturated Porous Medium," *Int. Comm. Heat Mass Transfer*, Vol. 17, pp. 791–800.

Masuoka, T., Tohda, Y., Tsuruta, T., and Yasuda, Y., 1986, "Buoyant Plume Above Concentrated Heat Source in Stratified Porous Media," *Trans. JSME*, Ser. B, pp. 2656–2662.

Nakayama, A., and Koyama, H., 1991, "Buoyancy-Induced Flow of Non-Newtonian Fluids Over a Non-isothermal Body of Arbitrary Shape in a Fluid-Saturated Porous Medium," *Appl. Sci. Res.*, Vol. 48, pp. 55–70.

Nield, D. A., and White, S. P., 1982, "Natural Convection in an Infinite Porous Medium Produced by a Line Heat Source," *Mathematical Models in Engineering Science*, A. McNabb, R. A. Wooding, and M. Rosser, eds., Dept. Sci. and Indust. Res., Wellington, New Zealand.

Yih, C. S., 1965, *Dynamics of Nonhomogeneous Fluids*, Macmillan, New York, p. 234.

Wooding, R. A., 1963, "Convection in a Saturated Porous Medium at Large Rayleigh or Peclet Number," *J. Fluid Mech.*, Vol. 15, pp. 527–544.

Reduced Heat Transfer Rate in Transient Phenomena: Cylindrical Geometry

S. Curilef[1] and F. Claro[1]

Nomenclature

a = radius of cylinder, cm
c = specific heat, erg/g K
f_0 = heat carrier equilibrium distribution
J = flux of heat, erg/cm^2 seg
k_B = Boltzmann constant, erg/K
l = mean free path, cm
$\mathbf{q}$ = phonon wave vector
q_D = Debye wavenumber, cm^{-1}
r = radial coordinate, cm
T = temperature profile, K

[1]Facultad de Física, Pontificia Universidad Católica de Chile, Casilla 306, Santiago 22, Chile.

Contributed by the Heat Transfer Division of THE AMERICAN SOCIETY OF MECHANICAL ENGINEERS. Manuscript received by the Heat Transfer Division November 1991; revision received October 1992. Keywords: Laser Processing, Materials Processing and Manufacturing Processes, Transient and Unsteady Heat Transfer. Associate Technical Editor: L. S. Fletcher.

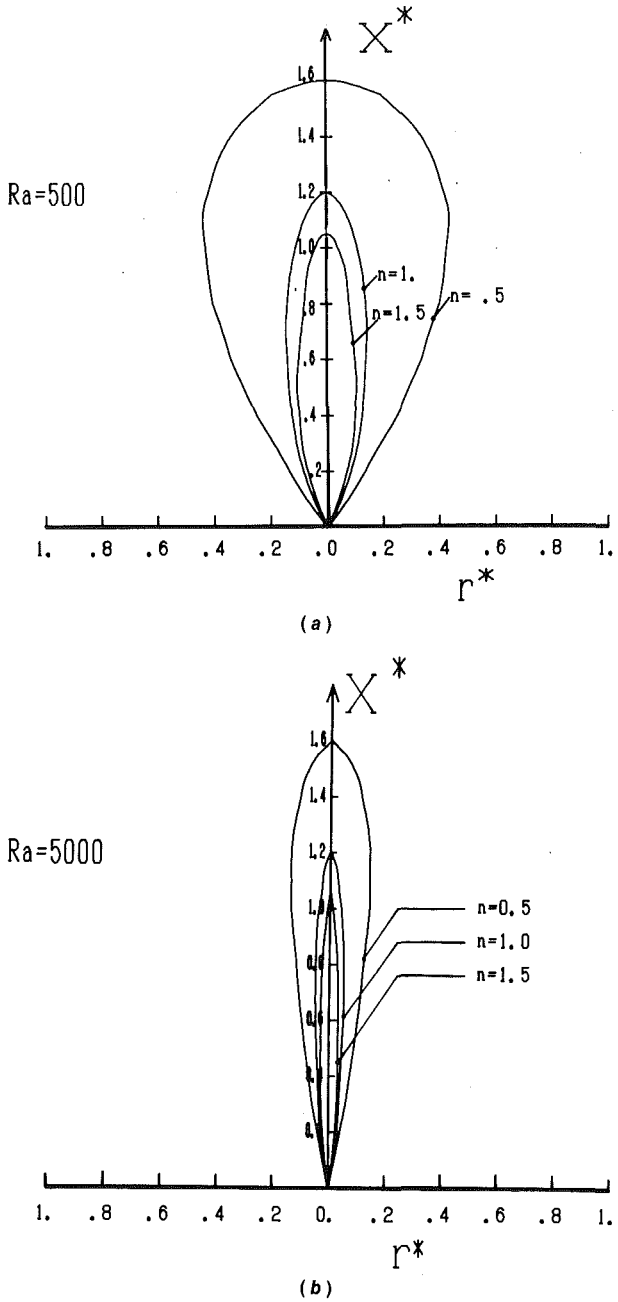

Fig. 5 Isotherms for $(T - T_e)/\Delta T_{ref} = 0.1$: (a) Ra = 500, (b) Ra = 5000

$$x^* = x/(q^*/k\Delta T_{ref})$$
$$r^* = r(q^*/k\Delta T_{ref})$$

and

$$\mathrm{Ra} = \left\{\frac{K^* \rho g \beta (q^*/k)^n}{\alpha^n \mu^* \Delta T_{ref}^{n-1}}\right\}^{1/n}$$

where ΔT_{ref} is an arbitrary temperature scale. The figures show that a high temperature zone expands farther for smaller n, as may be expected from the velocity and temperature profiles shown in Figs. 3 and 4. Comparison of Figs. 5(*a*) and 5(*b*) leads to the obvious conclusion that the effect of Ra is to make the plume slender.

Acknowledgments

The author would like to express his sincere thanks to Professors A. V. Shenoy and F. Kuwahara for helpful discussions.

References

Asano, N., 1992, "Transient Non-Darcy Forced Convection From a Flat Plate," M.S. Thesis, Dept. of Energy and Mechanical Engineering, Shizuoka University, Japan.

Bejan, A., 1978, "Natural Convection in an Infinite Porous Medium With a Concentrated Heat Source," *J. Fluid Mech.*, Vol. 89, pp. 97–107.

Bejan, A., 1984, *Convection Heat Transfer*, Wiley, New York.

Chen, H. T., and Chen, C. K., 1988a, "Free Convection of Non-Newtonian Fluids Along a Vertical Plate Embedded in a Porous Medium," ASME JOURNAL OF HEAT TRANSFER, Vol. 110, pp. 257–260.

Chen, H. T., and Chen, C. K., 1988b, "Natural Convection of a Non-Newtonian Fluid About a Horizontal Cylinder and a Sphere in a Porous Medium," *Int. Comm. Heat Mass Transfer*, Vol. 15, pp. 605–614.

Cheng, P., 1978, "Heat Transfer in Geothermal Systems," *Adv. Heat Transfer*, Vol. 14, pp. 59–60.

Christopher, R. V., and Middleman, S., 1965, "Power-Law Flow Through a Packed Tube," *Ind. Engng. Chem. Fundls.*, Vol. 4(4), pp. 422–426.

Dharmadhikari, R. V., and Kale, D. D., 1985, "Flow of Non-Newtonian Fluids Through Porous Media," *Chem. Engng. Sci.*, Vol. 40(3), pp. 527–529.

Hickox, C. E., and Watts, H. A., 1980, "Steady Thermal Convection From a Concentrated Source in a Porous Medium," ASME JOURNAL OF HEAT TRANSFER, Vol. 102, pp. 248–253.

Hickox, C. E., 1981, "Thermal Convection at Low Rayleigh Number From Concentrated Sources in Porous Media," ASME JOURNAL OF HEAT TRANSFER, Vol. 103, pp. 232–236.

Ingham, D. B., 1988, "An Exact Solution for Non-Darcy Free Convection From a Horizontal Line Source of Heat," *Wärme- und Stoffübertragung*, Vol. 22, pp. 125–127.

Lai, F. C., 1990, "Natural Convection From a Concentrated Heat Source in a Saturated Porous Medium," *Int. Comm. Heat Mass Transfer*, Vol. 17, pp. 791–800.

Masuoka, T., Tohda, Y., Tsuruta, T., and Yasuda, Y., 1986, "Buoyant Plume Above Concentrated Heat Source in Stratified Porous Media," *Trans. JSME*, Ser. B, pp. 2656–2662.

Nakayama, A., and Koyama, H., 1991, "Buoyancy-Induced Flow of Non-Newtonian Fluids Over a Non-isothermal Body of Arbitrary Shape in a Fluid-Saturated Porous Medium," *Appl. Sci. Res.*, Vol. 48, pp. 55–70.

Nield, D. A., and White, S. P., 1982, "Natural Convection in an Infinite Porous Medium Produced by a Line Heat Source," *Mathematical Models in Engineering Science*, A. McNabb, R. A. Wooding, and M. Rosser, eds., Dept. Sci. and Indust. Res., Wellington, New Zealand.

Yih, C. S., 1965, *Dynamics of Nonhomogeneous Fluids*, Macmillan, New York, p. 234.

Wooding, R. A., 1963, "Convection in a Saturated Porous Medium at Large Rayleigh or Peclet Number," *J. Fluid Mech.*, Vol. 15, pp. 527–544.

Reduced Heat Transfer Rate in Transient Phenomena: Cylindrical Geometry

S. Curilef[1] and F. Claro[1]

Nomenclature

- a = radius of cylinder, cm
- c = specific heat, erg/g K
- f_0 = heat carrier equilibrium distribution
- J = flux of heat, erg/cm^2 seg
- k_B = Boltzmann constant, erg/K
- l = mean free path, cm
- $\mathbf{q}$ = phonon wave vector
- q_D = Debye wavenumber, cm^{-1}
- r = radial coordinate, cm
- T = temperature profile, K

[1]Facultad de Física, Pontificia Universidad Católica de Chile, Casilla 306, Santiago 22, Chile.

Contributed by the Heat Transfer Division of THE AMERICAN SOCIETY OF MECHANICAL ENGINEERS. Manuscript received by the Heat Transfer Division November 1991; revision received October 1992. Keywords: Laser Processing, Materials Processing and Manufacturing Processes, Transient and Unsteady Heat Transfer. Associate Technical Editor: L. S. Fletcher.

v = phonon group velocity, cm/seg
ϵ = energy of heat carrier, erg
ν = $\cos(\mathbf{q}, \mathbf{r})$
ρ = density, g/cm^3
τ_r = carrier relaxation time, seg

1 Introduction

Laser-annealing experiments on planar surface layers of silicon and germanium using nanosecond synchrotron x-ray pulses have shown that, as heat enters the sample, the transient temperature profile evolves more slowly than predicted by standard theories based on Fourier's law (Larsen et al., 1986; Tischler et al., 1988). These theories assume that the temperature varies little over a length comparable to the mean free path, which need not be the case for the transient regime in ultrafast phenomena. In the experiments, temperature gradients as high as 10^9 K/m were produced during the first few nanoseconds after irradiation.

As shown in previous work dealing with the planar surface geometry, a nonlocal theory that takes into account the temperature change over the length scale of a mean free path is capable of explaining the reduction in the rate of heat transfer (Mahan and Claro, 1988, 1989; Claro and Mahan, 1989). In this paper we analyze a cylindrical geometry: The material that is heated initially is a cylinder, embedded in a cooler medium, through which heat flows radially. Compared to the local solution based on Fourier's law, our nonlocal results show a reduction of the rate of heat flow qualitatively similar to the one observed in a planar geometry.

2 Basic Relations and Boundary Conditions

Consider a cylinder of infinite length embedded in a uniform and infinite medium. We assume that the initial temperature profile $T(r, t = 0)$ is known. At later times the profile and the heat flux are related by the equation (Carslaw and Jaeger, 1959)

$$\rho c \frac{\partial T(r, t)}{\partial t} + \frac{1}{r} \frac{\partial r J(r, t)}{\partial r} = 0. \tag{1}$$

We shall assume that the temperature is high enough that heat is carried mainly by acoustic phonons (collective atomic vibrations). Treating phonons in the Debye approximation (Kittel, 1956), one has

$$J(r, t) = \frac{1}{(2\pi)^3} \int d^3\mathbf{q} \epsilon(\mathbf{q}) v \nu f(r, \nu, \mathbf{q}), \tag{2}$$

where the statistical distribution of carriers f obeys Boltzmann's equation,

$$\frac{\partial f}{\partial t} + v\nu \frac{\partial f}{\partial r} = -\frac{f - f_0}{\tau_r}, \tag{3}$$

Here the relaxation time approximation has been adopted (Reif, 1965). In the presence of a temperature gradient the solutions of Eq. (3) have transients with a characteristic decay time of the order of τ_r, which in turn is of the order of the time between collisions among the carriers. If this time is small compared to the time in which the temperature profile varies significantly, as is the case in semiconductors (Larsen et al., 1986), we need only consider the steady-state (time independent) solutions of Eq. (3). Substituting $f = f_0 + g$, Eq. (3) may be written in the form

$$\left(1 + \tau_r v \nu \frac{\partial}{\partial r}\right) g = -\tau_r v \nu \frac{\partial f_0}{\partial r}. \tag{4}$$

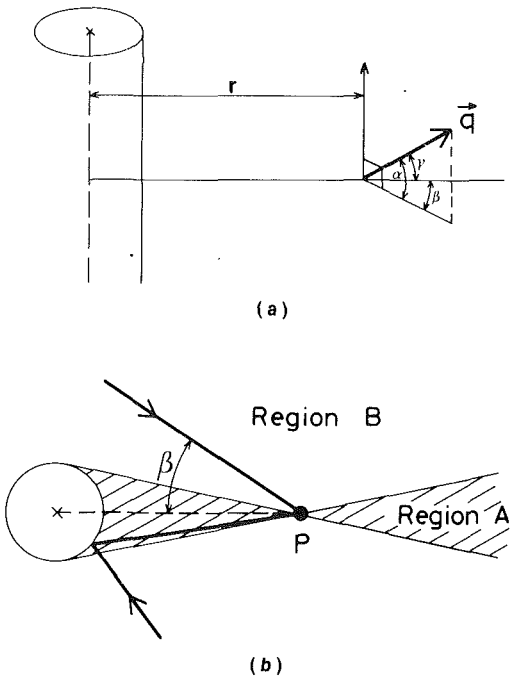

Fig. 1 Choice of angles that define the direction of propagation of the carriers (*a*). Different regions in space according to whether in their trajectories the carriers touch (region *A*) or do not touch (region *B*) the cylinder (*b*). A sample trajectory is shown in each region.

In semiconductors at long wavelengths $\tau_r = 1/q^2\eta(T)$ (Glassbrenner and Slack, 1964). We shall assume the more general form $\tau_r = l(\mathbf{q})/\xi(T)v$, with ξ a dimensionless quantity. The general solution of Eq. (4) is then

$$g(R, \nu, \mathbf{q}) = -e^{-\frac{1}{l}\int^R \frac{dR'}{\nu(R')}} \int^R dR' \frac{\partial f_0}{\partial R'} e^{\frac{1}{l}\int^{R'} \frac{dR''}{\nu(R'')}}, \tag{5}$$

where $R(r) = \int^r dr' \xi[T(r')]$. We call α the angle $\mathbf{q}$ makes with the plane perpendicular to the axis of the cylinder, and β the angle the projection of $\mathbf{q}$ on this plane makes with $\mathbf{R}$ (Fig. 1*a*). The integral that appears in the exponents is resolved using the identities $R\sin\beta = R' \sin\beta'$ and $\nu(R) = \cos\alpha\cos\beta$,

$$\int dR' \frac{1}{\nu(R')} = \frac{R'\cos\beta'}{\cos\alpha}. \tag{6}$$

Between scattering events, carriers travel in straight lines in all directions. Let us divide the space into two regions, as shown in Fig. 1(*b*). Region A contains trajectories that include the observation point P and hit the cylinder, while region B includes all remaining trajectories. The boundary conditions for $g(R, \nu, \mathbf{q})$ are obtained from the requirement that the cylinder have a constant temperature and the disturbance vanishes at infinity. This gives

$$g_>(R_a, v, \mathbf{q}) = -g_<(R_a, -\nu, \mathbf{q})$$
$$g_<(\infty, \nu, \mathbf{q}) = 0. \tag{7}$$

Using Eqs. (6) and (7) in Eq. (5) one gets

$$g_>(R, \nu, \mathbf{q}) = e^{-\frac{R\cos\beta}{l\cos\alpha}} \left(e^{\frac{2R_a\cos\beta_a}{l\cos\alpha}} \int_{R_a}^{\infty} dR' \frac{\partial f_0}{\partial R'} e^{-\frac{R'\cos\beta'}{l\cos\alpha}} + \int_{R_a}^{R} dR' \frac{\partial f_0}{\partial R'} e^{\frac{R'\cos\beta'}{l\cos\alpha}} \right),$$

$$g_<(R, \nu, \mathbf{q}) = e^{-\frac{R\cos\beta}{l\cos\alpha}} \int_{R_a}^{R} dR' \frac{\partial f_0}{\partial R'} e^{\frac{R'\cos\beta'}{l\cos\alpha}}. \tag{8}$$

In region B we use the boundary condition at infinity (7) and the continuity of the function g at the point S where ν changes sign (Fig. 1*b*),

$$g_>(R_S, \nu, \mathbf{q}) = g_<(R_S, -\nu, \mathbf{q}). \tag{9}$$

In these expressions $R_a = R(a)$, $R_S = R\sin\beta$, β_a is the angle at $R = R_a$, and the symbol $<$ $(>)$ is used to represent motion of the carriers with $\cos\nu$ less (greater) than zero. The contribution of the carriers in this region is then obtained using Eqs. (6) and (9) in Eq. (5),

$$g_>(R, \nu, \mathbf{q}) = e^{-\frac{R\cos\beta}{l\cos\alpha}}\left(\int_{R\sin\beta}^{\infty} dR' \frac{\partial f_0}{\partial R'} e^{-\frac{R'\cos\beta'}{l\cos\alpha}} - \int_{R\sin\beta}^{R} dR' \frac{\partial f_0}{\partial R'} e^{\frac{R'\cos\beta'}{l\cos\alpha}}\right),$$

$$g_<(R, \nu, \mathbf{q}) = e^{-\frac{R\cos\beta}{l\cos\alpha}} \int_{R}^{\infty} dR' \frac{\partial f_0}{\partial R'} e^{-\frac{R'\cos\beta'}{l\cos\alpha}}. \tag{10}$$

Equations (8) and (10) are the solutions to Eq. (4) that are of interest to us.

3 Evolution of the Temperature Profile

At temperatures higher than the Debye temperature (a case we assume to hold), $f_0 = 1/[\exp(\epsilon/k_BT) - 1] \approx k_BT/\epsilon$. Assuming ϵ to be a constant and writing $l = q_D/q^2$, we obtain from Eqs. (8), (10), (2), and (1) the equation for the time evolution of the temperature profile,

$$\frac{\partial T(y,\tau)}{\partial \tau} = \int_0^b \frac{du}{\sqrt{y^2-u^2}}\left[\int_b^\infty dy' \frac{\partial^2 T(y',\tau)}{\partial y'^2} F(y, y'; u) + \frac{\partial T(b,\tau)}{\partial y'} F(y, b; u)\right] - \int_b^y \frac{du}{\sqrt{y^2-u^2}}\left[\int_u^\infty dy' \frac{\partial^2 T(y',\tau)}{\partial y'^2} G(y, y'; u) + \frac{\partial T(u,\tau)}{\partial y'} G(y, u; u)\right]. \tag{11}$$

Here the quantities $y = q_DR$, $b = q_DR_a$, $u = y\sin\beta$, $w = \sin\alpha$, and $\tau = \xi q_D^4 k_B v t/6\pi^2\rho c$ are dimensionless. The functions $F(y, y'; u)$ and $G(y, y'; u)$ are defined by

$$F(y, y'; u) = -\frac{3}{5\pi}\int_{y'}^\infty dx\left[K\left(\sqrt{y^2-u^2} - 2\sqrt{b^2-u^2} + \sqrt{x^2-u^2}\right) + \operatorname{sign}(y-x) K\left(\left|\sqrt{y^2-u^2} - \sqrt{x^2-u^2}\right|\right)\right]$$

$$G(y, y'; u) = -\frac{3}{5\pi}\int_{y'}^\infty dx\left[K\left(\sqrt{y^2-u^2} + \sqrt{x^2-u^2}\right) - \operatorname{sign}(y-x) K\left(\left|\sqrt{y^2-u^2} - \sqrt{x^2-u^2}\right|\right)\right], \tag{12}$$

$$K(z) = 5\int_0^1 dw \int_0^1 dp p^4 e^{-\frac{zp^2}{\sqrt{1-w^2}}}.$$

The first (second) integral in Eq. (11) is the contribution of carriers in the region A (region B). The kernel $K(z)$ is a decreasing function of z with a decay length that characterizes the extent of the nonlocal contributions to the thermal flux. It is shown in Fig. 2.

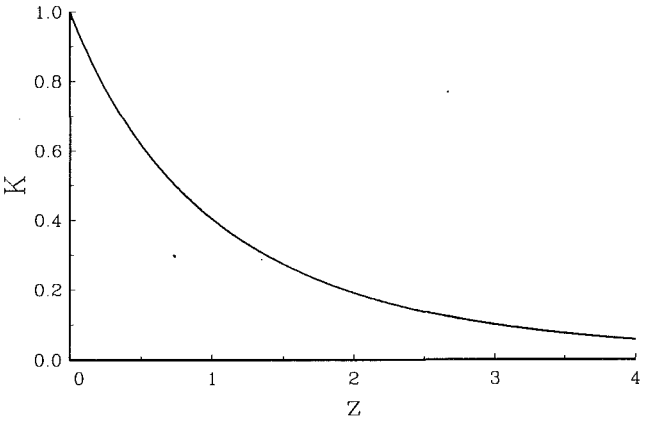

Fig. 2 The kernel *K(z)* controlling the extent in space of nonlocality

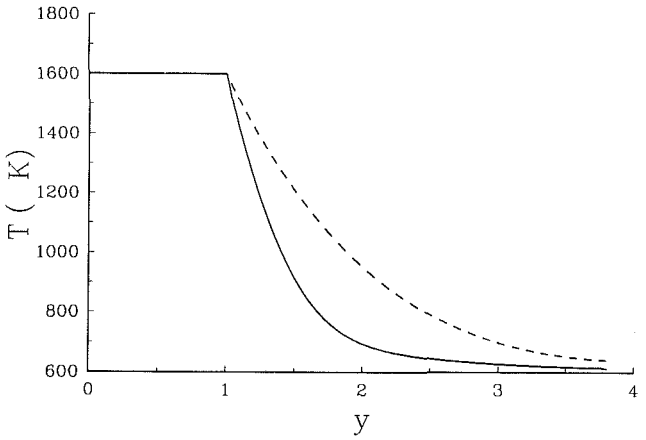

Fig. 3 Local (dashed line) and nonlocal (full line) temperature profile after an elapsed time $\tau = 1$

4 Numerical Example

We have solved Eq. (11) numerically using standard techniques. The time and space derivatives were treated as a forward difference and a central difference formula, respectively. Simpson's method was used to obtain the integral in Eq. (11). Increments were chosen to obtain better than 1 percent accuracy.

Figure 3 shows the temperature profile after a time $\tau = 1$ has elapsed. The solid line is our nonlocal solution and the dashed line, the corresponding solution based on Fourier's Law (Carslaw and Jaeger, 1959). Initially the cylinder was assumed to be at 1600 K and the medium surrounding it, at 600 K. Notice that at the cylinder edge the temperature has a discontinuous slope. The figure shows that the nonlocal profile lags behind the local result, indicating that heat transport is inhibited by nonlocal effects. As time progresses the nonlocal and local solutions become more similar, coinciding in the limit $\tau = \infty$. In this limit, and for the specified boundary conditions, the solution in both cases is $T(R = q_D\xi r, \infty) = \text{const}$.

Acknowledgments

This work was supported in part by Fondo Nacional de Ciencias, Grant 375/90. One of us (S.C.) would like to thank CONICYT for support.

References

Carslaw, H. S., and Jaeger, J. C., 1959, *Conduction of Heat in Solids*, Oxford University Press, 2nd ed., pp. 336–337.

Claro, F., and Mahan, G., 1989, "Transient Heat Transport in Solids," *J. Appl. Phys.*, Vol. 66, pp. 4213–4217.

Glassbrenner, C. J., and Slack, G. A., 1964, "Thermal Conductivity of Silicon and Germanium From 3°K to the Melting Point," *Phys. Rev.*, Vol. 134, pp. A1058–A1069.

Kittel, C., 1956, *Introduction to Solid State Physics*, Wiley, New York.

Larsen, B., Tischler, J., and Mills, D., 1986, "Nanosecond Resolution Time-Resolved X-Ray Study of Silicon During Pulsed-Laser Irradiation," *J. Mater. Res.*, Vol. 1, pp. 144–154.

Mahan, G., and Claro, F., 1988, "Nonlocal Theory of Thermal Conductivity," *Phys. Rev. B*, Vol. 38, pp. 1963–1969.

Mahan, G., and Claro, F., 1989, "Nonlocal Thermal Conductivity," *High Temp–High Pressures*, Vol. 21, pp. 1–6.

Reif, F., 1965, *Fundamentals of Statistical and Thermal Physics*, McGraw-Hill, New York.

Tischler, J. Z., Larsen, B. C., and Mills, D. M., 1988, "Time Resolved X-Ray Study of Ge During Pulsed Laser Melting," *Appl. Phys. Lett.*, Vol. 52, pp. 1785–1787.

Journal of Heat Transfer

Discussion

View Factor Algebra for Two Arbitrarily Sized Nonopposing Parallel Rectangles

L. W. Byrd[1]

Evaluation of the radiative heat transfer between two surfaces requires the use of a view factor, F_{1-2}, to give the fraction of radiation emitted from surface 1 that directly strikes surface 2. This discussion gives an equation to calculate the view factor between two arbitrarily sized nonopposing parallel rectangles in terms of view factors for opposing rectangles of the same size. This was originally presented by Hamilton and Morgan (1952) but their equation (referenced by Siegel and Howell, 1981, and Chapman, 1987) is missing one term. A closed-form solution derived by Hsu (1967) for the general case of two arbitrary parallel rectangles is also referenced as the recommended method for calculating the view factor. Hsu's approach is later generalized by Yuen (1980) to incorporate general polygons that do not have to be parallel to each other.

This discussion derives the expression for parallel rectangles that are not directly opposed. Using the notation of Fig. 1, this corresponds to $F_{1-9'}$. View factors for the geometries shown in Figs. 2 and 3 are used as building blocks for $F_{1-9'}$. The final result will be written entirely in terms of view factors for parallel opposing rectangular plates of the same size as shown in Fig. 4. This as well as basic view factor relations used in the derivation are given by Incropera and DeWitt (1990). The view factor $F_{a-b'}$ for the geometry shown in Fig. 2 can be found using the notation of Hamilton and Morgan as follows:

Let:

$$G_{i-j} \equiv A_i F_{i-j} \qquad G_{i-(ij)'} \equiv A_i F_{i-(ij)'}$$
$$G_{ij-i'} \equiv (A_i + A_j) F_{ij-i'} \qquad G_{i^2} \equiv G_{i-i'} \tag{1}$$

Then:

$$G_{(ab)^2} = G_{ab-(ab)'} = G_{a-(ab)'} + G_{b-(ab)'}$$
$$= G_{a^2} + G_{a-b'} + G_{b-a'} + G_{b^2} \tag{2}$$

Using a result from Siegel and Howell (1981), $G_{a-b'} = G_{b-a'}$ gives:

$$G_{a-b'} = 1/2\ (G_{(ab)^2} - G_{a^2} - G_{b^2}) \tag{3}$$

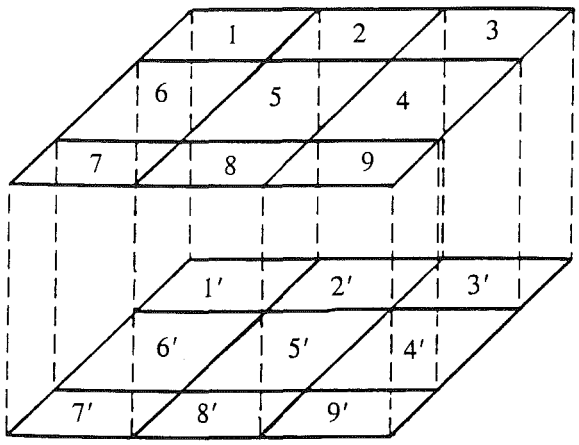

Fig. 1 Geometry for nonopposing parallel rectangles

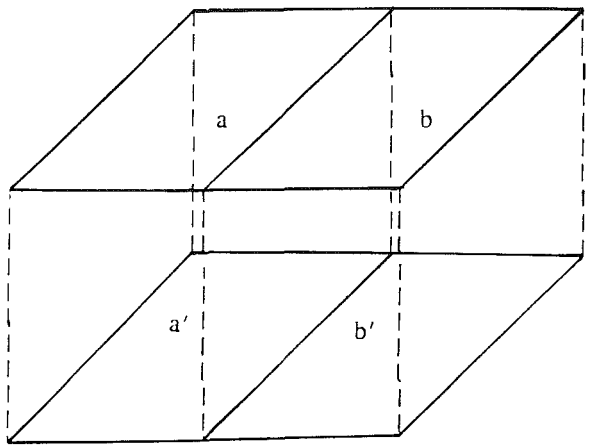

Fig. 2 Nonopposing parallel rectangles aligned on one edge

Similarly for Fig. 3:

$$G_{ce-(df)'} = G_{c-(df)'} + G_{e-(df)'} = 1/2\ (G_{(cdef)^2} - G_{(ce)^2} - G_{(df)^2}) \Rightarrow G_{c-d'} + G_{c-f'} + G_{e-d'} + G_{e-f'}$$
$$= 1/2\ (G_{(cdef)^2} - G_{(ce)^2} - G_{(df)^2}) \tag{4}$$

It can be shown that $G_{c-f'} = G_{e-d'}$ by writing them in integral form, interchanging the order of integration, and renaming the dummy variables of integration. This and rewriting $G_{c-d'}$ and $G_{e-f'}$ gives:

$$G_{c-f'} = 1/4\ [G_{(cdef)^2} + G_{c^2} + G_{d^2} + G_{e^2} + G_{f^2} - (G_{(cd)^2} + G_{(ce)^2} + G_{(df)^2} + G_{(ef)^2})] \tag{5}$$

Returning to Fig. 1, write $G_{1-9'}$ as:

[1]Mechanical Engineer, Flight Dynamics Directorate, Wright Laboratory WL/FIBEB, Air Force Systems Command, Wright-Patterson AFB, OH 45433-6553; Assoc. Mem. ASME.

Contributed by the Heat Transfer Division of The American Society of Mechanical Engineers. Manuscript received by the Heat Transfer Division October 1992; revision received January 1993. Keywords: Radiation. Associate Technical Editor: R. O. Buckius.

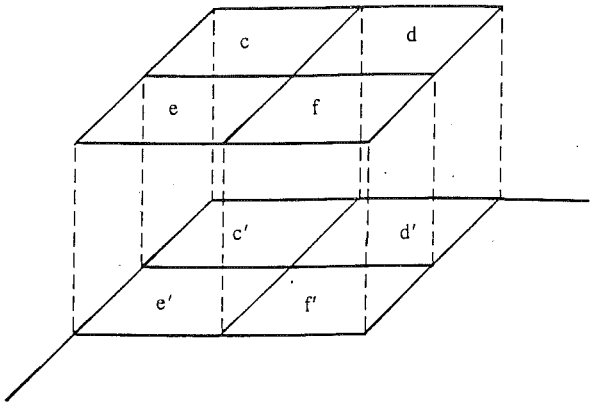

Fig. 3 Nonopposing parallel rectangles aligned on one corner

$$G_{1-9'} = G_{1-(4589)'} - G_{1-4'} - G_{1-5'} - G_{1-8'} \quad (6)$$

$G_{1-4'}$ and $G_{1-8'}$ can be rewritten:

$$G_{1-4'} = G_{1-(45)'} - G_{1-5'} \text{ and } G_{1-8'} = G_{1-(58)'} - G_{1-5'} \quad (7)$$

Use Eq. (5) to expand $G_{1-(4589)'}$, $G_{1-(45)'}$, $G_{1-5'}$, and $G_{1-(58)'}$ and combine Eqs. (6) and (7) to arrive at:

$$G_{1-9'} = 1/4\ [G_{(1234567789)^2} - (G_{(125678)^2} + G_{(234589)^2} + G_{(456789)^2} + G_{(123456)^2}) + (G_{(1256)^2} + G_{(2345)^2} + G_{(4589)^2} + G_{(5678)^2} + G_{(456)^2} + G_{(258)^2}) - (G_{(25)^2} + G_{(45)^2} + G_{(58)^2} + G_{(56)^2}) + G_5{}^2] \quad (8)$$

This equation is the same as that presented by Hamilton and Morgan except for the term $G_{5-5'}$, which was inadvertently omitted in the original paper. Equation (8) is sensitive to the values that are used for each term so it is recommended that graphs should not be used. Hsu's result is more general than Eq. (8) because it can also be used for rectangles that are directly opposed. Since the programming effort is similar for either method, Hsu's equation is recommended.

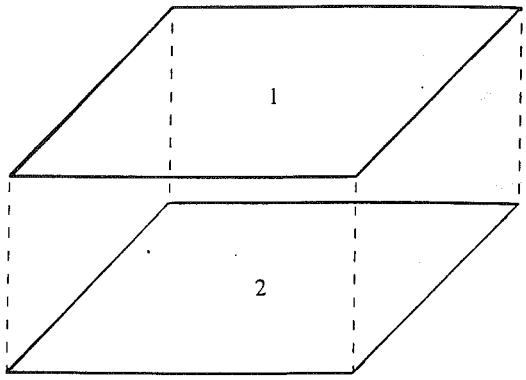

Fig. 4 Parallel opposing rectangles of the same size

References

Chapman, A. J., 1987, *Fundamentals of Heat Transfer*, Macmillan Publishing Company, New York.

Hamilton, D. C., and Morgan, W. R., 1952, "Radiant-Interchange Configuration Factors," NACA Tech Note 2836.

Hsu, C. J., 1967, "Shape Factor Equations for Radiant Heat Transfer Between Two Arbitrary Sizes of Rectangular Planes," *The Canadian Journal of Chemical Engineering*, Vol. 45, pp. 58–60.

Incropera, F. P., and DeWitt, D. P., 1990, *Fundamentals of Heat and Mass Transfer*, 3rd ed., Wiley, New York.

Siegel, R., and Howell, J. R., 1991, *Thermal Radiation Heat Transfer*, 2nd ed., Hemisphere Publishing Corp., New York.

Yuen, W. W., 1980, "A Simplified Approach to Shape-Factor Calculation Between Three-Dimensional Planar Objects," Vol. 102, pp. 386–388.